

University of Thessaly
Department of Civil Engineering
Laboratory of Structural Analysis and Design

Behaviour of structures under fire conditions after earthquake events

Daphne Pantousa
Civil Engineer, M.Sc.

Doctoral Dissertation

Submitted to
the Department of Civil Engineering
in Fulfillment of the Requirements
for the Degree of Doctor of Philosophy

Supervisor: Professor Euripidis Mistakidis

Volos, 2013

University of Thessaly
Department of Civil Engineering
Laboratory of Structural Analysis and Design

Behaviour of structures under fire conditions after earthquake events

Daphne Pantousa
Civil Engineer, M.Sc.

Doctoral Dissertation

Submitted to
the Department of Civil Engineering
in Fulfillment of the Requirements
for the Degree of Doctor of Philosophy

Examination Committee:

Euripidis Mistakidis, Professor at University of Thessaly (Supervisor)
Georgios Stavroulakis, Professor at Technical University of Crete (advisor committee)
Olympia Panagouli, Assistant Professor at University of Thessaly (advisor committee)

Ioannis Avramidis, Professor at Aristotle University of Thessaloniki
Charalampos Baniotopoulos, Professor at Aristotle University of Thessaloniki
Charalampos Gantes, Professor at National Technical University of Athens
Spiridon Karamanos, Associate Professor at University of Thessaly

Volos 2013

*This dissertation is dedicated to my
parents Olympia and Thomas*

Acknowledgments

Completing my PhD thesis is probably one of the most challenging activities of my life until now. The best and the worst moments of my doctoral journey have been shared with many people. After all these years of constant effort, first of all, I would like to express my sincere gratitude to my advisor Prof. Euripidis Mistakidis for his valuable support, guidance and successful collaboration during the course of the research. Apart from the significant assistance in the preparation of the present dissertation, my advisor introduced me in the field of scientific research and, moreover, inspired me to continue working on research in the future. I'm also grateful for giving me the chance to participate in the research European research program COST, through which I had the opportunity to gain further experience and knowledge in the field of fire engineering. Additionally, I want to thank my supervisor for helping me to be awarded by a scholarship in the context of Research Funding Program: Heracleitus II, through which my post-graduate studies were totally founded. But most of all, I'm truly indebted to him for his constant encouragement and support all these years.

Many thanks to my very dear friends Dr. Kyriaki Georgiadi-Stefanidi, Vassia Vassiliou, Apostolis Chlempos and Kalliopi Zografopoulou for their help during the preparation of the present manuscript. Furthermore, I would like to express them my sincere gratitude for all the real friendship which has been developed between during all these years.

Specially, I wish to thank my parents. Their love provided my inspiration and was my driving force. I owe them everything and I wish I could show them just how much I love and appreciate them.

My last and special debt of gratitude must go to my colleague and very close friend, Dr. Kosntantino Tzaro. His support and encouragement helped me during all this years. I really want to express him my real appreciation.

Finally, it is must be referred that this research has been co-financed by the European Union (European Social Fund – ESF) and Greek national funds through the Operational Program "Education and Lifelong Learning" of the National Strategic *Reference* Framework (NSRF) - Research Funding Program: Heracleitus II. Investing in knowledge society through the European Social Fund.

Contents

Chapter 1. Introduction	1
1.1 Overview	1
1.2 Aim	3
1.2.1 Basic concept	3
1.2.2 Research objectives	4
1.3 Organization.....	6
Chapter 2. State-of-the art / Literature review	10
2.1 Seismic performance of steel structures- Performance-based design trends	11
2.2 Fire (structural) performance of steel structures – CFD modeling.....	13
2.2.1 Fire (structural) performance.....	13
2.2.2 Numerical modeling of fire enclosure	15
2.2.3 Fire-structure interface	18
2.3 Fire after earthquake performance of steel structures.....	19
2.4 Ductility of steel beams at ambient and high temperatures.....	24
2.5 Contribution of the dissertation	26
Chapter 3. Elements of fire-behaviour in an enclosure	29
3.1 Description of the fire development in the fire-compartment	29
3.2 Modelling of the fire action according to guidelines of EN 1991-1-2	31
Chapter 4. Numerical simulation of natural fire	34
4.1 Fire modeling	34
4.2 Computational Fluid Dynamics in fire enclosure modeling	36
4.3 Fire Dynamics Simulator.....	36
4.3.1 General description	36
4.3.2 Input parameters	37
4.3.3 Output parameters.....	38
4.3.4 Governing equations and additional models	38
4.3.5 Numerical simulation techniques – Turbulence modeling.....	40
4.3.6 Solution procedure	40
4.3.7 Limitations and assumptions	40
Chapter 5. Elements of heat transfer theory	43
5.1 Convection	43
5.2 Radiation	43
5.3 Heat conduction	43
5.4 Boundary conditions	44
5.5 Temperature of unprotected steel sections	46
Chapter 6. Material properties at elevated temperatures	48
6.1 Structural steel	48
Chapter 7. Introduction to the case study – Definition of post-earthquake fire scenarios	51
7.1 Geometric characteristics of the library building	51
7.2 Post-Earthquake scenarios.....	53
Chapter 8. CFD modeling –Results of the numerical analysis	56
8.1 Numerical simulation.....	56
8.1.1 The numerical model	56
8.1.2 The numerical analysis.....	59
8.1.3 Thermal properties of the materials.....	59
8.1.4 Fire modeling and fire-spread modeling.....	60
8.1.5 Sprinkler system.....	65
8.2 Results	66
8.2.1 Spread of the fire.....	67
8.2.2 Heat Release Rate	69
8.2.3 Smoke and fire visualization.....	70
8.2.4 Velocity field	72
8.2.5 Gas -temperature distribution in the fire-compartment.....	75
8.2.6 Gas- temperature “near” the structural members.....	80
8.3 Interface between the CFD and the FEM structural analysis	88
Chapter 9. Seismic – gravity design / Non-linear structural analysis for seismic loading	117
9.1 Description of the problem	117
9.2 Design of the frame structure for gravity and seismic loading.....	118

9.3	Numerical modeling	122
9.3.1	Numerical model.....	122
9.3.2	Representation of seismic action.....	126
9.3.3	The numerical analysis.....	131
9.4	Eigenmode analysis	135
9.5	Evaluation of the seismic performance for the design spectrum	135
9.5.1	Static push-over analysis.....	136
9.5.2	Non-linear dynamic transient analysis based on the direct integration of the equations of motion.....	137
9.6	Incremental Dynamic Analysis (IDA)	146
9.6.1	Definition of the scaled seismic loading	146
9.6.2	Evaluation of the structural behaviour for different seismic levels	147
9.7	Characterization of the seismic “damage” in correlation with the seismic loading level.....	168
Chapter 10. Fire design/Non-linear structural analysis for fire loading		170
10.1	Numerical modeling	170
10.2	Simulation of fire loading.....	170
10.3	Results of numerical analyses	171
10.3.1	ISO-fire	171
10.3.2	Natural Fire.....	179
Chapter 11. Non-linear analysis for fire-after earthquake loading		180
11.1	Definition of the addressed problem	180
11.2	Representation of seismic and fire actions	181
11.3	Numerical modelling.....	182
11.4	Definition of the FAE scenarios.....	184
11.4.1	ISO-FAE scenarios.....	184
11.4.2	Natural-FAE scenarios	185
11.5	Results of the numerical analyses	188
11.5.1	ISO-FAE scenarios.....	188
11.5.2	Natural-FAE scenarios	200
11.5.3	Comparison between the ISO and Natural FAE scenarios	207
11.5.4	Conclusions	208
Chapter 12. Failure criteria of structural members at elevated temperatures		209
12.1	Description of the problem	210
12.2	Assessment of the member ductility in the structure	213
12.2.1	Simplified approach through the standard beam.....	213
12.2.2	Moment Rotation Curve - Definition of rotational capacity	216
12.2.3	Main factors affecting the member ductility of beams under fire conditions	219
12.2.4	Specification of the considered problem - Assumptions.....	220
12.3	Validation of the numerical model.....	222
12.3.1	The experimental program-The case study.....	222
12.3.2	The numerical model used for the validation.....	224
12.3.3	The numerical simulation.....	224
12.3.4	Comparison with the test results	225
12.4	Failure criteria	227
12.4.1	The simplified numerical model used for the assessment of the failure criteria.....	227
12.4.2	Case 1: Simulation of three point bending test at elevated temperatures.....	230
12.4.3	Case 2: Simulation of three point bending test at pre-damaged beams (due to cyclic loading) at elevated temperatures	252
Chapter 13. Determination of the fire-resistance of the structure for fire and FAE loading		278
13.1	Determination of the fire-resistance	278
13.2	Fire-resistance for the reference scenarios	283
13.3	Fire-resistance for the ISO-FAE scenarios	283
13.4	Fire-resistance for the natural- FAE scenarios	286
13.5	Conclusions.....	13-290
Chapter 14. Summary, conclusions and suggestions for further research.....		292
14.1	Summary and conclusions.....	292
14.2	Innovative points of the dissertation.....	296
14.3	Suggestions for further research.....	300
Appendix A. Finite Element Modeling.....		302
Appendix B. Results of CFD modeling.....		309

Gas-temperature “near” the structural members	309
Output of “dual-layer” post-processing model.....	350
References	362

Figures

Figure 1-1: Fully-coupled thermo-mechanical approach.	5
Figure 2-1: Schematic representation of the steps involved in the PEF performance evaluation of building frames (Mousavi <i>et al.</i> , 2008).	21
Figure 3-1 Description of the fire in an enclosure.....	29
Figure 3-2: Description of the pre-flashover and the post-flashover stages.....	31
Figure 3-3: The ISO fire curve.	32
Figure 4-1: Schematic representation of a burning solid fuel.	35
Figure 6-1: Stress-strain relationships of structural steel at elevated temperatures.	48
Figure 6-2: Stress-strain relationships of structural steel S275 at elevated temperatures. .	49
Figure 6-3: Thermal expansion of steel.....	50
Figure 6-4: Thermal conductivity of steel.	50
Figure 6-5: Specific heat of steel.....	50
Figure 7-1: The library building.	52
Figure 7-2: The structural system and a typical frame.	52
Figure 7-3: The fire-extinguishing system.	53
Figure 8-1: The numerical model for the natural fire-simulation.....	57
Figure 8-2: The numerical model for the first level and the limits of the computational domain.	57
Figure 8-3: Mesh of the type 2 is applied for definition of the exterior boundary of the computational domain (Gissi, 2010).	58
Figure 8-4: Section (not in-scale) of the panel and the different layers (dimensions in mm).	59
Figure 8-5: Variation of the specific heat of the insulation material with temperature.....	60
Figure 8-6: Variation of conductivity of the insulation material with temperature.....	60
Figure 8-7: The bookshelf setup and the burning stage.....	62
Figure 8-8: Experimental Heat Release Rate curve of the bookshelf test.	64
Figure 8-9: The experimental and the modified HRR curves used for the book shelving system.	64
Figure 8-10: Activation of the control devices for the different fire scenarios.	68
Figure 8-11: Envelope results for the activation of the control devices.....	69
Figure 8-12: Total HRR for the fire scenarios.....	70
Figure 8-13: Snapshots of rendering the HRRPUV for the scenario SC-75 (HRRPUV>40kW/m ³)......	71
Figure 8-14: Snapshots of rendering the mass fraction of soot and the HRRPUV (HRRPUV>40kW/m ³) for the SC-50C (Interior view).....	72
Figure 8-15: Snapshots of the velocity field for the SC-50B.	74
Figure 8-16: Inflow/Outflow at the windows positions at z=1m and z=2m (Time:1250sec).	75
Figure 8-17: Slices for the representation of the temperature field inside and outside of the fire-compartment.	76
Figure 8-18: Temperature distribution inside/outside of the fire-compartment at different slices for SC-00.	76
Figure 8-19: Temperature distribution inside/outside of the fire-compartment at different slices for SC-12.5.	77

Figure 8-20: Temperature distribution inside/outside of the fire-compartment at different slices for SC-25A.	77
Figure 8-21: Temperature distribution inside/outside of the fire-compartment at different slices for SC-25B.	78
Figure 8-22: Temperature distribution inside/outside of the fire-compartment at different slices for SC-50A.	78
Figure 8-23: Temperature distribution inside/outside of the fire-compartment at different slices for SC-50B.	79
Figure 8-24: Temperature distribution inside/outside of the fire-compartment at different slices for SC-50C.	79
Figure 8-25: Temperature distribution inside/outside of the fire-compartment at different slices for SC-75.	80
Figure 8-26: Temperature distribution inside/outside of the fire-compartment at different slices for SC-100.	80
Figure 8-27: Gas-phases devices at the steel-frames positions.	81
Figure 8-28: Gas-phase devices near the structural members (Section A-A').	81
Figure 8-29: Temperature distribution along the axis of the beams that lie at different frames for the SC-75.	83
Figure 8-30: Temperature distribution along the axis of the columns in different frames for the SC-75/ Time=800sec.	85
Figure 8-31: Temperature distribution along the axis of the columns in different frames for the SC-75/ Time=1200sec.	86
Figure 8-32: Temperature distribution along the axis of the columns in different frames for the SC-75/ Time=1600sec.	87
Figure 8-33: Temperature distribution along the axis of the columns in different frames for the SC-75/ Time=2000sec.	88
Figure 8-34: The plan-view of the library building with the layer zoning devices.	90
Figure 8-35: 3D view of the layer-zoning devices.	91
Figure 8-36: Plan view of the first floor-Virtual zones.	91
Figure 8-37: Longitudinal cross-section of the building – Virtual zones modeling.	91
Figure 8-38: Lower and upper layer temperature evolution with time for all the virtual zones/ SC-25A.	93
Figure 8-39: Lower and upper layer temperature evolution with time for all the virtual zones/ SC-25B.	94
Figure 8-40: Lower and upper layer temperature evolution with time for all the virtual zones/SC-50A.	95
Figure 8-41: Lower and upper layer temperature evolution with time for all the virtual zones/SC-50C.	96
Figure 8-42: Lower and upper layer temperature evolution with time for all the virtual zones/SC-75.	97
Figure 8-43: Lower and upper layer temperature evolution with time for all the virtual zones/SC-100.	98
Figure 8-44: Lower and upper layer temperature evolution with time for all the virtual zones/SC-SP40.	99
Figure 8-45: Lower and upper layer temperature evolution with time for all the virtual zones/SC-SP40.	100
Figure 8-46: Upper-Lower temperature and layer height at different virtual zones for SC-25B.	103
Figure 8-47: Upper-Lower temperature and layer height at different virtual zones for SC-75.	105

Figure 8-48: Time-history of the layer height z_{int} in the fire-compartment for different fire scenarios.	108
Figure 8-49: Temperature time history curves according to the two-zone model for the beams, with respect to the frame where the structural members are located.	111
Figure 8-50: Temperature time history curves according to the two-zone model for the HEB340 columns, with respect to the frame where the structural members are located. .	113
Figure 8-51: Temperature time history curves according to the two-zone model for the HEB450 columns, with respect to the frame where the structural members are located. .	115
Figure 9-1: The plan-view of the library building.	120
Figure 9-2: The area loads/ longitudinal view of the library building.	120
Figure 9-3: The typical frame.	120
Figure 9-4: Elastic versus design response spectrum for ground type D (5% damping). .	121
Figure 9-5: The cross-sections of the typical frame according to the design for seismic and gravity loading.	122
Figure 9-6: The numerical model.	123
Figure 9-7: Beam to column connections.	123
Figure 9-8: Discretization of the cross-section in four different branches and layers definition.	124
Figure 9-9: The CPM and the locations of the possible plastic hinges.	125
Figure 9-10: Structural system masses.	126
Figure 9-11: The user interface and the parameters used in this study.	128
Figure 9-12: Results of Rexel in terms of spectra and the scale factors for matching to the elastic response spectrum.	129
Figure 9-13: Scaled time-history acceleration records according to Rexel's results.	131
Figure 9-14: Time-history displacement records that are calculated through the double integration of the corresponding accelerograms.	134
Figure 9-15: The eigenmodes of the structural system (Scale factor =10).	135
Figure 9-16: Capacity of the structure in terms of (a) Force-displacement and (b) λ -global drift curve.	137
Figure 9-17: The global plastic hinge mechanism.	137
Figure 9-18: Roof displacement and base shear time history for the seven accelerograms.	139
Figure 9-19: Envelope results in terms of inter-storey drift angle for the seven accelerograms.	140
Figure 9-20: Equivalent plastic strain (layer 1) for the different time-history acceleration records (Visualization S.F. 2).	144
Figure 9-21: Equivalent plastic strain distribution at the ends of the beams at the first level of the structural system.	145
Figure 9-22: Base shear and roof displacement time history for the accelerogram 290xa and for various S.F.	148
Figure 9-23: Base shear and roof displacement time history for the accelerogram 293ya and for various S.F.	149
Figure 9-24: Base shear and roof displacement time history for the accelerogram 6142ya and for various S.F.	150
Figure 9-25: Base shear and roof displacement time history for the accelerogram 612xa and for various S.F.	151
Figure 9-26: Base shear and roof displacement time history for the accelerogram 1726xa and for various S.F.	152
Figure 9-27: Base shear and roof displacement time history for the accelerogram 1726ya and for various S.F.	153

Figure 9-28: Base shear and roof displacement time history for the accelerogram 5850xa and for various S.F.	154
Figure 9-29: Inter-storey and global drift angle along the height of the frame.....	156
Figure 9-30: Maximum and average values of the inter-storey drift angles.	157
Figure 9-31: Development of plastic hinge mechanism for S.F. 1.25, 1.50, 1.75 and 2.00 (290xa).	158
Figure 9-32: Equivalent plastic strain distribution at the 1 st level for increasing S.F (290xa).	159
Figure 9-33: Development of plastic hinge mechanism for S.F. 1.25, 1.50, 1.75 and 2.00 (293ya).	159
Figure 9-34: Equivalent plastic strain distribution at the 1 st level for increasing S.F (293ya).	160
Figure 9-35: Development of plastic hinge mechanism for S.F. 1.25, 1.50, 1.75 and 2.00 (6142ya).	160
Figure 9-36: Equivalent plastic strain distribution at the 1 st level for increasing S.F (6142ya).	161
Figure 9-37: Development of plastic hinge mechanism for S.F. 1.25, 1.50, 1.75 and 2.00 (612xa).	161
Figure 9-38: Equivalent plastic strain distribution at the 1 st level for increasing S.F (612xa).	162
Figure 9-39: Development of plastic hinge mechanism for S.F. 1.25, 1.50, 1.75 and 2.00 (1726xa).	162
Figure 9-40: Equivalent plastic strain distribution at the 1 st level for increasing S.F (1726xa).	163
Figure 9-41: Development of plastic hinge mechanism for S.F. 1.25, 1.50, 1.75 and 2.00 (1726ya).	163
Figure 9-42: Equivalent plastic strain distribution at the 1 st level for increasing S.F (1726ya).	164
Figure 9-43: Development of plastic hinge mechanism for S.F. 1.25, 1.50, 1.75 and 2.00 (5850xa).	164
Figure 9-44: Equivalent plastic strain distribution at the 1 st level for increasing S.F (5850xa).	165
Figure 9-45: IDA curves in terms of maximum inter-storey drift angle and PGA. Verification for different performance levels according to FEMA 356.....	168
Figure 9-46: Identification of the ends of the beams that are presented in Table 9-18.....	169
Figure 10-1: Temperature profile of the structural members for the ISO <i>reference</i> scenario.	171
Figure 10-2: Deformed configuration of the structural sub-system at the end of analysis.	172
Figure 10-3: Equivalent plastic strain evolution with time at the Left end of Beam 1A (node 2437).	172
Figure 10-4: Equivalent plastic strain evolution with time at the Right end of Beam 1A (node 2439).	173
Figure 10-5: Equivalent plastic strain evolution with time at the Mid-span of Beam 1A (node 3240).	173
Figure 10-6: Equivalent plastic strain evolution with time at the upper end of Column 1B (node 1178).	173
Figure 10-7: Equivalent plastic strain evolution with time at the upper end of Column 1A (node 2543).	174

Figure 10-8: Axial force and horizontal displacement at the first level of the frame during the fire exposure.	175
Figure 10-9: Evolution of mid-span deflection of Beam 1A during fire-exposure.	175
Figure 10-10: Von Mises stress evolution with temperature at the UF and LF in the Left end of Beam 1A.	176
Figure 10-11: Von Mises stress evolution with temperature at the UF and LF in the Right end of Beam 1A.	176
Figure 10-12: Von Mises stress evolution with temperature at the upper and the lower flange in the Mid-span end of Beam 1A.	177
Figure 10-13: Hogging (support) and sagging (mid-span) of Beam 1A during the fire exposure.	178
Figure 10-14: Normal stress at the Left end of Beam 1A during the fire exposure.	178
Figure 10-15: Normal stress at the Right end of Beam 1A during the fire exposure.	178
Figure 10-16: Normal stress at the Mid-span of Beam 1A during the fire exposure.	179
Figure 11-1: Stabilization of the ground motion (1726ya record).	184
Figure 11-2: Temperature time-history curves for the beams with respect to the PEF scenarios.	187
Figure 11-3: Calculation of the critical temperature according to the simple calculation model.	188
Figure 11-4: Deformed shape of the structural system and the equivalent plastic strain distribution (Layer 1) during the FAE loading for scenario E290xa-1.00-FISO.	191
Figure 11-5: Vertical displacement and axial force time-history for scenario E290xa-1.00-FISO.	191
Figure 11-6: Eq. plastic strain distribution in the cross-section for scenario E290xa-1.00-FISO.	192
Figure 11-7: Rotation z time-history for scenario E290xa-1.00-FISO.	192
Figure 11-8: Deformed shape of the structural system and the equivalent plastic strain distribution (Layer 1) during the FAE loading for scenario E290xa-1.25-FISO.	193
Figure 11-9: Vertical displacement and axial force time-history for scenario E290xa-1.25-FISO.	193
Figure 11-10: Eq. plastic strain distribution in the cross-section for scenario E290xa-1.25-FISO.	194
Figure 11-11: Rotation z time-history for scenario E290xa-1.25-FISO.	194
Figure 11-12: Deformed shape of the structural system and the equivalent plastic strain distribution (Layer 1) during the FAE loading for scenario E290xa-1.50-FISO.	195
Figure 11-13: Vertical displacement and axial force time-history for scenario E290xa-1.50-FISO.	195
Figure 11-14: Eq. plastic strain distribution in the cross-section for scenario E290xa-1.50-FISO.	196
Figure 11-15: Rotation z time-history for scenario E290xa-1.50-FISO.	196
Figure 11-16: Deformed shape of the structural system and the equivalent plastic strain distribution (Layer 1) during the FAE loading for scenario E290xa-1.75-FISO.	197
Figure 11-17: Vertical displacement and axial force time-history for scenario E290xa-1.75-FISO.	197
Figure 11-18: Eq. plastic strain distribution in the cross-section for scenario E290xa-1.75-FISO.	198
Figure 11-19: Rotation z time-history for scenario E290xa-1.75-FISO.	198
Figure 11-20: Vertical displacement (d_y) at the mid-span of Beam 1A versus temperature.	200

Figure 11-21: Axial force and vertical displacement evolution with time for the natural-FAE scenarios (accelerogram290xa).	201
Figure 11-22: Equivalent Von Mises stress during the fire exposure at the Left end of Beam 1A for the natural FAE scenarios (accelerogram 290xa).....	203
Figure 11-23: Equivalent Von Mises stress during the fire exposure at the Right end of Beam 1A for the natural FAE scenarios (accelerogram 290xa).....	204
Figure 11-24: Equivalent Von Mises stress during the fire exposure at the Mid-span of Beam 1A for the natural FAE scenarios (accelerogram 290xa).....	204
Figure 11-25: Equivalent plastic strain during the fire exposure at the Left end of Beam 1A for the natural FAE scenarios (accelerogram 290xa).....	205
Figure 11-26: Equivalent plastic strain during the fire exposure at the Right end of Beam 1A for the natural FAE scenarios (accelerogram 290xa).	206
Figure 11-27: Equivalent plastic strain during the fire exposure at the Mid-span of Beam 1A for the natural FAE scenarios (accelerogram 290xa).....	206
Figure 11-28: Comparison of the results of the ISO and the natural FAE scenarios in terms of mid-span deflection.....	207
Figure 12-1: Evolution of $\sqrt{\frac{k_{E,\theta}}{k_{y,\theta}}}$ with temperature.....	212
Figure 12-2: Standard beams.....	214
Figure 12-3: Decomposition of the moment resisting frames using standard beams.	214
Figure 12-4: Decomposition of the moment resisting frame for the fire combination.	216
Figure 12-5: Moment-rotation curve for SB1.	217
Figure 12-6: Plastification of the SB1.....	218
Figure 12-7: Definition of the rotational capacity.....	219
Figure 12-8: Loading procedure- First case.	221
Figure 12-9: Loading procedure- Second case.....	221
Figure 12-10: Simplification of the problem from a continuous beam to a simply supported beam.	223
Figure 12-11: The structural system and the cross section (dimensions of the cross section in mm).	223
Figure 12-12: The numerical model.....	224
Figure 12-13: Results of the buckling analysis.	225
Figure 12-14: The boundary conditions.	225
Figure 12-15: Comparison of the numerical analysis results with the test results for the specimen S2-1 at 415 ⁰ C.....	227
Figure 12-16: Deformed shape of the steel beam at the failure.	227
Figure 12-17: Geometry of the numerical model.....	228
Figure 12-18: Results of the buckling analysis.	229
Figure 12-19: Discretization of the cross-section and boundary conditions at the support and at the mid-span.	230
Figure 12-20: Case 1: loading procedure.	230
Figure 12-21: Deformed shape of the beam and the distribution of equivalent plastic strain at different increments for temperature equal to T=20°C and T=400°C (amplitude of initial imperfections equal to 2mm).....	232
Figure 12-22 : Deformed shape of the beam and the distribution of Von mises at different increments for temperature equal to T=20°C and T=400°C (amplitude of initial imperfections equal to 2mm).....	233

Figure 12-23: Deformed shape of the beam and the distribution of equivalent plastic strain at different increments for temperature equal to $T=20^{\circ}\text{C}$ and $T=400^{\circ}\text{C}$ (amplitude of initial imperfections equal to 5mm).....	234
Figure 12-24: Load-deflection curves at 20°C and 400°C	235
Figure 12-25: The stress-strain relationship of steel (S275) for temperature levels 20 and 400°C	236
Figure 12-26: Deformed shape of the beam and the distribution of equivalent plastic strain at different increments and for temperature equal to $T=500^{\circ}\text{C}$ and $T=700^{\circ}\text{C}$ (amplitude of initial imperfections equal to 2mm).	237
Figure 12-27: Distribution of equivalent plastic strain for $d=50\text{mm}$ (amplitude of initial imperfection equal to 2mm).	238
Figure 12-28 Von Mises stress distribution at $T=500^{\circ}\text{C}$ (amplitude of initial imperfection equal to 2mm).....	239
Figure 12-29: Von Mises stress distribution at $T=700^{\circ}\text{C}$ (amplitude of initial imperfection equal to 2mm).....	240
Figure 12-30: Load-deflection curves at 500°C and 700°C (amplitude of initial imperfection equal to 2mm).....	241
Figure 12-31: Definition of the rotation of the plastic hinge.....	242
Figure 12-32: Rotation that is used in this study.....	242
Figure 12-33: Procedure for the evaluation of the rotation.	243
Figure 12-34: Moment-rotation curves at different temperature levels and for various amplitudes of initial imperfections.	245
Figure 12-35: Deformed shape and failure mode of the beam during the unloading stage at 200°C	247
Figure 12-36: The evolution of the available rotation with the temperature and the effect of the amplitude of the initial imperfections.....	248
Figure 12-37: Dimensionless moment-rotation curves.	249
Figure 12-38: Effect of the temperature on the moment-rotation diagrams for different amplitudes of initial imperfections.	251
Figure 12-39: The evolution of the rotational capacity with the temperature and the effect of the amplitude of the initial imperfections.	251
Figure 12-40: The evolution of the ultimate available rotation with the temperature and the effect of the amplitude of the initial imperfections.	252
Figure 12-41: Different configurations concerning the cyclic loading.	253
Figure 12-42: Case 2: loading procedure.	253
Figure 12-43: Cyclic loading patterns.	254
Figure 12-44: Reaction force-displacement curves for the different patterns of cyclic loading.	256
Figure 12-45: Local buckling at the flanges for different cyclic loading patterns.	258
Figure 12-46: Local buckling at the webs for different cyclic loading patterns.....	259
Figure 12-47: The equivalent plastic strain distribution at the end of cyclic loading.	260
Figure 12-48: Evolution of the plastic strain distribution of the beam during the monotonic loading stage at 20°C , 400°C and 600°C	262
Figure 12-49: Moment-rotation curves for the monotonic loading stage during the numerical simulation of three-point bending test concerning pre-damaged beams (amplitude of initial imperfections equal to 0.5mm).....	264
Figure 12-50: Moment-rotation curves for the monotonic loading stage during the numerical simulation of three-point bending analysis test concerning pre-damaged beams (amplitude of initial imperfections equal to 2mm).....	265

Figure 12-51: Moment-rotation curves for the monotonic loading stage during the numerical simulation of three-point bending test concerning pre-damaged beams (amplitude of initial imperfections equal to 5mm).....	266
Figure 12-52 Available rotation for beams that are damaged due to cyclic loading.	268
Figure 12-53: Dimensionless moment-rotation curves for the monotonic loading stage during the numerical simulation of three-point bending test at pre-damaged beams.	271
Figure 12-54 The effect of the temperature rise to the behaviour of the pre-damaged beams during the monotonic loading stage depending on the ‘level of damage’ and the amplitude of initial imperfections.	271
Figure 12-55 Available rotational capacity of the pre-damaged beams for different levels of damage considering the effect of the initial imperfections.	273
Figure 12-56 Proposed procedure for the definition of the ‘level of damage’.....	275
Figure 12-57: Ultimate available rotation of the pre-damaged beams for different levels of damage considering the effect of the initial imperfections.	277
Figure 13-1: Failure criteria according to the standard beam approach for different amplitudes of initial imperfections and for the perfect model.	280
Figure 13-2: Calculation of the fire-resistance of heated beams in terms of temperature and time.....	282
Figure 13-3: Comparison of fire-resistance time for ISO and Natural FAE scenarios (in ISO-fire time).	13-290

Chapter 1. Introduction

1.1 Overview

In urban areas fire-following earthquake is a rather common phenomenon and, occasionally, can be catastrophic. The aftermath of the fire exposure after an earthquake has been witnessed internationally in recent years (Northridge 1994, Kobe 1995, Chile 2010, Tohoku 2011). In many cases, urban environment characteristics (gas piping system, electricity wiring system, etc.) and post-earthquake conditions (multiple ignition points, malfunction of the active fire-protection systems, etc.) are combined and the fire-following earthquake becomes the predominant cause of damage and loss of human life (Scawthorn, 2005). Earthquake shaking causes damage both to structural and non-structural components of buildings. Ignition sources are related with several kinds of non-structural damage, for example damaged electrical devices, gas-service in damaged buildings, electricity distribution wiring system, electrical equipment that remains operating during the earthquake action, etc. Furthermore, non-structural damage, can be associated with the release of flammable gases or other combustible materials, coming into contact with ignition sources and leading to uncontrolled outbreak of fire. On the other hand, post-earthquake non-structural damage is related to the air flow conditions in the fire-compartment and to the active fire protection systems (e.g. breakage of windows that allows free air inflow, blocking of fireproof doors, failure of the sprinkler system, etc.) and may affect significantly the conditions of growth and spread of fire.

Fire control in post-earthquake conditions becomes more demanding than in ordinary ones. It has been recorded that 50-75% (FM Global, 2013) of the post-earthquake initiated fires start simultaneously and immediately after the event. Additionally, the delayed response of the fire-fighting rescue system may lead to uncontrolled fire growth. This is commonly attributed to the distributed large number of fires and emergencies and to the traffic jam in the access roads. Other issues that become critical during the post-earthquake conditions and contribute to the delay of the fire suppression are the impaired fire-protection systems, the reduced water supplies due to the increased demand and damages to the water piping system.

Fire has been the most catastrophic seismic consequence in both Japan and United States during the twentieth century, according to Scawthorn (2005). The post-earthquake fires in San Francisco (1906) and in Tokyo (1923) have been recorded as the largest urban fires in history. It is interesting to notice that the scenario of post-earthquake fire has been little studied until now. San Francisco earthquake still remains the largest earthquake in terms of economical and life cost in U.S. history (over 3,000 people were killed and 28,000 buildings were destroyed). And this record has only been exceeded during the Tokyo earthquake (140,000 people were killed and 575,000 buildings were destroyed, 77% of the

buildings were destroyed by the fires). The impact of fire after earthquake problem has been emphasized again during more recent earthquakes in Northridge (1994) and in Kobe (1995).

Nowadays, structural design according to the current codes is performed independently for the seismic and thermal actions. Many studies have been published in the last 20 years on the seismic behaviour of structures. The resulting knowledge has been incorporated into seismic design regulations in Europe and elsewhere. Concurrently, there has been considerable research on the behaviour of steel and composite structures in fire. Recently, this research has progressed beyond the behaviour of materials and isolated structural members, to the behaviour of real structures in fire. Thus, the interaction of heated members with the rest of the structural components is taken into account. Large-scale experiments have been performed in European level (e.g. the Cardington full-scale fire tests which were carried out by CORUS and BRE, Kirby, 1996 and 1997). These have led to the identification of additional mechanisms through which structures resist loads at elevated temperatures. Moreover, these studies underlined the need for robustness. Parts of this research have been consolidated in the latest versions of fire design rules (particularly Parts 1.2 of EN 1993-1, EN 1994-1, EN 1991-1).

Despite this progress in research on structural response to earthquake and fire independently, research on their combined effect has started only recently and, moreover, the post-earthquake fire-design is not a normative requirement. Specifically, fire design codes assume that when a fire starts, the structure is intact, and that all fireproofing measures are active (profile protection, sprinkler systems, etc.). This is not valid when structures have been damaged due to seismic action. In order to conduct an integrated study for the post-earthquake fire-performance of structures, the seismic damage of both structural and non-structural components should be taken into account. Both kinds of damage can alter significantly the fire-performance of the structure and reduce the fire-resistance time. The reduction of the fire-resistance, in time domain, is referred with respect to the fire-design *reference* case where the structure is not initially damaged.

The damage induced to the structural members can be qualified and quantified through the plastic deformations and cracking strains for steel and concrete respectively. It is expected that in post-earthquake fire-conditions the resistance of the structure will be limited and dependent on the “level of damage” induced during the seismic action. On the other hand, earthquake damage to active and passive fire-protection systems (e.g. peeling of fireproof coatings due to intense plastic deformation, sprinkler failure etc) may also limit the structural fire resistance. Seismic non-structural damage can affect the geometric characteristics of the fire-compartments (eg. blocking of fireproof doors etc). In this case the calculations for the fire-resistance of the structure according to the fire-design codes are not valid. Another important issue which is not included in the fire-design of the structures according to the current codes, is connected to the different post-earthquake fire-

scenarios, generated due to the modification of the air-flow conditions in the fire-compartments after the seismic event (e.g. breakage of windows allowing free air inflow).

It is evident that the response of the structure during the post-earthquake fire conditions is strongly dependent on the level of both structural and non-structural damage induced due to the seismic action and that the problem should be approached through the performance based philosophy.

1.2 Aim

1.2.1 Basic concept

The main problem addressed in this dissertation is the assessment of the behaviour of steel frame structures at elevated temperatures, considering that the starting point is a state of permanent damage caused by a prior seismic event, using the numerical methods. It is noted that the seismic damage to both structural and non-structural members is taken into account. The study focuses on the determination of the fire-resistance (in time domain) of structures during post-earthquake fire event. In this way the fire-resistance calculated depends on the damage caused by the earthquake.

The dissertation is focused on a steel-frame building that is used as a library. However, the developed methodology can be applied to any structural typology. Initially, the basic steps of the well-known seismic and gravity loading design are followed. The idea is to study the fire-performance of the structural system that is damaged due to seismic actions that are scaled-up, with respect to the earthquake intensity, in order to represent more severe earthquake with lower probability of occurrence. Moreover, it is assumed that the building can suffer different levels of damage (induced to both structural and non-structural components) depending on the earthquake probability of existence. To this end, first the verification of the performance of the structure is conducted through the comparison of the available capacity with the required one (Gioncu and Mazzolani, 2002).

In this study the capacity is measured in terms of the story drift. The four-level seismic design approach is followed. The interest is focused on the basic safety objectives of Life Safety and Collapse Prevention where the non-structural damage is considered to be extensive and uncontrolled for the different cases respectively. In this dissertation the objective is to study the behaviour of the structure for different Post-Earthquake Fire (PEF) scenarios that are related to scaled seismic actions. *Here, the term Post-Earthquake Fire Scenario is related only to the non-structural damage.* Different PEF scenarios are generated, taking into account various levels of non-structural damage, resulting to different boundary conditions for the thermal problem. As a result, different time-temperature distributions in the fire-compartment are obtained. Specifically, the idea is that the structure that is already designed according to the current codes, can suffer different PEF scenarios depending on the earthquake intensity. For the different scenarios, the fire-

resistance of the structure is expected to be modified, depending on the level of the structural and non-structural damage.

Another goal is to evaluate the reduction of the fire-resistance of the structure due to the earthquake induced damage. The reduction is referred with respect to the case where the structure is not damaged. In the latter case, the fire resistance is indicated as the *reference* one in this dissertation. The comparison of the results concerning the Fire after Earthquake (FAE) scenarios with the *reference* case indicates the reduction of the fire resistance due to the induced damage. It is noted that in this study the term FAE is related to both structural and non-structural damage and thus is different from the term PFE. The FAE scenarios include scaled seismic actions (directly connected to structural damage) and different PEF scenarios (directly connected to non-structural damage).

Briefly, the basic concept of this dissertation is described in the following. The structure is designed for the gravity and seismic loading according to the current regulations. The different PEF scenarios are generated using the principles of Computational Fluid Dynamics (CFD) and they are represented through different time-history gas-temperature distributions. Two different goals are defined.

- The **first** one is to obtain the *reference* fire resistance of the structure which is calculated using numerical analysis. At this point, two different cases are considered. In the first case the fire action is simulated through the ISO fire (prescriptive *reference* fire resistance), according to the guidelines of the current codes for the fire-design of the structure. In the second case the fire action is simulated using the principles of CFD.
- The **second** goal is to obtain the fire resistance of the structure for the PEF scenarios, taking into account seismic actions with different return periods. To this end, the next step is to scale-up the seismic action in order to represent more severe earthquakes. At this point it is assumed that the structure can suffer different PEF scenarios, depending on the earthquake intensity. The comparison of the post-earthquake fire-resistance with the *reference* value indicates the reduction due to the combined action. Finally, the problem is approached through a more simple methodology, using the ISO-fire curve instead of the PEF scenarios. In this way, the reduction of the fire-resistance due to earthquake damage is calculated with respect to the *reference* fire-resistance.

1.2.2 Research objectives

This dissertation actually is focused on two different areas. The first one is the numerical simulation of the fire enclosure while the second one is the simulation of the structural behaviour at elevated temperatures. The complexity of the problem is attributed to the fact that both structural and fluid mechanics are involved. An integrated approach is to conduct a fully-coupled thermo-mechanical analysis. This analysis involves three different issues. The first issue is the fire development in the fire-compartment, the second is the calculation of the temperatures that arise in the structural members while the last is the

structural behaviour during the fire exposure. Here, the term fully-coupled is referred to the interaction between the three different stages (Figure 1-1). This approach is quite complex.

In this dissertation the phenomenon is not assumed to be fully coupled. First, the fire is simulated through the principles of CFD. The output of this analysis yields the gas-temperatures which are used as input for the thermal analysis and the structural analysis is the last step.

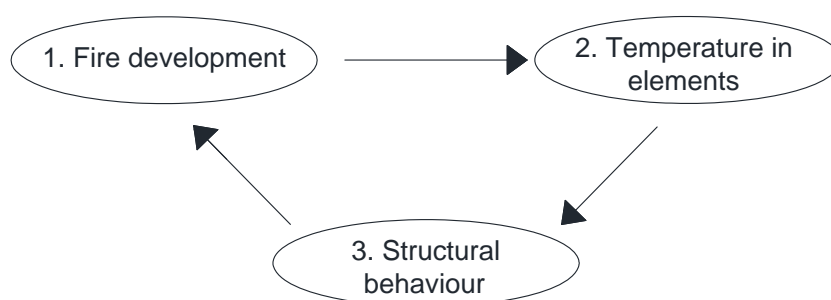


Figure 1-1: Fully-coupled thermo-mechanical approach.

The basic objective is to conduct the latter procedure for the determination of the fire-resistance of the structure for both the *reference* case and the PEF scenarios.

Considering the *reference* case, the first target is the simulation of the natural fire through the principles of CFD. The simulation is conducted through Fluid Dynamics Simulator (FDS McGrattan *et al.*, 2010a,b). This is a CFD model of fire-driven fluid flow. The output of FDS (McGrattan *et al.*, 2010a,b) is the spatial distribution of gas temperature in the fire-compartment. As it has already been explained, in the *reference* case the structure is not-damaged due to earthquake and it is assumed that all the fire-protection systems are active. After the definition of the *reference* scenarios, the goal is to study the structural behaviour during the fire-exposure. The numerical simulation is carried out using the non-linear finite element code MSC-Marc (2011). Non-linear numerical analysis is conducted using beam finite elements. At this point, the aim is to study the behaviour of the structure at elevated temperatures and to determine the *reference* fire-resistance.

The determination of the fire-resistance of the structure for the PEF scenarios is more complex. Here, the initial objective is the numerical simulation of the structural behaviour for the earthquake loading. To this end, non-linear dynamic analysis is conducted and the seismic action is simulated through time-history accelerograms. The loading is scaled-up in order to represent earthquakes with lower probability of existence. The target is to study the structural damage and to classify the results depending on the probability of existence of earthquake.

The second target is to make the calculations for the PEF scenarios through FDS (McGrattan *et al.*, 2010a,b), taking into account different levels of non-structural damage. The latter is simulated for two different non-structural components, the windows and the sprinkler system. Specifically, the breakage of the windows and the malfunction of the

sprinkler fire-extinguishing system are considered. Regarding the breakage of the windows, the different levels of non-structural damage are connected to different percentage of the windows that are broken due to earthquake. The malfunction of the sprinkler fire-extinguishing system can be partial or complete, thus the differentiation to the percentage of the operational sprinkler system is related to different levels of non-structural damage. The gas-temperature time history records that arise, yield the PEF scenarios.

The final goal is to study the behaviour of the structure that is damaged due to earthquake for different PEF scenarios, in order to identify the failure mode and to calculate the corresponding fire-resistance. Two-dimensional beam finite element models are developed in order to simulate the behaviour of the structure for the combined loading of fire-after earthquake. The structure is submitted to the seismic action taking into account different time-history acceleration records. The accelerograms are scaled-up in order to represent more severe earthquakes. The performance of the structure is verified through the performance levels that are defined in FEMA 356. Then, the damaged structure is submitted to thermal loading according to the gas-temperature history records of the PEF scenarios.

At this point, it is noted that a critical issue is the determination of the failure criteria during the fire exposure, that will be used for the calculation of the fire-resistance time. In this study the criterion that is proposed in order to assess the fire-resistance of the structure, is based on the rotational capacity of the structural members at elevated temperatures. To this end, the behaviour of isolated beams at elevated temperatures is studied in detail. Three-dimensional numerical models employing shell elements are developed in order to simulate the behaviour of steel beams at elevated temperatures. The objective is to determine the limit values of the rotational capacity, depending on the temperature level. The case of the damaged structural components that are exposed to fire is also studied. In this case the isolated beams are first submitted to cyclic loading and then to thermal loading. In this way, the limit values of the rotational capacity are obtained taking into account different levels of initial damage.

1.3 Organization

The dissertation is organized in fourteen chapters. The second Chapter presents a detailed literature overview concerning the older and the most recent published research studies related to the objectives of this dissertation. Specifically, the literature overview is focused on four different issues. The first part is focused on the current trends for the analysis of structures under seismic loading and presents the developments in performance-based design in seismic engineering. The second part of this Chapter is devoted on the fire engineering and involves both the study of the structural response of structures under fire loading and the modeling of the fire evolution in a compartment (using CFD numerical methods). The same part includes also a detailed presentation of the current methods regarding the interface models that are proposed in the literature in order to transfer the

results of the CFD fire simulation to the finite element model used for the mechanical analysis of structures during fire exposure. The third part of this Chapter discusses the studies devoted to the simulation of the structural behaviour during the fire-after-earthquake loading. The fourth part presents the state-of-the-art review concerning the research for the ductility of steel structural members at ambient temperature. The limited studies that are conducted for the study of the ductility of structural members at elevated temperatures are also discussed. Finally, the contribution of the dissertation in the area of the fire-after-earthquake analysis of structures is presented.

Chapter 3 provides information on the fire-behaviour in an enclosure. The basic aspect of this Chapter is to describe fires that take place in an enclosure that is defined as a fire-compartment in this dissertation. The basic stages of an enclosure fire are described in detail. The interest is focused on the post-flashover fire, which is the stage of the fire development that will be addressed in this dissertation. Another issue is the presentation of the basic guidelines provided by EN 1991-1-2 for the fire simulation.

The pyrolysis and combustion models used for the simulation of fire are presented in Chapter 4. Moreover, a brief review of the basic principles of the CFD used for the simulation of the fire development in an enclosure is provided in this Chapter. Specifically, this Chapter presents the governing equations that are solved, the limitations and the assumptions that are used in the code and the solution procedures that are available in FDS (McGrattan *et al.*, 2010a,b). Emphasis is given in the formulation of the problem for the fire-driven fluid flow. The Navier-Stokes equations appropriate for low-speed, thermally-driven flow, with an emphasis on smoke and heat transport from fires and the turbulence modelling are discussed.

Chapter 5 focuses on the basic principles of heat transfer theory and on the basic concepts concerning the modeling in the context of fire engineering. First, the basic mechanisms of heat transfer, convection, conduction and radiation are discussed. In the sequel, the basic elements for the application of the theory to the numerical simulation of heat transfer are presented. This Chapter contains also the solutions that are suggested by EN 1991-1-2 in order to find analytical solutions for the heat transfer problem in the case of steel sections.

The sixth Chapter deals with the material properties of steel at elevated temperatures. Both the mechanical and the thermal properties are discussed. The first aspect is the mathematical model used in order to describe the non-linear temperature dependent stress-strain relationship at elevated temperatures, according to guidelines of EN 1993-1-2. Finally, the thermal properties, including the thermal conductivity and the specific heat are provided.

Chapter 7 presents the library- building that is studied in the dissertation. The “*reference scenarios*” are defined, taking into account that the structure is not damaged due to earthquake. Additionally, the PEF scenarios that are used in order to study the effect of the non-structural damage on the fire evolution in the enclosure, are defined. In this

dissertation the PEF scenarios are generated using as parameters the ventilation conditions and the functionality of the fire-sprinkler system.

Chapter 8 presents the numerical model that is developed for the simulation of the natural-fire in the library building. The study is focused on the structural system of the steel building. The basic aspect in this Chapter is the definition of the gas-temperature distribution in the fire-compartment for both the *reference* and the PEF scenarios and to study the effect of non-structural damage to the fire evolution in the enclosure through different aspects. The evolution of the gas-temperature with time provides the input data for the calculation of the temperature profile of the structural members during the fire exposure in the next Chapters (Chapters 10 and 11). For this reason, the next issue is the development of an interface in order to link the CFD and the FEM structural analyses, conducted in Chapters 10 and 11. Finally, the temperature profiles of the structural members are calculated for the PEF scenarios.

The study of the behaviour of the structural system for the seismic loading is presented in Chapter 9. The first aspect is the design of the structure studied in this dissertation for gravity and seismic loading according to the guidelines of EN 1993-1-1 and EN 1998-1-1. The modeling of the seismic action through different time-history acceleration records and the development of the numerical model follow. The basic issue of this Chapter is to present the outcomes of the time-history dynamic analysis which is carried out using the non-linear finite element code MSC-Marc (2011). Different earthquake scenarios are studied by scaling-up the time-history acceleration records.

The non-linear analysis of the frame structure for the fire loading follows, in Chapter 10. The fire-response of the structural system studied in this dissertation is discussed in detail in order to understand the mechanisms of failure at elevated temperatures. In this Chapter, the fire-loading is represented through the *reference* scenarios (both ISO and natural fire).

Chapter 11 deals with the study of the behaviour of the structure during the Fire after Earthquake (FAE) loading. The first issue is the definition of the FAE scenarios. Two categories are distinguished, depending on the simulation of the fire action: the ISO-FAE scenarios and the natural-FAE scenarios. The structure is first submitted to different scaled time-history acceleration records as they are defined in Chapter 9. The second stage is the fire loading. The main target of this Chapter is to obtain in detail the behaviour of the structure for the different FAE scenarios.

Chapter 12 deals with the identification of the failure criteria of the structure during the fire exposure. Advanced three-dimensional numerical models are developed for the determination of the rotational capacity of the steel beams under fire conditions. The three-dimensional models are based on shell finite elements and take into account the initial imperfections of the steel members. Parametric analyses are conducted with respect to the amplitude of the initial imperfections, in order to obtain moment – rotation curves for steel beams at elevated temperatures. In order to take into account the seismic damage, the

moment-rotation curves are obtained also for beams which are pre-damaged due to cyclic loading. Finally, the limit values for the rotation of the structural members at elevated temperatures are obtained.

Finally, the fire-resistance of the structural system is calculated, in Chapter 13, taking into account the failure criteria that are defined in Chapter 12 for both the undamaged structure (*reference* fire scenarios) and for the case where the structure is damaged due to earthquake (FAE scenarios). The fire-resistance is calculated in time and temperature domain. The comparison between the fire-resistance of the undamaged and damaged structures specifies the reduction, in time domain, in the case of the FAE loading.

Chapter 14 summarizes the objectives of the dissertation, the techniques that are used for the study of the behavior of the structure under the combined scenario of FAE and presents the main findings. Moreover, the innovative points of the dissertation and the suggestions for further research are presented.

Chapter 2. State-of-the art / Literature review

The objectives of this dissertation are covering three different scientific areas which are the earthquake engineering, the fire engineering, the ductility of structural members. This Chapter presents the literature review and a state-of-the-art report about the main scientific regions of interest in the dissertation. Specifically, the literature overview is organized in four basic sections:

- ✓ Numerical methods for the structural analysis for earthquake loading.
- ✓ Structural analysis during fire exposure, enclosure-fire modelling using the principles of Computational Fluid Dynamics and the interface that is required in order to connect the aforementioned analyses.
- ✓ Modeling/analysis of the structural behaviour for the fire-after-earthquake loading.
- ✓ Ductility of structural members at ambient and elevated temperatures

Finally, is described the contribution of this dissertation in the area of the fire-after-earthquake analysis of structures.

Many theoretical and experimental studies for the behaviour of structures under seismic loading have been published and the knowledge has been incorporated in the current codes for the seismic design. The objective of the conventional methods of seismic design is to provide life safety and damage control. The last years an international agreement exists in the scientific community that the design of structures should be conducted according to the performance based idea (Fajfar, 1998, Ruiz-Garcia and Miranda, 2002, Ghobarah, 2001). This Chapter presents a state-of-the-art review of the current trends, regarding the analysis of structures under seismic loading and presents the developments in performance-based design in seismic engineering (Section 2.1).

The fire engineering field involves both the fire-response of the structures and the field modeling approaches (CFD). Today, the structural fire design is currently based on prescriptive approaches either through standard fire tests on individual building components or empirical approaches (Kodur *et al.*, 2012). In the last years, there has been consensus in the scientific community that the fire should be treated as a load, like the earthquake or the wind. This Chapter presents a review of the most important studies concerning the fire-behaviour of structural members and frame sub-structures (Section 2.2.1).

The simulation of the fire in an enclosure is a complex issue since fluid dynamics, combustion and radiation are combined and provide a physical and chemical phenomenon (Novozhilov, 2001). The approach of CFD or field modeling is significantly developed in the last years. Today, the CFD modeling is considered to be fundamental since it can provide the basis for the not yet developed performance-based fire design. The increasing

research led to sophisticated models and the validation through the experimental data make them more reliable. This Chapter presents a state-of-the-art for the CFD modeling of compartment fires (Section 2.2.2).

Section 2.2.3 is devoted to the interface that is required in use to link the output of the CFD analysis as an input for the finite element analysis, conducted for the study of the fire-response of the structures. Today, the scientific research in this area is limited. This section presents the models that are proposed in the literature for linking the different type of analyses.

Despite the progress in the research in fire and earthquake fields, the research on the combined effect of seismic and thermal actions is rather limited. The book edited by Scawthorn *et al.* (2005) emphasizes the fact that the fire following earthquake is a significant problem in urban regions with the potential of catastrophic losses. This book covers in detail the historical experiences of post-earthquake fires and presents a quantitative framework that can be used to examine the effectiveness of various mitigation strategies. This Chapter examines in detail the scientific published studies that are related to the post-earthquake fire-behaviour of steel structures (Section 2.3).

The last part of this Chapter is devoted to the literature review about the assessment of the ductility of structural members. The review is focused on the most important studies regarding the evaluation of the member ductility at room temperature and the research activity at high temperatures (Section 2.4).

2.1 Seismic performance of steel structures- Performance-based design trends

The major objective of the current regulations for the seismic design of buildings is to ensure life safety. The design is conducted either using linear methods and the most popular are the lateral force method (where it is supposed that the structural behaviour is dominated by the first mode) and the modal superposition method which takes into account the contribution of higher modes of the structure. In both cases, the inelastic behaviour of the structure is considered through the behaviour factor q and this implements several uncertainties in the design. The lessons of the recent earthquakes identify that the buildings designed according to the modern codes, performed as expected and life loss was minimal. On the other hand, the economic loss was enormous. The economic impact of physical damage and loss of function was huge and this indicates that damage control should be considered. For this reason, the performance-based framework was introduced in the seismic design of buildings (Gioncu and Mazzolani, 2002). The idea is that the building should achieve predefined performance objectives (Fajfar, 1998). Specifically, the structure should resist minor earthquakes without significant damage, moderate earthquakes with repairable damage and severe earthquakes with the no-collapse requirement. Many research studies focus on the performance –based seismic design: Teran-Gilmore (1998a), Fajfar (1998), Leelataviwat (1999), Fajfar (2000), Yamawaki

(2000), Ruiz-Garcia and Miranda (2002), Ruiz-Garcia and Miranda (2005).

According to Gioncu and Mazzolani (2002), in the context of a cohesive strategy for seismic design, the structure must be verified for rigidity at serviceability level, for strength at damageability level and for ductility at survivability level. Consequently, the rigidity, strength and ductility must be verified for different levels of seismic actions and this requires linear elastic and non-linear analyses. The idea of the performance-based design appears also in several guidelines as ATC-40 (1995) and FEMA-273 (2000). The latter approach was first proposed by Freeman *et al.* (1975) and it was modified by Fajfar (1999). The capacity spectrum method gives a graphical presentation and makes possible a visual evaluation of how the structure will perform when subjected to earthquake ground motion. The intersection of the capacity spectrum with the demand spectrum provides an estimate of the inelastic acceleration (strength) and displacement demands. It is clear that the non-linear analysis methods are of great importance in the modern seismic design of structures. In this point of view, the worldwide research interest was focused on the refinement and verification of the non-linear static analysis (pushover). This is an alternative way for predicting the non-linear dynamic response of structures without the excessive computational cost which is required for the inelastic dynamic analysis. A detailed review for the pushover analysis is presented in Elnashai (2001). According to the aforementioned study, the use of the inelastic static analysis in earthquake engineering dates back to the work of Gulkan and Sozen (1974). Simplified procedures for Multi Degree of Freedom systems have been proposed by Saiidi and Sozen (1981) and Fajfar and Fischinger (1988). A lot of research studies are devoted to the advantages and disadvantages of this method (Lawson *et al.*, 1994), to the improvement of the procedure (Sakaki *et al.* 1996) and to the comparison with inelastic time-history procedures (Kim and D'amore, 1999). In order to improve the efficiency of the method different non-linear static procedures have been proposed in the literature (Gupta and Kunnath, 2000, Antoniou and Pinho, 2004, Manoukas *et al.*, 2011 and 2011a, etc). The drawbacks of the conventional pushover analysis (Reinhorn, 1997, Bracci *et al.*, 1997, Antoniou and Pinho, 2004) spurred to the adaptive pushover methods that take into account the updated modal characteristics of the structure during the progressive loading.

In the recent years the computer processing power has increasingly grown and this leads to the implementation of more accurate analysis methods. The non-linear time history analysis has been extended to the Incremental Dynamic Analysis (IDA). In the IDA the ground motion records are scaled in order to describe the structural behaviour until collapse. As it reviewed in Vamvatsikos and Cornell (2002), the concept of the IDA has been cast in several forms in the work of many researchers, including Yun *et al.* (1992), Bazzurro and Cornell (1994a, 1994b), Luco and Cornell (1998 and 2000), Dubina *et al.*(2000) and De Matteis *et al.* (2000). Several researchers published numerical studies in order to validate the results of the adaptive pushover analyses by comparing capacity curves with IDA curves (Gupta and Kunnath, 2000, Elnashai, 2002, Ferracuti *et al.*, 2009).

2.2 Fire (structural) performance of steel structures – CFD modeling

Fire enclosure modeling includes three different stages: the fire modelling, the heat transfer and the structural model. Usually, they are considered as uncoupled and the interaction between them is neglected.

2.2.1 Fire (structural) performance

An extensive review for the structures in fire, which has recently been published (Kodur *et al.*, 2012), summarizes the state-of-the-art review and identifies the research and training needs for improved fire safety. In this study, it is underlined that there is a lack in experimental data, the numerical modeling tools are underdeveloped and few specifications for performance-based structural fire safety design exist. Also it is noted that fire, which is a low probability - high consequence event, is not included in the typical design of buildings like other loading such as wind and earthquake. The trend is the development of a performance-based fire design which indicates that the structures should be designed against fire, based on a target structural response.

In the past years, many theoretical studies were published for the behaviour of the laterally restrained steel beams under fire conditions (Burguess *et al.* 1990, 1991, El-Rimawi *et al.* 1997, Liu 1998, 1999, Usmani *et al.* 2001, Yin and Wang 2005a and 2005b). The studies reveal that the utilization of the connection capacity in fire leads to an increased fire-resistance time.

In the study of Yin and Wang (2005a), a general analytical method for providing the catenary action of steel beams with uniform temperature profile at large deformation is proposed. The model is suggested as a design method to enable engineers to make use of the catenary action. In this way, the fire-resistance time of the beam could be much higher than that obtained from the current design method based on bending moment capacity. The companion paper (Yin and Wang, 2005b) indicates that for design purposes it is not necessary to determine precisely the beam's non-uniform temperature profile since the results show that the different non-uniform temperature profile does not have effect on a beam's catenary force.

The theoretical studies concerning the longitudinally and axially restrained beams reveal that the level of restraint (both rotational and axial) is the dominant parameter at the early stages of heating, before the catenary action takes place (Elghazouli and Izzuddin, 2000, Usmani *et al.*, 2001).

Several finite element codes have been developed during the last years that are specialized to the fire analysis of structures. The most popular codes are Vulcan and Safir which include both the heat transfer and the structural modeling.

The numerical modeling is mainly limited to the fire-behaviour of isolated structural members (Liu and Davies, 2001, Yin and Wang, 2004, Tan and Huang, 2005, Huang and

Tan, 2007, Li *et al.*, 2007). In this way the interaction of the structural members with the adjacent members is simulated through axial and rotational boundary conditions.

In the study of Tan and Huang (2005) the axial restraint is represented by a linear elastic spring, whereas the rotational restraint is simulated as a semi-rigid rotational spring. The developments of beam internal forces, cross-sectional stresses and strains, together with displacements are examined. Moreover, the effects of some important factors such as load utilization factor, beam slenderness ratio and axial and flexural restraint ratios, are also studied. Numerical analyses show that the critical temperature is reduced by axial restraint but increased by semi-rigid rotational restraint.

The catenary action of axially restrained steel beams at elevated temperatures is studied in Yin and Wang (2004). The parameters investigated include beam span, uniform and non-uniform temperature distributions, different levels of applied load, different levels of axial and rotational spring stiffness at the beam ends and the effect of lateral torsional buckling. The results of the numerical analysis indicate that the level of axial restraint is the most important factor as it affects the beam deflection and the axial force under catenary action. As it is stressed in the study, as the axial restraint is increased, the beam deflection is reduced and this is favorable for the integrity of the fire-compartment in which the restrained beam is located. It is concluded that the large deflection behaviour of steel beams can significantly affect their survival temperature in fire and that the fire engineering design will need to consider the effect of axial forces in the beam on the adjacent structure, including the connections.

A method for the analysis of the non-linear structural behaviour of axially restrained steel beams at elevated temperatures is presented in Li *et al.* (2007). This method employs the axis arc-length and section rotation of the deformed beam as basic variables. The model is validated against results from the finite element method employing shell elements and the comparison showed a good agreement. Parametric studies demonstrate that the load ratio and axial restraint stiffness have great influence on the structural behaviour of the axially restrained steel beam at elevated temperatures, while the effect of the temperature gradient across the section or along the length is small. However, the temperature gradient across the section may cause a hog moment in the axially restrained beam, which fails in the catenary action model.

The behaviour of frame structures was the subject of several numerical studies (Wang *et al.* 1995, Wang and Moore, 1995, Najjer and Burgess, 1996, Liew *et al.*, 1998, Kaewkulchai and Williamson, 2004, Khandelwal *et al.*, 2009, Kim *et al.* 2011, Sun *et al.* 2012).

The study of Liew *et al.*, 1998 demonstrates that standard fire tests carried out on isolated beams or columns cannot provide anything more than a very crude pointer to structural performance. In real buildings, the individual members exposed to any fire are part of a

larger structure, much of which may remain cold and may support the fire-weakened members. Traditional fire-resistance design may be conservative because structural behaviour is estimated on the element level taking into account the time–temperature relationship of the ISO standard fire.

In the study of Sun *et al.* (2012) the progressive collapse mechanisms of steel-framed structures were studied. Twenty cases have been analysed to provide a comprehensive view of the mechanisms of progressive collapse for these frames, with different bracing systems under different fire conditions. The influences of stiffness and strength of the bracing systems are also analyzed. The results indicate that the pull-in of columns is one of the main factors which generate progressive collapse. Moreover, it was concluded that a bracing system can enhance the capacity of a steel frame to resist progressive collapse under fire conditions. The bracing system increases the redundancy of the structure and provides alternative load-sharing paths after a local instability occurs.

Numerous fire tests were conducted during the last decades. The behaviour of steel beams is usually studied through standard fire tests. The most extended experimental program concerning the bending behaviour of steel beams at elevated temperatures was conducted in UK. The compendium of UK's fire tests (Wainman and Kirby 1987, 1988) provides useful data for the fire response of beams. As it is noticed in Kodur *et al.*, (2012) today there is a lack of minimum data for steel beams under restrained conditions. The first full scale fire tests were conducted in the Fire Research Station in U.K. (Cooke and Latham, 1987). The most significant full scale tests were undertaken by the Building Research Establishment (BRE) in Cardington in U.K (Kirby, 1996 and 1997). The observation and the data from the fire tests on the multistory composite steel buildings provided useful information for the behaviour of structural and non-structural components under natural fire conditions.

2.2.2 Numerical modeling of fire enclosure

Compartment fire is the topic of a large number of experimental, analytical and numerical studies. The experimental studies provide useful data for understanding the physical phenomena that are involved during the fire development in the enclosure. The scientific research in this field is significant, but it is out of scope of this dissertation to discuss the experimental studies.

Today, the simulation of the natural fire is based on analytical zone and CDF models (Yeoh *et al.*, 2003 a and b, Sherman *et al.*, 2004, Pope and Bailey, 2006, Utiskul, 2006, Hasib *et al.*, 2007, Rinne *et al.*, 2007, Merci and Maele, 2008, Yang *et al.*, 2010, Suard *et al.*, 2011, Rein *et al.* 2011, Chi-ming *et al.*, 2013,). Due to the large number of published studies that are devoted to the fire modeling, here the literature review is limited to the numerical simulation of the enclosure fire using CFD principles.

The last decade the available computational power and knowledge of fire dynamics have

grown sufficiently. As a result, the simulations in real-size building enclosures are carried out using grids that are fine enough to reproduce fire-driven flows reasonably well. Regardless of model type – zone, RANS (Reynolds-Averaged Navier-Stokes), LES (Large Eddy Simulation) models – there is fairly high confidence to model transport phenomena. In other words, if the fire's heat release rate is given, the compartment temperatures can be predicted on accuracy of 20% at worst and at best to within experimental accuracy (McGrattan, 2005).

A detailed review for the computational fluid dynamics modeling of compartment fires is presented from Novozhilov (2001). The review discusses the trends and perspective of the mathematical fire modeling and highlights the need for extensive validation studies and interaction between theoretical and experimental investigations. The state-of-the-art review of fire modeling is such that given a fire of known size and power (evolution of the heat release rate (HRR)), CFD models calculate the resulting temperature and smoke concentration fields. The fire source is therefore treated as an input into the model by means of a prescribed HRR as a function of time. This poses a problem in the study of accidental fires where the HRR is unknown. Predicting the evolution of the HRR (i.e., spread rate and growth pattern) instead of measuring it, is among the most challenging pending issues in fire research. Most modelling work in the literature corresponds to scenarios with simple fire sources, like pool fires or a single burning item of constant or near constant HRR. This type of scenario avoids the more complex processes of flame spread and fire growth observed in real fires. Little research has been done in comparing simulations with real-scale fire tests that use realistic fuel loads.

The last decades, several software have been developed for the numerical simulation of the natural fire in a compartment. The most popular is the Fire Dynamics Simulator (FDS (Mcgrattan *et al.*, 2010a,b) from NIST (National Institute of Standards and Technology). Many researchers use FDS (Mcgrattan *et al.*, 2010a,b) in order to predict the temperature in the enclosure, the velocity field, the smoke movement, the gas concentration. Some recent studies about the CFD modeling are presented in this section.

In the study of Chi-ming *et al.* (2013) FDS (Mcgrattan *et al.*, 2010a,b) simulations and full-scale experiments were carried out to measure the impact of natural ventilation conditions and installation of a natural ventilation shaft, on smoke layer descent during different fire scenarios. It was observed that when outdoor air blows into the interior, it causes the smoke layer temperature to become unstable. It is concluded that FDS (Mcgrattan *et al.*, 2010a,b) simulations can reliably model the fire smoke layer height.

Numerical simulation results of full-scale fire tests in a small compartment are presented in the study of Merci and Maele (2008). A range of total fire heat release rates, fire source areas and ventilation roof opening areas is covered. Both two-zone model calculations and field model simulations are considered. For the different configurations, profiles of mean temperatures and temperature fluctuations were reported. Furthermore, the mean flow field and temperature field in the compartment were extensively discussed, providing insight in the entrainment and mixing phenomena in the plume in the compartment. The smoke layer

depth was determined for all configurations. It was concluded that the computational fluid dynamics (CFD) simulations agree well with experimental observations. According to the authors, the total fire heat release rate value has the strongest influence on the hot smoke layer average temperature rise, while the influence of the fire source area and the roof opening is smaller. It was observed that the hot smoke layer depth, determined from the mean temperatures, is hardly influenced by the total fire heat release rate and that the roof opening has a moderate influence in the range considered. The largest impact on the layer depth was due to the fire source area, with an increase of the depth as the fire source area increases. Correlations were given for the average hot smoke layer temperature rise and the total smoke mass flow rate out of the compartment, as a function of the different parameters mentioned. A study of the buoyancy *reference* velocity led to the verification of a formula to estimate the total smoke mass flow rate out of the compartment. Finally, the performance of different entrainment models in zone model calculations was discussed in relation to the obtained CFD results.

The paper of Rein *et al.* (2011) reports a series of CFD simulations (with FDS, Mcgrattan *et al.*, 2010a and b) conducted to reproduce the large-scale Dalmarnock Fire Test One. This test involved several real burning items leading to a complex fire spread process. No previous fire simulation had this large amount of data available for comparison. Simulations were compared against average and local measurements. The heat release rate was reconstructed from additional laboratory tests and upper and lower bounds for the fire growth are found. Within these bounds and after adjusting uncertain parameters, the level of agreement reached with the measurements was of 10 to 50% for the evolution of the average hot layer temperatures and between 20% and 200% for local temperatures.

This study of Rinne *et al.* (2007), presents an experimental validation of FDS (Mcgrattan *et al.*, 2010a,b) simulations of PMMA (polymethyl-methacrylate), wood, heptane, and toluene fires in a test compartment. The numerical predictions of smoke and gases concentrations, vertical temperature profile, smoke layer height, and visibility are compared against experimental results. Simulations and visualizations were done using FDS (Mcgrattan *et al.*, 2010a,b) and Smokeview- Version 5 (Forney, 2007). The results showed that the simulations of CO₂ and O₂ concentrations and vertical temperature profiles were in good agreement with the measurements. The agreement of the CO concentrations was better in case of toluene and heptane than in case of PMMA and wood. In case of gas concentrations, strong dependency on the grid cell size was observed. For heptane and toluene fuels, the use of default values of Smokeview (Forney, 2007) and FDS (Mcgrattan *et al.*, 2010a,b) leads to good predictions of the view inside a fire-compartment.

Hasib *et al.* (2007) analyzed the experimental results, obtained in a compartment fire experiment by using CFD modelling. Experiments were conducted in a compartment by burning methanol as a fuel. Temperatures vs. time were recorded at 11 different locations in the compartment for three sizes of fires. CFX-version 5.7.1(2005) was the software package used for the analysis. The predictions of temperatures with time at selected locations showed good agreement with the experimental results. Furthermore, the predicted

profile of horizontal component of velocity at the door centreline was in agreement with usual assumption, made in zone models that the neutral plane exists at about the door mid height. Above this plane the hot gases leave the compartment, while below it fresh air enters into the compartment from the outside. According to the authors view, CFX which is a general purpose CFD software, may be applied to complex fire scenarios for the analysis and developing fire safety regulations.

2.2.3 Fire-structure interface

In the case of the modeling of natural fire using the CFD principles, an important issue that arises is the heat transfer in solids (structural members). This is critical for the determination of the fire response of the structure. In this point of view, an interface must be developed in order to transfer the results of the CFD fire simulation to the finite element model. The scientific research in this subject is limited.

An algorithm is proposed by Prasad and Baum (2005a, b) and it was adopted in the study of Hamins *et al.* (2005). The Fire Structural interface (FSI) is described in detail in Prasad and Baum (2005a). The paper describes the collapse of the World Trade Center towers, resulting from a combination of the aircraft impact damage and the fires that followed. A methodology was developed to calculate the heat transfer to structural elements. The simple radiative transport model assumes that the compartment can be locally divided into a hot, sooty layer and a cool relatively clear lower layer. The properties of the two layers are extracted from temporal averages of the results of the fire simulation using CFD. Specifically, the approach that is proposed in this study takes into account the fact that the horizontal dimensions of each floor of the WTC towers are much greater than the height of the individual floor. Hence, in this case the temperature and the soot concentration change quite rapidly in the vertical direction but much more slowly in the horizontal directions. This simplification is very similar to the “zone models” of fire dynamics that ignore the variation of thermal properties in the horizontal directions. Taking into account this simplification, the radiative transport equation can be solved explicitly and the heat flux can be obtained as a function of temperature, hot layer depth, soot concentration and orientation of the structural element. The local spatial and temporal averages that are required in order to define the properties of the layers (temperature, soot concentration and layer height) are extracted from the output results of FDS (Mcgrattan *et al.*, 2010a,b). Spatial averaging is defined by the grid size that is used in FDS (Mcgrattan *et al.*, 2010a,b) simulation. The time intervals used for the averaging are chosen to be compatible to the time required for the heat to diffuse through the smallest structural element. Another important simplification that is introduced in this study is the concept of grey gas, whose properties are independent of frequency. If the spectral absorption coefficient is replaced by certain average value, the radiative transport equation is simplified. The solution, that yields the heat flux, is obtained taking into account constant values for the temperature and the absorption coefficient at the upper hot layer. This formulation can be used directly as input into finite element analyses codes where the numerical simulation is based on three-dimensional models.

The Research Fund of Coal and Steel (RFCS) project called FIRESTRUCT (Kumar *et al.*, 2005) dealt with different approaches for the FSI employing different softwares. In the study of Tondini *et al.* (2012), a weak coupling approach between the CFD software FDS (Mcgrattan *et al.*, 2010a,b) and the FE code SAFIR is presented. The FSI method requires that the fire development is simulated in FDS (Mcgrattan *et al.*, 2010a,b) and the thermal and mechanical analysis are conducted in SAFIR using linear elements for the simulation of the structural members. Specifically, at the end of the CFD analysis a transfer file, which contains all the required information (temperature of gas, convection factors and radiant intensities from various direction), is generated. The target is to compute the fluxes at the surface of the structural members in the FE software by integrating the radiant intensities. The directions of the intensities which are required to perform the integration are generally not the directions in which the intensities are given by the CFD analysis. For this reason, a spherical interpolation is performed in order to obtain the radiant intensities in the directions required by the numerical integration. The most important limitations, which are implied in the FSI, are the following: 1) the dimensions and the deflections of the structural elements must be small, compared to the dimensions of the compartment, in order not to affect the fluid motion in the compartment, 2) the CFD model does not include the structural members.

The new concept of the adiabatic surface temperature is introduced in the study of Wickström *et al.* (2007). The concept can be used successfully when the exposure conditions are obtained either for a CFD model or directly from measurements during a fire test. The adiabatic surface is a surface of a perfect insulator exposed to the same heating conditions as the real surface. Its temperature is the adiabatic surface temperature. The basic characteristic of the adiabatic surface is that the total net heat flux is by definition zero. The adiabatic surface temperature can be obtained from the output of a CFD model or it can be measured in real fire tests using devices as the plate thermometer. The adiabatic temperature is the interface between the fire and the structural models. Initially, the adiabatic temperature can be calculated since the total net heat flux is zero. The incident radiation heat flux and the corresponding gas-temperature adjacent to the surface, at every surface point, that are resulting from the CFD modeling, are required for the calculation. The time-history of the adiabatic temperature is stored in a file. Then, the heat flux to the surface can be computed to the structural model using the adiabatic temperature. Actually, the net heat flux of the fire model is translated into a temperature and then the temperature is translated back to a net heat flux in the structural model. This is more efficient since it is required to transfer only one quantity than three different quantities (a heat flux, surface temperature and convective heat transfer coefficient).

2.3 Fire after earthquake performance of steel structures

The literature review concerning the disasters that are attributed to the post-earthquake fires in urban regions, is extensive. Several studies (Buchanan, 2001, Cousins *et al.*, 2001, Scawthorn *et al.*, 2005) are devoted to the historical events and indicate the mitigation

strategies for the reduction of the post-earthquake fire losses in urban regions. The idea for the design of structures for the fire following earthquake action can be accomplished through the performance based design procedure. Chen *et al.* (2004) indicate a methodology about this aspect and highlight that the structural damage, the damage of the fire protection of the structural members and the non-structural damage should be considered. The effect of the earthquake level to the non-structural passive fire protection systems is studied in Collier (2008). This study reveals that the post-earthquake performance of the fire-protection systems is considerably reduced. The fire-behaviour of structural components with damaged fire protection was studied experimentally by Li and Wang (2008) and Pessiki *et al.* (2006).

The scientific research on the fire-behaviour of unprotected steel structures started recently and is limited. The problem of structures under fire after earthquake scenarios was studied in C26 COST action with title “Urban habitat constructions under catastrophic events”. In the context of the action, several studies for the fire-behaviour of earthquake-damaged structures were published. A state-of-the-art review for the structural analysis in case of fire after earthquake was presented by Faggiano *et al.* (2008). An interesting study was carried out by Faggiano *et al.* 2007 for the fire analysis of damaged portal frames due to earthquake according to the performance based procedure.

A study concerning the assessment of post-earthquake fire performance of steel-frame buildings was presented in the 14th World Conference on Earthquake Engineering by Yassin *et al.* (2008). The paper highlights that there is a need for developing a systematic approach to the evaluation of the post-earthquake fire-response. A scheme for the evaluation of PEF performance of structural systems for buildings proposed by Mousavi *et al.* (2008) is shown in Figure 2-1. Moreover a preliminary study of limited steel frames was presented. The study was conducted numerically, using SAFIR. In particular, a single-story and a two storey one bay moment resisting steel building frames have been considered and two types of structural models have been developed, one with fixed support condition, and the other with hinged support conditions. Concerning the fire load, the standard fire curve was used. The structure was analyzed using SAFIR. The earthquake was simulated through lateral loading. The analyses were performed for different magnitudes of the lateral loads. It was concluded that performance evaluation of building under fire or under earthquake separately is not sufficient. Building should be evaluated under the combined effect of fire following earthquake. The level of seismic performance of the structure should be correlated with the fire performance of the structure.

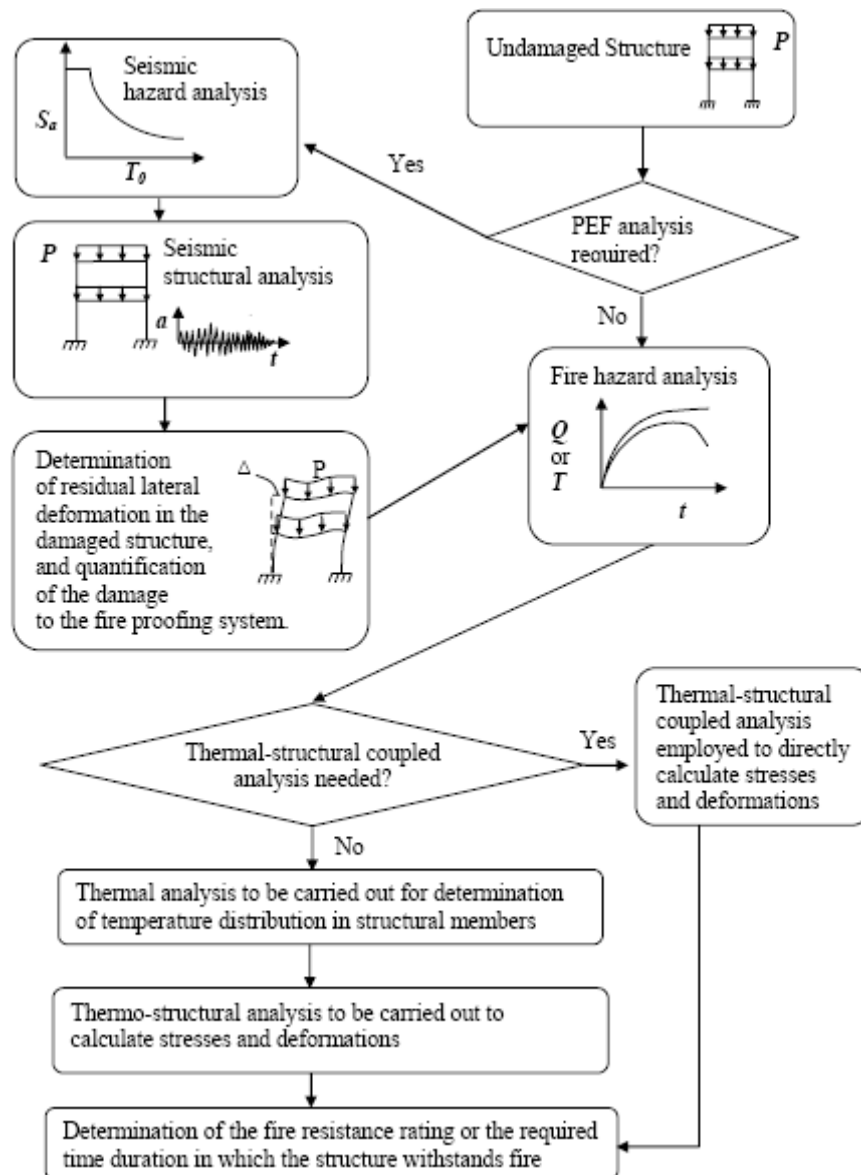


Figure 2-1: Schematic representation of the steps involved in the PEF performance evaluation of building frames (Mousavi *et al.*, 2008).

The combined scenario was also studied by Zaharia *et al.* (2007, 2008 and 2009). The study of Zaharia and Pintea (Zaharia and Pintea 2009), presents the evaluation of the fire-resistance time for four unprotected steel moment resisting frames that are damaged due to earthquake for both ISO and natural fire scenarios. The steel frames are designed for moderate and severe seismic actions. The design is conducted according to the Romanian seismic code adopted from the corresponding European standard CEN (2004). The design for one of the frames was governed by the fundamental load combination for gravity loading, while for all the other cases the design was governed by the seismic combination. The seismic response was evaluated through push-over analysis. The frame, where the critical combination corresponds to the gravity loading, remains undamaged. The rest frames remain undamaged for lower intensity earthquakes and in the case of more severe earthquake the behaviour corresponds to the Life Safety performance level according to FEMA 356 (2002). The fire is simulated through both the ISO fire curve and natural fire

curves. Specifically, the parametric model that is proposed in EN 1991-1-2 is used for the simulation of the natural fire in the compartment and the Ozone (Cadarin *et al.*, 2003) software is utilized for the production of the gas-temperature time-history. Two fire curves were produced for each building. The “before earthquake” curves (where all the fire-protection measures are active) are fuel controlled, having lower design fire load density and the flashover does not take place. The “after earthquake” curves are ventilation controlled. In this case, it was considered that the sprinkler system and the automatic fire detection are damaged due to earthquake and that are not active. The thermal analysis is conducted using SAFIR (Franssen *et al.*, 2010) software and the temperature profile of the structural members is obtained. The results of the structural analysis indicate two different collapse modes for both the ISO and the natural fire. It is concluded that the fire resistance time of damaged structures is influenced by the damage level. The highest differences, in terms of fire resistance, appear in the global mechanism. Moreover, it was observed that the structures that are designed for severe seismic actions have an important reverse of resistance in fire and fire after earthquake scenarios.

An interesting study was conducted by Della Corte *et al.* (2003). This paper studies numerically the effect of structural earthquake-induced damages on the fire resistance of moment resisting steel frames. Two different design strategies have been used for dimensioning the two selected frames. The first frame was designed for the Ultimate limit State (ULS) requirement of EN 1998, while the second frame was designed for the serviceability and the ULS requirements. The seismic action was modeled through eight different accelerograms which were scaled with respect to the PGA according to the well-known methodology of Incremental Dynamic Analysis (IDA). Temperature was assumed uniform in the selected compartment and monotonically increasing in accordance with the time-temperature curve suggested by the standard ISO-834. A basic issue of the study was the interpretation of the earthquake-induced damage, which has been schematized as the combination of two damage types: a ‘geometrical damage’, which consists of the residual deformation of the structure and a ‘mechanical damage’, which consists of the reduction of the main mechanical properties of the structural components (stiffness and strength degradation). At the end of each dynamic analysis, the residual lateral storey displacements of the frame were extracted from the numerical results, in order to compute the residual inter-storey drift angles. Then, the damaged frame was subjected to gravity-related loads and to the action of the fire scenario. The structural fire-resistance analysis has been conducted in the time domain, by checking the stability either of the whole frame or of one of its members. It is concluded that for low and medium seismic intensities and for well-engineered steel frames (e.g. those satisfying the serviceability requirement of seismic design) the effect of earthquake-induced damage can be neglected. Contrary, in areas of strong seismic intensities or for structures designed considering only the ULS seismic design requirement, the reduction of the fire resistance produced by earthquake induced damage could be significant and should be taken into account. Furthermore, the results were re-evaluated taking into account a limit value for the plastic rotation of beam-to-column connections. The *reference* target value was assumed to be equal to 0.03 rad as

representing a minimum satisfied by almost all well-engineered seismic moment connections according to FEMA 350 (2001). Accordingly, the numerical results that were obtained are considered to be valid in the range where the plastic rotation developed during the earthquake was less than 0.03rad. Taking into account the previous, it was revealed that in the case of the ULS frame, the reduction of the fire-resistance time was significant. On the contrary, for the frame designed considering the serviceability limit state seismic requirement, the fire resistance rating reduction seems to be negligible in the range of non-degrading seismic behaviour (small residual deformations).

Recently, a dissertation was conducted in the Lehigh University (Keller, 2012) about the thermo-mechanical response of steel moment-frame beam-column connections during post-earthquake fire exposure. The study considers the residual post-earthquake stress/strain field in the damaged assembly, the fragility of spray-applied fire-resistive material (SFRM) in moment-frame beam hinge regions and the thermal degradation and distortion of heat-affected steel. A case study of a ten-story steel moment frame, representative of a typical office building is developed. A non-linear dynamic response model for the test structure was developed in the finite element code OpenSees (OpenSees, 2011). The earthquake was simulated through recorded ground motions using the guidelines of FEMA P695 (2008). The normalized ground-motion records were scaled so that the median pseudo-acceleration response equaled the prescriptive spectral acceleration demand from ASCE/SEI 7-05. The deformation demands and the anticipated damage to SFRM insulation have been evaluated through non-linear response time-history dynamic analysis. In the sequel, a three-dimensional thermo-mechanical finite element model was developed for a representative moment frame beam-column assembly in the test structure, using Abaqus (Abaqus, 2011). It was noted that only one record caused side-way collapse of the structure. Inelastic deformations were shown to concentrate in the beam hinge regions, while the column and panel zone region remained within the elastic range. The fire was simulated through compartment fire models using large-scale fire test data. An idealized damage model for SFRM insulation was developed based on experimental findings. A multi-step sequential analysis procedure was developed to simulate the response of the beam-column sub-model during the earthquake excitation and post-earthquake fire exposure. In the first phase of the analysis the earthquake was simulated by imposing nodal displacement histories, which resulted from the dynamic analyses of the global structure, to the respective boundary nodes. In the post-earthquake stage the sub-model was submitted to two different fire scenarios and the moment –rotation response was obtained. The results lead to reductions in rotational stiffness of 30-50% and a 20-30% reduction in flexural capacity. Moreover, thermo-mechanical simulations of moment-frame beam-column sub-assembly response during post-earthquake fire exposure indicate that seismic damage to spray-applied fire-resistive (SFRM) insulation in beam hinge regions leads to increased heat penetration and temperature-induced softening of the moment-rotation response for the beam-column assembly. In the sequel, a numerical model for the global structure was developed in the nonlinear finite element software Abaqus (Abaqus, 2011) to study side-way response of the test structure during post-earthquake fire exposure.

The model utilizes the moment-rotation response extracted from the beam-column sub-assembly, for the members that lie within the fire-compartment. In this way the temperature effects are included in the model. The test structure remained stable during the post-earthquake fire scenarios. This was attributed to the robust moment-frame design and to the considerable rotational stiffness retained in the heat-affected beam hinge regions. Finally, it was observed that the extent of thermal degradation in moment-frame beam hinge regions and moment –frame columns was shown to have a significant effect on drift response during the post-earthquake fire-exposure.

2.4 Ductility of steel beams at ambient and high temperatures

The last decades, the ductility of steel structural members in terms of the rotational capacity was the subject of numerous experimental, analytical and numerical studies. The scientific research is mainly conducted at ambient temperature. The research is focused on the geometric factors that affect the development of local buckling and lead to the deterioration of the ductility of the structural members and on the calculation of the required values for the rotational capacity. A brief review follows, including only few representative studies. Kuhlmann (1989) conducted an experimental study for the definition of the flange slenderness limits on the basis of rotational capacity values. The study revealed that the basic parameters that affect the rotational capacity are the flange and web slenderness and the steepness of the moment gradient. An analytical approach for the prediction of local buckling and rotational capacity is proposed in the study of Daali and Korol (1995). The model can predict the rotational capacity at maximum moment i.e. when local buckling is initiated, given some specific values for flange and web slenderness. The determination of rotational capacity requirements was the subject of the study that was conducted by Choo and Nethercot (1995). The method that is proposed is based on the use of moment-curvature relationships and simplifies the determination of support rotations required for specific percentage redistributions of support members. A detailed theoretical study was conducted by Gioncu and Petcu (1997a) for the available rotational capacity of wide-flange beams and beam-columns limited by local plastic buckling. The most important factors that are included in the study are the material properties, the member dimensions, the interaction between flange and web, plastic buckling and cyclic loading. A computer program is presented for the evaluation of the ultimate plastic rotation. The study indicates that the concept of the cross-section behavioural classes should be substituted by the concept of member behavioural classes. Moreover, it proposes limits for the classification of the member behavioural classes (High, medium and low ductility). The companion paper (Gioncu and Petcu 1997b) presents the comparison of the theoretical results of the first study with experimental and numerical tests. The main factors affecting the rotational capacity are systematically studied. The results confirm that the provisions for ductility classes, given in codes, are not sufficient for a proper design. The research conducted by Earls (2000) uses experimentally verified non-linear finite element modeling techniques to identify two distinct inelastic modal manifestations that occur in compact I-shaped beams at failure. It is emphasized that a bifurcation point appears at the equilibrium path, at a load level close to the plastic

capacity of the cross-section. At this point there is a transition between the so-called Mode-1 and Mode-2 inelastic buckling manifestations. It is also concluded that the techniques used for the determination of the rotational capacity should consider cross-sectional geometry, unbraced length, yield stress and the strain hardening modulus. The study of Davies (2005) focuses on the strain hardening, local buckling and lateral torsional buckling in plastic hinges. In this study it is suggested that the local buckling of the compression flange, together with the interaction with lateral torsional buckling can offset the advantage of using strain hardening in the elastic-plastic stability design of plane steel frames. The more recent study conducted by Gioncu *et al.* (2012) presents new improvements for the determination of the rotational capacity of wide flange beams. The study presents the new version of DUCTROT which considers both the out-of-plane and in-plane plastic mechanisms and includes the application of gradient and quasi moments. The companion paper (Anastasiadis *et al.*, 2012) discusses the importance to eliminate, through constructional details, the out-of-plane buckling mode. Several solutions are proposed depending on the cross-sectional type. For preliminary design, a simple rule of thumb is to select the flange and the web thickness to be of the same order. In the experimental study conducted by D'Aniello *et al.* (2012) it is highlighted that the loading conditions have significant influence on the rotational capacity. During the experimental program a wide range of cross-section typologies is tested under monotonic and cyclic loading. It was observed that the rotational capacity is reduced under cyclic loading conditions with respect to the monotonic loading conditions due to web buckling, which occurs after the flange buckling. Additionally, it was detected that for I and H shapes the cyclic flexural over-strength could be larger than the one in monotonic tests due to the isotropic hardening. Finally, it is highlighted the need of further research to determine the rotational capacity of flexural members under seismic and non-seismic conditions.

Unlike the extensive research activity related to the ductility of structural members at ambient conditions, the research at elevated temperatures is limited. A strain-based approach to local buckling of steel sections subjected to fire is proposed in Knobloch and Fontana (2006). This study stresses that the local buckling under fire conditions needs to be considered in the context of a wide range of cross-sectional slenderness than at ambient temperature. This can be attributed to the non-linear behaviour of steel at elevated temperatures and moreover to the fact that large strains are required for the achievement of the cross-sectional capacity. The novel design method that is proposed in this paper can be used for the calculation of the resistance of stiffened and unstiffened elements at elevated temperatures. The design method is validated against results that arise from numerical simulations of steel under fire conditions. The advantage of the approach is that it can be used for any type of cross-section. The strain-based approach results to the calculation of the load-deflection behaviour (including the descending branch), which is necessary to determine the ductility and to avoid the marginal strain limitations necessary in stress-based design which leads to unsafe predictions.

An extensive experimental program was conducted to investigate the rotational capacity of

steel I-beams under fire conditions (Dharma and Tan, 2007a). It is noted that the specific experimental program was the first one that was conducted worldwide for the investigation of the rotational capacity of steel beams at elevated temperatures. The main objectives were to determine the effects of temperature on the rotational capacity and to identify the key parameters that affect the rotational capacity. Totally nine steel beams were tested with four varied parameters: temperature, flange slenderness, web slenderness and effective length. All the specimens were designed in order to achieve their plastic moment capacity at elevated temperatures. The specimens (simply supported beams) were heated up to the desired temperature level (415 °C or 615 °C) and then they were subjected to a mid-span point load until failure. The results of the fire tests showed that no local or global buckling took place before the plastic moment capacity was reached. Two failure modes were observed: local buckling of the beam flange near the mid-span and global lateral torsional buckling (LTB). The local buckling of the compression flange was more obvious with respect to the web buckling and the LTB was a result of spread of yielding after plastic moment capacity was reached. Moreover, the test results indicated that shorter effective lengths provide greater rotational capacity and change the failure mode from LTB to local buckling of flange and web. This study highlights that the rotational capacity is reduced at elevated temperatures and that the primary difference of moment-rotation curve at elevated temperature compared to the corresponding one at ambient temperature is the non-linear pre-buckling stage, which takes place due to the non-linear stress-strain relationship of steel at elevated temperatures. In the companion paper (Dharma and Tan, 2007b) numerical models were developed for the prediction of the rotational capacity at elevated temperatures. The finite element (FE) model was developed using the finite element code MSC-Marc (2011) and it was validated against published test results at ambient temperature. The objectives of this study was to investigate the feasibility of applying the finite element method to study the moment-rotation relationship of steel I-beams at elevated temperatures and to conduct parametric analyses in order to find out the main parameters that affect the phenomenon. The results of the parametric analyses, concerning the temperature level, showed that for temperature greater than 300 °C, the rotational capacity is significantly reduced. This is attributed to the reduction in the modulus of elasticity and to the reduced value of the proportionality limit. Finally, a simple moment-rotation relationship at elevated temperature was developed for use in design. This simple model consists of three parts: a non-linear pre-peak curve, a horizontal plateau set conservatively at the plastic moment capacity, and a softening curve. Comparisons between the design model, FE predictions and test results showed that this design model is comparatively accurate, hence useful for design purposes, without recourse to finite element modeling.

2.5 Contribution of the dissertation

The progress in the research and the state-of-the-art review concerning all the scientific areas that are of interest in the current dissertation were discussed in previous Sections of this Chapter. The contribution of the dissertation is mainly focused on three different fields: the fire-structure interface, the modeling/analysis for structures under the combined

effect of fire after earthquake and the assessment of the rotational capacity of steel beams at elevated temperatures.

In the case of the modeling of natural fire through the CFD principles, the transition of the data from the CFD analysis to the structural model is of great importance since the determination of temperature profile of the structural members is an absolutely critical parameter during the structural analysis. The study of the literature indicates that the “fully-coupled” approach is a hard task and for this reason it is not used. Moreover, the scientific research for the Fire-Structure Interface (FSI) is limited. The contribution of this dissertation in this field is the development of a FSI model, which is referred in this document as simplified “dual-layer” model. The model can be utilized at the post-processing stage of CFD analysis and it is based on the gas-temperature field (spatial and temporal) of the fire-compartment. The model can be used for design purposes in the cases where fire-compartments exceed the “regular” dimensions, as they are defined by the guidelines of the codes. Specifically, the main objective is the numerical determination of the gas-temperature (discrete) function along the height of the fire-compartment, at discrete plan-view points. The model “compresses” the point data to (spatial) virtual zones, which are divided into two layers (with respect to the height of the fire-compartment) of uniform temperature: the upper (hot) layer and the lower (cold) layer. In this study, the modeling of the natural fire is conducted in FDS, but, in general, any code can be used. In this way, the gas-temperature time-history is determined at the virtual-zones and the calculation of the temperature profile of the structural members can be conducted according to the guidelines of EN 1991-1-2. The main advantage of this methodology is that actually, only three different variables (height of interface, upper and lower layer temperature) are required during the post-processing stage of the CFD analysis. Moreover, the calculation of the temperature profile of the structural members becomes an easy task, since it can be handled through the simplified guidelines of EN 1991-1-2.

The main contribution of this study is in the field of numerical modeling and analysis of steel structures under FAE loading. The first point of contribution of this dissertation is that the study of the behaviour of steel structures for the combined loading is based on the damage, that is induced due to earthquake, to both structural and non-structural members. The literature review reveals that the structural damage is taken into account in all the published studies. Additionally, it is noticed that the effects of the non-structural damage to the fire-behaviour of the damaged structure and finally, to the fire-resistance has not yet been studied. It is specified that in this dissertation the non-structural damage is simulated through the percentage of the windows that are broken during the earthquake and through the quantification of the damage induced in the sprinkler system. This is taken into account during the CFD simulation. The consideration of the above, results in different ventilation conditions in the fire-compartment, and subsequently, to different gas-temperature time history results. In this way different FAE are generated, with respect to the fire loading stage.

The second contribution point of this dissertation in the field of FAE is the modelling and numerical analysis techniques, that are proposed for the determination of the fire-structural performance of the earthquake-damaged structures. Specifically, an integrated numerical model is proposed, which simulates accurately the behaviour of the structure for both the fire and the seismic loading and it can be utilized for design purposes taking into account the FAE loading. The model incorporates the dynamic characteristics that are required for the simulation of the response of the structure during the seismic action and in the same time it includes the temperature dependent mechanical and thermal properties of steel at elevated temperatures. Specifically, the two-dimensional model that is developed, utilizes beam finite elements and it is formulated taking into account the concept of the concentrated plasticity. Moreover, this dissertation proposes techniques for the numerical analysis in the case of FAE loading. The techniques are referred to the problems that arise in this case connected to the different scale of the duration of earthquake and fire events. The earthquake lasts few minutes, while the duration of the fire exposure is estimated to be almost one hour. Thus, the incorporation of the different events in the same analysis introduces several problems concerning the required time step that has to be solved.

The third contribution point of this dissertation in the area of the FAE is associated to the calculation of the fire-resistance of the structure, taking into account failure criteria that are based on the ductility of structural members at elevated temperatures. The criteria are defined in Chapter 13. The literature review identifies that the criteria used in other studies are based on the strength or stability of structural members or on the global stability of the structure. In this study, the failure criteria take into account the rotational capacity of beams at elevated temperatures. Moreover, different criteria are used depending on the 'level of damage' that is induced in the structure during the earthquake loading.

Finally, the contribution of the study in the field of the assessment of the ductility of structural members at elevated temperatures should be mentioned. As it has already been referred in Section 2.4, the scientific research in the specified area is limited. This dissertation proposes three-dimensional numerical models for the calculation of the rotational capacity of steel I-beams under fire conditions. The models take into account the possible local buckling that may arise as the temperature increases, while the possible lateral torsional buckling is excluded. Moreover, the study in this area is further extended to the determination of the rotational capacity of beams that are damaged due to cyclic loading. In this point the contribution is totally innovative, since there is no scientific research in the specific field. Parametric analyses are conducted with respect to the level of induced damage and to the amplitude of the considered initial imperfections. The results are interpreted in rotational criteria, used for the determination of the structural fire-resistance in time and temperature domain

Chapter 3. Elements of fire-behaviour in an enclosure

This chapter deals with the fires that take place in an enclosure of a fire-compartment. This case is different from the fire development in the exterior. The development of the compartment-fire has three distinct stages, the growth period, the steady burning stage and the decay phase. In the very early stage of the growth period, the combustion, which happens due to the ignition sources is limited to local areas and the temperature of the gases are low. The important issue during this stage is the smoke concentration which reduces the visibility in the fire-compartment and the toxic gases that are released. According to the literature (Purkiss, 2007), a large number of fires never get beyond this stage either due to insufficient fire load or due to deficiency of airflow in the fire-compartment. The interest of the fire research community is focused in this stage in order to study the ignition, the combustion and the production of smoke and to control the evacuation of the building. However, most fire-structural engineers focus on the post-flashover (steady burning) period where the fire is fully developed, since all the available combustible materials are burnt and the temperature of the hot-gases is very high.

3.1 Description of the fire development in the fire-compartment

The stages of development of the fire in an enclosure are described in Figure 3-1. During the fire growth period, the fire is limited in a small area and only localized temperature rise can be detected. The temperature distribution in the fire-compartment is highly non-uniform. The danger during this stage can be attributed only to the release of toxic gases and to the thick layer of smoke. The fire will not pass to the next stage if the fire-protection systems are fully active. Also, if the first ignition point is not too close with other ignition sources or combustible materials, the fire will immediately pass to the decay period. Another possibility that would prevent the fire from the flashover is the insufficient supply of oxygen. It is noted that in many cases the human intervention supplies the fire-compartment with fresh air and this may lead to sudden flashover, which is possible to be very dangerous for the fire-fighters.

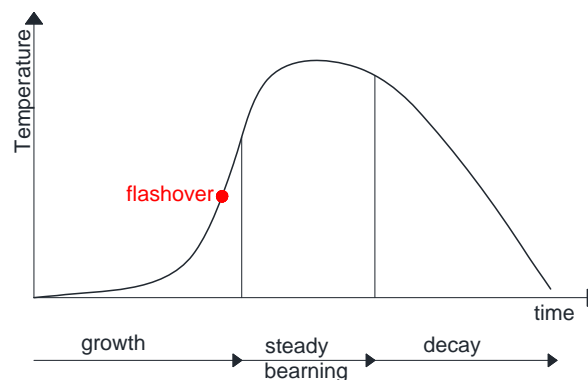


Figure 3-1 Description of the fire in an enclosure.

In fire engineering, it is assumed that the ventilation conditions will contribute to the fully fire-spread in the compartment. According to Wang (2002), during the fire growth stage the hot gases that are released from the burning of the combustible materials are rising to the ceiling of the fire-compartment due to the buoyancy. At the same time, if the air supply is sufficient, more smoke is released. When the smoke layer covers the whole area of the ceiling, it will move down therefore heating the walls of the fire-compartment. As the air supply continues, the layer of the smoke becomes thicker and, at a certain time, it reaches the level of an opening (window, door etc.). Then, the smoke flows out of the compartment until the phenomenon is stabilized. At this stage the fire-compartment is divided into two different zones, the upper layer and the lower layer. At the upper layer there is an outflow of the smoke and at the lower layer there is an inflow of the fresh air.

During this stabilization phase, the smoke layer is supplied with more combustible gases and the temperature rises in the fire-compartment. At the same time, the flame becomes higher and fire spreads due to high concentration of the partially burnt fuels in the smoke layer. The fire-spread is accelerated due to the radiation of the flames and the fire passes to the flashover period when the radiation of the unburned combustible materials becomes high. The flashover is defined as the time when, suddenly, all the combustible materials in the enclosure ignite almost simultaneously due to the high rise of the temperature. The fire is no more a local phenomenon. The stage of the fire growth is referred also as pre-flashover period and the subsequent stage as post-flashover period. The transition between the two stages is very quick. During the post-flashover stage the temperature in the fire-compartment increases rapidly and it is possible to reach the value of 1000°C in the fire enclosure. Both stages are schematically described in Figure 3-2.

In the post-flashover stage, the fire enters to the steady burning stage. In most cases, there are enough combustible materials in the fire-compartment and the fire burning rate depends on the supply of fresh air. In this case, the fire is referred as ventilation controlled. In the case where the amount of the combustible materials is not enough, the burning rate depends on the area of the burning fuels and the fire is indicated in the literature as fuel-bed controlled. In the sequel, the rate of the fuel combustion decreases and the fire passes to the decay phase and the temperature in the fire-compartment decreases. The fire ends when all the combustible materials have been consumed.

The fire that is developed in an enclosure depends on the fire-department characteristics, the ventilation conditions and the available combustible materials, is commonly referred as *natural fire*.

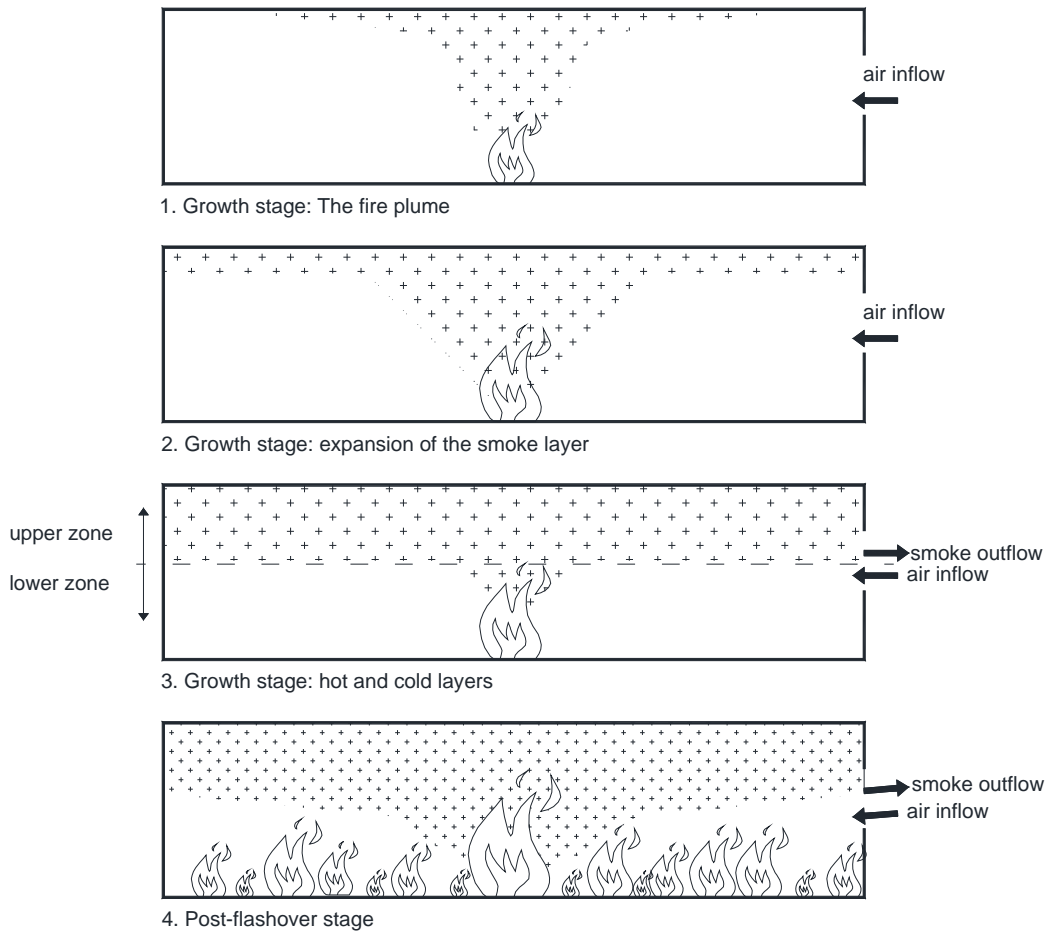


Figure 3-2: Description of the pre-flashover and the post-flashover stages.

3.2 Modelling of the fire action according to guidelines of EN 1991-1-2

According to the guidelines of EN 1991-1-2, the thermal action can be represented either by the nominal temperature-time curves or by natural fire models. The term nominal is used to express the fact that these curves do not represent real fire-conditions. Actually, the “nominal” fire-curves are arbitrary and they should be used only for prescriptive requirements. In this sense, the equivalent time used in these expressions should not be compared to the real time needed for the evacuation of the building (Franssen, 2010). The standard ISO temperature-time fire curve is commonly used today for the determination of the fire-resistance of structural and non-structural components. The standard curve which represents a fully developed fire in a compartment is given by the mathematical expression (1) and it is represented in Figure 3-3:

$$\theta_g = 20 + 345 \log_{10}(8t + 1) \tag{3.1}$$

where θ_g is the gas-temperature in °C and t is the time in minutes.

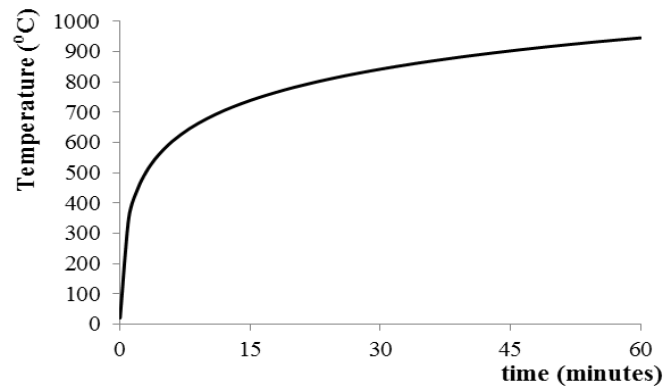


Figure 3-3: The ISO fire curve.

The natural fire models are divided into simplified models and advanced ones. The simplified models (parametric temperature-time curves) take into account the most fundamental parameters that influence the physical phenomenon, which are the geometry of the fire-compartment, the thermal properties of the enclosure (walls, floor and ceiling), the fire load density and the openings. The temperature in this case is assumed to be uniform in the fire-compartment. These models are limited to fire-compartments of area up to 500m², of height up to 4m without roof openings.

The advanced models are the Computational Fluid Dynamics (CFD) and the zone models. The CFD modelling is the most accurate and detailed technique and it is applied in a wide range of problems. The fire-compartment is divided in control volumes. Following the principles of CFD, the partial equations of mass, momentum and energy transfer are formulated. The appropriate boundary and initial conditions are applied, the equations are assembled and the numerical solution is obtained. The CFD modeling is used for both the prediction of the production and flow of smoke during the pre-flashover stage and for the simulation of the fire spread during the post-flashover stage of the natural fire. The main output of the CFD simulation is the temperature evolution in the fire-compartment in a completely time dependent and space dependent manner. Additional results are the heat release rate, the mass loss rate, the burning rate, the pressure distribution, the velocity field etc.

A more simple approach is the zone modeling. This technique is less complicated than the CFD models but the results are less detailed. A basic advantage of this technique is that it can be used for multiple, adjacent fire-compartments. Zone models are based on the balance equations of mass and energy. The main parameters that are taken into account are the same that are considered in the case of the parametric models, in a more detailed manner. The exact positions and the dimensions of the openings on the walls and ceiling are taken into account. Additional possibilities are included as the forced ventilation conditions and the opening of a window (human intervention) at a given time or by giving a temperature criterion (breakage of the window). Another important issue is the fact that the HRR (Heat Release Rate) curve can be used as an input.

Two different types of zone models (two-zone and one-zone) are used. Regarding the pre-flashover stage, the fire-compartment is divided into two different zones, the hot smoke (upper) zone and the cold air (lower) zone. It is assumed that the temperature is uniform at each layer. The zone models are also used for the post-flashover stage. In this case the fire-compartment is considered as one zone with uniform temperature. Also it is possible to start the simulation with two zones and in the sequel to shift to one-zone, provided that some specific criteria are satisfied. From the above it is clear that the zone models are a powerful tool for the study of fire in an enclosure. Zone modeling is a popular technique in fire-structural engineering, since it is simple and offers a good qualitative approach for the fire development in the enclosure.

It is noted that all the previous techniques, are actually deterministic approaches of natural fire. The random character of the physical phenomenon involves many uncertainties and it should be studied through probabilistic models. Random factors are the position of ignition source of fire, the wind velocity outside of the fire-compartment, the ventilation conditions of the enclosure (open doors and windows), the available combustible materials, etc. Many researchers tried to develop probabilistic models but due to the complicated characteristics of the fire-development in an enclosure, the models are not definite and have not been incorporated in guidelines or regulations (Wang, 2002).

Chapter 4. Numerical simulation of natural fire

This chapter concerns the numerical simulation of the fire development in an enclosure through the principles of computational fluid dynamics. In this dissertation the numerical simulation is conducted in Fire Dynamics Simulator (FDS, McGrattan *et al.*, 2010a,b), a Computational Fluid Dynamics code for the simulation of thermally driven flows with an emphasis on smoke and heat transport from fires.

The simulation of fire is the first issue. Both the pyrolysis and the combustion are discussed. Two different approaches for the pyrolysis modeling are presented. Since fires involve combustible gases the dynamic behaviour of the gases as fluid is encountered. This is accomplished taking into account the fundamental laws of fluid mechanics and heat transfer that are briefly discussed in this Chapter. Another goal of this Chapter is to present the numerical techniques of FDS (McGrattan *et al.*, 2010a,b). The mathematical model that is incorporated in the code is briefly described. Specifically, this Chapter presents the governing equations that are solved, the limitations and the assumptions that are used in the code and the solution procedures that are available in FDS (McGrattan *et al.*, 2010a,b). Concerning the solution procedures, the issue that arises is the treatment of turbulence. Compartment fires are generally turbulent. Despite the significant research on this issue, it is still not feasible to solve the conservation equations directly within the required accuracy. Turbulent flows are extremely complex time-dependent flows and special turbulent models have been proposed in the literature. This Chapter presents a brief description of turbulence modeling as it applied for the needs of fire simulation.

4.1 Fire modeling

Most fires involve combustible solids. However, in certain occasions (e.g. industry) liquid and gaseous fuels are met. According to Drysdale (2002) the term fuel can be used to describe whatever is burning (solid, liquid or gas). Fire engineering problems are related to fuels that are carbon-based. All fuels burn under appropriate conditions, reacting with oxygen from the air, generating combustion products and releasing heat. Flame is a visible portion of the volume, where the oxidation occurs. Specifically, flame is a gas phase phenomenon and in the case of solids fuels, the conversion to gaseous form should be involved. Regarding the burning liquids, the process is normally simple evaporation at the boiling point. For solids, the chemical decomposition (or pyrolysis) yields products of sufficient low molecular weight that can volatilize from the surface and enter the flame. Since the energy required for pyrolysis is much higher compared to simple evaporation of the fluids, the temperature of the surface is usually very high (typically 400°C).

The volatiles comprise a complex mixture of pyrolysis products, ranging from simple molecules to high molecular weight chemical compositions. The combustible volatiles react with the oxygen in the air which enters the combustion zone. The air entrance may be free or driven by forces depending on the ventilation conditions of the fire-compartment (Figure 4-1). In the case of combustible solids, the rate of burning (\dot{m}'') depends on the rate of supply of volatiles from the fuel surface and to the rate of heat transfer to the fuel. The most important parameter that characterizes the fire is the rate at which the energy is released. This is defined through equation:

$$\dot{Q}_c = \chi \dot{m}'' A_f \Delta H_c \quad (4.1)$$

where,

\dot{Q}_c is the released energy rate,

χ is a factor (<1.0) included to account for the incomplete combustion,

\dot{m}'' is the rate of burning,

A_f is the fuel surface area,

ΔH_c is the heat combustion of the volatiles.

An illustrative description for a carbon based fuel is given in Yeoh and Yuen (2009). In this case the chemical reaction generates the combustion products such as carbon dioxide and water vapor. Actually, a series of elementary reactions steps take part during the combustion. Heat is released following the chemical reaction, which is an exothermic process. Smoke is produced during the fire. Apart from the combustion products, smoke may contain high-concentration of finely dispersed particles, known as soot, or gases such as carbon monoxide, depending on the nature of the fuels that are involved. Radiation from these hot gases and flames is very important. Due to the radiation, heat is supplied by the visible flame into the solid surface. Moreover, volatiles are continuously supplied into the combustion zone for flaming combustion.

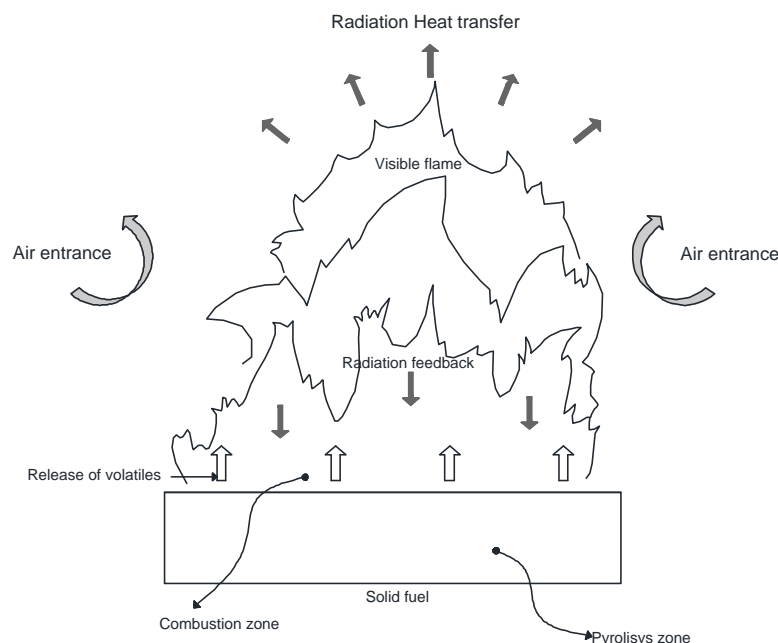


Figure 4-1: Schematic representation of a burning solid fuel.

In order to simulate numerically the fire, the pyrolysis model is adopted. This model includes the solid phase reactions in order to describe the chemical decomposition of the solids, which is conducted for the production of the volatiles that escape from the surface to in the sequel they burn in the flame. The combustion model is also required. This model describes the reaction between the fuel and the oxygen, which are initially separate and they burn in the region where they mix (diffusion flames).

The fire-engineering community usually bypasses this complexity, by relying on the results of real tests instead of using a pyrolysis model. This approach, adopted for the fire simulation, is based on a specified heat release rate (HRR) of a fire-test. This means that the heat release rate is just entered as an input to the solution process and no calculations are required. In this case, the desired HRR is transformed into mass flux for fuel at a given solid surface, which is usually called surface burner.

4.2 Computational Fluid Dynamics in fire enclosure modeling

The equations describing the transport of mass, momentum, and energy by the fire-induced flows must be simplified so that they can be efficiently solved for the fire scenarios of interest. The general equations of fluid dynamics describe a rich variety of physical processes, many of which have nothing to do with fires. Retaining this generality would lead to an enormously complex computational task, that would shed very little additional insight on fire dynamics. The simplified equations, developed by Rehman and Baum (1978), have been widely adopted by the larger combustion research community, where they are referred to as the “low Mach number” combustion equations. They describe the low speed motion of a gas driven by chemical heat release and buoyancy forces. Oran and Boris provide a useful discussion of the technique as applied to various reactive flow regimes. They comment that “There is generally a heavy price for being able to use a single algorithm for both fast and slow flows, a price that translates into many computer operations per time step often spent in solving multiple and complicated matrix operations.”

4.3 Fire Dynamics Simulator

4.3.1 General description

Fire Dynamics Simulator (FDS) is a Computational Fluid Dynamics model of fire driven fluid flow. FDS (Mcgrattan *et al.*, 2010a,b) is a Large Eddy Simulation (LES) code for low speed thermally driven flow emphasizing mainly on smoke and heat transport deriving from fires. The partial derivatives of the conservation equations of mass, momentum and energy are approximated as finite differences, and the solution is updated in time on a three-dimensional, rectilinear grid. A finite volume technique is being used in order to calculate the thermal radiation on the same grid as the flow solver and smoke movement, sprinkler discharge and fuel sprays are simulated with the use of Lagrangian particles.

Along with FDS, an accompanying visualization program, Smokeview (Forney, 2007), produces images and animations of the results and it is able to visualize fire and smoke in a fairly realistic way. Three-dimensional realistic renderings of the fire and smoke

development can be produced by Smokeview, along with the described geometry.

The code was originally developed by the National Institute of Standards and Technology (NIST) and the first version was publicly released in 2000.

This software is aiming at solving practical fire problems in fire engineering, but it can also be used as an analytical tool for fire dynamics and combustion. As a fire engineering tool it can be implemented in the analysis of: (a) Low speed transport of heat and combustion products of fire, (b) Radiative and convective heat transfer between gas and solid surfaces and (c) Sprinkler, heat detector and smoke detector activation. More advanced physical phenomena such as pyrolysis, flame spread and fire growth, sprinkler activation and fire suppression by water, can also be modeled with this software.

FDS software is considered to be a suitable candidate for fire related professions such as the fire service, as well as for the study and analysis of residential and industrial fires by engineers. It is highly important though, that this software is used as a supplement to the informed and qualified engineer and not as a predictive tool, mainly cause of the complexity of the phenomena that are modeled and the large number of parameters that need to be provided. So far, 50% of the model applications have been applied in designing smoke control systems and for sprinkler/detector activation studies and the other half aim at residential and industrial fire reconstructions.

4.3.2 Input parameters

All the necessary input parameters of the model and the corresponding fire scenario are described in a text file. The basic parameters are:

- information regarding the numerical grid (it consists of one or more rectilinear meshes with (usually) uniform cells. All geometric features must conform to the specified grid, and all objects smaller than the grid are either ignored or approximated as a single cell. Due to the rectilinear grid, all the building's entities are described as a series of rectangle blocks, and the geometric description detail is defined by the mesh refinement.)
- ambient environment
- building geometry
- material properties (defined by their thermal conductivity, specific heat, density, thickness, and burning behaviour)
- combustion kinetics
- desired output quantities.

When simulating real fire scenarios in real structures, all the properties regarding building's walls, floors, ceilings and furnishings need to be provided. All these objects are treated as multi-layered solids, therefore many real object physical parameters can only be viewed as approximations to the actual properties. The accurate and appropriate description of the properties of these materials define the fire development, thus user's attention is highly required. Although many material properties databases can be found scripted or online, their description can be very challenging for the user. Thermal

properties such as conductivity, specific heat, density, and thickness can be found in various handbooks, or in manufacturers' literature, or from bench-scale measurements, whereas materials' burning behaviour at various heat fluxes is rather difficult to be described, and the properties more difficult to be obtained.

4.3.3 Output parameters

All the variables described in the equations (temperature, density, pressure, velocity and chemical composition) that are used to perform the numerical calculations, can be used as output parameters and they are all available in every grid cell for every discrete simulation time step. Moreover, the temperature, heat flux, mass loss rate, and various other quantities can be computed by FDS at solid surfaces. Due to the excessive amount of the produced output quantities cause of the large number of grid cells and time steps, which are usually in the magnitude of thousands or millions, and the huge data files requirements, the user is advised to choose in advance the output quantities that should be recorded, as it would be done in the case of a real experiment.

Typical output quantities for the gas phase include: gas temperature, velocity, density and species concentration (water vapor, CO₂, CO, N₂), smoke concentration and visibility estimates, pressure, heat release rate per unit volume, mixture fraction (or air/fuel ratio) and water droplet mass per unit volume.

On solid surfaces, FDS can predict quantities associated with the energy balance between gas and solid phase, such as: (a) Surface and interior temperature, (b) Radiative and convective heat flux, (c) Burning rate and (d) Water droplet mass per unit area.

Global quantities recorded by the program include:

- Total Heat Release Rate (HRR)
- Sprinkler and detector activation times
- Mass and energy fluxes through openings or solids

The various quantity time histories at single points are simple data sets that can be easily plotted. The more complex field or surface data are visualized with the use of Smokeview (Forney, 2007) in 3D surfaces or section slices.

4.3.4 Governing equations and additional models

In order to provide the fire-compartment flow, mass, momentum and energy conservation equations are used. Additional models that include the turbulence, the combustion, the smoke production – movement and the solid pyrolysis are required in practical fires, in order to capture the entity of the physical phenomenon and these models are included in the numerical model. Here are presented the basic components of FDS and the additional models.

Hydrodynamic Model

FDS solves numerically a form of the Navier-Stokes equations appropriate for low speed, thermally-driven flow with an emphasis on smoke and heat transport from fires. The core algorithm is an explicit predictor-corrector scheme that is second order accurate in space and time. Turbulence is treated by means of the Smagorinsky form of Large Eddy Simulation (LES). It is possible to perform a Direct Numerical Simulation (DNS) if the underlying numerical grid is fine enough. LES is the default mode of operation.

Combustion Model

FDS uses a combustion model based on the mixture fraction concept for the majority of applications. The mixture fraction is a conserved scalar quantity that is defined as the fraction of gas at a given point in the flow field that originates as fuel. Fuel and oxygen reaction is not necessarily instantaneous and complete, and the extent of combustion in under-ventilated spaces can be predicted by several optional schemes designed for that purpose. The mass fractions of all of the major reactants and products can be derived from the mixture fraction by means of “state relations,” expressions arrived at by a combination of simplified analysis and measurement.

Radiation Transport

The model also includes radiative heat transfer via the solution of the radiation transport equation for a gray gas. A better spectral accuracy can be provided by the use of a wide band model instead of the gray gas model. Finite Volume Method (FVM) is used to solve the radiation equation with the use of a technique similar to a finite volume method for convective transport. *Given the complexity of radiation heat transfer, the finite volume solver requires only 20 % of the total CPU time of a calculation, using approximately 100 discrete angles.*

Geometry

FDS approximates the governing equations on one or more rectilinear grids. The user prescribes rectangular obstructions that are forced to conform to the underlying grid.

Boundary Conditions

Thermal boundary conditions and information about material’s burning behaviour are assigned to all solid surfaces. Heat and mass transfer to and from solid surfaces can be calculated either with applying the Direct Numerical Simulation (DNS), or via empirical correlations.

Sprinklers and Detectors

Simple correlations of thermal inertia for sprinklers and heat detectors are used for modeling the activation of sprinklers and heat detectors, whereas transport lag is used for smoke detectors. Lagrangian particles are used to model the sprinkler sprays and they represent a sampling of the water droplets ejected from the sprinkler.

4.3.5 Numerical simulation techniques – Turbulence modeling

Large eddy simulation (LES)

The phrase LES refers to the description of turbulent mixing of the gaseous fuel and combustion products with the local atmosphere surrounding the fire. The outcome of this process is the determination of the burning rate in most fires and the ability to control the spread of smoke and hot gasses. The above characteristics can not be predicted accurately in an easy way though and this refers to both fire research and all phenomena involving turbulent fluid motion. Large Eddy Simulation (LES) is based on the observation that the small turbulent structures are more universal in character than the large eddies and therefore it is only important to calculate the momentum and energy transfer of the large eddies and not the momentum and energy transfer of these small turbulent structures which can modeled separately. More specific, in the case of combustion modeling, we consider that the equations of fluid dynamics can accurately calculate the eddies that account for most of the mixing of the gaseous fuels and combustion products with the atmosphere of the fire, without including the calculation of the small scale eddies in the computational mesh.

Direct numerical simulation

Direct Numerical Simulation (DNS) is the most straightforward approach. The solution is obtained by solving directly the Navier-Stokes equations without any turbulence model. This means that the turbulence must be resolved in the computational mesh. A mesh capable of such a task would have to account for the whole range of spatial and temporal scales of the turbulence. This approach requires very high computational recourses, which are still unavailable for the usual problems of engineering, such as the simulation of building fires.

4.3.6 Solution procedure

FDS uses a second-order accurate finite-difference approximation to the governing equations on a series of connected recti-linear meshes. The flow variables are updated in time using an explicit second-order Runge-Kutta scheme.

4.3.7 Limitations and assumptions

Although FDS can address most fire scenarios, there are limitations in all of its various algorithms.

Low Speed Flow Assumption

FDS's usage is limited to a low-speed flow - specifically to Mach numbers less than 0.3 - and the focus stays on the heat transport and smoke from fires. Based on this presumption, it is impossible to use this particular model for any outline that requires flow speeds which are close to the speed of sound (for example explosions, detonations or choke flow at nozzles)

Rectilinear Geometry

The performance of FDS is caused by the clarity of its rectilinear numerical grid and, also, by using a fast and direct solver for the pressure field. This might be a limitation in certain situations where particular geometrical features are not conforming to the rectangular grid, although most components of building do. It should also be noted the fact that in FDS there are techniques to lessen the effect of “sawtooth” obstructions useful for the representation of the nonrectangular objects, these cannot be expected to produce a good result, if, for example, the reason for the calculation is to study boundary layer effects. In general, for the practical large-scale simulations, the increased grid resolution afforded by the fast pressure solver offsets the approximation of a curved boundary by small rectangular grid cells.

Fire Growth and Spread

Due to the fact that the model was created initially to analyze industrial-scale fires, it can also be easily used when the heat release rate (HRR) of the fire is specified, and the main purpose of the simulation is the transport of heat and exhaust products. In cases like these, the model can provide information about flow velocities and temperatures with an accuracy within 10% to 20% of the experimental measurements, taking into account the resolution of the numerical grid.

Nevertheless, for fire scenarios where the heat release rate is predicted and not specified, the uncertainty of the model can be higher. Some of the reasons are as follows:

- It is often difficult to obtain the properties of real materials and fuels; at time, these can also be unknown;
- The FDS representations of processes of radiation, combustion and solid phase heat are simpler than the actual physical processes;
- The calculation results are sensitive to physical and numerical parameters as well.

Modeling fire growth and spread stands in need of a proficient level of user skill and judgment than the one required for modeling the transport of heat and smoke from specified fires.

Combustion

FDS utilizes a mixture fraction-based combustion model for most applications. This mixture fraction is a conserved scalar quantity that is defined as the fraction of gas at a given point in the flow field that originated as fuel. When in its most simple form, the model ensures that combustion is mixing controlled, and also, that regardless of the temperature, the reaction of oxygen and fuel is infinitely fast. This assumption is great for well-ventilated, large-scale fires. Nonetheless, if a suppression agent like water mist or CO₂ is introduced, or if the fire is in a poorly ventilated compartment, oxygen and fuel can mix without burning, according to a several empirically-based criteria. The physical mechanisms underlie that these phenomena are tied closely to the temperature of the flame, the local strain rate, none of which can be found available in simulations of fire on a large scale. Subgrid-scale modeling of gas phase suppression and extinction is still an area of active research in the combustion community. In expectation of the development of

reliable models for building-scale fire simulations, basic empirical rules are utilized to prevent burning from occurring when the atmosphere encompassing the fire cannot sustain the combustion.

Radiation

Radioactive heat transfer is included in the model through the radiation transport equation (RTE) for a gray gas, and, in certain limited cases, by using a wide band model. The RTE is solved by using a technique similar to finite volume methods for convective transport, hence its name: Finite Volume Method (FVM). This model does present a few limitations:

- The radiation transport is discretized through approximately 100 solid angles; the user can choose to use more angles. When dealing with targets far away from a localized radiation source, like for example a growing fire, the discretization may lead to a fluctuating distribution of the radiant energy. This error is known as “ray effect” and it is visible in the visualization of surface temperatures, where “hot spots” show the outcome of the finite number of solid angles. The issue can be mitigated by including more solid angles, which will also cause longer computing times. Generally, the radioactive flux to farther targets is less important than the one in the near-field ones, where a much better coverage of the default angles.

-

- The absorption coefficient for the smoke-laden gas is a complex function of its temperature and composition. Due to the basic nature of the combustion model, the chemical composition of smoky gases (and especially the soot content) may affect emission and absorption of thermal radiation.

Chapter 5. Elements of heat transfer theory

This Chapter focuses on the heat transfer theory, applied in fire-engineering problems, for the determination of the temperature-profile of the structural members. Since, the problem of the fire development in the enclosure is solved; the gas-temperature time-history is obtained. The heat transfer from the hot-gases to the surfaces of the structural members takes place through convection and radiation. Then, the heat is transferred through the conduction mechanism. The differential equation that describes the problem of heat conduction is solved by the application of the appropriate solid-fluid boundary conditions that describe radiation and the convection mechanisms. It is noted that the governing equations of the problem are non-linear and the problem should be solved numerically, using the finite element method. The last part of the Chapter presents analytical, simplified solutions that are suggested in EN 1993-1-2 for the determination of the temperature profile of steel sections.

5.1 Convection

Convection is the heat transfer at the interface between a fluid and a solid element. The distinction between the forced and natural convection depends on the motion of the fluid. Free or natural convection takes place when the heat is transferred by the circulation of fluids (in this case the hot air) due to buoyancy from the density changes induced by the heating itself. On the other hand, in the case where the fluid flows on the solid surface at speed, the convection is called forced. Heat transfer through convection takes place only when a fluid comes in contact with a solid surface.

5.2 Radiation

Thermal radiation is the exchange of energy by means of electromagnetic waves that are emitted from a surface or an object. As in the case of light, these electromagnetic waves can be absorbed, transmitted or reflected on a surface. Heat transfer through radiation always takes place when the temperature of a fluid or a solid increases, regardless it comes in contact with another body.

5.3 Heat conduction

The one-dimensional heat conduction is governed by the well-known law of Fourier which is written in the form

$$\dot{Q} = -k \frac{dT}{dx} \quad (5.1)$$

where dx is an infinitesimal thickness of a specific material, \dot{Q} (resp. dT) is the heat flux (resp. the temperature difference) across this thickness and k is the thermal conductivity of

the material. The thermal conductivity is normally dependent on the material temperature and this fact makes the solution of even the simplest problems nonlinear, requiring a numerical method for their treatment. Values for the thermal conductivity for different structural materials can be found in many sources. EN 1993-1-2 has incorporated the thermal conductivity properties for the various structural materials. Details for steel and concrete will be given in the sequel.

In civil engineering structures, heat transfer occurs usually in three dimensions. In this case, an infinitesimal material volume $dx \times dy \times dz$ is considered. The application of the energy conservation principle in this case implies that for stationary heat transfer the heat inflow in the element should be equal to the heat outflow from it and leads to the partial differential equation:

$$k_x \frac{\partial^2 T}{\partial x^2} + k_y \frac{\partial^2 T}{\partial y^2} + k_z \frac{\partial^2 T}{\partial z^2} = 0 \quad (5.2)$$

where k_x, k_y, k_z are the thermal conductivities of the material in each one of the three spatial directions. In transient state heat transfer, the temperature on a material volume increases or decreases over time. The transient state heat conduction partial differential equation is written in the form:

$$k_x \frac{\partial^2 T}{\partial x^2} + k_y \frac{\partial^2 T}{\partial y^2} + k_z \frac{\partial^2 T}{\partial z^2} = \rho C \frac{\partial T}{\partial t} \quad (5.3)$$

where ρ is the density of the material and C is its specific heat. As in the case of the thermal conductivity coefficient, the specific heat is normally dependent on the temperature of the material. In cases that phase changes occur, the function that describes the specific heat may not be continuous. Moreover, in the case of porous materials, as e.g. the concrete, the specific heat is affected by the evaporation phenomena that occur over a range of temperatures. Details for the materials treated here will be given in Chapter 6.

5.4 Boundary conditions

Boundary conditions should be applied in order to find a solution to equation 5.3. In heat transfer, the boundary conditions are of three general types.

Adiabatic boundary conditions

Adiabatic boundaries can be treated as a special case of the general fixed flux boundary conditions. No heat exchange takes place across such a boundary and the adiabatic boundary condition is written in the form:

$$-k_n \frac{\partial T}{\partial n} = 0 \quad (5.4)$$

Adiabatic boundaries are used in order to simulate symmetry conditions (no heat exchange takes place along the symmetry axis or surface) or boundaries which are almost completely insulated.

Fixed temperature boundary conditions

This is the simplest form of boundary conditions, where in specific points of the material, or along edges or surfaces the temperature is assumed known:

$$T = T_0 \quad (5.5)$$

Fixed flux boundary conditions

In this case, the heat flux in a direction normal to a boundary surface is assumed known. This boundary condition is written in the form

$$-k_n \frac{\partial T}{\partial n} = \dot{q}_0 \quad (5.6)$$

where k_n is the thermal conductivity measured in the direction normal to the boundary surface and \dot{q}_0 is the known heat flux. A special case of this boundary condition is that of an adiabatic boundary. Across such a boundary no heat exchange takes place, therefore the heat flux is equal to zero. The adiabatic boundary condition is therefore written in the form:

$$-k_n \frac{\partial T}{\partial n} = 0 \quad (5.7)$$

Adiabatic boundary conditions are used in order to simulate symmetry conditions (no heat exchange takes place along the symmetry axis or surface) or boundaries which are almost completely insulated.

Boundary conditions at solid-fluid boundaries

In the case that solid boundaries are in contact with moving fluids, the following boundary condition can be written:

$$-k_n \frac{\partial T}{\partial n} = h_f (T_f - T_s) = h_f \Delta T \quad (5.8)$$

where h_f is the heat transfer coefficient and ΔT is the temperature difference between the fluid and the solid boundary surface. In this case T_f is the fluid ambient temperature (assumed as known) and T_s is the temperature of the solid surface, which is not a priori known, but is calculated as a result of the solution process. For cases which are of interest in structural analysis problems, both convective and radiation heat exchange takes place and Equation 5.8 can be written in the form

$$-k_n \frac{\partial T}{\partial n} = a(T_f - T_s)^\beta + \Phi \varepsilon_r \sigma (T_f^4 - T_s^4) \quad (5.9)$$

where

a and β are coefficients that depend on the side of the structural elements (fire side or ambient temperature air side)

Φ is the configuration or view factor,

ε_r is the resultant emissivity (which depends on the fluid and solid emissivities) and σ is the Stefan-Boltzmann constant.

The first part of the r.h.s. of Equation 5.9 is known as the convective term whereas the second one is known as the radiative term.

The term ε_r can be evaluated by the simple formula

$$\varepsilon_r = \varepsilon_f \times \varepsilon_s \quad (5.10)$$

where ε_f is the emissivity of fire (usually taken equal to 1.0) and ε_s is the emissivity of the structural material.

5.5 Temperature of unprotected steel sections

EN 1993-1-2 provides a simple equation for calculating the thermal response of unprotected steel members. Assuming an equivalent uniform temperature distribution throughout the cross section, the increase in temperature $\Delta\theta_{\alpha,t}$ in an unprotected steel member during a time interval Δt is given by:

$$\Delta\theta_{\alpha,t} = k_{sh} \frac{A_m / V}{c_\alpha \rho_\alpha} \dot{h}_{net,d} \Delta t \quad [^\circ C] \quad (5.11)$$

where,

k_{sh} - is the correction factor for the shadow effect, from Eq. (5.12)

$$k_{sh} = 0.9[A_m / V]_b / [A_m / V] \quad (5.12)$$

where,

$[A_m / V]_b$ is the box value of the section factor. The box value of the section factor of a steel section is defined as the ratio between the exposed surface area of a notional bounding box to the section and the volume of steel. In all other cases, the value of k_{sh} shall be taken as:

$$k_{sh} = [A_m / V]_b / [A_m / V] \quad (5.13)$$

Ignoring the shadow effect (i.e., $k_{sh} = 1$) leads to conservative solutions.

A_m / V - is the section factor for unprotected steel members, (≥ 10) [m^{-1}]

A_m - is the surface area of the member per unit length, [m^2 / m]

V - is the volume of the member per unit length, [m^3 / m]

c_α - is the specific heat of steel, [J / kgK]

$\dot{h}_{net,d}$ - is the design value of the net heat flux per unit area according to Eq. (5.14)

$$\dot{h}_{net} = \alpha_c (\theta_g - \theta_m) + \Phi \varepsilon_f \varepsilon_m \sigma [(\theta_r + 273)^4 - (\theta_m + 273)^4] \quad (5.14)$$

where,

$\sigma = 5.67 \times 10^{-8}$ [$W / m^2 K^4$] is the Stephan Boltzmann constant

representing the thermal actions and reproduced here. This flux is the sum of a convective

part $\dot{h}_{net,c}$ and a radiative part $\dot{h}_{net,r}$:

$$\dot{h}_{net,d} = \dot{h}_{net,c} + \dot{h}_{net,r} \quad [W / m^2] \quad (5.16)$$

where,

$$\dot{h}_{net,c} = \alpha_c (\theta_g - \theta_m) \quad [W / m^2] \quad (5.17)$$

and

$$\dot{h}_{net,r} = \Phi \cdot \varepsilon_f \cdot \varepsilon_m \cdot 5.67 \times 10^{-8} \cdot [(\theta_r + 273)^4 - (\theta_m + 273)^4] \quad [W / m^2] \quad (5.18)$$

where,

- α_c - is the coefficient of heat transfer by convection
- θ_g - is the gas temperature of the fire-compartment, [$^{\circ}C$]
- θ_m - is the surface temperature of the steel member,
- Φ - is the view factor or configuration factor that is usually taken equal to 1.0,
- ε_m - is the surface emissivity of the member,
- ε_f - is the emissivity of the fire (usually $\varepsilon_f = 1.0$),
- θ_r - is the radiation temperature of the fire environment normally taken $\theta_r = \theta_g$
- ρ_a - is the unit mass of steel, 7850 [kg / m^3]
- Δt - is the time interval [s] (≤ 5 [s]).

Chapter 6. Material properties at elevated temperatures

The properties of steel at elevated temperatures are very important for the analysis of structures subjected to fire. Taking into account the conclusions of studies that have been conducted in the past from various researchers, it is obvious that it is of great importance to simulate numerically the dependence of material properties to temperature, in order to study the response of structures in fire conditions. The dependence of all mechanical-thermal properties of materials to temperature contributes to a more complex numerical analysis. The following section describes the mechanical and thermal properties of steel, which are adopted in the present study, complied with the mathematical models as are proposed in EN 1993-1-2.

6.1 Structural steel

For heating rates between 2 and 50 K/min, the strength and deformation properties of steel at elevated temperatures are obtained by the stress-strain curve of Figure 6-1. The stress-strain curve of structural steel at high temperatures is quite different from that at ambient temperature as it is illustrated in Figure 6-2. The elastic range is followed by an elliptic branch, occurring until the suggested strain limit of $\varepsilon_{y,\theta}=2\%$. A yield plateau appears in the last part of the curve until strain is up to $\varepsilon_{t,\theta}=15\%$. The variation of the stress-strain relationship, for structural steel S275, as the temperature increases is presented in Figure 6-2. Structural steel begins to lose strength at temperatures above 400 °C. The reduction is immediate and at the temperature of 800 °C the yield stress is equal to 11% of its initial value. In the present study, it is assumed that steel melts at the temperature of 1200 °C where its strength is becoming zero.

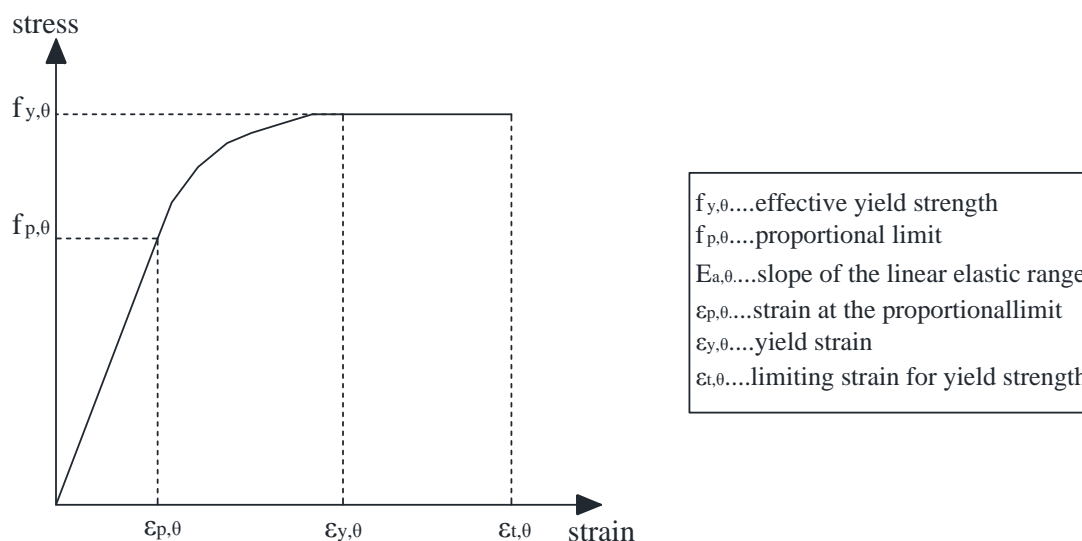


Figure 6-1: Stress-strain relationships of structural steel at elevated temperatures.

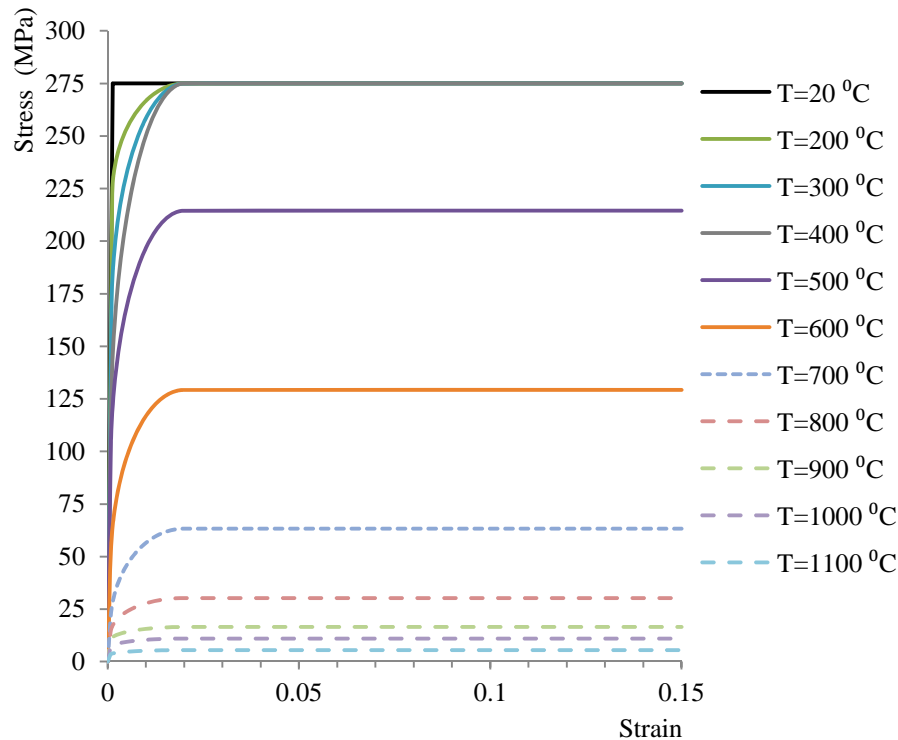


Figure 6-2: Stress-strain relationships of structural steel S275 at elevated temperatures.

At elevated temperatures, effective yield strength, proportionality limit and slope of linear elastic range are reduced according to factors specified on Table 3.1 EN 1993-1-2 for structural steel.

An important issue that determines the behaviour of steel during fire exposure is the temperature induced strains. These strains include the thermal expansion and the creep strain. The thermal expansion coefficient of steel α has a great importance in modeling composite structures under fire conditions. The dependence of the coefficient α on temperature is illustrated in Figure 6-3. Additionally, it is well known that the creep strain appears during the heating of metals. In fire-engineering only the primary and the secondary creep strains are considered, due to the short time of fire-exposure. Various models have been proposed in the literature (Plen model, Dorn-Harmathy model etc.). The incorporation of the creep strain models in the calculations is a demanding task. For simplicity, the effect of creep is implicitly taken into account to the stress-strain relationship, according to EN 1993-1-2.

The temperature dependent thermal properties are thermal conductivity and specific heat. It is obvious from equation (2) that the thermal conductivity k and the specific heat C are the basic thermal properties defining the temperature distribution in a structural member. The thermal conductivity of structural steel reduces as the temperature increases as it is shown in Figure 6-4.

The specific heat is increasing slightly at elevated temperatures until 600 °C. In the range between 600 °C and 900 °C the specific heat increases rapidly until the value of 5000

J/kg K at 735 °C (Figure 6-5). This occurs due to the phase transition of steel at this temperature. The thermal properties of reinforcing steel and structural steel are identical.

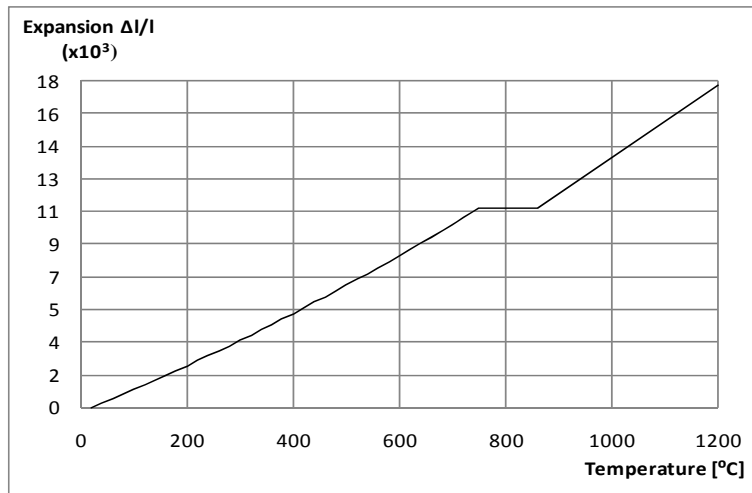


Figure 6-3: Thermal expansion of steel.

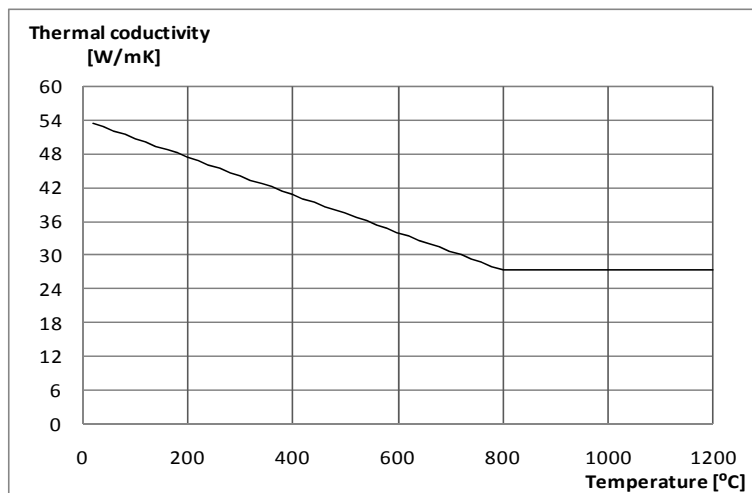


Figure 6-4: Thermal conductivity of steel.

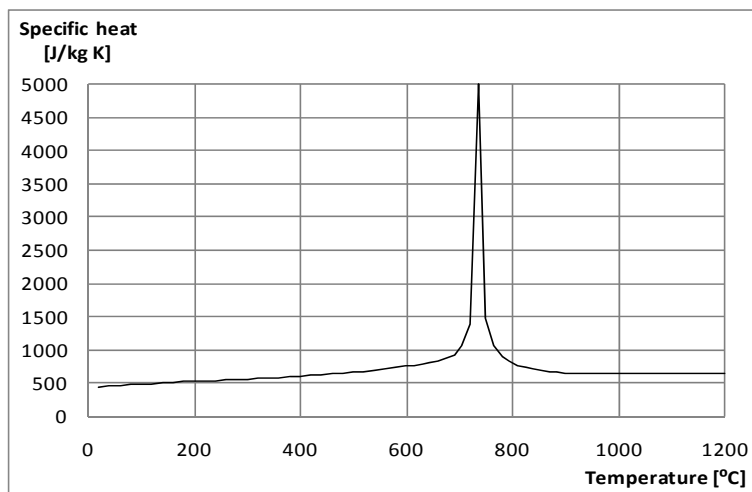


Figure 6-5: Specific heat of steel.

Chapter 7. Introduction to the case study – Definition of post-earthquake fire scenarios

The goal of this Chapter is to present in detail the building that is studied in the dissertation and to define the Post Earthquake Fire (PEF) scenarios that are used in order to study the effect of the non-structural damage to the fire evolution in the enclosure. As it is referred in Chapter 3, the geometry of the fire-compartment, its fire loads and ventilation influence strongly the temperature distribution and spread of fire. Thus, due to the complex character of the fire development in a fire enclosure it is crucial to focus the study on structures where most parameters are well-defined. Examples for this kind of buildings are office buildings, library buildings, hotels and shopping centers. These types of buildings usually are constructed with many normative restrictions to room-area, -height and -openings. Additionally, they can be considered as model structures as it is rather easy to define the fire-loads. In this study the interest is focused on a library building. The particularity of this building is that the dimensions of the fire-compartments are not following the restrictions of the regulations due to special requirements of the architectural design. The fire-design of this building cannot be based on the guidelines of EN 1991-1-2 and it is both interesting and demanding to study the fire-evolution in the enclosure through special software based on CFD theory.

The fire scenarios can be based on the variation of several parameters, such as the heat release rate, fire load, geometry of the fire-compartment and ventilation conditions and the performance of the fire-protection systems. In this dissertation the PEF scenarios are defined using as parameters the ventilation conditions and the functionality of the fire-sprinkler system.

7.1 Geometric characteristics of the library building

The building that is considered in this dissertation is a 4-storey steel framed structure used as a library and it is illustrated in Figure 9-1. The dimensions of the plan-view of the building are 60 x 16 m. All the levels are similar and the height of the floor is equal to 3.5m. The total area of the windows is equal to 120m² at every level. In order to simplify the modeling, the windows are divided into 15m² sections representing 8% of the total compartment window area at each level. The accurate allocation of the windows is defined in Figure 9-1. Specifically, eight windows of 7.50 x 2.00 m are placed at each level along the 60m sides of the building.

The combustible materials consist mostly of paper documents in folders, placed on 2.50 m high shelving systems arranged in rows, as indicated in Figure 9-1. The distance between the shelving systems is 1.20 m, and the dimensions of the plan-view of the shelves are 0.50

x 10.00 m. The exterior doors are not defined since it is assumed that are closed during the fire evolution. The structural system of the building consists of eleven double span steel frames on every floor at a distance of 3.00 m as it is represented in Figure 7-2. The geometrical dimensions of a typical frame of the building are presented in the same figure.

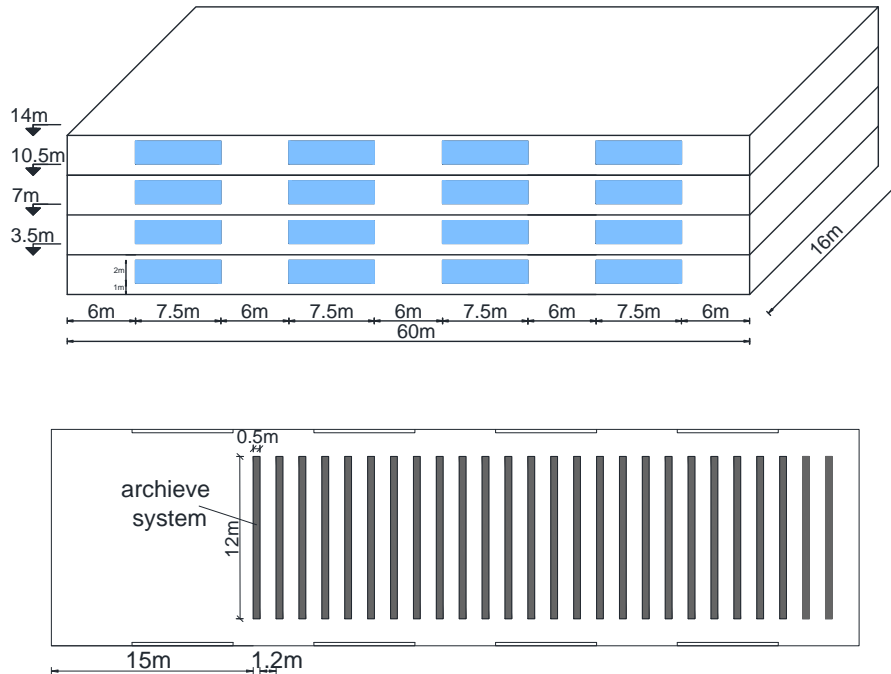


Figure 7-1: The library building.

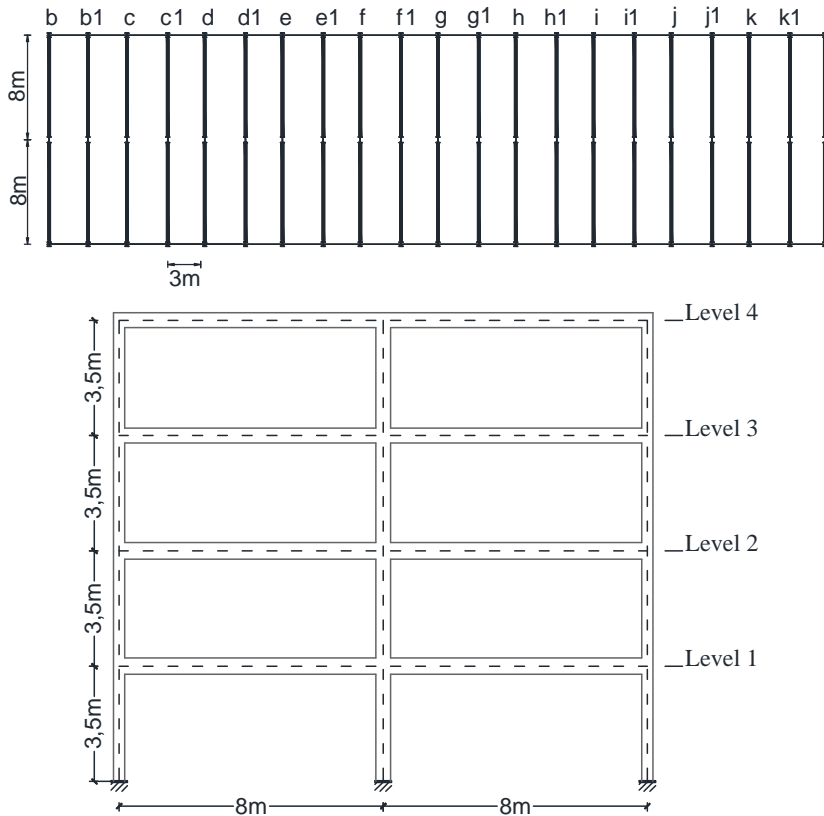


Figure 7-2: The structural system and a typical frame.

A special feature of the library building is that every floor is a separate fire-compartment and the total area is equal to 960m^2 . A fire-extinguishing system which consists of 60 sprinklers is installed at each floor (Figure 7-3).

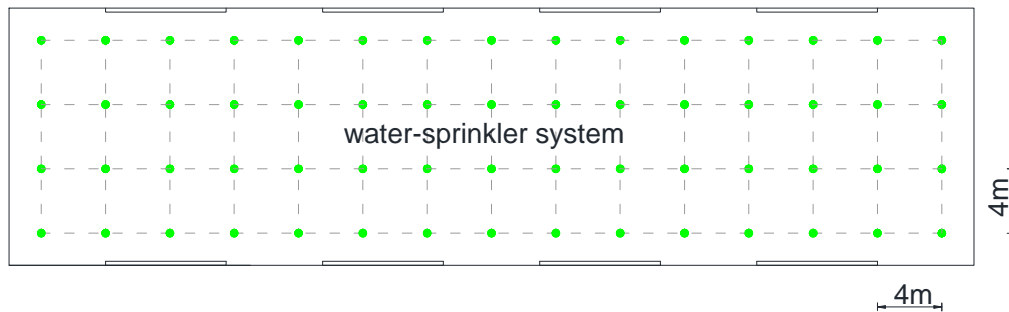


Figure 7-3: The fire-extinguishing system.

7.2 Post-Earthquake scenarios

Post-Earthquake fire scenarios are defined in order to study the influence of the ‘level of damage’ induced to the non-structural components due to earthquake to the fire evolution in the enclosure. In the current study the non-structural damage is simulated taking into account two different issues:

- the breakage of windows
- the malfunction of the sprinkler fire-extinguishing system.

Different levels of damage are considered. Regarding the breakage of windows, different levels are connected to various percentages of the windows that are broken due to earthquake. The percentage and the position of the broken windows modifies the ventilation conditions leading to different PEF scenarios, and consequently, to different gas temperature time-history distributions in the fire-compartment. Consequently different temperature profiles develop at the structural members. The malfunction of the sprinkler fire-extinguishing system can be partial or general, thus the differentiation to the percentage of the operational sprinkler system is related to different levels of non-structural damage.

Twelve different PEF scenarios are defined. Nine scenarios include variations in the ventilation conditions by changing the number and allocation of the broken windows. The remaining scenarios are referred to a different percent of the operational sprinkler system. The scenarios are illustrated in Table 7-1.

The following parameters are given for all the scenarios:

- percentage of broken windows to the total area of openings in the fire-compartment
- percentage of the broken openings to the total wall area (532m^2)
- position of the broken windows
- percentage of the functional water sprinklers.

The scenarios SC-00 and SC-SP100 are defined as the *reference scenarios* since the non-structural damage is not considered in both cases. This designation will be used in the next Chapters.


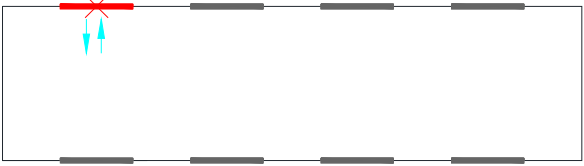


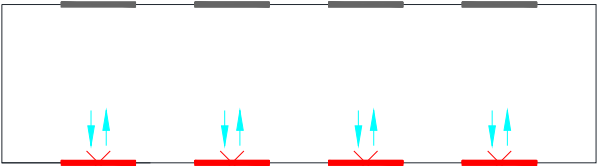
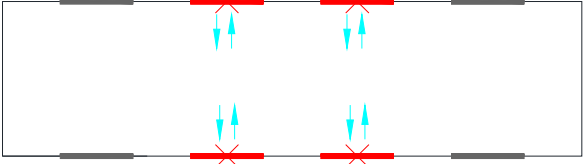
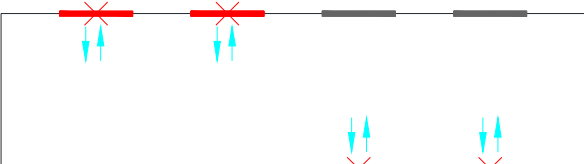
Post-Earthquake scenario	% of broken windows	% of broken windows / wall area	% of operational sprinkler system
SC-00	0	0	0
			
SC-12.5	12.5	2.75	0
			
SC-25A	25	5.5	0
			
SC-25B	25	5.5	0
			
SC-50A	50	11	0
			
SC-50B	50	11	0
			
SC-50C	50	11	0
			

Table 7-1: Post-Earthquake Fire scenarios. (continued)

SC-75	75	16.5	0
SC-100	100	22	0
SC-SP100	50	11	100
SC-SP40	50	11	40
SC-SP20	50	11	20






	non-damaged/closed window		functional sprinkler		air inflow/outflow
	broken/open window		damaged sprinkler		

Table 7-1: Post-Earthquake Fire scenarios.

Chapter 8. CFD modeling –Results of the numerical analysis

The main objectives of this Chapter are to present the numerical model that is developed for the simulation of the natural-fire in the library building, to obtain the gas-temperature distribution in the compartment and to calculate the temperatures time-history curves for the structural members. Initially, the numerical model is presented. The thermal properties of the materials that are incorporated in the fire-compartment, the combustible materials and the technique used for the fire spread in the enclosure are discussed in detail. Additionally, the simulation of the fire-sprinkler system that is used for the suppression of the fire is presented. The outcomes of the CFD analyses, for the PEF scenarios that were presented in Chapter 7 follow. The goal is to study the effect of non-structural damage to the fire evolution in the enclosure through different aspects. The main issues that are discussed are the Total Heat Release rate and the gas-temperature “near” the structural members. In the sequel, the main target is to provide the input data for the simulation of the fire action during the mechanical analysis that is presented in Chapter 10 and Chapter 11. Actually, initially the goal is to obtain the fire evolution, which is represented through the gas-temperature history, in the fire-compartment and then to calculate the temperature of the structural members. The latter defines the input data for the mechanical analysis that follows (Chapter 10 and Chapter 11).

To this end, the interface between the CFD and the FEM structural analysis is the most important issue that has to be solved. In order to address this issue, an alternative two-zone model is developed, utilizing the results of the CFD analysis. This model provides the spatial gas-temperature distribution in the fire-compartment.

8.1 Numerical simulation

8.1.1 The numerical model

The numerical model is developed using Fire Dynamics Simulator (FDS, McGrattan *et al.*, 2010a,b) and is presented in Figure 8-1. As it has already been mentioned, each floor constitutes a single fire-compartment of total area 960m². In this study it is assumed that the fire breaks out at the first floor of the building and that the fire cannot spread to the upper levels. Taking into account the previous, it is not required to simulate the higher levels. The numerical model that is used in this dissertation is depicted in Figure 8-2.

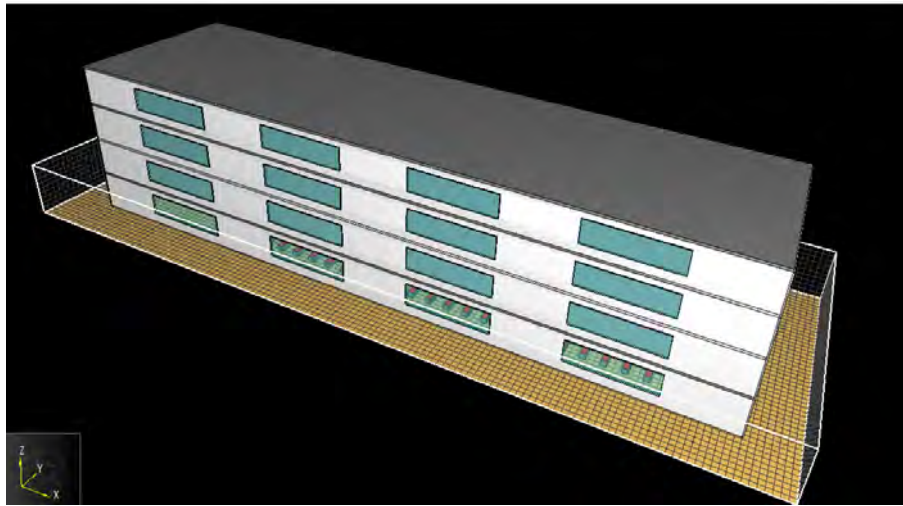


Figure 8-1: The numerical model for the natural fire-simulation.

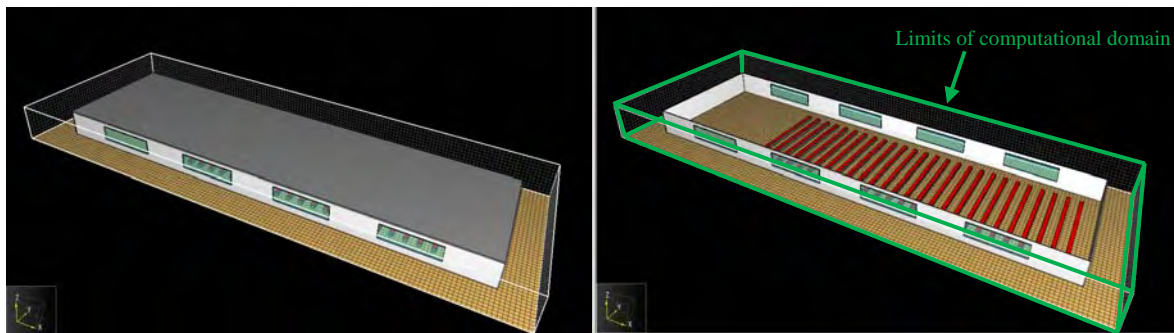


Figure 8-2: The numerical model for the first level and the limits of the computational domain.

The boundaries of the computational domain are illustrated in Figure 8-2. As it can be observed, the computational domain is not restricted to the outline of the building but it is extended around it, in order to simulate in a realistic way the ambient atmospheric conditions. The domain is extended 4m in x and y directions and 2m in the z direction. The predefined boundary condition OPEN, which is included in FDS (Mcgrattan *et al.*, 2010a,b), is used for the description of the exterior boundary of the computational domain. The OPEN boundary condition assumes that ambient conditions exist around the building and the flow in and out of the building is treated naturally as part of the solution of the governing equations as it is described in Figure 8-3 (Gissi, 2010). Specifically, in this study, the OPEN boundary condition is applied at the outer limits of the computational mesh in $-x$, $+x$, $-y$, $+y$ and $+z$ directions. In the $-z$ direction it is not allowed any interaction with the soil. It is noted that the ambient temperature and pressure are set equal to 20°C and 1Pa respectively. Moreover, the extended mesh is useful for the representation of the heat transfer and the smoke movement at the surroundings of the building.

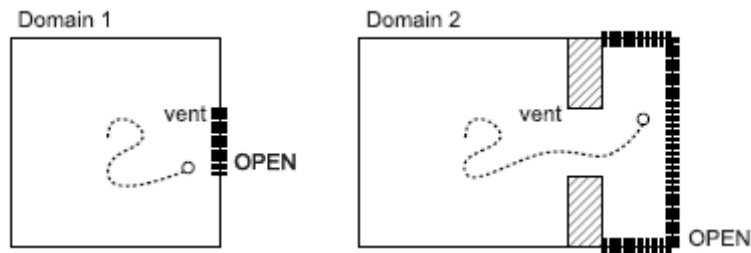


Figure 8-3: Mesh of the type 2 is applied for definition of the exterior boundary of the computational domain (Gissi, 2010).

A basic parameter for the numerical simulation is the definition of the grid cell size for the computational domain. FDS (Mcgrattan *et al.*, 2010a,b) approximates the governing equations on a rectilinear grid cell. Taking into account results from the literature (Rinne *et al.*, 2007) regarding the mesh sensitivity, the grid cell size is selected to be 0.50x0.48x0.50m for the directions x , y and z respectively. In this way, totally 68,000 mesh cells are included in the numerical model.

At this point it is noted that the structural members are not included in the numerical model. This assumption is required in order to simplify the calculations. Actually, the problem that is studied involves three different physical phenomena that interact. The first is the fire-evolution in the compartment, the second is the heat transfer in the solids and the third is the mechanical response of the structural system. This indicates that three different mathematical problems have to be solved in order to obtain the gas-temperature time-history in the fire-compartment, the temperature profile of the structural members and the stress-strain field of the structural system.

The most integrated methodology for the solution of the problem is to conduct “fully-coupled” thermo-mechanical analysis. The term “fully-coupled” is referred to the interaction between the fire-evolution in the fire-compartment and the structural members. The fire development induces thermal loading in the structural members that deform due to the concurrent mechanical and thermal actions. The deformations of the structural members cause continuous modifications of the initial configuration of the structural system during the fire-evolution and this can affect the gas-temperature distribution in the enclosure.

This approach is extremely complex to be applied, due to the fact that the structural members should be included in the numerical model which is used for the CFD analyses. It is clear that it is difficult to couple the different types of analyses due to the different spatial scale of the interacting phenomena. The incorporation of the structural members in the CFD model requires a very dense mesh in the corresponding positions and, consequently, leads to excessive computational cost. Thus, it is necessary to simplify the calculations and to uncouple the involved problems. In the current study it is taken into account the fact that the dimensions of the structural elements are small enough compared to the dimensions of the fire-compartment and it this specifies that the structural system does not significantly affects the air-flow and the temperature distribution in the fire-

compartment. Moreover, the loss of radiation due to the structural members can be neglected. Thus, the thermal and the mechanical analysis of the structure are disconnected from the fluid analysis and the structural members are not included in the CFD model.

8.1.2 The numerical analysis

In this study, the Large Eddy simulation is used and the Radiation Transport solver is enabled. The duration of the fire event is set equal to 3600th sec for all the PEF scenarios. The computational time step is adjusted not to exceed the value of 0.1sec. Specifically, the time step can be decreased during the analysis if the solution does not converge.

The total computational time is significantly affected by the incorporation of the sprinkler system. The duration of the analyses concerning the scenarios where the sprinkler system is not used varies between 4 and 5 hours, while the corresponding values for the rest scenarios is about 10 hours.

8.1.3 Thermal properties of the materials

The walls of the library building are composed of typical insulation panels. The total width of the panel is equal to 0.2m and three different layers are considered, as it is illustrated in Figure 8-4. The external layers are made of steel while the interior layer is the insulation material. It is noted that the connection of one panel to another is considered to be airproof so there is no extra ventilation from the walls into the compartment. The floors are assumed to be concrete slabs and the total thickness of the slabs is equal to 0.2m. The thermal characteristics of the materials are presented in Table 8-1.

For simplification purposes, the windows are either considered as a void in the wall when they are open/damaged, or either they are considered to be of the same material of the wall, when they are closed/ undamaged. The specified simulation technique is proposed in the manual of FDS (Mcgrattan *et al.*, 2010a,b). The simulation of glass is not necessary, because the main function of the windows is to act as vents changing the ventilation conditions of the compartment. Any radiation loss through the undamaged/closed windows is considered to be negligible.

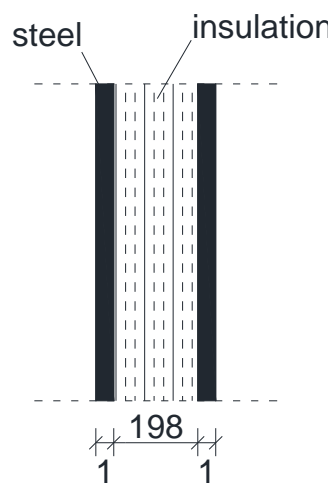


Figure 8-4: Section (not in-scale) of the panel and the different layers (dimensions in mm).

Material	Density (kg/m^3)	Specific heat ($kJ/(kg\cdot K)$)	Conductivity ($W/(m\cdot K)$)	Emissivity	absorption coefficient ($1/m$)
Steel	7850	0.46	45.8	0.95	50000
Insulation	208	Variable ¹	Variable ²	0.9	50000
concrete	2280	1.04	1.8	0.9	5000

Variable ¹: The variation with the temperature is depicted in Figure 8-5
Variable ²: The variation with the temperature is depicted in Figure 8-6

Table 8-1: Thermal characteristics of materials.

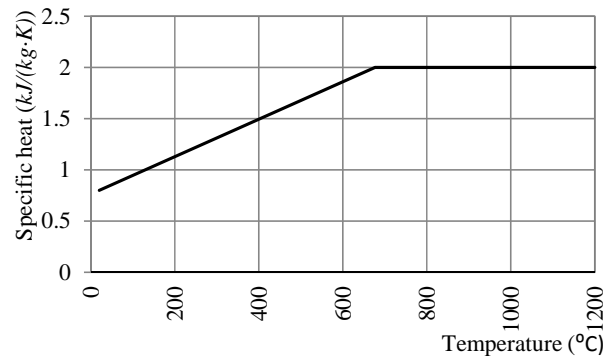


Figure 8-5: Variation of the specific heat of the insulation material with temperature.

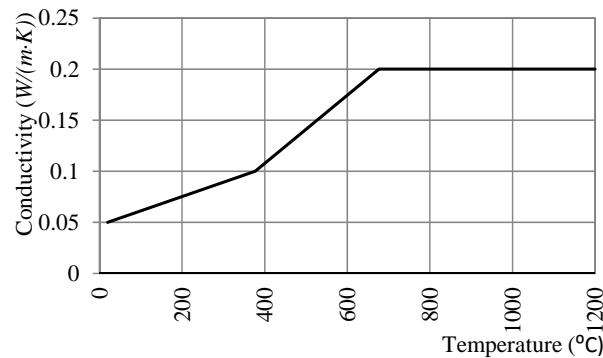


Figure 8-6: Variation of conductivity of the insulation material with temperature.

8.1.4 Fire modeling and fire-spread modeling

The term fire modeling involves two different phases. The first one is the pyrolysis while the second is the combustion phase. The former refers to the generation of the volatiles from a solid surface, while the second is the reaction of the volatiles and oxygen.

Regarding the pyrolysis modeling, two different techniques are available in FDS (Mcgrattan *et al.*, 2010a,b). The first is to explicitly specify the Heat Release Rate per Unit Area (HRRPUA) on a surface and then apply the surface ID to an obstruction (in FDS the obstruction is defined as a solid volume). In FDS (Mcgrattan *et al.*, 2010a,b) this is indicated as a burner. The HRRPUA can be either constant or variable with time. Actually, in this case FDS (Mcgrattan *et al.*, 2010a,b) creates a gas burner, whose fuel flow is controlled by the prescribed Heat Release Rate (HRR) curve that is specified by the user.

The second choice is to specify solid phase thermal and pyrolysis properties on a surface and then apply this boundary condition to an obstruction. The surface can be divided in multiple layers in order to include various materials. In this way the chemical reactions of the materials that occur at different temperatures are simulated. In this case FDS (Mcgrattan *et al.*, 2010a,b) predicts the HRR of the fire.

The second method is rather complicated and several problems arise during the numerical modeling. First of all, the pyrolysis takes place in a small scale compared with the dimensions of the fire-evolution in the compartment. In order to model accurately the pyrolysis, a dense discretization of the fire-compartment is required, which is not compatible with the looser grid that can be applied for the simulation of the fire spread. Thus, the numerical modeling of both pyrolysis and fire-evolution requires dense meshing and the computational time becomes excessive.

Additionally, in most cases it is difficult to know the exact composition of the burning materials. The burning fuels can be parted by a large number of different materials. Thus, it is very difficult to define the required thermal properties. Usually, for fire engineering purposes it is preferred to use specified HRR that comes from real or small scale experiments. Taking into account the previous, the approach of the predefined HRRPUA is used in this thesis, since the second method is rather complicated. Moreover, the numerical simulation of the pyrolysis is beyond the scope of this thesis, since it requires further background material on solid phase pyrolysis.

Regarding the simulation of the combustion, the so-called *mixture fraction model* is used by default in FDS (Mcgrattan *et al.*, 2010a,b). This model takes into account for the evolution of the fuel gas from its surface of origin through the combustion process. The alternative way for the simulation of the combustion is the *finite-rate approach*, where all of the individual gas species which are involved in the combustion process are defined and tracked individually. In this case the combustion process is modeled as one or more finite-rate reactions of these species. This is a costlier and more complicated approach than the mixture fraction model. In this study the mixture-fraction model is used. It is noted that the combustion can take place if the fuel/oxygen mixture fraction satisfies specific requirements. If the oxygen is not enough for the combustion, there will be no heat release from the gas burner.

Fire modeling

The combustible materials in the first floor of the building, where the fire takes place, consist mainly of paper and document folders which are placed in the shelving systems of the library. In this study, the definition of the HRR curve for the simulation of the burning of the shelving system is based on the results of an extensive experimental program conducted by Rein *et al.*, (2007). Laboratory fire tests have been conducted at the BRE Center for Fire Safety Engineering at the University of Edinburg in conjunction with the

Dalmarnock Fire tests¹. Among others, a bookshelf fire-test has been conducted. According to the report, a fully loaded shelf unit, identical to those that were used in Dalmarnock fire tests was burned under the calorimeter hood.

The ignition and configuration was similar to the tests in Dalmarnock, thus a wastepaper basket stuffed with crumpled newspaper which was moistened with heptane was used for the ignition. Unfortunately, the extraction system of the lab's exhaust hood was not able to remove all the smoke produced by the shelf fire. Therefore the test had to be stopped, by extinguishing the fire, before the shelf had burnt out. For this reason the entire heat release curve of the shelf was not obtained. The bookshelf set-up and a snapshot of the burning phase are illustrated in Figure 8-7.

The custom Heat Release Rate (HRR) curve according to the experimental report is presented in Figure 8-8. According to the fire tests report, the second peak is attributed to the control of the smoke extraction in the hood,. By increasing the extraction volume more air is entrained which could have contributed to fire growth. When the fire was extinguished, the HRR curve had passed its peak and was decreasing significantly. As stated above it was unfortunately not possible to record a full heat release curve until burnout.



Figure 8-7: The bookshelf setup and the burning stage.

In order to take into account the difference in the scale of the test bookshelf and the real scale shelving units, the heat release rate curve of the test is modified according to the

¹ The Dalmarnock Fire tests are a series of fire experiments that were conducted in a real high-rise building in Dalmarnock, Glasgow. The 23-storey building was scheduled for demolition and hence was evacuated of tenants. Three main experiments were conducted.

scaling laws that are defined in Fong and Fong (2003). The Heat Release Rate curve is modified according to equation 8.1, while the time is transformed according to equation 8.2.

$$\frac{Q_M}{Q_R} = \left(\frac{L_M}{L_R} \right)^{5/2} \quad (8.1)$$

$$\frac{t_M}{t_R} = \left(\frac{L_M}{L_R} \right)^{1/2} \quad (8.2)$$

where Q is the total HRR, L is the length and t is the time.

The subscripts M and R indicate the *Model* (or experimental) and the *Real* (or scaled) parameter, respectively. The total floor-plan area of the book-shelf that was used during the experimental program is 0.27m^2 ($1 \times 0.27\text{m}$) and the height was equal to 1.80m . The corresponding values of a book-shelf unit in the library building are 6m^2 ($12 \times 0.50\text{m}$) and 2.50m , respectively. The scaling is conducted according to the following. First the maximum HRR is scaled according to (8.1) using the values $L_M = 1.8\text{m}$ and $L_R = 2.5\text{m}$ and is calculated to be equal to 1023KW . In order to take into account the change of the floor-plan area due the change of the height of the bookshelf unit, the corresponding scaling is conducted and the scaled area results to be equal to 0.52m^2 . Taking into account the previous, the maximum HRRPUA results to be $1023/0.52 = 1964\text{KW}/\text{m}^2$. The time is scaled according to (8.2) for the values $L_M = 1.8\text{m}$ and $L_R = 2.5\text{m}$. After the transformation in the time domain the overall duration is extended from 1600^{th} sec to 1886^{th} sec and the real (or scaled) curve is obtained.

The experimental and scaled HRR curves are illustrated in Figure 8-8. For the numerical simulation the scaled curve is used. In FDS (Mcgrattan *et al.*, 2010a,b) the book-shelf units are modeled by 26 heat release burners, at the exact position of the real shelves in the floor plan. At the point when the burner is activated it starts to release heat in the prescribed manner, given that the oxygen is enough to support the combustion. It is clarified that the Heat Release burners are applied to the surface properties of the obstructions that represent the book-shelving units. The plan-view of the obstructions is identical to the book-shelves and the height is assumed to be 0.5m . This assumption is adopted due to the fact that the fire evolution in the enclosure will be affected significantly in the case where the height of the obstructions is set equal to real height of the book-shelves. Another advantage of this assumption is that the material properties used for the simulation of the obstructions are not important since their total area is small compared to the corresponding area of the fire-compartment.

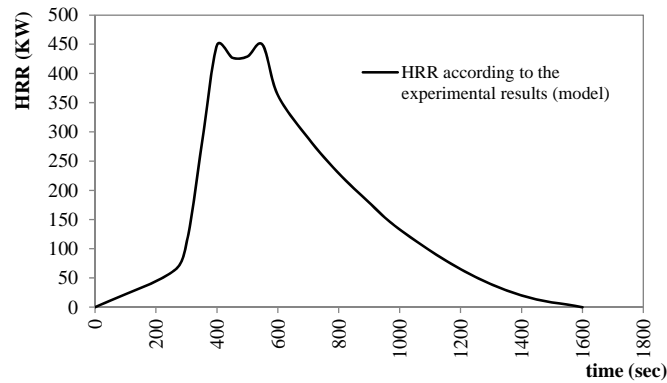


Figure 8-8: Experimental Heat Release Rate curve of the bookshelf test.

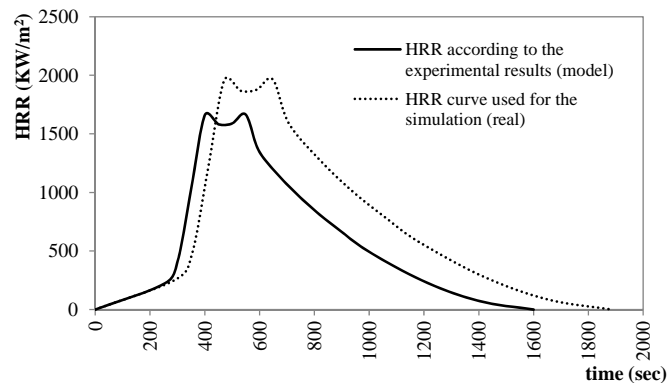


Figure 8-9: The experimental and the modified HRR curves used for the book shelving system.

It is important to notice that the goal of the numerical simulation of the natural fire in the library building is to reproduce parametric fire scenarios. There is no intention to obtain real fire scenarios. In this case the HRR curve should be modified further in order to take into account for the environmental conditions during the fire-test. Several factors such as the variation in air entrainment, complete/non-complete combustion, free/non-free burning and other can change significantly the HRR curve. In this study the scaled HRR curve is used and the intention is to obtain the parametric PEF scenarios based on the modification of the ventilation conditions and on the malfunction of the fire-sprinkler extinguishing system. The next key issue of the fire modeling is to define the criteria for the activation of the Heat Release burners and the simulation of the fire spread from one bookshelf unit to another.

Modeling the spread of fire

The ignition source of fire is supposed to be at the middle (with respect to the y-direction) of the first row (left side) of the array of book-shelves. It is noted that changing the ignition point of fire, the results are completely different. In this study the selection of the ignition point is completely random, since the matter is to define the parametric PEF scenarios taking into account the same ignition point in all cases. The activation of fire is implemented by the assumption that the Heat Release burner that corresponds to the ignition source is active from the starting point of the simulation.

The simulation of fire spread is an extremely complicated issue, since it depends on several factors involving the combustible materials, the available oxygen, the orientation of the burning surface (Novozhilov, 2001) etc. Although FDS (Mcgrattan *et al.*, 2010a,b) offers the capability to define the rate of fire spread, it is quite difficult to define this value since the experimental data on this issue are limited. An alternative simulation of the fire spread is adopted in this study (Zografopoulou, 2013a,b). It is assumed that the basic requirement for fire spread between combustible materials at a distance, is that the temperature reaches a specified value near the surface of the material. The specified temperature indicates that the pyrolysis reaction starts.

Actually, the simulation is based on the activation temperature of the Heat Release burning surface placed on the obstructions that represent the book-shelving units. Specifically, the activation is controlled by a sensor 2.50 m above the center of the section. This control device activates the Heat Release burner when the temperature at the sensor reaches 250 °C. The temperature that is used corresponds approximately to the auto ignition temperature of wood (Babrauskas, 2002) and paper (Graf, 1949). It is clear that this approach results in gradual activation of the heat release sections and that it depends on the temperature distribution in the compartment. Another required condition for the combustion to occur is an oxygen index >0.15. If this is not satisfied, the fire is suppressed due to lack of oxygen.

8.1.5 Sprinkler system

A water sprinkler system is installed in the compartment as a means of fire suppression in a fire event. The activation temperature of sprinkler heads is set equal to 74 °C. The simulation of the effect of the activation of the water sprinkler system in the analysis is performed by presenting the released water in the form of water droplets which have the material properties presented in Table 8-2. The water discharge of each sprinkler head in the compartment is converted to a certain number of water droplets based on the set particle size and sprinkler flow. The particle upon entering the computational space with the assigned velocity, interacts with the surfaces of the obstacles in the compartment. If the surface is vertical the droplets continues its motion downwards. If the surface is horizontal and the particles velocity is in the *z*-direction only, a random direction is chosen when the droplet hits the surface.

Water particles	
Density (kg/m ³)	1000.0
Specific heat (kJ/(kg·K))	4.184
Vaporization temperature (°C)	100
Heat of Vaporization (kJ/(kg))	1.80
Droplet median diameter (µm)	500
Droplets per second	5000
Insertion interval (sec)	0.1

Table 8-2: Properties of the water particles.

The actual effect that a water sprinkler system has in the suppression of fire is very complex, and impossible to be simulated fully because the physical mechanisms take place in a scales many times smaller than the mesh cell size. During the combustion (in the gas phase) the water influences the flame development by lowering the temperature and diluting the oxygen supply. In the solid phase, the water cools the pyrolysis surface, decreases the fuel supply and interferes with the corresponding chemical reactions.

In the computational analysis, the burning of the materials is represented by Heat Release Rate sections and there were not any actual fuel objects placed in the compartment to be undergo pyrolysis. The fire suppression is implemented with the use of an extinguish coefficient on the Heat Release sections. An assumption is made in the software that the water that interacts with the HR section absorbs energy from the surface, and reduces the pyrolysis rate and the burning rate of the fuel. A parameter in FDS (Mcgrattan *et al.*, 2010a,b) defines the suppression rate of the surface and reduces the Heat Release Rate of the surface in correlation to the mass of the water that reaches the certain surface.

The local mass loss rate of the fuel is expressed in the form

$$\dot{m}_f''(t) = \dot{m}_{f,0}''(t)e^{-\int k(t)dt} \quad (8.3)$$

Here $\dot{m}_{f,0}''(t)$ is the user-specified burning rate per unit area when no water is applied and k is a function of the local water mass per unit area, m_w'' , expressed in units of kg/m².

$$k(t) = E_{COEFFICIENT} m_w''(t) \quad (8.4)$$

The E_{COEF} is obtained experimentally and is expressed in m²/kg/s. The use of the extinguish coefficient is preferable when the fuel type is complex.

In the current analysis the E_{COEF} was set at 0.4 and was based on the work of Jukka Vaari *et al.* (2012), who conducted a research project on fire suppression of large water based systems and their simulation in Fire Dynamics Simulator. Their work aimed in the development and improvement of the code to describe water spray dynamics, flame extinguishment and suppression of large complex solid fire loads. The chosen value is based on their best representation of water fire suppression of a burning stack of wooden pallets.

8.2 Results

In order to study the effect of non-structural damage to the fire evolution in the enclosure, different issues are examined. Initially, the fire spread in the fire-compartment is presented. The HRR curve of the fire denotes in a vibrant manner the effect of both the ventilation conditions and the operative sprinkler system on the fire development in the enclosure. The smoke movement and the velocity field are also obtained in order to get an integrated overview of the air-flow in the compartment. An important part of the results is dedicated to the gas-temperature “near” the structural members. For the needs of the present dissertation, a “dual-layer model” has been developed which actually represents the interface between the CFD and the FEM mechanical analysis. It is noted that the “dual-layer model” model that is developed in this study is based on the philosophy of the two-zone models that are proposed in EN 1991-1-2 but actually, it is not the same model. Here,

the model is developed in the post-processing stage of the CFD analyses as it is explained in detail in Section 8.3. The outcomes of the dual-layer models” designate the spatial gas-temperature distribution in the compartment. Finally, the time-history temperature curves that correspond to the structural members are obtained.

8.2.1 Spread of the fire

As it was described in Chapter 3, during the fire growth period, the fire is limited in a small area and only localized temperature rises can be detected. In the sequel, as the smoke layer is supplied with more combustible gases, the temperature rises in the fire-compartment. At the same time, the flame becomes higher and fire spreads due to the high concentration of the partially burnt fuels in the smoke layer. Here it is demonstrated that the fire-spread is strongly dependent on the ventilation conditions. As it has already been mentioned in Section 8.1.4, the fire spread is controlled by a temperature sensor 2.50 m above the center of the Heat Release burning surface, which is activated when the temperature of the sensor is equal to 250 °C. Totally 28 special devices are used, corresponding to the different burners. Figure 8-10 presents the results of the analyses considering the activation of the control devices, for all the PEF scenarios. The ON/OFF status is indicated by -1/1. The activation is denoted by 1. If the sensor is not activated the status is recorded as -1.

In the *reference* scenario SC-00, where the windows are considered to be closed, numerous devices are not activated and consequently the corresponding heat release burners are not activated. This indicates that the temperature of the corresponding sensors does not exceed the value of 250 °C. The fire starts from the ignition point and spreads to the adjacent bookshelves. Due to the lack of oxygen the combustion stops and the book-shelves are partially burned. Consequently, the temperature in the fire-compartment is low and the activation of the rest burners does not take place. Regarding the *reference* scenario SC-SP100, the heat release burners are not activated. In this case the temperature of the sensors does not reach the required value of 250 °C due to the reduced burning rate that is imposed by the activation of the sprinklers.

Additionally, it can be observed that as the percentage of the broken windows increases, the activation of the heat release burners is delayed and it takes place more gradually. The activation of the heat release burners starts approximately at the 500th sec of the fire. In the extreme case of SC-00 the fire spreads quickly and the last burner is activated at the 600th sec of the analysis. In the reverse case (SC-100) where all the windows are considered to be broken, the fire spreads more slowly and activation of the burners is finalized at the 1200th of the analysis. This delay can be attributed to the different ventilation conditions in the fire enclosure. Specifically, when a window is open, it is treated as a hole in the wall. In this aspect, the inflow/outflow of the gas is possible. As a result, the velocity field and the temperature distribution in the fire-enclosure are affected. Specifically, the temperature in the compartment is reduced, as the surface of the open windows is increased and the fire spread is delayed.

Regarding the scenario SC-SP40 where the 40% of the sprinkler system is operational, some of the control devices are not activated due to the low temperature values near the active sprinklers. As the percentage of the active sprinklers is reduced, the fire spread is accelerated and all the control devices are activated.

Figure 8-11 presents in a more systematic manner the results and the activation of the first and the last control device is highlighted. The value -1 corresponds to status where none of the devices in the compartment is active. The value 1 indicates that all the devices are active. It is noted that the term “all devices” is referred not to the entity of the devices that are installed in the fire-compartment but to those devices that are finally activated during the fire. Each curve of Figure 8-11 corresponds to the envelopes values of the corresponding diagram in Figure 8-10.

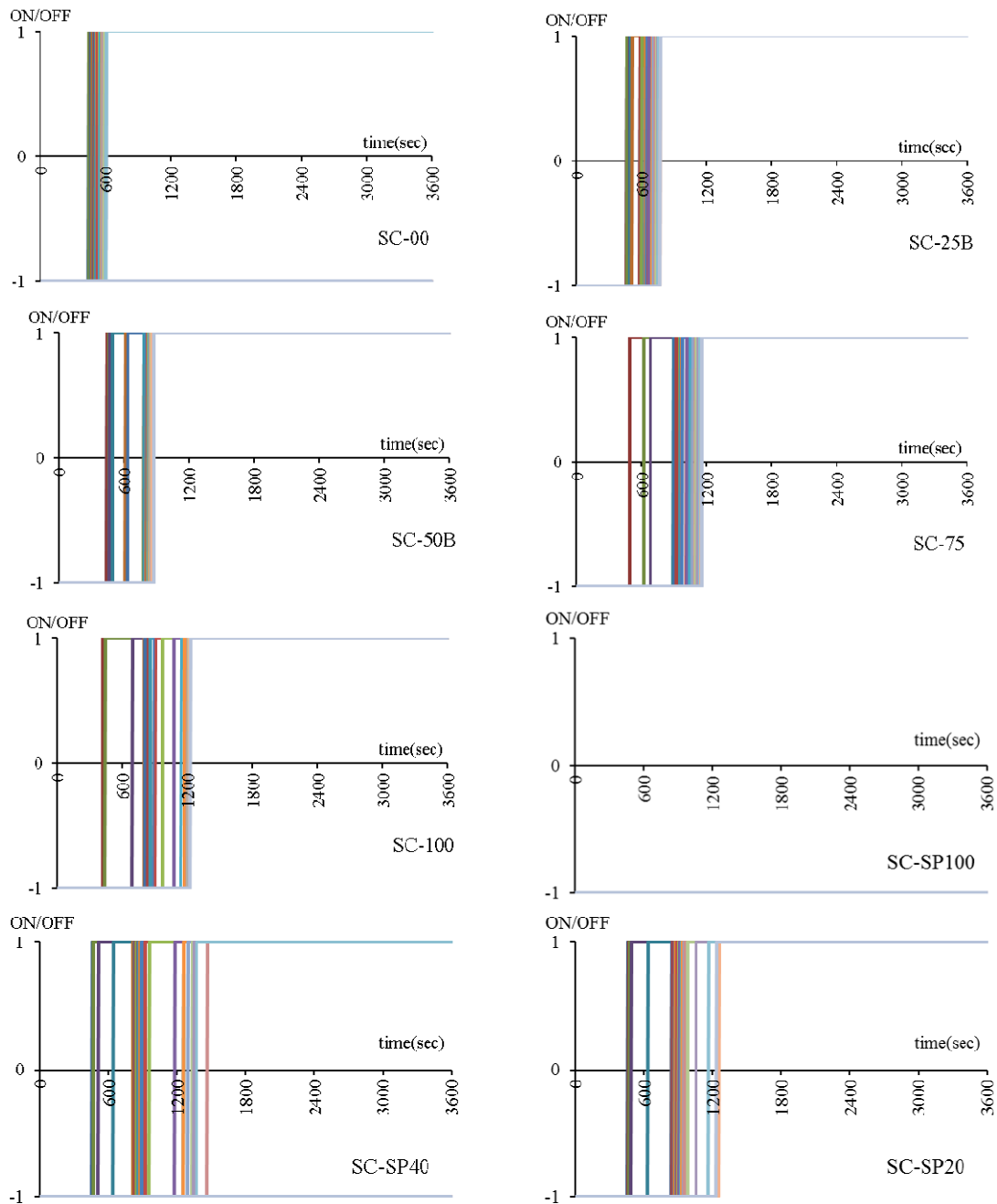


Figure 8-10: Activation of the control devices for the different fire scenarios.

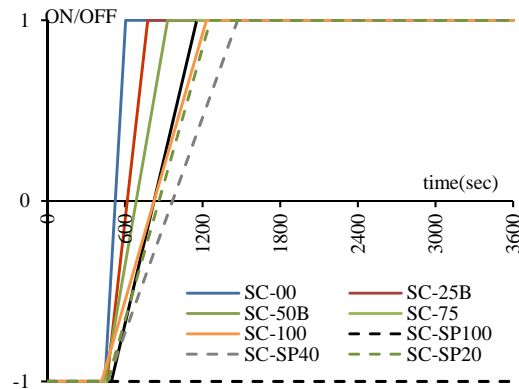


Figure 8-11: Envelope results for the activation of the control devices.

8.2.2 Heat Release Rate

During the fire spread in the enclosure, the HRR burners are activated. The next stage is the growth of the fire. This is controlled by two different factors. The first is the available combustible materials while the second is the available oxygen for the combustion of the fuel volatiles. If the fire is fully developed, the flashover occurs and the maximum HRR is recorded. After this, the fire passes to the decay phase. During the fire, the Heat Release changes as a function of time and it is very crucial, since it characterizes the rate of growth of fire. The results of the analyses regarding the total HRR are presented in Figure 8-12. It is obvious that the fire is ventilation controlled, since the evolution of the total HRR with time depends strongly on the ventilation conditions.

Concerning the *reference* scenario SC-00, the fire is self-suppressed and the flash-over is prevented due to insufficient air supply while, regarding the *reference* scenario SC-SP100, the fire is suppressed due to the fully-operational sprinkler system. In the rest scenarios the fire is fully developed. The “flashover branch” can be detected in the HRR curves that correspond to the fully-developed fires. The flashover is characterized by the steep ascending branch of the HRR curve. It is noted that after the fire spread in the enclosure the flashover immediately takes place.

For example, taking into account the SC-100, the fire-spread is completed at the 1230th sec of the analysis. This means that HRR burners are activated. It can be observed that flashover takes place between the 1250th sec and the 1500th sec of the analysis. Next, the fire is fully developed and the maximum value of the total HRR is recorded.

It is clear that the time where the maximum HRR is recorded is controlled by the accomplishment of the fire spread. Subsequently, the occurrence of the peak value of the total HRR “delays” as the percentage of the broken windows increases, as it can be identified in Figure 8-12.

Additionally, it can be observed that as the area of the damaged (open) windows is increased, the maximum value of the total HRR is amplified. This indicates that the peak value that is recorded depends on the available oxygen in the fire enclosure. Exception to

the previous is the SC-100 where the total HRR is slightly decreased. The maximum value is recorded in SC-75 approximately at the 1700th sec of the analysis.

The position of the damaged windows does not affect the evolution of the total HRR with time, as it is indicated in Figure 8-12. As it is expected, the percentage of the active fire-sprinkler system affects strongly the total HRR in the fire-compartment.

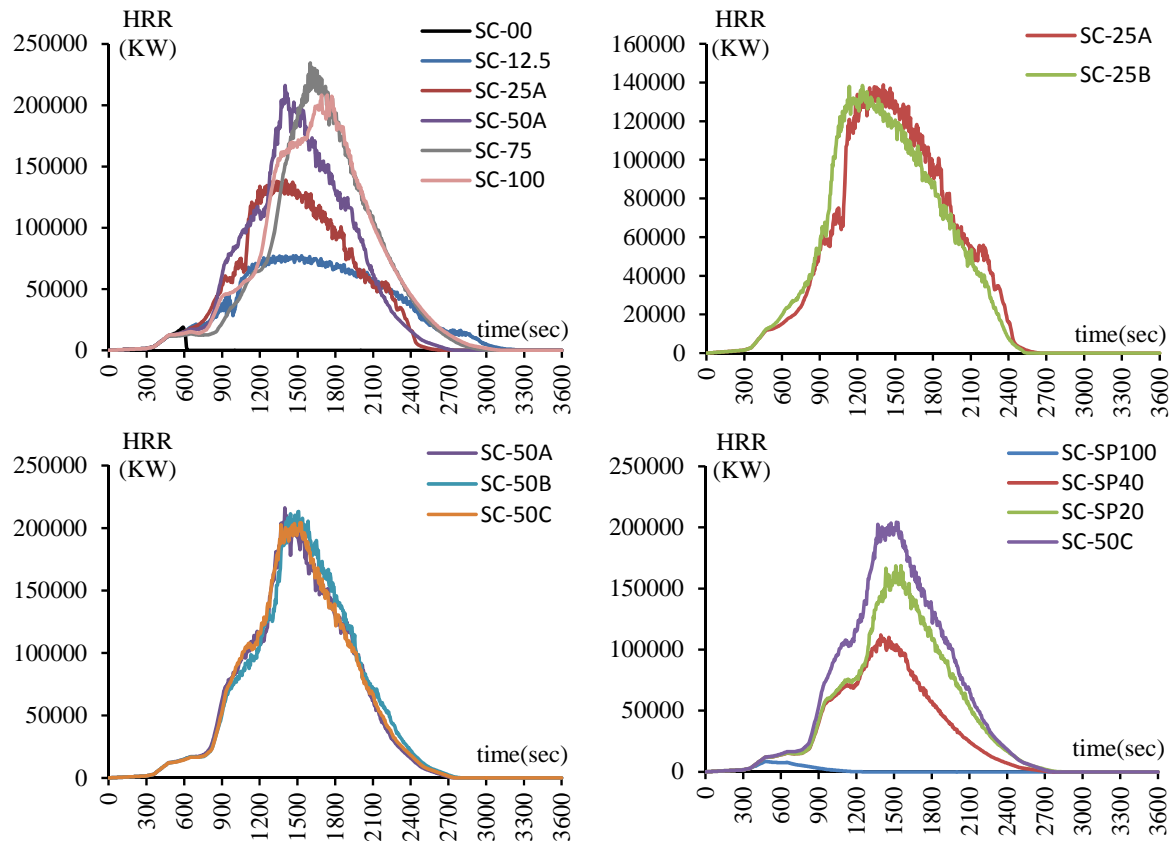


Figure 8-12: Total HRR for the fire scenarios.

8.2.3 Smoke and fire visualization

In order to obtain more integrated aspect of the fire spread and growth in the compartment, the output of the analyses concerning the Heat Release Rate per Unit Volume (HRRPUV) and mass fraction of smoke are presented. The results are rendered by Smokeview (Forney, 2007) as realistic looking for fire and smoke. It is out of scope of this dissertation to study in detail the smoke movement and the energy released during the fire, therefore some illustrative cases are only given. Figure 8-13 depicts six snapshots of the rendering of HRRPUV in the interior and the exterior of the fire-compartment for the SC-75. It can be clearly seen that fire spreads from the ignition point towards the adjacent shelving systems and that at the 1400th of the analyses the fire is fully developed. It is interesting to notice that the flames are extended in the exterior of the compartment in the positions of the open/damaged windows. Additionally it is obvious that the position of open windows affects the fire evolution.

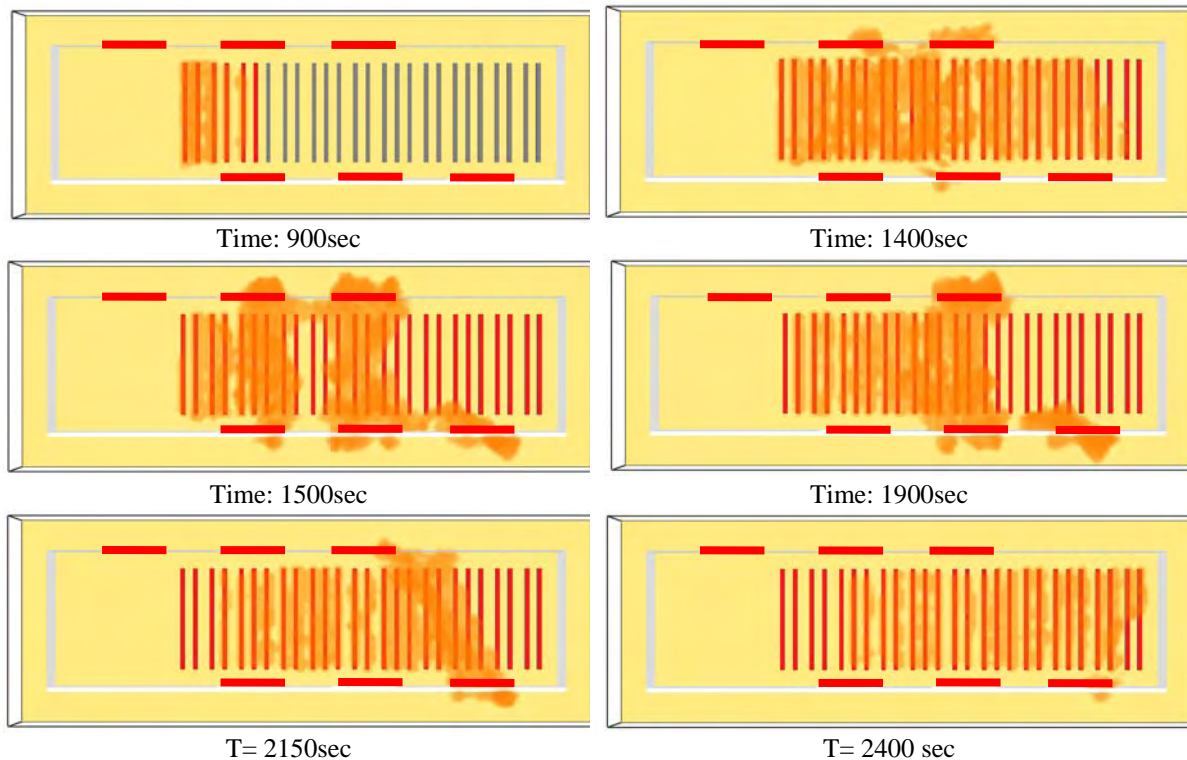


Figure 8-13: Snapshots of rendering the HRRPUV for the scenario SC-75 ($\text{HRRPUV} > 40 \text{ kW/m}^3$).

Figure 8-14 depicts the rendering of the mass fraction of soot in the interior and the exterior of the fire-compartment for the SC-50C. By default, FDS (Mcgrattan *et al.*, 2010a,b) assumes that the smoke from a fire is generated in direct proportion to the heat release. The smoke generation rate is 0.01 of the fuel burning rate. The “smoke” in this case is not explicitly tracked by FDS (Mcgrattan *et al.*, 2010a,b) but rather is assumed to be a function of the mixture fraction. Soot data or smoke is visualized in Smokeview (Forney, 2007) using a variation of a 2D shaded contour, where transparency rather than color is used to represent the opacity or optical thickness of smoke. The method used for visualizing the smoke flow involves a method known as volumetric rendering. Smoke flow is visualized using the optical properties of soot noting that the amount of light obscured by smoke (and hence its shade of grey) depends on the amount of smoke between the observer and the background. Smokeview (Forney, 2007) then integrates the smoke opacity on a grid plane at a time.

The interior view of the fire-compartment is illustrated in Figure 8-14. The HRRPUV is also visualized. An observer is supposed to “walk” in the interior in order to capture the snapshots. The height of the observer is set equal to 2m. It is interesting to notice that the visibility in the fire-compartment is reduced significantly from the early stages of the fire. Similar remarks, concerning the smoke and the fire evolution, hold for all the fire scenarios that are studied.

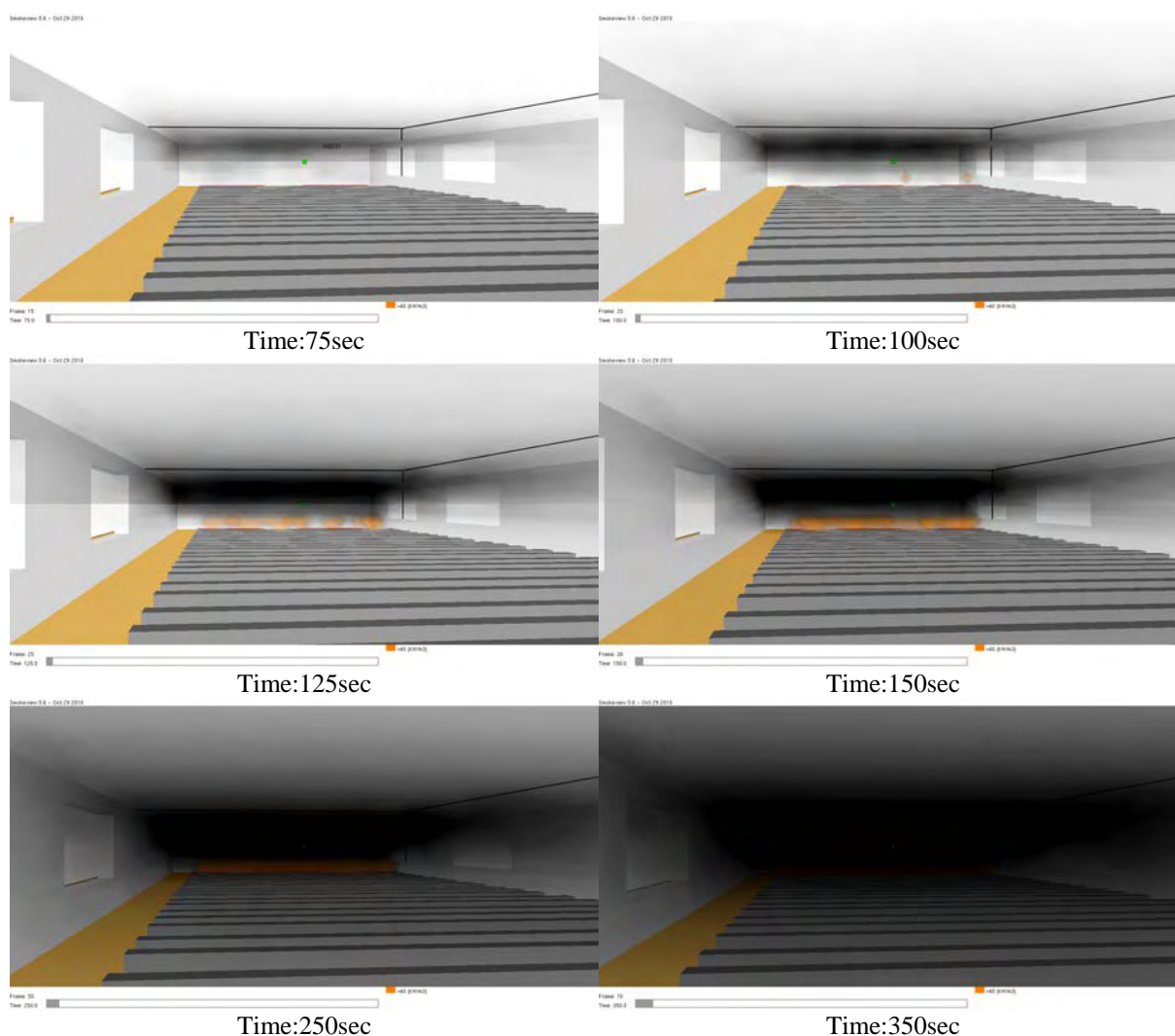


Figure 8-14: Snapshots of rendering the mass fraction of soot and the HRRPUV ($\text{HRRPUV} > 40 \text{ kW/m}^3$) for the SC-50C (Interior view).

8.2.4 Velocity field

The velocity field is also obtained in order to understand more thoroughly the flow of the hot gases in the enclosure and in the surroundings of the fire-compartment. An illustrative example is presented, due to the fact that the specific topic is out of the dissertation's objectives. Figure 8-15 depicts snapshots of the velocity field during the analysis for SC-50C. The vector velocity field is depicted in a slice located at the x - y plane where z is equal to 2m. In the snapshots that correspond to the 450th and the 800th second of the analysis it is noted that the flow is laminar far away from the ignition point and becomes transitional near the region where the combustion takes place. At the next snapshots it is observed that as the fire spreads in the fire-compartment the flow becomes turbulent. Additionally, Figure 8-16 illustrates the inflow and the outflow of gas at the position of the windows at levels $z=1\text{m}$ and $z=2\text{m}$ at the 1250th second of the analysis. It can be noticed that at the lower level ($z=1\text{m}$) the air flows into the fire-compartment while at the upper level ($z=2\text{m}$) the gas flows out of the enclosure. The visual representation of the velocity field constitutes a qualitative verification of the results of the CFD analysis since the fuel flow

evolution in the compartment is in accordance with the description of the fire development which is presented in Section 3.1. In general, the same remarks hold for all the studied scenarios.

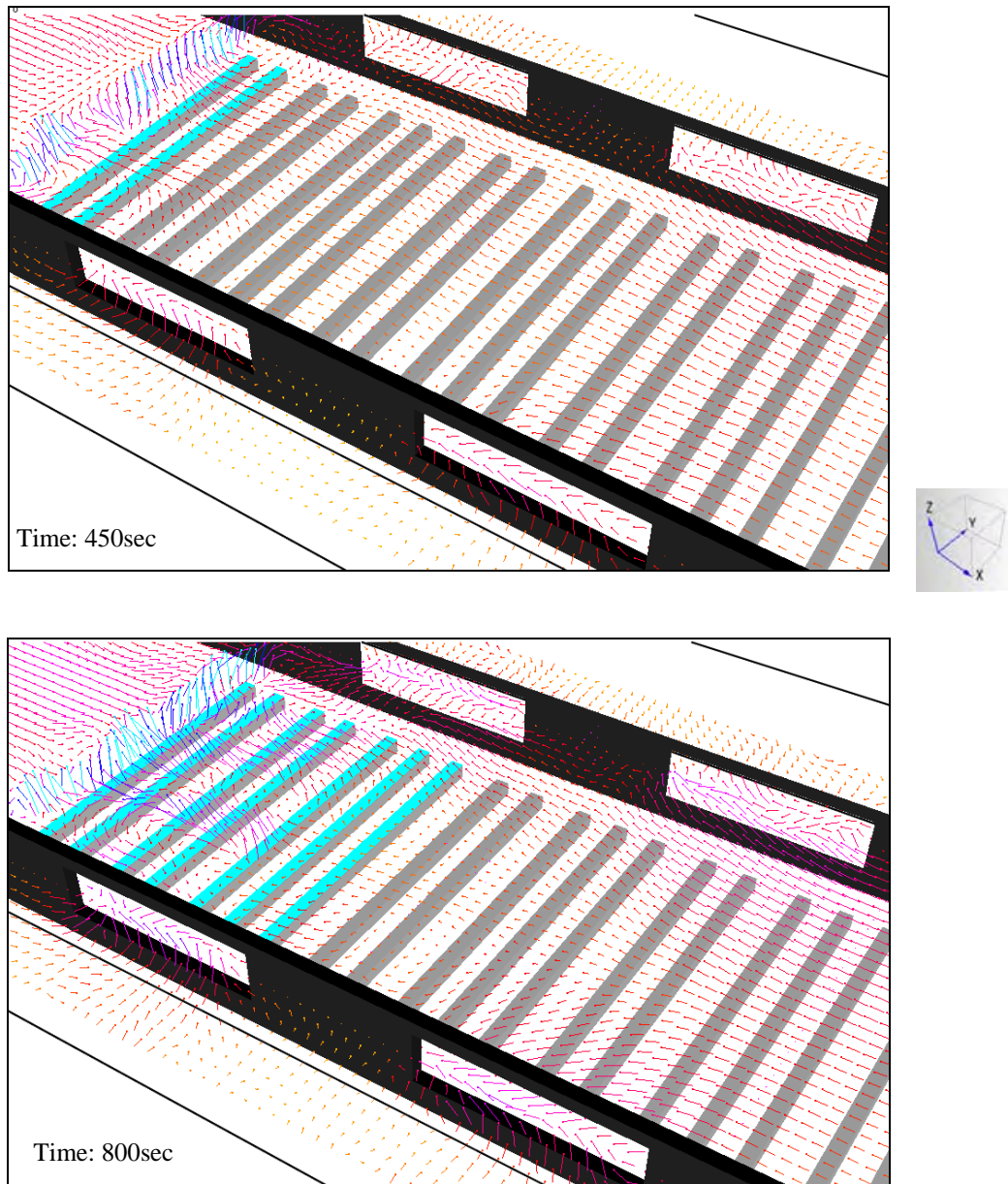


Figure 8-15: Snapshots of the velocity field for the SC-50B.(continued)

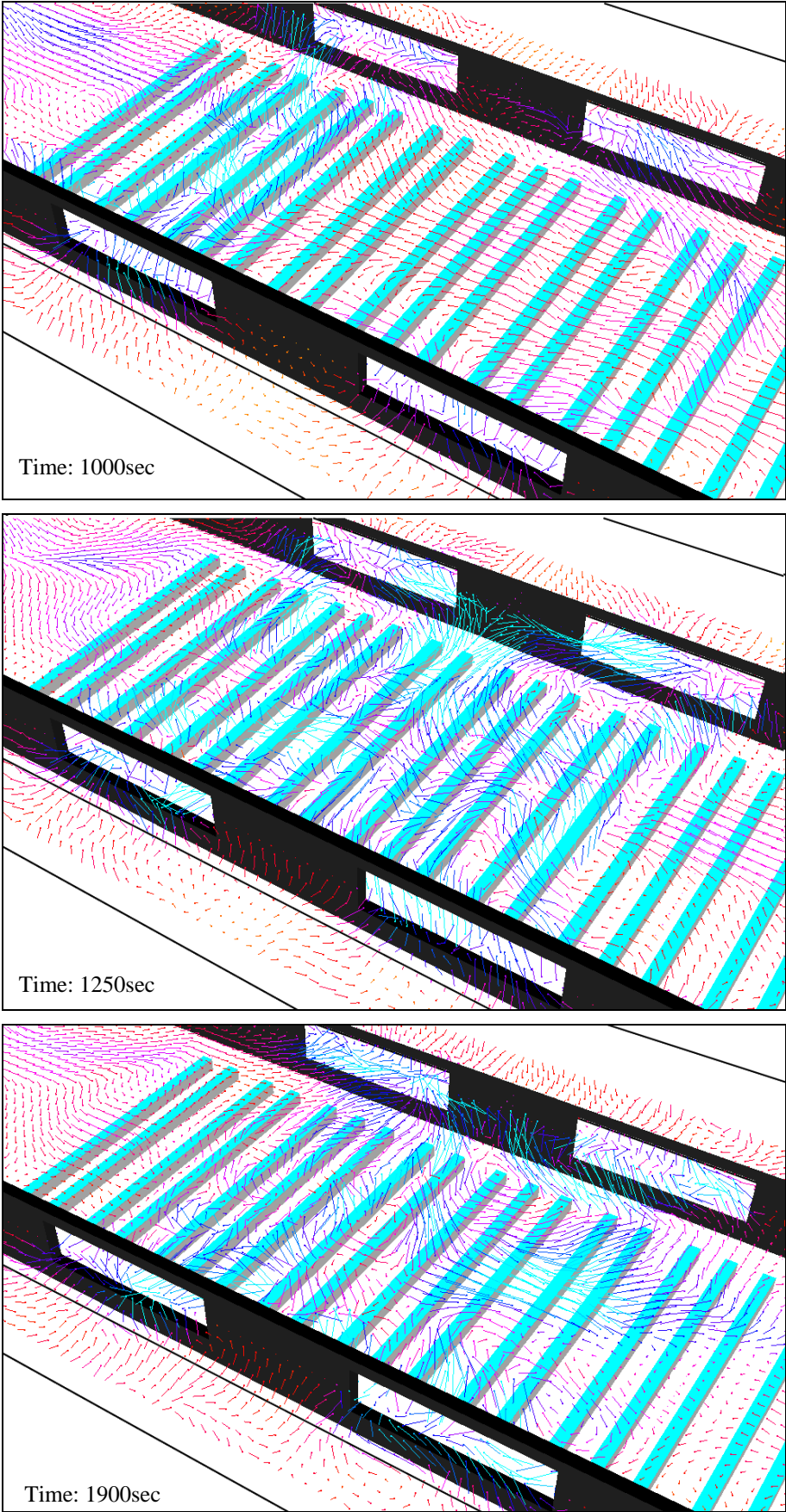


Figure 8-15: Snapshots of the velocity field for the SC-50B.

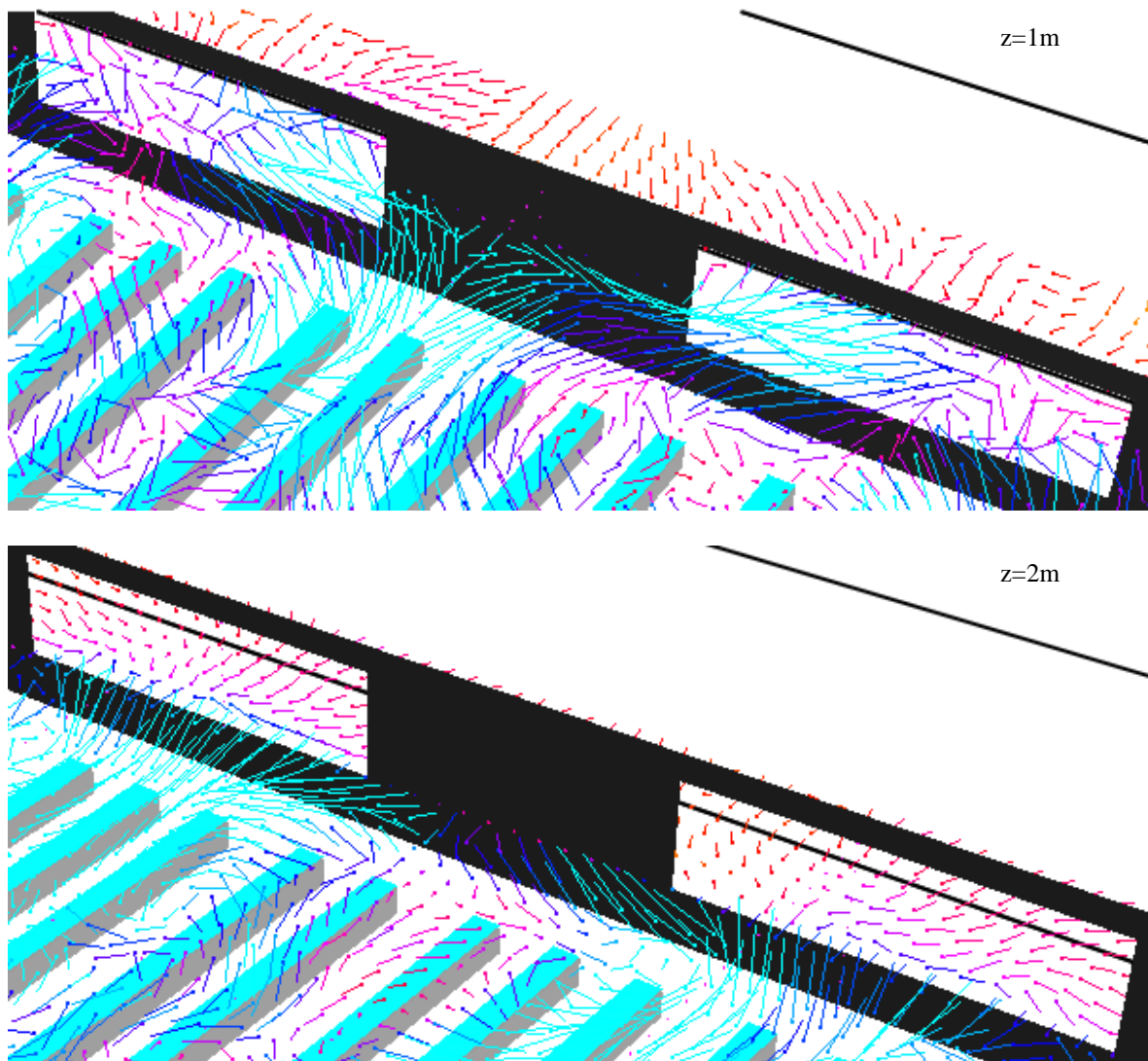


Figure 8-16: Inflow/Outflow at the windows positions at $z=1\text{m}$ and $z=2\text{m}$ (Time:1250sec).

8.2.5 Gas -temperature distribution in the fire-compartment

The temperature distribution in the fire-compartment is presented at different slices in the x- and y-direction (Figure 8-17). The results that are presented in this section are generated using the visualization program Smokeview (Forney, 2007). A “slice” refers to a subset of the whole domain. Normally, FDS (Mcgrattan *et al.*, 2010a,b) averages slice file data at cell corners. For example, gas temperatures are computed at cell centers, but they are linearly interpolated to cell corners and output to a file that is read by Smokeview (Forney, 2007).

Concerning the *reference* scenario SC-00 it noted that the temperature in the enclosure does not exceed the value of $270\text{ }^{\circ}\text{C}$ and that the fire is self-suppressed very quickly (Figure 8-18). Taking into account that one window is damaged due to earthquake (Figure 8-19) the maximum temperature that is recorded in the fire-compartment is considerably increased and it is approximately $720\text{ }^{\circ}\text{C}$. As it is illustrated in the corresponding figure, the phenomenon is localized near the area of the damaged (open) window. For this reason,

SC-12.5 will not be studied further in this dissertation. The results concerning the fire scenarios SC-25A and SC-25B are presented in Figure 8-20 and Figure 8-21 respectively. It is observed that the position of the broken windows affects the temperature distribution in the enclosure and the maximum values that are recorded. After the growth stage of the fire, which is completed approximately at the 1300th second of the analysis, the gas-temperature remains high near the region where the windows are open. The same remarks are valid for the scenarios SC-50A, 50B and 50C that are illustrated in Figure 8-22, Figure 8-23 and Figure 8-24. The most severe seem to be the scenarios SC-75 and SC-100 (Figure 8-25 and Figure 8-26), since the maximum recorded gas-temperature is approximately 1000 °C and the phenomenon is extended in the compartment. In general, it is concluded that the temperature distribution in the enclosure is non-uniform and changes rapidly with the evolution of time. It becomes evident that it is difficult to obtain the gas-temperature time-history for the next stage of the study which is the determination of the temperature profile of the structural members. Thus, the next objective is to focus the study on the gas-temperature “near” the frames of the library building.

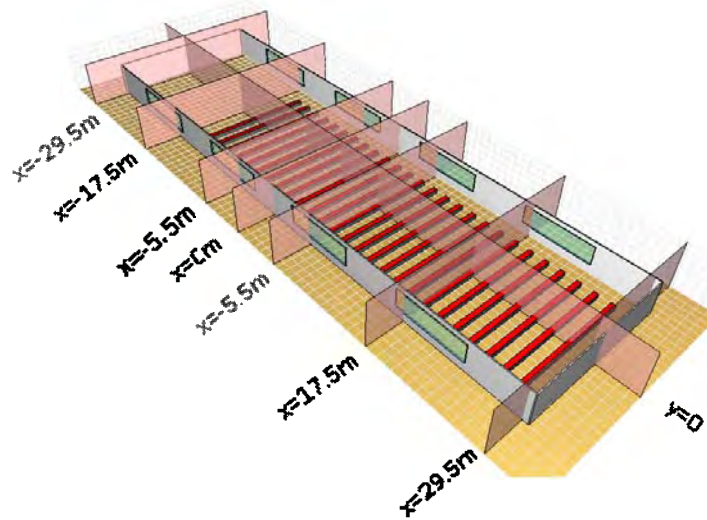


Figure 8-17: Slices for the representation of the temperature field inside and outside of the fire-compartment.

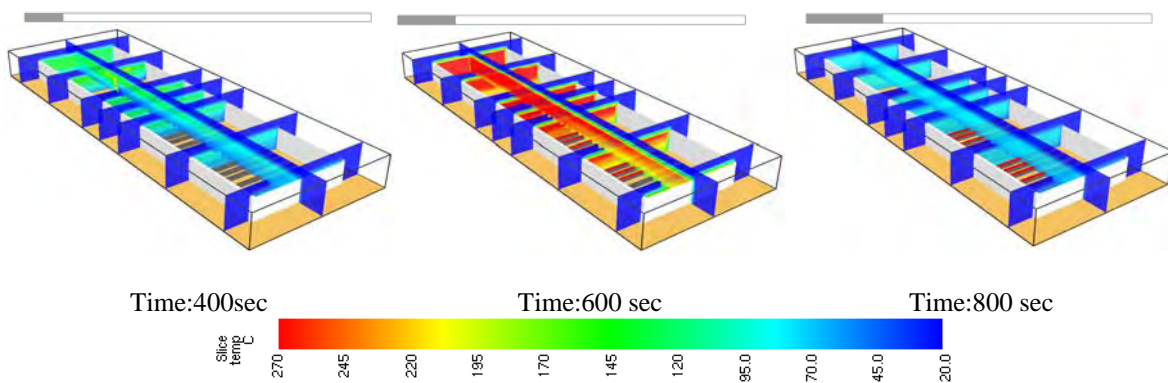


Figure 8-18: Temperature distribution inside/outside of the fire-compartment at different slices for SC-00.

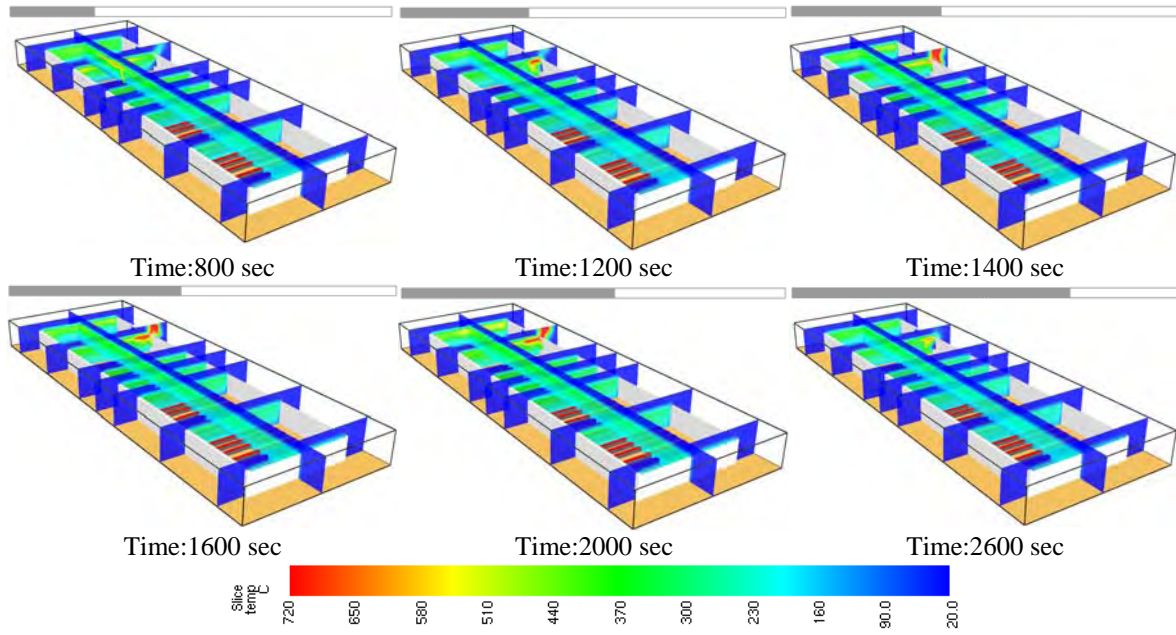


Figure 8-19: Temperature distribution inside/outside of the fire-compartment at different slices for SC-12.5.

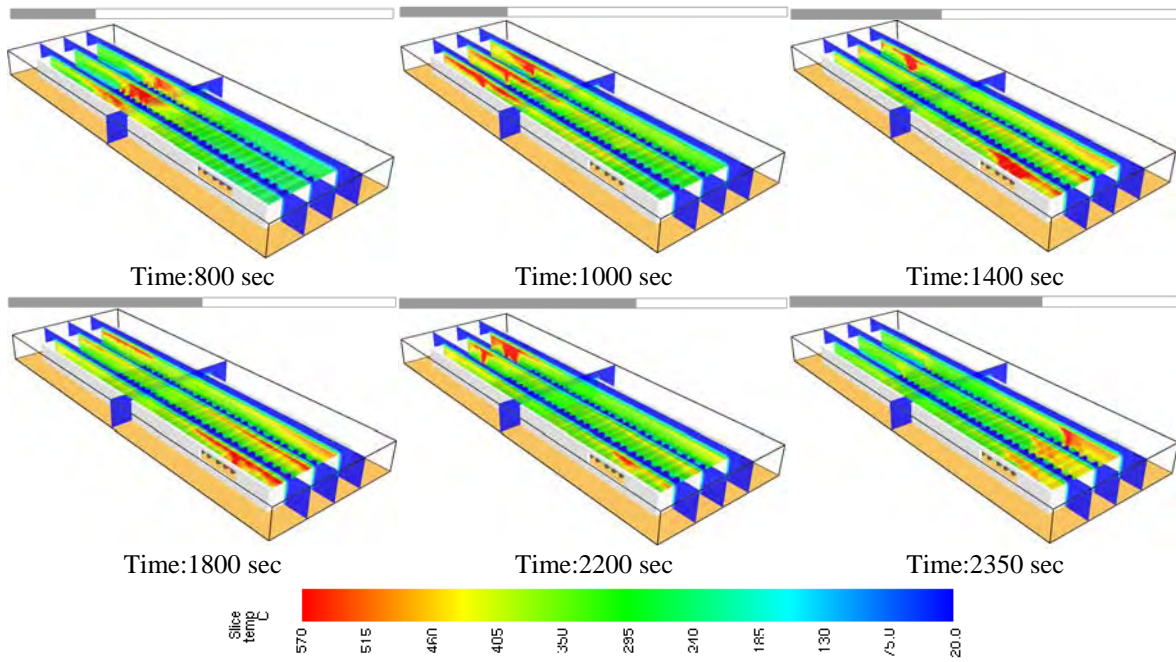


Figure 8-20: Temperature distribution inside/outside of the fire-compartment at different slices for SC-25A.

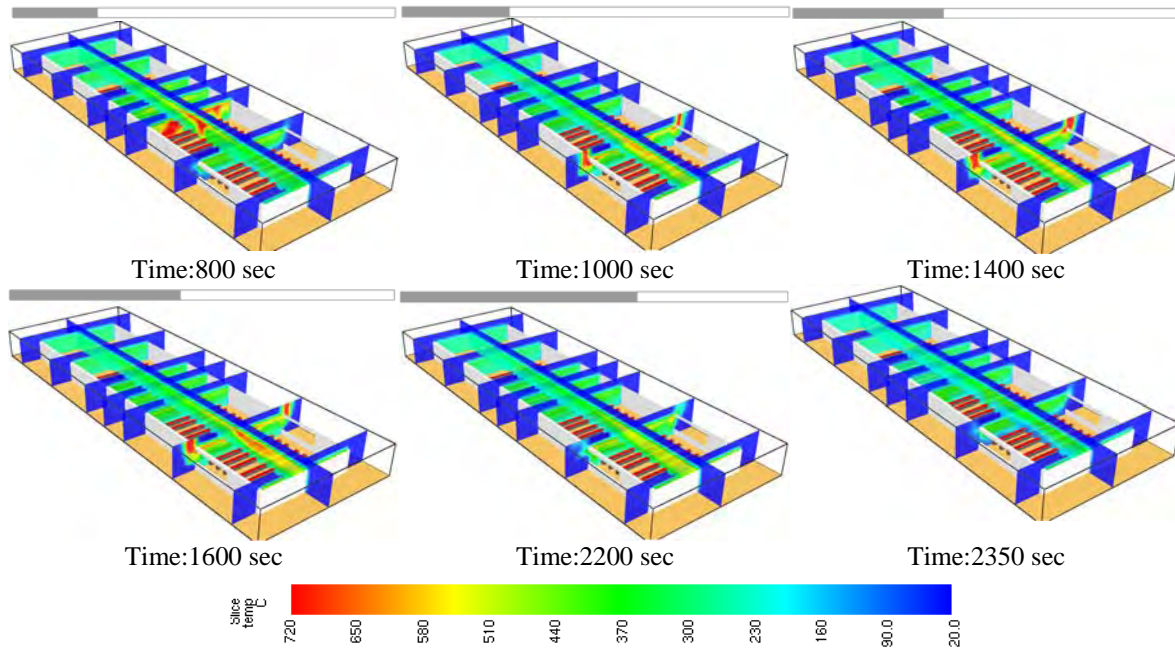


Figure 8-21: Temperature distribution inside/outside of the fire-compartment at different slices for SC-25B.

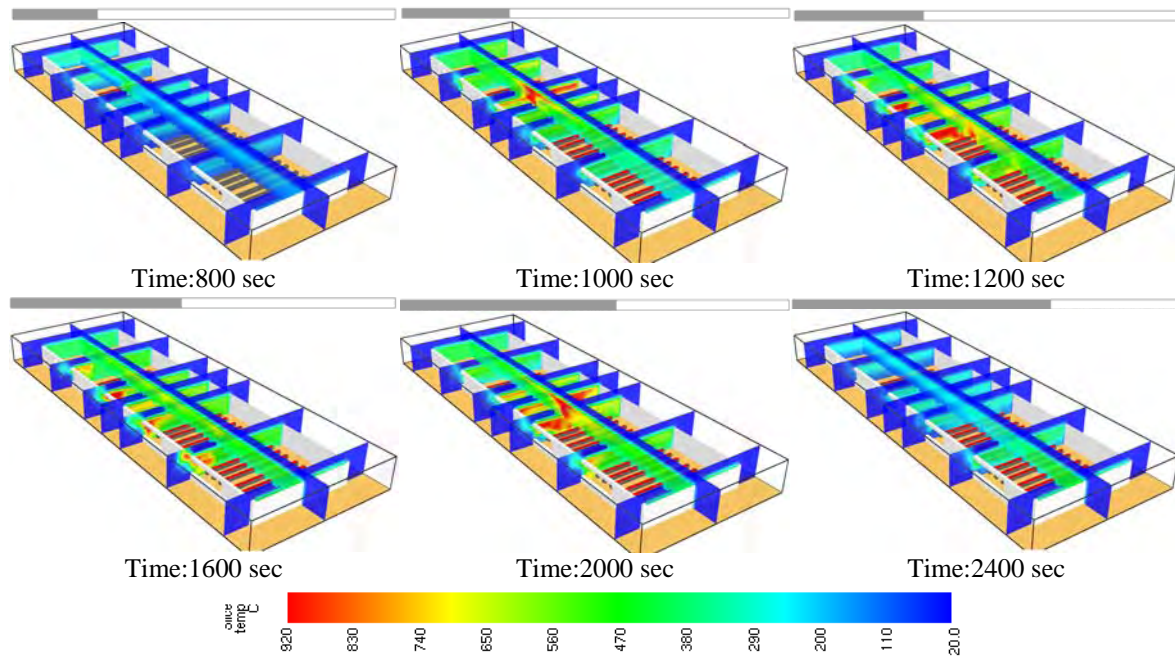


Figure 8-22: Temperature distribution inside/outside of the fire-compartment at different slices for SC-50A.

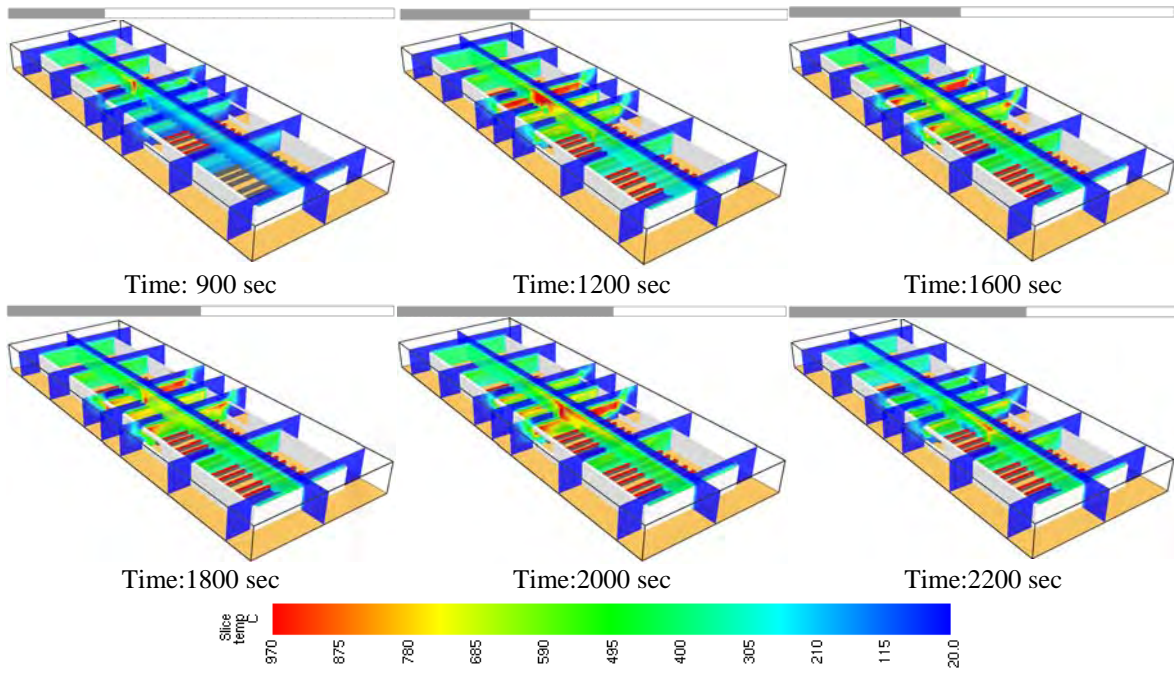


Figure 8-23: Temperature distribution inside/outside of the fire-compartment at different slices for SC-50B.

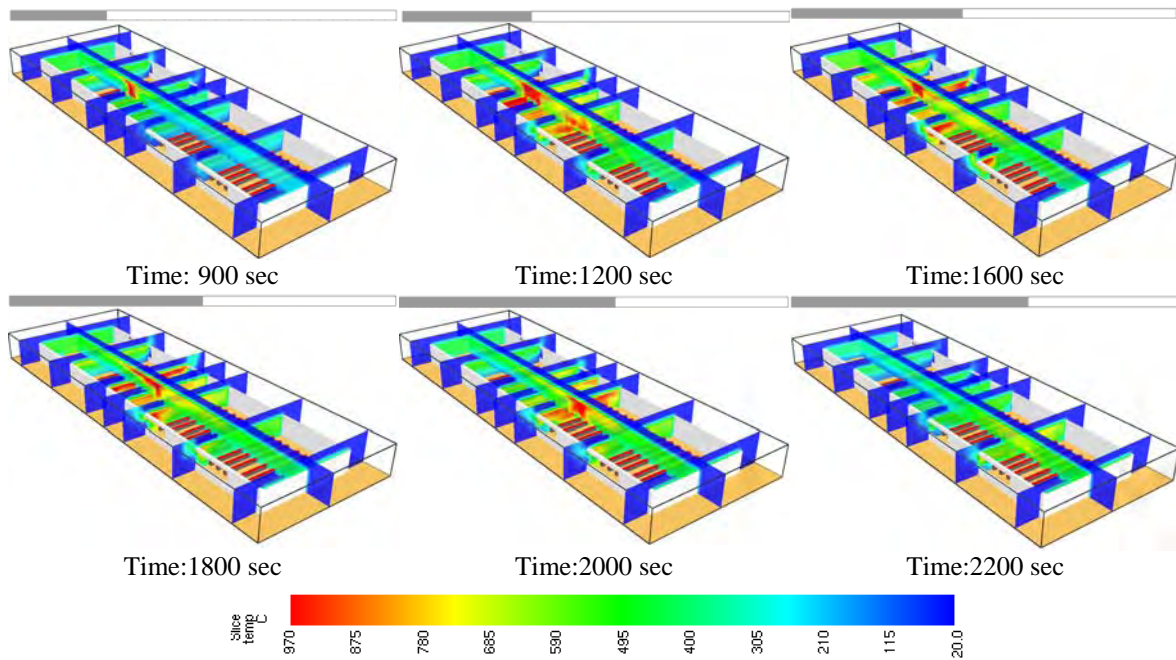


Figure 8-24: Temperature distribution inside/outside of the fire-compartment at different slices for SC-50C.

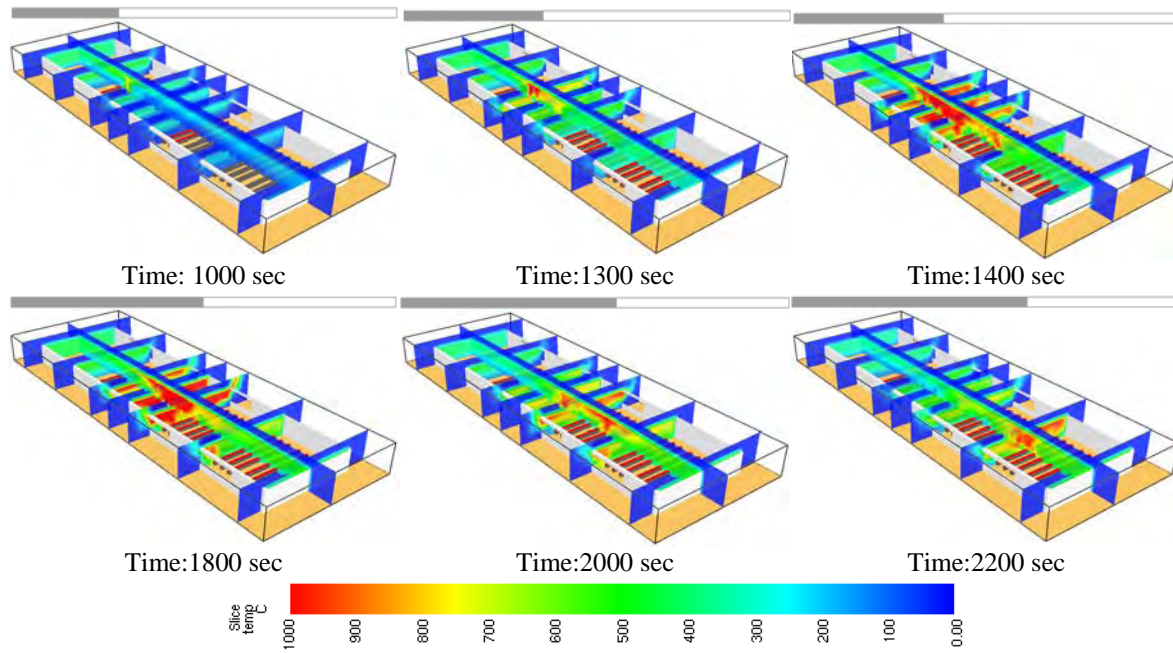


Figure 8-25: Temperature distribution inside/outside of the fire-compartment at different slices for SC-75.

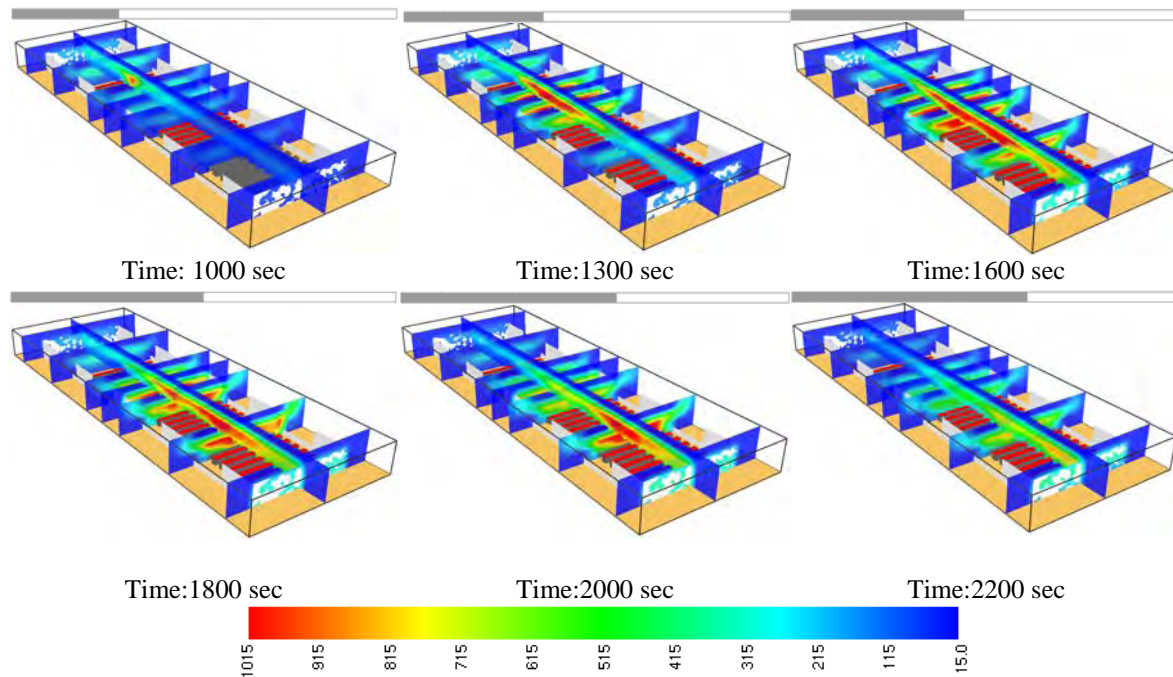


Figure 8-26: Temperature distribution inside/outside of the fire-compartment at different slices for SC-100.

8.2.6 Gas- temperature “near” the structural members

The goal in this Section is to study in detail the gas-temperature distribution near the structural members. To this end, 572 gas-phase devices are used for the recording of the temperature near the frames as it is illustrated in Figure 8-27.

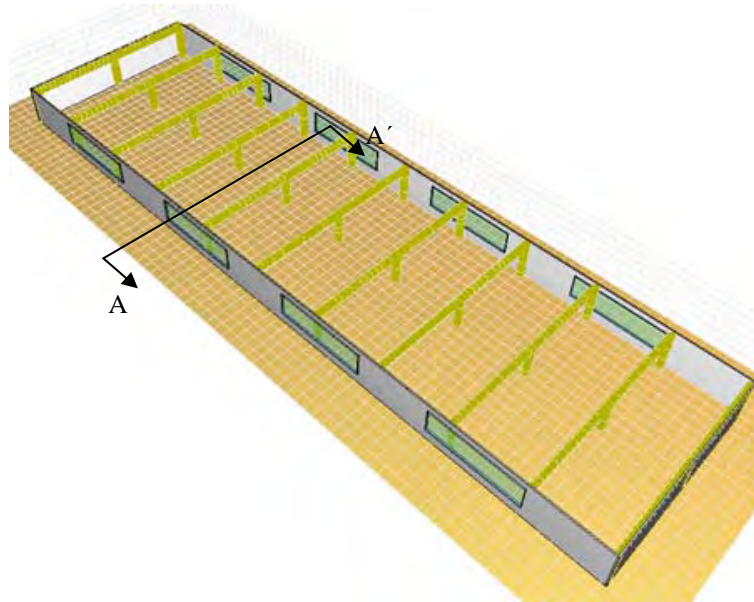


Figure 8-27: Gas-phases devices at the steel-frames positions.

Specifically, the gas temperature was recorded at 52 points around every frame as it is indicated in Figure 8-28. The orientation that is specified for the devices is different for beams and columns. Since the devices are located at a specific point of the mesh, FDS (Mcgrattan *et al.*, 2010a,b) reports the value of the temperature in the cell where the point XYZ is located. The data are recorded in a time interval of 5 sec for the total time history of 3600 sec for all the PEF scenarios.

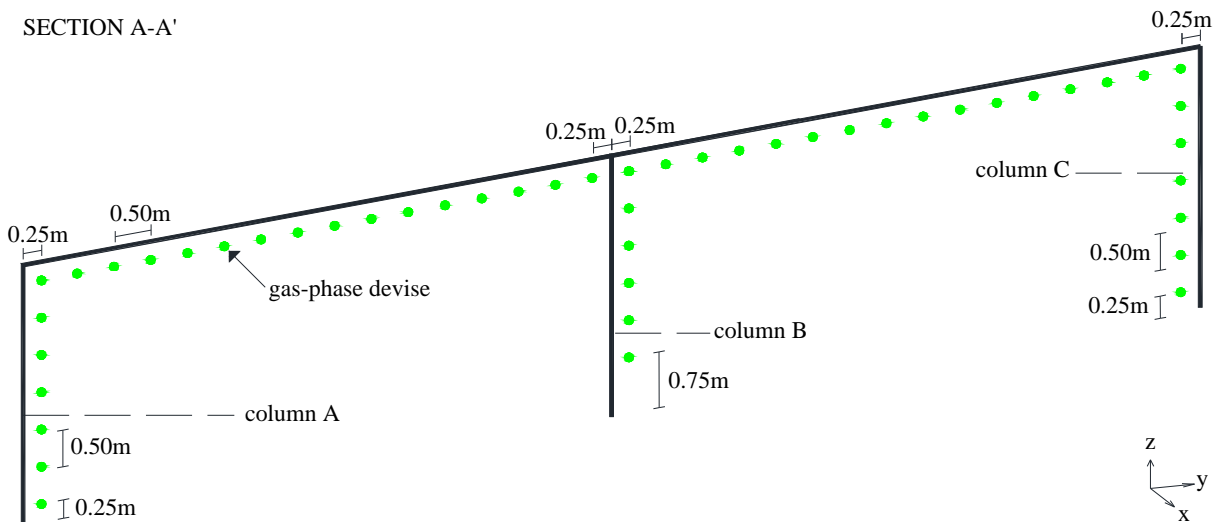


Figure 8-28: Gas-phase devices near the structural members (Section A-A').

The main issue that is addressed at this stage of the dissertation is to understand thoroughly the temperature profile near the structural members in order to decide which is the “critical frame” for every fire scenario. This term “critical frame” is referred to the frame that is more encumbered due to the thermal actions. The identification of the “critical frame” is rather complicated since the temperature is highly non-uniform in the fire-compartment

and it changes rapidly, as it was concluded in the previous section. To this end, the time-history temperature records are plotted along the axis of the members for the entity of the frames that are included in the compartment. Moreover, different snapshots are presented due to the strong variation of the temperature during the analysis.

The results are presented separately for the beams and the columns in order to see more clearly the gas-temperature distribution along the members. The results concerning the SC-75 are presented in the next sections.

Beams

The temperature distribution along the axis of the beams is presented in Figure 8-29 for the time-frames 800, 1200, 1600 and 2000 sec. Six different frames are selected for the representation of the results in order to have a comprehensible view of the temperature distribution. The axial distance between the selected frames is 12m as it is indicated in Figure 7-2. The designation of the frame names is illustrated in the same figure. As it is expected, the temperature along the beams is not uniform and this becomes more intense for the higher temperature values. For example in the snapshot that corresponds to the 1200th sec of the analysis, the temperature of the beam that lies in frame F varies between 820 °C and 1020 °C. In the same snapshot the temperature along the beam located at frame L is quite constant. Moreover, it is clear that the critical beam changes during the evolution of the fire. Regarding the snapshot at the 800th second of the analysis the critical beam is located at frame D and according to Figure 8-29 the position changes to frame F for the snapshots at the 1200 and 1600sec. Finally at the 2000th second the critical beam lies at frame H. Finally, it is noted that the values of the temperature that correspond to the critical beams are touching the value of 1000 °C.

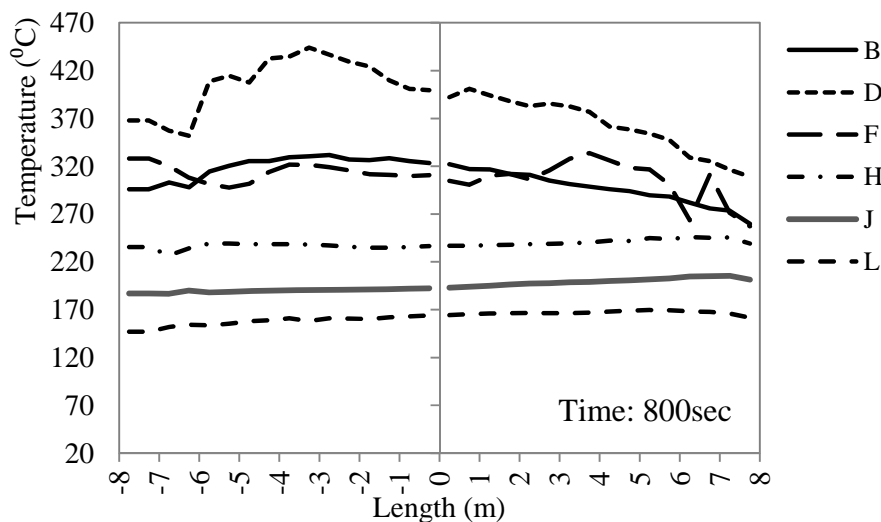


Figure 8 29: Temperature distribution along the axis of the beams that lie at different frames for the SC-75.
(continued)

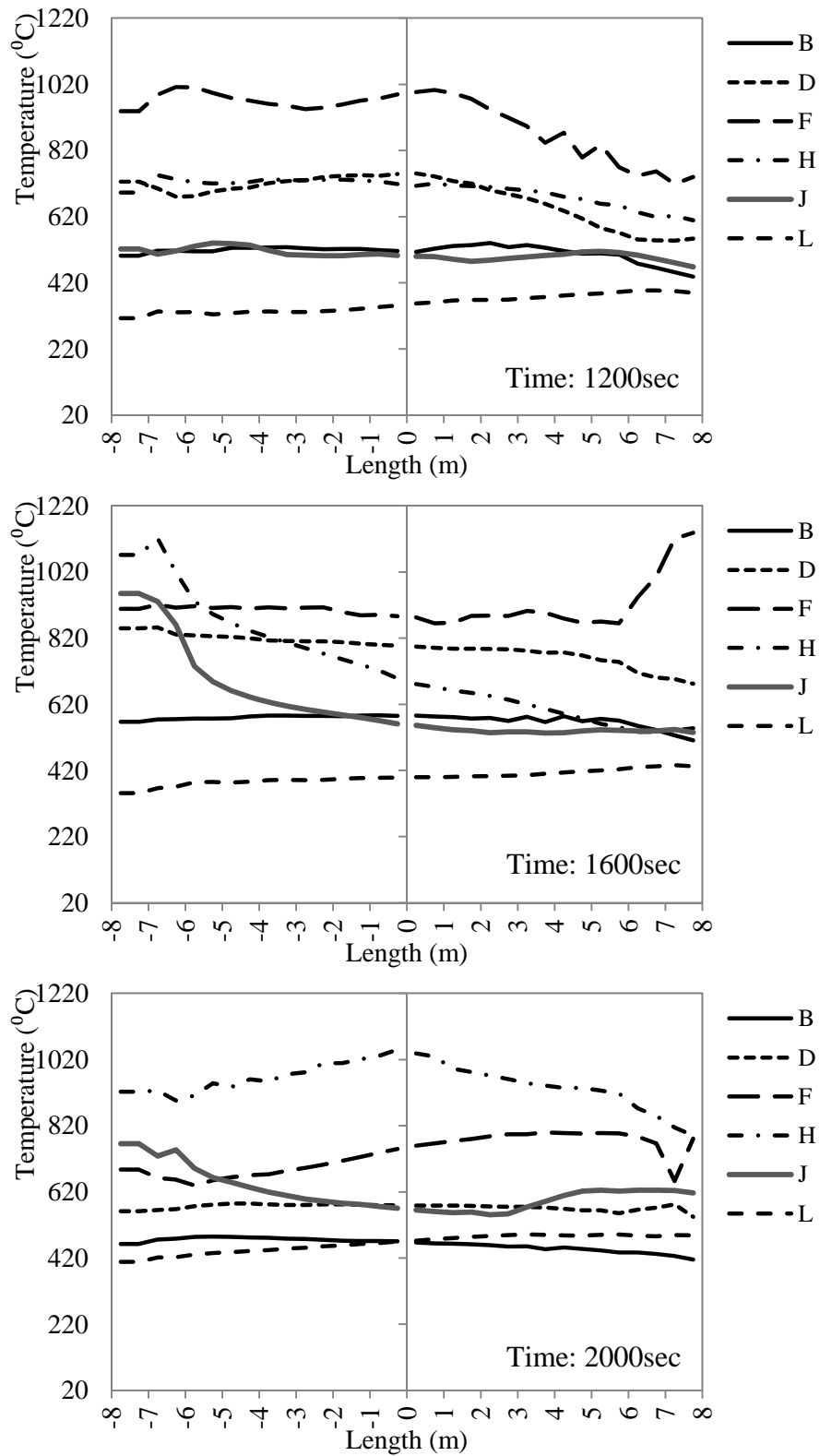


Figure 8-29: Temperature distribution along the axis of the beams that lie at different frames for the SC-75.

Columns

The temperature distributions along the axis of the columns are indicated in Figure 8-30, Figure 8-31, Figure 8-32, Figure 8-33, and Figure 8-36 for the time-frames 800, 1200, 1600th sec and 2000th sec respectively. Each diagram illustrates the temperature profile along the axis of the three columns that are included in every frame. The designation of the column names is given in Figure 8-28. It is noted that regarding the columns A and C, the temperature records over the level $z=0.75\text{m}$ are presented. The records that correspond to the devices that are placed under this level are not of interest due to the very low temperature values that resulted (approximately 25 °C). In the case of column B, the temperature is recorded above the level $z=0.75\text{m}$, due to the presence of the burners in the fire-compartment. It is reminded that the burners are located on obstructions of height equal to 0.50m. The comparison of the temperature profile of the columns that lie in the same frame is completely different. This holds for all the frames at the different snapshots. Moreover, it is obvious that it is almost impossible to define the critical column due to the non-homogenous profiles.

It is reminded that the gas-temperature distributions that are presented in this section are recorded “near” the structural members. The next objective is to use the outcomes of the CFD analyses in order to obtain the temperature profile of the structural members. If the results were to be used in the manner that is presented in this section several issues would arise. The first one is the term “near” which includes the distance between the gas-phase devices and the structural members. Due to the fact that in FDS (Mcgrattan *et al.*, 2010a,b) the temperature is calculated at the center of the cell where the device is placed, in this study the distance is set equal to 0.25m since the meshing size that is applied is about 0.5m in all directions. From the previous it is clear that the term “near” depends on the density of the discretization. As the density meshing that is applied increases, the term “near” is approximated in a better way. On the other hand, the dense discretization results to huge computational time due to the large dimensions of the fire-compartment. The second issue is the strong spatial non-homogeneity and the intense time variation of the gas-temperature profile near the structural members. The last problem is that the CFD model does not actually include the structural members. The devices are just located near to the positions of the frames and the radiation of the structural members is actually ignored.

The previous make clear that an interface between the CFD and the FEM mechanical analysis should be developed in order to link the different kind of analyses. The difficulties that arise during the development of the interface are described in detail in the next section. In fact, this issue is still open in the scientific community and several approaches have been proposed in the literature.

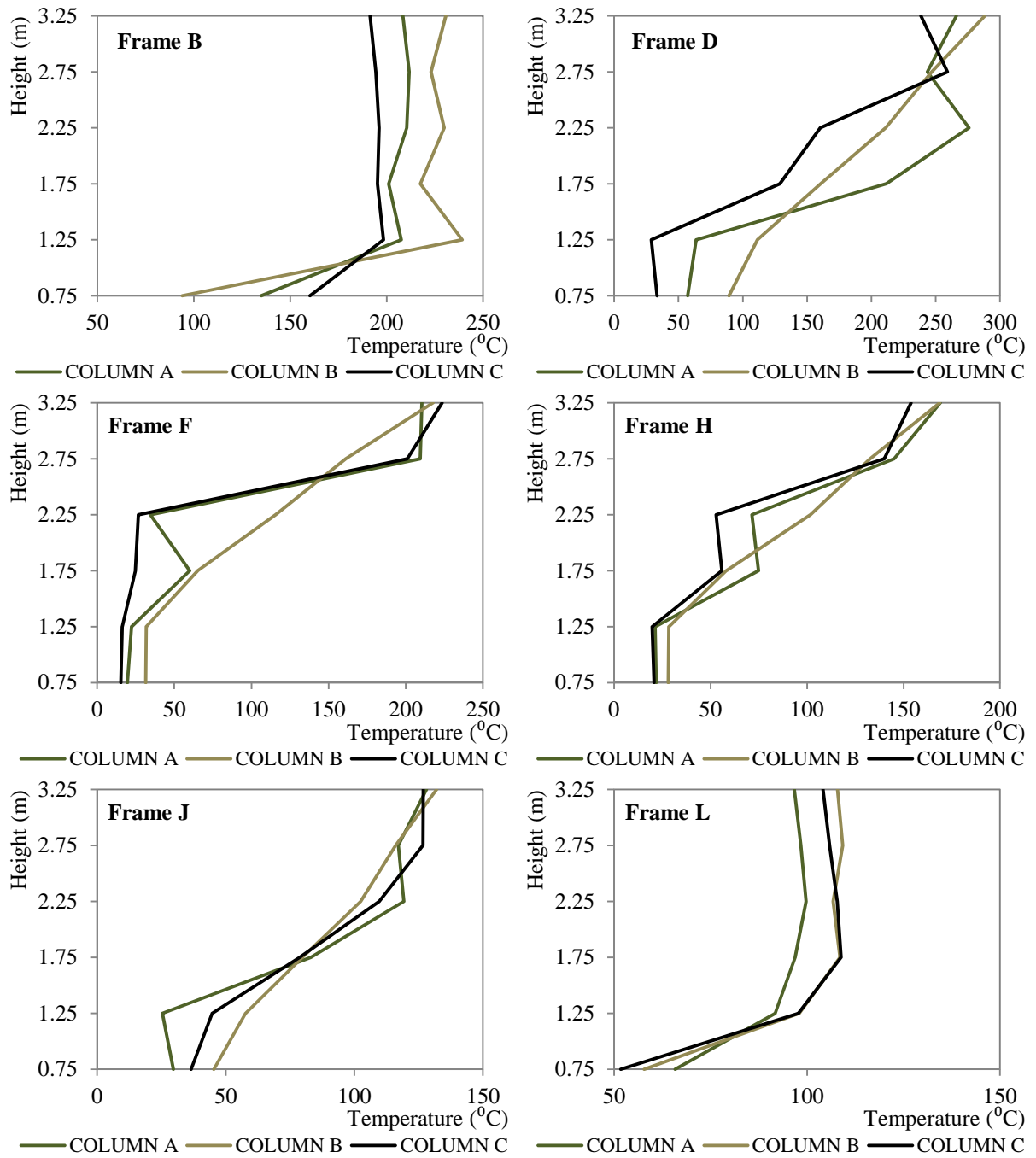


Figure 8-30: Temperature distribution along the axis of the columns in different frames for the SC-75/
Time=800sec.

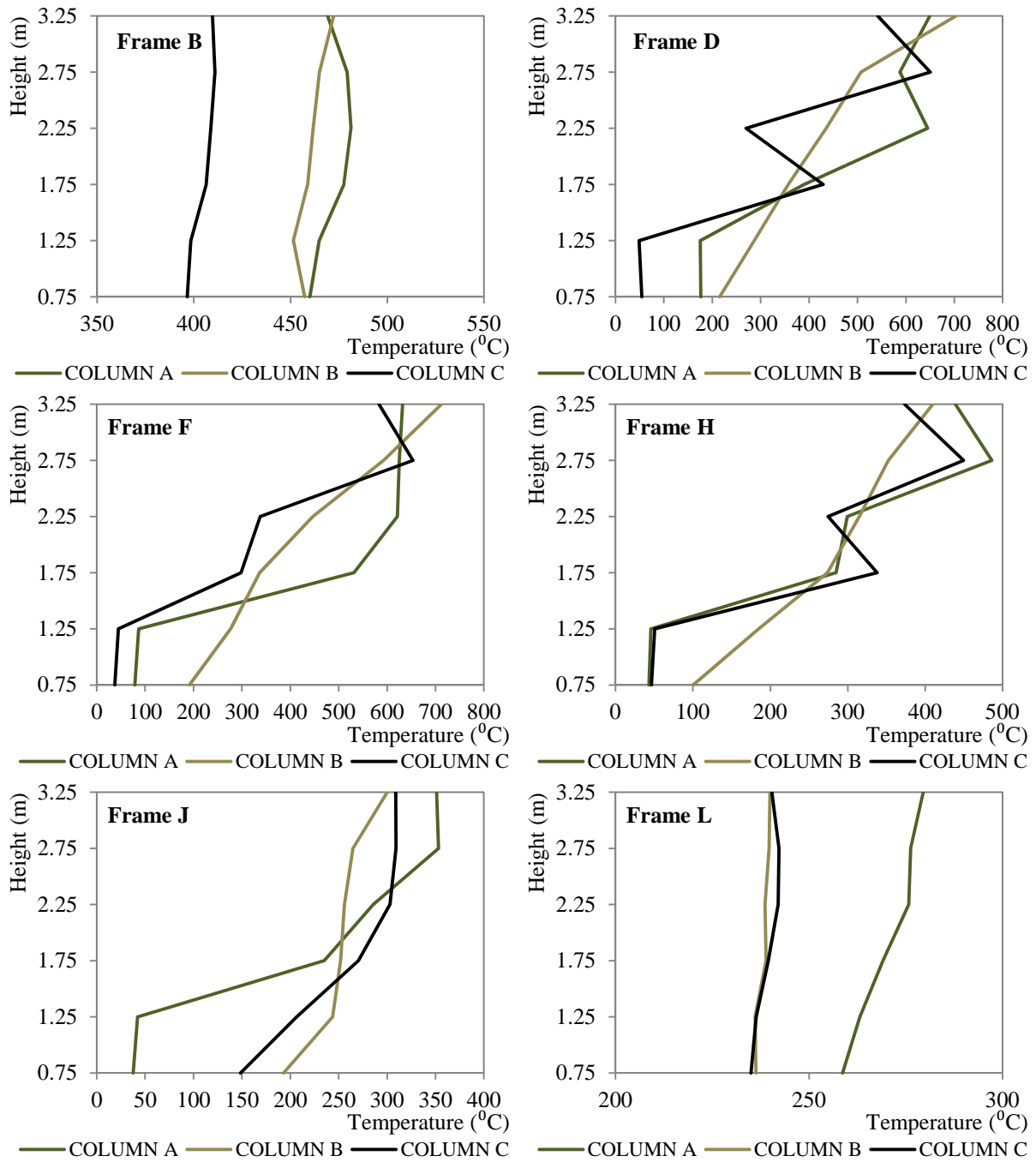


Figure 8-31: Temperature distribution along the axis of the columns in different frames for the SC-75/
Time=1200sec.

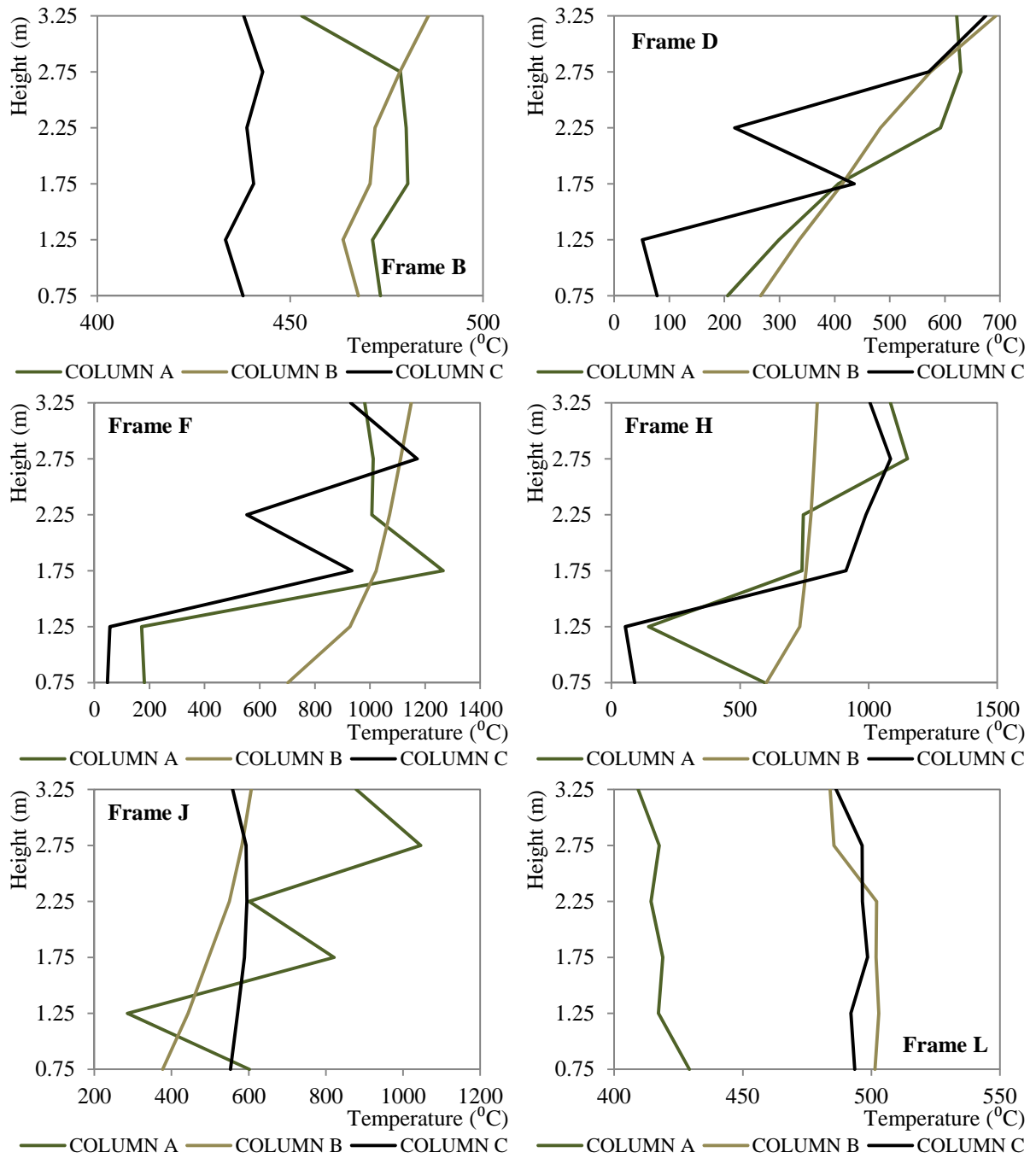


Figure 8-32: Temperature distribution along the axis of the columns in different frames for the SC-75/
Time=1600sec.

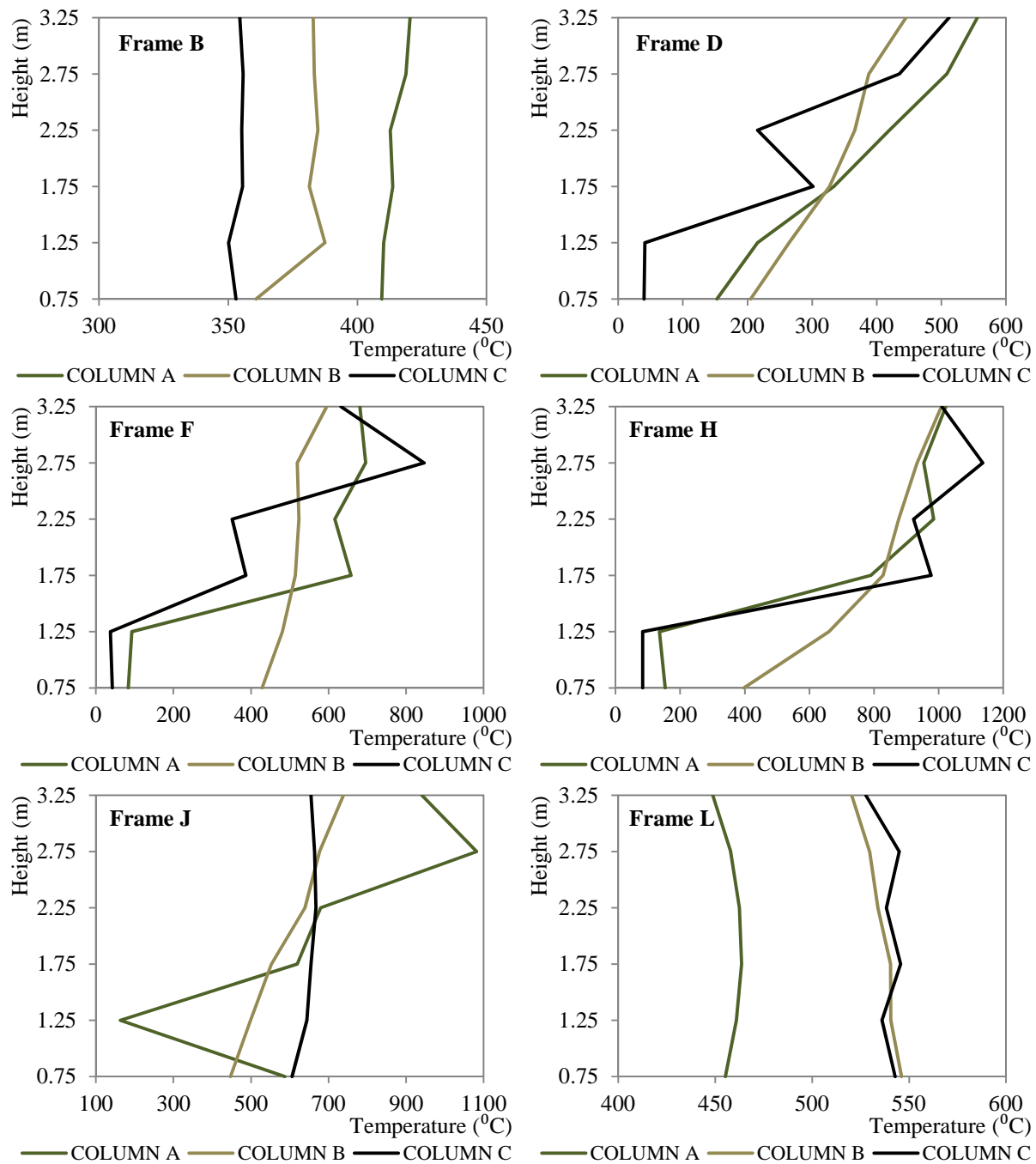


Figure 8-33: Temperature distribution along the axis of the columns in different frames for the SC-75/
Time=2000sec.

8.3 Interface between the CFD and the FEM structural analysis

The next step is to develop the interface between the CFD and the FE structural analysis. The results of the CFD analysis indicate the time evolution of this spatial temperature field in the fire-compartment. Since it is quite complex to evaluate and use the spatial gas-temperature field, a more flexible strategy is followed in this dissertation and the so-called “dual-layer model” is developed. The model is based on the idea that the fire-compartment can be divided into two different layers, the hot smoke (upper) layer and the cold air (lower) layer and that the temperature is uniform at each layer, following the general idea

of the two-zone models that are proposed in EN 1991-1-2. However, the herein developed “dual-layer model” is totally different and the calculations are conducted in the post-processing stage of the CFD analysis. As it is presented in Section 8.2, the results of the CFD analysis do not indicate two distinct zones but rather a continuous profile of the temperature. In order to overcome this difficulty the special layer zoning devices that are included in FDS (Mcgrattan *et al.*, 2010a,b) are used in this dissertation. These devices estimate the layer height and the upper and lower temperature of each layer at a specific point (x,y) using the continuous vertical profile of the temperature along the z -direction.

In the literature several methods have been proposed (Hamins *et al.*, 2005, Prasad and Baum, 2005a, Wickström *et al.*, 2007, Tondini *et al.*, 2012) for the estimation of the two zone characteristics (upper and lower temperature and layer height). The method used in FDS (Mcgrattan *et al.*, 2010a,b) is described in detail in (Janssens and Tran, 1992). First the continuous function $T(z)$ is obtained which defines the temperature T as a function of the height above the floor z , where $z = 0$ is the floor and $z = H$ is the ceiling. The question that arises is how to calculate the unknown variables z_{int} , T_u and T_l , from a series of temperature measurements at a discrete number of heights. T_u represents the upper layer temperature and T_l the lower layer temperature, and z_{int} as the interface height (actually the lower layer height). Quintiere *et al.* (1984) proposed the method that is used in this study. Initially, T_u is defined as the average of the upper layer temperature. Then, z_{int} and T_l are calculated from the integral equations:

$$(H - z_{\text{int}})T_u + z_{\text{int}}T_l = \int_0^H T(z)dz = I_1 \quad (8.1)$$

$$(H - z_{\text{int}})\frac{1}{T_u} + z_{\text{int}}\frac{1}{T_l} = \int_0^H \frac{1}{T(z)} dz = I_2 . \quad (8.2)$$

Here, the Simpson’s Rule is applied for the numerical integration of I_1 and I_2 . T_u is defined as the average upper layer temperature via:

$$(H - z_{\text{int}})T_u = \int_{z_{\text{int}}}^H T(z)dz . \quad (8.3)$$

Actually, (8.1) is the equation that describes mathematically the two-zone model and has no-physical meaning, although is very close to the requirement for the equivalence of enthalpy. Equation (8.2) describes the mass equivalence (Keski-Rahkonen, O. and Hostikka, S., 2002).

In the current study the layer zoning devices are placed every one meter along the x - and y -directions on the model plan as it is illustrated in Figure 8-34. The three-dimensional view of the devices is presented in Figure 8-35. Totally 1036 layer zoning devices are installed in the library interior. Then, the fire-compartment is separated into 10 different virtual zones, each corresponding to the “effective area” for every *two* frames (effective length equal to 6m), as illustrated in Figure 8-36. It is noted that each virtual zone is assumed to include two sub-frames e.g. the sub-frames are f-b and f-b1 are included in zone b, the sub-

frames are f-c and f-c1 are included in zone c, etc. The effective length is set equal to 6m in order to compress the results. A more dense discretization (“effective area” for every frame) of the area of the building, in virtual zones, leads to extended results and there is no actual profit, since, the gas-temperature of adjacent sub-frames (e.g. f-c and f-c1) results to be very close (according to the results of several trial analysis that were conducted with respect to the length of the virtual zones). For this reason, in the following, the temperatures that arise for each virtual zone are referred to the corresponding sub-frames, as it was defined in the previous (i.e. the temperature for the sub-frame f-c results to be identical to the temperature of sub-frame f-c1).

Regarding each virtual zone, the mean value of the output results for the layer zoning devices (layer height, upper and lower zone temperature), are calculated. This indicates that the gas-temperature is assumed to be uniform along every virtual zone. Moreover, it is highlighted that the temperature is assumed uniform at the upper and the lower layers, in z-direction. This becomes vibrant through Figure 8.37. Taking into account the previous, the problem is simplified and three different time-histories are calculated in each virtual zone: the layer height and the gas-temperature of the upper and the lower layers.

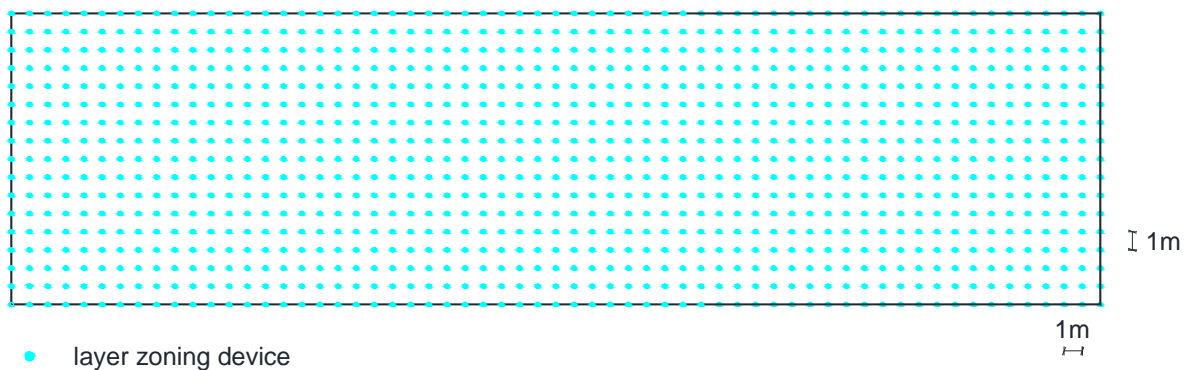


Figure 8-34: The plan-view of the library building with the layer zoning devices.

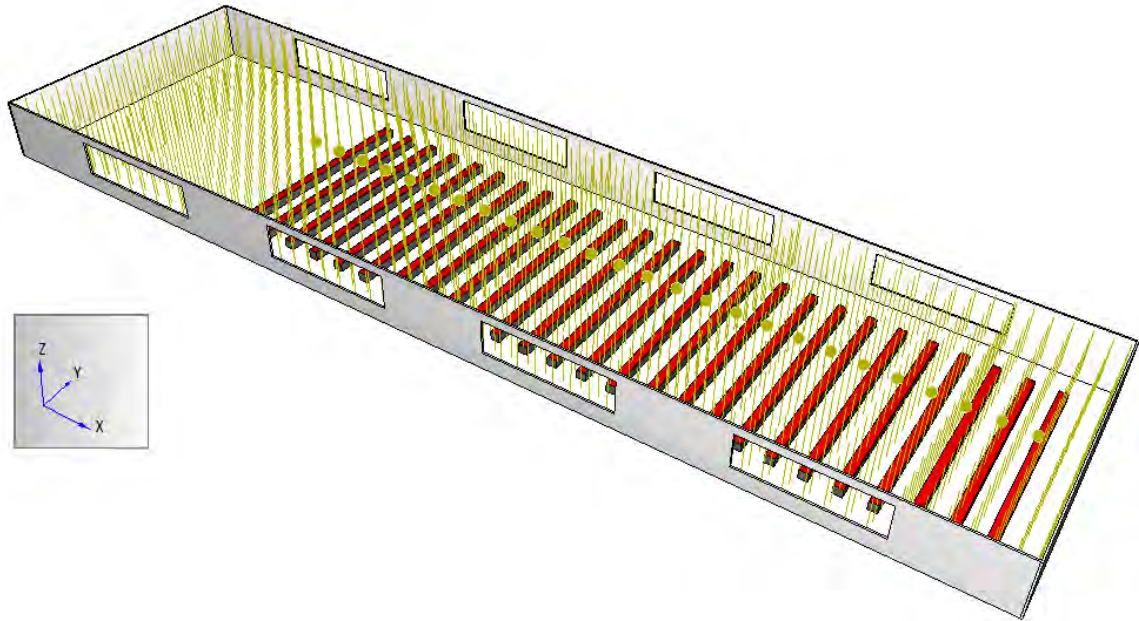


Figure 8-35: 3D view of the layer-zoning devices.

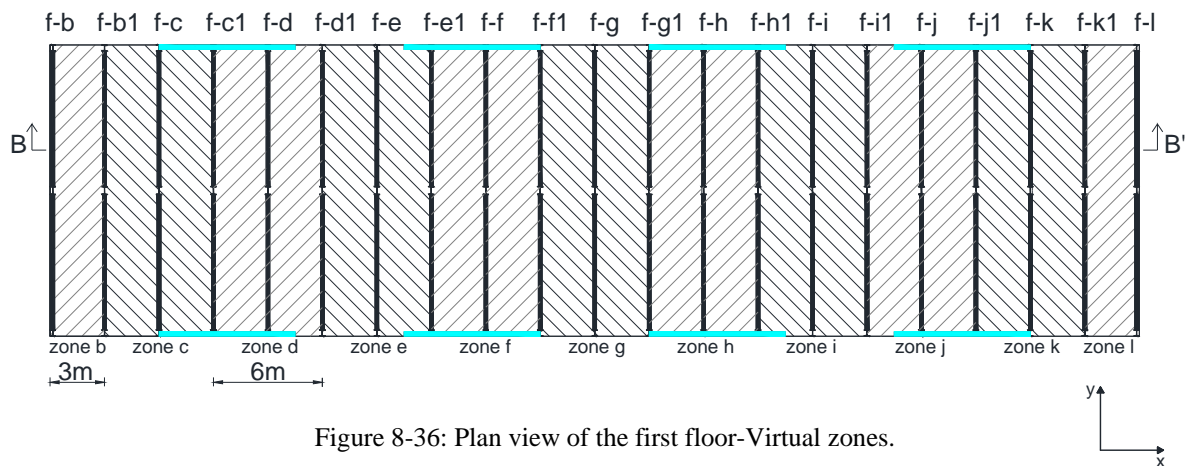


Figure 8-36: Plan view of the first floor-Virtual zones.

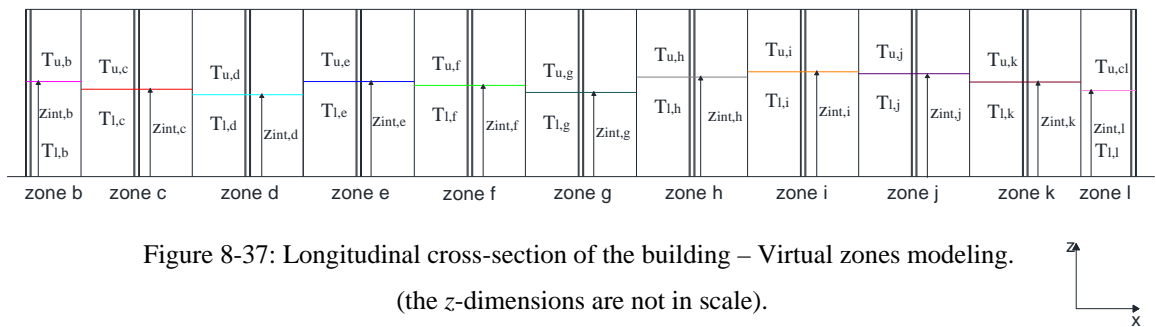


Figure 8-37: Longitudinal cross-section of the building – Virtual zones modeling.

(the z-dimensions are not in scale).

The results of the “interface model” that is developed in order to link the CFD analyses with the FEM mechanical analyses are presented in two different sections. Initially, the gas-temperature of the lower and the upper layers are presented for all the scenarios that are considered in the study. In the sequel the time evolution of the height of the layer z_{int} is given, in order to understand more clearly the “dual-layer” post-processing model.

Gas-temperature at the Lower and upper layers

The evolution of the gas-temperature with time for the upper and the lower layers are presented in Figure 8-38 up to Figure 8-45 for all the fire scenarios. The results concern all the virtual zones that are included in the “interface model”, in order to understand the spatial temperature variation in the fire-compartment.

In the scenario SC-25A (Figure 8-38) it is observed that at first the temperature increases, and a peak is recorded approximately between the 600th sec and the 900th sec of the analysis. This peak is recorded at different time-frames for each on the virtual zones, and it can be attributed to the fire spread in the compartment. In the sequel, the temperature remains quite constant. Regarding the lower layer, the temperature varies between 200 °C and 300 °C while the corresponding values for the upper layers are 300 °C and 500 °C. After the constant branch, a second peak is recorded. This is a local phenomenon and can be connected to the sudden heat release from the burners located at zones j, k and l. This is also visualized in Figure 8-20. After this, the temperature decreases rapidly in both layers. The spatial gas-temperature distribution in the enclosure during the analysis is quite constant, since the variations between the layers are small. The same remarks, concerning the peak values and the constant branch, hold also for the SC-25B scenario. In this case the difference lies on the fact that the curves that correspond to the different virtual zones (especially for the upper layer) are more discrete and this indicates that the spatial temperature distribution in the enclosure is non-uniform. As the percentage of the broken/open window increases, (SC-50A and SC-50C) the temperature distribution in the enclosure is completely non-uniform. The time evolution is different for each virtual zone and this strongly depends on the position of the broken windows. The spatial variation is strongly non-uniform, especially in the upper layer, where the zones are well-separated. This behaviour conforms to the temperature distribution as it is presented in Figure 8-22 and Figure 8-24. The spatial distribution of the gas-temperature is totally non-uniform for the scenarios SC-75 and SC-100. It is noted that in both cases the gas-temperature is high in the lower layer for most of the virtual zones. Finally, it is observed that for low percentage of the broken/open windows a constant plateau (with respect to the time evolution) can be detected in most of the virtual zones. This plateau is not present in the cases that the percentage of open/broken windows is higher and it is replaced by a single peak. This is more obvious in SC-100.

Concerning the scenario SC-SP40, where 40% of the sprinkler system is active, it is observed that the temperature of all the virtual zones is decreased, compared to the gas-temperature distribution that is recorded in SC-50C. In the virtual zones where the sprinklers are active, the temperature is considerably reduced. Especially in the lower layer the maximum recorded gas-temperature fluctuates approximately at 200 °C. The reduction of the temperature is more obvious as the percentage of the broken sprinklers increases (SC-SP20).

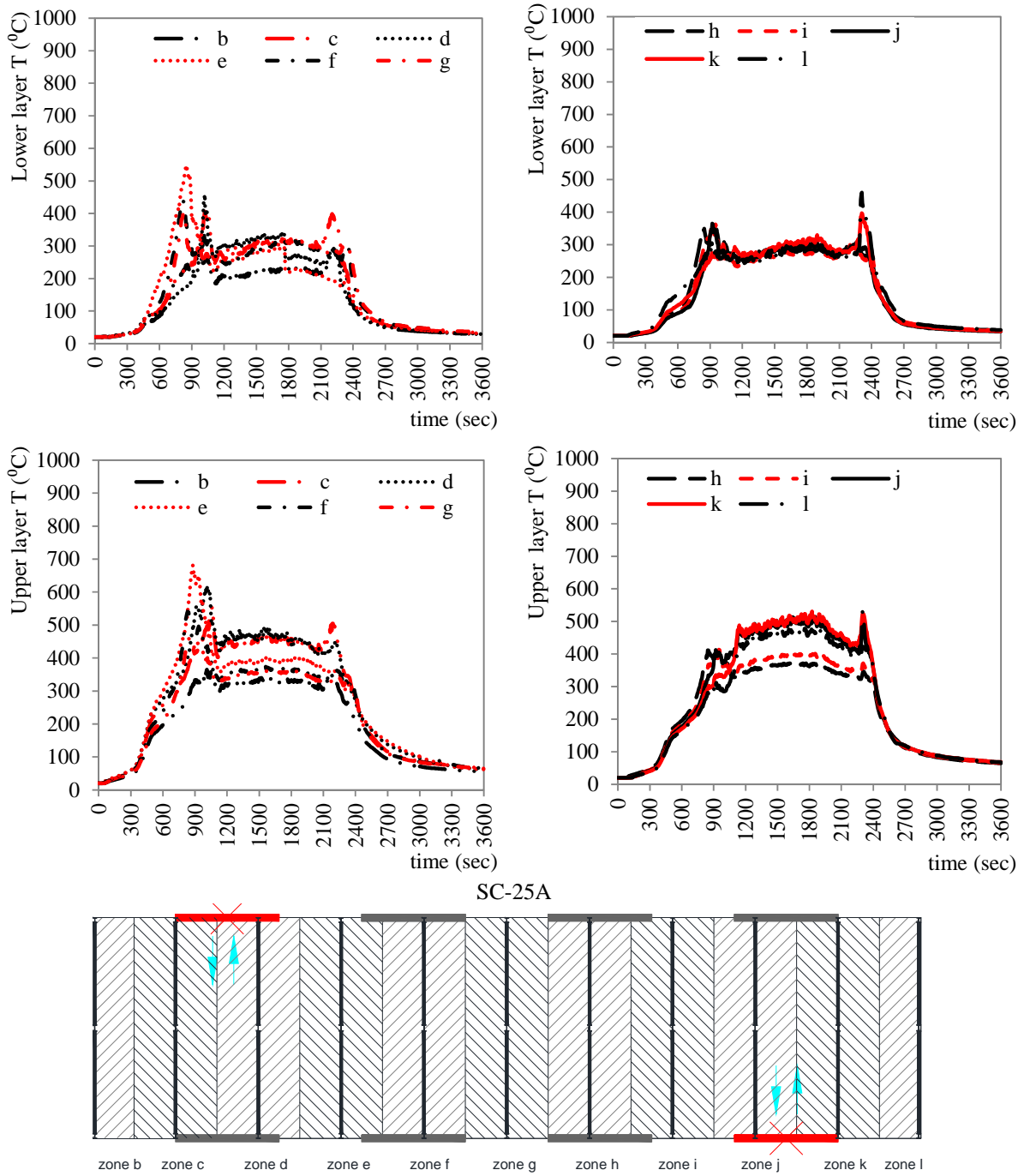


Figure 8-38: Lower and upper layer temperature evolution with time for all the virtual zones/ SC-25A.

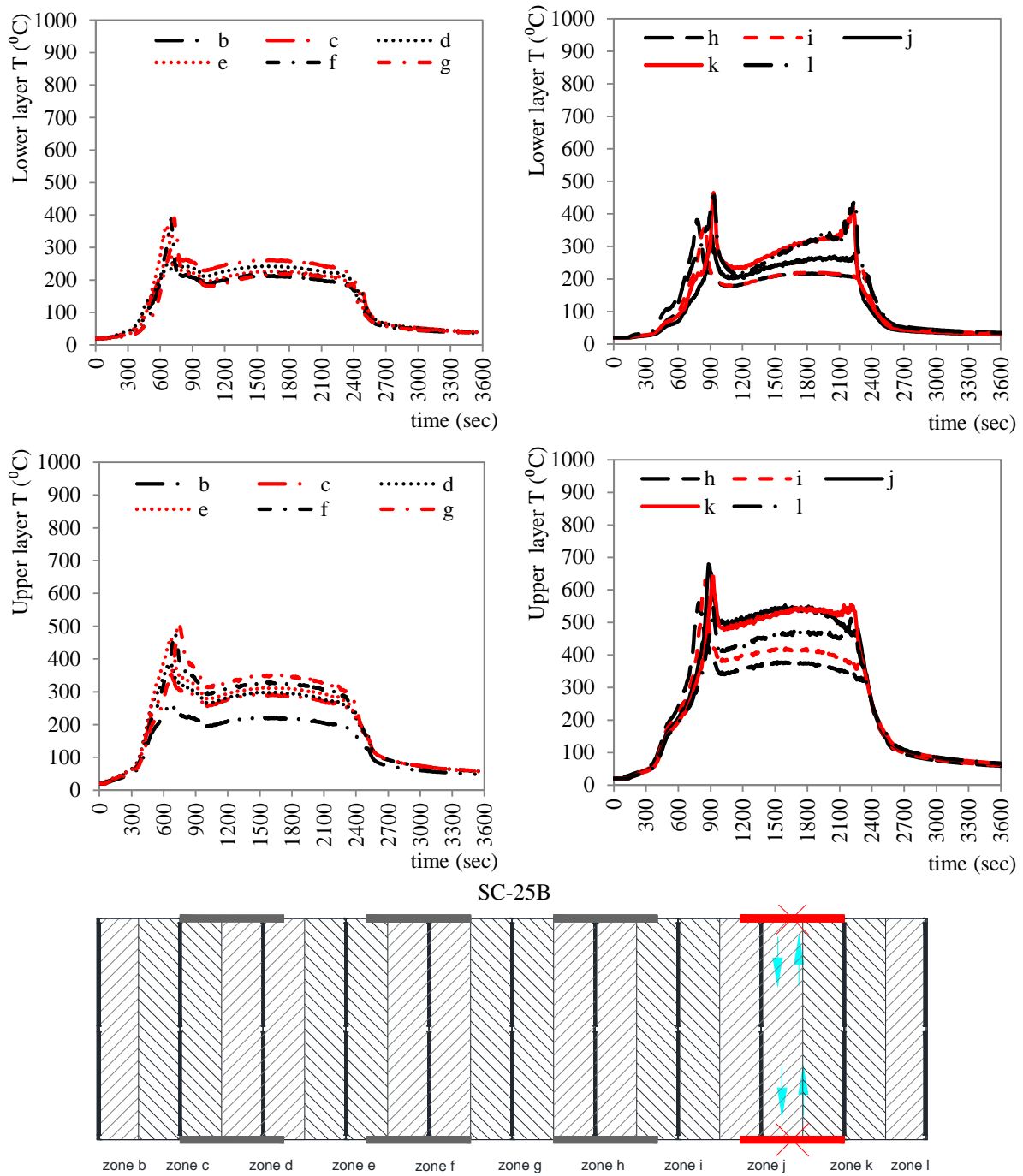


Figure 8-39: Lower and upper layer temperature evolution with time for all the virtual zones/ SC-25B.

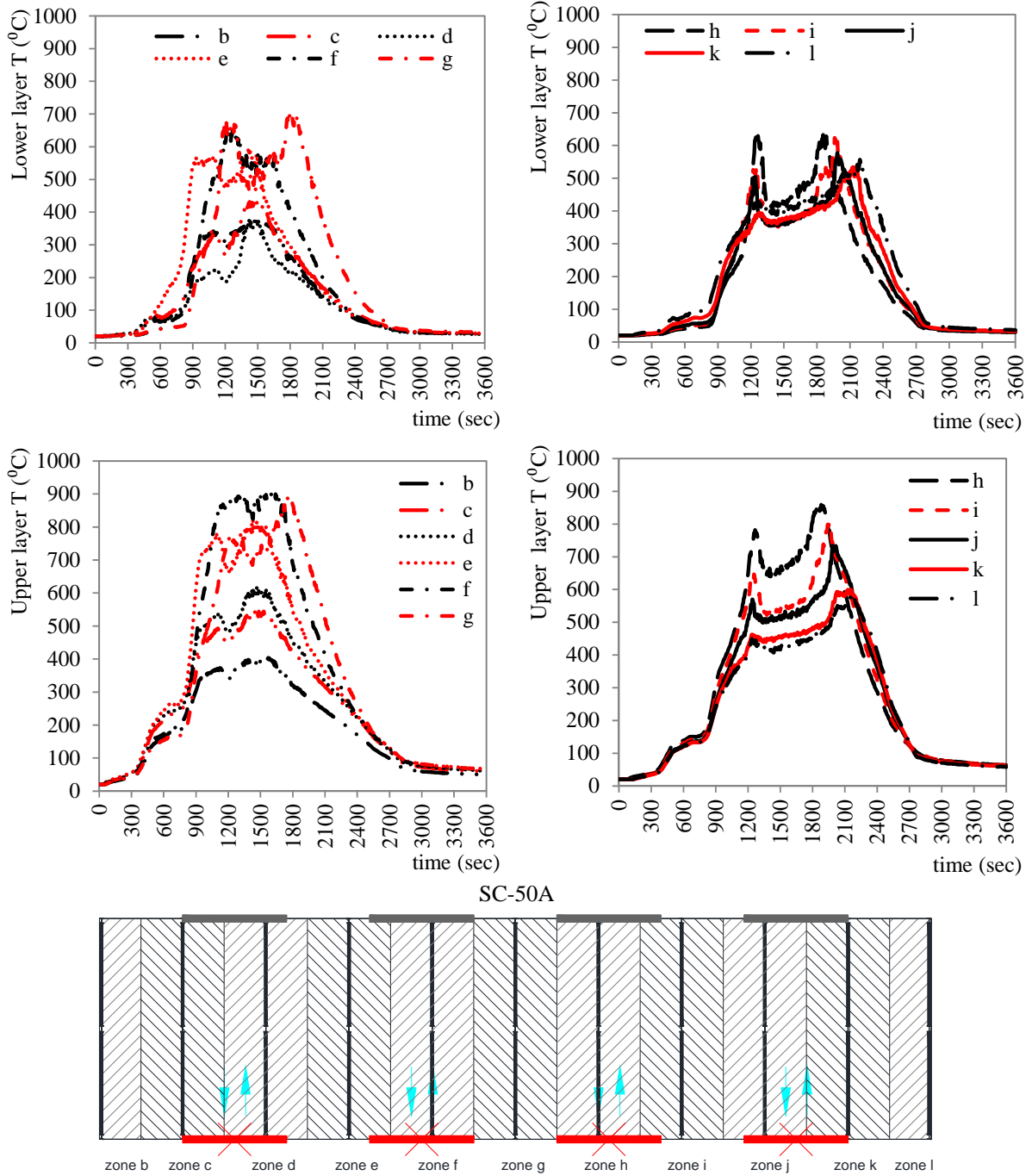


Figure 8-40: Lower and upper layer temperature evolution with time for all the virtual zones/SC-50A.

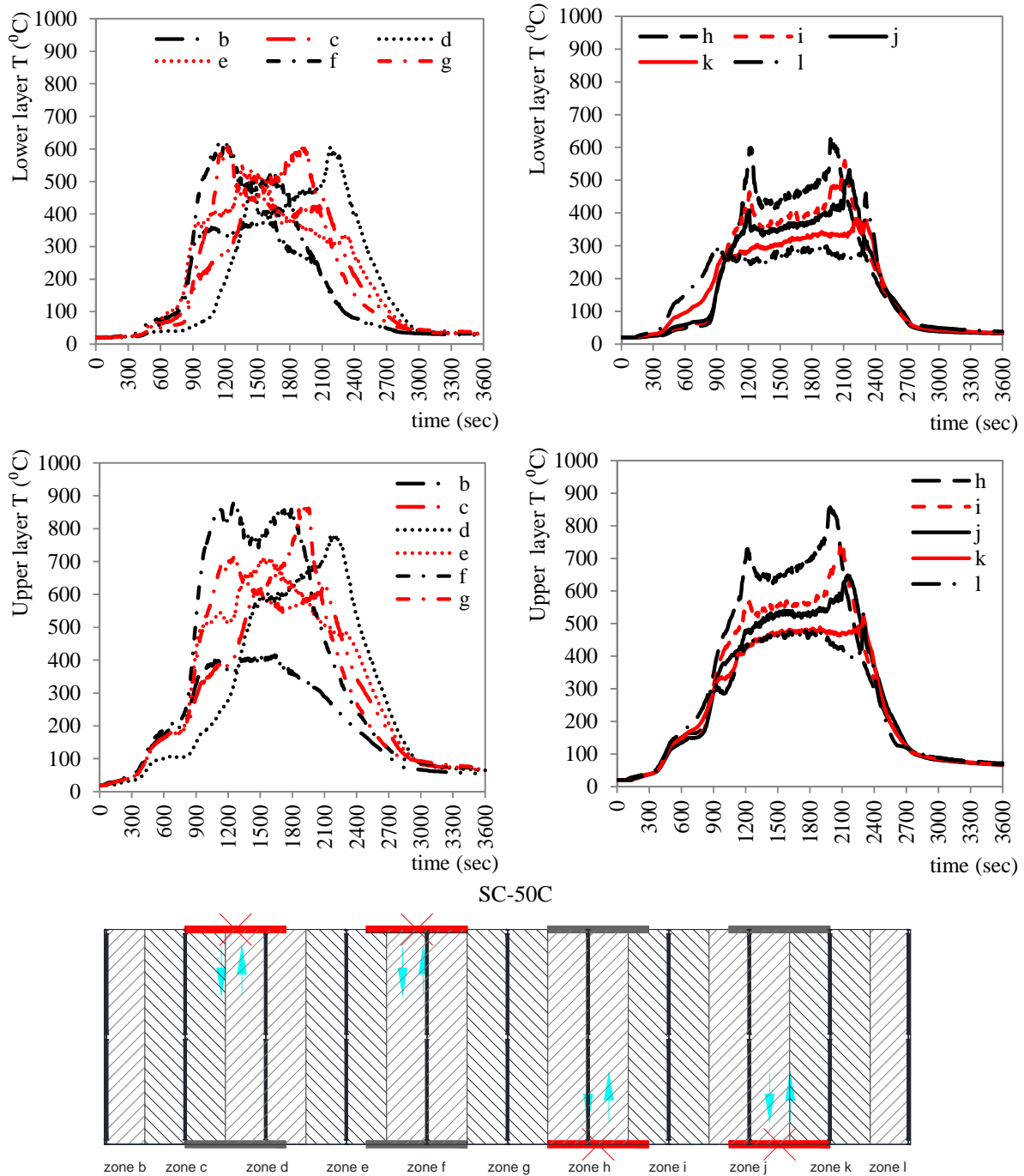


Figure 8-41: Lower and upper layer temperature evolution with time for all the virtual zones/SC-50C.

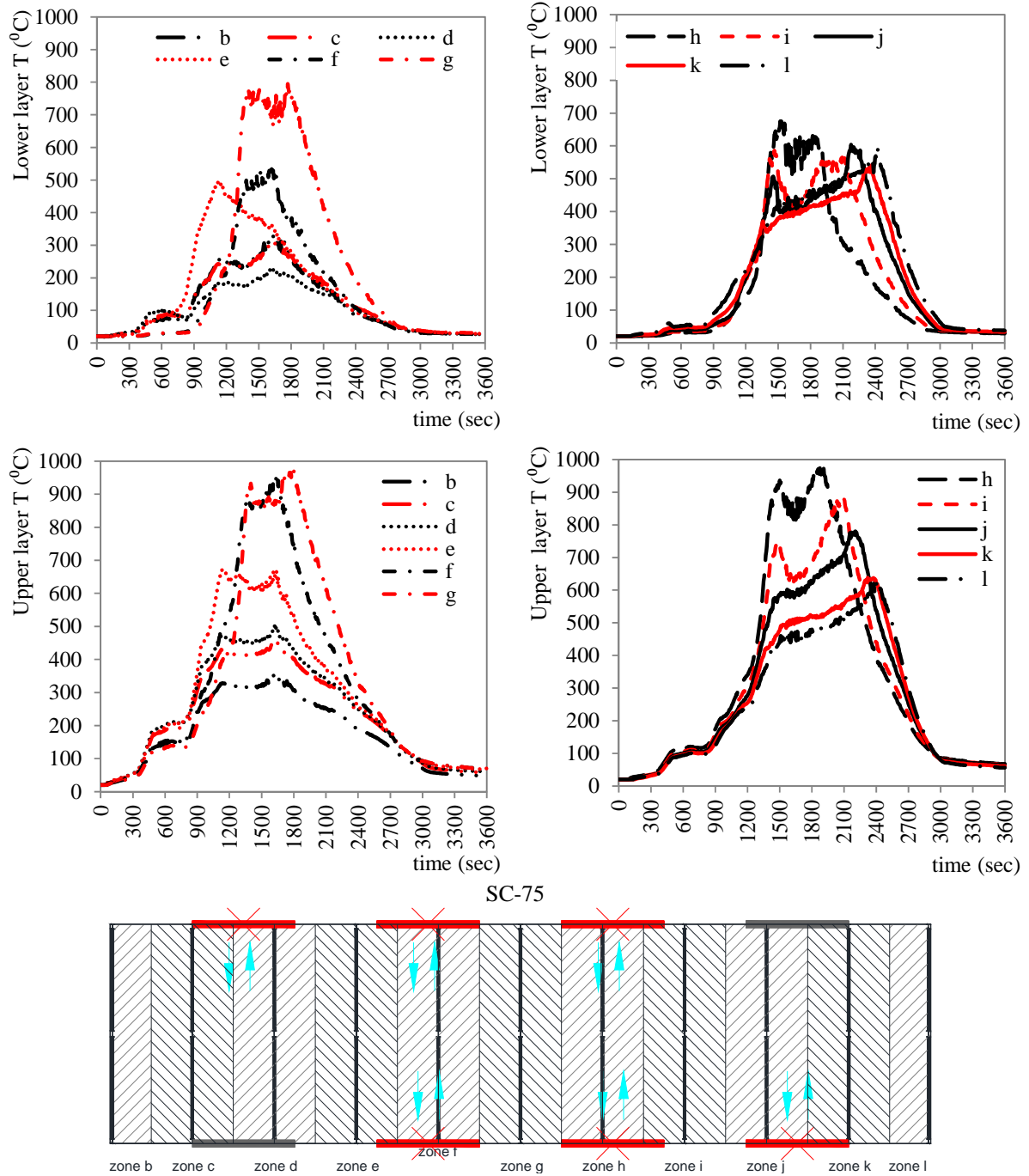


Figure 8-42: Lower and upper layer temperature evolution with time for all the virtual zones/SC-75.

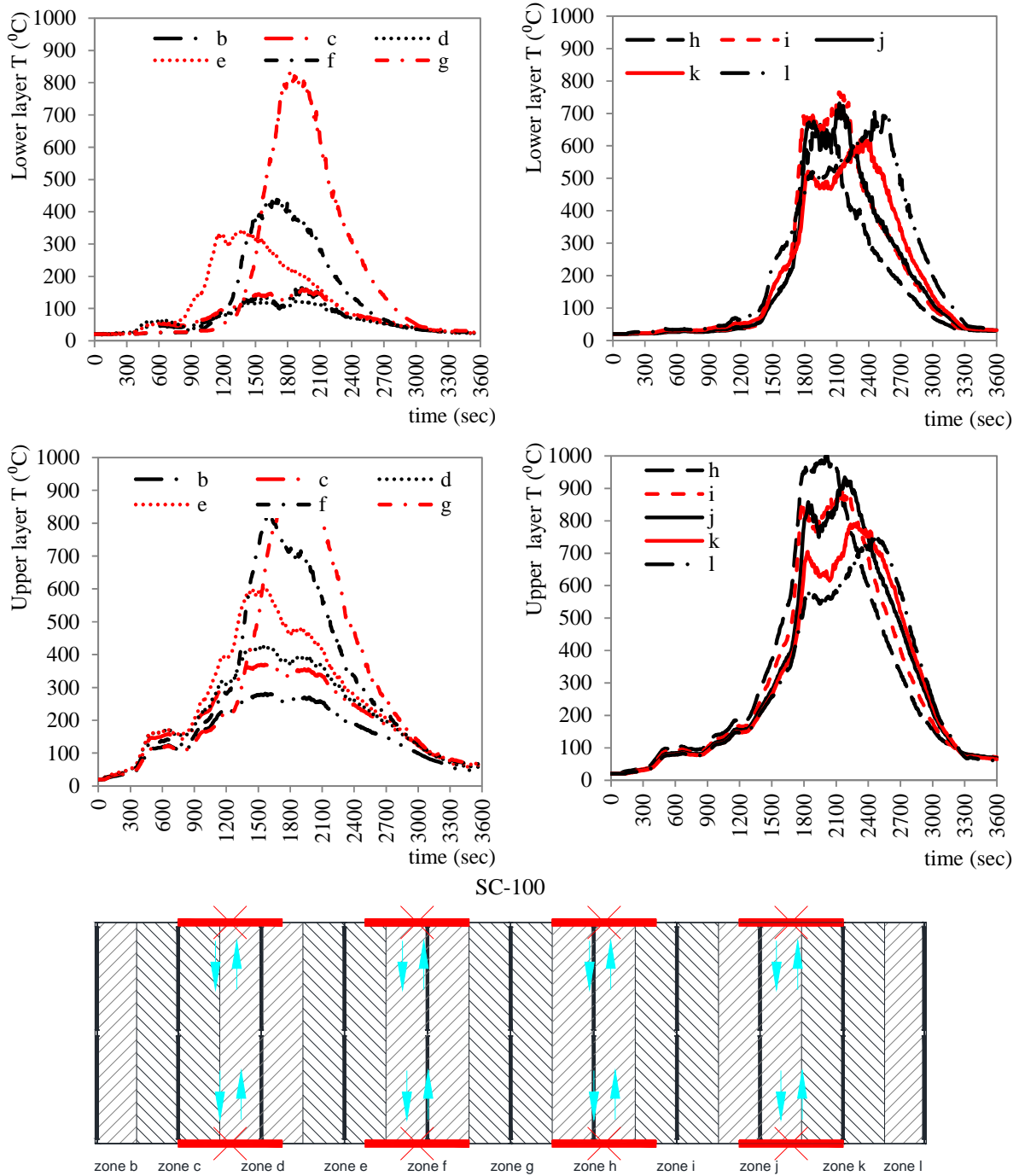


Figure 8-43: Lower and upper layer temperature evolution with time for all the virtual zones/SC-100.

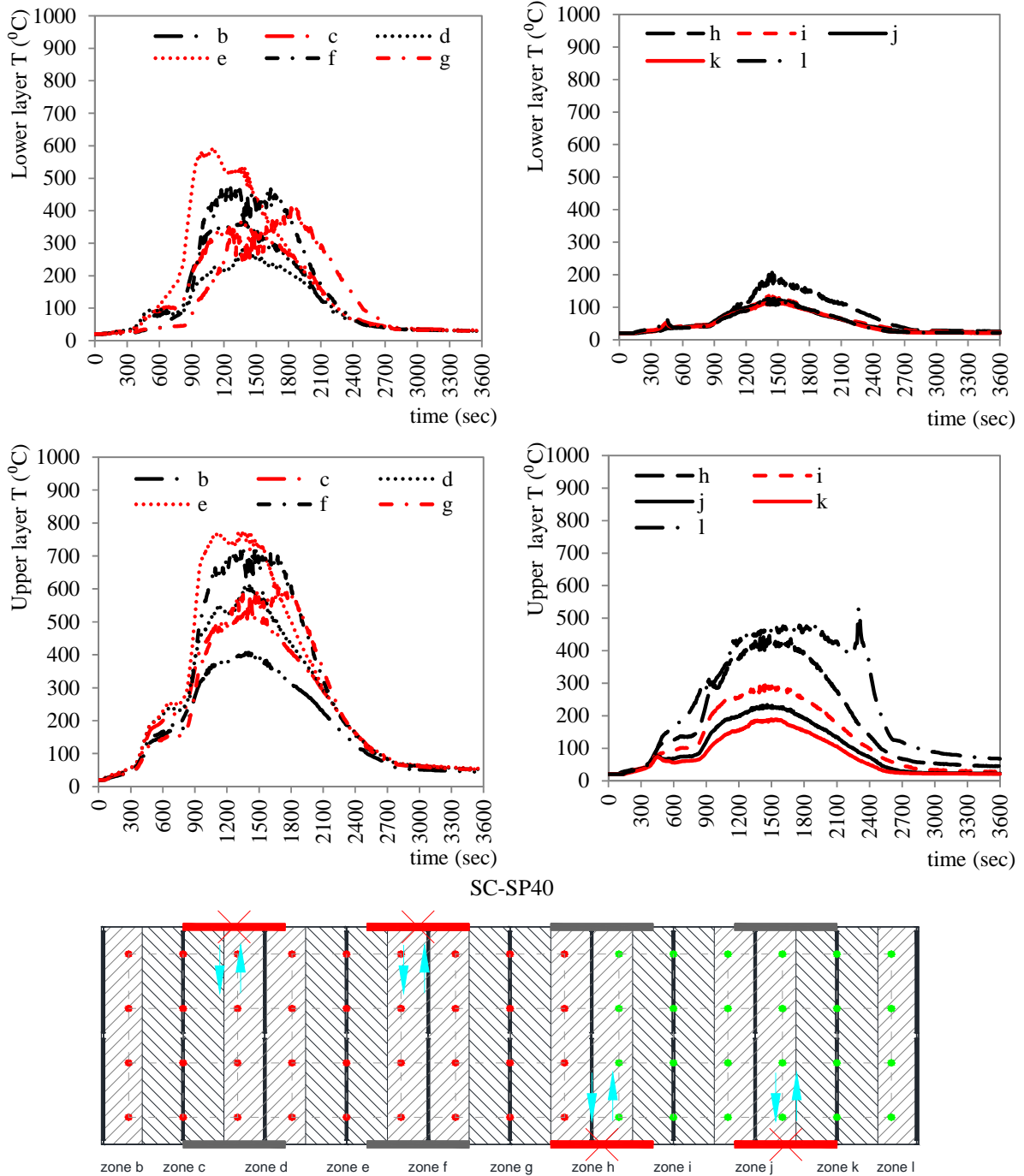


Figure 8-44: Lower and upper layer temperature evolution with time for all the virtual zones/SC-SP40.

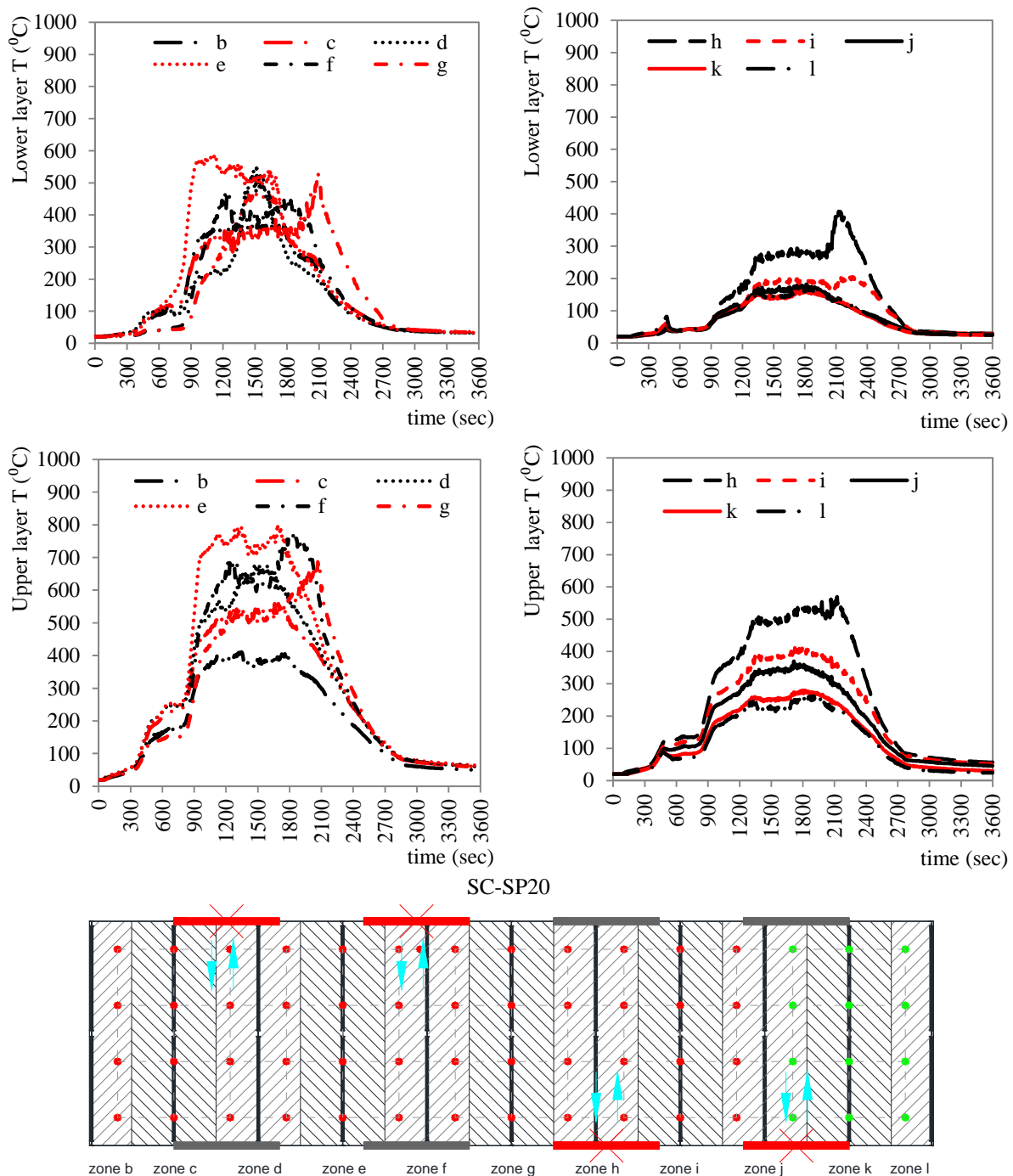


Figure 8-45: Lower and upper layer temperature evolution with time for all the virtual zones/SC-SP40.

Layer height

The next objective is to study the time-history evolution of the layer height. In order to study systematically the relation of the layer height with the gas-temperature profile at the two distinct layers, two demonstrative cases are presented. In the first case (Figure 8-46) which concerns the SC-25B scenario, the time-history of the layer height is presented in correlation with the upper/lower layer gas-temperature time-evolution for all the virtual zones. The corresponding data are illustrated in Figure 8-47 for SC-75. The scenarios discussed here are considered to be representative, since a different behaviour is noticed in each of them.

In the first case (Figure 8-46) the temperature distribution in the fire-compartment is quite uniform, concerning the zones that are far away from the broken windows (virtual zones b, c, d and f) where it varies between 200 °C and 350 °C (the peaks are not included in this range since they are considered to be simultaneous). Near the area of the broken windows (virtual zones g, h, I, j, k and i) the temperature appears larger spatial variation. Another characteristic of SC-25B is that the time-history of the layers includes the temperature plateau as it was mentioned in the previous section.

On the other hand, in SC-75 (Figure 8-47) the variation of the temperature of the virtual zones is high and this indicates highly non-uniform spatial profile during the fire exposure. Moreover, the time-history of the layers does not include the plateau and a single temperature peak appears. The results concerning the rest scenarios are included in Appendix B.

It is clarified that the layer height is actually the height of the lower layer. Concerning both scenarios, it is obvious that in the cases that the different layers are well-separated (which means that the difference between the temperature of the upper and the lower layer is considerable), the layer height is decreased. This is independent from the values of the temperature of both layers. Actually, the parameter that determines the layer height is the difference between the temperatures that are recorded in the distinct layers.

In SC-25B it is observed that during the fire exposure the layer height is quite constant, especially for the steady branch as it is indicated in the HRR diagram that is included in Figure 8-46. The layer height varies between 1.00m and 1.20m in the most zones, except zones b and c. The value of the interface height, which corresponds to the steady burning stage, is marked on the diagrams of Figure 8-46 as $z_{int/av}$. This indicates that in this region (zones b and c) the temperature profile is uniform with respect to the z-axis and the temperature varies between 200 °C and 300 °C. In the rest virtual zones the difference between the temperature recorded at the upper and the lower layer is large. The maximum values are noted at zones j and k, where the open/damaged windows are located.

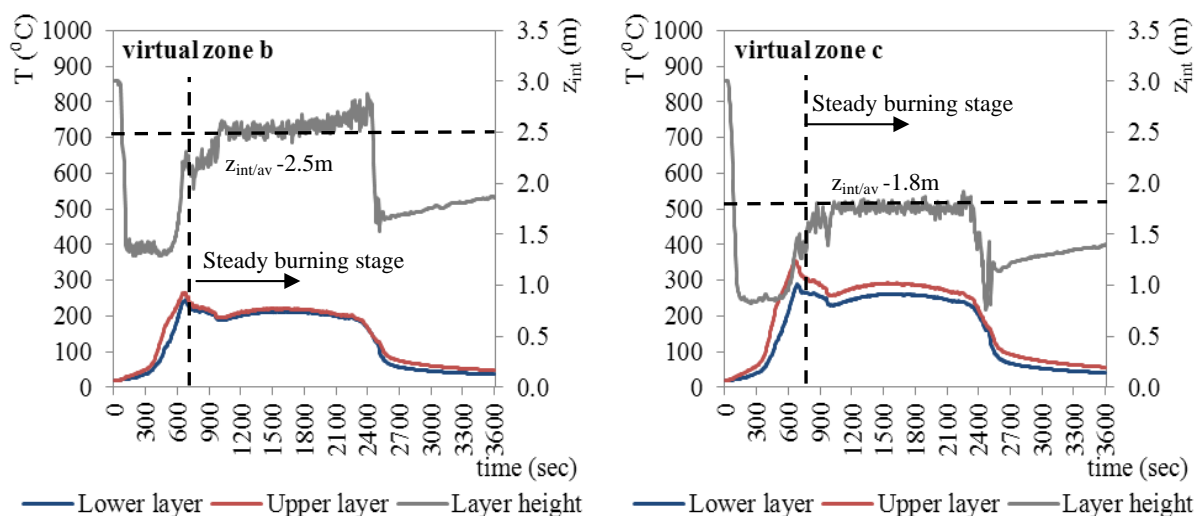


Figure 8-46: Upper-Lower temperature and layer height at different virtual zones for SC-25B. (continued)

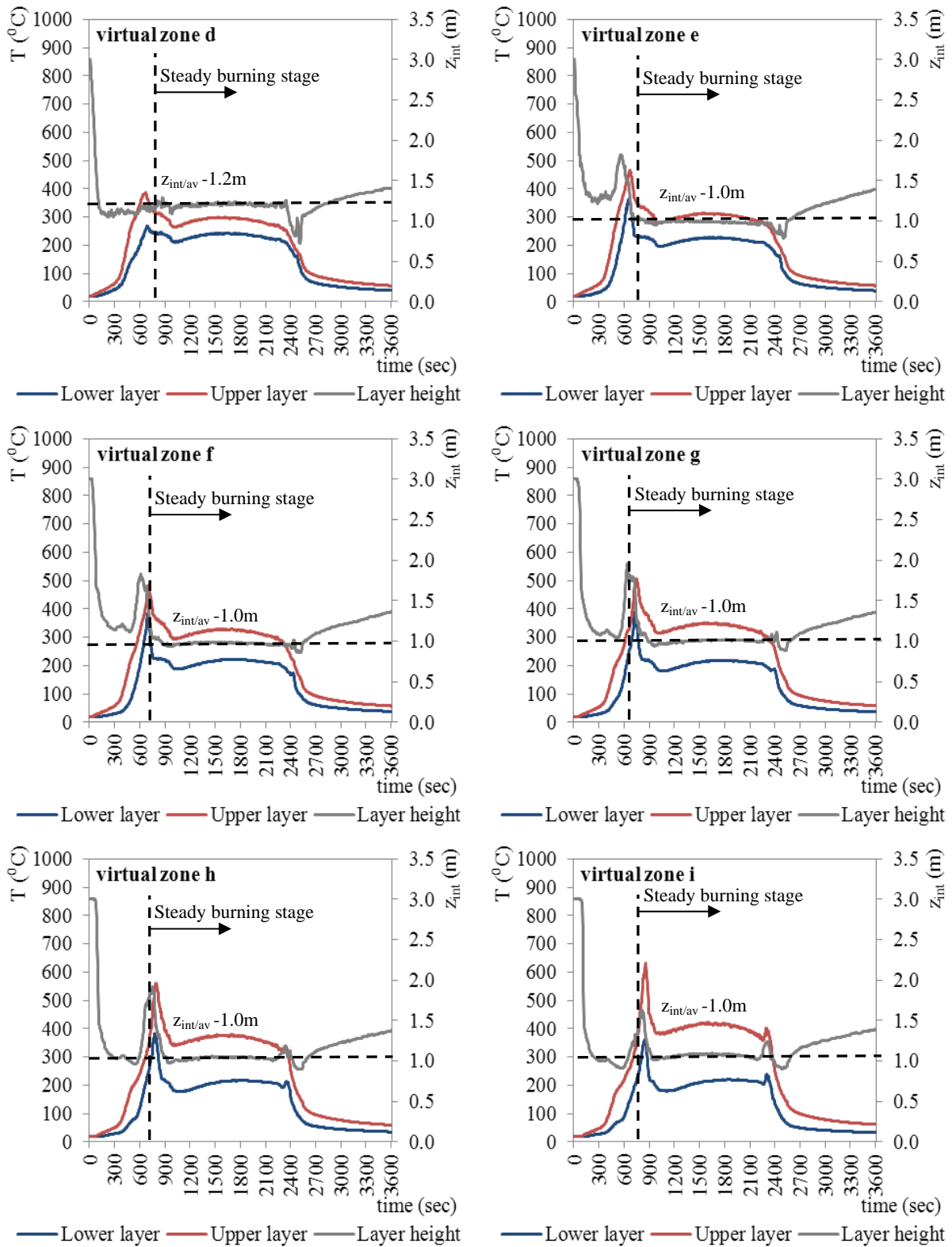


Figure 8 46: Upper-Lower temperature and layer height at different virtual zones for SC-25B. (continued)

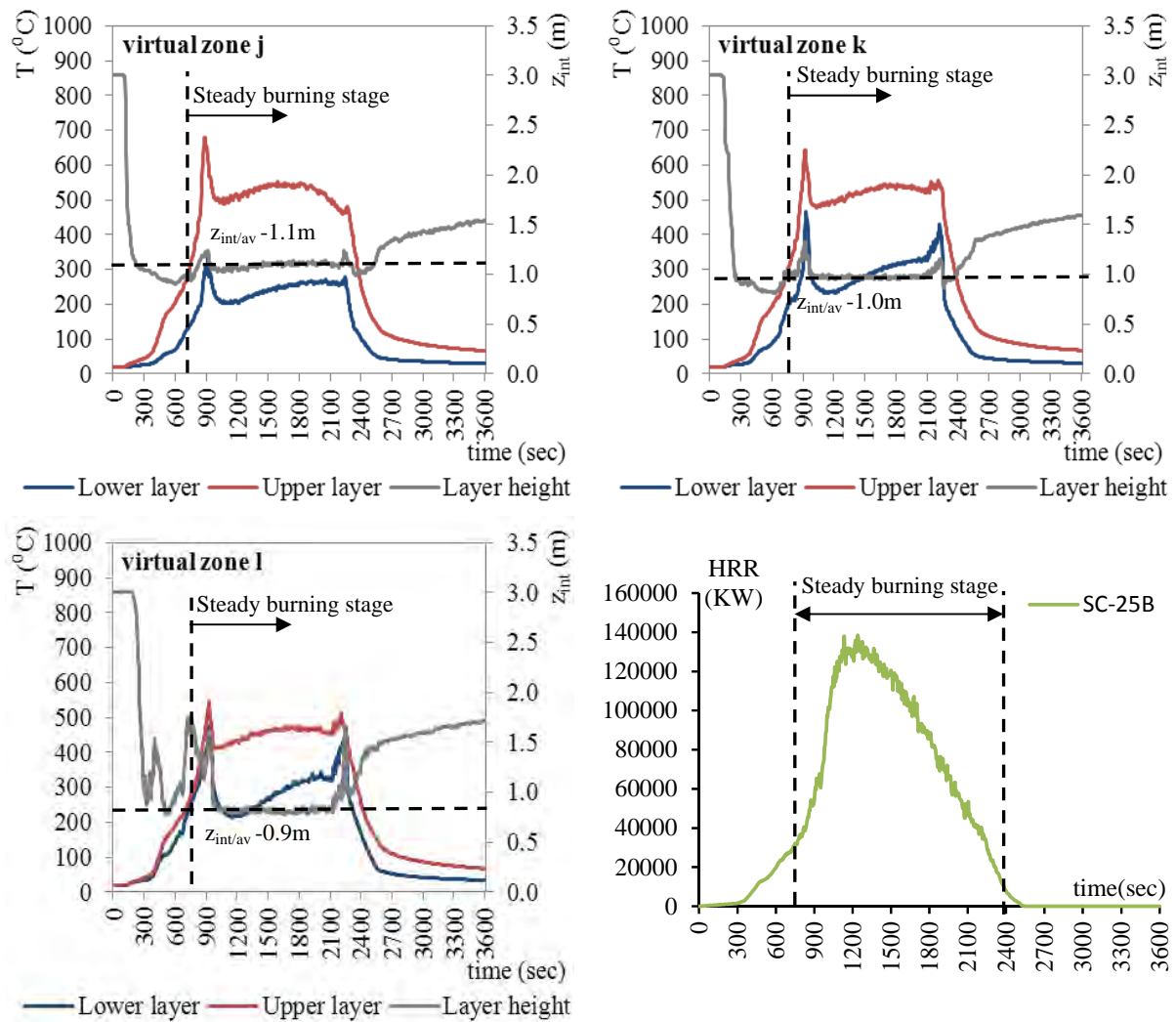


Figure 8-46: Upper-Lower temperature and layer height at different virtual zones for SC-25B.

In the case of SC-75 (Figure 8-47) the layer height is characterized by a continuous variation during the fire exposure. During the early stages of the fire exposure, in virtual zones b, c, j and k the layer height is almost constant and in the rest zones it decreases. During the time interval 3000-3600 sec of the decay phase of the fire, the lower zone temperature is slightly increased. A more “stable” behaviour is observed during the steady burning stage in all virtual zones, except b and l. These regions present strong fluctuations and this can be attributed to the fact that the zones are located at the boundaries of the enclosure. In the rest zones, the layer height varies between 1m and 1.5m. The previous indicate that the differences between the temperatures that are recorded at the distinct layers are considerable. This can be verified through the time evolution of the gas-temperature of both layers, as it is illustrated in Figure 8-47. The maximum temperatures are recorded in the region that includes the virtual zones f, g, h, i and j.

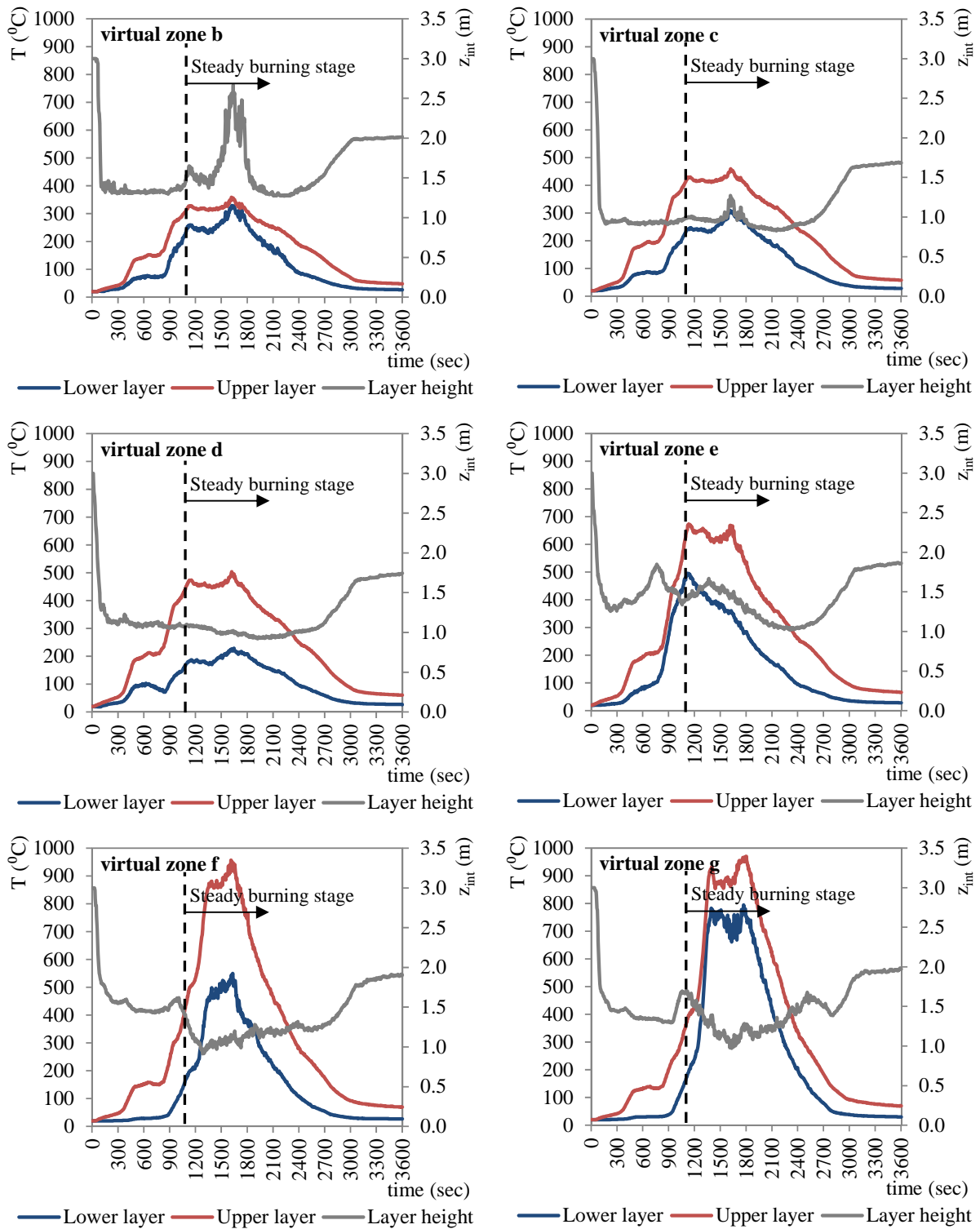


Figure 8-47: Upper-Lower temperature and layer height at different virtual zones for SC-75. (continued)

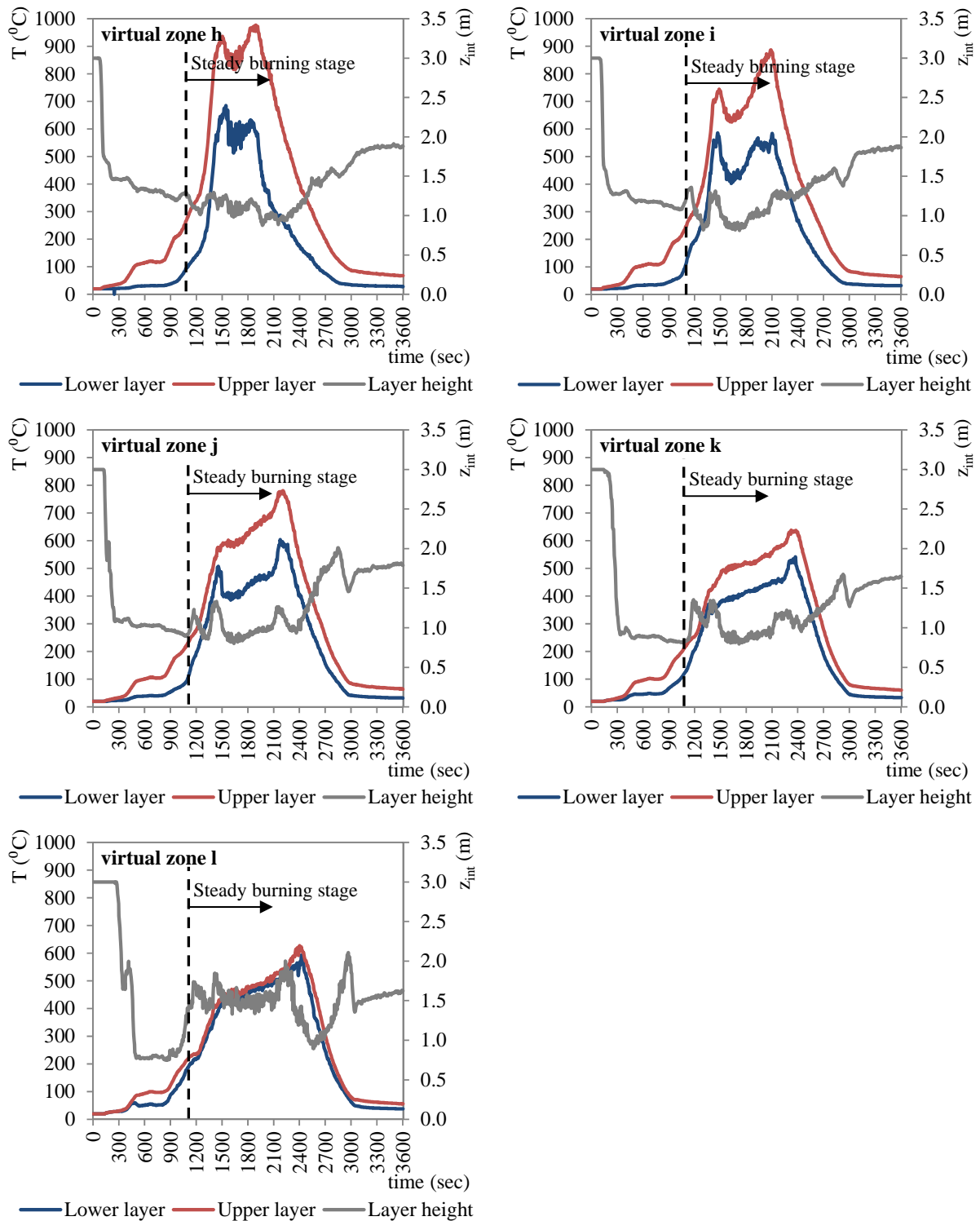


Figure 8-47: Upper-Lower temperature and layer height at different virtual zones for SC-75.

The results of the analyses concerning the time-history of the layer height z_{int} , for all the PEF scenarios, are presented in Figure 8-48. In general, it is noted that the temperature profile is uniform with respect to the z -axis near the boundaries of the compartment (virtual zones b and l). This holds for all the scenarios except the SC-100 one. In this case the different layers (upper and lower) are well-separated in the fire-enclosure. Additionally, it is observed that the layer height varies between 0.80m and 1.5m for all the scenarios. This

is not valid near the boundaries of the compartment, where the layer height is up to 2m. Also, this remark holds for the time period between the flashover and the end of the decay phase.

It is concluded that the “dual-layer” post-processing model that is developed for the interface between the CFD and the mechanical analysis can describe sufficiently the temperature distribution in the fire-compartment. The phenomenon is depicted in a simple way through three different variables which are the temperature of the upper and the lower layer and the layer height. Certainly, this interface model is based on two important assumptions. The first is that the structural members are not included in the CFD model. The second is that the temperature in all virtual zones is uniform. The evaluation of the results indicates that it is a good approximation for the qualitative representation of the very complex spatial temperature distribution in the enclosure during the fire evolution, although the local phenomena cannot be represented accurately. The model can be used for design purposes in the cases where fire-compartments exceed the “regular” dimensions as they are defined by the guidelines of the codes.

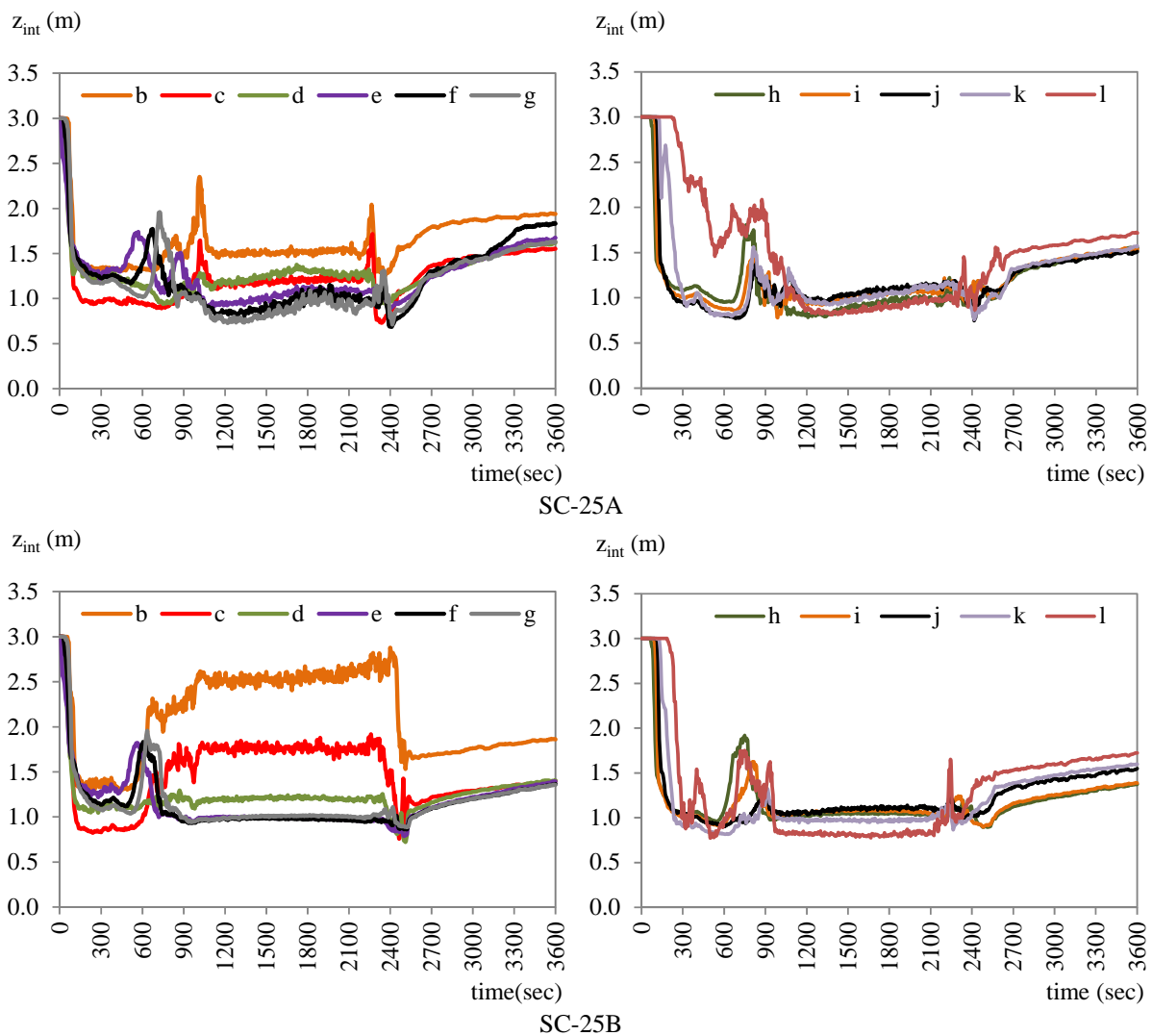


Figure 8 48: Time-history of the layer height z_{int} in the fire-compartment for different fire scenarios. (continued)

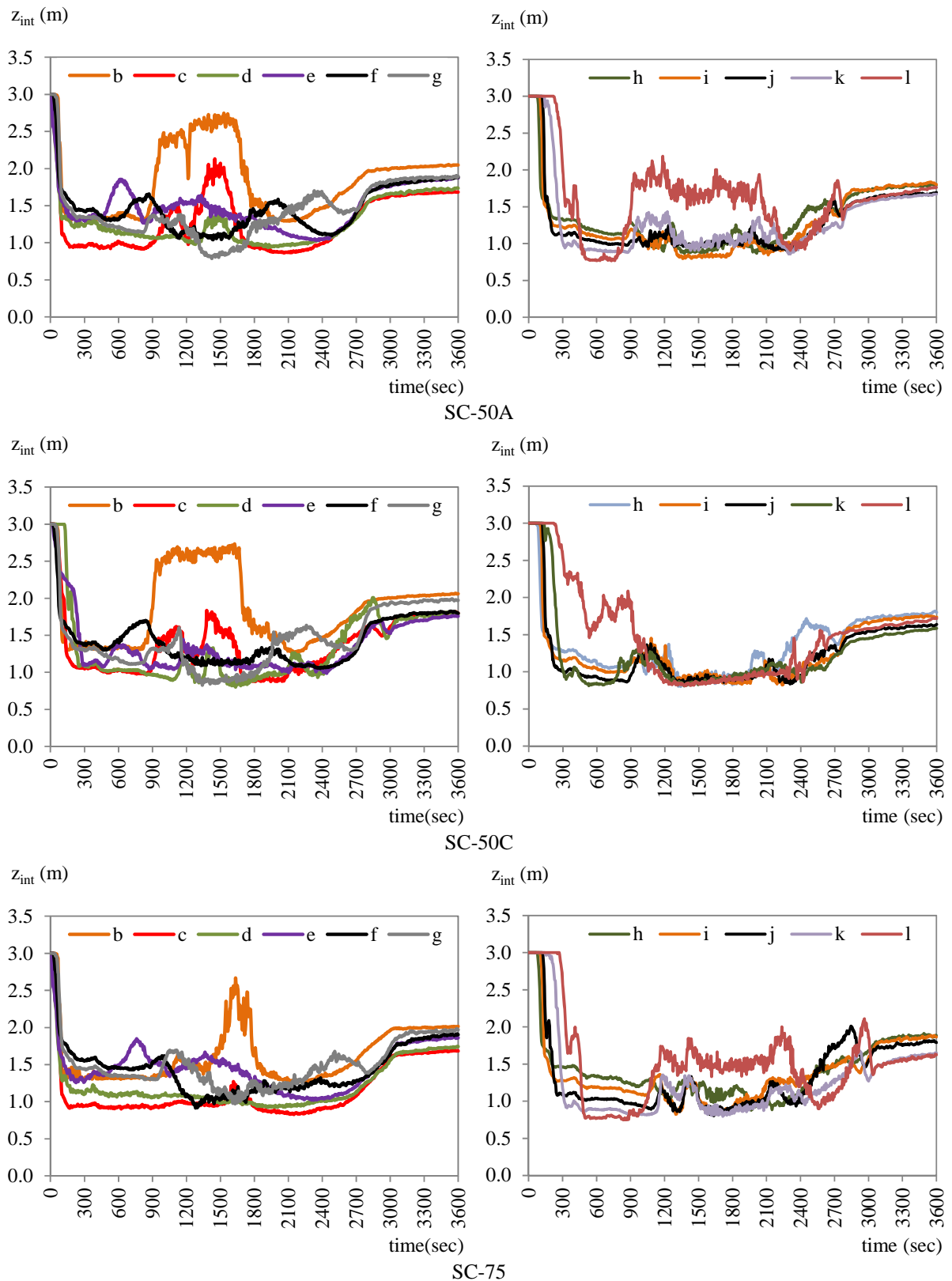


Figure 8-48: Time-history of the layer height z_{int} in the fire-compartment for different fire scenarios. (continued)

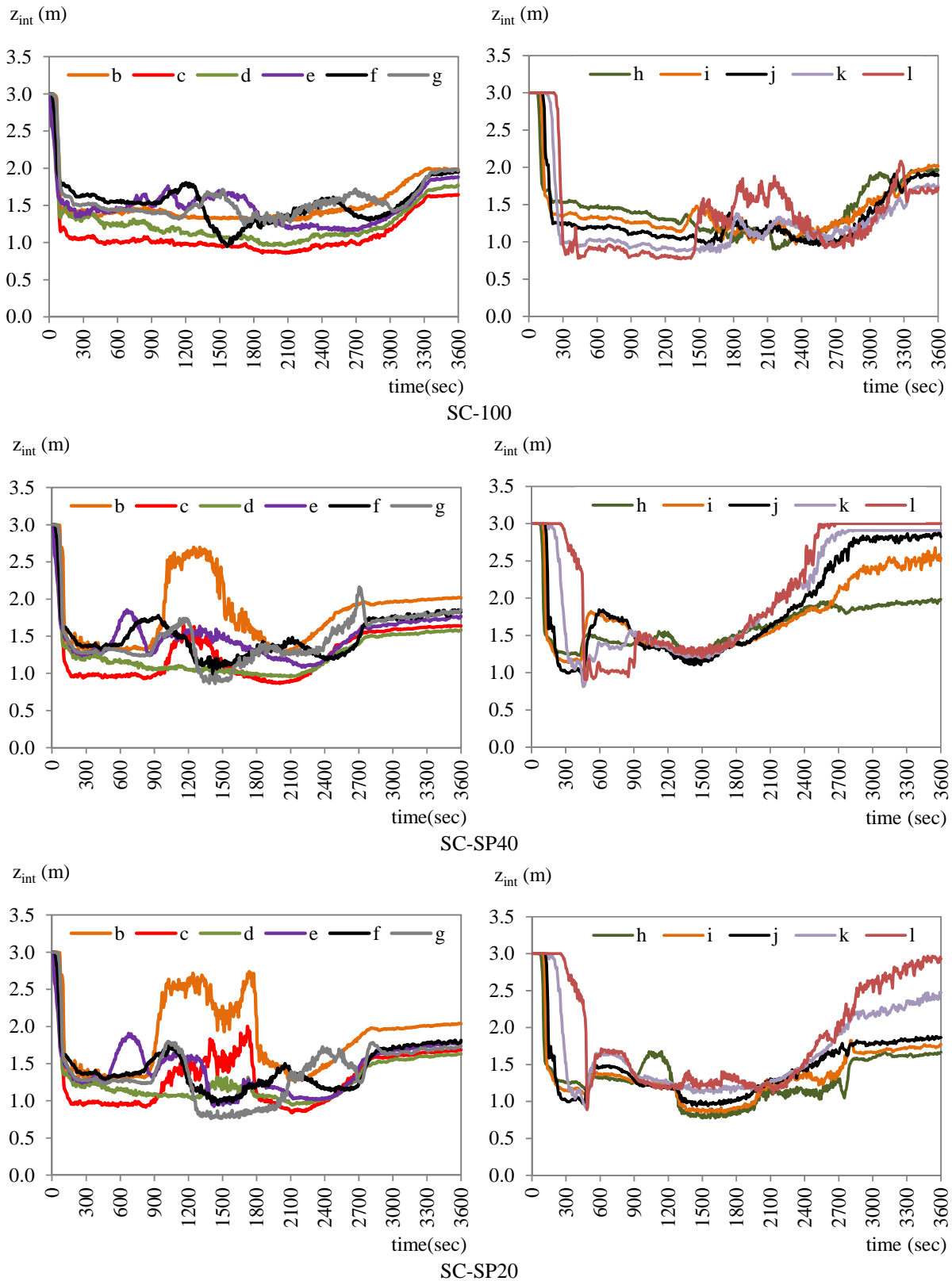


Figure 8-48: Time-history of the layer height z_{int} in the fire-compartment for different fire scenarios.

Temperature of structural members according to the guidelines of EN 1993-1-2

Finally, the temperature of the structural members is calculated using the methodology that is proposed in EN 1991-1-2 and described in Section 5.5. It is noted that the calculation of the temperature profile of the structural members is based on the assumption that the temperature is uniform along the members and the gradient in the cross-sections is ignored. Specifically, the temperature of the structural members is strongly dependent on the gas-temperature time-history and the cross-section dimensions. The gas-temperature time-history is the temperature of the upper and lower layer that is derived in the previous Section.

This assumption is accurate enough for the needs of this dissertation. The results for the beams are presented in Figure 8-49 with respect to the frame where the beams are allocated and the respective results for the columns are included in Figure 8-51. Actually, the temperature profile of the beams is calculated using the gas-temperature time-history of the upper layer, depending of the virtual zone that the frame is located. The temperature profile of the columns is different in the upper and the lower layers, since the gas-temperatures are different. Moreover, two different cases arise, depending on the cross-section of the columns. As it will be explained in detail in the next Chapter, the cross-section of the outer columns results to be HEB340 while the cross-section of the middle column is HEB450, according to the calculation that are conducted for the seismic and the gravity loading design purposes. Figure 8-51 presents the temperature time-history for both outer and middle columns, taking into account the upper layer for each virtual zone. The results concerning the lower layer are included in Appendix B. The maximum recorded values are summarized in Table 8-3, Table 8-4 and Table 8-5 for the beams, the outer columns and the middle column respectively. It can be observed that the maximum values of temperature are recorded at different frame locations for the various PEF scenarios and this depends strongly on the ventilation conditions and on the structural member that is studied. Moreover, for a specific frame, the maximum temperature values are recorded for the scenarios SC-75 and SC-100 in most of the frames. This holds for both the beams and the columns.

At this point, it should be noted that the temperatures of the structural members that correspond to the scenarios that take into account the malfunction of the fire-extinguishing system (SC-SP20, SC-SP40 and SC-SP100), are not presented here, due to the fact that the aforementioned scenarios are “overlapped” from SC-50C. According to both the results of the gas-temperature “near” the structural members and the outcomes of the “dual-layer” model, it was concluded that the gas-temperature that corresponds to the scenarios SC-SP20, SC-SP40 and SC-SP100 is lower comparing to SC-50C. It is reminded that the aforementioned scenarios (SC-SP20, SC-SP40 and SC-SP100) are based on the arrangement of the open/damaged windows accordingly to SC-50C. For this reason, these scenarios are not further studied (Chapter 11 and 13).

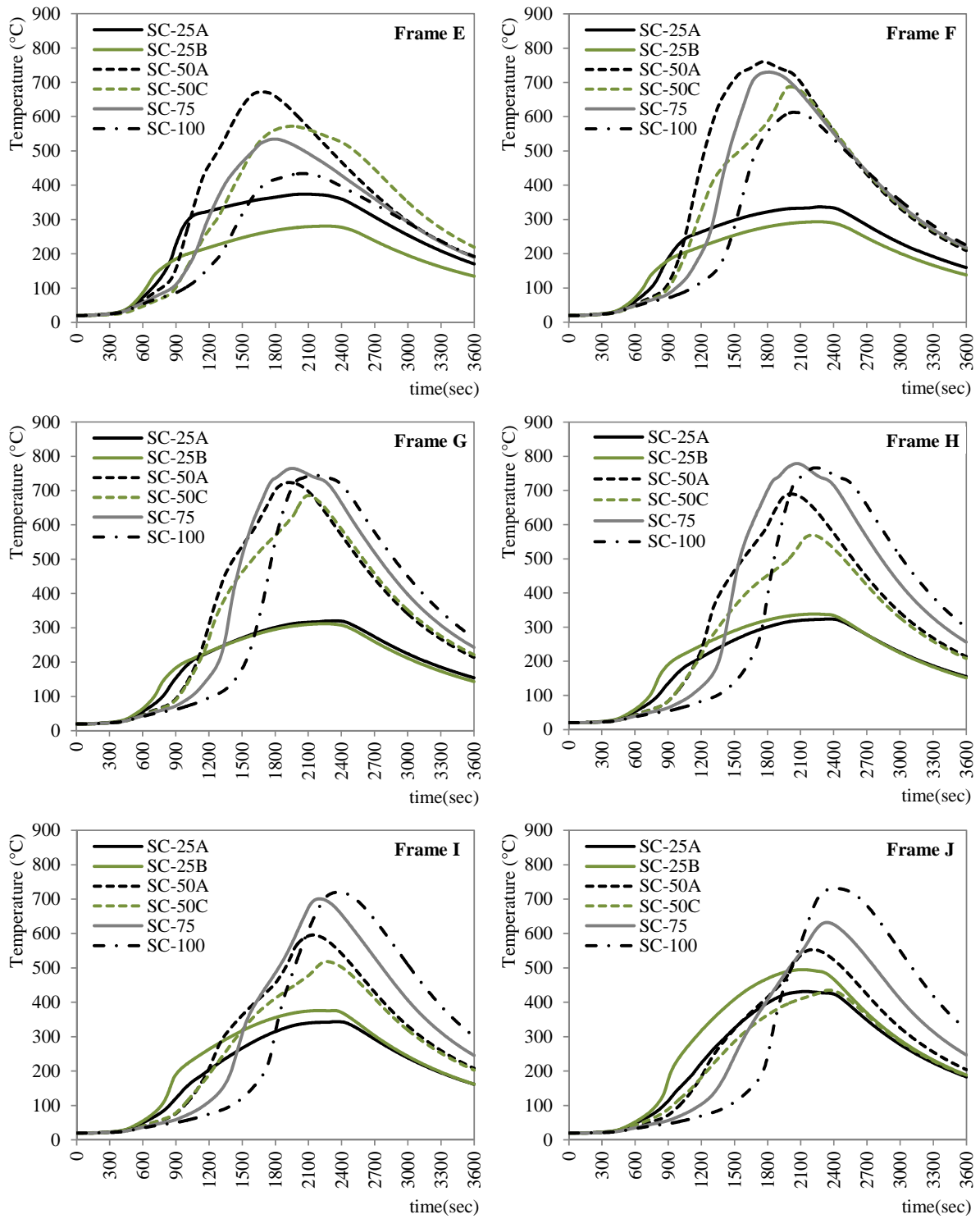


Figure 8-49: Temperature time history curves according to the two-zone model for the beams, with respect to the frame where the structural members are located. (continued)

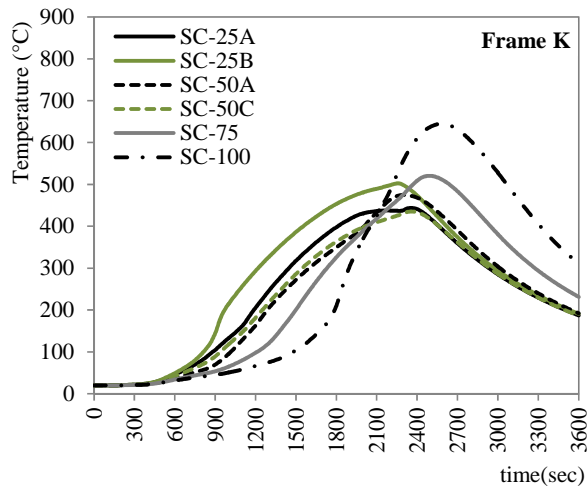


Figure 8-49: Temperature time history curves according to the two-zone model for the beams, with respect to the frame where the structural members are located.

Frame	E	F	G	H	I	J	K	Upper Value
SC-25A								
Max T(°C)	374.00	336.86	320.33	323.86	343.74	431.30	443.70	443.70
Time (sec)	2080	2275	2350	2360	2355	2155	2350	(Frame K)
SC-25B								
Max T(°C)	280.73	293.36	311.96	338.22	376.08	494.87	502.65	502.65
Time (sec)	2260	2255	2250	2245	2330	2120	2260	(Frame K)
SC-50A								
Max T(°C)	672.45	760.31	723.67	689.88	595.53	553.24	474.84	760.31
Time (sec)	1680	1765	1925	2015	2140	2210	2305	(Frame F)
SC-50C								
Max T(°C)	571.92	687.62	685.41	569.25	518.26	435.22	435.22	569.25
Time (sec)	1955	2010	2100	2210	2265	2355	2355	(Frame F)
SC-75								
Max T(°C)	534.39	730.19	764.69	778.89	700.93	632.15	520.64	778.89
Time (sec)	1790	1810	1955	2070	2200	2345	2490	(Frame H)
SC-100								
Max T(°C)	433.97	612.82	745.18	766.28	720.74	730.80	644.62	766.28
Time (sec)	2035	2035	2150	2230	2380	2425	2580	(Frame H)
Upper Value	672.45	730.19	764.69	778.89	720.74	730.80	644.62	
	SC-50A	SC-75	SC-75	SC-75	SC-100	SC-100	SC-100	

Table 8-3: Maximum temperatures values (°C) of the beams for all the PFE scenarios.

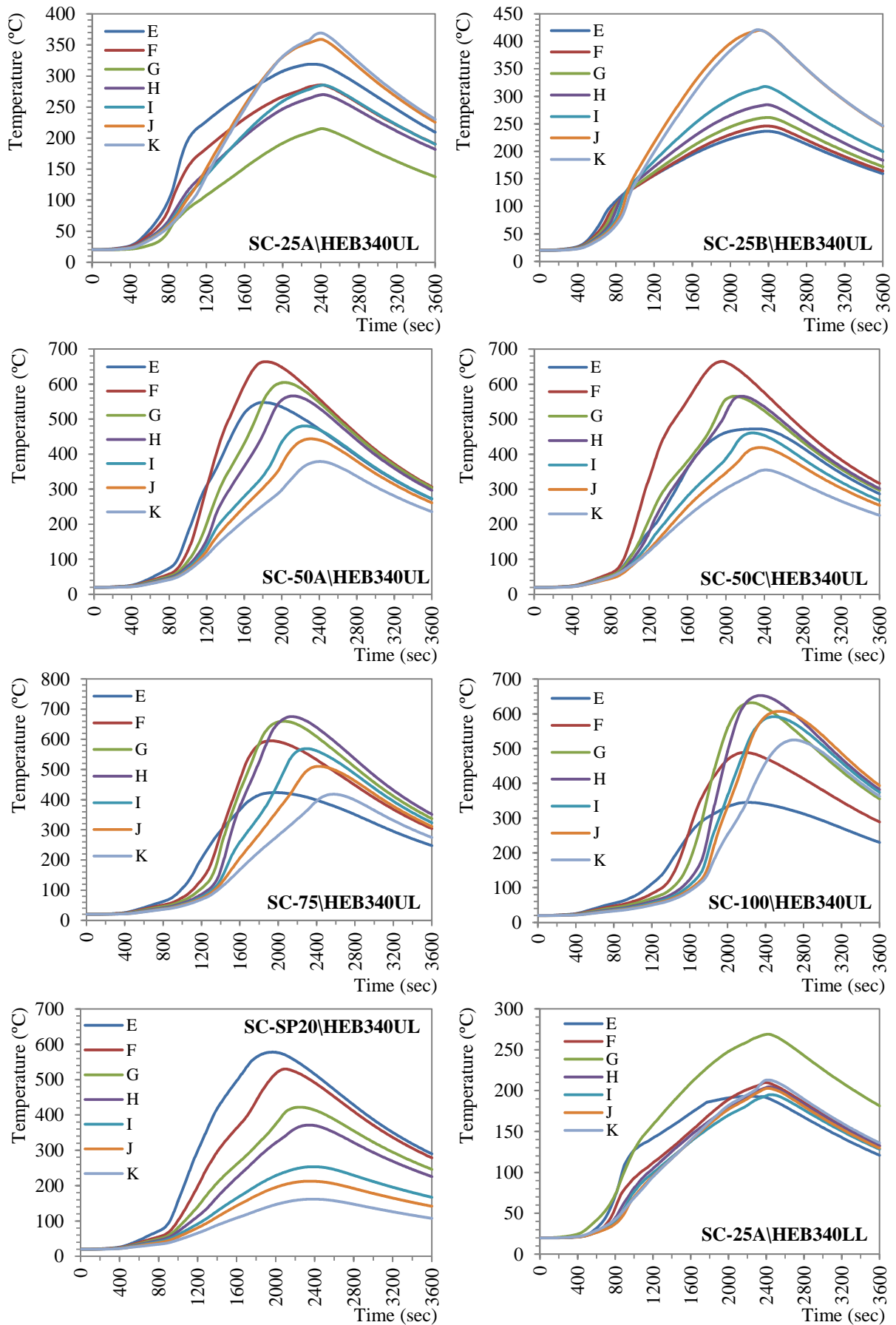


Figure 8-50: Temperature time history curves according to the two-zone model for the HEB340 columns, with respect to the frame where the structural members are located. (continued)

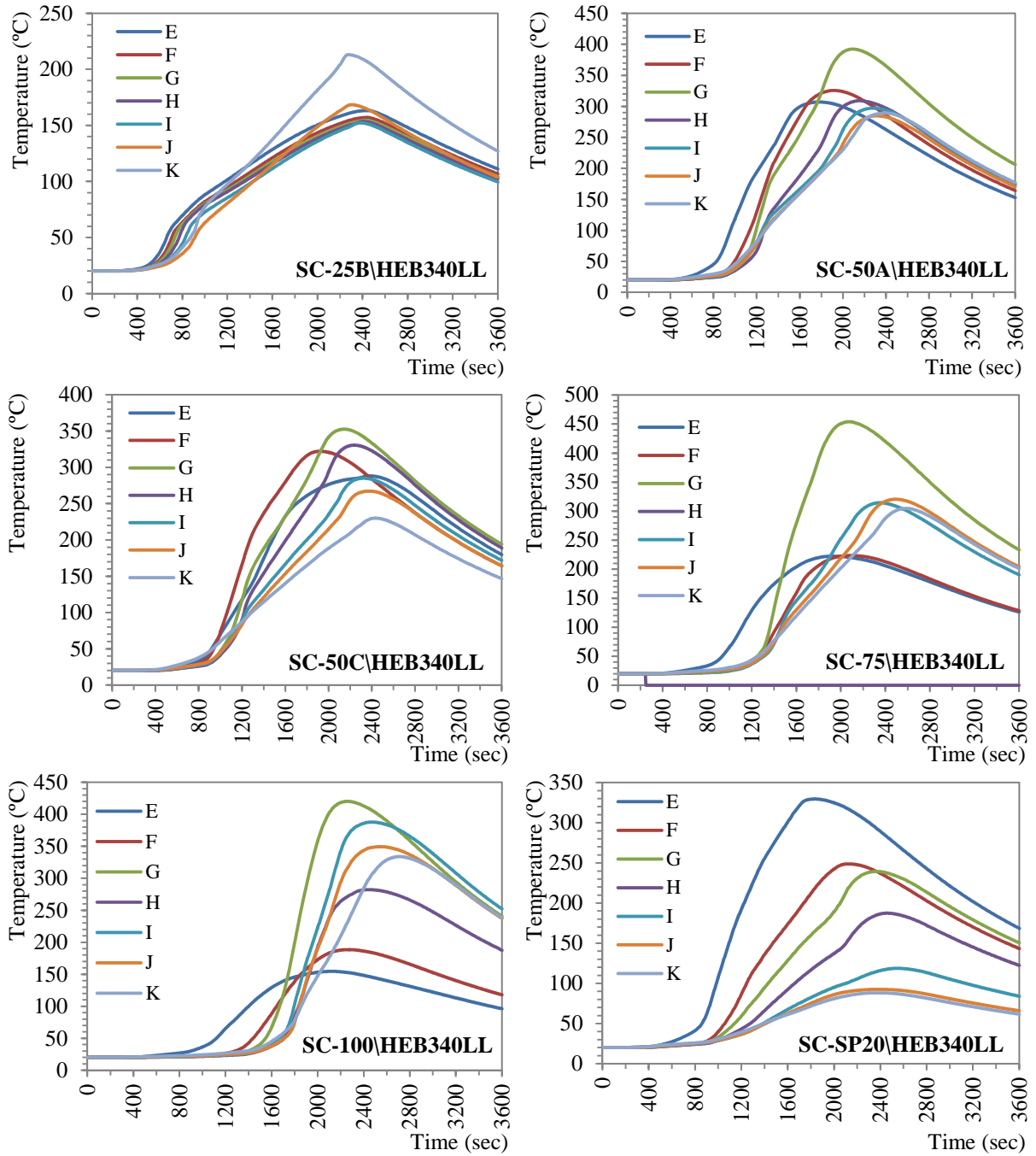


Figure 8-50: Temperature time history curves according to the two-zone model for the HEB340 columns, with respect to the frame where the structural members are located.

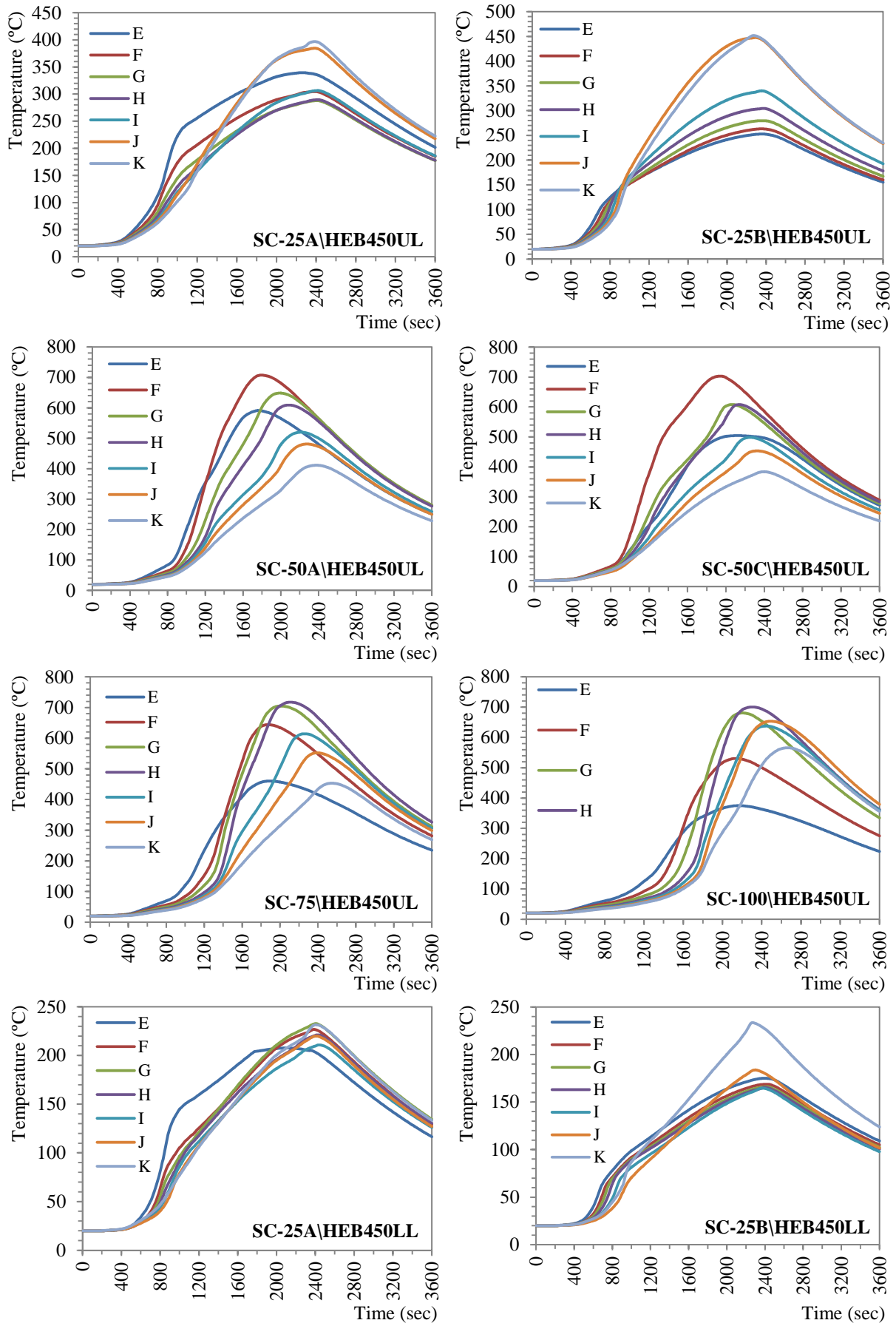


Figure 8-51: Temperature time history curves according to the two-zone model for the HEB450 columns, with respect to the frame where the structural members are located. (continued)

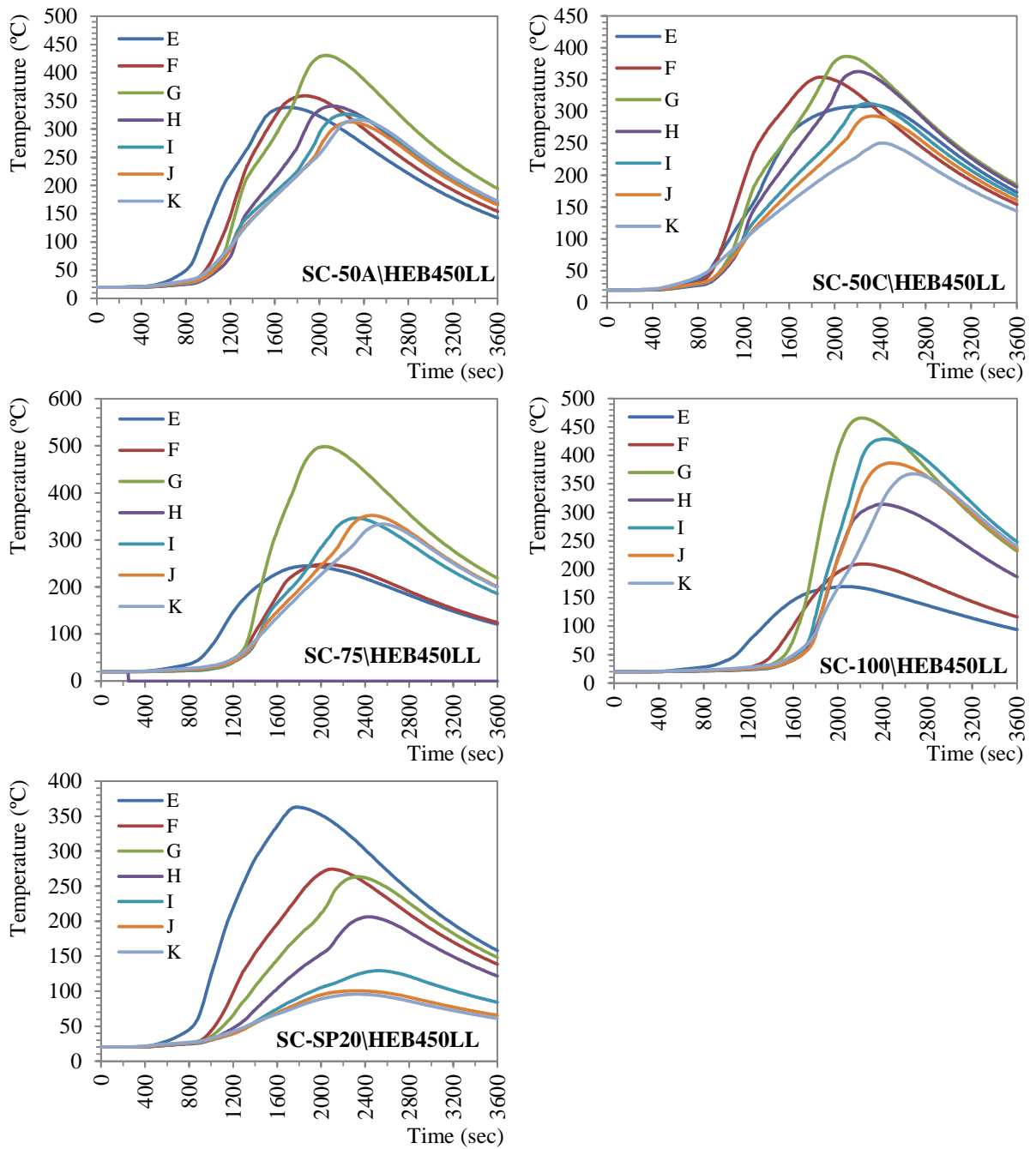


Figure 8-51: Temperature time history curves according to the two-zone model for the HEB450 columns, with respect to the frame where the structural members are located.

Frame	E	F	G	H	I	J	K	Upper Value
SC-25A								
Max T(°C)	193.08	209.87	269.07	204.59	195.06	202.82	213.04	269.07
Time (sec)	2205	2390	2420	2435	2450	2420	2425	(Frame G)
SC-25B								
Max T(°C)	236.66	246.07	261.61	284.78	317.91	420.26	421.19	421.19
Time (sec)	2385	2380	2395	2385	2365	2310	2285	(Frame K)
SC-50A								
Max T(°C)	547.69	663.65	604.45	566.23	480.54	443.60	379.00	663.65
Time (sec)	1800	1825	2035	2125	2240	2310	2410	(Frame F)
SC-50C								
Max T(°C)	472.56	664.98	565.46	565.55	460.94	419.03	355.26	664.98
Time (sec)	2330	1965	2085	2165	2275	2355	2415	(Frame F)
SC-75								
Max T(°C)	423.62	595.03	659.68	675.05	568.97	510.39	417.97	675.05
Time (sec)	1965	1930	2060	2135	2295	2425	2575	(Frame H)
SC-100								
Max T(°C)	345.21	488.77	631.97	652.78	591.86	607.28	524.82	652.78
Time (sec)	2215	2180	2255	2345	2485	2540	2695	(Frame H)
Upper Value	547.69	664.98	659.68	675.05	591.86	607.28	524.82	
	SC-50A	SC-SP20	SC-75	SC-75	SC-100	SC-100	SC-100	

Table 8-4: Maximum temperatures values (°C) of the columns at the upper layer for all the PFE scenarios for the outer columns (cross-section HEB 340).

Frame	E	F	G	H	I	J	K	Upper Value
SC-25A								
Max T(°C)	339.61	304.59	288.01	289.78	306.64	384.57	396.90	396.90
Time (sec)	2265	2390	2410	2415	2415	2385	2385	(Frame K)
SC-25B								
Max T(°C)	252.77	263.25	279.74	304.48	340.11	447.75	451.79	451.79
Time (sec)	2355	2355	2360	2375	2355	2290	2270	(Frame K)
SC-50A								
Max T(°C)	590.90	707.69	648.59	609.10	519.89	480.96	411.32	707.69
Time (sec)	1760	1795	1990	2090	2215	2275	2375	(Frame F)
SC-50C								
Max T(°C)	504.40	703.09	608.31	607.90	498.64	453.28	383.73	703.09
Time (sec)	2120	1935	2070	2135	2250	2325	2400	(Frame F)
SC-75								
Max T(°C)	460.04	643.90	704.68	717.45	614.45	552.18	453.13	717.45
Time (sec)	1890	1870	2000	2105	2260	2390	2545	(Frame H)
SC-100								
Max T(°C)	374.94	530.74	680.91	700.60	637.68	653.38	566.08	700.60
Time (sec)	2160	2135	2205	2310	2445	2495	2665	(Frame H)
SC-SP40								
Upper Value	590.90	707.69	704.68	717.45	637.68	653.38	566.08	
	SC-SP20	SC-50A	SC-75	SC-75	SC-100	SC-100	SC-100	

Table 8-5: Maximum temperatures values (°C) of the columns at the upper layer for all the PFE scenarios for the middle column (cross-section HEB 450).

Chapter 9. Seismic – gravity design / Non-linear structural analysis for seismic loading

The library building that is presented in Chapter 7, is initially designed in order to resist the gravity and seismic loading. It is important to notice that this dissertation is devoted to the case where the structures are “well-designed” according to the guidelines of EN 199-1-1 and EN 1993-1-1. In other cases, if the buildings do not conform to the seismic and gravity design rules, the results would be completely different and for this reason these cases are out of the scope of this study. The first aim of this Chapter is to present the seismic and the gravity design of the library building. To this end, the principles and the procedures that are given in the current regulations are followed. The next objective is to verify the seismic performance of the structure and to study in detail the behaviour during earthquake loading. This is accomplished numerically and non-linear dynamic transient analysis with direct integration of the equations of motion is applied. The seismic action is represented through accelerograms. Specifically, seven time-history acceleration records are selected and properly scaled to match the design spectrum. In the sequel the records are further scaled-up in order to represent more severe earthquakes. Then the performance of the structure is verified through the comparison of the available capacity with the required one. The verification is based on the results of the numerical analysis and it is conducted in terms of storey drift depending on the performance level. The main goal of this Chapter is to present the results of the numerical analyses concerning the different seismic levels. Finally, the ‘level of damage’ that is induced to the structural system due to the scaled seismic actions is systematically classified according to the findings of the numerical analyses.

9.1 Description of the problem

The main goal of the dissertation is to study the behaviour of the library building which is presented in Chapter 7 for the combined loading of Fire after Earthquake (FAE) and to calculate the fire resistance in time domain. To this end, the first step is the design of the frame structure. The design in this study is performed individually for the seismic and the thermal actions according to the current codes. The seismic design of the structure is presented in the first part of this Chapter (section 9.2). The fire design is included in the next Chapter.

The study is conducted numerically and it is based on the FEM. The numerical model and the method used for the analysis are presented in detail in section 9.3. The first objective is to study in detail the behaviour of the structure for the earthquake action as it is defined from the design spectrum (section 9.5). Thus, the seismic action is represented through seven different time-acceleration records.

In the sequel the seismic loading is scaled in order to represent more rare earthquakes with lower probability of existence. The seismic action levels are defined in section 9.6.1. To this end Incremental Dynamic Analysis is conducted. The response of the structure is obtained for scaled accelerograms. The scaling is based on the Peak Ground Acceleration. The results are obtained mainly in terms of maximum inter-storey and global drift angle in order to classify the response of the structural system with respect to the scaled earthquake intensity.

The next target of this Chapter is to present the verification of the seismic performance of the structure for the seismic levels that are considered (section 9.6.2). The limits for the verification are taken according to the multi-level design approach of FEMA which includes four different seismic performance levels (Operational, Immediate Occupancy, Life safety and Collapse Prevention). Taking into account the fact that the structure is initially designed according to EN 1998-1-1 for the ULS performance level, it is expected that the seismic performance of the building lies between the LS (Life Safety) and the CP (Collapse Prevention) as the intensity of the seismic action is scaled-up. To this end, the performance of the structural system is verified through the storey drifts limits as they are defined in FEMA for the different performance levels.

Finally, the damage that is induced to the structural system during the earthquake is studied. In this dissertation the damage is expressed and further quantified through the equivalent plastic strain. In this point of view, the damage depends on the time-history accelerogram that is used and is different for the various structural members that form the structural system. The dissertation is focused on the members of the first level of the structure where the fire is assumed to take place. The ‘level of damage’ is summarized in a table taking into account different time-history acceleration records that are scaled for the representation of different levels of earthquake intensity.

9.2 Design of the frame structure for gravity and seismic loading

The study of the frame structure is based on the consideration that the building can be decomposed in particular sub-structural systems in order to simplify the calculations. Specifically, the design of the library building is conducted individually for the two different main axes of the plan view, which are indicated as x -, y - directions in Figure 9-1. This can be performed due to the regularity of the building. Actually the typical frames are repeated in x -axis every 6m and the loading that is transferred is the same in all the frames except those that are located at the left and the right boundaries ($x=-30$ and $x=30$). These frames undertake the half of the loading comparing with the rest due to the half effective area that corresponds to the specific sub-structural systems. The study is focused on a typical frame oriented in the y -direction of the building as it is indicated in Figure 9-1. The study is conducted for the frames that are aligned with the y -direction. The sub-structural systems that are resisting the loads at the x -axis are not further studied here. The area loads (permanent and live) that are considered according to EN 1991-1-1 for the design of the library building are illustrated in Figure 9-2. The area loads are transferred properly to the

two-dimensional typical frame.

The details related to the geometrical dimensions and the permanent /live loads that are considered for the gravity and the seismic design of the typical frame are presented in Figure 9-3. Initially the frame is designed for the Ultimate Limit State (ULS) combination of actions for the gravity loading. The ULS combination can be simplified in the following expression $E_d = 1.35G + 1.50Q$, where G is the permanent load (including the dead load) and Q is the live load as they are indicated in Figure 9-3. It is noted that a concrete slab, of total depth equal to 0.2m, is assumed to be present at each floor of the building. The seismic design of the structure is conducted according to EN 1998-1-1. The design effect of actions for the seismic actions can be obtained using the combination for accidental situation. The combination is simplified to the expression $G + \psi_2 Q \pm E$. The value of the coefficient ψ_2 that is applied to the variable action Q is considered to be equal to 0.8 according to EN 1990.

Specifically the frame is designed to withstand the design seismic action without local or global collapse, thus retaining the structural integrity and a residual load bearing capacity after the seismic events. The previous, according to the guidelines of EN 1998-1-1, define that the frame is designed to meet the ULS (or “no-collapse”) requirements.

The first objective is the definition of the seismic action. In this dissertation, the seismic action is represented through the elastic response spectrum ($S_e(T)$) of Type 1. The soil type is considered to lie in the D category which indicates that the soil factor S is equal to 1.35 and the lower/upper limits of the period of the constant spectral acceleration branch (T_B and T_C) are equal to 0.2 sec and 0.8 sec respectively. According to the type of the soil the value of the period that defines the beginning of the constant displacement response range (T_D) is also defined and is equal to 2sec. The design ground acceleration on type A ground α_g is taken equal to 0.36g.

The design spectrum ($S_d(T)$) that is used in this study is based on the elastic one taking into account that the behaviour factor q is equal to 4. The value of the behaviour factor is selected according to the specific rules for steel buildings and indicates that the frame is designed according to the concept of the dissipative behaviour. Specifically, according to Tables 6.1 and 6.2 of EN-1998-1-1 this behaviour factor corresponds to the medium ductility class and it corresponds to regular buildings that are formed using moment resisting frames. The elastic and the design response spectrum are depicted in Figure 9-4.

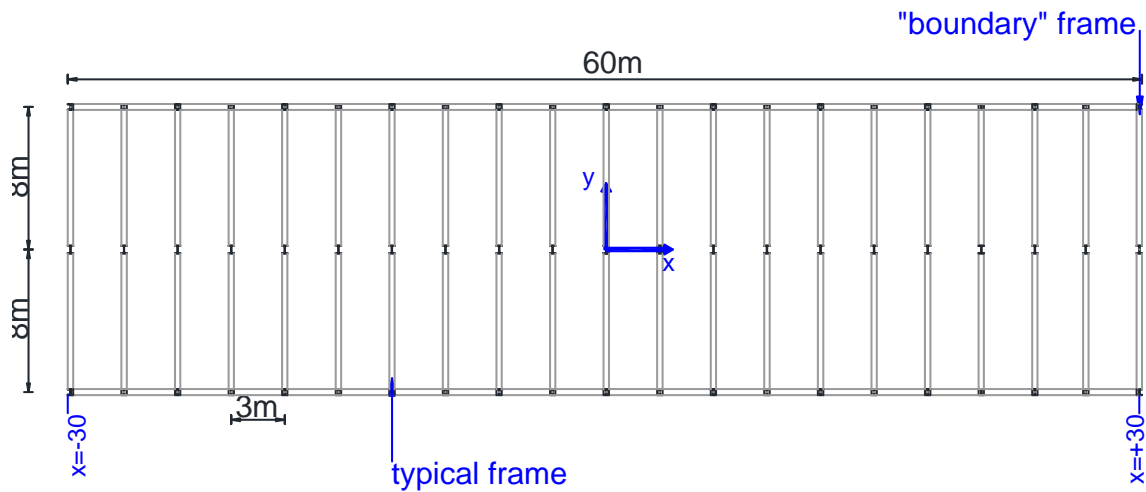


Figure 9-1: The plan-view of the library building.

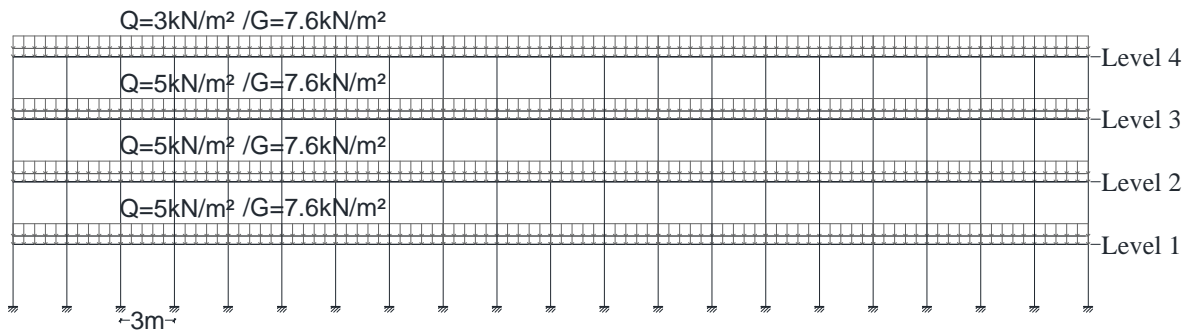


Figure 9-2: The area loads/ longitudinal view of the library building.

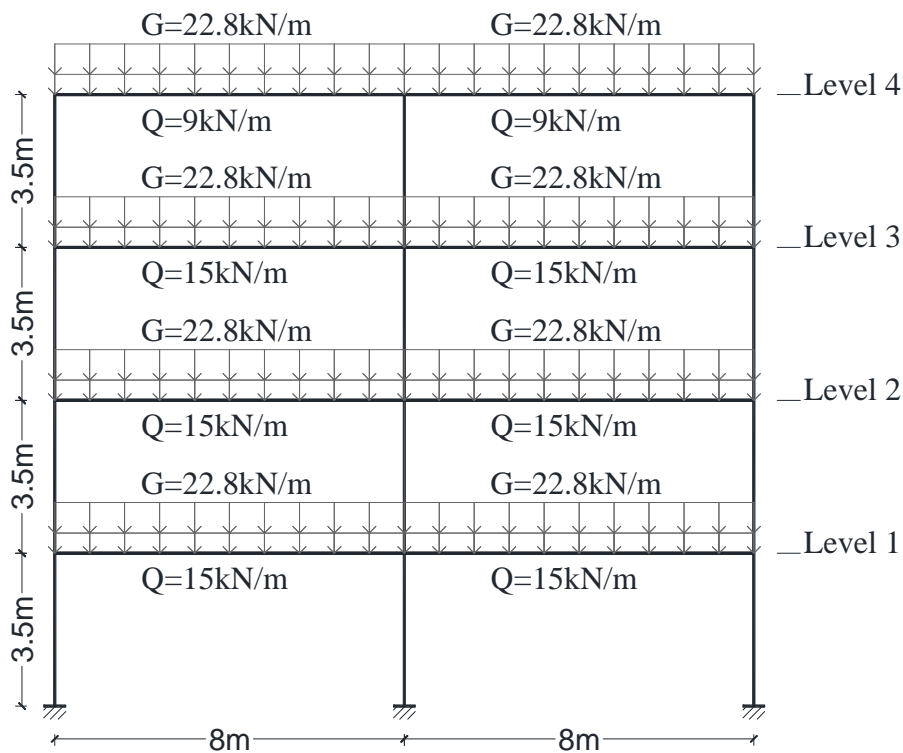


Figure 9-3: The typical frame.

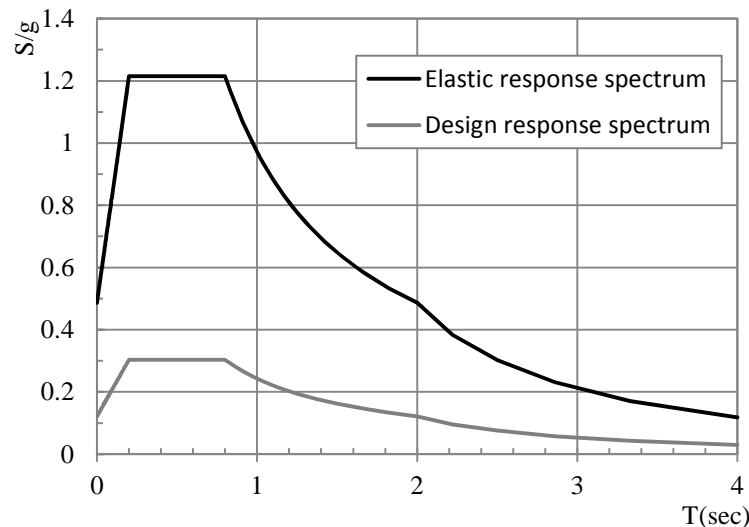


Figure 9-4: Elastic versus design response spectrum for ground type D (5% damping).

In order to verify the design requirements the lateral force method of analysis is used. This is feasible since the building satisfies the requirements for the application of the linear-elastic analysis. The requirements are defined in order to ensure that the response of the building is not significantly affected by the contributions from modes of vibration higher than the fundamental one. In this case study, this is ensured since the building follows the requirements concerning the regularity in elevation. Moreover, the fundamental period of vibration of the frame is calculated to be equal to 0.878 sec and the restrictions that arise in section 4.3.3.2.1 of EN 1998-1-1 are satisfied. The calculation of the fundamental period of the frame is included in detail in section 9.5 where the results of the modal analysis are presented.

The verification of the ULS requirement is based on the fulfillment of the conditions regarding the resistance, ductility and equilibrium. The resistance of the cross-sections of the structural members is verified through the inequality:

$$E_d \leq R_d \quad (9.1)$$

where E_d is the design value of the action effect, due to the seismic design situation and R_d is the corresponding design resistance of the element.

The global and local ductility condition is verified in order to ensure that both the structural members and the structure as a whole, possess adequate ductility. This indicates that the soft storey plastic mechanism is prevented. Moreover, the capacity design rules are verified according to general requirements included in section 4.2.3 of EN 1998-1-1 and the specific rules for steel buildings that are given in section 6.6 of EN 1998-1-1. Since the capacity design rules are satisfied, it is ensured that for the plastic hinges the full plastic moment of resistance and rotational capacity are not decreased by compression and shear forces. Additionally, the capacity design indicates that the plastic hinges are formed in the beams ends but not in the columns. This is only violated at the base of the moment resisting frame. Finally, in the current study, the plastic mechanism of the building is

verified using push-over analysis and the results confirm the capacity design demands. The outcomes of the push-over analysis are presented in detail in section 9.5.

The cross-sections of the structural members that result according to the design procedure are summarized in Figure 9-5.

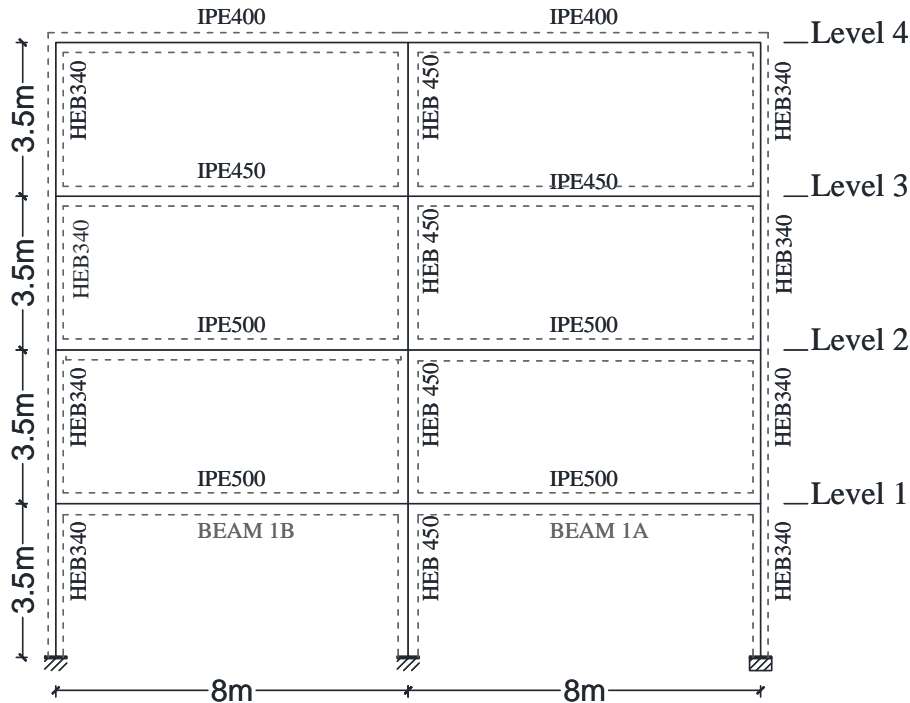


Figure 9-5: The cross-sections of the typical frame according to the design for seismic and gravity loading.

9.3 Numerical modeling

9.3.1 Numerical model

The numerical model is developed using the nonlinear finite element code MSC-Marc (2011). The two-dimensional model that is developed for the simulation of the behaviour of the steel frame uses the element of type 98 of the library of MSC-Marc (2011). This is a straight beam in space which includes transverse shear effects (more details are included in Appendix A). The geometrical dimensions of the numerical model and the cross-sections that are used are those that arise from the design procedure and they are indicated in Figure 9-5. Totally 595 finite elements are used for the numerical simulation. The size of the beam finite elements is equal to 0.175m for the columns and the corresponding value for the beams varies between 0.1m and 0.25m. The discretization is not uniform in order to decrease the total number of the finite elements that are used in the simulation due to the high computational time that is required for the analysis. Regarding the beams, the mesh is more dense at the support position and at the mid-span for the more accurate simulation of the behaviour. The numerical model and the mesh that is adopted are presented in Figure 9-6. It is noted that the beam-column joints details are not included in the numerical model. For this reason, rigid offsets are used in order to model the connections between the beams and the columns. This indicates that the joint are assumed to be rigid. The details about the joint modeling are presented in Figure 9-7.

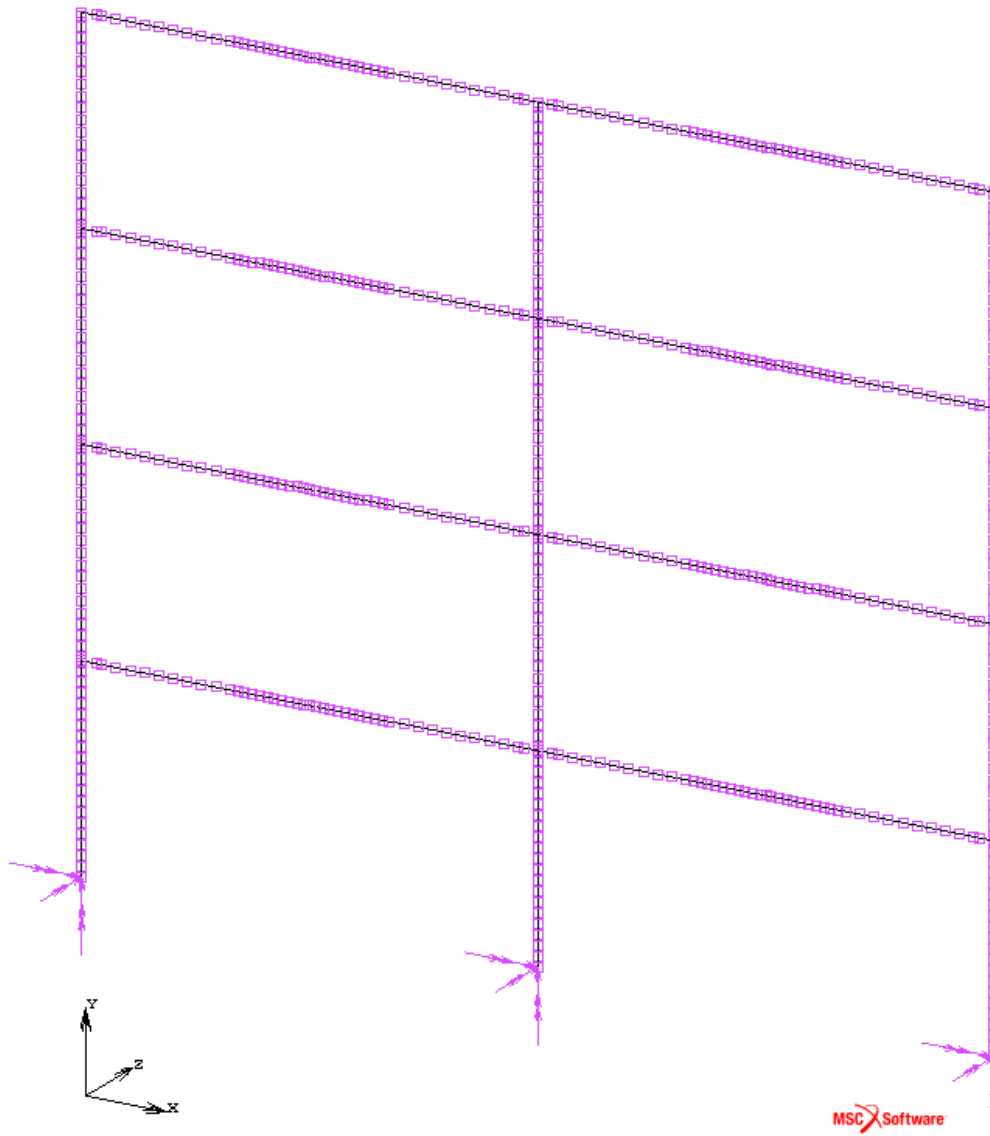


Figure 9-6: The numerical model.

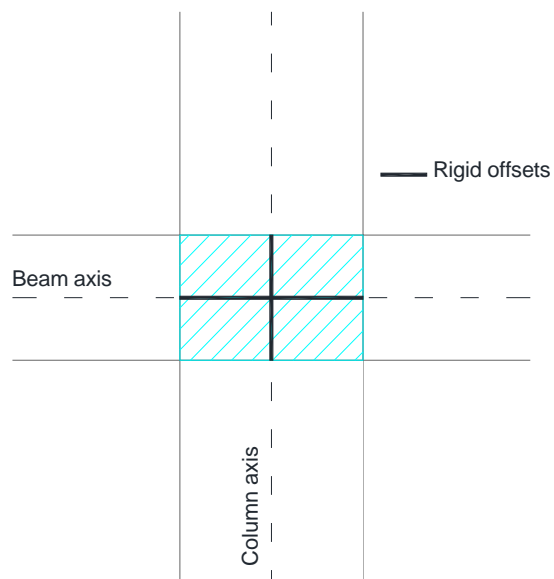


Figure 9-7: Beam to column connections.

Cross-sections simulation

The cross-section of the finite element used for the numerical modelling, is a user-defined solid numerically integrated one. Four different branches are defined for the sections of the structural members: the upper flange, the web (which is divided into two parts for more accurate results) and the lower flange branch as it is depicted in Figure 9-8. Depending on the order of the numerical integration that is selected for every branch of the cross-section, the stress-strain law is integrated through solid sections using the Newton-Cotes rule. Specifically, the order of the integration is equal to 5x5 for all the branches of the cross-section (Figure 9-8). This indicates that 25 different integration points are defined for every branch. The results are exported to different layers, corresponding to the position of the integration points. In this way, totally 100 layers are generated as it is illustrated in Figure 9-8.

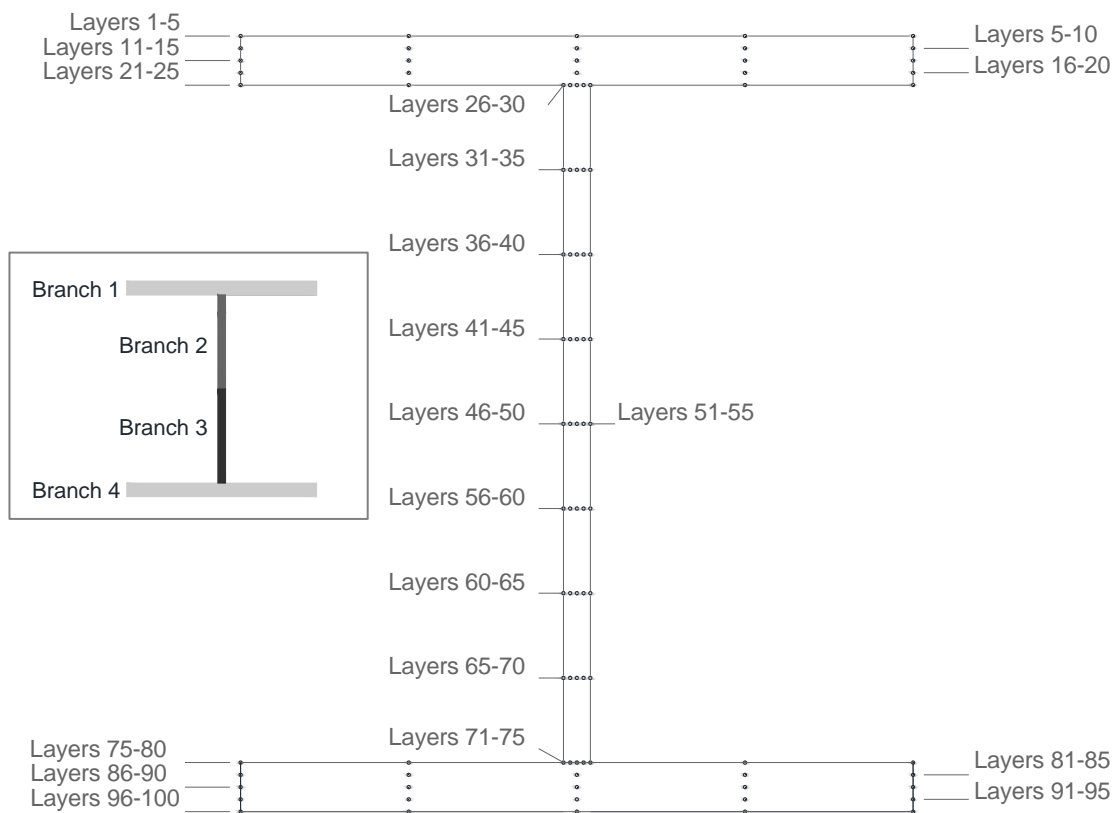


Figure 9-8: Discretization of the cross-section in four different branches and layers definition.

Material properties-plasticity modelling

The yield stress of the structural steel is assumed to be equal to 275MPa at room temperature (S275 structural steel). It is highlighted that the strain hardening of the steel for temperature range 20⁰C-400⁰C is neglected in order to simplify the problem. Two different models are developed. In the first model all the finite elements are using the elastic-perfect plastic material law (distributed plasticity model), while the second model is based on the concentrated plasticity approach. In the second model the elastic-plastic behaviour of the model is consolidated at the ends of beams and columns and at the mid-span of the beams. The rest of the finite elements are considered to be elastic. Specifically,

first the plastic hinge mechanism of the frame structure is verified from the results of the analyses of the model that includes the distributed plasticity (DPM). Taking into account the previous results, the possible positions of the plastic hinges are defined and the concentrated plasticity model is developed. Specifically, the elastic-plastic material law is attached at the finite elements that correspond to the possible plastic hinge locations as it is illustrated in Figure 9-9.

At this point it is critical to decide the size-length of the finite elements where the elastic-plastic material law is used. In this study the length is set to be equal to 0.1m as it is clarified in Figure 9-9.

The first model, which demonstrates more accurately the frame behaviour, is developed in order to study carefully the seismic response. The second model, which is based on the assumption of the concentrated plasticity (CPM), is developed in order to simplify the numerical analyses. Moreover the results of the analyses of the CP model can be directly connected to the findings of Chapter 12 as it is explained in detail in the section 12.4.3.

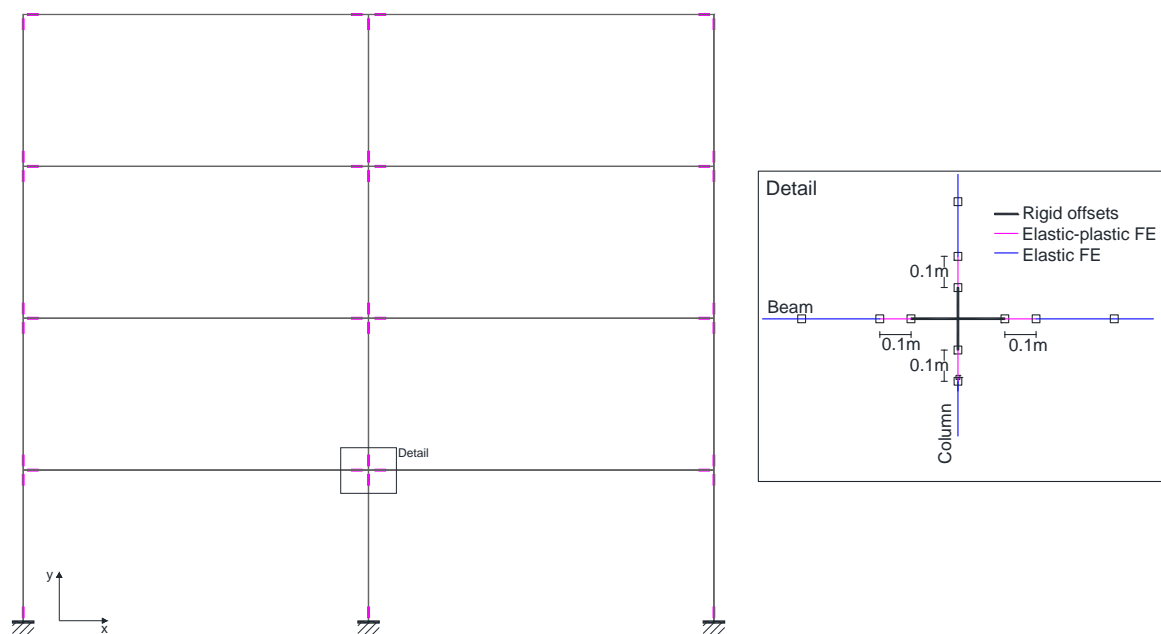


Figure 9-9: The CPM and the locations of the possible plastic hinges.

Mass and damping modeling

The system mass is defined through both distributed and concentrated masses. The numerical model uses two different mass approaches. Distributed masses are defined for elements through the mass density material property and they simulate the self-weight of the structure. To this end, the density of the steel is considered equal to 7850kg/m^3 . The contribution of the masses that correspond to the dead and the live load is simulated through the lumped-mass idealization. Specifically, the mass associated with the translational DOF in x -direction are indicated at each level as it is illustrated in Figure 9-9. Regarding the masses connected to the rotational DOF, they are assumed to be zero. The

total mass of the system is equal to 228.42tn.

The dissipated energy of the structure during the earthquake excitation is modeled through the Rayleigh damping type according to the procedure that is presented in Appendix A.

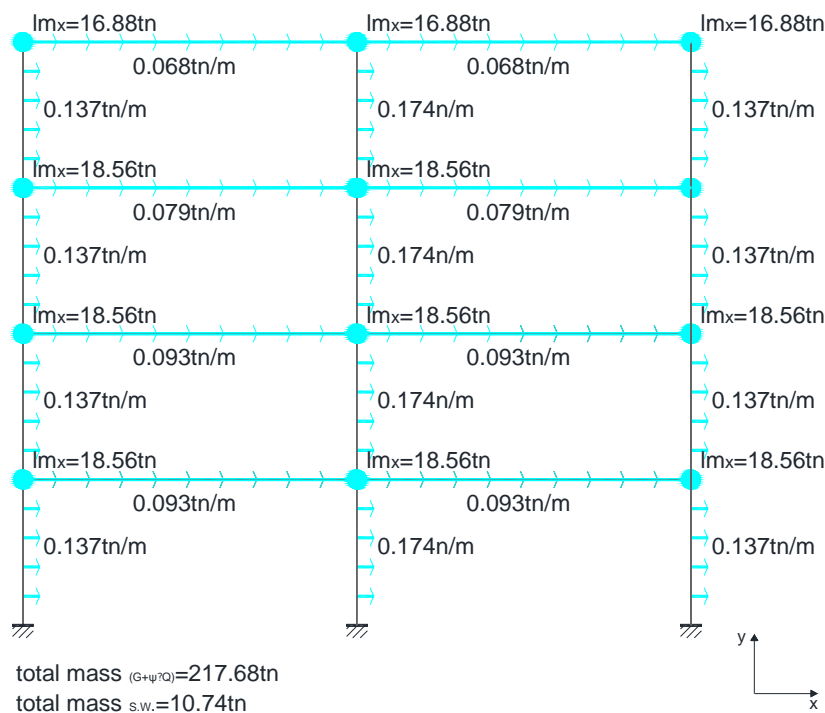


Figure 9-10: Structural system masses.

9.3.2 Representation of seismic action

Artificial accelerograms are generated in order to represent the seismic action. To this end the Roxel (Iervolino *et al.*, 2010) software is used. Which is a computer aided record selection tool for code based seismic structural analysis. It features a MATHWORKS-MATLAB graphic user interface (Figure 9-11) and a FORTRAN engine, based on the software developed for the studies of Iervolino *et al.* (2008).

In particular, the software is developed to search for combinations of seven accelerograms compatible in the average with the *reference* spectra according to the criteria that are defined in codes. In the specific study the guidelines included in EN 1998-1-1 are used which are the following:

- *A minimum of three accelerograms should be used*
- *The mean of the zero period spectral response acceleration values (calculated from the individual time histories) should not be smaller than the value of $a_g S$ for the site in the question*
- *In the range of the periods between $0.2T_1$ and $2T_1$, (where T_1 is the fundamental period of the structure in the direction where the accelerograms will be applied), no value of the mean 5% damping elastic spectrum, calculated from all time*

histories, should be less than 90% of the corresponding value of 5% design elastic response spectrum.

It is also possible to reflect in selection the characteristics of the source, in terms of magnitude (M), epicentral distance (R) and EC8 soil classification. The steps that are followed in order to obtain the accelerograms are the following:

1. The *reference* elastic response spectrum is defined (Figure 9-4). It is clarified that the spectra used here is not scaled according to the behaviour factor q . The records have to match on the spectra according to the criteria that are defined in Step 3.
2. Preliminary search in the European Strong motion Database² which falls into the magnitude and distance limits. Regarding the epicentral distance, the limit values used in this study are $R_{min}=30km$, $R_{max}=50km$, while the corresponding values for the magnitude are $M_{min}=6$ and $M_{max}=7$. Rexel returns the number of records available in these intervals. The list constitutes the inventory of records in which the search for suites of seven records, which are compatible with the spectrum defined in Step 1, will be finally conducted. No criteria are used for the site class. This means that the search is conducted for any site class. It is noted that if the site class that corresponds to the *reference* elastic spectra is used (site class D), Rexel does not return any results in the preliminary search.
3. Assignment of the spectrum matching criteria. These are the period range where the average spectrum has to be compatible with the *reference* spectrum and the tolerances in compatibility. In this study the limit values for the definition of the period range are $0.2T_1=0.175 sec$ and $2T_1=1.757 sec$. The lower tolerance is set equal to 10% according to the rules presented in the previous. EC8 does not provide any indication about the upper tolerance limit. In general, it is better to reduce as much as possible the overestimation of the spectrum. For this reason this value is set equal to 30%.
4. Running the software for the combination of seven records which include one component of motion that match the elastic response spectrum according to the parameters that are defined in Step 3.

² The European strong-motion database is a platform that provides an interactive, fully relational database and databank with more than 3,000 uniformly processed and formatted European strong-motion records and associated earthquake, station and waveform-parameters. The user can search the database and databank interactively and download selected strong-motion records and associated parameters. Information about European organizations involved in strong-motion recordings are also available. The database is available at the webpage: http://www.isesd.hi.is/ESD_Local/frameset.htm.

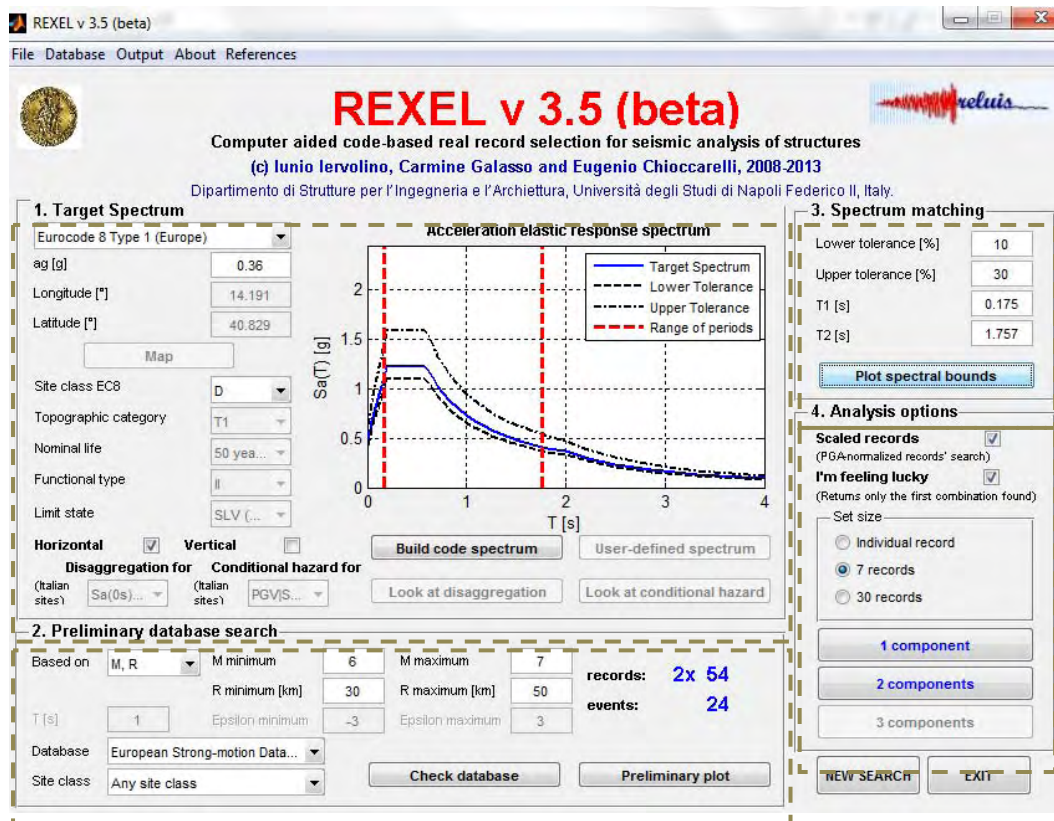


Figure 9-11: The user interface and the parameters used in this study.

The outputs of REXEL are depicted in Figure 9-12 in terms of response spectra. Specifically, the figure illustrates the target-reference spectrum, the upper and the lower tolerance limits, the period range, the average spectrum and the spectra that are matched according to the parameters defined to Step 3. The time-history acceleration records that result from REXEL are properly scaled in order to match the elastic spectrum using the appropriate scale factors. The characteristics of the seven accelerograms that are used in this study are summarized in Table 9-1. The scaled accelerograms are presented in Figure 9-13.

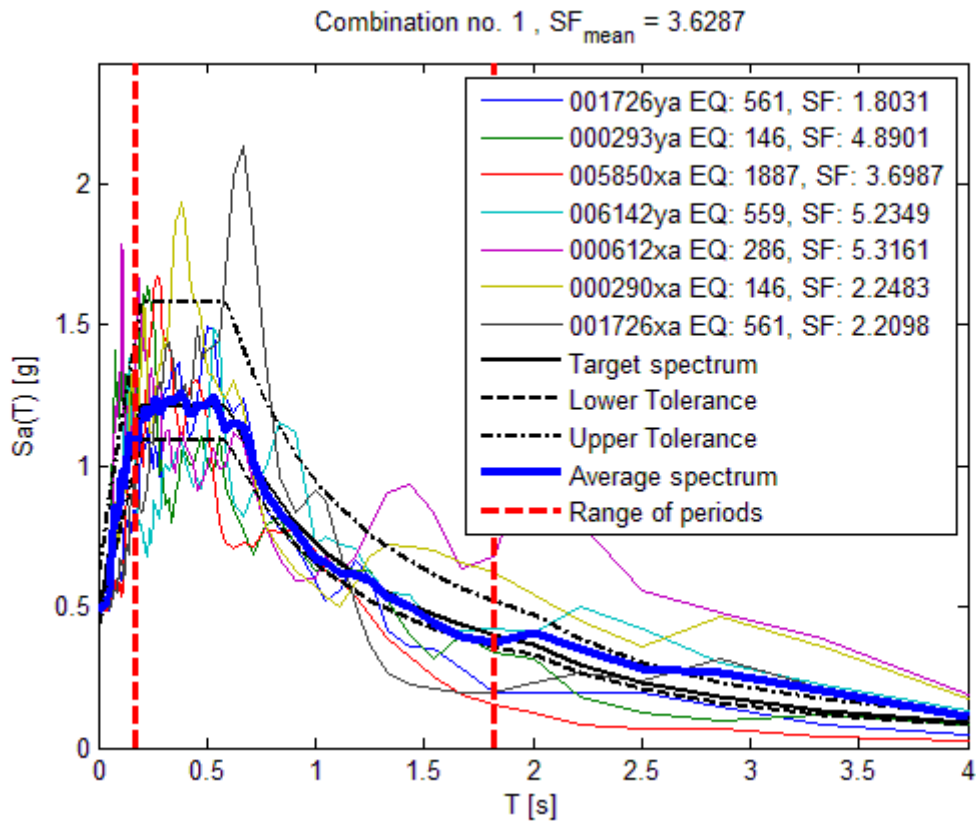


Figure 9-12: Results of REXEL in terms of spectra and the scale factors for matching to the elastic response spectrum.

Waveform ID	Earthquake Name	\overline{M}_w	Fault Mechanism	Duration (sec)	Epicentral Distance [km]	EC8 Site class	PGA [m/s ²]	Scale factor
290xa	Campano Lucano	6.9	normal	71.93	32	A	2.248	2.121
293ya	Campano Lucano	6.9	normal	83.94	33	B	4.890	0.975
6142ya	Aigion	6.5	normal	39.5	43	B	5.235	0.911
612xa	Umbria Marche	6	normal	106.21	38	B	5.316	0.897
1726xa	Adana	6.3	strike slip	29.2	30	C	2.210	2.158
1726ya	Adana	6.3	strike slip	29.18	30	C	1.803	2.644
5850xa	Strofades	6.6	oblique	65.43	38	B	3.699	1.289

Table 9-1: The time-history acceleration records used for dynamic analyses.

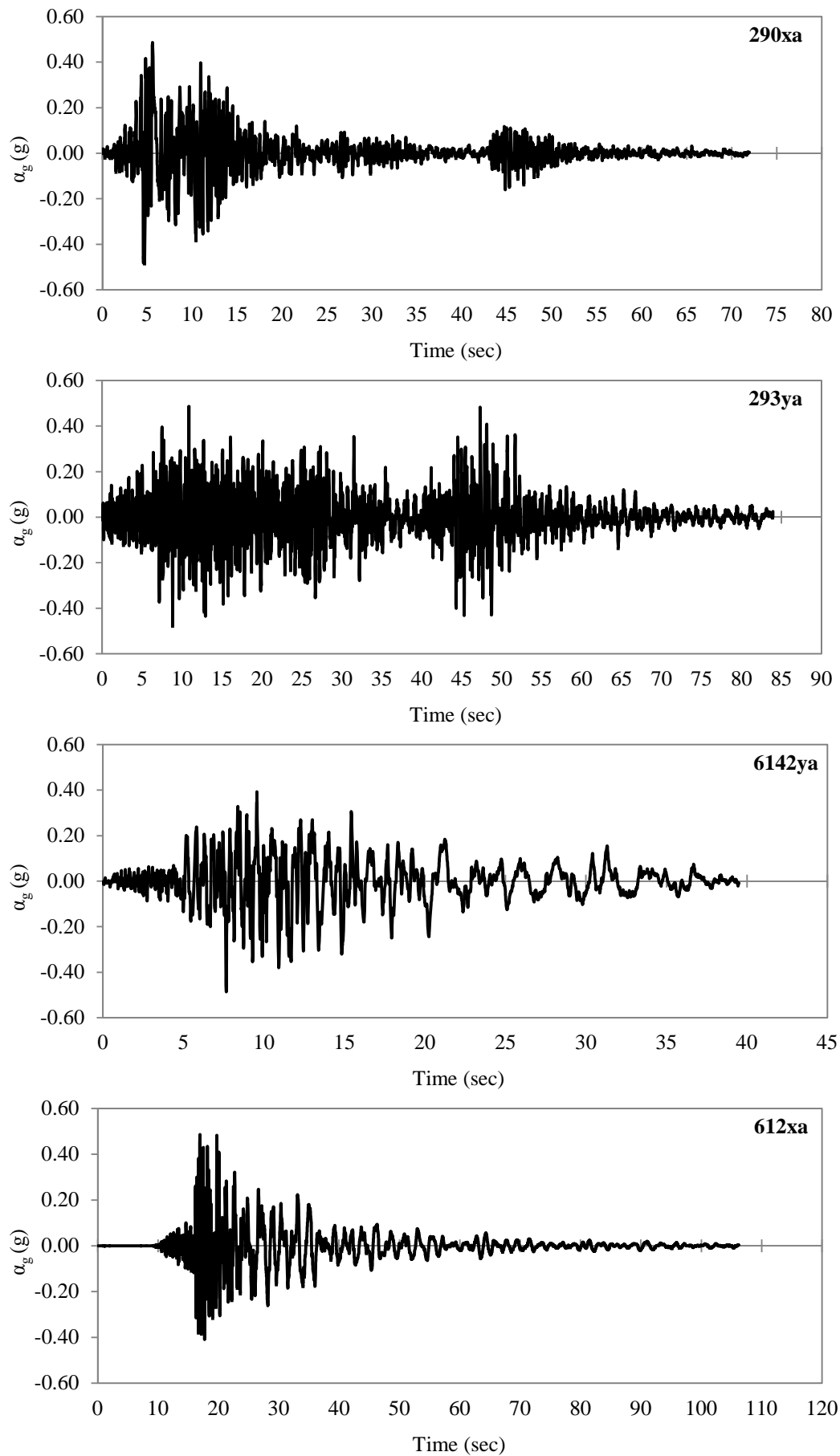


Figure 9-13: Scaled time-history acceleration records according to Rexel's results. (continued)

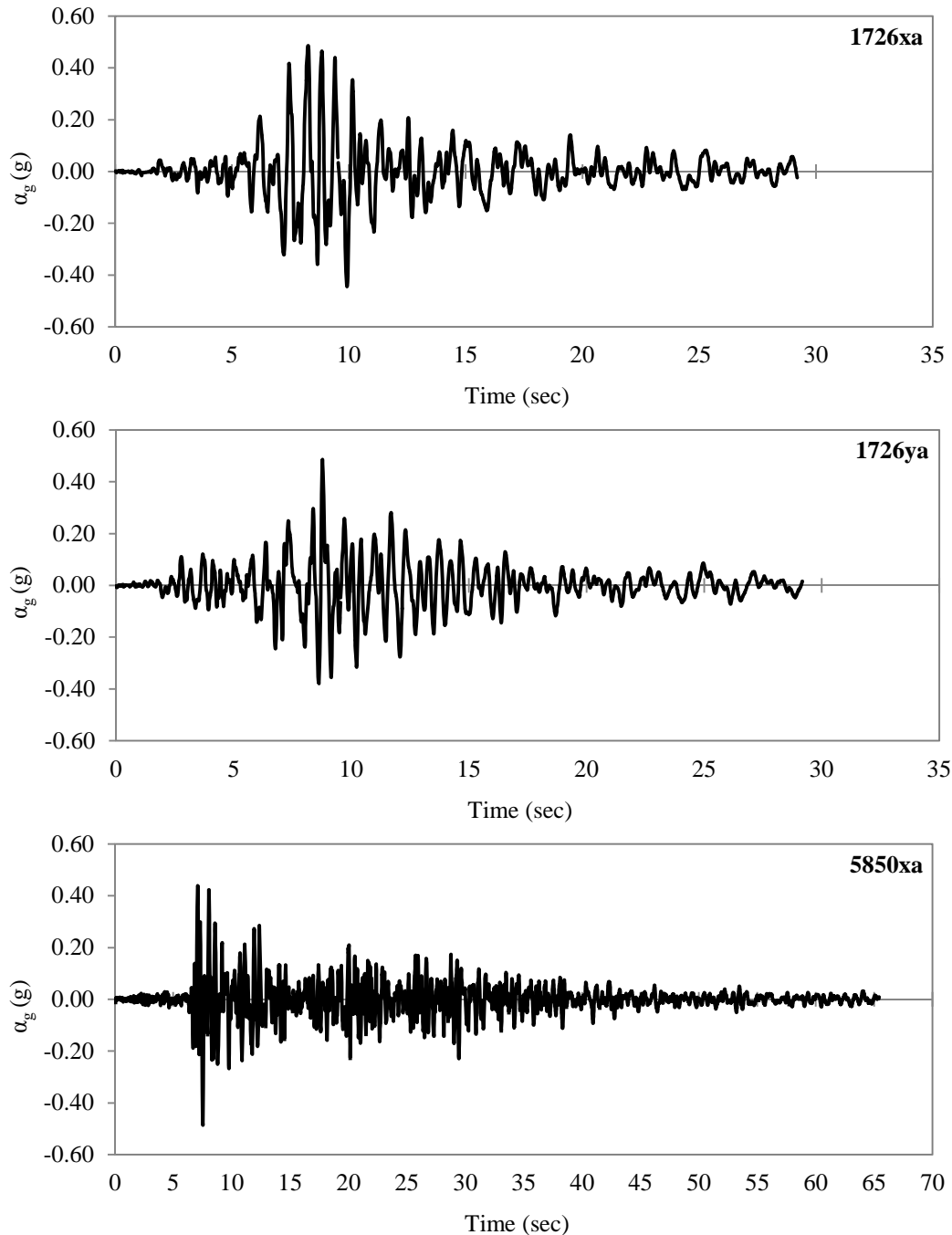


Figure 9-13: Scaled time-history acceleration records according to Rexel's results.

9.3.3 The numerical analysis

The problem is solved numerically using the FEM through dynamic transient analysis with direct integration of the equations of motion and the “large strain formulation” is used. The details regarding the specified analysis are included in Appendix A.

The selection of the numerical procedure used for the time integration of the differential equations is crucial. The three important requirements are referred to the convergence of the solution, the stability and the accuracy. In this study the Newmark-Beta method is used applying the linear acceleration scheme ($\gamma = 0.5$ and $\beta = 0.25$). The time-step of the

analysis is set to be constant and equal to 10^{-3} sec. The total time of the analyses and the computational time are dependent on the time-history record duration and they are presented in Table 9-2. It is noted that in the case of the DP model the results are recorded at every time step while in the case where the CD model is used, the output is recorded every 10 time steps.

Accelerogram ID	Duration t_a (sec)	Total analysis time t_{tot} (sec)	Time steps	Computational time (sec) -CP model-	Computational time (sec) -DP model-
290xa	71.93	90	90,000	22,146	44,143
293ya	83.94	110	110,000	22,120	48,858
6142ya	39.50	60	60,000	11,679	20,135
612xa	106.21	130	130,000	26,305	56,873
5850xa	65.43	85	85,000	18,931	42,821
1726xa	29.20	50	50,000	15,630	26,208
1726ya	29.18	50	50,000	11,334	27,045

Table 9-2: Total analyses time and computational time.

It is important to notice that the total analysis time does not concur with the duration of the corresponding time-history acceleration record. Actually, the total analysis time is obtained by the addition of approximately 20 sec to the duration of the accelerograms. This time is approximately required in order to ensure that the oscillation of the structural system is totally damped. Specifically, the earthquake excitation, according to the time-history acceleration record, ends at the t_a sec of the analysis. After this point, the structure performs a damped free vibration ($\zeta=0.05$) since there is no external dynamic excitation. The motion decays as the time passes, due to the energy dissipation and this time period is controlled by the damping characteristics of the structural system. When the oscillation is totally damped, the residual configuration of the structure is obtained. This consideration is critical in this study due to the fact that the final goal is to study the fire-performance of the damaged structural system. This indicates that the results of the seismic (dynamic) analyses will be further used in order to conduct the FAE analyses. The initial configuration for the analyses that are conducted at the second stage (fire loading) is the residual configuration that is obtained at the end of the dynamic-seismic analyses.

Moreover, the issue that arises at this point is related to the type of loading used for the dynamic excitation (time history acceleration, velocity or displacement). This is explained in detail in Chapter 11. Briefly, the problem comes from the fact that the time where the earthquake excitation stops (t_a) corresponds to a non-zero value for the ground acceleration. It is apparent that the acceleration should be eliminated. In other words, if the ground displacement remains constant the velocity and the acceleration become zero. In this study, first the ground displacement time-history is obtained through the double integration of the ground acceleration time-history. Then, the displacement is artificially stabilized. The stabilization is gradual and a second order curve is used. In this way the ground acceleration is gradually decreased and finally is eliminated. A visual

representation of the stabilization of the acceleration is given in Figure 11-1 in Chapter 11. The earthquake excitation is applied as time-history displacement to the x -translational DOF to the corresponding nodes of the numerical model. The time-history displacement records that are used are depicted in Figure 9-14. It is noted that the stabilization of the displacement is not included in the diagrams of Figure 9-14.

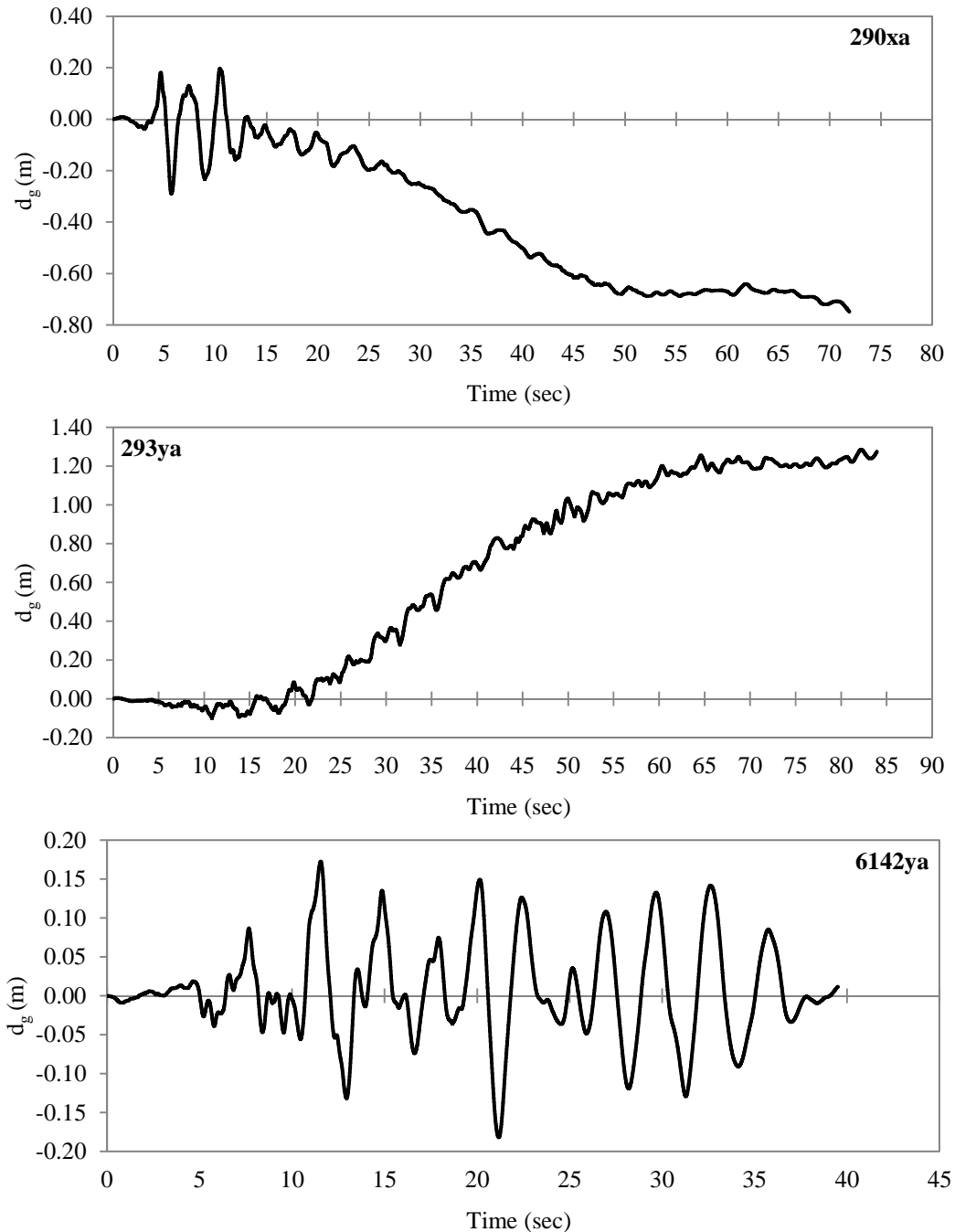


Figure 9-14: Time-history displacement records that are calculated through the double integration of the corresponding accelerograms. (continued)

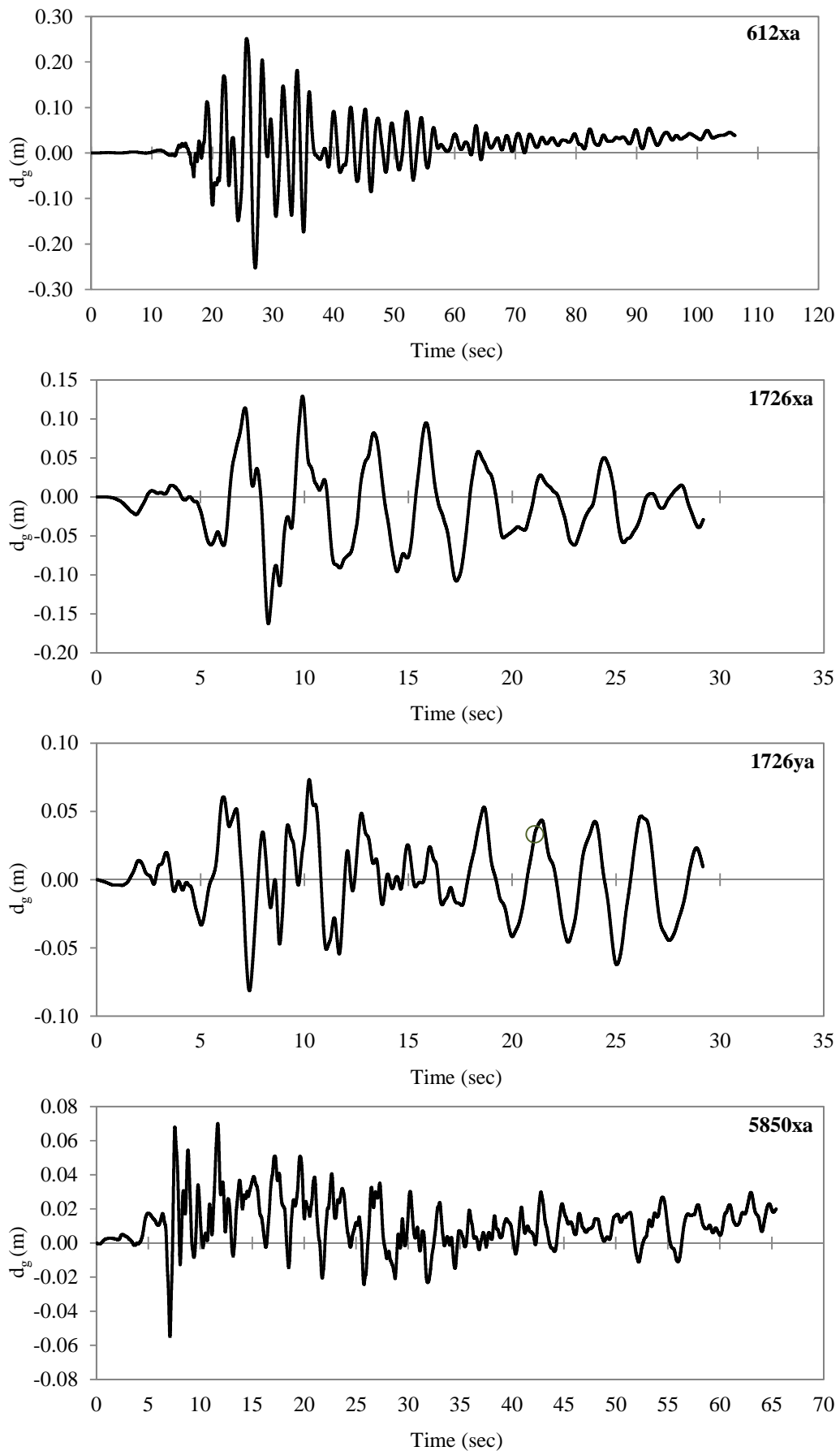


Figure 9-14: Time-history displacement records that are calculated through the double integration of the corresponding accelerograms.

Boundary conditions – loading

The frame structure is clamped at the basis of the columns. This specifies that all the degrees of freedom displacement x , y , z and rotation x , y , z are fixed at the support nodes. Both the permanent and the live loads are applied with respect to the combination of actions $E_d = G + 0.8Q$. As it is explained in the previous section, the seismic excitation is applied at the support nodes in terms of imposed displacement in x -direction.

9.4 Eigenmode analysis

Initially, eigenmode analysis is conducted in order to obtain the basic dynamic characteristics of the structural system. The analysis is conducted using the finite element code MSC Marc (2011). The numerical model has already been presented in Section 9.3.1. The results of the modal analysis regarding the eigenmodes are illustrated in Figure 9-15. A scale factor equal to 10 is used for better visualization of the deformed configuration of the frame.

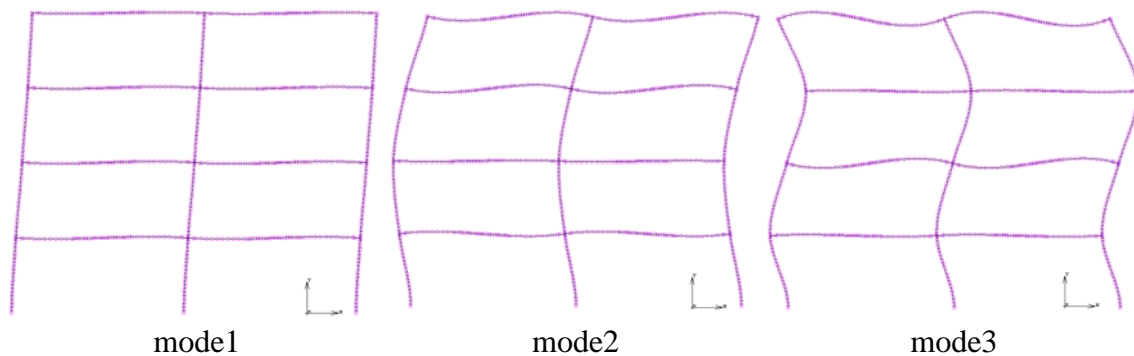


Figure 9-15: The eigenmodes of the structural system (Scale factor =10).

The natural cyclic frequency of vibration f_n and the natural period of vibration T_n for the first, the second and the third mode are summarized in Table 9-3.

n^{th} eigenmode	Natural frequency f_n (sec^{-1})	Natural period T_n (sec)
1	1.138	0.878
2	3.527	0.284
3	7.017	0.143

Table 9-3: Natural period and frequency for various eigenmodes.

9.5 Evaluation of the seismic performance for the design spectrum

The behaviour of the structural system is evaluated through two different approaches. First push-over analysis is conducted in order to determine the capacity of the system in terms of base-shear and roof displacement curve. In this way the inelastic behaviour of the structural system is obtained and the objective is to evaluate the global plastic-hinge mechanism and the drift displacements. In the sequel the behaviour of the system is studied in detail through the non-linear dynamic analysis. The seven accelerograms that are properly scaled to match the elastic spectrum are used. In this way a more realistic

perspective for the behaviour of the structural system is obtained. The results are presented in terms of the time-history of the base shear and drift displacements.

9.5.1 Static push-over analysis

During the push-over analysis the structural system is subjected to lateral loads under the combination of actions that correspond to the seismic loading $E_d = G + 0.8Q$. The lateral forces represent the inertia forces of the structure that appear during the ground motion. The issue is that the actual force distribution during the seismic loading changes continuously during the earthquake excitation. Thus, the selection of the appropriate lateral load pattern is crucial for the results of the push-over analysis. Several approaches are proposed in the literature and the most common are the uniform distribution, the modal pattern proportionality to lateral forces consistent with the lateral force distribution in the linear analysis (lateral force method or modal response spectrum analysis). In this study, the distribution of the lateral forces is relevant to the scheme used for the elastic lateral force method. The analysis was conducted using the software Statik (2007).

As the lateral loads are incrementally increased, the structural members yield and plastic hinges are formed. The push-over linear limit analysis that is used in this study is conducted under the consideration of concentrated plasticity. This indicates that the plastic hinges are formed instantaneously and the elastic-perfectly plastic approach is adopted. The results of the push-over analysis are represented through the non-linear force-displacement curve in terms of base shear and roof displacement, as it is illustrated in Figure 9-16. In the same figure the curve is presented also in an alternative form. In the vertical axis the lateral force coefficient λ is defined as the ratio of the base shear to the total seismic mass of the structural system. On the horizontal axis the global drift displacement with respect to the total height of the structure is presented. The push-over curve extends up to the point where the roof displacement corresponds almost to 4% of global drift.

At this point the plastic hinge mechanism of the structure is completely formed as it is depicted in Figure 9-17. The strong beam-weak column plastic hinge mechanism that results indicates that the plastic hinges are formed at the ends of the beams and at the bases of the columns. This follows the requirements of the capacity design of the structural system. Also, it can be observed that the structural system process an over-strength which can be demonstrated using the ratio between the value of λ at the point where the drift is equal to 4% to the value of λ which corresponds to the occurrence of the first plastic hinge. In this way the over-strength factor is determined to be equal to 1.93.

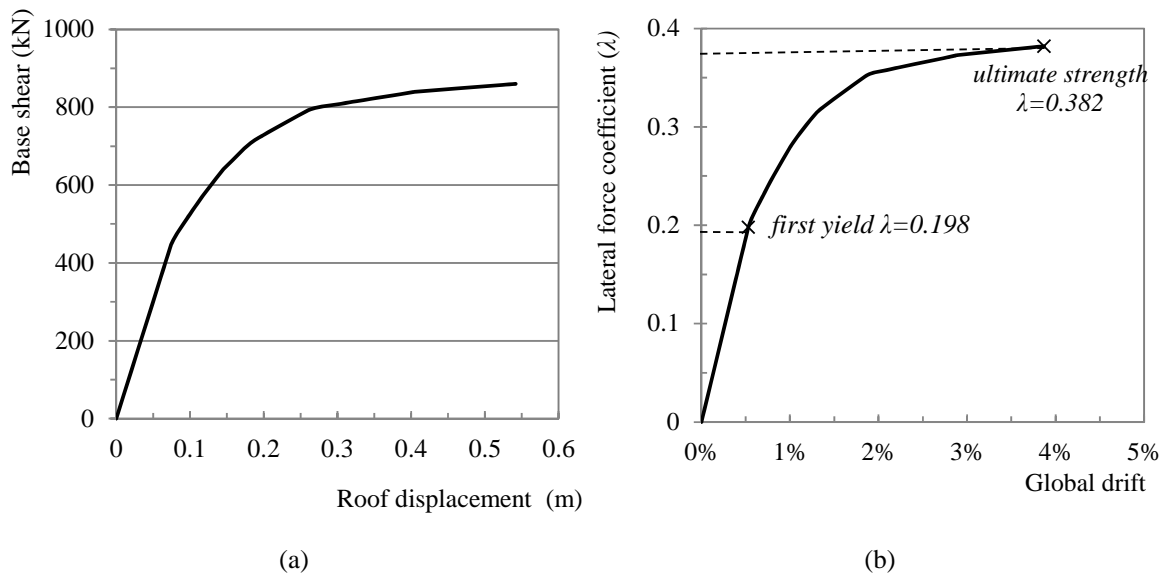


Figure 9-16: Capacity of the structure in terms of (a) Force-displacement and (b) λ -global drift curve.

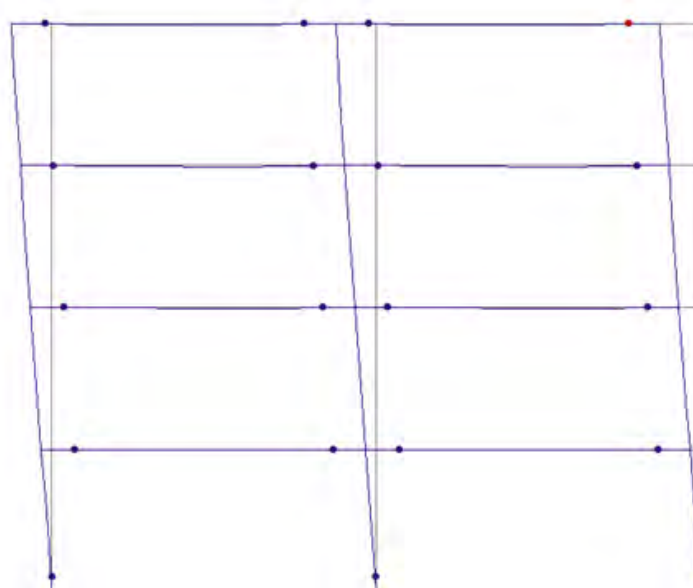


Figure 9-17: The global plastic hinge mechanism.

9.5.2 Non-linear dynamic transient analysis based on the direct integration of the equations of motion

Base-shear versus global drift

Figure 9-18 presents the time history evolution of the absolute values of the global drift and the base shear of the structural system for the seven different accelerograms that are properly scaled in order to match the elastic spectrum. It is observed that the maximum values for both the global drift and the base shear are recorded at different times and this depends on the accelerogram that is used. Moreover, it should be clarified that the time where the maximum drift is recorded is not the same with the time when the maximum shear is recorded. In order to evaluate the behaviour of the structural system under the

dynamic loading both the maximum global and the maximum base shear are presented in detail in Table 9-4. For each accelerogram two different sets of data are given. The first, is the maximum global drift and the corresponding shear and time of the analysis. The second set includes the maximum base shear and the corresponding total drift and time of the analysis. It is clear that the maximum roof displacement and the maximum base shear occur in a short time interval. The peak values appear for the time-history acceleration records 1726xa and 6142ya for the global drift and the base shear respectively. It is noted that the values for both the maximum global drift and the base shear, regarding all the dynamic analyses, are reasonable taking into account the values that appear at the capacity curve that results from the pushover analysis. In this study the evaluation of the dynamic analysis is conducted in terms of drift values and this is presented in Section 9.6.2.

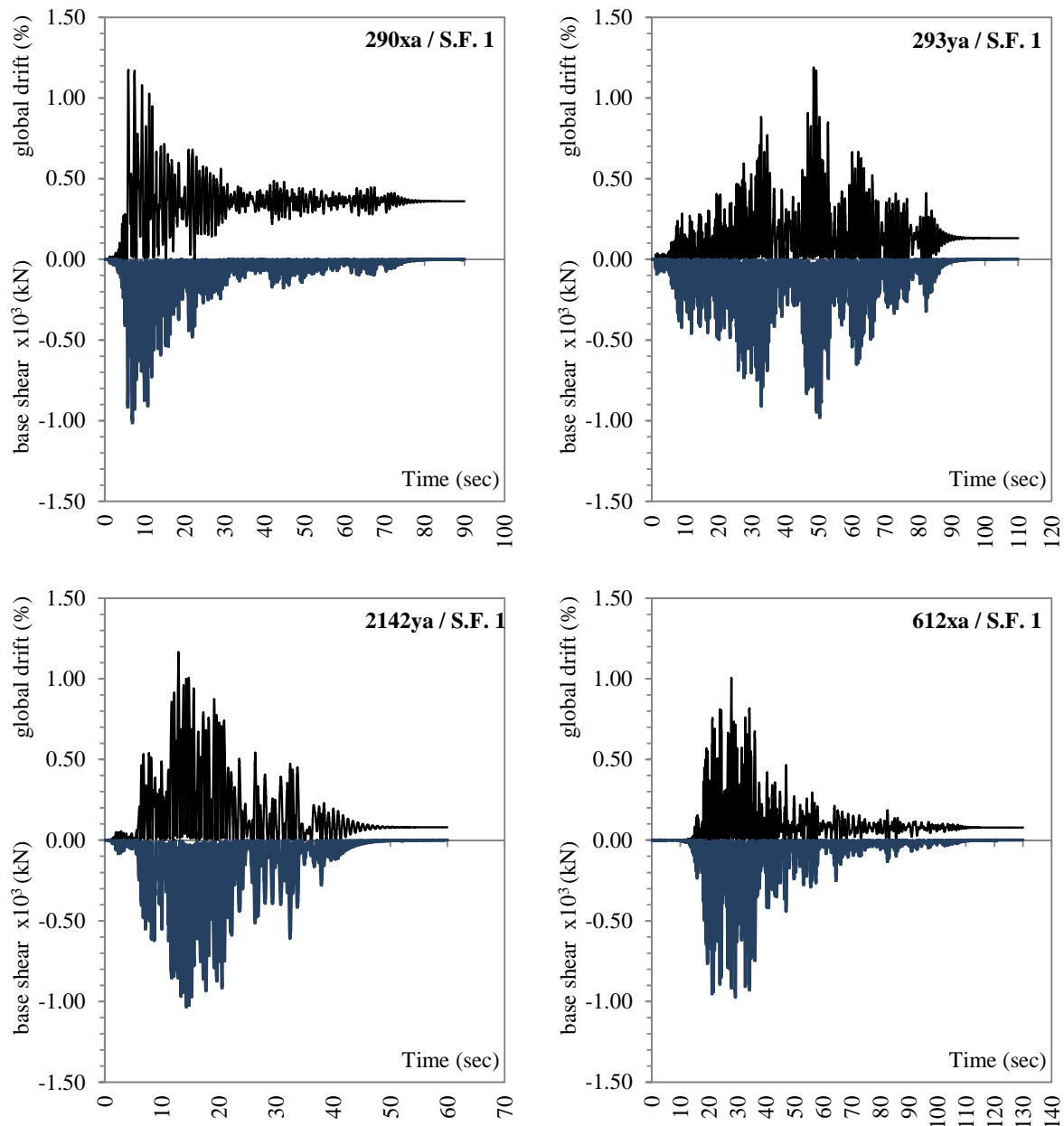


Figure 9-18: Roof displacement and base shear time history for the seven accelerograms. (continued)

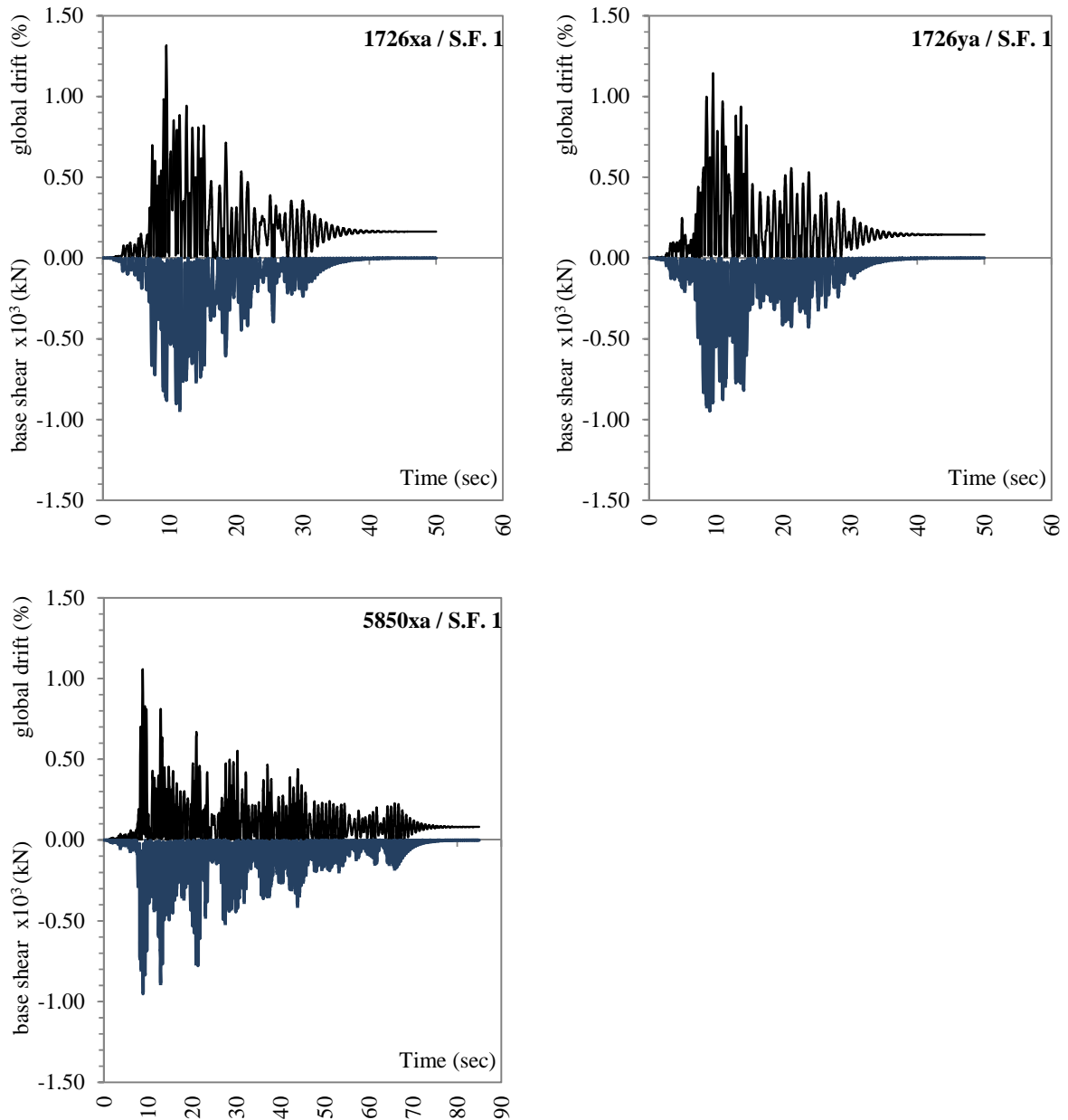


Figure 9-18: Roof displacement and base shear time history for the seven accelerograms.

Accelerograms	290xa	293ya	6142ya	612xa	1726xa	1726ya	5850xa
Maximum global drift	1.17%	1.19%	1.17%	1.01%	1.32%	1.14%	1.06%
Base shear (kN)	563.5	735.5	844.8	894.2	849.0	851.4	681.8
Time (sec)	5.89	48.59	12.91	27.90	9.53	9.56	8.78
Maximum Base shear (kN)	1008.9	976.0	1029.1	947.9	939.4	917.5	834.1
Global drift	0.51%	0.86%	0.98%	0.72%	0.86%	0.61%	0.84%
Time (sec)	6.95	50.39	14.30	29.29	11.55	9.06	8.89

Table 9-4: Peak values for the base shear and the global drift.

Inter-storey drifts

On the other hand, it is interesting to notice that the maximum values of the drift angle are corresponding to the inter-storey drifts and not to the global drift. Table 9-5 presents the maximum values that are recorded during the analyses and the corresponding maximum global value. It is observed that the peak values are obtained for the first, second or the third level. Figure 9-19 presents the envelope results concerning the inter-storey drifts taking into account the results of the entire dynamic analyses. Finally, it is noted that the peak value is recorded at the second level and is equal to 0.0161rad.

accelerogram	1 st level	2 nd level	3 rd level	4 th level	global
290xa	1.08%	1.43%	1.41%	1.23%	1.17%
293ya	1.04%	1.42%	1.46%	1.19%	1.19%
6142ya	1.42%	1.38%	1.35%	1.16%	1.17%
612xa	0.98%	1.26%	1.08%	0.75%	1.01%
1726xa	1.22%	1.61%	1.47%	1.03%	1.32%
1726ya	1.05%	1.38%	1.27%	0.92%	1.14%
5850xa	0.92%	1.18%	1.36%	1.24%	1.06%

Table 9-5: The maximum recorded values for the inter-storey drifts and the global drift.

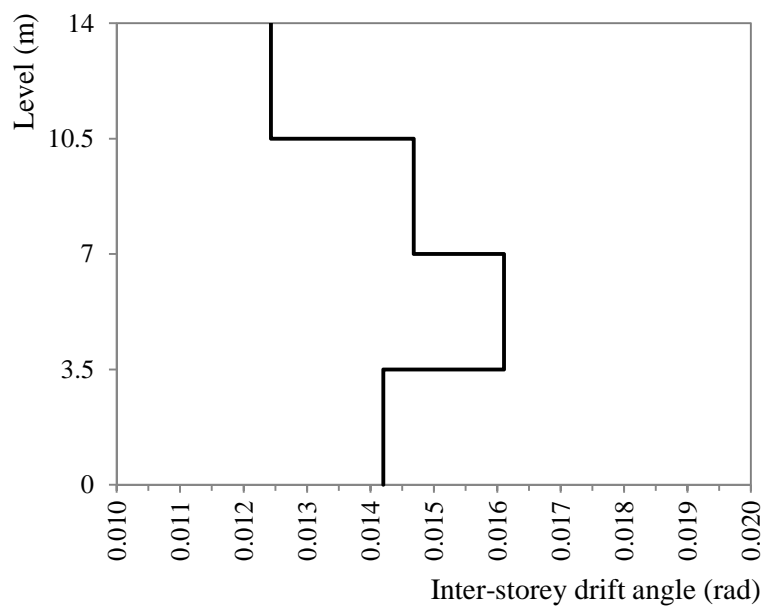


Figure 9-19: Envelope results in terms of inter-storey drift angle for the seven accelerograms.

Plastic hinge mechanism

The results of the dynamic analyses do not directly indicate the plastic hinge mechanism of the structural system. Figure 9-20 illustrates the field of the equivalent plastic strain at the end of the corresponding analysis. The distribution of the equivalent plastic strain along the cross-section should be studied in order to reveal if the plastic hinge has been formed. In general, it can be observed that the plastic hinges are formed or more correctly tend to be formed at the ends of the beams and not at the columns. Exception to the previous is the basis of the structural system. This indicates that the structure follows the capacity rules concerning the seismic design. Furthermore, the allocation of the plastic hinges is different and this depends on the time-history acceleration record that is used. In Figure 9-21 the equivalent plastic strain variation in the cross sections of the beams of the first level are depicted. The notation of beams is depicted in Figure 9-5. It is clear that the plastic hinges are well formed and this is valid for all the analyses and in all the cross-sections that are considered. The distribution along the cross-section is symmetric and this indicates that the effect of the axial forces is negligible. The values of the equivalent plastic strain depend on the accelerogram that is used in order to represent the earthquake excitation. The peak values are recorded in the case of 6142ya time-history acceleration record in the cross-sections.

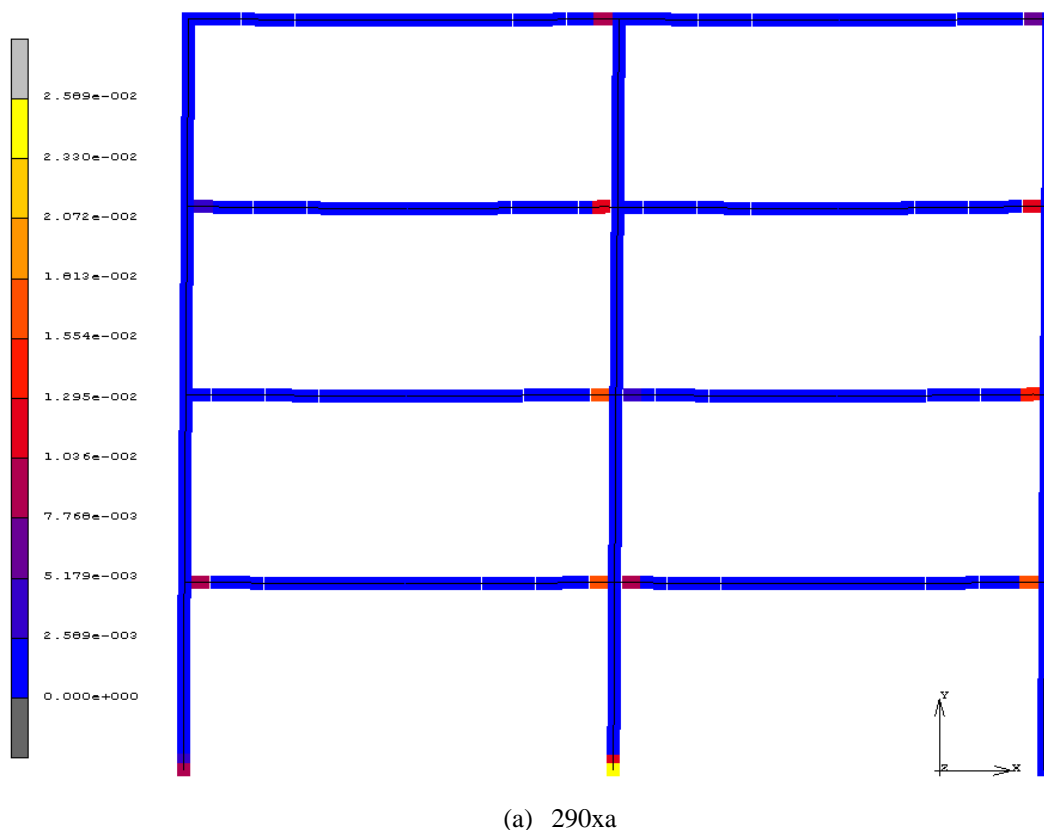
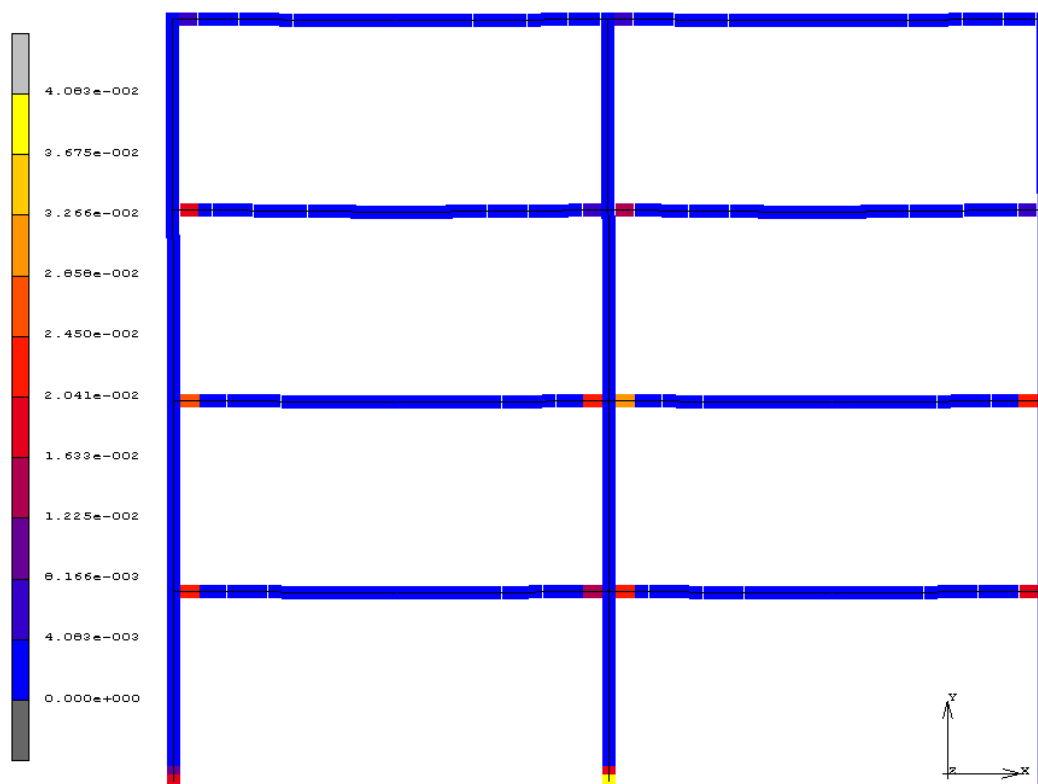
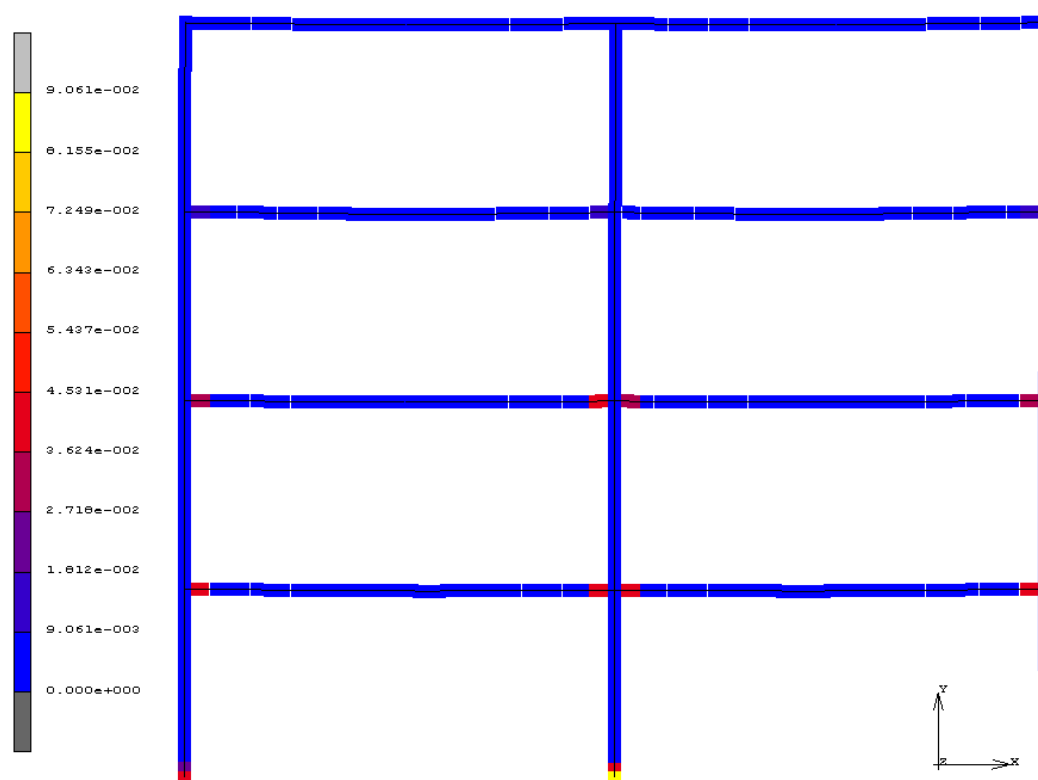


Figure 9 20: Equivalent plastic strain (layer 1) for the different time-history acceleration records
(Visualization S.F. 2). (continued)

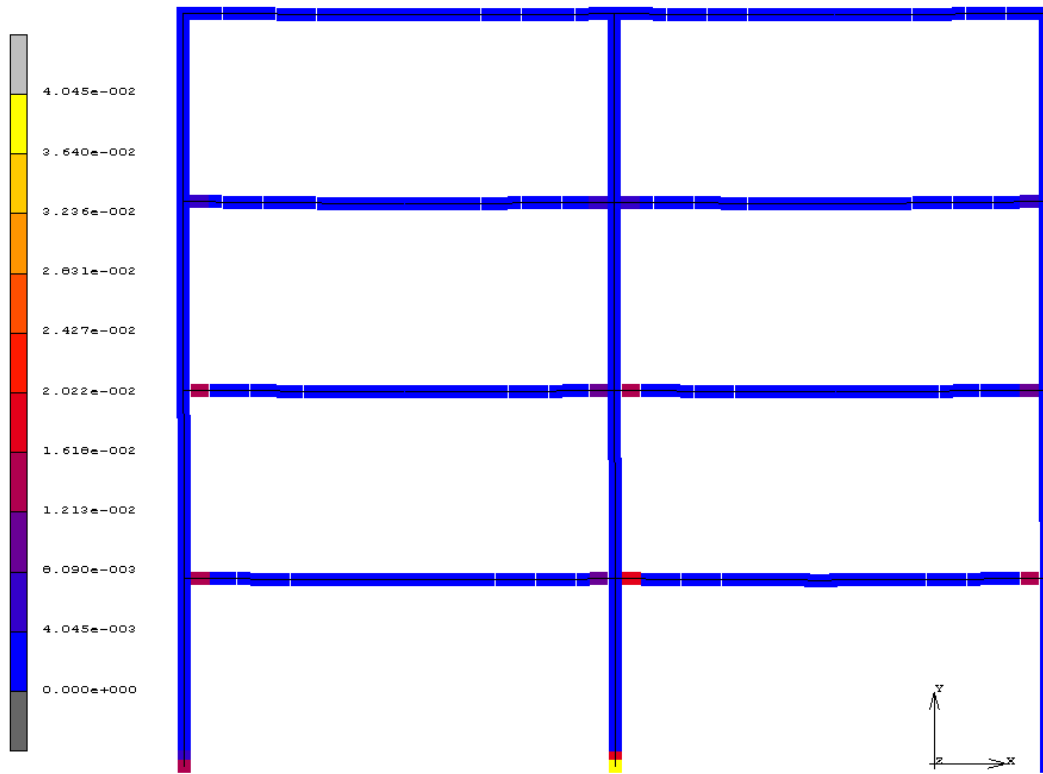


(b) 293ya

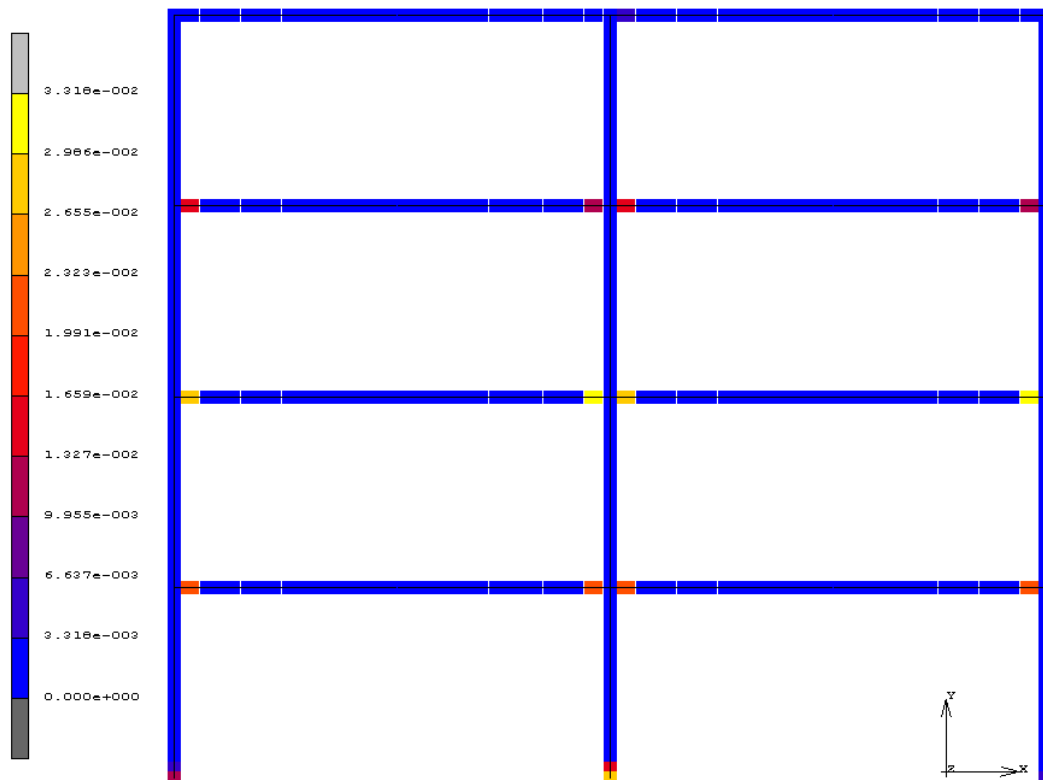


(c) 6142ya

Figure 9 20: Equivalent plastic strain (layer 1) for the different time-history acceleration records (Visualization S.F. 2). (continued)

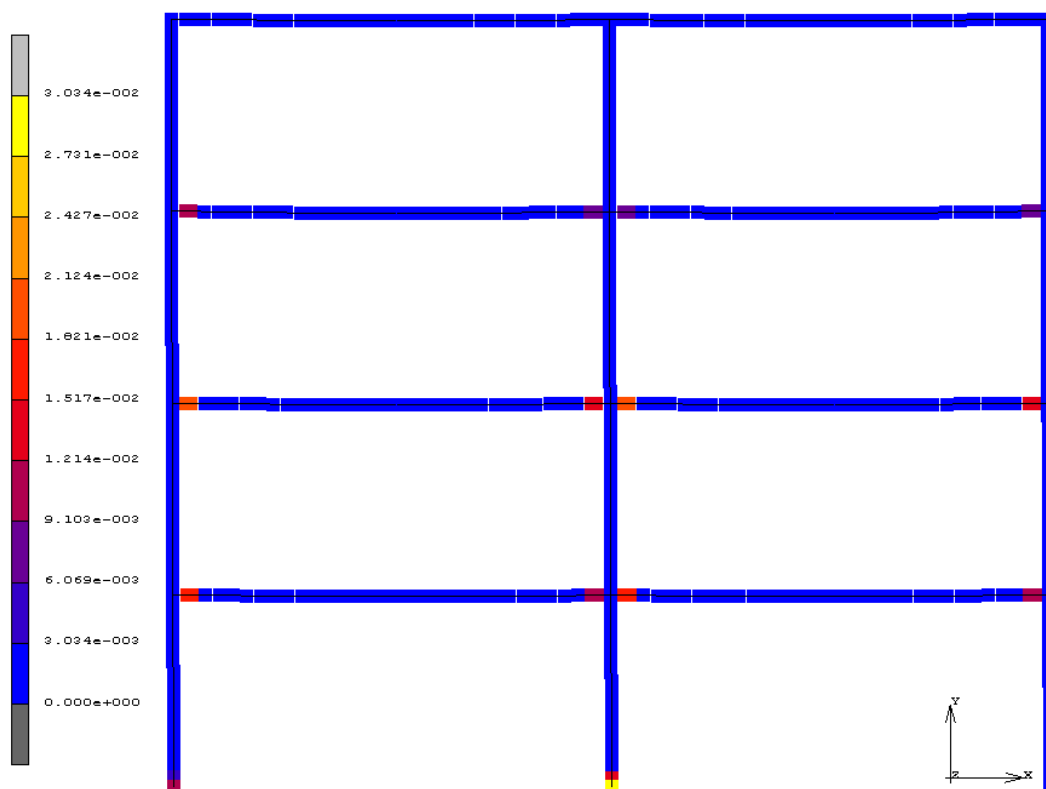


(d) 612xa

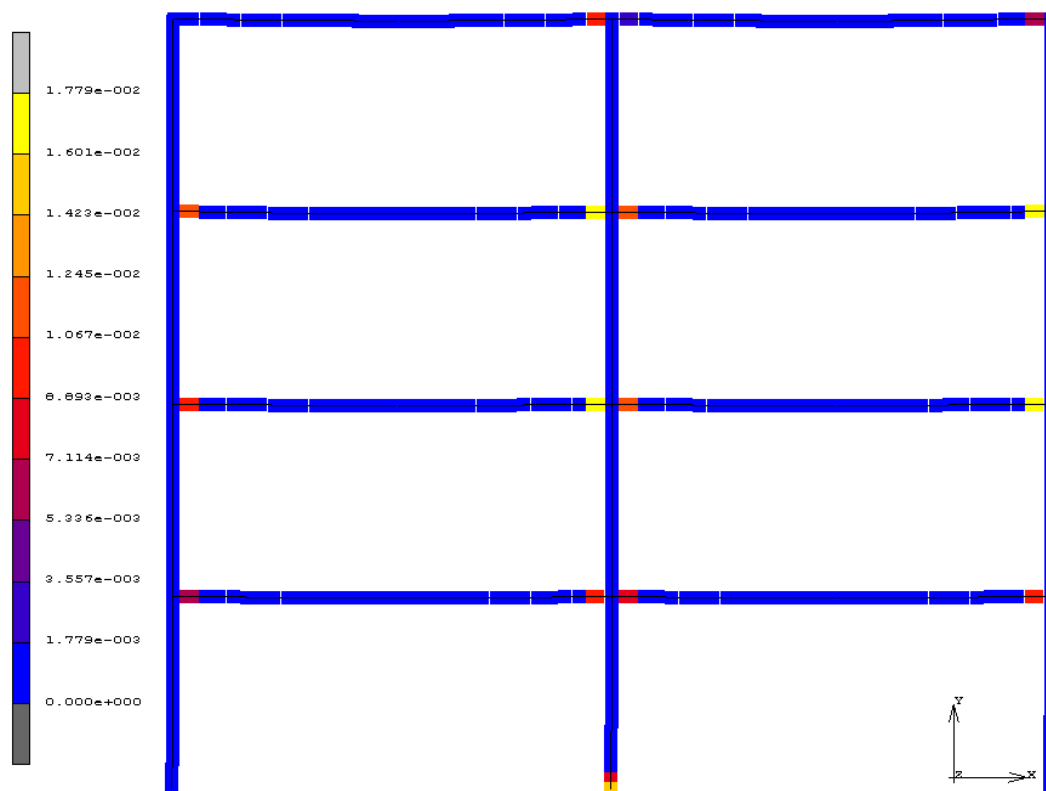


(e) 1726xa

Figure 9 20: Equivalent plastic strain (layer 1) for the different time-history acceleration records (Visualization S.F. 2). (continued)



(f) 1726ya



(g) 5850xa

Figure 9-20: Equivalent plastic strain (layer 1) for the different time-history acceleration records (Visualization S.F. 2).

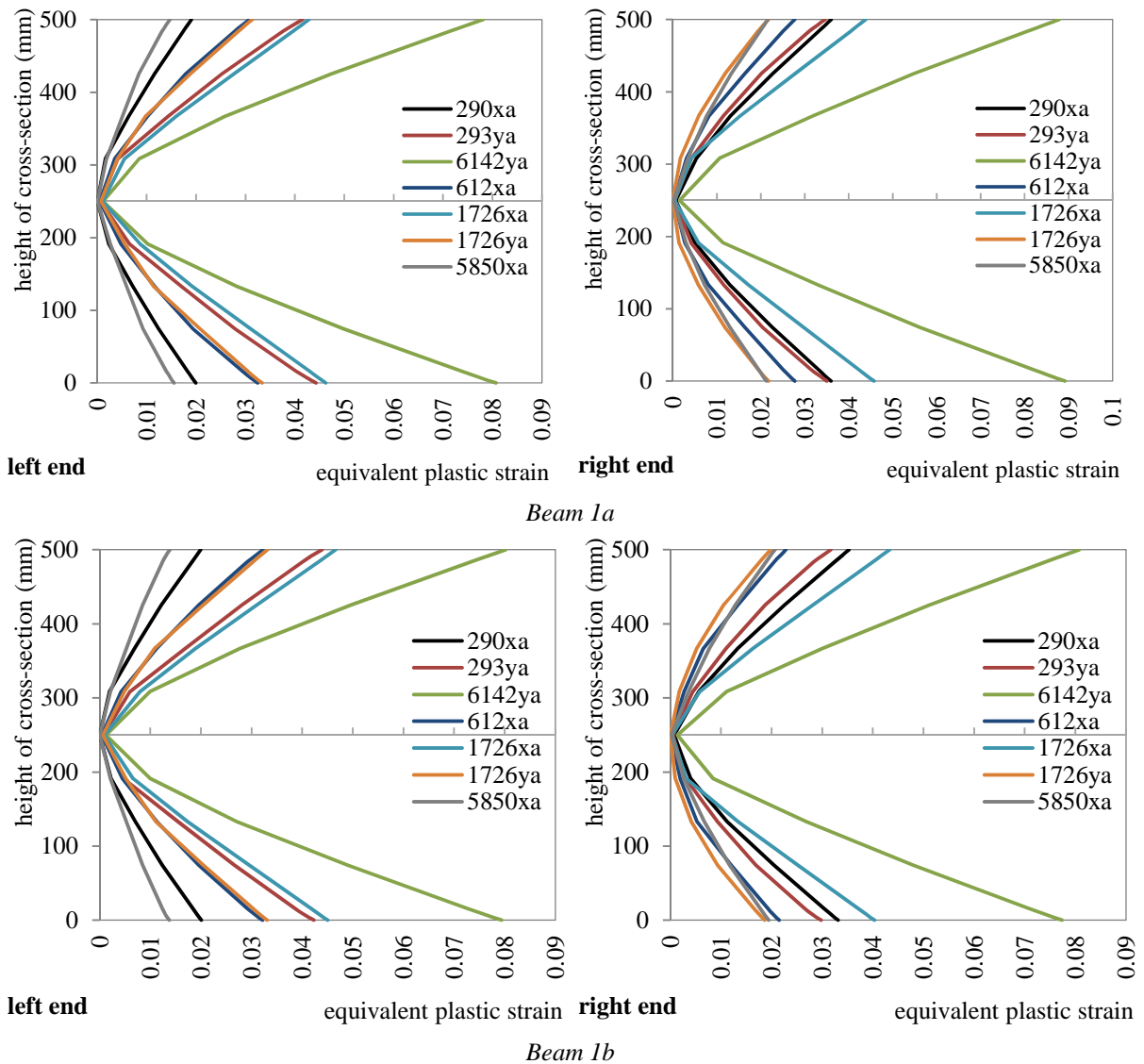


Figure 9-21: Equivalent plastic strain distribution at the ends of the beams at the first level of the structural system.

Residual drifts

Finally, the residual drifts at the end of the earthquake excitation are given in Table 9-6. The values that are presented correspond to the maximum value between the global and the inter-storey drifts. The peak value corresponds to the analysis where the 290xa time-history acceleration record is used.

Accelerograms	290xa	293ya	6142ya	612xa	1726xa	1726ya	5850xa
Maximum residual drift	0.39%	0.24%	0.22%	0.09%	0.10%	0.25%	0.15%

Table 9-6: Peak values for the residual drifts.

At this point it is noted that the numerical model, which is developed in this, can predict two basic failure modes. The first one is the failure through possible elastic or plastic buckling of the structural members. Alternatively, the failure can be provided if an unstable global or local mechanism takes place due to the formulation of plastic hinges.

The possible type of failure that can be developed due to local buckling or due to extensive strains is not included in the model. In order to encounter this issue, the plastic strain field is studied in detail and possible extreme values will be excluded from the results. In general, considering the results of the dynamic analyses for the seven accelerograms compatible to the elastic spectrum of EN 1998-1-1, it can be concluded that the structural system follows the principles of the design for the seismic actions.

9.6 Incremental Dynamic Analysis (IDA)

The next step of the study is the evaluation of the earthquake response of the structure through Incremental Dynamic Analysis. IDA is a parametric analysis method for the estimation of the structural performance under seismic loads (Vamvatsikos and Cornell, 2002). Specifically, the structure is subjected to one (or more) ground motion records, each scaled to multiple levels of intensity. In this way the behaviour of the structure can be represented through response curves parameterized versus intensity level. Initially, two issues must be addressed in order to proceed to the IDA analysis. The first one is the definition of the quantity that characterizes the intensity of the ground motion. The second is to determine a response quantity for the classification of the structural behaviour. In the literature several quantities are proposed to characterize the intensity of the ground motion such as the Peak Ground acceleration (PGA), Peak Ground Velocity, the 5% damped Spectral Acceleration that corresponds to the structures first mode period, the normalized factor $R = \frac{\lambda}{\lambda_{yield}}$ etc. In this study the intensity of the ground motion record is represented

through the PGA. On the other hand the response of the structural system is represented through both the base shear and the maximum drift angle. It is noticed that the aforementioned response quantity is the maximum between the peak inter-storey drift and the global drift angles.

9.6.1 Definition of the scaled seismic loading

The seven accelerograms that are presented in section 9.3.2 are scaled with respect to the PGA using the factors that are defined in Table 9-7. Due to the fact that the accelerograms are pre-scaled in order to match the elastic spectrum, the PGA is the same for all the ground motion records. In this way, the PGA that results after the scaling that is presented in this section remains the same for all the earthquake records that are considered in this study. As the scale factor increases the time-history acceleration records represent more severe ground motions and the return period is higher.

Scale Factor (S.F.)	1.25	1.50	1.75	2.00
PGA	0.608g m/sec ²	0.729g m/sec ²	0.851g m/sec ²	0.972g m/sec ²



Lower probability of existence – More severe earthquakes

Table 9-7: Scaling of the seismic action.

Totally, 28 (7 accelerograms x 4 S.F.) non-linear dynamic analyses are conducted taking into account the scaled accelerograms.

9.6.2 Evaluation of the structural behaviour for different seismic levels

The response of the structural system for the scaled time-history acceleration records is evaluated in the following sections.

Base shear versus roof - global drift

The results of the non-linear dynamic analyses are presented in terms of the absolute values of base shear versus global drift time history in Figure 9-22 to Figure 9-28 for the seven different accelerograms. The base shear is depicted at the negative of the vertical axis only for the better visualization of the results. Thus, the negative values do not have any physical meaning. Moreover, the results are tabulated in Table 9-9 to Table 9-14. Specifically, every table corresponds to a specific accelerogram and summarizes the peak values of the global drift angle (the corresponding base shear and the time at which is recorded) and the maximum values of the base shear (and the corresponding time) during the analyses for the different scale factors.

As it is expected, as the S.F. increases the global drift that is recorded during the analyses is non-linearly increased. It is interesting to observe the evolution of base shear that correspond to the peak values of the global drift as the S.F. increases. It is noticed that as the S.F. increases ($1 \leq S.F. \leq 1.75$) the base shear that corresponds to the peak global drift is increased. Moreover, the peak values of the base shear are increased as the seismic action becomes more severe. Additionally, it can be observed that the peak values of the base shear are not recorded at the same time with the peak global drift. This holds for all the accelerograms. As the S.F. increases the time interval between the peak values of base shear and the global drift is enlarged.

Table 9-15 presents the average values for the peak roof displacement (or global drift) and the corresponding base shear (or pseudo-acceleration) for the S.F. that are considered in this study.

Accelerogram: 290xa

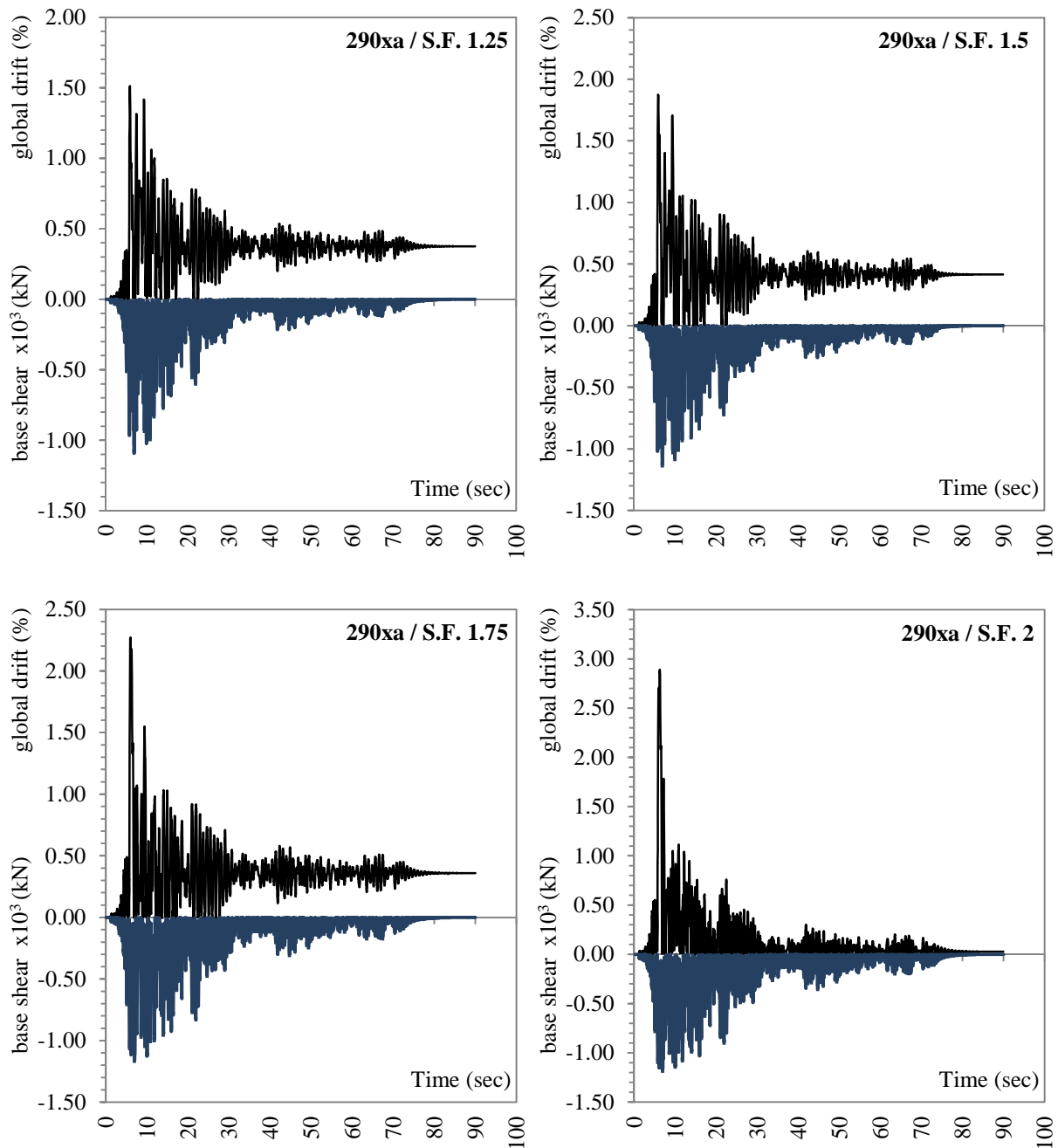


Figure 9-22: Base shear and roof displacement time history for the accelerogram 290xa and for various S.F.

	S.F. 1.00	S.F. 1.25	S.F. 1.50	S.F. 1.75	S.F. 2.00
Maximum global drift	1.17%	1.51%	1.87%	2.27%	2.89%
Base shear (kN)	563.51	606.47	-613.67	784.91	639.54
Time (sec)	5.89	5.90	5.92	5.95	6.24
Maximum Base shear (kN)	1008.90	1092.52	1134.43	1161.81	1181.38
Time (sec)	6.95	6.96	6.94	6.95	6.92

Table 9-8: Evolution of peak values for global drift and base shear as the SF increases (290xa).

Accelerogram: 293ya

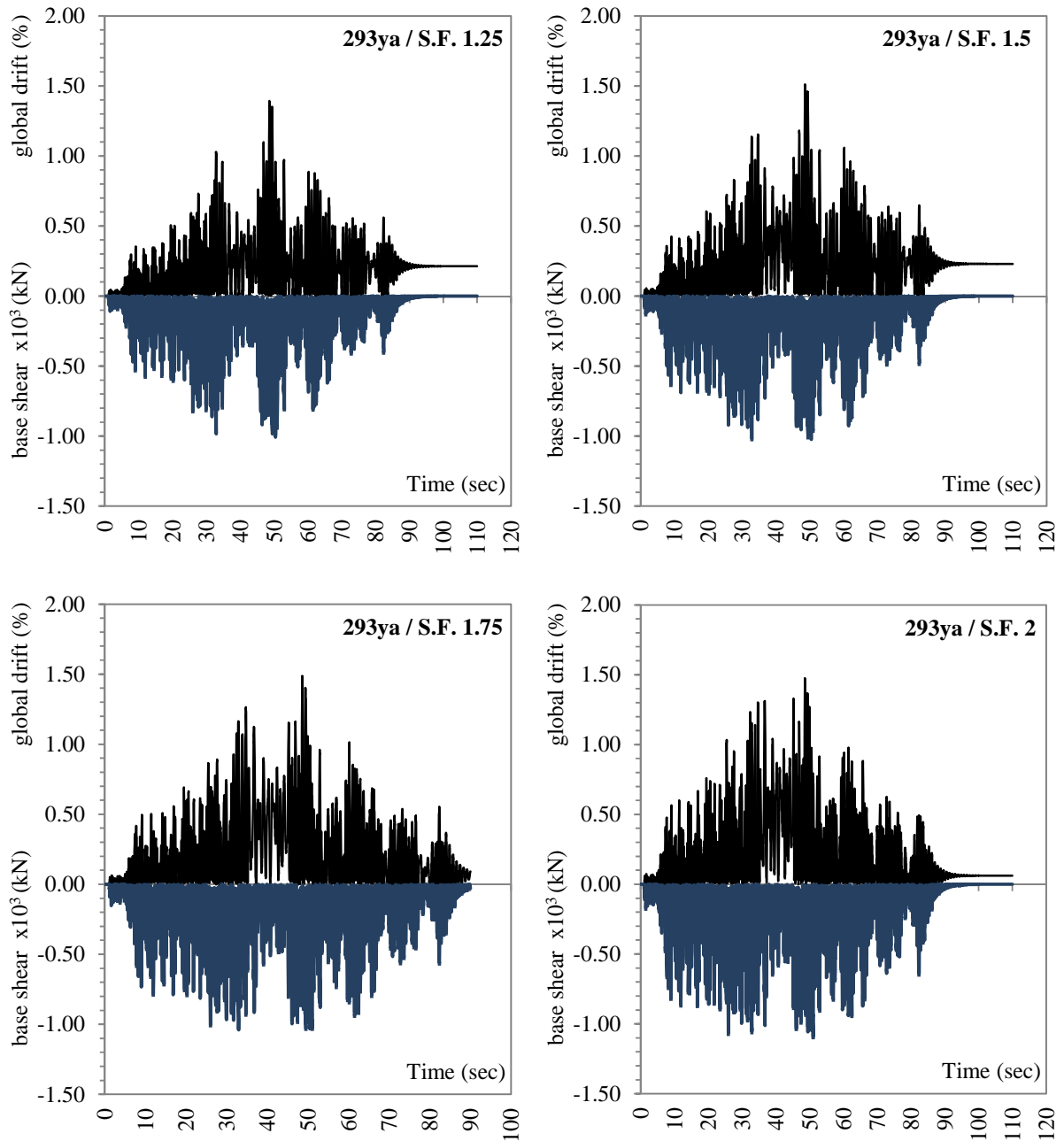


Figure 9-23: Base shear and roof displacement time history for the accelerogram 293ya and for various S.F.

	S.F. 1.00	S.F. 1.25	S.F. 1.50	S.F. 1.75	S.F. 2.00
Maximum global drift	1.19%	1.39%	1.51%	1.49%	1.48%
Base shear (kN)	735.46	732.07	705.34	686.82	699.89
Time (sec)	48.59	48.60	48.60	48.60	48.61
Maximum Base shear (kN)	976.03	1007.51	1024.20	1038.64	1094.66
Time (sec)	50.39	50.43	50.45	32.91	51.05

Table 9-9: Evolution of peak values for global drift and base shear as the SF increases (293ya).

Accelerogram: 6142ya

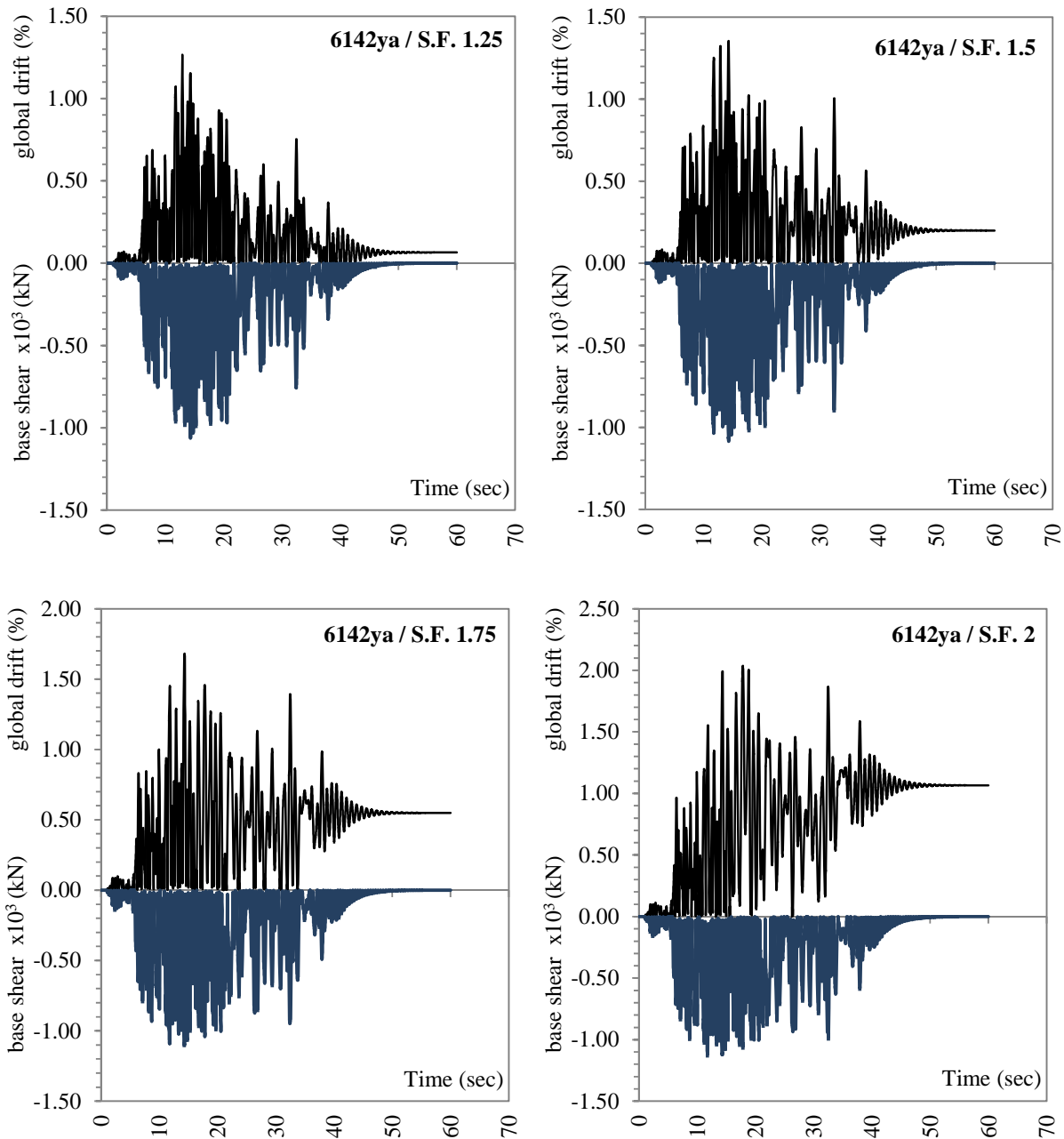


Figure 9-24: Base shear and roof displacement time history for the accelerogram 6142ya and for various S.F.

	S.F. 1.00	S.F. 1.25	S.F. 1.50	S.F. 1.75	S.F. 2.00
Maximum global drift	1.17%	1.26%	1.35%	1.68%	2.04%
Base shear (kN)	844.76	857.02	1075.02	1048.64	1060.18
Time (sec)	12.91	12.90	14.31	14.34	17.84
Maximum Base shear (kN)	1029.14	1061.93	1085.07	1101.00	1126.96
Time (sec)	14.30	14.31	14.32	14.32	11.77

Table 9-10: Evolution of peak values for global drift and base shear as the SF increases (6142ya).

Accelerogram: 612xa

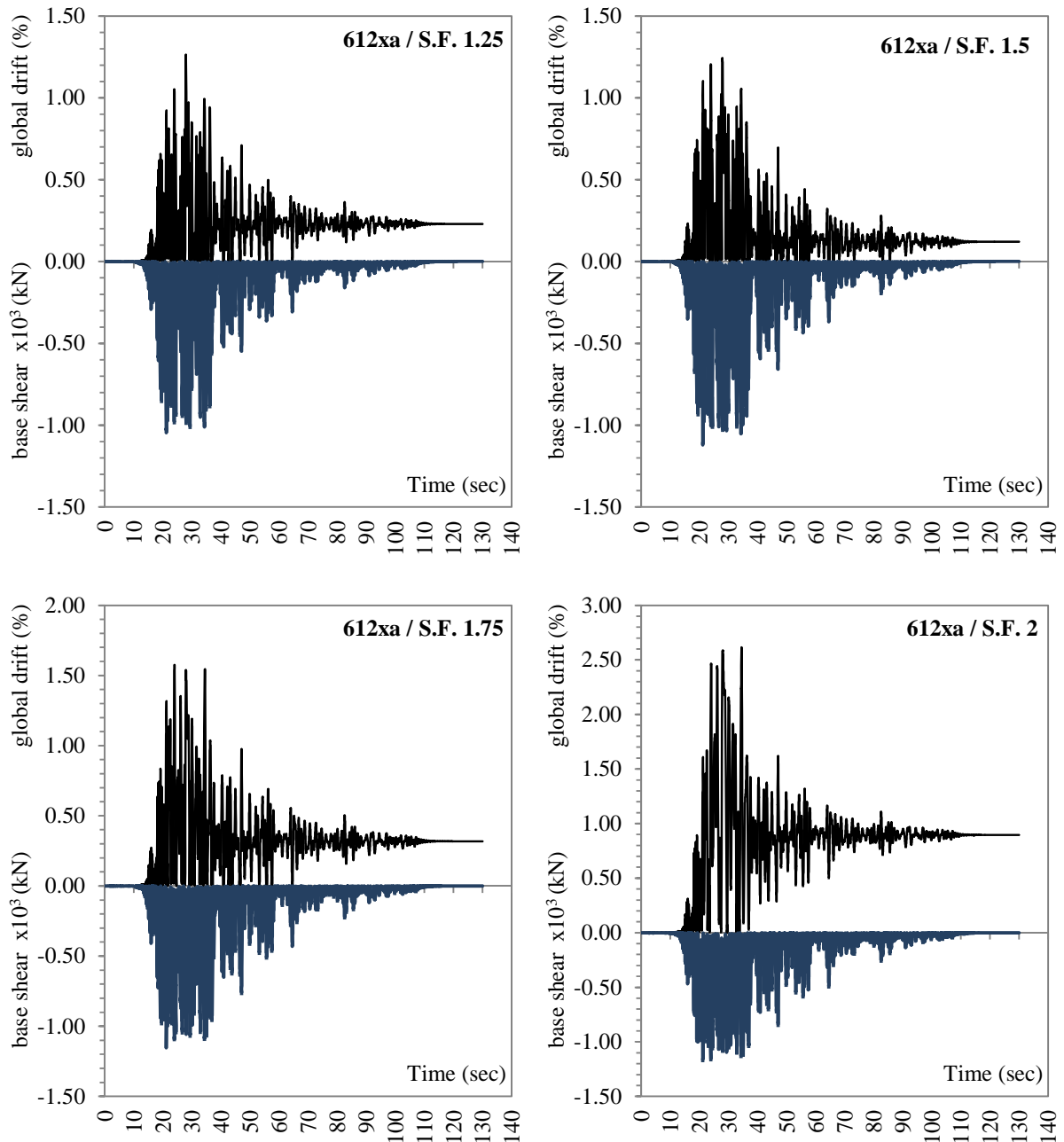


Figure 9-25: Base shear and roof displacement time history for the accelerogram 612xa and for various S.F.

	S.F. 1.00	S.F. 1.25	S.F. 1.50	S.F. 1.75	S.F. 2.00
Maximum global drift	1.01%	1.26%	1.24%	1.57%	2.62%
Base shear (kN)	894.16	902.59	919.10	856.95	777.15
Time (sec)	27.90	27.91	27.92	23.99	34.49
Maximum Base shear (kN)	972.47	1045.11	1119.96	1153.93	1166.19
Time (sec)	29.29	21.18	21.17	21.17	21.17

Table 9-11: Evolution of peak values for global drift and base shear as the SF increases (612xa).

Accelerogram: 1726xa

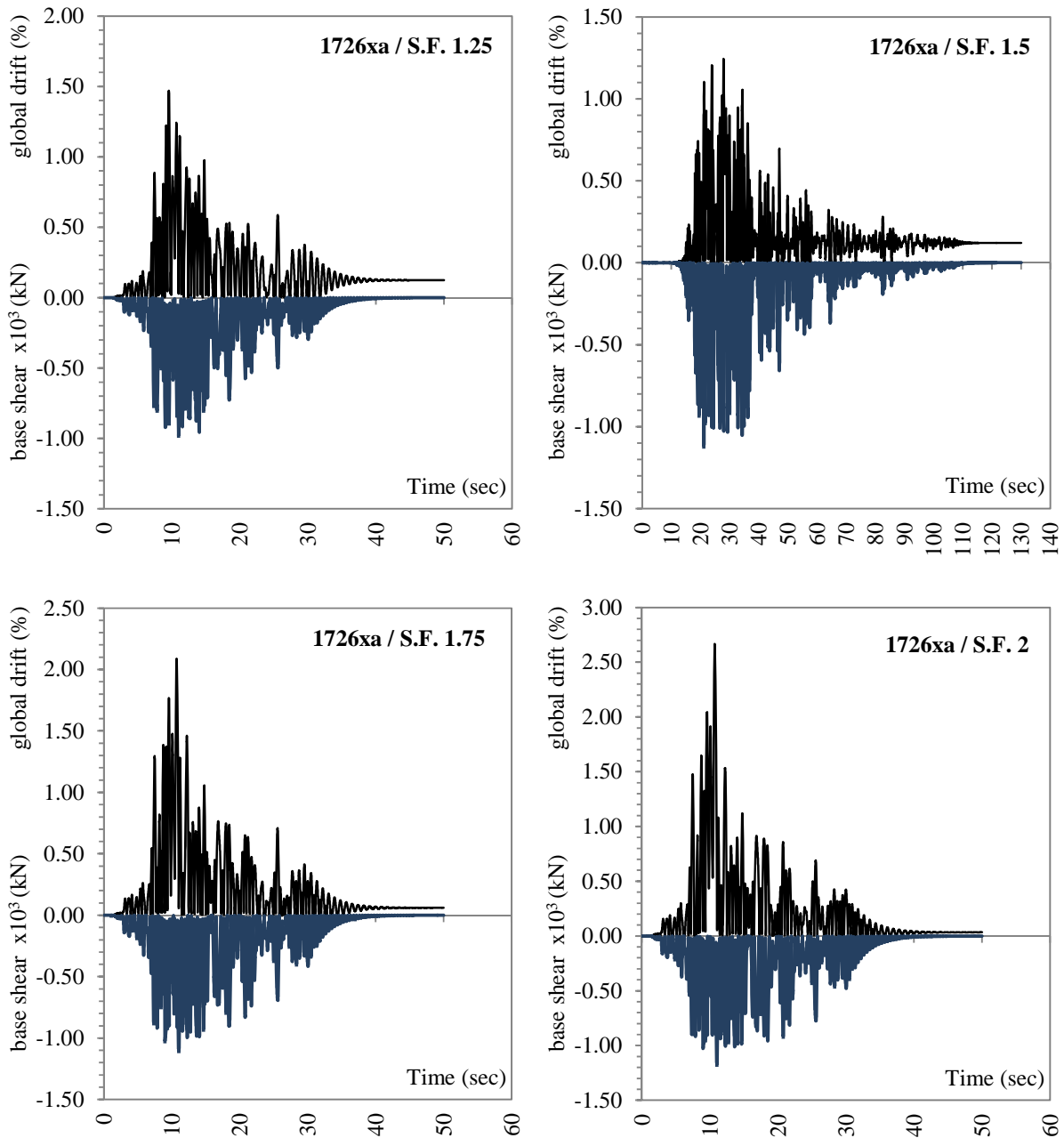


Figure 9-26: Base shear and roof displacement time history for the accelerogram 1726xa and for various S.F.

	S.F. 1.00	S.F. 1.25	S.F. 1.50	S.F. 1.75	S.F. 2.00
Maximum global drift	1.32%	1.47%	1.61%	2.09%	2.67%
Base shear (kN)	848.97	847.69	777.75	747.86	691.02
Time (sec)	9.53	9.55	10.68	10.69	10.71
Maximum Base shear (kN)	939.41	979.01	1027.12	1103.03	1172.97
Time (sec)	11.55	10.98	11.00	11.01	11.02

Table 9-12: Evolution of peak values for global drift and base shear as the SF increases (1726xa).

Accelerogram: 1726ya

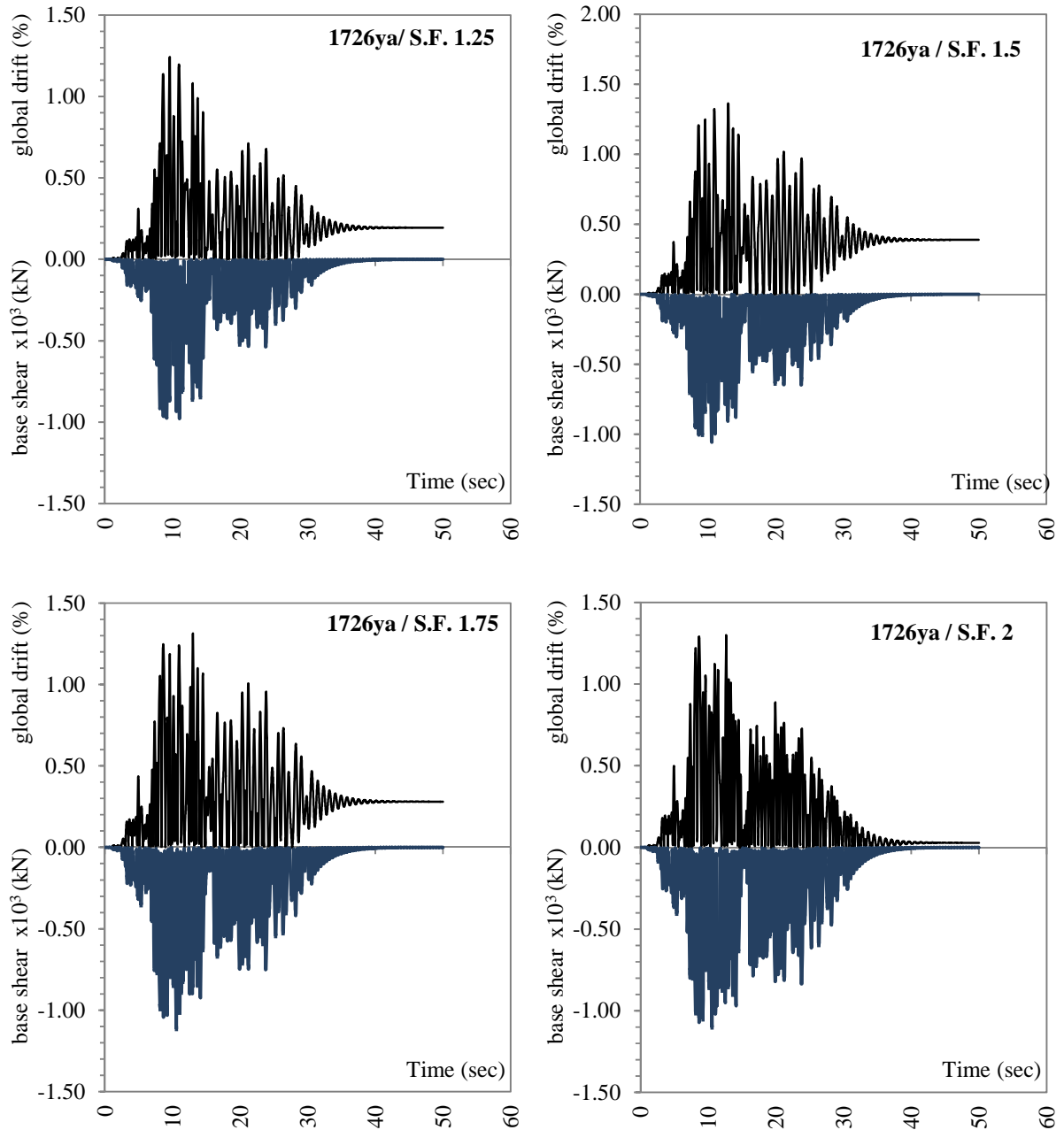


Figure 9-27: Base shear and roof displacement time history for the accelerogram 1726ya and for various S.F.

	S.F. 1.00	S.F. 1.25	S.F. 1.50	S.F. 1.75	S.F. 2.00
Maximum global drift	1.14%	1.24%	1.36%	1.31%	1.30%
Base shear (kN)	851.39	870.17	852.98	852.29	-631.11
Time (sec)	9.56	9.57	13.00	13.01	12.65
Maximum Base shear (kN)	946.59	978.44	1057.00	1114.32	1101.77
Time (sec)	9.06	11.02	10.55	10.57	10.56

Table 9-13: Evolution of peak values for global drift and base shear as the SF increases (1726ya).

Accelerogram: 5850xa

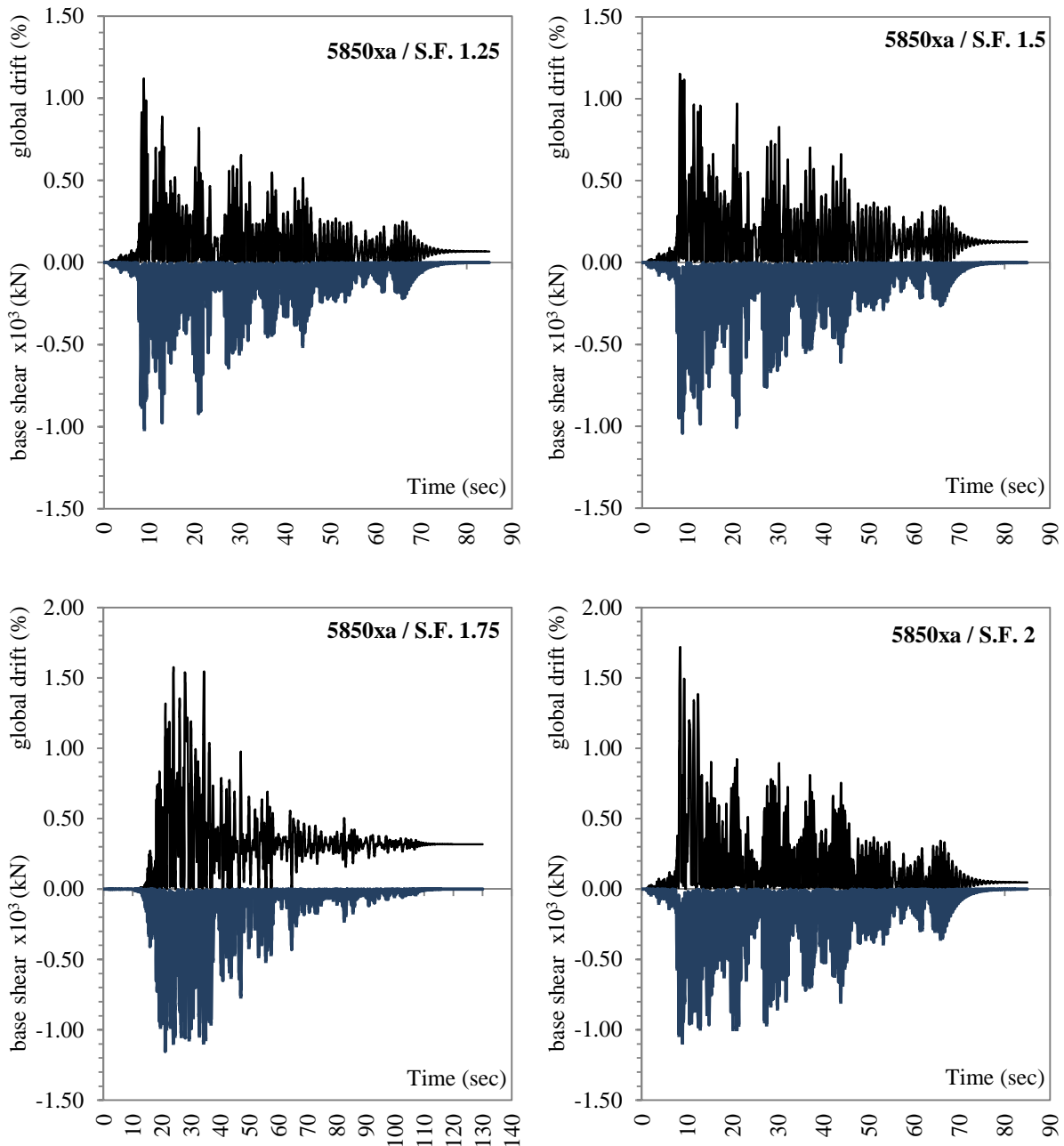


Figure 9-28: Base shear and roof displacement time history for the accelerogram 5850xa and for various S.F.

	S.F. 1.00	S.F. 1.25	S.F. 1.50	S.F. 1.75	S.F. 2.00
Maximum global drift	1.06%	1.12%	1.15%	1.42%	1.72%
Base shear (kN)	681.80	746.99	869.67	895.59	888.03
Time (sec)	8.78	8.79	8.36	8.38	8.43
Maximum Base shear (kN)	950.10	1014.08	1041.63	1063.69	1089.26
Time (sec)	8.89	8.91	8.93	8.95	8.95

Table 9-14: Evolution of peak values for global drift and base shear as the SF increases (5850xa).

S.F.	Average roof displacement (m)	Average drift angle (rad)	Average- Corresponding base shear (kN)	Pseudo-acceleration (m/sec ²)
1.00	0.161	0.0115	774.29	0.339
1.25	0.185	0.0132	794.71	0.347
1.50	0.202	0.0144	830.50	0.363
1.75	0.237	0.0169	839.01	0.367
2.00	0.294	0.021	769.56	0.337

Table 9-15: Average values for the global drift (or roof displacement) and the corresponding shear (or pseudo-acceleration).

Inter-storey drifts

Figure 9-29 presents the distribution of the inter-storey and global drift angles along the height of the frame for all the accelerograms. The maximum values that are recorded during the analyses are used. It can be observed that in most cases the pattern of the inter-storey drift angles depends on the accelerogram that is used for the non-linear dynamic analysis and changes as the S.F. increases. In the analyses where the accelerograms 290xa, 612xa and 1726ya are used in order to represent the seismic action, the critical level is the second one for low values of the S.F. As the intensity of earthquake is scaled-up, the maximum inter-storey drift angles take place at the first level. The same phenomenon is observed for the accelerograms 1726xa and 5850xa where the critical level changes from 2nd to 3rd and from 3rd to 2nd respectively as the earthquake loading is increased. Regarding the time-history acceleration records 293ya and 6142ya, the critical level is the first and the second respectively for the entire range of S.Fs. The envelope of the maximum inter-storey drift angles and the average values with respect to the accelerogram that is used are illustrated in Figure 9-30 and they are tabulated in Table 9-16. Comparing the patterns of the envelope results with the average values with respect to the S.F., it is clear that the critical level is the second for S.F. ≤1.75. Only in the case of the maximum S.F. the first level becomes the critical. Finally it should be noticed that the values of the global drifts are lower comparing with the inter-storey drifts. This holds for the accelerograms that are studied and for all the range of the scale factors that are considered.

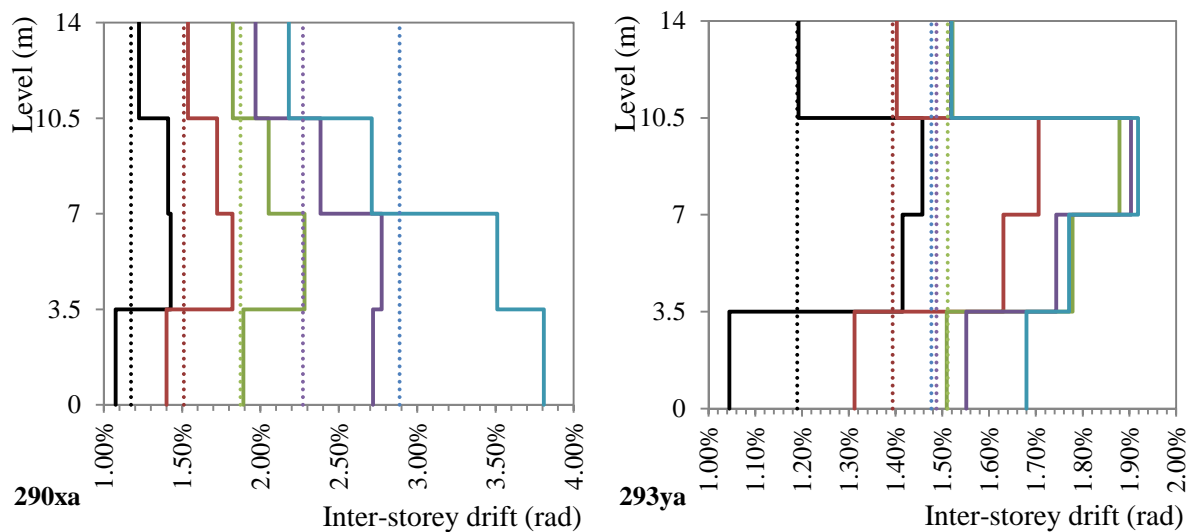


Figure 9 29: Inter-storey and global drift angle along the height of the frame. (continued)

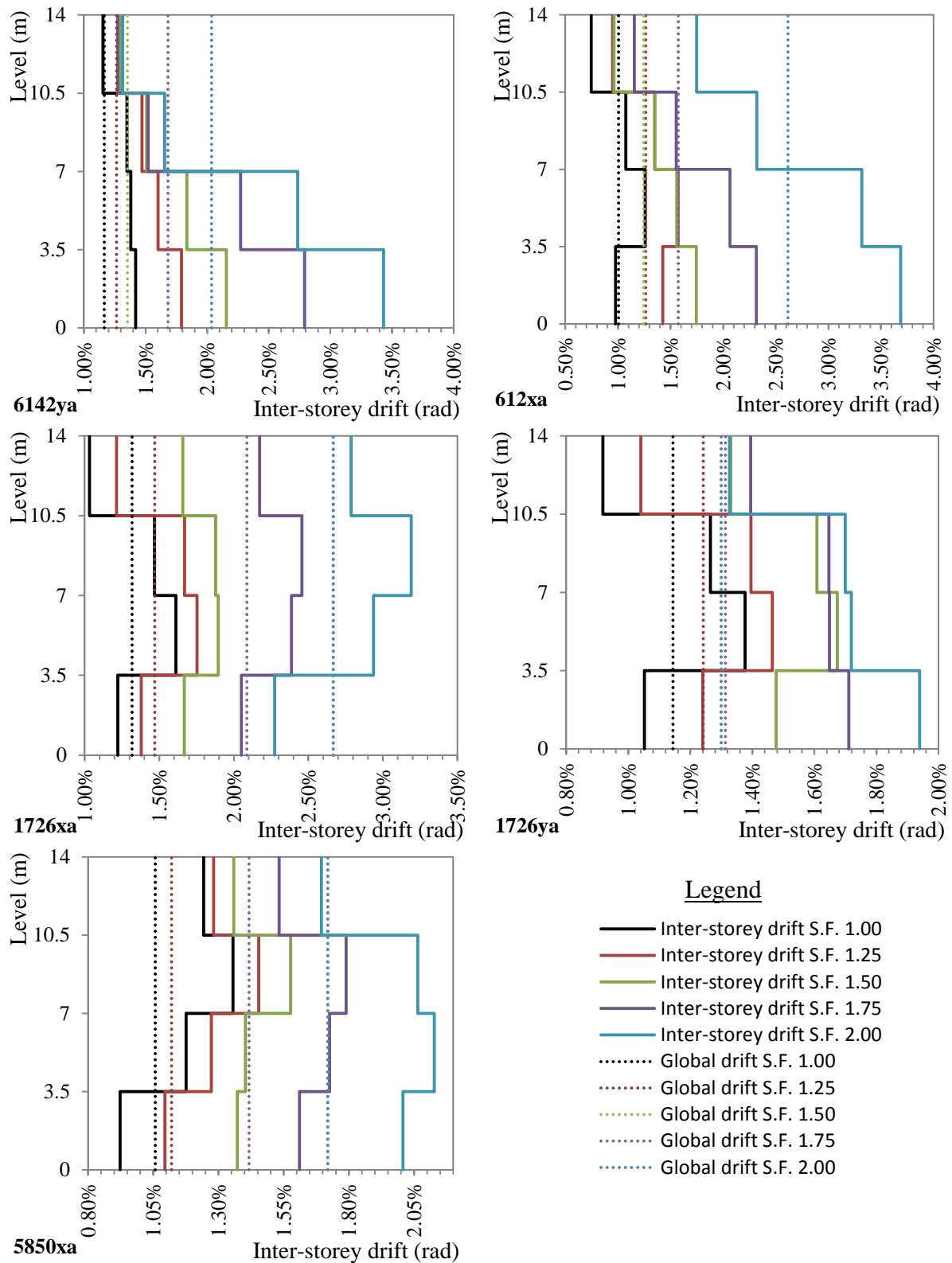


Figure 9-29: Inter-storey and global drift angle along the height of the frame.

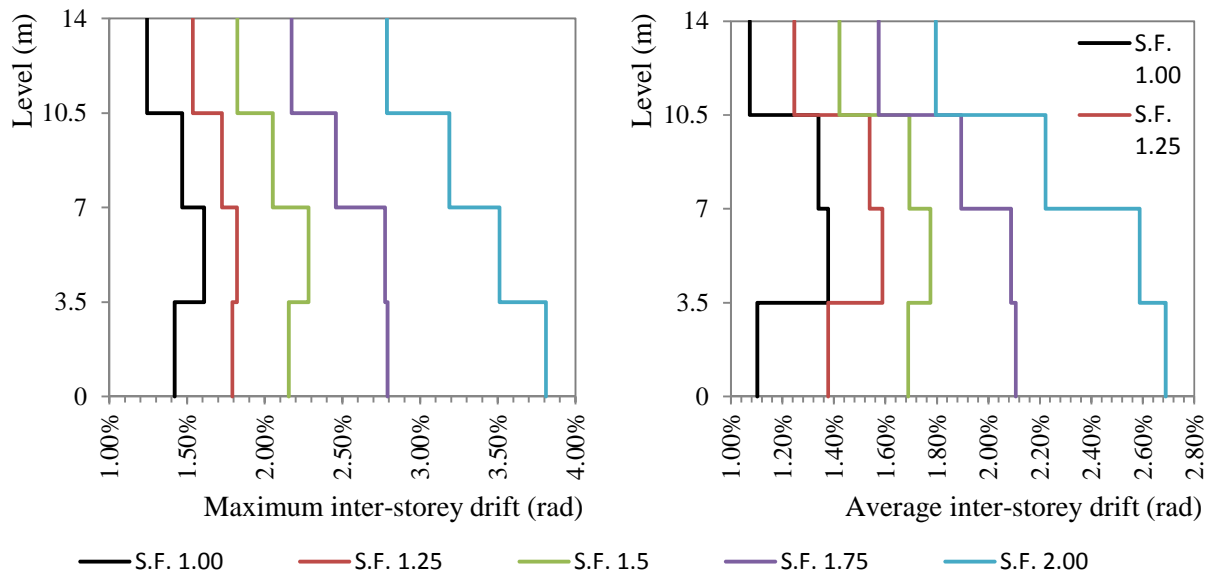


Figure 9-30: Maximum and average values of the inter-storey drift angles.

	S.F.	1 st level	2 nd level	3 rd level	4 th level
Average values	1.00	1.10%	1.38%	1.34%	1.07%
	1.25	1.38%	1.59%	1.54%	1.25%
	1.50	1.69%	1.78%	1.69%	1.42%
	1.75	2.11%	2.09%	1.89%	1.57%
	2.00	2.69%	2.59%	2.22%	1.80%
Peak values	1.00	1.42%	1.61%	1.47%	1.24%
	1.25	1.79%	1.82%	1.72%	1.54%
	1.50	2.16%	2.28%	2.05%	1.82%
	1.75	2.79%	2.77%	2.46%	2.17%
	2.00	3.81%	3.51%	3.19%	2.79%

Table 9-16: Tabulated data for the maximum and the average drift angles.

Plastic hinge mechanism

The plastic hinge mechanism of the structural system at the end of the seismic loading for the increasing levels of the earthquake intensity are presented in Figure 9-31, Figure 9-33, Figure 9-35, Figure 9-37, Figure 9-39, Figure 9-41 and Figure 9-43 for the accelerograms 290xa, 293ya, 6142ya, 612xa, 1726xa, 1726ya and 5850xa respectively. Specifically, the figure presents the values of the equivalent plastic strain for the layer of the cross section. Despite the fact that this values do not specify if the plastic hinge is “fully” formed, a good approximation can be obtained depending on the values of the upper layer. For values of equivalent plastic strain greater that 0.01 (grey color), the plastic hinge is fully developed. The other values indicate the potential for the plastic hinge formulation. It is observed that the plastic hinges are formed at the ends of the beams and at the basis of the structural system as long as the scale factor is less or equal to 1.75. For the maximum value of the S.F. plastic hinges sporadically appear also in the columns of the first and the second level. The behaviour of the structural system is similar for all the accelerograms that are studied.

The distribution of the equivalent plastic strain along the height of the cross-section at both the ends of the beams of the first level are depicted in Figure 9-32, Figure 9-34, Figure 9-36, Figure 9-38, Figure 9-40, Figure 9-42 and Figure 9-44 for all the accelerograms. The negative values are used only in order to distinguish the **R**ight and the **L**eft end of the beams and there is no physical meaning.

It is noticed that the plastic hinges are “fully” formed at the ends of both beams of the first level of the frame. Moreover, it is observed that the distribution of the equivalent plastic strain is almost symmetric with respect to the centroid axis of the cross-section and this is valid for all the range of the scaled earthquake levels. The amplitude of the equivalent plastic strain is considerably increased for $S.F. > 1.75$. For this reason the results for the S.F. 2 are not depicted in the corresponding diagrams and not further studied in Chapter 11 and Chapter 13.

Accelerogram: 290xa



Figure 9-31: Development of plastic hinge mechanism for S.F. 1.25, 1.50, 1.75 and 2.00 (290xa).

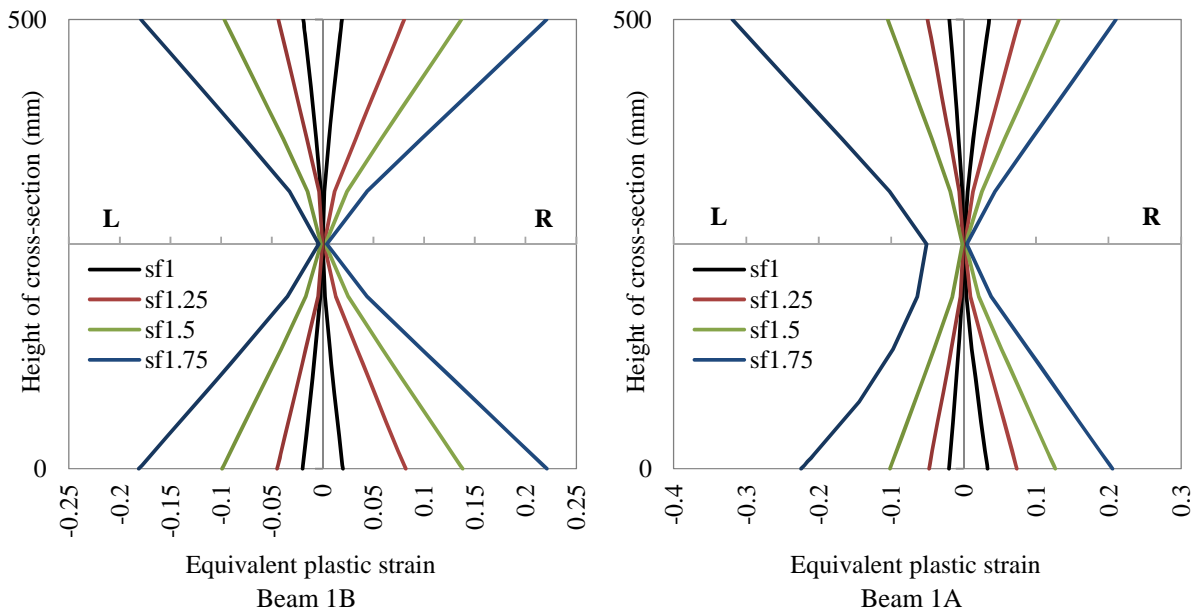


Figure 9-32: Equivalent plastic strain distribution at the 1st level for increasing S.F (290xa).

Accelerogram: 293ya

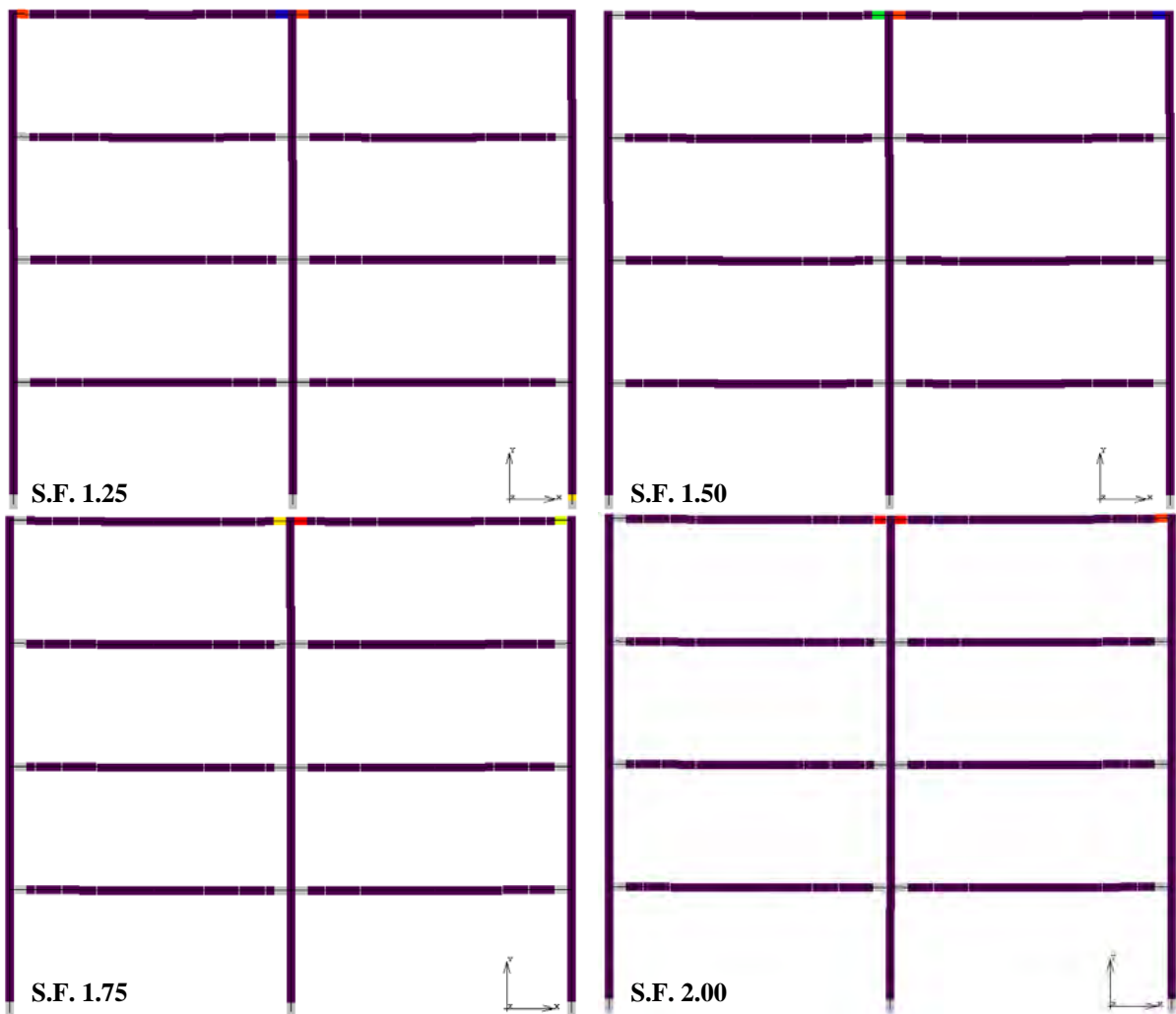


Figure 9-33: Development of plastic hinge mechanism for S.F. 1.25, 1.50, 1.75 and 2.00 (293ya).

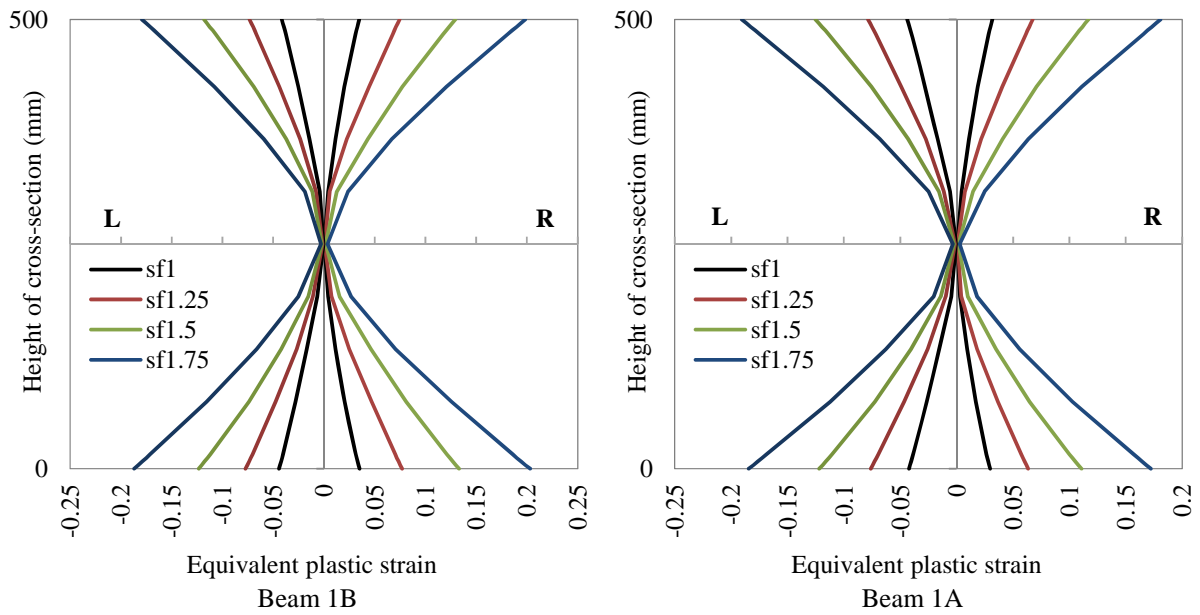


Figure 9-34: Equivalent plastic strain distribution at the 1st level for increasing S.F (293ya).

Accelerogram: 6142ya



Figure 9-35: Development of plastic hinge mechanism for S.F. 1.25, 1.50, 1.75 and 2.00 (6142ya).

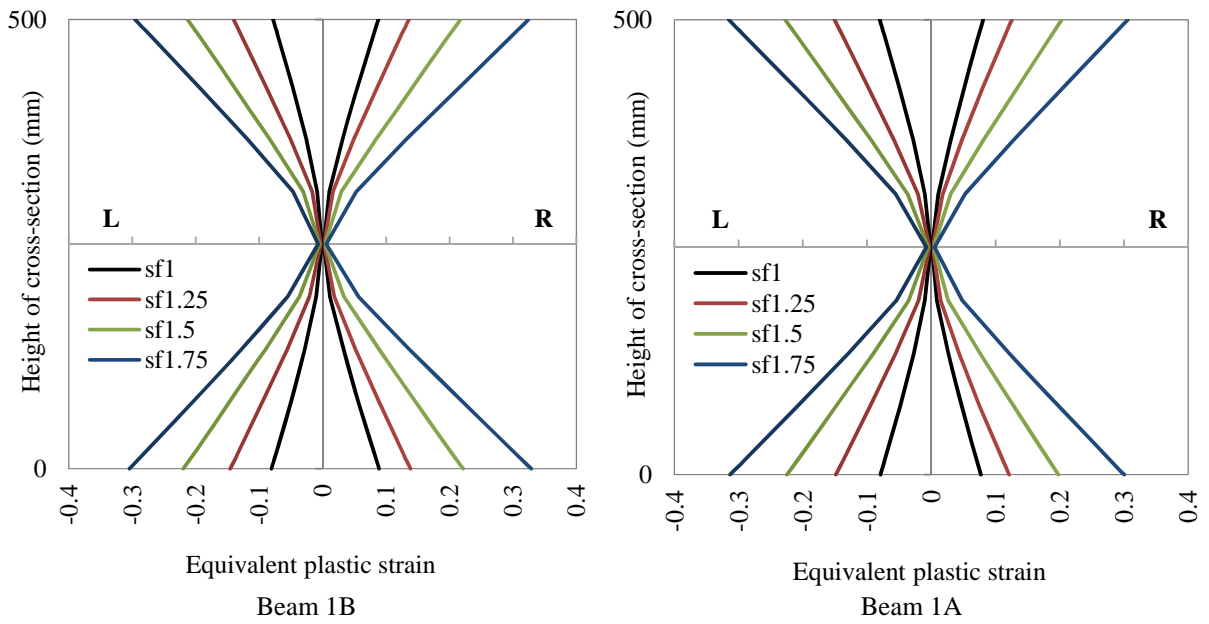


Figure 9-36: Equivalent plastic strain distribution at the 1st level for increasing S.F (6142ya).

Accelerogram: 612xa



Figure 9-37: Development of plastic hinge mechanism for S.F. 1.25, 1.50, 1.75 and 2.00 (612xa).

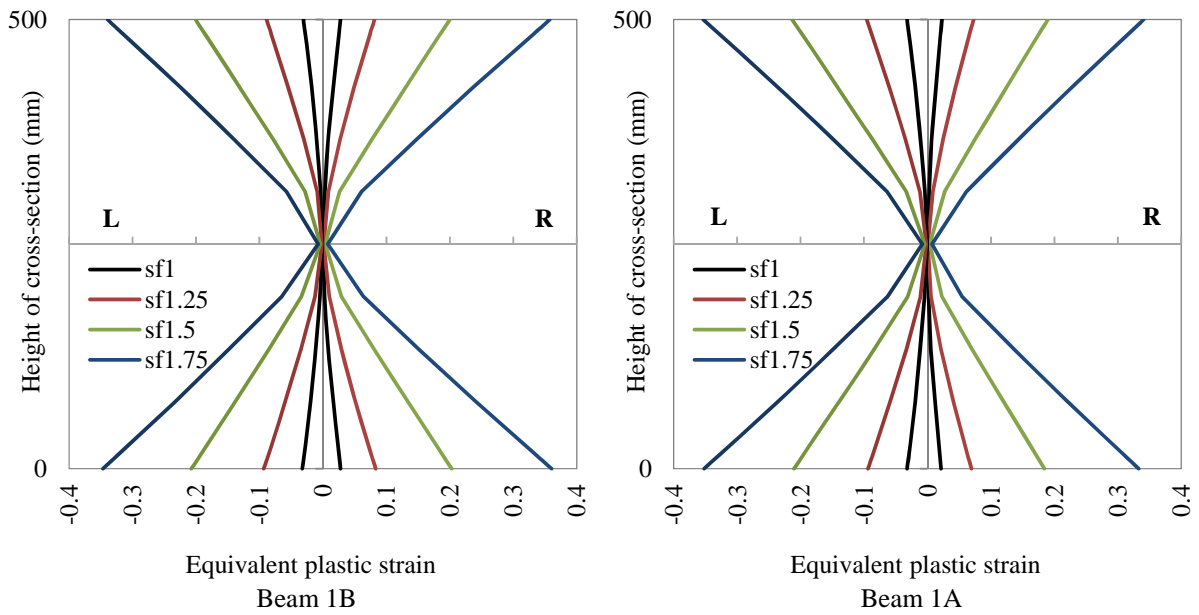


Figure 9-38: Equivalent plastic strain distribution at the 1st level for increasing S.F (612xa).

Accelerogram: 1726xa

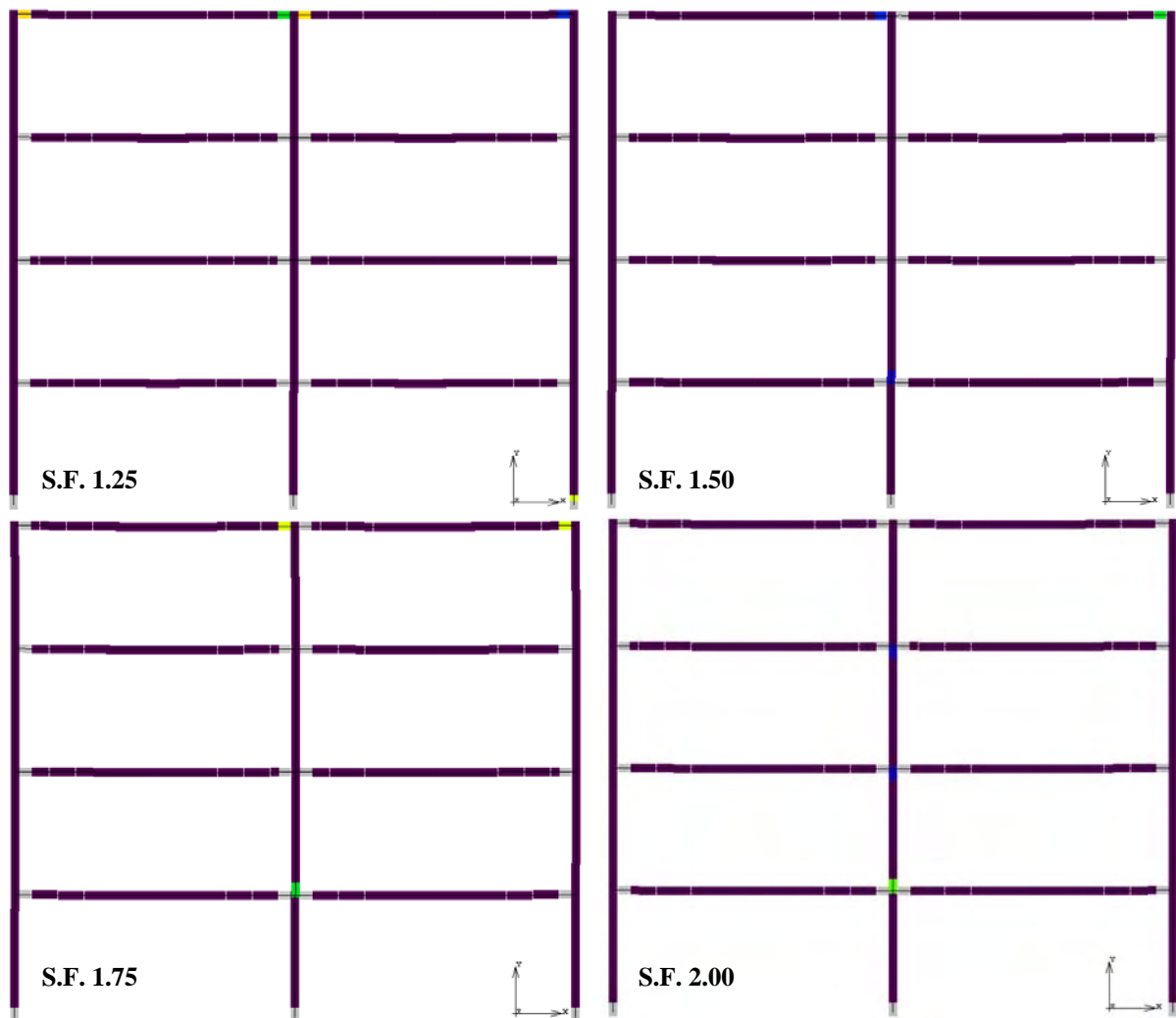


Figure 9-39: Development of plastic hinge mechanism for S.F. 1.25, 1.50, 1.75 and 2.00 (1726xa).

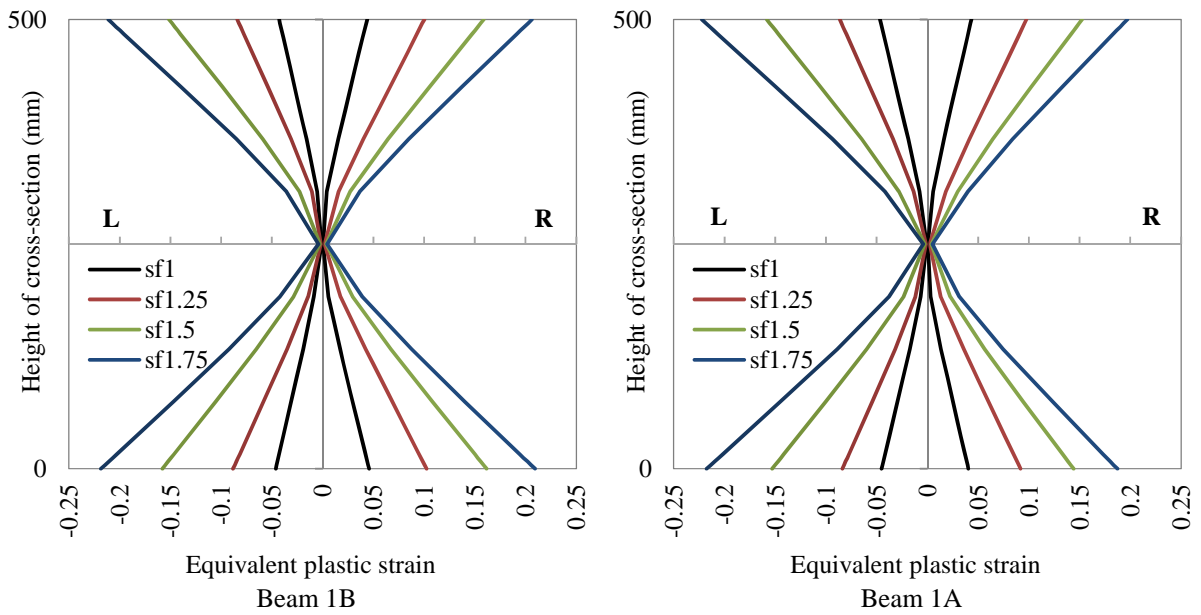


Figure 9-40: Equivalent plastic strain distribution at the 1st level for increasing S.F (1726xa).

Accelerogram: 1726ya



Figure 9-41: Development of plastic hinge mechanism for S.F. 1.25, 1.50, 1.75 and 2.00 (1726ya).

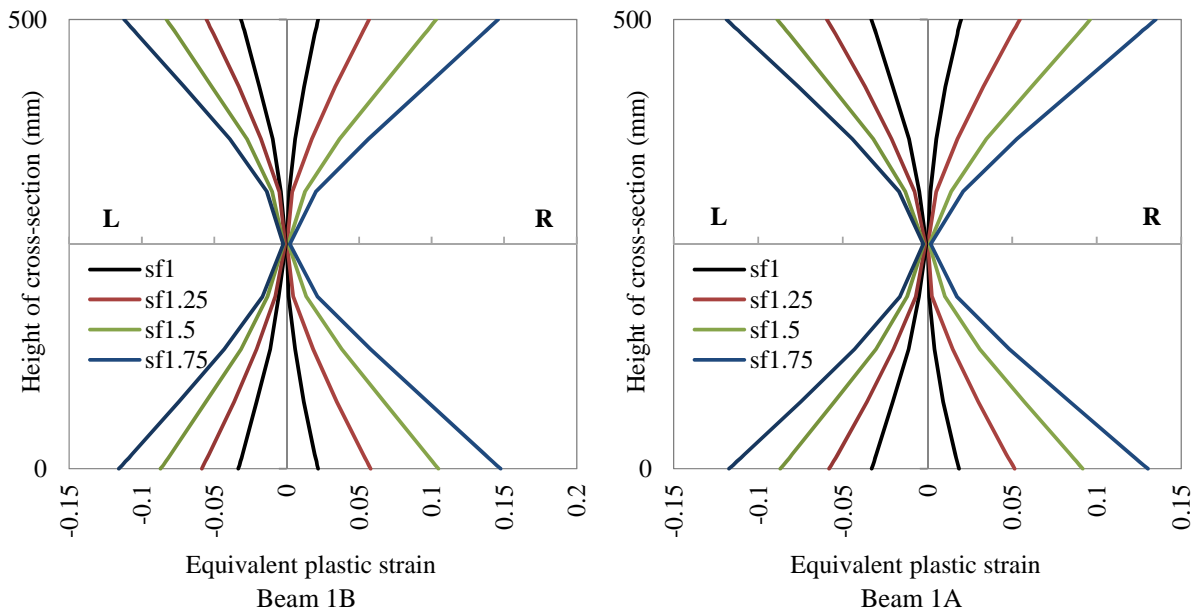


Figure 9-42: Equivalent plastic strain distribution at the 1st level for increasing S.F (1726ya).

Accelerogram: 5850xa



Figure 9-43: Development of plastic hinge mechanism for S.F. 1.25, 1.50, 1.75 and 2.00 (5850xa).

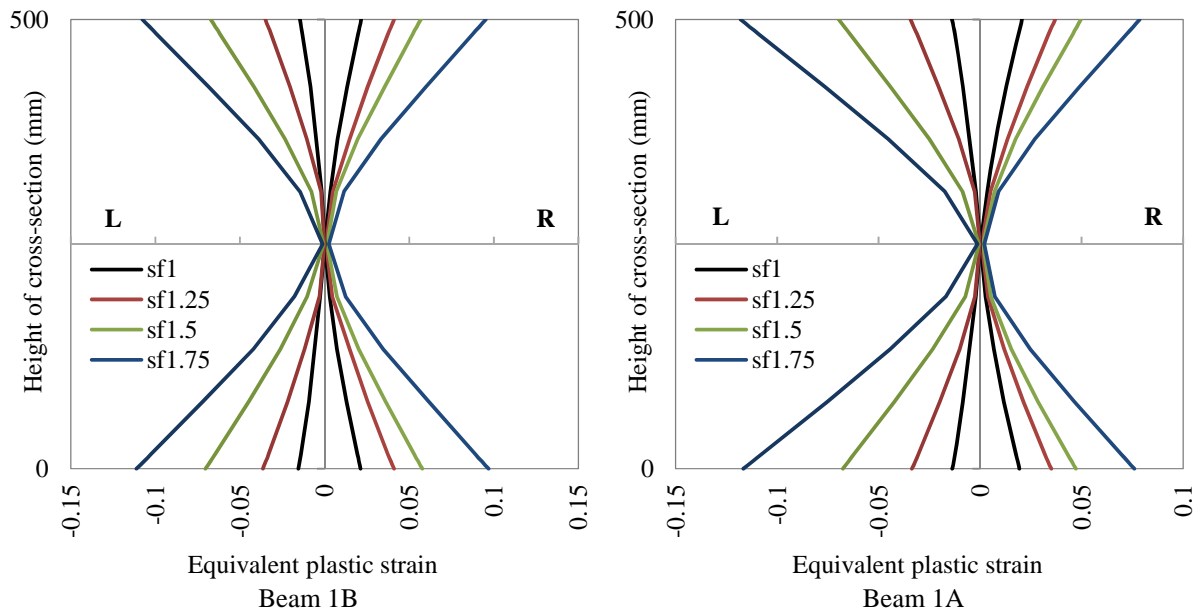


Figure 9-44: Equivalent plastic strain distribution at the 1st level for increasing S.F (5850xa).

Residual drifts

The residual displacements are dependent on both the accelerogram that is used for the representation of the earthquake and on the scale factor. Figure 9-19 presents the maximum of the drift angles taking into account both the inter-storey values. The comparison of the values with respect to the accelerogram that is used indicates that the peak values are corresponding to the 290xa time history acceleration record for $1 \leq S.F. \leq 1.50$ while for more severe earthquake levels the peak residual drift angles are noted for the 6142ya accelerogram.

accelerogram	S.F. 1.00	S.F. 1.25	S.F. 1.50	S.F. 1.75	S.F. 2.00
290xa	0.39%	0.50%	0.61%	0.67%	0.75%
293ya	0.24%	0.34%	0.37%	0.26%	0.22%
6142ya	0.22%	0.29%	0.51%	1.10%	2.06%
612xa	0.09%	0.36%	0.15%	0.39%	1.05%
1726xa	0.10%	0.28%	0.40%	0.38%	0.32%
1726ya	0.25%	0.36%	0.52%	0.42%	0.08%
5850xa	0.15%	0.22%	0.44%	0.68%	0.46%
AVERAGE	0.21%	0.33%	0.43%	0.56%	0.71%

Table 9-17: Peak residual drift angles.

Verification of performance levels

Finally the results of the IDA are presented in terms of inter-storey drift angle versus PGA. Actually, two different IDA curves are obtained for a single accelerogram. The first one uses the maximum recorded (transient) inter-storey drift angle while the second corresponds to the residual drifts (Figure 9-45). At this point, the response of the structural system is verified with respect to the limit values for the drift angles that are recommended in FEMA 356. Specifically, the limit values for the drift angles of steel moment frames that correspond to three different performance levels are adopted. For the Collapse Prevention

(C.P.) performance level the limit value for permanent or transient drift is defined to be equal to 5%. In the case of the Life Safety (L.S.) performance level the limit values are 2.5% for the transient drift and 1% for the permanent. Finally, more severe limits are used in the Immediate Occupancy (I.O.) performance level where it is recommended that the transient drift angles should not exceed the limit of 0.7% and the residual angles should be negligible. In order to define the term negligible the limit value is set equal to 0.1%. The structural performance limits are depicted in the diagrams of Figure 9-45. It is concluded that according to the specific limits for the transient drift, the structural response lies between the I.O. and the L.S. performance levels when the S.F. is bounded at the interval 1.00 up to 1.75. This is valid for all the accelerograms that are studied except the cases of 290xa and 6142ya. In the specific cases the structural response for S.F. equal to 1.75 is allocated between the L.S. and the C.P. states. Taking into account the permanent drift angles, the response of the structure is limited between the I.O. and the L.S. limits.

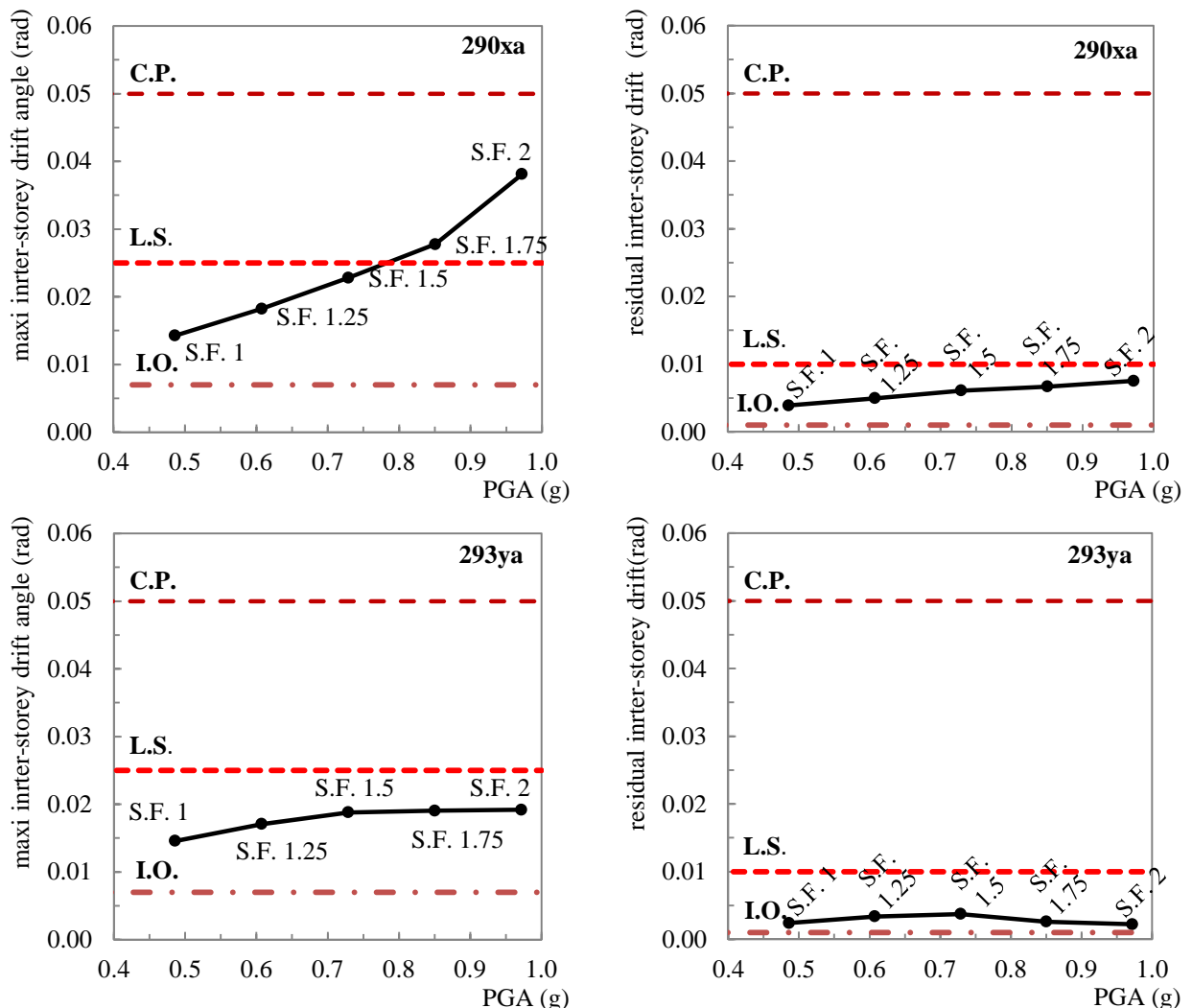


Figure 9 45: IDA curves in terms of maximum inter-storey drift angle and PGA. Verification for different performance levels according to FEMA 356.(continued)

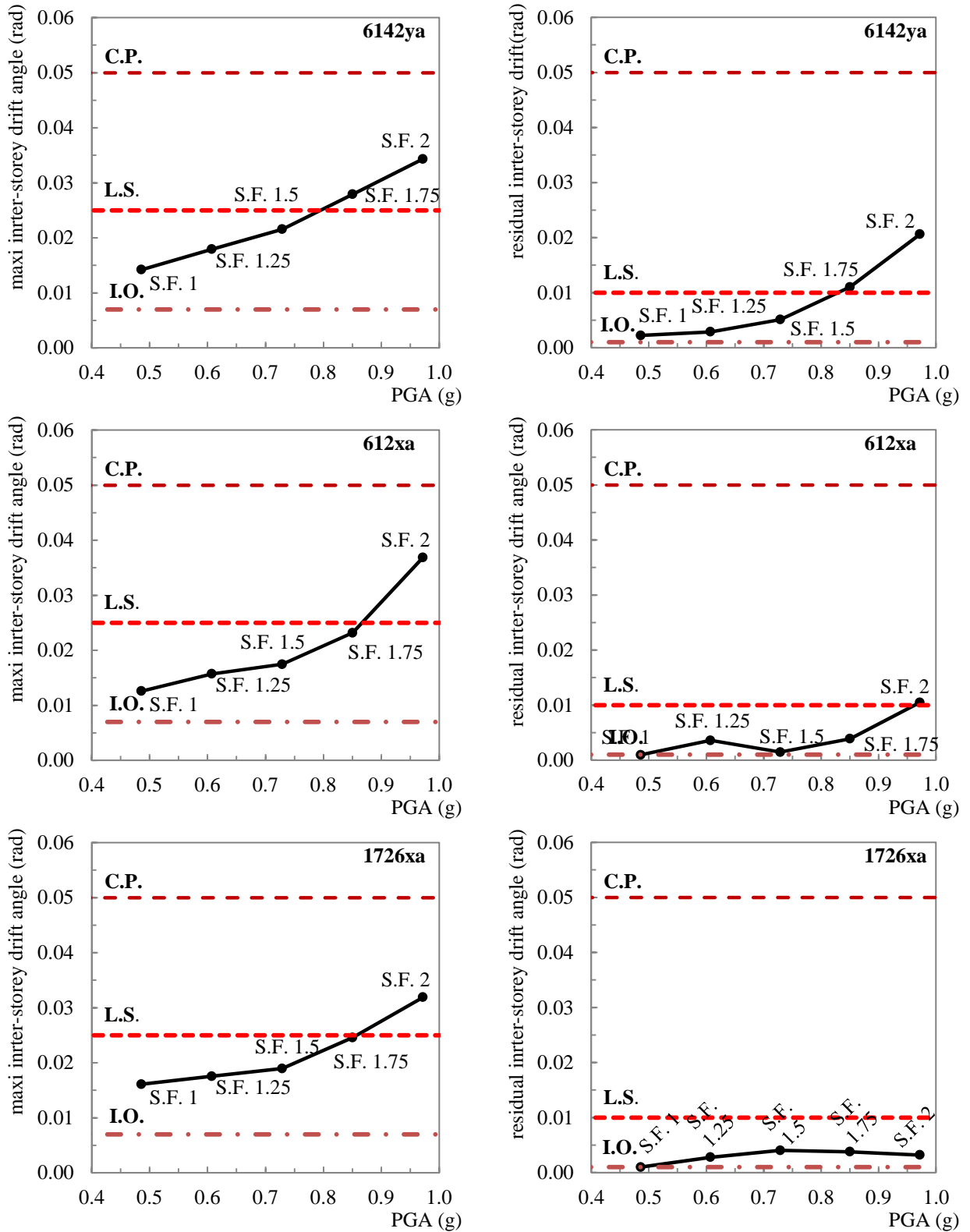


Figure 9-45: IDA curves in terms of maximum inter-storey drift angle and PGA. Verification for different performance levels according to FEMA 356. (continued)

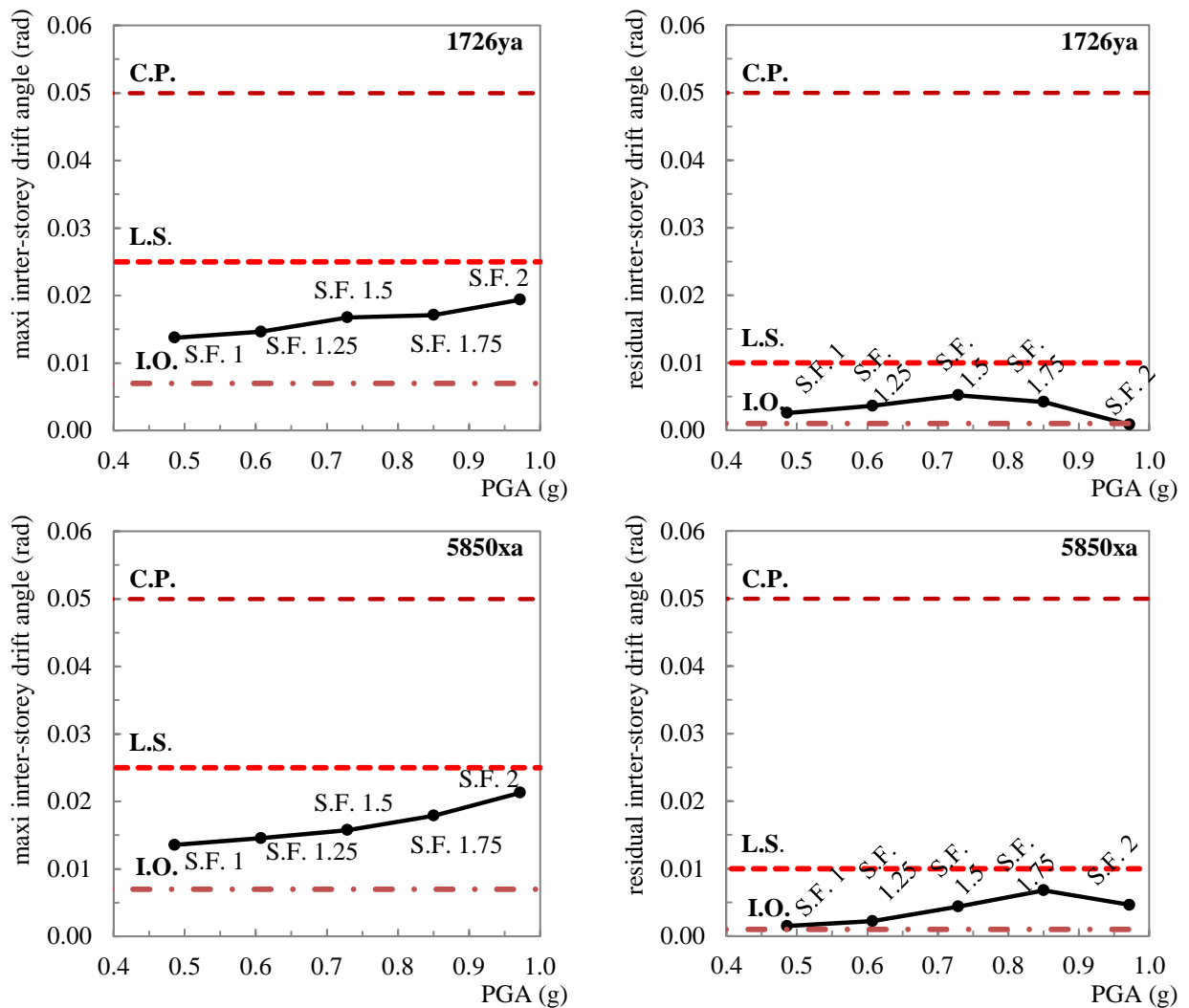


Figure 9-45: IDA curves in terms of maximum inter-storey drift angle and PGA. Verification for different performance levels according to FEMA 356.

9.7 Characterization of the seismic “damage” in correlation with the seismic loading level

The final goal is to study the ‘level of damage’ that is induced to the structural system due to the earthquake hazard. Various damage indices are proposed in the literature (Cosenza and Manfredi, 2000, Kappos, 1997, Fontana *et al.*, 2012). The damage measures for the non-linear structural response are defined either for individual structural elements (local indices) or they are related to the entire global structure (global indices) and they are used in order to define the damage potential in global or local level. The approaches that are proposed are based mainly in terms of plastic dissipated energy and on the ductility of the structural systems. In this dissertation a more simplified approach is obtained. It is noted that the “damage level” that is used here intends only to the characterization of the damage of the structural components at the end of the earthquake. The characterization is further used in Chapter 13 in order to determine the fire resistance of the structural system through (local type) failure criteria.

In this point of view, the characterization of the damage must be based on a scalar that depends on the intensity of the earthquake. Thus, the global (global damage) or the inter-storey drift (sub-local damage) angles could be used to characterize the damage.

In order to focus to individual structural members, the maximum equivalent plastic strain at the plastic hinge locations at the end of the seismic excitation is used. In this way, the ‘damage level’ is completely localized and is defined only at the positions where the plastic hinges are partially or fully formed. It is clear that the ‘damage level’ depends on the plastic hinge mechanism allocation at the end of the earthquake. Hence, it strongly depends on the time-history acceleration record and on the intensity of the earthquake. At this point the dissertation focuses on the structural members of the first level of the structural system where the fire exposure takes place in the next stage of the study (Chapter 11). Table 9-18 is developed in order to take into account the different time-history acceleration records which are scaled for the representation of more severe earthquakes. Specifically, the maximum of the equivalent plastic strain between the upper and the lower layers (Layers 1 and Layer 100) is selected for both the ends (**Left** and **Right**) of the each beam (Beam 1A and Beams 1B) as they are illustrated in Figure 9-46.

Accelerogram/Beam		S.F. 1.00		S.F. 1.25		S.F. 1.50		S.F. 1.75	
		L	R	L	R	L	R	L	R
290xa	Beam 1A	0.020	0.020	0.045	0.082	0.099	0.138	0.181	0.221
	Beam 1B	0.020	0.035	0.050	0.077	0.105	0.131	0.319	0.210
293ya	Beam 1A	0.044	0.035	0.077	0.077	0.123	0.133	0.187	0.203
	Beam 1B	0.044	0.032	0.079	0.067	0.125	0.117	0.191	0.181
6142ya	Beam 1A	0.081	0.089	0.146	0.139	0.220	0.222	0.305	0.329
	Beam 1B	0.080	0.081	0.151	0.126	0.227	0.203	0.315	0.306
612xa	Beam 1A	0.032	0.028	0.093	0.083	0.207	0.203	0.347	0.361
	Beam 1B	0.032	0.023	0.096	0.073	0.213	0.190	0.353	0.341
1726xa	Beam 1A	0.046	0.046	0.088	0.102	0.158	0.162	0.218	0.209
	Beam 1B	0.047	0.043	0.086	0.098	0.158	0.152	0.222	0.197
1726ya	Beam 1A	0.033	0.022	0.059	0.058	0.087	0.105	0.116	0.148
	Beam 1B	0.033	0.020	0.059	0.055	0.089	0.096	0.119	0.135
5850xa	Beam 1A	0.016	0.022	0.037	0.041	0.070	0.058	0.111	0.097
	Beam 1B	0.014	0.021	0.034	0.037	0.070	0.050	0.118	0.079

Table 9-18: Level of seismic damage according to the eq. plastic strain at the ends of the beams of the first level.

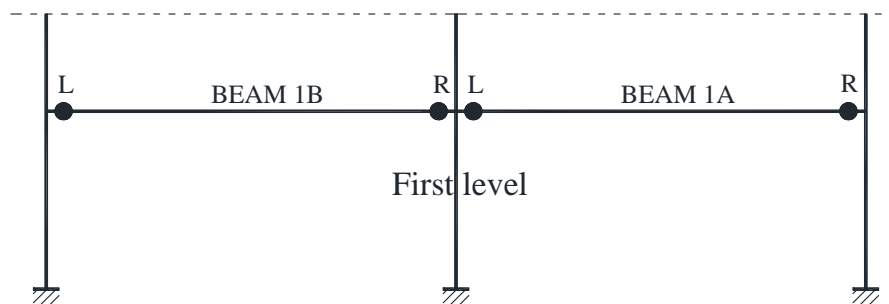


Figure 9-46: Identification of the ends of the beams that are presented in Table 9-18.

Chapter 10. Fire design/Non-linear structural analysis for fire loading

The goal of this Chapter is to study in detail the behaviour of the structural system, presented in Chapter 7 and Chapter 9, for the *reference* fire scenarios as they are defined in Chapter 7. The *reference* scenarios are determined either using the ISO fire curve (SC-ISO) or through the simulation of the natural fire through CFD (SC-00). The first objective is to calculate the temperature profiles of the structural members for the *reference* scenarios. At this point it is highlighted that the structure is considered to be undamaged and thus the results of the study indicate the inherent fire-resistance of the structural system. It is noted that, actually, the fire design of the structural system is conducted through numerical analysis. The results of the analysis indicate the response of the structural system under the fire exposure, taking into account the concurrent loading combination of permanent and live actions according to the guidelines of EN 1993-1-2. Different aspects are studied, including the strain field, the stresses, the bending moments, the axial forces and the displacements. The final issue that arises is the determination of the fire-resistance of the structural system in time or temperature domain. According to the literature, this can be defined using several criteria related to local or global instabilities and criteria based on the deflections of the structural members. The criteria that are used in this study are temperature dependent and they are based on the ductility of the structural members under fire conditions (Chapter 12).

10.1 Numerical modeling

The numerical model that is developed for the simulation of the fire-response of the structural system is the same with the one presented in Chapter 9. The model uses beam finite elements and the material properties (mechanical and thermal) are taken according to the guidelines of EN 1993-1-2. It is noted that the strain hardening of steel for the temperature range between 20 °C and 400 °C is neglected and the material behaviour is considered to be elastic-perfectly plastic. The yield stress of steel is equal to 275MPa at room temperature.

The problem is solved through non-linear dynamic analysis as it is described in section 9.3.3. Since the fire is classified as an accidental action (EN 1990), the design effect of actions for the fire situation can be obtained using the combination for accidental situation. The combination is simplified to the expression $G + \psi_2 Q$. The value of the coefficient ψ_2 that is applied to the variable action Q is considered to be equal to 0.8, according to the guidelines of EN 1990 for library buildings.

10.2 Simulation of fire loading

In the case of the ISO-*reference* scenario, the temperature in the fire-compartment is

assumed to be uniform. The temperature profile of the structural members is presented in Figure 10-1. It should be emphasized that no thermal analysis is conducted and the temperature profile for the structural members is calculated according to the guidelines of EN 1991-1-2, depending on the cross-section dimensions. Moreover it is assumed that the temperature is uniform along the member and the thermal gradient in the cross-section is not taken into account. Regarding the *reference* scenarios SC-00 and SC-SP100, which are generated using the CFD model for the fire simulation, the temperature profiles of the structural members are presented in section 8.3.

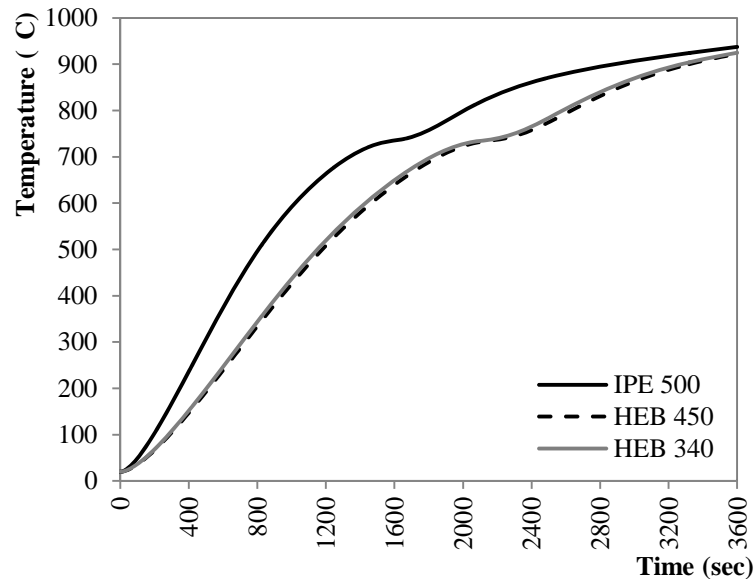


Figure 10-1: Temperature profile of the structural members for the ISO *reference* scenario.

10.3 Results of numerical analyses

10.3.1 ISO-fire

The deformed shape of the structural system at the end of the numerical analysis is illustrated in Figure 10-2. The analysis stops at the 1584th sec (26.4 min) due to convergence failure. The same figure presents the equivalent plastic strain distribution taking into account the Layer 1 of the cross sections (for the beams this corresponds to the upper flange). Figure 10-3, Figure 10-4 and Figure 10-5 represent the evolution of the equivalent plastic strain with time, at the upper, lower and middle layers of the cross-section of Beam 1A. The same diagrams are plotted for the upper end of Columns 1A and 1B. It can be observed that at the end of analysis, the plastic hinges are formed at the ends and at the mid-span of Beam 1A. The same holds for Beam 1B. Moreover, it is noted that the plastic hinges are formed in the upper ends of columns (Column 1A and 1B) in the early stages of fire exposure (approximately at the 10th min). The same holds for the lower ends of both columns (support nodes). This indicates that the columns can be considered as *simply supported* from the early stages of the fire exposure. It is clear that the analysis failed to converge due to the unstable (local) mechanism (three continuous hinges) that develops at both the beams 1A and 1B.

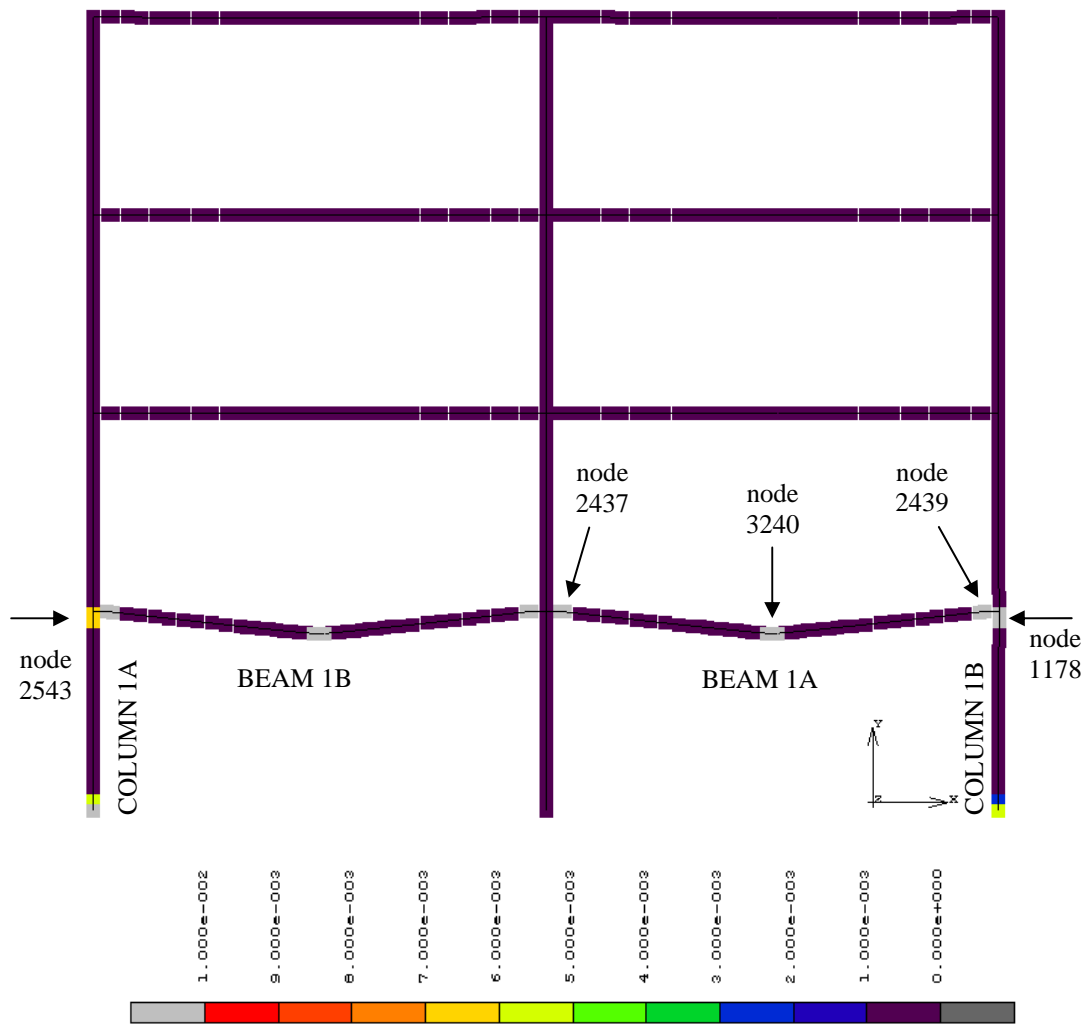


Figure 10-2: Deformed configuration of the structural sub-system at the end of analysis.

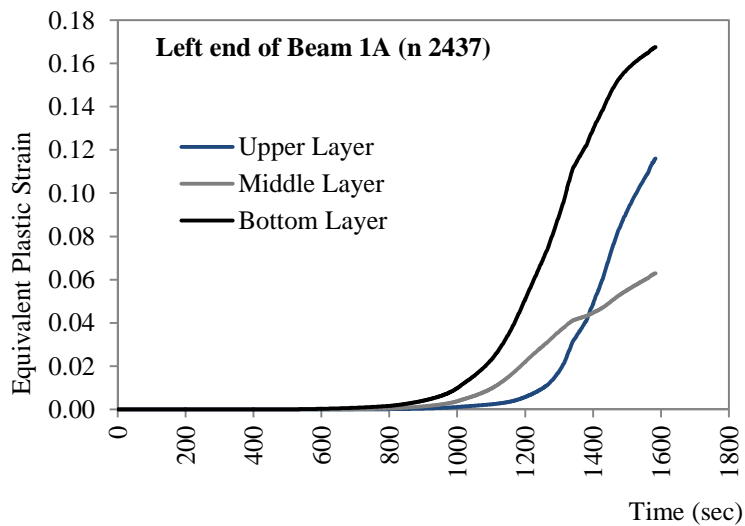


Figure 10-3: Equivalent plastic strain evolution with time at the Left end of Beam 1A (node 2437).

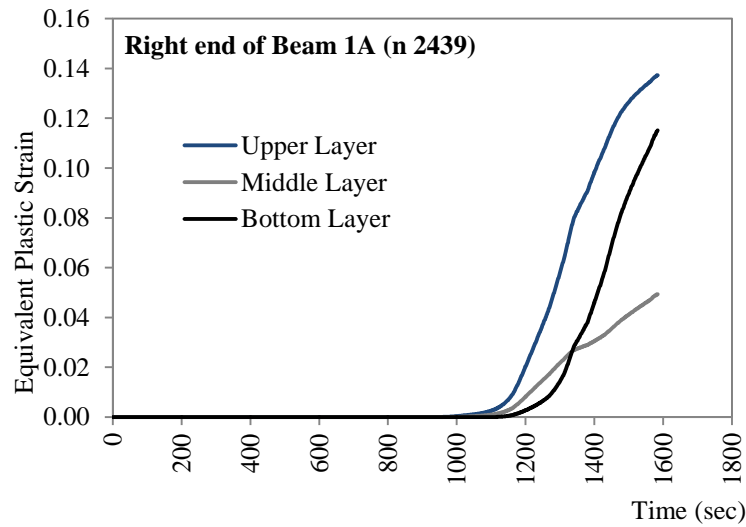


Figure 10-4: Equivalent plastic strain evolution with time at the Right end of Beam 1A (node 2439).

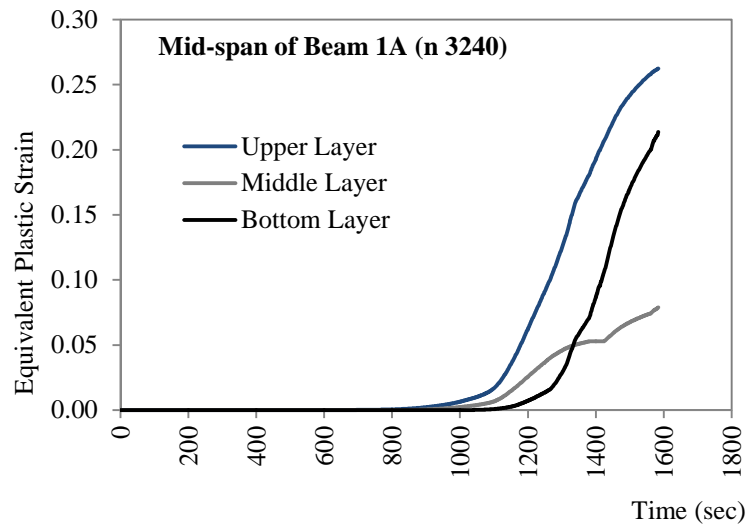


Figure 10-5: Equivalent plastic strain evolution with time at the Mid-span of Beam 1A (node 3240).

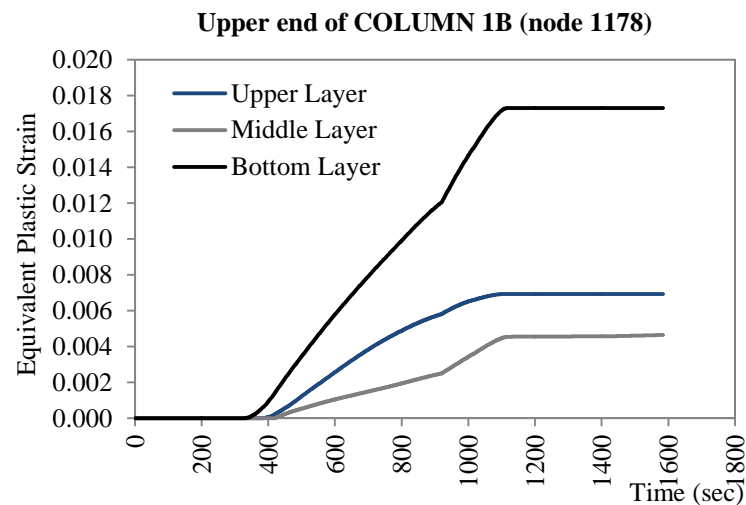


Figure 10-6: Equivalent plastic strain evolution with time at the upper end of Column 1B (node 1178).

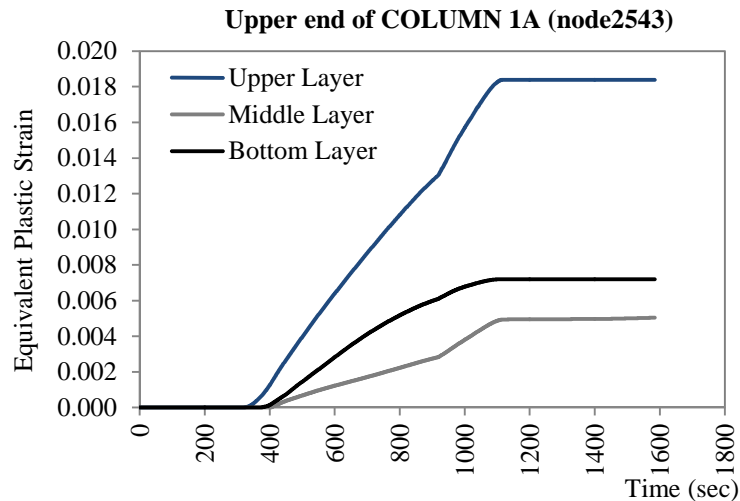


Figure 10-7: Equivalent plastic strain evolution with time at the upper end of Column 1A (node 2543).

In order to understand in detail the behaviour of the beams during the fire exposure and the failure mode of the structural system, the temporal evolution of axial force for the Beam 1A is plotted in Figure 10-8. The remarks that follow are valid as well for the Beam 1B. This diagram demonstrates in a comprehensive way the mechanisms that take place during the fire exposure of a beam that is located in a structure. The beam is laterally and axially restrained due to the adjacent members and the restraints are not the same at the Left and the Right ends of the beam. It is reminded that the temperature gradient in the cross-section of the beam is not considered here.

In the early stages of the fire exposure, the behaviour of the beam is dominated by the restrained thermal expansion. The longitudinal restraint reacts to the thermal expansion of the beam and generates the compressive axial force. The compressive force is quickly developed and the maximum value that is recorded is equal to 696kN. In the same time (13.5 min) the temperature of the beam is 512 °C. This stage, which starts at the beginning of the fire exposure and is terminated at the maximum recorded value of the compression force is the *restrained thermal elongation* stage. It is noted that during this stage the yield stress of the beam is not significantly reduced due to the increase of temperature. Moreover the mid-span deflection of the beam is quite small (Figure 10-9). The evolution of the horizontal deflection of the beam is presented in Figure 10-8. It is observed that the maximum value of the horizontal deflection of the beam during the *restrained thermal elongation* stage is approximately 40mm.

As the temperature increases, the behaviour of the beam is mainly affected by the bending and the degradation of the material properties (yield stress, proportionality limit and elastic modulus). In this study this stage is referred as *increase of curvature* stage. During this stage, the plastic hinges are formed, first in the ends of the beam (nodes 2437 and 2439) and next in the mid-span (node 3240). At the same time, the compressive force is reduced and the length of the beam is progressively decreased (reduction of the horizontal displacement). During this stage the vertical mid-span deflection is rapidly increased as it

can be observed in Figure 10-9. When the vertical deflection of the beam becomes sufficiently large, the shortening of the beam's length (due to bending) is gradually overtaken by the beam's thermal expansion and thereafter, a tensile force develops and the *catenary action* stage starts. The transition temperature, where the axial force of the beam becomes zero, is equal to 713.26 °C. At this stage all the three plastic hinges are formed in the beam. The bending moment capacity of the beam is negligible but the beam is able to resist the applied load due to the existence of the tensile force. Finally the analysis stops for temperature equal to 734.5 °C.

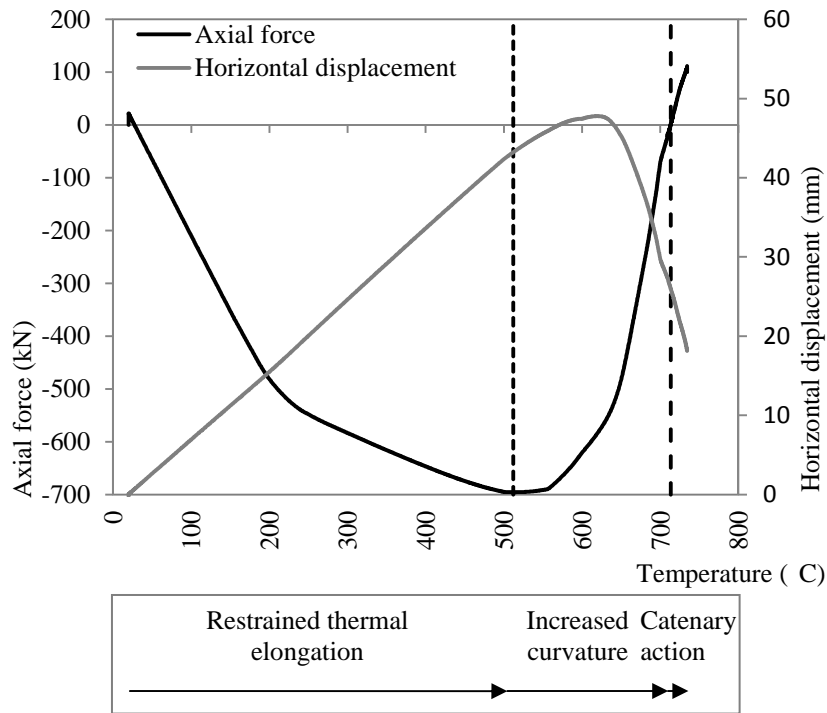


Figure 10-8: Axial force and horizontal displacement at the first level of the frame during the fire exposure.

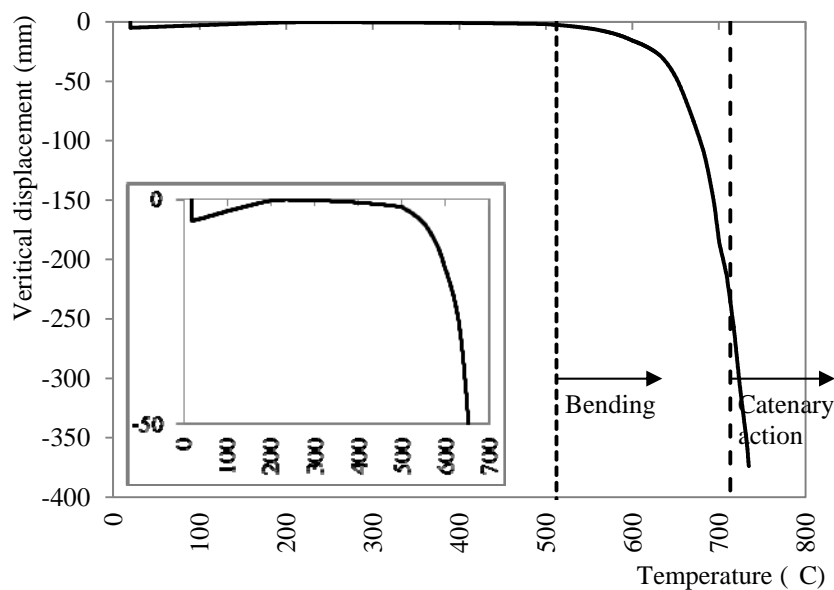


Figure 10-9: Evolution of mid-span deflection of Beam 1A during fire-exposure.

The Von Mises stress at the Upper Flange (UF) and the Bottom Flange (BF) for the Nodes 2437 (Left end), 2439 (Right end) and 3240(Mid-span) are presented in Figure 10-10, Figure 10-11 and Figure 10-12 respectively. All the figures include the reduction of both the yield and the proportionality limit stresses (according to EN1993-1-2) as the temperature increases. It is observed that the stress of the BF at the left support reaches the proportionality limit value (A) for a temperature approximately equal to 320 °C (520th sec). This indicates that plastic strains appear in the cross-section. Next, the proportionality limit is attained at compression flange at the mid-span (point B) for a temperature equal to 380 °C (610thsec). The stress at the UF at the left support becomes equal to the proportionality limit (point C, 475 °C, 765th sec) and the same happens very quickly for both the bottom and the upper flange of the right support (points D and E, 490 and 540 °C, 790th and 880th sec). Finally, the flange under tension at the mid-span (F, 564 °C, 935th sec) reaches the proportionality limit. Moreover, it is noted that both at the supports and at the mid-span, the stresses of the upper and the lower flanges of the beams reach the yield limit in the *increased curvature* stage. Finally, it is interesting to observe that the Von Mises stress time-evolution is completely different at the left and the right ends of the beam. This is attributed to the different rotational and axial restrains that are provided by the adjacent members at the respective positions.

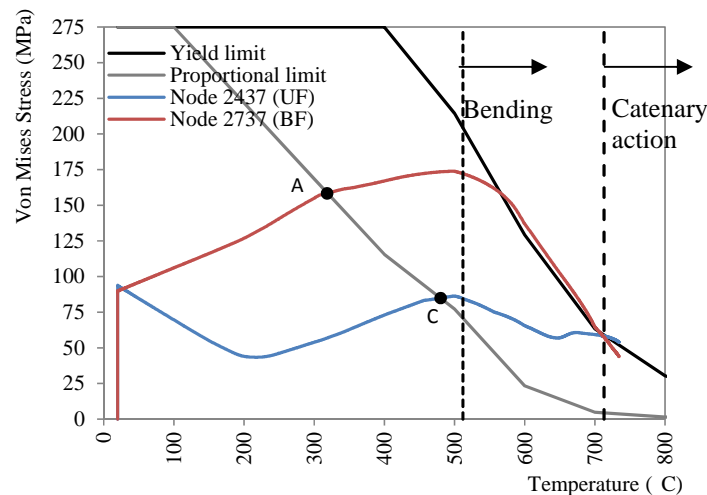


Figure 10-10: Von Mises stress evolution with temperature at the UF and LF in the Left end of Beam 1A.

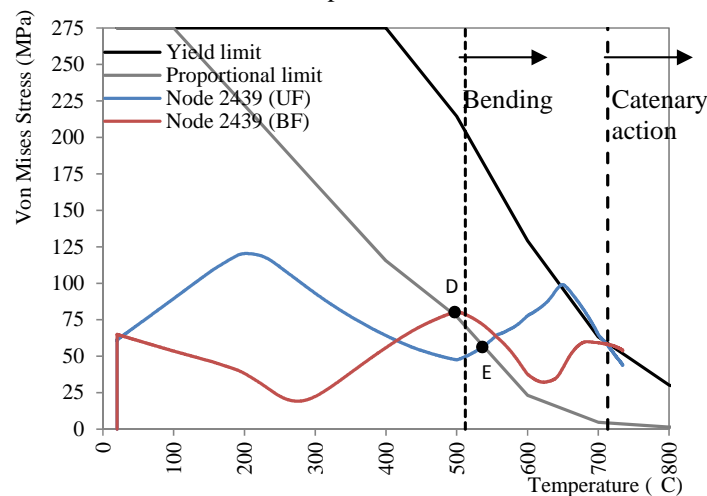


Figure 10-11: Von Mises stress evolution with temperature at the UF and LF in the Right end of Beam 1A.

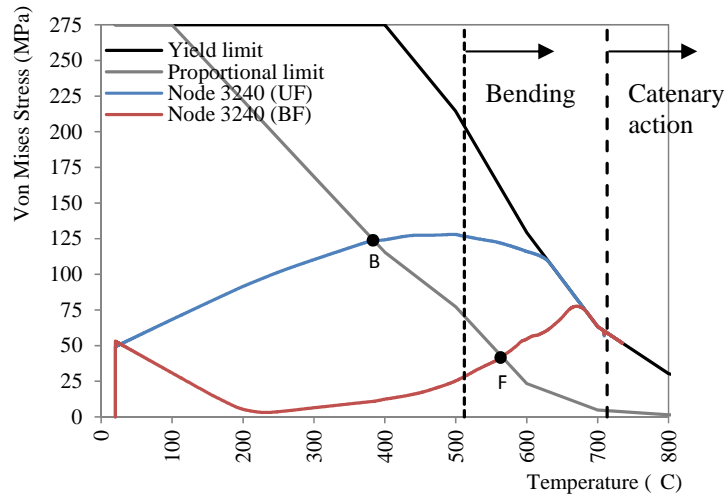


Figure 10-12: Von Mises stress evolution with temperature at the upper and the lower flange in the Mid-span end of Beam 1A.

Figure 10-13 presents the temporal evolution of the bending moments during the fire exposure, at the supports (Left end and Right end) and at the mid-span of Beam 1A. The normal stresses at the BF and the UF of the beam at the same locations are provided in Figure 10-14, Figure 10-15 and Figure 10-16 respectively. During the early stages of the fire exposure the mid-span deflection of Beam 1A is slightly increased (in the opposite direction of the initial deflection that arises due to gravity loading) due to the restrained thermal elongation as it can be observed in Figure 10-9. Due to this “negative bending” at the early stages of the fire exposure the moment at the mid-span and at the right support is slightly reduced while the moment at the left support is increased.

As the temperature increases, during the *restrained thermal expansion* stage, the moment is enlarged at both the left support and the mid-span due the compressive axial force action while at the right support the moment increases and it turns to positive values.

At the time where the *restrained thermal expansion* stage is terminated, the bending moments at both the supports and the mid-span are reduced. At this stage the axial force is decreased and the bending is the main action. At the Left support, where the proportionality limit has already been attained in the previous stage, the moment is reduced due to the reduction of the mechanical properties of steel. Concerning the Left support, the behaviour is more complicated. The normal stress at the BF is reduced (and finally slightly increased) and the opposite happens at the LF. This can be attributed to the combined effect of the bending and the simultaneous decreasing axial force. Additionally, it should be taken into account the fact that there is main difference between the left and the right beam-to-column joint. In the right side, the balance of moments in the joint includes both the moment of the heated beam, the moment of the heated column (lower side) and the moment of the cold column (upper side). At the Left end, the moment balance in the joint includes only the moment of the heated beams (Beam 1A and 1B), since the moment of the central column is zero. Finally, in the Mid-span the normal stresses at the UF are decrease mainly due to the reduction of the axial force and the LF stresses are increased mainly due to bending. As a result the moment is slightly decreased.

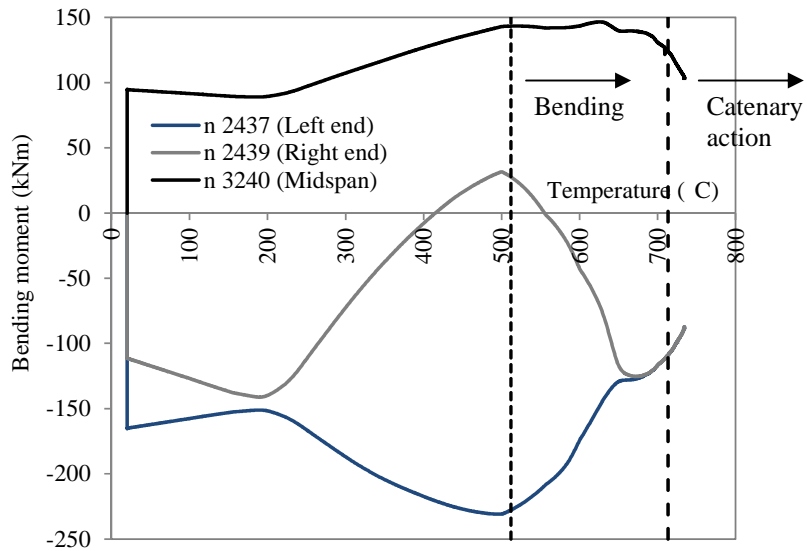


Figure 10-13: Hogging (support) and sagging (mid-span) of Beam 1A during the fire exposure.

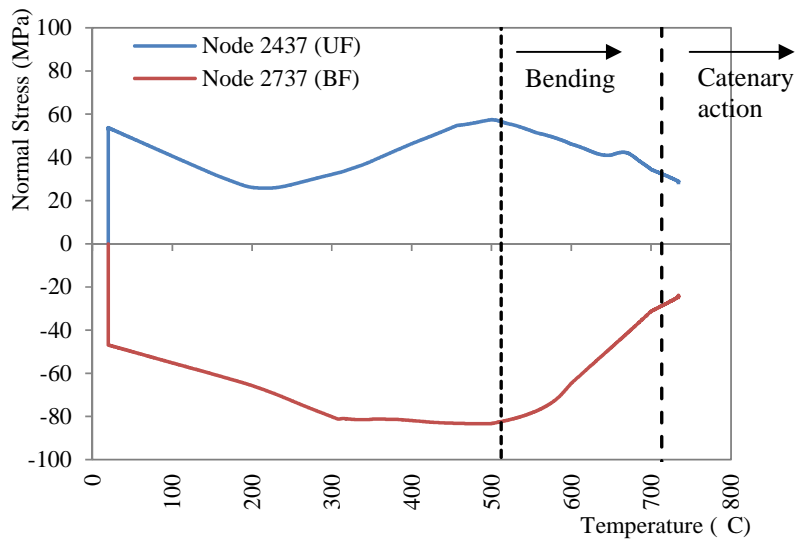


Figure 10-14: Normal stress at the Left end of Beam 1A during the fire exposure.

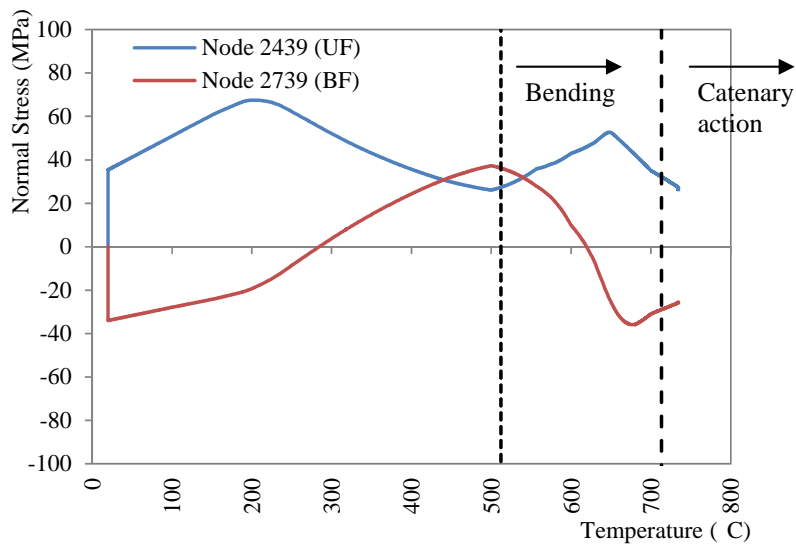


Figure 10-15: Normal stress at the Right end of Beam 1A during the fire exposure.

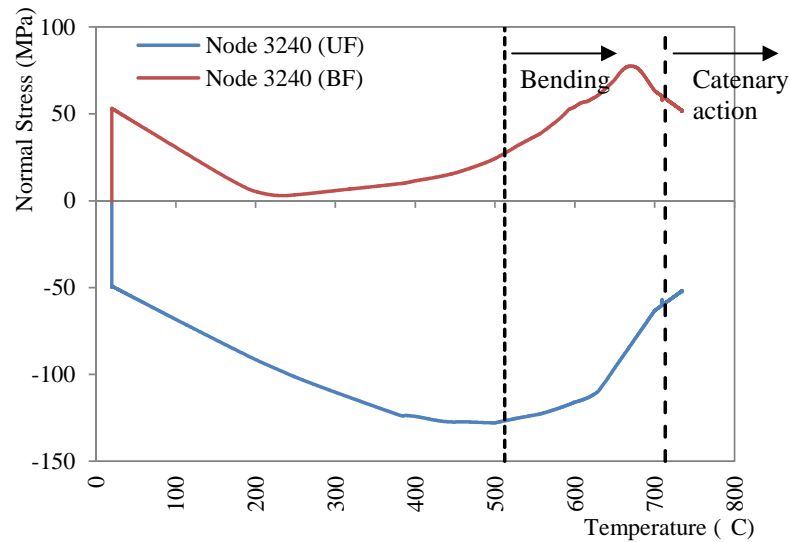


Figure 10-16: Normal stress at the Mid-span of Beam 1A during the fire exposure.

10.3.2 Natural Fire

Considering the natural *reference* scenario, the maximum recorded temperatures for the heated beam and columns do not exceed the value of 200°C and the structural system does not fail during the fire exposure. Moreover, due to low temperature profile of the structural members, the results concerning the stresses, the strains and the deflections are not presented.

Chapter 11. Non-linear analysis for fire-after earthquake loading

The main objective of this Chapter is to study the behaviour of the structural system, which has been presented in the previous Chapters, for the Fire after Earthquake (FAE) loading. Briefly, it is mentioned that the structural system is initially designed for the seismic actions (Chapter 9) and the fire-performance of the steel frame (undamaged structural system) for the *reference* scenarios is presented in Chapter 10. In this Chapter, first the frame is submitted to the seismic loading and then the fire-behaviour of the damaged structural system is obtained. The study is conducted numerically using the finite element code MSC Marc (2011). The seismic action is represented through the time-history acceleration records that are obtained in section 9.3.2 and the intensity of the earthquake loading is scaled-up according to section 9.6.1. Regarding the fire loading, two different cases are considered. In the first case the fire is simulated through the ISO-fire curve while in the second case the Post Earthquake Fire (PEF) scenarios are used. The PFE scenarios are defined taking into account different levels of non-structural damage as they are presented in Chapter 7.

The first goal of this Chapter is the determination of the FAE scenarios. Two different categories are distinguished, depending on the simulation of the fire action: the *ISO-FAE scenarios* and the *natural-FAE scenarios*. In the second case, the fire- behavior is studied taking into account the fact that the structural system can suffer different PEF scenarios (which are directly related to the level of the non-structural damage), depending on the probability of occurrence of earthquake (which is directly related to the scaling of the earthquake intensity).

The main target of this Chapter is to obtain in detail the behaviour of the structure for the different FAE scenarios. The results of the non-linear numerical analyses are systematically presented in order to detect the main parameters that affect the fire response of the damaged structural system. The fire-resistance of the structural system for the various FAE scenarios is calculated in Chapter 13 according to the criteria that are defined in Chapter 12.

11.1 Definition of the addressed problem

The main problem that is addressed here is the study the response of the structural system under fire conditions taking into account the seismic structural and non-structural damage. It is expected that the fire-performance of the structural system will be different, depending on the 'level of damage' caused to the structural members by the seismic loads. Furthermore, the non-structural damage leads to different time-history temperature

distribution in the fire-compartment and, subsequently, to various fire-loading scenarios for the structural members.

First, the problem is approached through the ISO-FAE scenarios in order to take into account only the structural damage. The findings of the numerical analyses indicate the variation of the fire-behaviour of the structural system as the earthquake intensity level is scaled-up. The next step is to study the problem through the natural-FAE scenarios. This approach is quite complicated since it involves the variation of the seismic damage to both the structural and the non-structural components. At this point the target is to obtain the fire-performance that yields from the correlation of the earthquake PGA level to the non-structural performance level. Specifically, the seismic action is defined according to Section 9.6.1 where the PGA of the earthquake is scaled-up for the representation of stronger earthquake motions. On the other hand, the performance level is defined from the 'level of damage' (broken windows) of the non-structural members, as it is indicated in the PEF scenarios (Chapter 7). The correlation of the earthquake return period with the non-structural performance level indicates the target point. Actually, the approach that is used in this dissertation connects directly the seismic levels to different PEF scenarios. The results indicate the variation of the fire-response of the structural system as the earthquake becomes more severe and, subsequently, the induced non-structural damage is increased. The behaviour of the structure is mainly depicted in terms of deformations, rotations and plastic strains. The final objective is the calculation of the fire-resistance of the structural system which is presented in Chapter 13.

11.2 Representation of seismic and fire actions

The seismic action is simulated through the time-history acceleration records that are presented in Section 9.3.2. It repeated that the accelerograms are further scaled according to Section 9.3.2.

The fire action is simulated through temperature time-history curves. Briefly, it is reminded that, in order to simplify the calculations, the temperature of every structural member is assumed to be uniform along the length of the member and the thermal gradient in the cross-section is not taken into account. The time-history temperature curves are obtained through the procedure that is described in Section 5.5 and the calculations are based on gas-temperature time history records. Actually, the temperature time-history curve for a distinct structural member depends mainly on the geometric cross-section characteristics and on the gas temperature time-history record.

Two different cases are considered. In the first case the gas temperature time-history record is defined to be the ISO-fire curve. The temperature time-history curves for the structural members that are used in this Chapter, are identical with those that are presented in Chapter 10 (Section 10.2). In the second case the gas temperature time-history records are obtained from the simulation of the enclosure fire. The temperature time-history curves of the beams and the columns of the first level of the library building have already been

presented in Section 8.3 (Figure 8-49) with respect to the location of the frame where the beams belong.

11.3 Numerical modelling

The numerical model is identical with the one that is described in Chapter 9 (section 9.3.1). Moreover, the type of analysis that is described in Chapter 9 is used and the problem is solved through dynamic analysis based on the direct integration of equations of motion. All the details concerning the type of the numerical analysis are the same as they are referred in Section 9.3.1.

The numerical analysis consists of two different stages. In the first stage the structural system is submitted to the seismic action until the oscillation is totally damped. In the second stage the structural members of the first level of the frame structure are exposed to fire.

The issue that appears at this point is connected to the different scale of the time duration of earthquake and fire actions that must be incorporated in the same analysis. In order to encounter this issue it is essential to divide the analysis into two separate ones. In the first analysis, the steel frame is subjected to the seismic action while in the second one the analysis restarts and the deformed structure is exposed to fire for 60 minutes. It is necessary to split the analysis into two different parts in order to use the desired time step at the corresponding stages (earthquake and fire). The duration of the earthquake event varies between 50 sec and 130 sec, while the fire lasts 3600 sec. Taking into account the fact that the selection of the time step is a crucial decision when conducting dynamic analysis with direct integration of the equations of motion, it is crucial to decide the required time step for each analysis. Regarding the seismic analysis, the desired time step is required to be equal to 10^{-3} sec, while for the fire analysis it is sufficient to use time step equal to 1 sec. Consequently, if a single analysis is conducted, adopting the minimum time step (10^{-3} sec), it is estimated that the earthquake excitation can be imposed using 50,000 to 130,000 increments, while for the case of the fire loading 3,600,000 increments would be required. In this way, the computational cost would be enormous. In order to overcome this difficulty, it was decided to split the analysis into two parts and to use the desired time step in the corresponding analyses. It is noted that at the start point of the fire analysis, where the analysis restarts, the code “reads” the output file of the seismic analysis, which includes all the results of the previous stage, comprising the kinematic results, the stress and strain output, and the temperature field. Thus, at the start point of the fire analysis, both the geometric damage (deformed shape of the steel frame) and the material degradation (formulation of plastic hinges) are taken into account. It is noted that in the seismic analysis the boundary conditions that are related with the fire loading are not included in the modeling. On the other hand during the fire analysis the boundary conditions that correspond to the earthquake excitation are not further used and they are not included in the input of the analysis.

When the problem is solved through two subsequent analyses, the issue that arises is related to simulation of the earthquake excitation. During the seismic analysis, the structural system is submitted to the earthquake excitation which can be depicted through ground acceleration, velocity or displacement. This numerically can be simulated either by using the time-history acceleration record or through the ground displacement time-history using the corresponding DOF (Degree of Freedom) of the support nodes of the structural system. The time-history acceleration records as they are illustrated in Figure 9-13, specify that the time at which the earthquake excitation stops corresponds to non-zero value for the ground acceleration. If the seismic analysis is terminated at this time-frame, the boundary conditions that are related with the earthquake motion (acceleration or displacement at the support nodes) are not zero. In this case, when the analysis is restarted, the output file of the seismic analysis, which is actually the input file for the fire analysis, includes the non-zero values for the acceleration or the displacement for the corresponding DOF of the support nodes of the frame. This indicates that the prescribed values are used in the second (fire) analysis and the structural system actually is submitted to a ground motion of constant acceleration. In order to overcome this problem, the ground acceleration should become zero at the end of the earthquake analysis. This indicates that the time-history acceleration records should be modified in order to include a descending branch that would lead to the elimination of the ground acceleration. But this option is still problematic because in this case the ground velocity is not eliminated but remains constant. The better choice is to stabilize the ground displacement. If the displacement remains constant, both the velocity and the acceleration become zero. To this end, in this study, first the ground displacement time-history is obtained through the double time-integration of the ground acceleration time-history. Then, the displacement is artificially stabilized. The stabilization is gradual and a second order curve is used. In this way the ground acceleration is gradually decreased and finally eliminated. The earthquake excitation is applied as time-history displacement at the x -translational DOF to the corresponding nodes of the numerical model.

Finally, it is noticed that the branch that corresponds to the constant ground displacement is lengthened for about 20sec. As it is explained in Section 9.3.3, this time period is required in order to ensure that the oscillation of the structural system is totally damped. An illustrative example for the artificial stabilization of the ground motion is depicted in Figure 11-1.

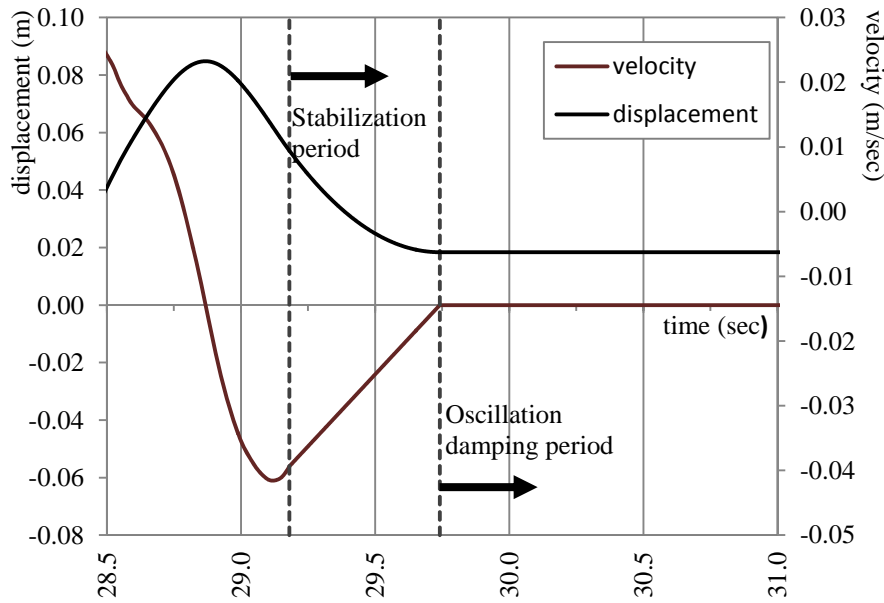


Figure 11-1: Stabilization of the ground motion (1726ya record).

11.4 Definition of the FAE scenarios

The FAE scenarios consist of two distinct stages. The first stage is the earthquake excitation while the second one is the fire-exposure (in the first level of the library building). In this study two different categories are defined according to the gas temperature time-history record that is used for the calculation of the temperature of the structural members. In both categories the same characteristics of the earthquake loading are used.

11.4.1 ISO-FAE scenarios

The ISO-FAE scenarios are concentrated in Table 11-1. Four FAE-scenarios are defined for one accelerogram according to the scaling factors that are used for the intensity of the earthquake action. Thus, totally $4 \times 7 = 28$ ISO-FAE scenarios are generated.

		Time-history acceleration record						
S.F.		290xa	293ya	6142ya	612xa	1726xa	1726ya	5850xa
1.00		E290xa/1.00	E293ya/1.00	E6142ya/1.00	E612xa/1.00	E1726xa/1.00	E1726ya/1.00	E5850xa/1.00
	FISO	FISO	FISO	FISO	FISO	FISO	FISO	FISO
1.25		E290xa/1.25	E293ya/1.25	E6142ya/1.25	E612xa/1.25	E1726xa/1.25	E1726ya/1.25	E5850xa/1.25
	FISO	FISO	FISO	FISO	FISO	FISO	FISO	FISO
1.50		E290xa/1.50	E293ya/1.50	E6142ya/1.50	E612xa/1.50	E1726xa/1.50	E1726ya/1.50	E5850xa/1.50
	FISO	FISO	FISO	FISO	FISO	FISO	FISO	FISO
1.75		E290xa/1.75	E293ya/1.75	E6142ya/1.75	E612xa/1.75	E1726xa/1.75	E1726ya/1.75	E5850xa/1.75
	FISO	FISO	FISO	FISO	FISO	FISO	FISO	FISO

Table 11-1: ISO-FAE scenarios.

11.4.2 Natural-FAE scenarios

The natural-FAE scenarios are defined through the approach that the structural system can suffer different PEF scenarios (related to the level of the non-structural damage), depending on the return period of earthquake (related to the scale factor used for the scaling of the seismic action). According to this approach, the structure can be subjected either moderate or more severe earthquakes. On the other hand, it is considered that the structure can undergo the earthquake through slight, moderate or heavy damage to both structural and non-structural components. These levels of damage depend on the earthquakes intensities and they are connected to both the structural and non-structural components. The idea that is used in this study is that the damage of the non-structural components can generate different PEF scenarios. Thus, the structural system can suffer different PEF scenarios as the earthquake becomes stronger.

The procedure that is used in this study is described in the following. It is considered that as the intensity of the seismic actions is scaled-up using the appropriate scale factors for the PGA, the seismic action level is modified in order to represent more severe actions. Moreover, the non-structural damage is characterized by the breakage of the windows. In this point of view, the level of non-structural damage is connected to the PEF scenarios. In this way, four district levels of damage are considered which are directly related to PEF SC-25, SC-50, SC75 and SC-100.

The natural-FAE scenarios are generated according to the following:

- The structure is submitted to an earthquake of intensity scaled to 1 and *slight* damage is expected (SC-25 and SC-50).
- The structure is submitted to an earthquake of intensity scaled to 1.25 and *moderate* damage is expected (SC-50 and SC-75).
- The structure is submitted to an earthquake of intensity scaled to 1.50 and *severe* damage is expected (SC-75 and SC-100).
- The structure is submitted to an earthquake of intensity scaled to 1.75 and more *severe* damage is expected (SC-100).

The natural-FAE scenarios are specified in Table 11-2, depending on the accelerogram that is used. The name differs according to the code of the accelerogram for example E290xa/1.00-FSC25 or E5850xa/1.00-FSC100. In this way totally 7x7=49 natural-FAE scenarios are generated.

	SC-25 (A or B)	SC-50 (A or C)	SC-75	SC-100
S.F. 1.00	Eaccel/1.00-FSC25	Eaccel/1.00-FSC50		
S.F. 1.25		Eaccel/1.25-FSC50	Eaccel/1.25-FSC75	
S.F. 1.50			Eaccel/1.50-FSC75	Eaccel/1.50-FSC100
S.F. 1.75				Eaccel/1.75-FSC100

Table 11-2: Definition of natural-FAE scenarios for an individual accelerogram.

Taking into account the fact that the study is focused on an *individual* typical structural frame system of the building and that the temperature in the fire-compartment is non-homogenous, the “critical” frame should be identified. This depends on the PEF scenario that is considered. Figure 11-2 illustrates the variation of the temperature of the beams in the fire-compartment with respect to the PEF scenarios. The temperature of the columns is not presented at this point due to the fact that the section factor of the columns is greater compared to the corresponding one of the beams and, consequently, the resulting temperatures of the columns are lower during the fire evolution³. Thus, in this study the selection of the critical frame absolutely depends on the temperature of the beams.

Considering the fact that the final objective is the determination of the fire-resistance of the structural system, the “critical” frame is defined by two different variables. The first one is the “critical” temperature, taking into account the spatial distribution, and the second one is the time when the “critical” temperature takes place. The second variable is set in order to ensure that the fire resistance, in time domain, is the most critical. For example, if the same critical temperature is recorded for two different structural members at different time-frames of the fire exposure, the “critical” one is the one where the maximum temperature (in time-domain) is first reached. Here, the term “critical” temperature is obtained through a “simple calculation” model. Specifically, a fixed beam “replaces” the beam of the first level of the structural system. The temperature at which the fixed beam fails due to the formulation of unstable system (three plastic hinges) can be easily obtained by simple calculations. The calculation of the “critical” temperature is illustrated in Figure 11-3 and, according to the data, is calculated equal to 700 °C. In the case where the temperature of the structural member does not exceed the “critical” one during the fire exposure, the maximum temperature that is recorded is used instead of the critical one.

³ It is noted that the frames B, C, D and L are not included in the diagrams due to the fact that the gas-temperature is very low in the corresponding zones. Moreover the SC12.5 is not presented due to the low temperature field in the compartment. Concerning the three different scenarios where the 50% of the windows are broken, the most unfavorable scenarios are considered here which are the SC-50A and SC-50B.

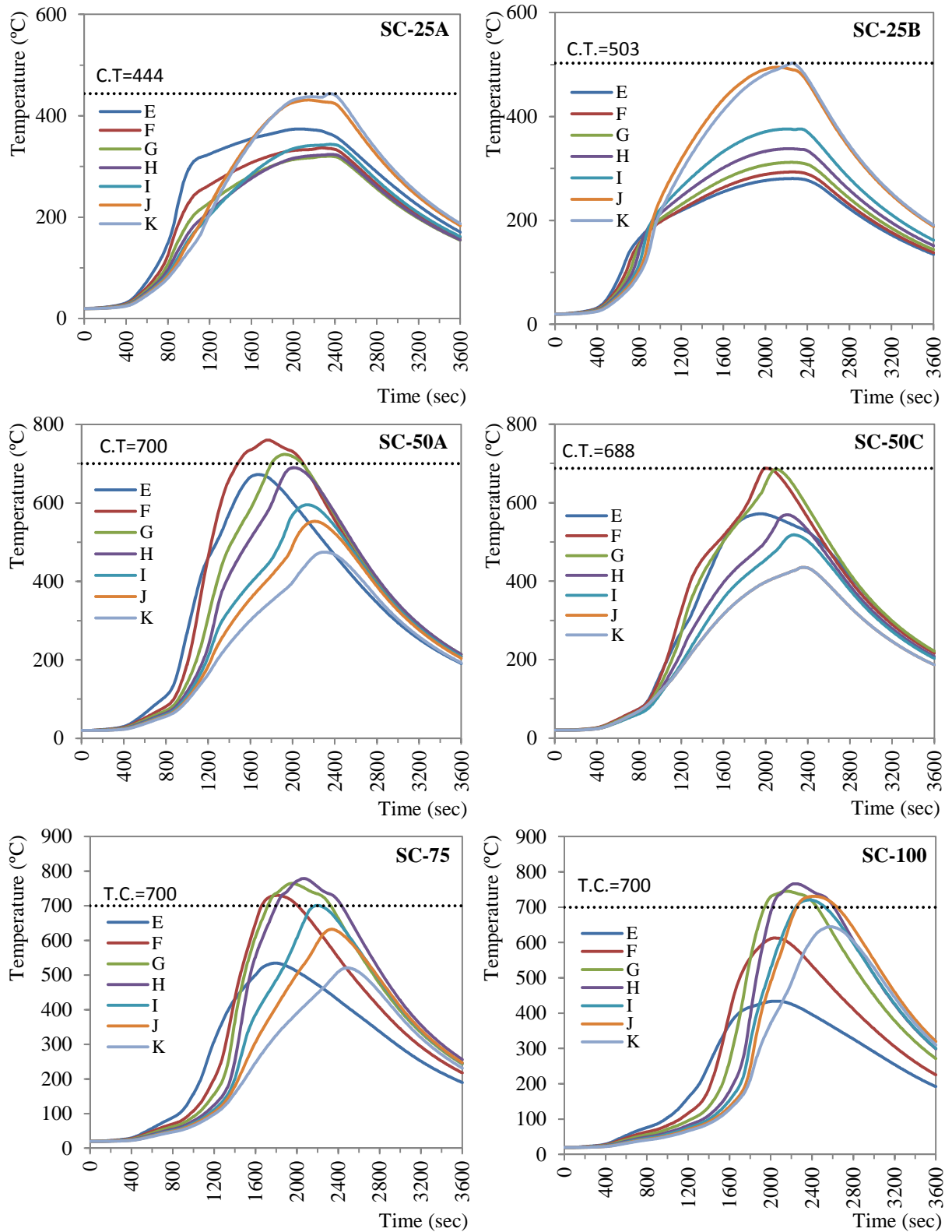


Figure 11-2: Temperature time-history curves for the beams with respect to the PEF scenarios.

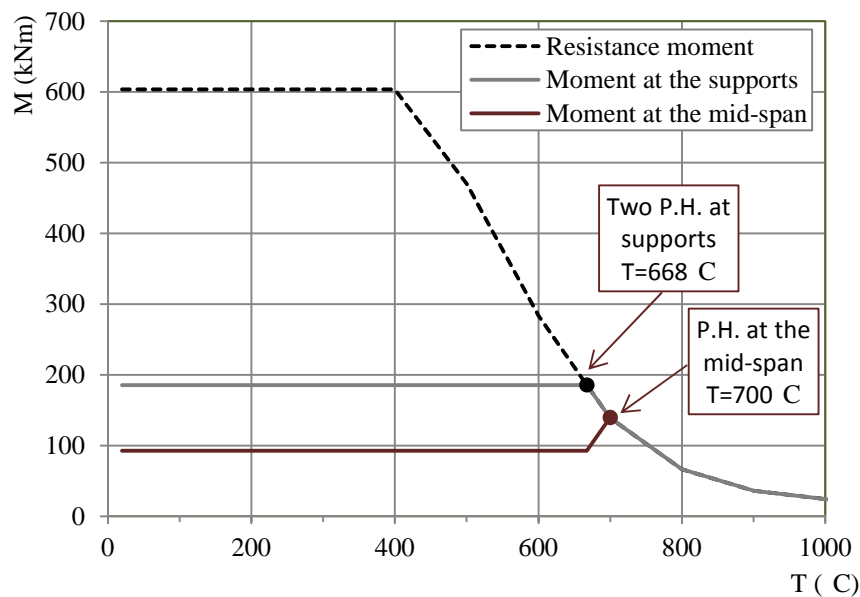


Figure 11-3: Calculation of the critical temperature according to the simple calculation model.

According to the previous, the critical frames are selected and they are depicted in Table 11-3 for the different PFE scenarios.

PFE scenario	SC-25A	SC-25B	SC-50A	SC-50C	SC-75	SC-100
Critical frame	K	K	F	F	F	G
Peak temperature	443.70 °C	502.65 °C	760.31 °C	687.62 °C	730.19 °C	745.18 °C

Table 11-3: The critical frames of the structure according to the PEF scenarios.

Regarding the PEF scenarios where the 25% and the 50% of the windows are broken, the most unfavorable case is chosen between the SC-25A /SC-25B and SC-50A /SC-50C respectively. The selection is based on the maximum peak temperature that is recorded. The comparison indicates that the maximum temperatures are met in SC-25B and SC-50A. Thus, the natural-FAE scenarios will be based on the particular PEF scenarios. The SC-25A and SC-50C are not further studied.

11.5 Results of the numerical analyses

The results are presented in two different sections for the ISO and the natural FAE scenarios respectively.

11.5.1 ISO-FAE scenarios

The deformed shape of the structural system at characteristic time instants during the fire exposure and the equivalent plastic strain field (Layer 1) are illustrated in Figure 11-4, Figure 11-8, Figure 11-12 and Figure 11-16 for the FAE scenarios E290xa-1.00-FISO, E290xa-1.25-FISO, E290xa-1.50-FISO and E290xa-1.75-FISO respectively. It is noted that in all cases the analysis stops due to convergence failure. Moreover, in all the FAE scenarios, the plastic hinges are formed at both the upper and the lower ends of the exterior

columns of the fire-compartment. It can be observed that the rest members of the structural system are not strongly influenced during the fire exposure.

The axial force that is developed in both the beams (Beam 1A and Beam 1B) and the mid-span vertical displacement during the thermal loading are presented in Figure 11-9, Figure 11-13, Figure 11-17 and Figure 11-20 for the seismic scale factors 1.00, 1.25, 1.50 and 1.75 (E290xa-FSIO) respectively. Comparing the behaviour of Beam 1A and Beam 1B, it is clear that, taking into account the deflection and the axial force, the behaviour of both beams is almost identical, and this is independent from the factor that is used for the escalation of the seismic intensity. The evolution of the axial force with time and the maximum recorded values do not change significantly for the different FAE scenarios. Specifically, the maximum recorded axial force fluctuates between 710 and 730kN and the corresponding temperature lies between 500 and 520°C. Moreover, it is observed that for moderate earthquake excitations (E290xa-1.00 and E290xa-1.25) the catenary action takes place. Considering the evolution of the mid-span deflection, it is observed that the vertical displacement of the beams is rapidly increased during the *increase of curvature stage* and this holds for all the scenarios. The evolution of the mid-span deflection is absolutely dependent on the value that is recorded at the end of the seismic loading. Actually, as the seismic intensity is scaled up, the deflection curve is shifted downwards, depending on the mid-span deflection that is imposed due to earthquake (Figure 11-20).

At this point it is noted that deflection limits are imposed in practice, in order to avoid excessive deformations. For flexural members the limit value that is usually used is equal to $d_{lim} = L^2 / 400d$, where L is the length of the span and d is the depth of the section in mm. The application of the above criterion for the case treated here gives 320mm.

It can be observed that unstable mechanisms (three continuous plastic hinges) are formed at both beams that are exposed to fire, at the end of the analyses. The distributions of the equivalent plastic strains along the cross-sections of the structural elements at the support and at the mid-span locations (for both the fire-exposed beams) are presented in Figure 11-6, Figure 11-10, Figure 11-14 and Figure 11-18 for the scenarios E290xa-1.00-FISO, E290xa-1.25-FISO, E290xa-1.50-FISO and E290xa-1.75-FISO respectively. Each diagram includes four curves for different instants of the fire exposure. These instants represent characteristic points of the fire exposure. The first one corresponds to the starting point, the second to the thermal expansion stage (600th sec), the third to the early phase of the *increase of curvature* stage (1000sec) and the last to the ending of the same stage (1400th sec). It can be observed that at both supports, the plastic strain distribution is symmetric with respect to the centroid axis of the cross-section. This distribution remains unchanged and identical to the profile at the end of the earthquake loading, during the *restrained thermal expansion* phase and until the early stages of the *increase of curvature* phase. As the temperature increases, the plastic strains increase quickly and the profile becomes unsymmetrical. Considering the mid-span, plastic strains are developed at the upper (compression) flange of the beam during the *restrained thermal expansion* phase and the

profile is not-symmetric with respect to the centroid axis of the cross-section. The values of the plastic strain increase rapidly during the *increase of curvature* stage and the values become extremely large at the compression flange. In general, the amplitude of the equivalent plastic strain is higher at the support locations with respect to the corresponding values at the mid-span. Additionally, the profile is not identical at the Left (L) and the Right (R) end of the beams, due to the different axial and rotational degree of restraint that is provided from the adjacent members. Moreover, as the seismic intensity is scaled-up, increased values of equivalent plastic strain are recorded.

The temporal evolution of the rotation, at the support positions of both beams, is presented in Figure 11-7, Figure 11-11, Figure 11-15 and Figure 11-19 for the ISO-FAE scenarios that correspond to accelerogram 290xa. It is noticed that the results are not the same for the two beams (Beam 1A and 1B) that are exposed to fire. Moreover, the rotation at the support locations of each beam is different.

In general, the rotation that develops at the ends of the beams is dependent on the imposed rotation at the end of the earthquake loading. At this point, it should be clarified that the rotation that is used here is the rotation of the plastic hinge that is located at the end of the heated beam. It can be observed that at the early stages of the fire exposure (*restrained thermal expansion* stage) the rotation curves that correspond to the Left (L) and the Right (R) supports are completely different. As the temperature increases, the values are significantly increased and they are almost the same for both ends of the beams. The previous remarks are valid for all the FAE scenarios.

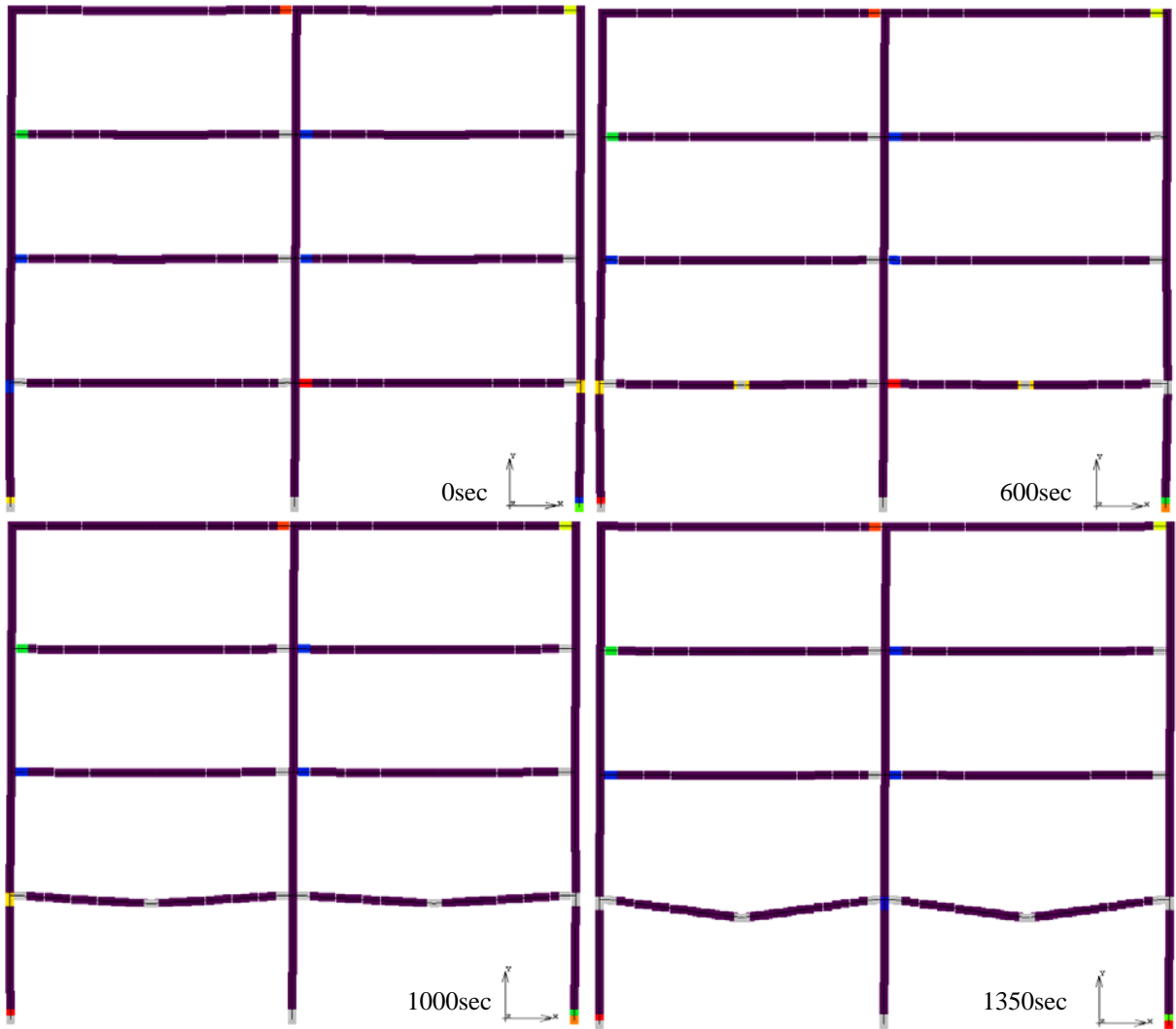


Figure 11-4: Deformed shape of the structural system and the equivalent plastic strain distribution (Layer 1) during the FAE loading for scenario E290xa-1.00-FISO.

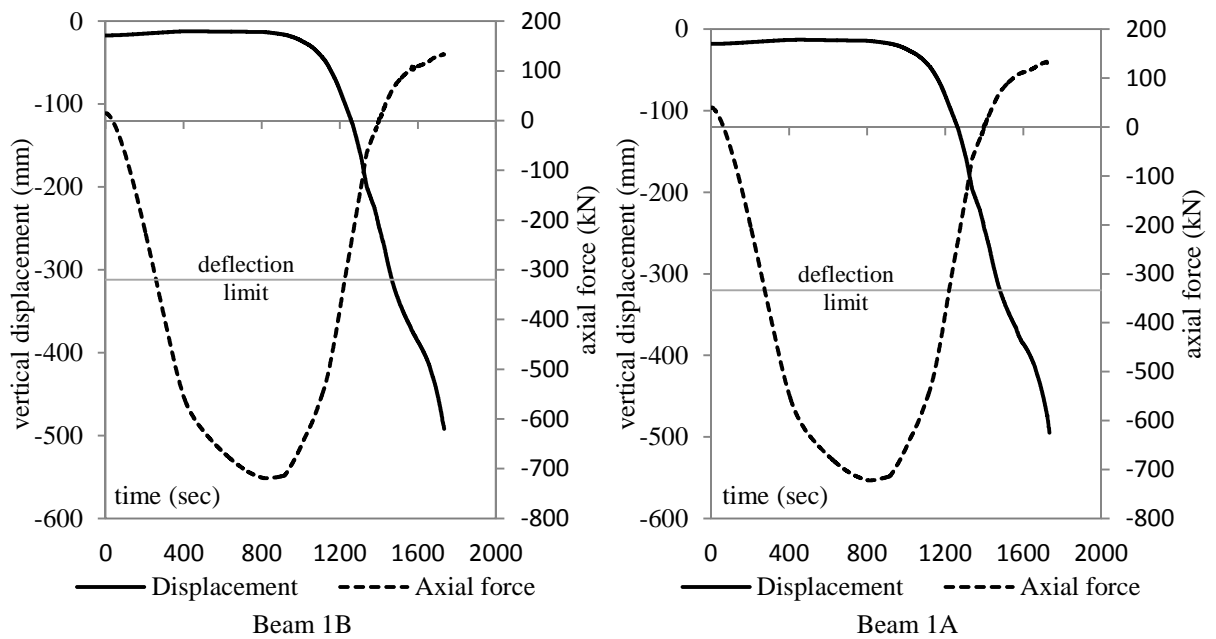


Figure 11-5: Vertical displacement and axial force time-history for scenario E290xa-1.00-FISO.

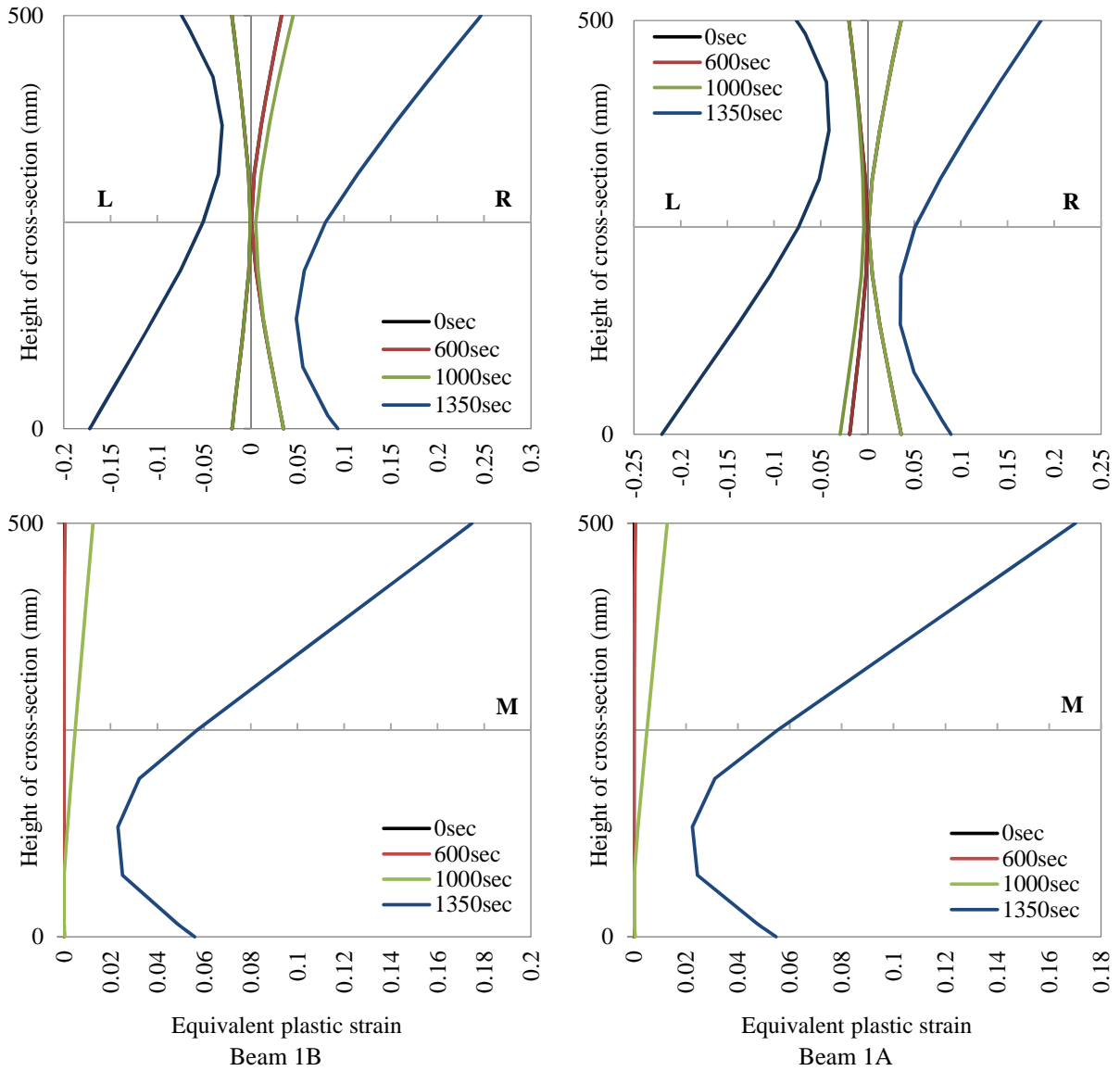


Figure 11-6: Eq. plastic strain distribution in the cross-section for scenario E290xa-1.00-FISO.

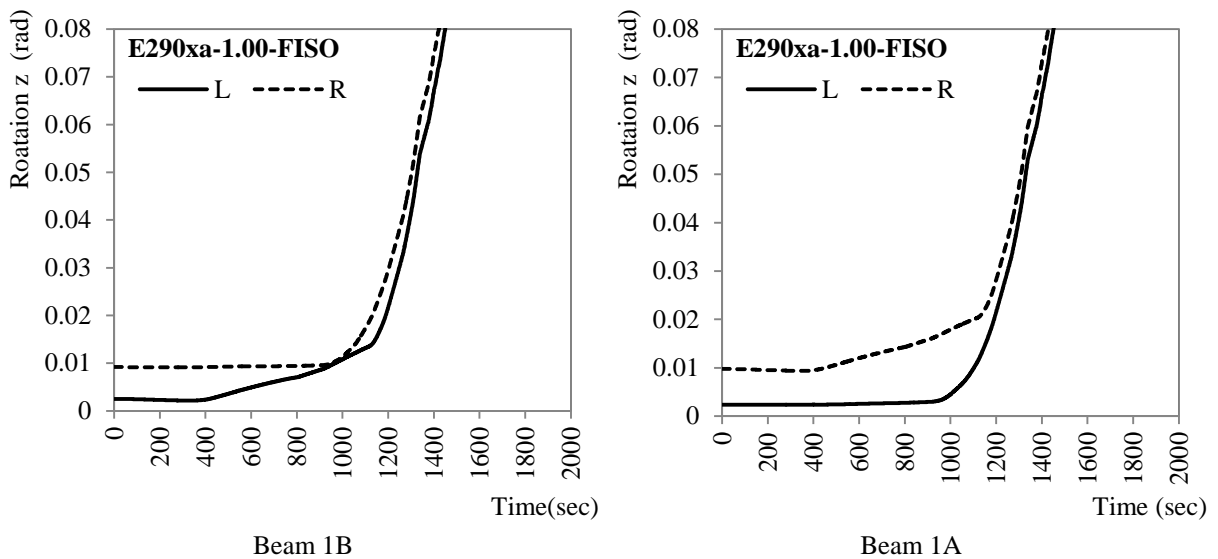


Figure 11-7: Rotation z time-history for scenario E290xa-1.00-FISO.

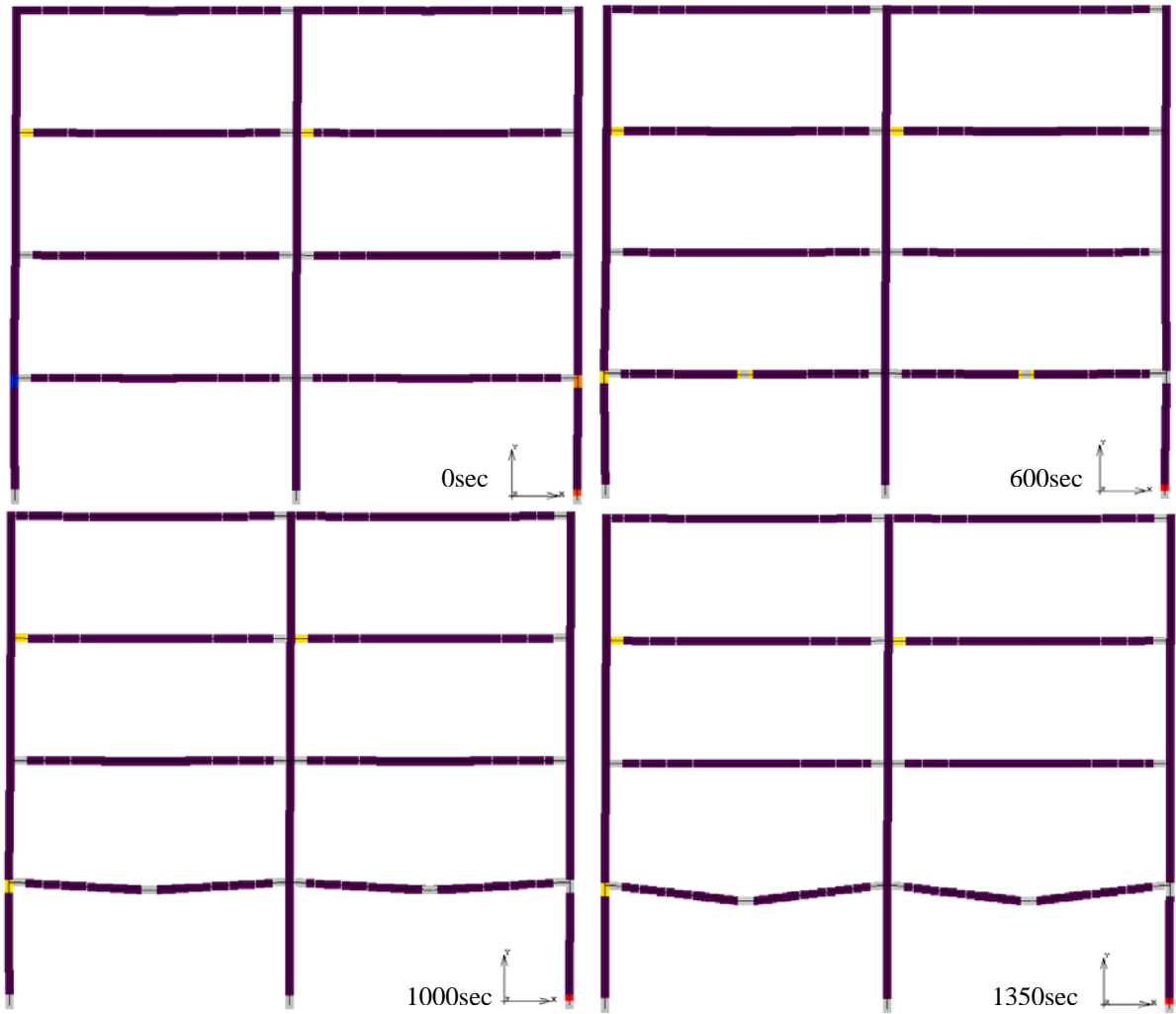


Figure 11-8: Deformed shape of the structural system and the equivalent plastic strain distribution (Layer 1) during the FAE loading for scenario E290xa-1.25-FISO.

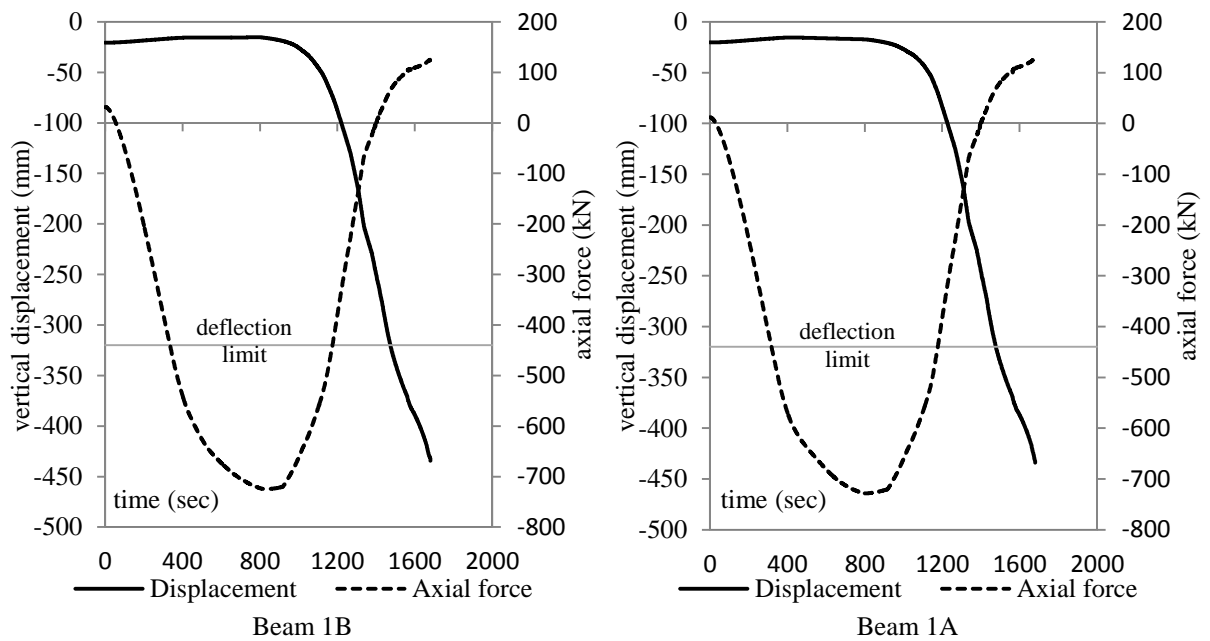


Figure 11-9: Vertical displacement and axial force time-history for scenario E290xa-1.25-FISO.

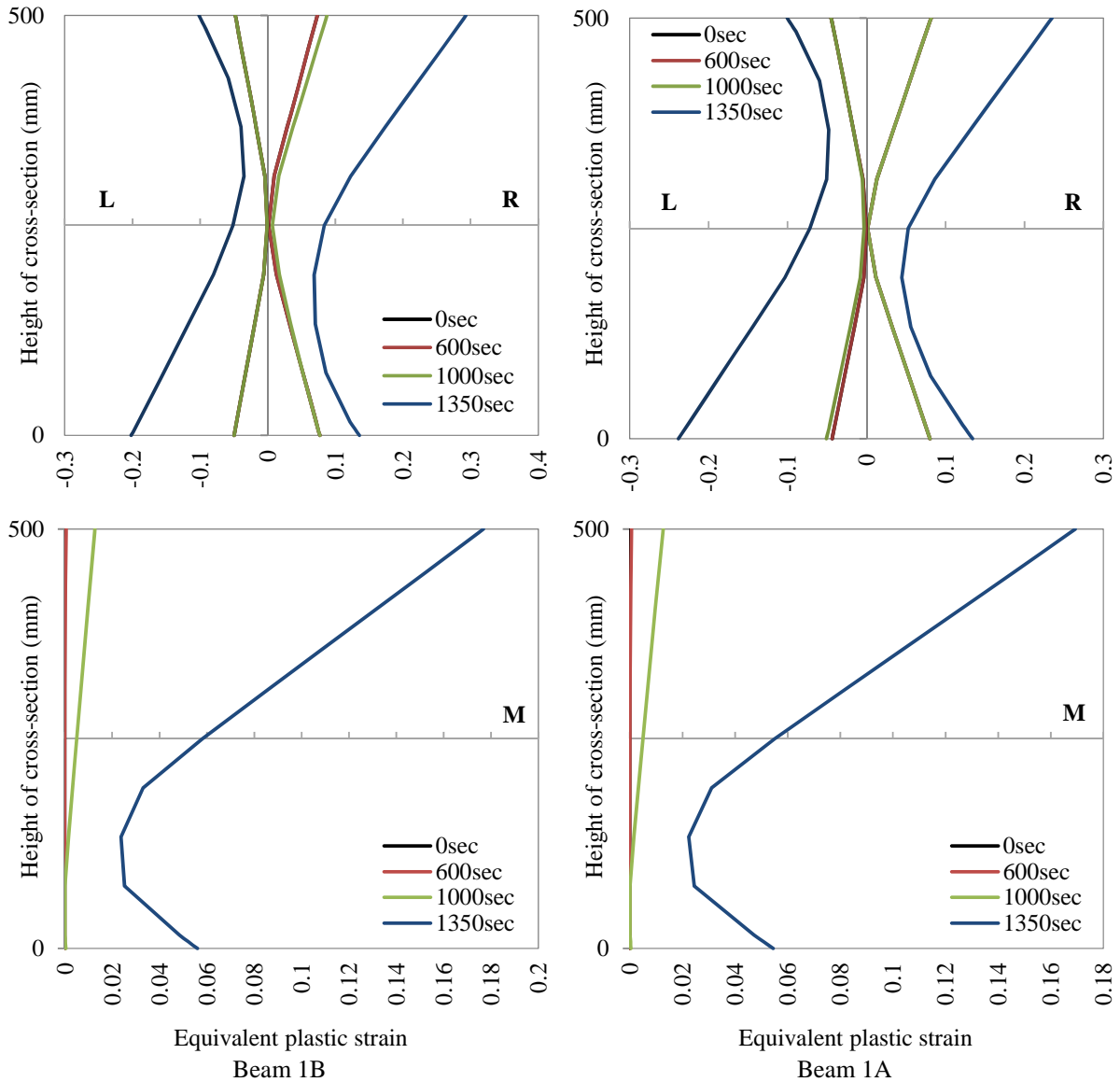


Figure 11-10: Eq. plastic strain distribution in the cross-section for scenario E290xa-1.25-FISO.

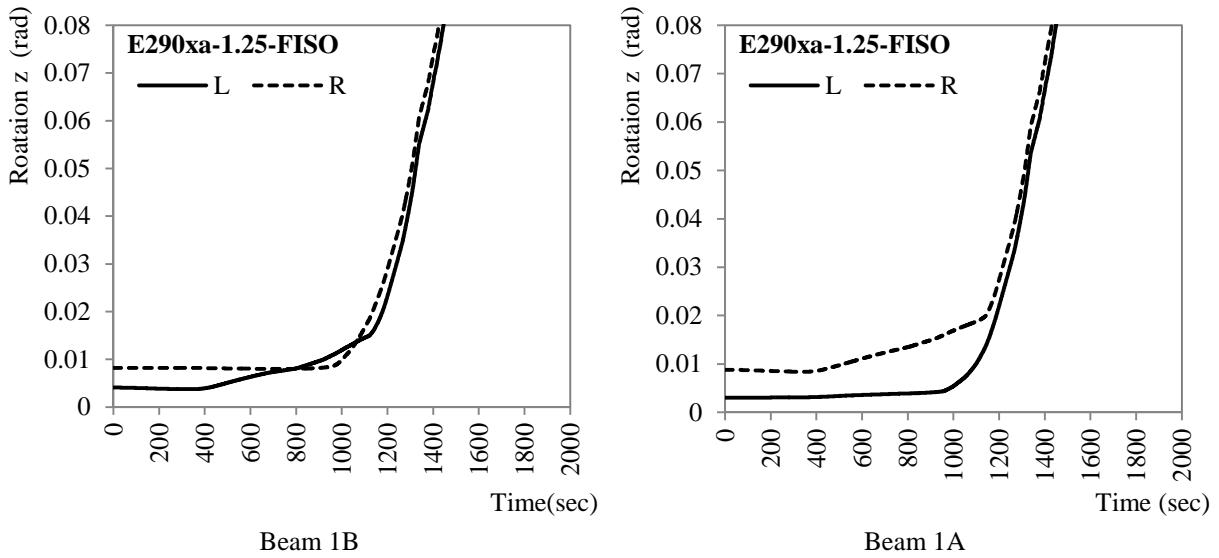


Figure 11-11: Rotation z time-history for scenario E290xa-1.25-FISO.



Figure 11-12: Deformed shape of the structural system and the equivalent plastic strain distribution (Layer 1) during the FAE loading for scenario E290xa-1.50-FISO.

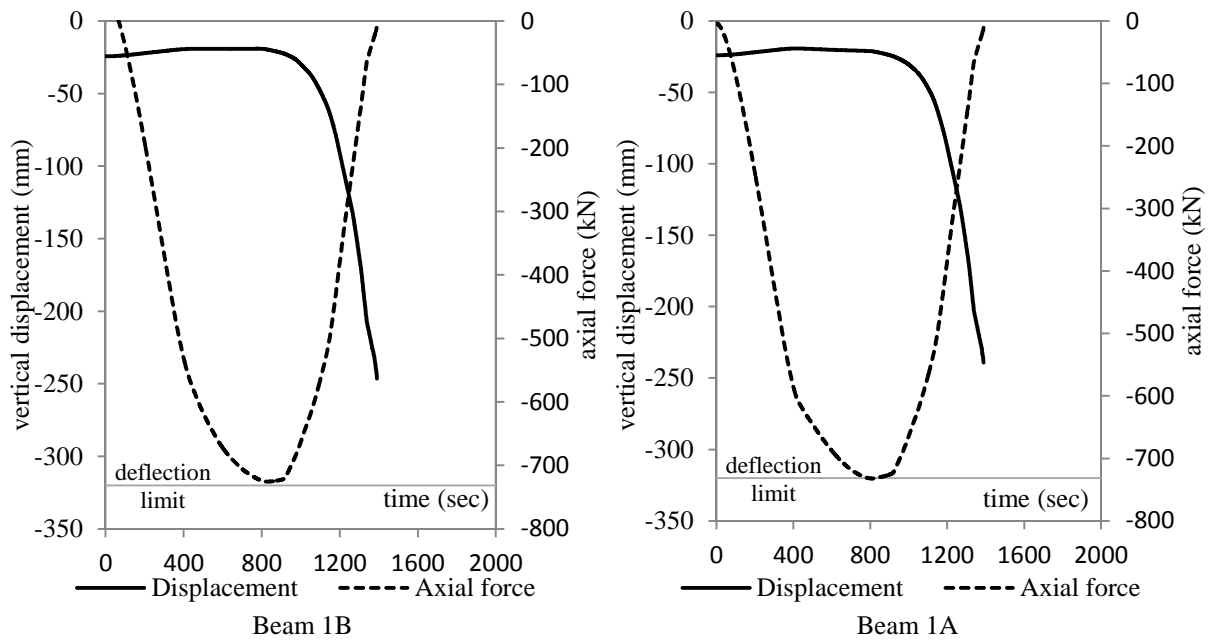


Figure 11-13: Vertical displacement and axial force time-history for scenario E290xa-1.50-FISO.

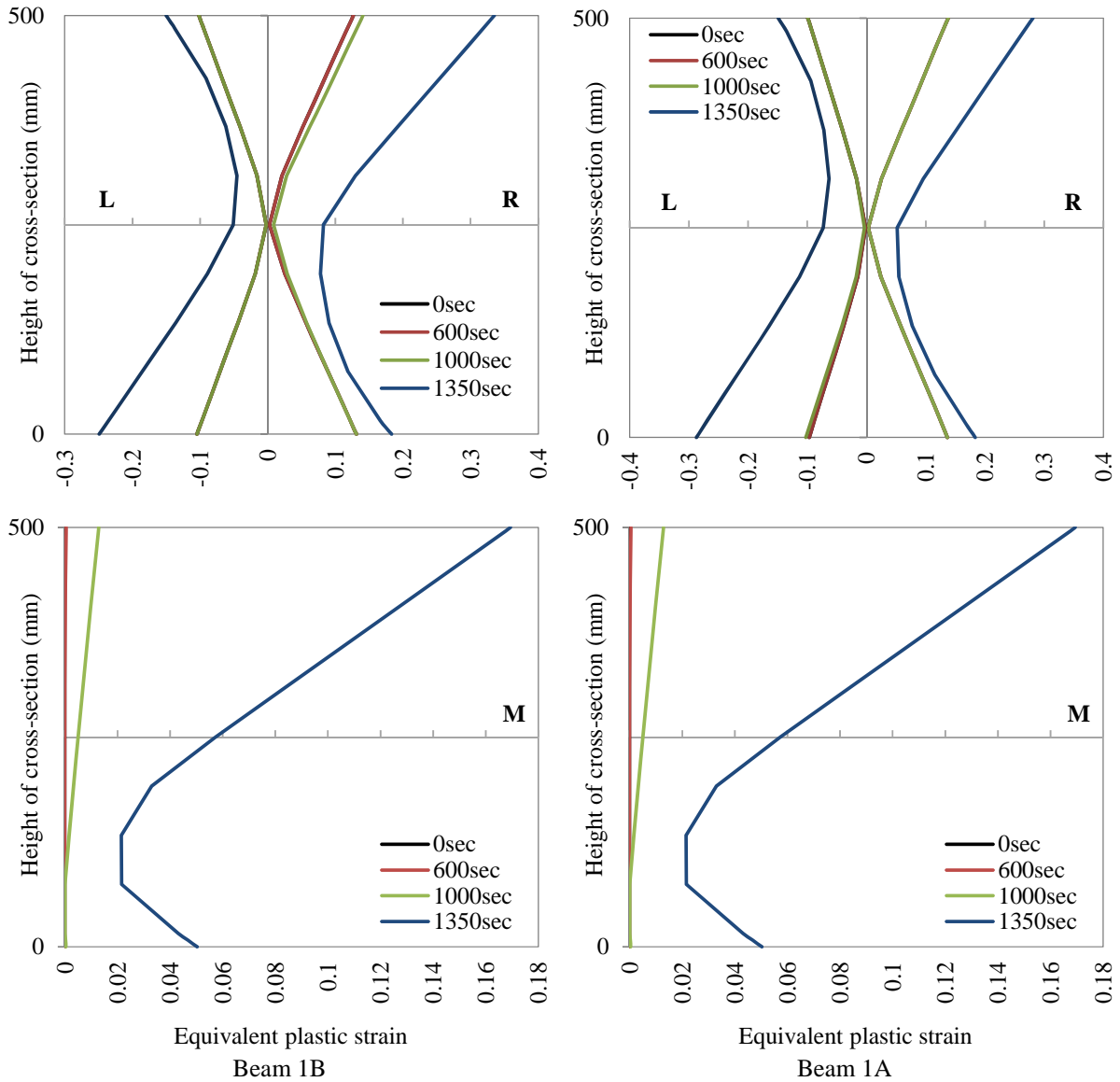


Figure 11-14: Eq. plastic strain distribution in the cross-section for scenario E290xa-1.50-FISO.

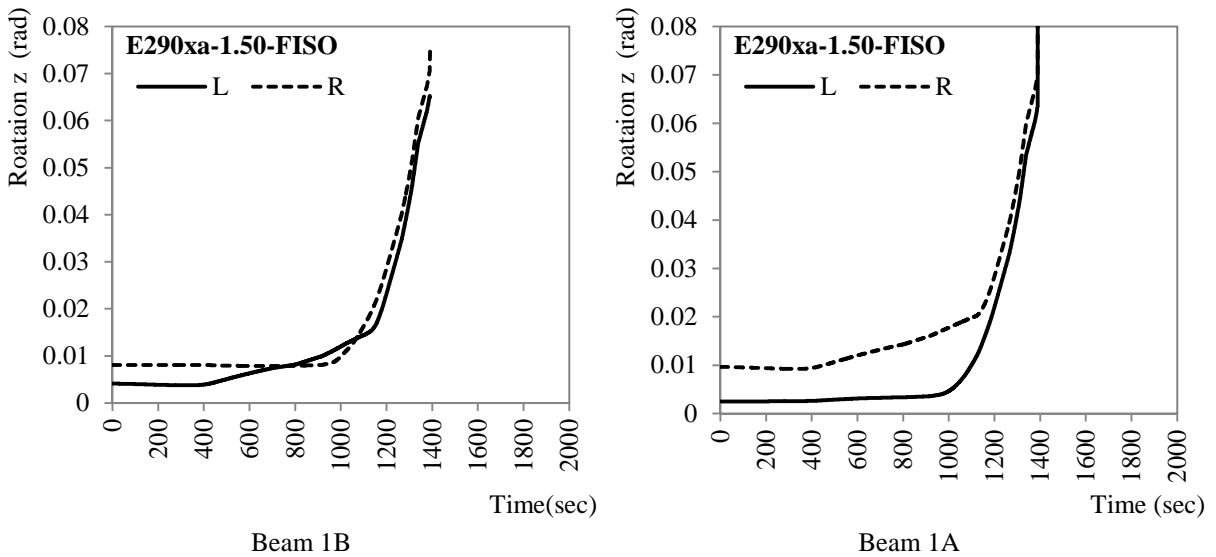


Figure 11-15: Rotation z time-history for scenario E290xa-1.50-FISO.

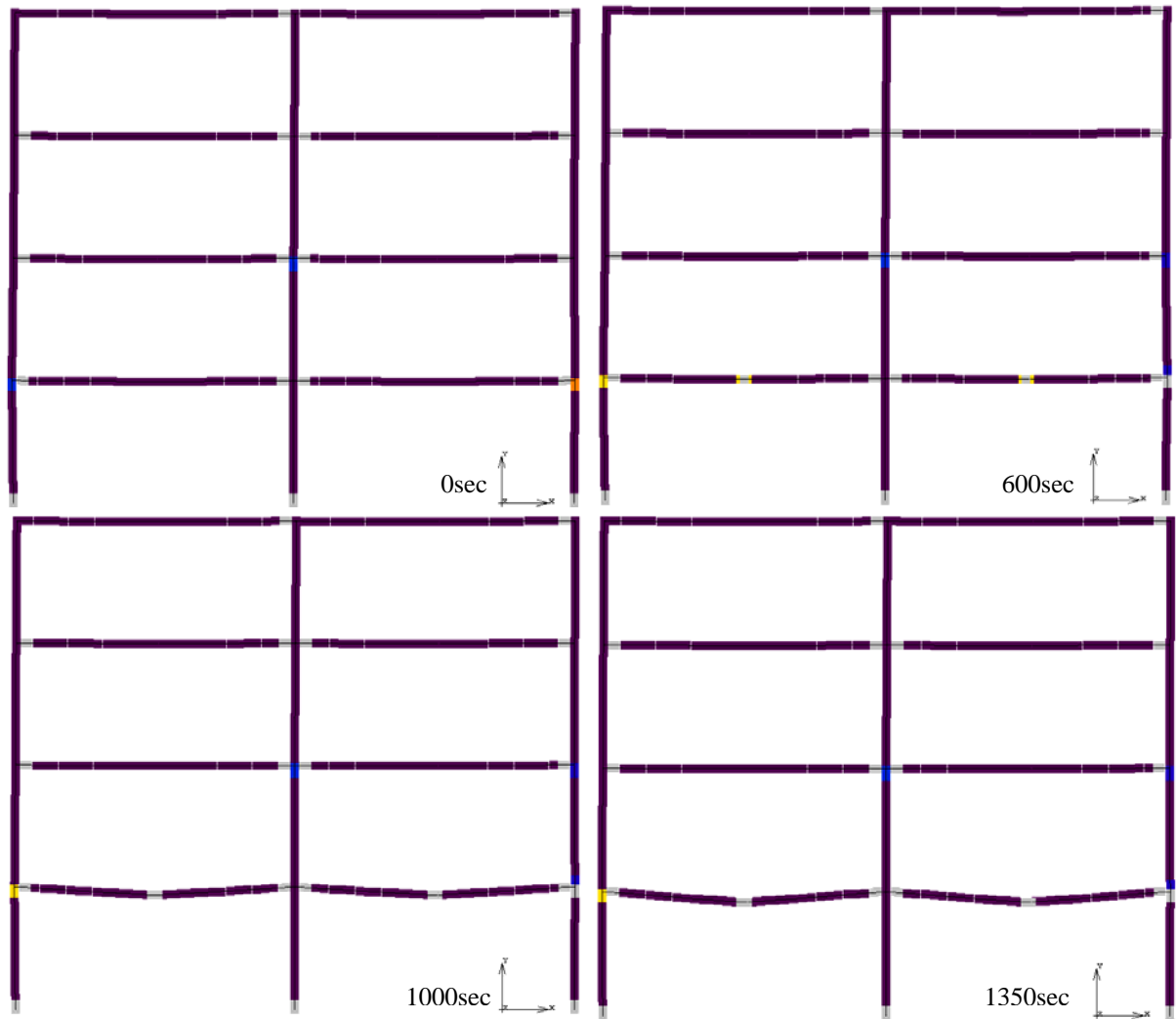


Figure 11-16: Deformed shape of the structural system and the equivalent plastic strain distribution (Layer 1) during the FAE loading for scenario E290xa-1.75-FISO.

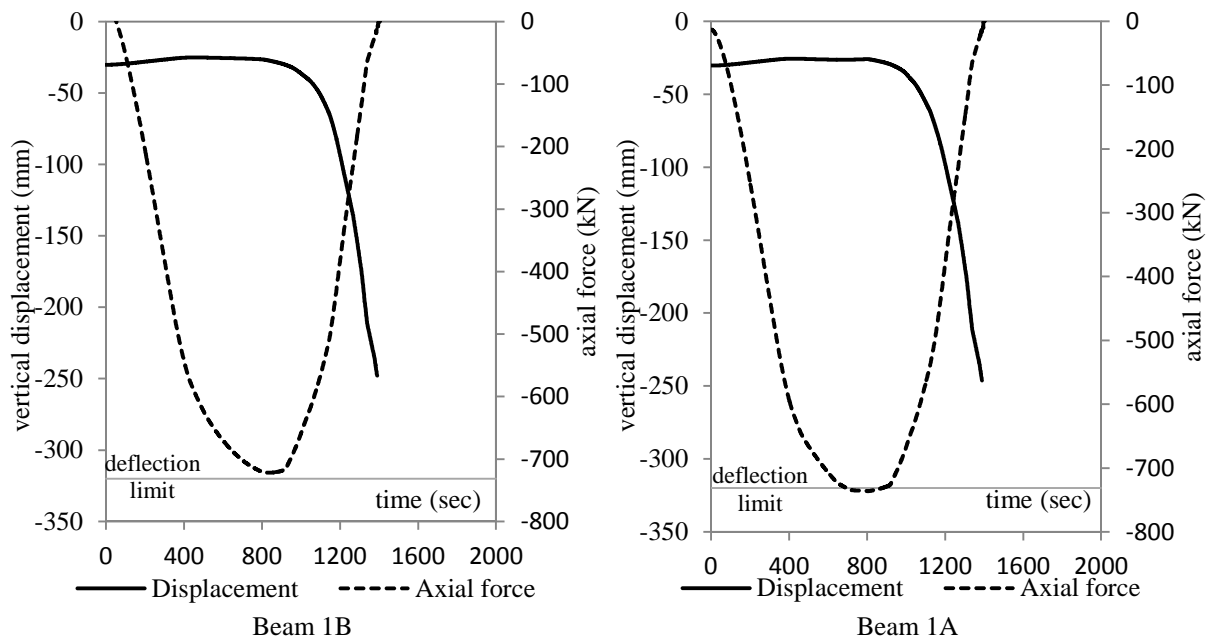


Figure 11-17: Vertical displacement and axial force time-history for scenario E290xa-1.75-FISO.

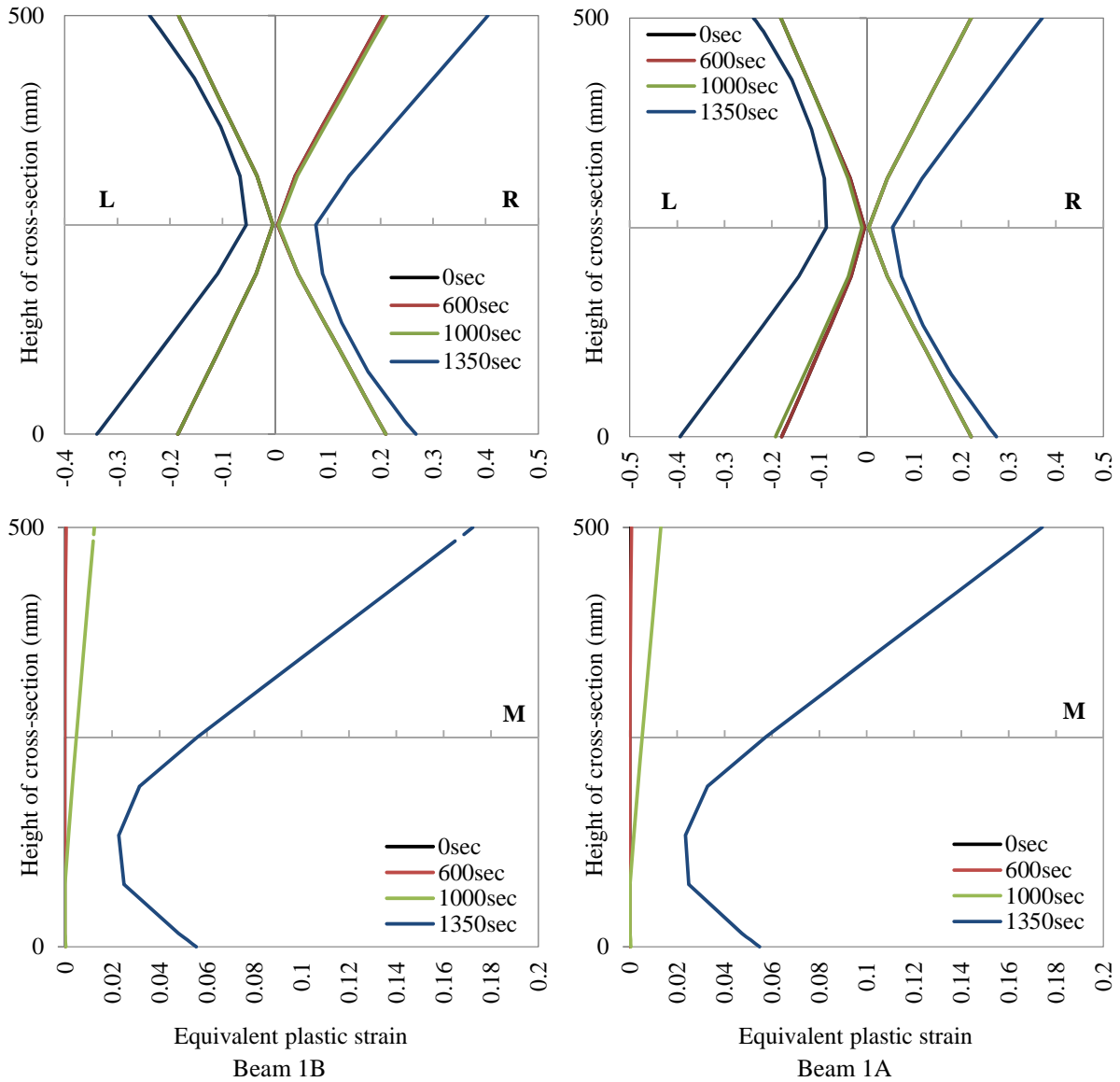


Figure 11-18: Eq. plastic strain distribution in the cross-section for scenario E290xa-1.75-FISO.

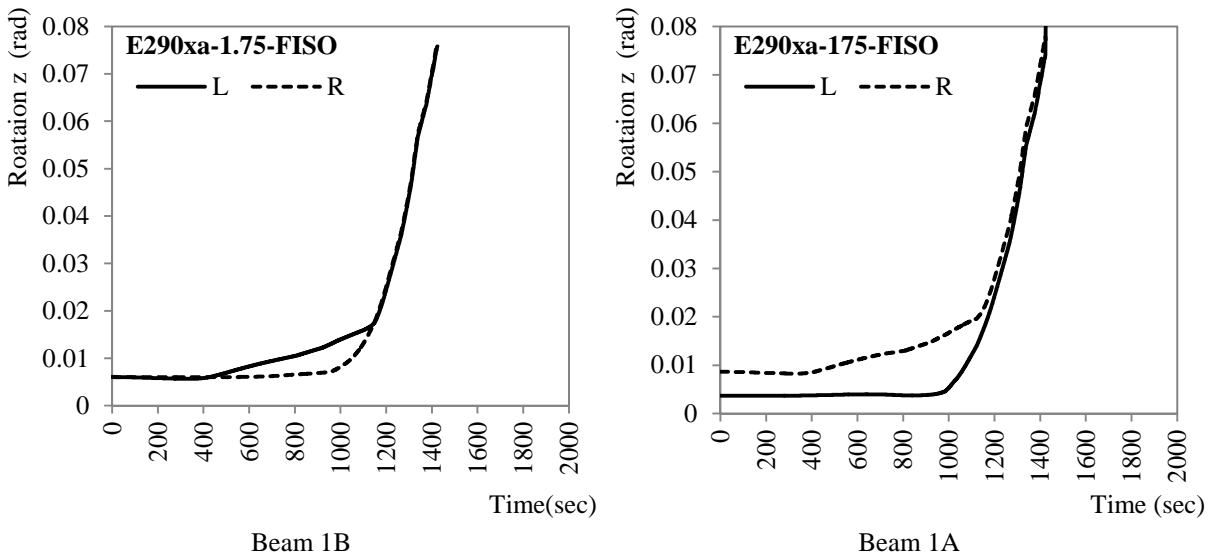


Figure 11-19: Rotation z time-history for scenario E290xa-1.75-FISO.

Figure 11-20 presents the evolution of the mid-span deflection of Beam 1A with time for all the ISO –FAE scenarios. Each diagram corresponds to a specific ground motion acceleration record. As the scale factor, used for the amplification of the earthquake intensity increases, the mid-span deflection curve is shifted accordingly. This holds for all the cases that are considered in this study.

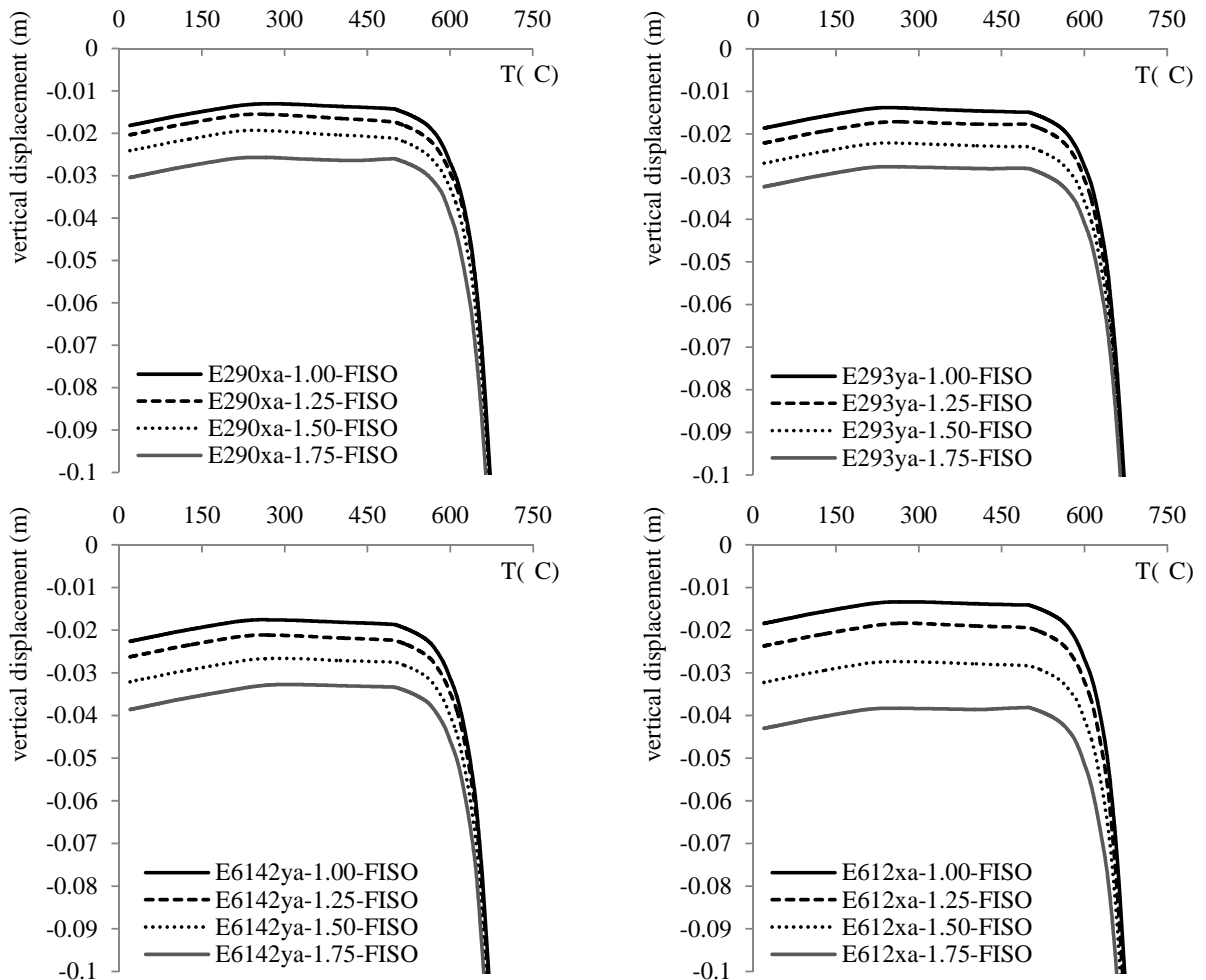


Figure 11-21: Vertical displacement (dy) at the mid-span of Beam 1A versus temperature. (continued)

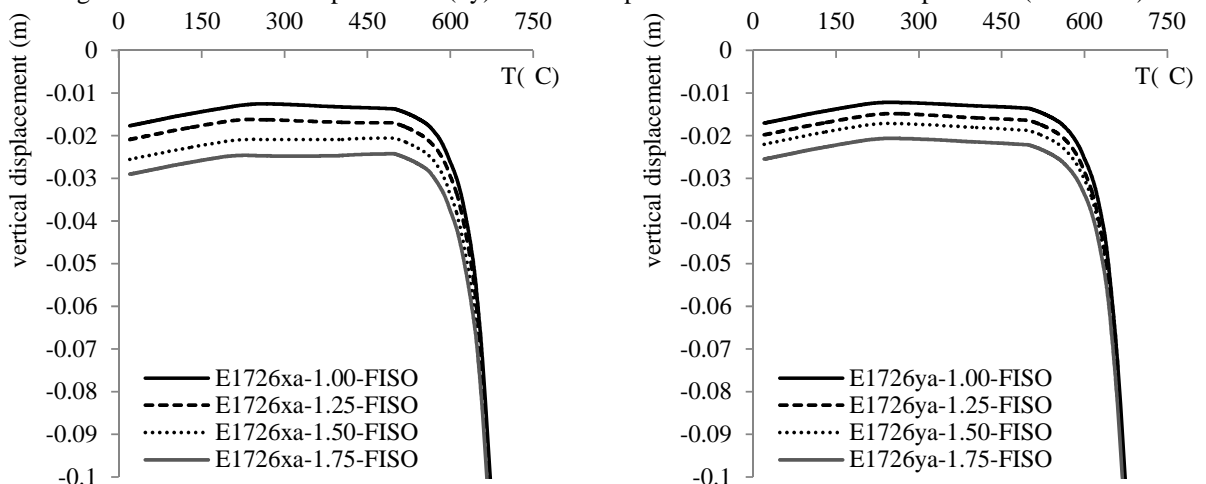


Figure 11 20: Vertical displacement (dy) at the mid-span of Beam 1A versus temperature. (continued)

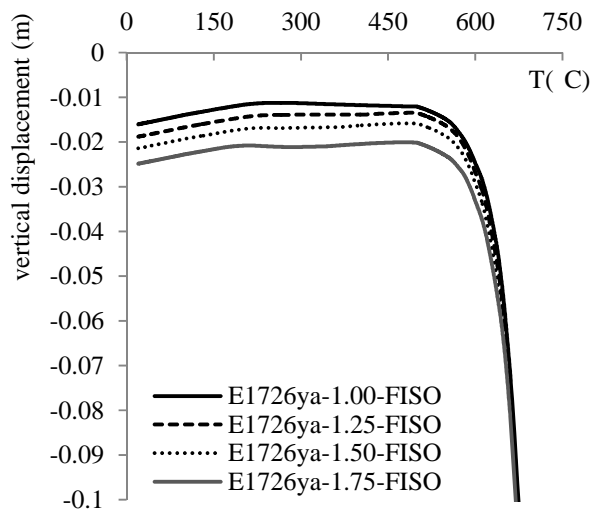


Figure 11-20: Vertical displacement (d_y) at the mid-span of Beam 1A versus temperature.

11.5.2 Natural-FAE scenarios

This section studies the behaviour of the structure for the natural-FAE scenarios. Figure 11-21 presents the axial force (N) and the vertical displacement (d_y) at mid-span for the natural-FAE scenarios that are generated using accelerogram 290xa. Each diagram corresponds to a specified scale factor of the seismic intensity and includes the corresponding PEF scenarios. In all the cases, there is a clear distinction between the *restrained thermal expansion* and the *increase of curvature* stages. It is observed that, for a specific scale factor of the earthquake intensity which indicates a certain level of structural damage, the temporal evolution of both the axial force and the vertical mid-span deflection during the fire exposure is dependent on the level of the non-structural damage. Specifically, the duration of the *restrained thermal expansion* stage is absolutely dependent on the temperature of the structural element. This stage is terminated in all cases when the beam temperature is between the 475°C and 500°C. This indicates that the temperature which corresponds to the maximum axial force is not strongly dependent on the scale factor that is used for the escalation of the accelerogram, neither to the PEF scenario. On the other hand, the time that corresponds to the termination of the thermal expansion stage depends on the temperature of the structural member. As it is presented in Table 11-4, the duration of the *restrained thermal expansion* stage takes place until the 1231st, 1474th and 1861st sec for the SC50, SC-75 and SC-100, regardless of the scale factor of the earthquake intensity used. It is observed that as the structural damage is escalated, the duration of the *restrained thermal expansion stage* is elongated. This is attributed to the temperature time-history of the beam which follows the temporal “delay” of the HRR curve as it is explained in Section 8.2.2. The maximum recorded values of the axial force are presented in Table 11-5. It is observed that the maximum recorded axial force is reduced as the scale factor of the earthquake intensity is amplified.

The following stage, which is dominated by the bending behaviour of the beam and the mid-span deflections are significantly increased, is terminated approximately at the same temperature level (approximately 715°C) for all the FAE scenarios that are studied. The

time that corresponds to the termination of the *increase of curvature* stage depends on the scale factor of the seismic intensity. This indicates that the duration of this stage is decreased as the level of the structural damage that is induced due to earthquake is amplified. Additionally, it is noted that for the more severe earthquake actions, the catenary action does not take place (E290xa-1.50-FSC100 and E290xa-1.75-FSC100).

In the case of E290xa/1.00-FSC25 the maximum temperature is 444°C and the structural system does not fail during the fire exposure.

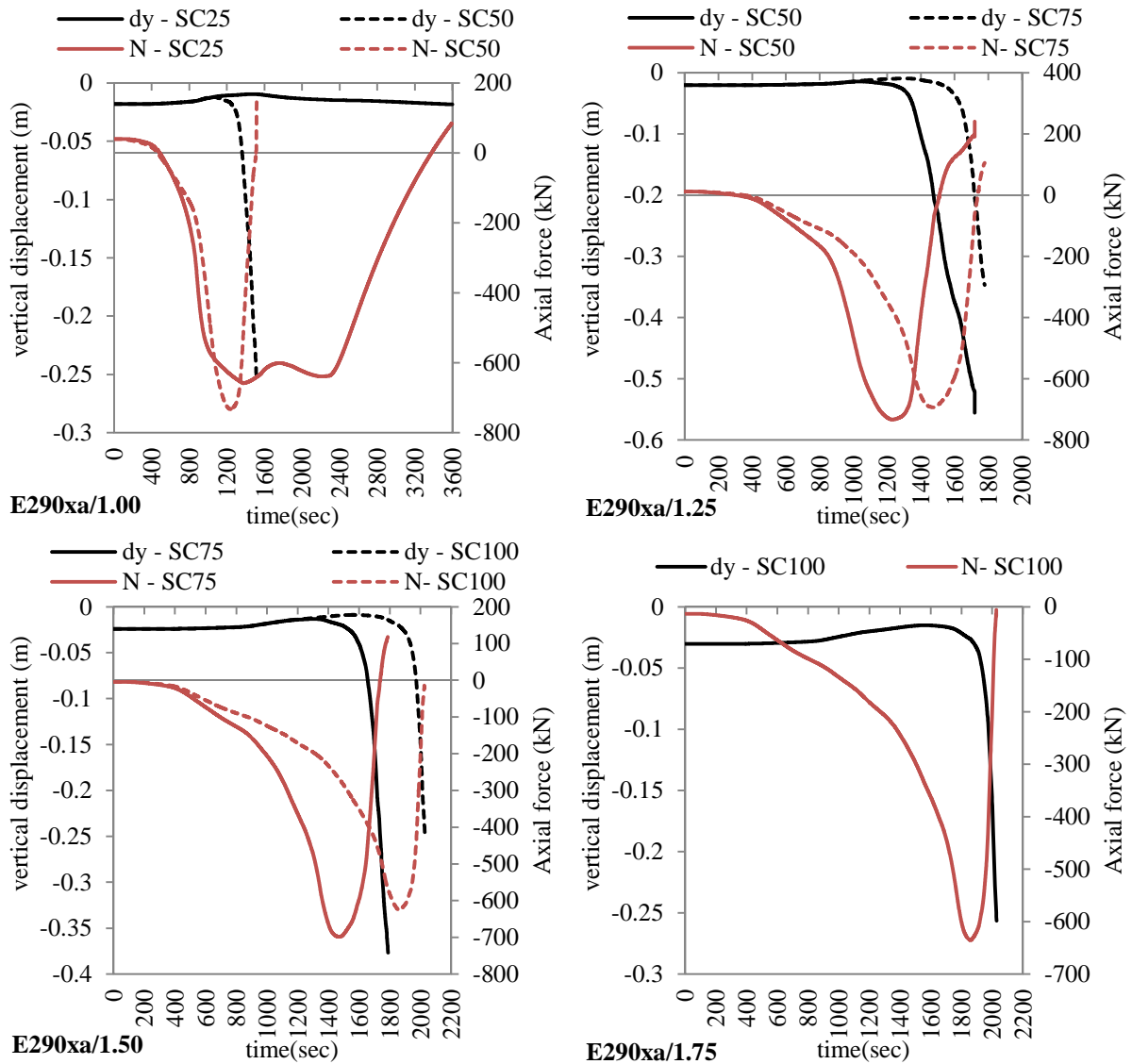


Figure 11-21: Axial force and vertical displacement evolution with time for the natural-FAE scenarios (accelerogram290xa).

FAE scenario	<i>Restrained thermal expansion stage</i>		<i>Increase of curvature stage</i>		
	Termination (time)	Termination (Temperature)	Termination (time)	Termination (Temperature)	Duration
290xa/ 1.00/SC25	645 sec	374°C	-	-	
290xa/ 1.00/SC50	1231 sec	500°C	1512 sec	714°C	281 sec
290xa/ 1.25/SC50	1231 sec	500°C	1511 sec	714°C	280 sec
290xa/ 1.25/SC75	1474 sec	476°C	1737 sec	712°C	263 sec
290xa/ 1.50/SC75	1472 sec	474°C	1737 sec	713°C	265 sec
290xa/ 1.50/SC100	1861 sec	501°C	2030 sec	713°C	169 sec
290xa/ 1.75/SC100	1860 sec	499°C	2030 sec	712°C	170 sec

Table 11-4: The distinct stages of the fire exposure for the FAE scenarios.

	SC-25	SC-50	SC-75	SC-100
290xa/ 1.00	658kN	-733 kN		
290xa/ 1.25		-734 kN	-693kN	
290xa/ 1.50			-698kN	-626kN
290xa/ 1.75				-636kN

Table 11-5: Maximum axial force for the natural-FAE scenarios.

The equivalent Von Mises stress at the Upper (Upper Layer -UL) and the Lower flanges (Lower Layer-LL) of Beam 1A are presented in Figure 11-22, Figure 11-23 and Figure 11-24 for the Left end, the Right end and the Mid-span of Beam 1A respectively. Each diagram corresponds to a specific scale factor of the earthquake intensity and the related PEF scenarios are included. The corresponding diagrams for the equivalent plastic strain are presented in Figure 11-25, Figure 11-26 and Figure 11-27. Moreover, the evolution of the yield stress with time is introduced in each diagram and this curve is dependent on the fire scenario studied. Considering the Left end of the beam, it is observed that the Von-Mises temporal evolution during the restrained thermal expansion stage depends on both the scale factor of the seismic damage and on the PEF scenario that is used. Moreover, during the *increase of curvature* stage, the Lower flange, which is in compression, yields earlier than the Upper flange. On the contrary, during the same stage the behaviour is different in the Right end of the beam and the Upper flange reaches the yield limit earlier than the Lower flange. This is valid for all the PEF scenarios that are studied here. Concerning the mid-span, it can be observed that in all the cases the Von Mises stress in the Upper flange is increased during the *thermal expansion stage* until the maximum value is reached. In the sequel, the stress decreases and during the *increase of curvature* stage the flange yields. The stress at the lower (tension) flange during the *thermal expansion stage* is initially decreased. In the following, the stress is slightly increased until the end of this stage. During the *increase of curvature* stage the stress at the lower flange continues to decrease until yielding. In both flanges the yield limit is attained approximately at the same time. Finally, it can be noticed that the equivalent plastic strains remain almost constant during the *thermal expansion stage*. In the stage that follows, the values of the plastic strains are significantly increased.

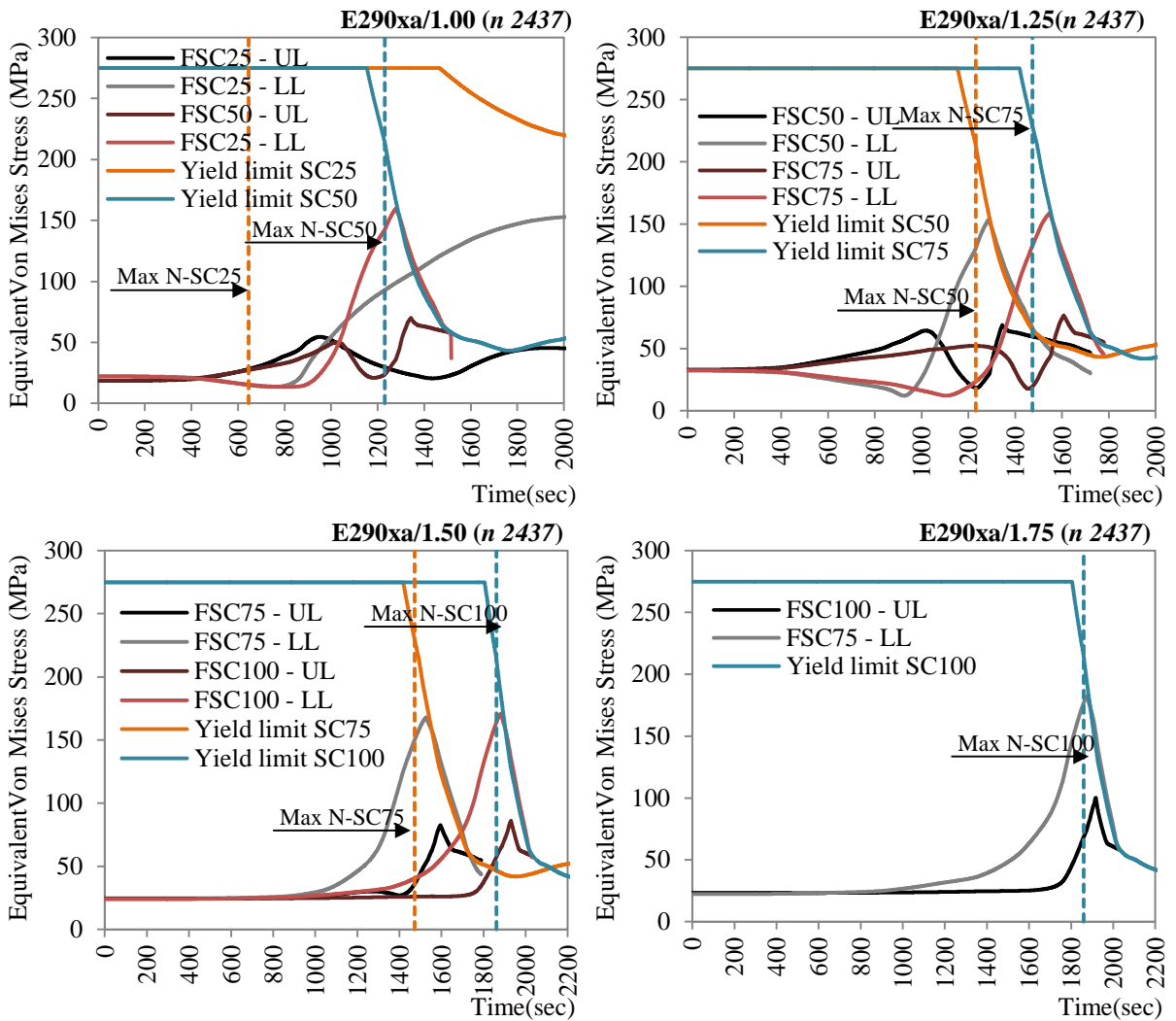


Figure 11-22: Equivalent Von Mises stress during the fire exposure at the Left end of Beam 1A for the natural FAE scenarios (accelerogram 290xa).

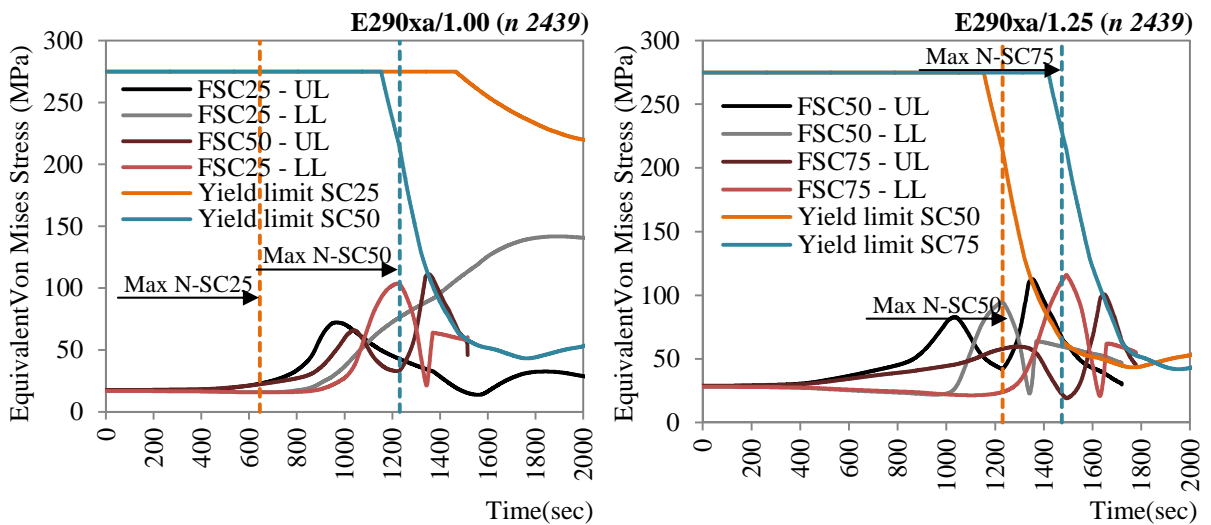


Figure 11-23: Equivalent Von Mises stress during the fire exposure at the Right end of Beam 1A for the natural FAE scenarios (accelerogram 290xa). (continued)

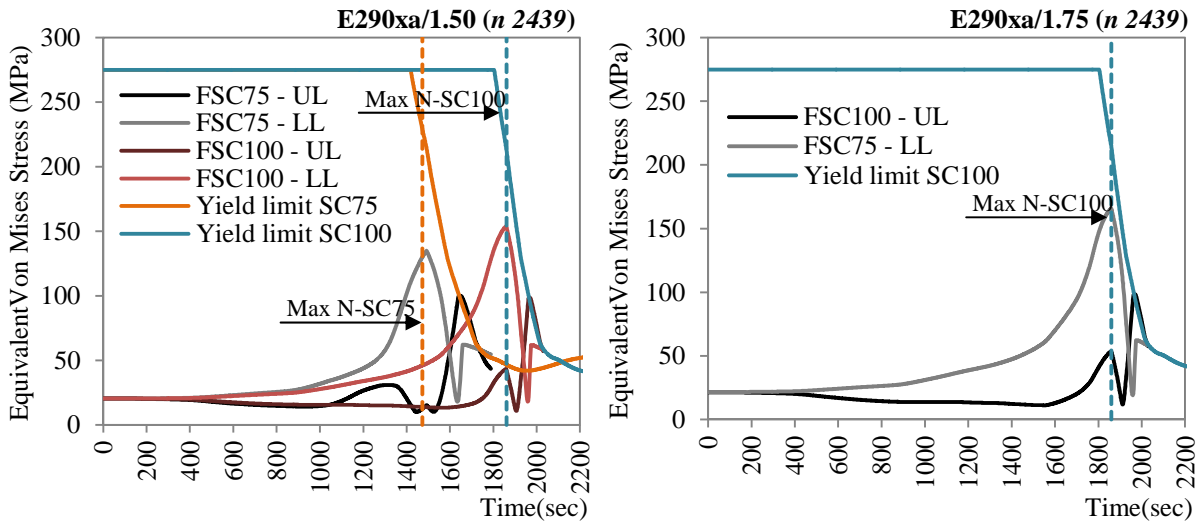


Figure 11-23: Equivalent Von Mises stress during the fire exposure at the Right end of Beam 1A for the natural FAE scenarios (accelerogram 290xa).

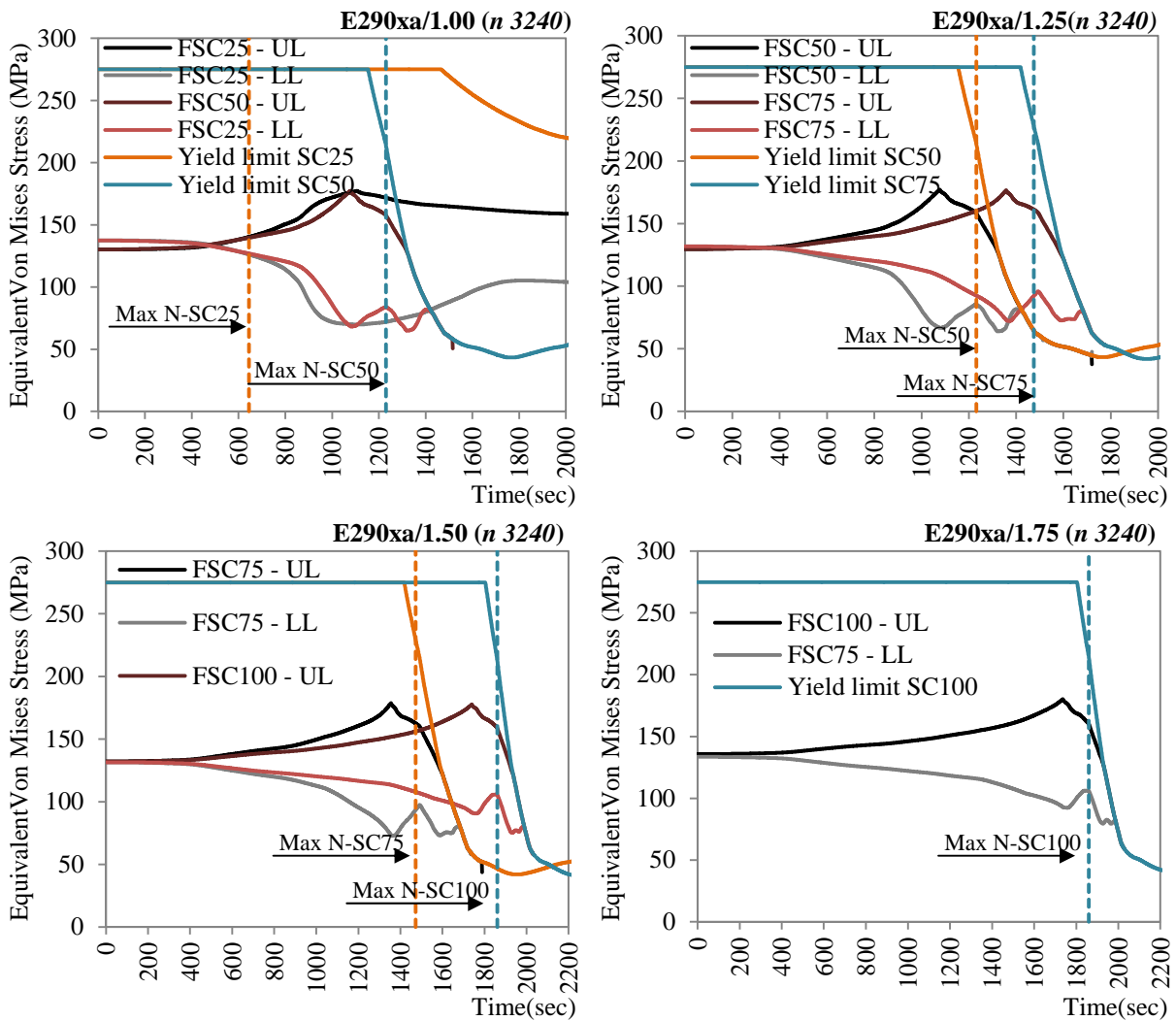


Figure 11-24: Equivalent Von Mises stress during the fire exposure at the Mid-span of Beam 1A for the natural FAE scenarios (accelerogram 290xa).

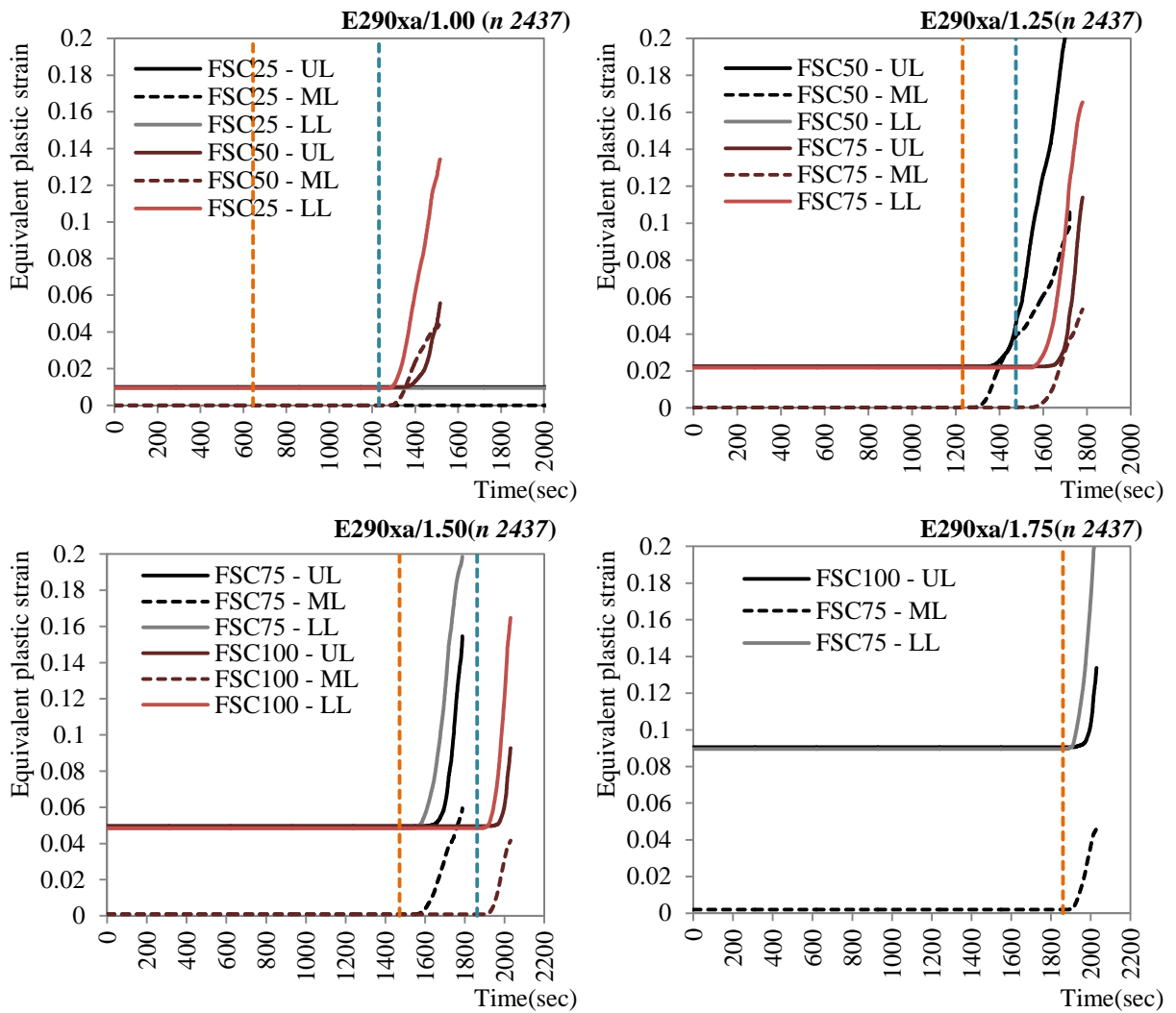


Figure 11-25: Equivalent plastic strain during the fire exposure at the Left end of Beam 1A for the natural FAE scenarios (accelerogram 290xa).

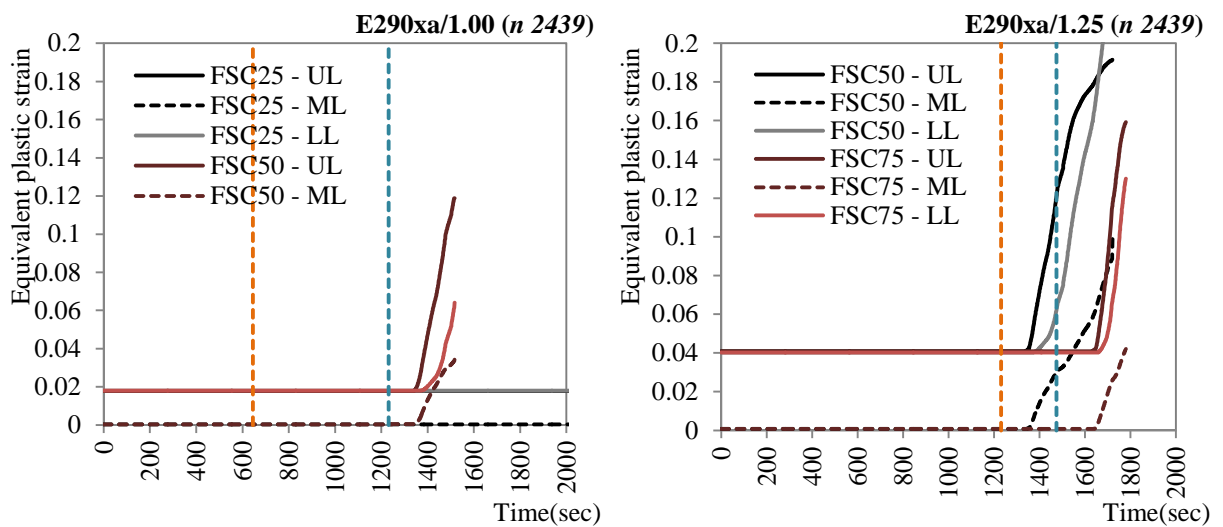


Figure 11-26: Equivalent plastic strain during the fire exposure at the Right end of Beam 1A for the natural FAE scenarios (accelerogram 290xa). (continued)

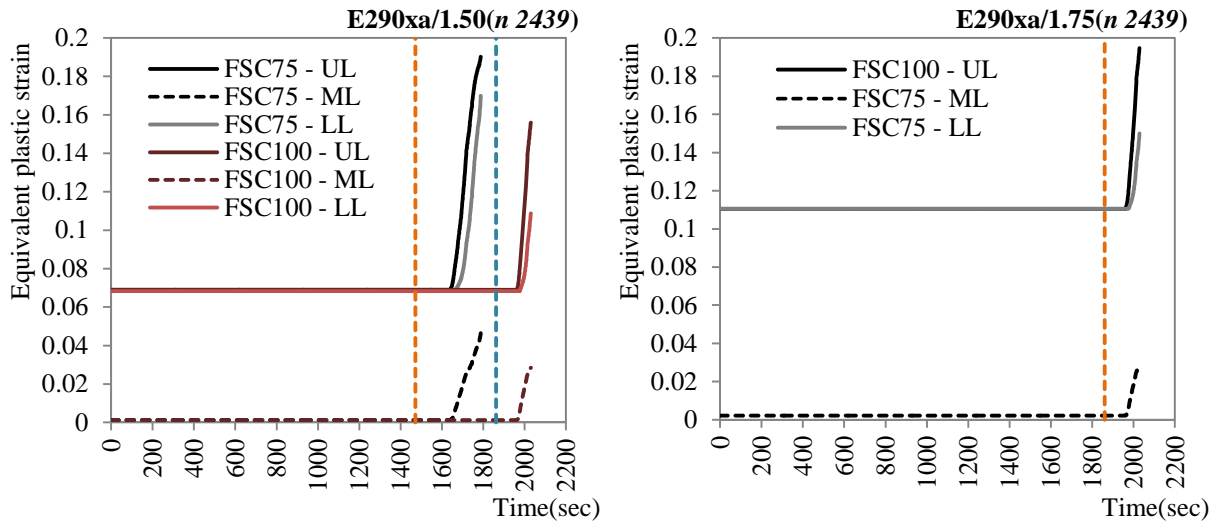


Figure 11-26: Equivalent plastic strain during the fire exposure at the Right end of Beam 1A for the natural FAE scenarios (accelerogram 290xa).

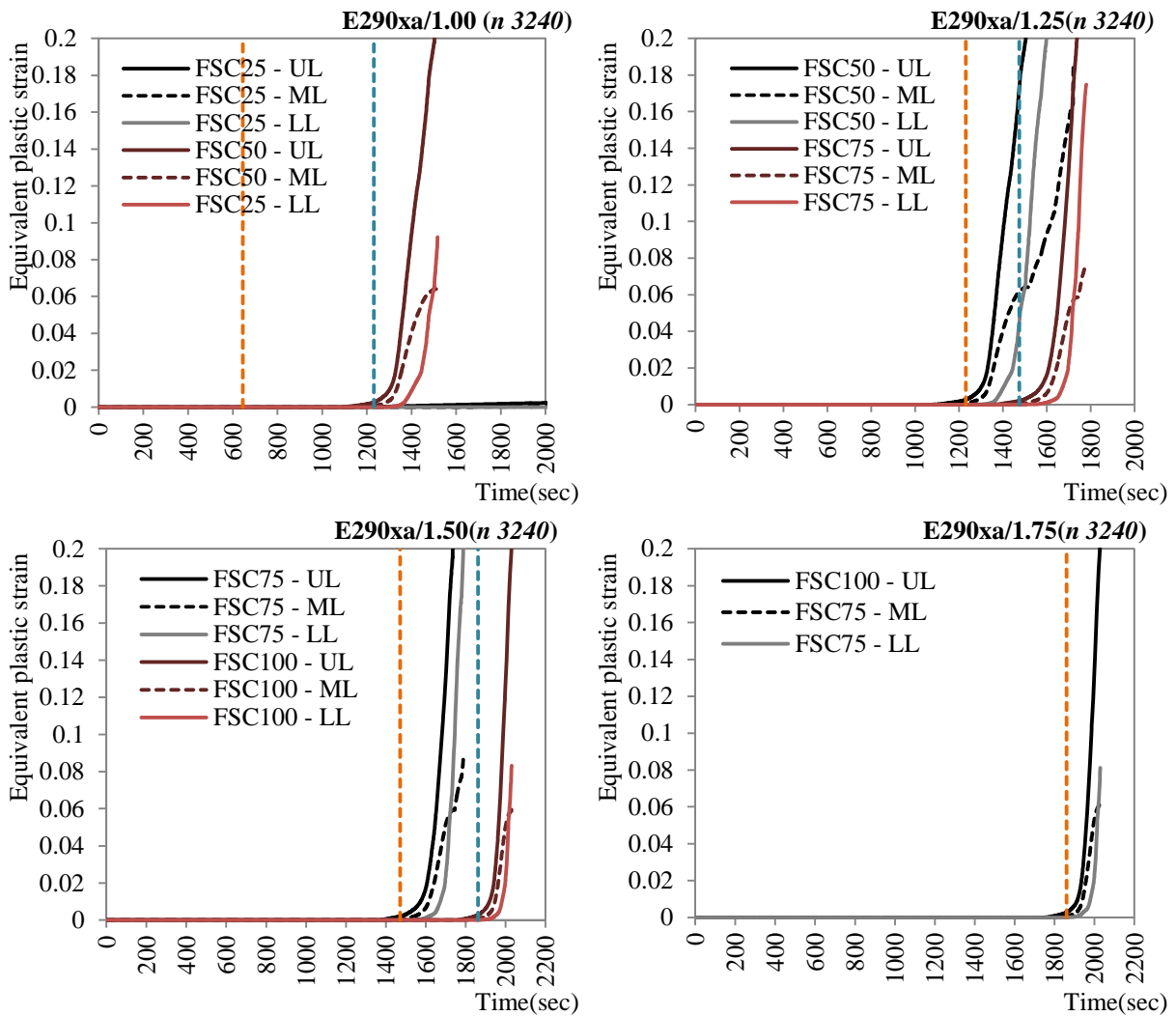


Figure 11-27: Equivalent plastic strain during the fire exposure at the Mid-span of Beam 1A for the natural FAE scenarios (accelerogram 290xa).

At this point it is noted that the numerical model does not take into account the unloading

branch that appears at the stress-strain law of steel at elevated temperatures. This branch (Figure 6-2) indicates that steel fails due to fracture under tension for strain equal to 0.2. According to the outcomes of the numerical analyses, the values of the equivalent plastic strain overcome this value in most of the scenarios that are studied. This may lead to fracture in the tension flange or to plastic local buckling if the flange is under compression. In order to address this issue, the limits that are defined in the next Chapter (Chapter 12) are used in order to take into account the local failure that may take place.

11.5.3 Comparison between the ISO and Natural FAE scenarios

In general, the comparison between the two cases is not straight-forward due to the fact that the ISO-fire curve is used to simulate the gas-temperature during the steady burning stage. Thus the comparison in time-domain is not absolutely correct. In order to compare the results of the ISO and the natural fire scenarios, the mid-span deflection of Beam 1A is plotted against the temperature of the beam. In this point of view, the comparison indicates that the behaviour of the beam is the almost identical for all the PEF scenarios (ISO or natural fire) for a specified ‘level of damage’ induced during earthquake (specific scale factor of the earthquake intensity). Figure 11-28 compares the temporal evolution of the mid-span deflection for the ISO and natural FAE scenarios.

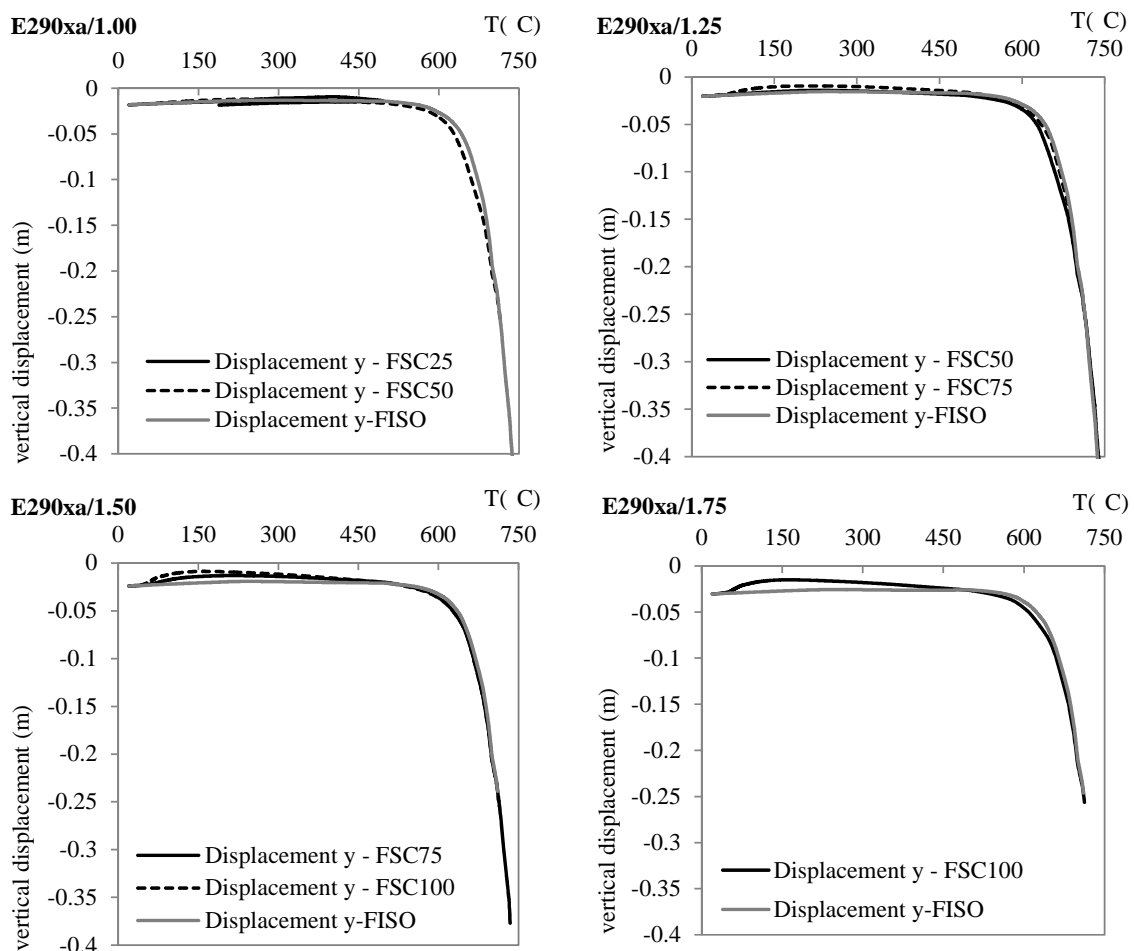


Figure 11-28: Comparison of the results of the ISO and the natural FAE scenarios in terms of mid-span deflection.

11.5.4 Conclusions

This Chapter discusses the behaviour of the structural system under FAE loading for both the ISO and Natural FAE scenarios. In all the cases that are studied, at the end of the numerical analysis a local unstable mechanism is developed at both beams that are exposed to fire. For this reason, the study is mainly focused on the fire-response of the heated beams. The results are presented in terms of mid-span deflection and rotation at the ends of the beams. It is observed that the mid-span deflection of the heated beam is increased as the scale factor of the seismic action is enlarged. Moreover, the axial force that develops during fire exposure is studied. The temporal evolution of the axial force indicates the different stages that take place during the thermal loading. It is noticed that the maximum recorded values of the compression forces are not influenced by the 'level of damage' that is induced during the earthquake but they are affected from the PEF scenario that is used.

Moreover, the temporal evolution of the equivalent plastic strain field and the Von Mises stress are studied in detail, in order to understand thoroughly the formulation of the unstable mechanism at the heated beams. In general, it can be concluded that numerical analysis stops due to convergence failure due to the formulation of an unstable local mechanism at the heated beams. For the FAE scenarios that take into account low values of the seismic scale factor, the catenary action takes place.

Taking into account the previous, it is obvious that the fire resistance of the structural system cannot be easily defined. The deflection criteria that are usually used in practice, are not appropriate in the present case, since they tend only to limit the extensive deflections that take place during the fire-tests. The criteria should take into account the deterioration of the mechanical properties at elevated temperatures. Moreover, in the case of the structures that are damaged due to earthquake, the criteria should be modified depending on the 'level of prior damage'. Therefore, it is demanding to define integrated criteria in order to calculate the fire-resistance of the structural system during the fire exposure. The definition of such criteria will be done in the next Chapter.

Chapter 12. Failure criteria of structural members at elevated temperatures

The main goal of this Chapter is the definition of the criteria which are required for the determination of the fire-resistance of the frame structure. According to the guidelines of the current regulations, the structural fire design can be based either to “simple” or “advanced” calculation models. The “simple calculation models” are simplified design methods for individual members, based on conservative assumptions. Actually, the load bearing capacity function of the members is calculated and the verification of the fire-resistance is conducted through the comparison of the required and the available values:

$$E_{fi,d} \leq R_{fi,d,t} \quad (12.1)$$

where,

$E_{fi,d}$ is the design effect of actions for the fire design situation

$R_{fi,d,t}$ is the corresponding design resistance of the steel member, for the fire design situation, at time t .

This method includes several limitations. The most important are the hypothesis of uniform temperature distribution in the structural member and the fact that the indirect thermal actions are not considered. The indirect thermal actions are mainly attributed to the thermal expansion of the structural members. Some examples are the thermal expansion of members affecting other members outside the fire-compartment, non-linear thermal gradient in the cross-section etc.

The “advanced calculation models” are defined as advanced models that should provide realistic analysis of structures exposed to fire. Regarding the objective of the fire design, it is mentioned that the design should take into account the ultimate limit state beyond which the calculated deformations of the structure would cause failure due to the loss of adequate support to one of the members. This implies that the performance of the structure lies to the survivability level. In this case, the analysis should include both the geometric and material non-linearity in order to verify the fire-performance of the structure. The determination of the fire-resistance in time domain should be based on integrated criteria, considering apart of the strength the ductility of the structure as well. For this reason, in this dissertation the criteria used for the determination of the fire-resistance are based on the ductility of the structural members, i.e. emphasis is given to the determination of the rotational capacity. For this purpose the standard beam approach is used.

The first objective of this Chapter is to propose advanced three-dimensional models based on the use of shell elements that can be used for the simulation of the structural steel behaviour under fire conditions. The problem is handled through coupled thermo-

mechanical analysis in the context of the finite element method. The basic target is to ensure that the developed numerical models can describe adequately the complex behaviour of structural steel at elevated temperatures. For this purpose, an experimental study, available in the literature, is used for comparison. The three – dimensional numerical model that is proposed in the current study, is developed using the non-linear finite element code MSC Marc (2011). The first step is to simulate the behaviour of steel I-beams studied experimentally in (Dharma and Tan, 2007a) and compare the test results with the corresponding values from the numerical analysis.

The next goal is to obtain moment – rotation curves for the structural members at elevated temperatures. A mathematical model for the description of the curves can be established. This model can subsequently be used for the analysis of frame structures under fire conditions, through simpler software packages utilizing beam finite elements with concentrated nonlinear behaviour. On the other hand, in this dissertation, the moment-rotation curves are used for the determination of the rotational capacity of the structural members and additionally for the calculation a limit rotation value for the steel member at elevated temperatures. These values are actually defining the criteria, used in Chapter 13, for the determination of the fire-resistance of the frame structure. Finally, the objective is to define the moment-rotation curve and subsequently the rotational criteria, for structural members that are pre-damaged due to cycle loading. These criteria are used in Chapter 13, for the determination of the fire-resistance of the frame structure.

12.1 Description of the problem

The steel frame structure, which is presented in Chapter 7 and Chapter 8 9, is designed according to regulations for earthquake (Chapter 9) and thermal actions (Chapter 10) individually. According to the principles of the seismic design, the building follows the requirements of the capacity design rules. This means that the plastic hinges are expected to be formed at the ends of the beams and at the bases of the columns. This is verified through the findings of the push-over and the dynamic analysis that are presented in Chapter 9.

According to the guidelines of EN 1998-1-1 for the seismic design, the cross-sections of the members should be limited in classes 1 or 2 in order to assure that the full plastic moment resistance is not decreased by compression or shear forces. The same classification is used under fire loading and EN 1993-1-2 that the structural members of class 1 can form plastic hinges, without reduction of the plastic moment resistance.

In the case of the Fire-After-Earthquake (FAE) loading, the structure is first undergoing inelastic deformations due to the seismic action and then it is submitted to the thermal loading. This means that at the starting point of the fire, the plastic hinges are already formed at the ends of the beams. In this case, the plastic moment resistance of the cross-section may be reduced due to the interaction of several phenomena (initial imperfections, temperature rise). Hence, the question that arises is referred to the remaining available rotational capacity at the plastic hinges locations at the end of the earthquake loading which is actually the starting point of the fire.

On the other hand, the classification of the cross-sections should be reconsidered during the fire design. In the case of the fire design of steel structures, the classification of the cross sections is conducted in the same way as in room temperature, except that a factor of 0.85 is used for the calculation of parameter ε i.e. it is:

$$\varepsilon_{\theta} = 0.85 \left[235 / f_y \right]^{0.5} \quad (12.1)$$

where

f_y is the yield strength at 20°C.

As it is stated in EN 1993-1-2, the reduction factor ε considers influences due to the increased temperature. Parameter ε is included in the calculation of the normalized plate slenderness $\overline{\lambda}_p$ which is a critical value for the classification of IPE cross-sections. The normalized plate slenderness depends on the material properties, the geometric dimensions and the support conditions of the plate and it is calculated according to the expression:

$$\overline{\lambda}_p = \sqrt{\frac{f_y}{\sigma_{cr}}} \quad (12.2)$$

where, σ_{cr} is the elastic buckling critical stress which is calculated, as it is well known, according to:

$$\sigma_{cr} = \frac{k_{\sigma} \pi^2 E}{12(1-\nu^2)} \left(\frac{t}{b} \right)^2 \quad (12.3)$$

where

k_{σ} is a factor depending on the support conditions of the plate and on the moment distribution

t is the thickness of the plate

b is the width of the plate.

Substituting equation (7.3) in (7.2) the plate normalized slenderness $\overline{\lambda}_p$ can be expressed in an alternative way by:

$$\overline{\lambda}_p = \frac{b/t}{28.4 \varepsilon \sqrt{k_{\sigma}}} \quad (12.4)$$

where,

$$\varepsilon = \sqrt{\frac{235}{f_y}} \sqrt{\frac{E}{210000}} \quad (f_y, E \text{ in MPa}) \quad (12.5)$$

At room temperature, regarding the carbon steel case, the elastic modulus E is considered to be constant and equal to 210GPa. In this way, equation (7.5) yields to the well-known equation (7.6) for the calculation of the dimensionless number ε .

$$\varepsilon = \sqrt{\frac{235}{f_y}} \quad (12.6)$$

On the other hand, at elevated temperatures, both the modulus of elasticity and the yield stress are not constant and they are temperature dependent. Consequently, equation (7.5) is modified according to the following:

$$\begin{aligned}\varepsilon_{\theta} &= \sqrt{\frac{235}{f_{y,\theta}}} \sqrt{\frac{E_{\theta}}{210000}} = \sqrt{\frac{235}{k_{y,\theta} f_y}} \sqrt{\frac{k_{E,\theta} E}{210000}} \Rightarrow \\ \varepsilon_{\theta} &= \sqrt{\frac{k_{E,\theta}}{k_{y,\theta}}} \sqrt{\frac{235}{f_y}} \approx 0.85 \sqrt{\frac{235}{f_y}}\end{aligned}\quad (12.7)$$

The ratio $\sqrt{\frac{k_{E,\theta}}{k_{y,\theta}}}$ depends on the temperature and it is illustrated in Figure 12-1. In order to

simplify the calculations, EN 1993-1-2 suggests to set $\sqrt{\frac{k_{E,\theta}}{k_{y,\theta}}} = 0.85$. As it can be observed in Figure 12-1 this simplification is not accurate over the entire temperature range.

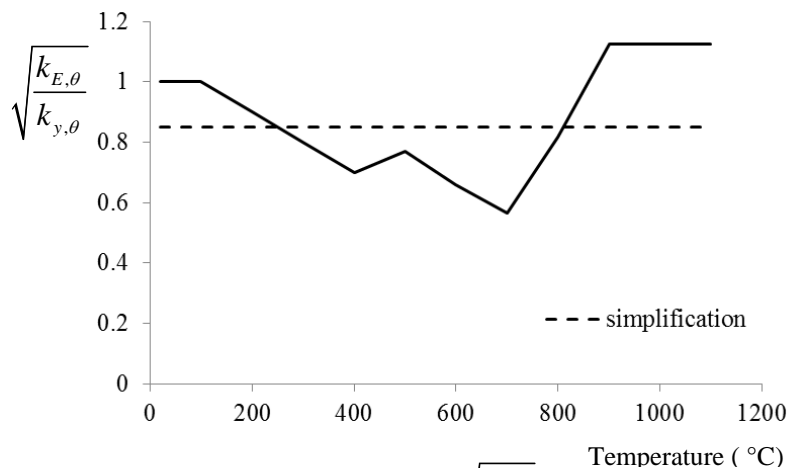


Figure 12-1: Evolution of $\sqrt{\frac{k_{E,\theta}}{k_{y,\theta}}}$ with temperature.

Moreover, this simplification implies that during fire-exposure the cross-sections are able to attain the plastic moment resistance and that at the plastic hinge locations the structural members have sufficient rotational capacity. This could be conservative or not since the factor ε does not take into account several factors that affect the rotational capacity of steel members under fire conditions, as the lack of strain hardening in the stress-strain relationship after the temperature of 400°C, the effect of the initial imperfections etc. These parameters may lead to a premature occurrence of local or lateral torsional buckling in the plastic range, therefore limiting the available rotational capacity. It is clear that during the fire loading the problem should be treated through the member ductility and not through the cross-section resistance. Specifically, the criteria that are used in this dissertation for the determination of the fire-resistance of the structure are based on the rotational capacity of the steel beams at elevated temperatures.

12.2 Assessment of the member ductility in the structure

The assessment of the local ductility of the members using numerical methods, depends strongly on the modeling method that is chosen. The latter should take into account the interaction of the member with the rest of the structure. An integrated approach is to detect the member behaviour through the modeling of the behaviour of the entire structure. This method is quite complicated since it requires the development of detailed, three-dimensional models of the structure in order to take into account several nonlinear phenomena that arise during fire exposure. In this case the numerical model should involve the possible local buckling, the multiple global buckling modes, the interaction of the previous, the special time-temperature distribution in the fire-compartment, the material non-linearity etc. Moreover, in the case of FAE loading, the study should take into account the seismic damage induced at the beginning of the fire. This method would lead to accurate results but it is impractical for the design purposes.

A simpler approach is the isolation of the member from the structure in order to study local ductility. This method is less complicated compared to the first one but it is still demanding, since it requires the development of three-dimensional detailed finite element models for the prediction of the local and global instabilities that are expected to occur. Additionally, several issues have to be solved. First of all the kinematic boundary conditions should be applied. These include the rotational and the axial restraints at the ends of the member in order to take into account the effect of the adjacent structural members and the axial forces that are present during fire exposure. The effect of the lateral restrains is also an important issue for the determination of the behaviour of the beam-columns at elevated temperatures.

Alternatively, several researchers suggest the use of the “standard beam approach” for the determination of the ductility of structural members. This approach is already used for the seismic design of structures EN 1998-1-1 and in this dissertation it is extended for the determination of the failure criteria of the steel structures under fire and FAE loading. This method is also complicated since the numerical modeling is demanding in order to take into account the local, global instabilities and the material non-linearity.

12.2.1 Simplified approach through the standard beam

According to literature (Gioncu and Mazzolani, 2002), the method of the standard beam can be used in design practice. The evaluation of the ductility of structural members is simplified, by substituting the actual members with a simple member having a similar behaviour. The new member is called *standard beam*. The name is attributed to the fact that many theoretical and experimental studies have been performed in such beams. Two different cases are defined depending on the loading conditions. The standard beam 1 (SB1) is actually a simply supported beam and a point load is applied at mid-span, resulting to a steep moment gradient. Regarding the standard beam 2 (SB2) two

concentrated loads are applied for leading to a weaker moment gradient. These are also known as three-point and four-point bending beams respectively (Figure 12-2).

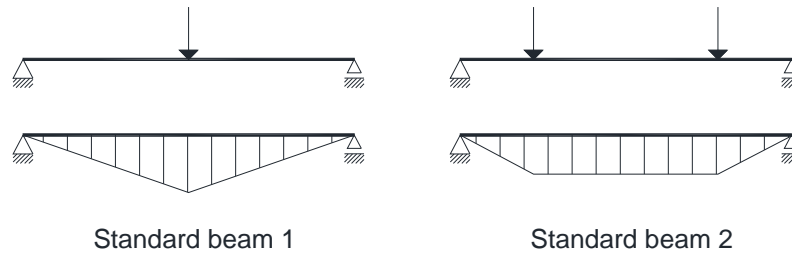


Figure 12-2: Standard beams.

The standard beam approach can be used for either continuous beams or for moment resisting frames where the global failure mechanism follows the capacity design philosophy and the plastic hinges are formed at the ends of the beams and at the bases of the columns. Considering the case that are mentioned above, it can be observed in Figure 12-3, that each structural member can be divided into two parts, depending on the position of the point where the moment diagram becomes zero. In this way, each actual member of the structure can be replaced using a combination of SB1 and SB2 as it is illustrated in Figure 12-3.

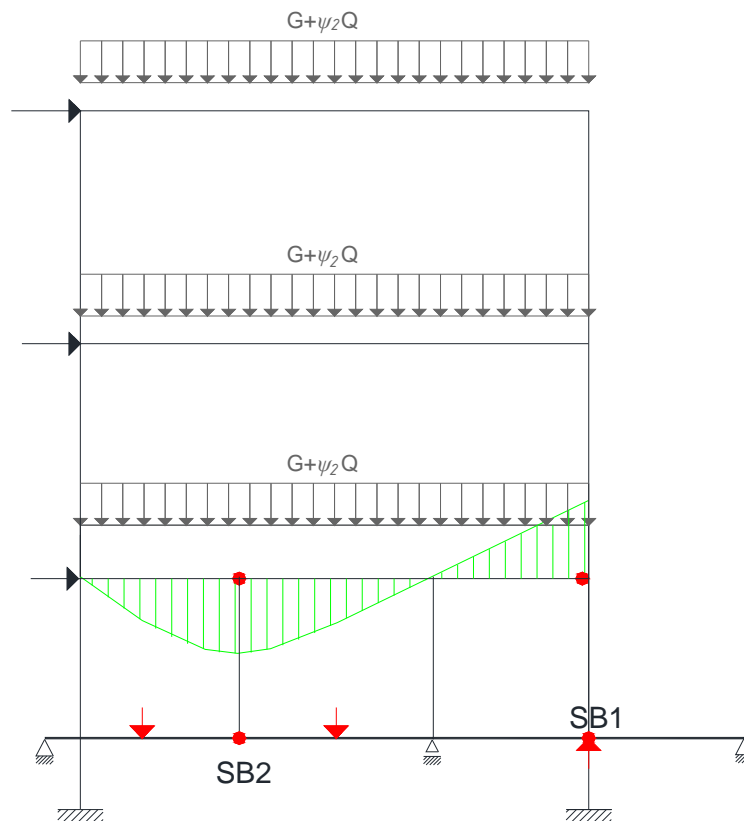


Figure 12-3: Decomposition of the moment resisting frames using standard beams.

In this dissertation the standard beam approach is adopted and it is extended for the fire design. Specifically, the first step is the decomposition of the structural system using the standard beams. The study focuses on the structural members that are exposed to fire. At

this point, a key parameter that has to be considered is the fact that the frame structures considered in this dissertation are initially designed for seismic action. According to the current regulations the behaviour of the structures that follow the capacity design rules is dominated from the “weak beams-strong columns” formulation (the behaviour is verified from the results of both the push-over and dynamic analyses in Chapter 9). This denotes two different aspects for the fire-behaviour of the structural members. The first is, concerning the fire design combination, the columns are over-designed compared to the beams. The second aspect is that during fire exposure it is expected that the temperature of the columns will be lower compared to the corresponding temperature of the beams since the section factors decrease as the dimensions of the cross-sections are becoming larger (this is verified from the findings of Chapter 8). Taking into account the previous, it is expected that the beams are the more vulnerable parts of the steel moment resisting frames. For this reason the study is focused specifically on the beams that are exposed to fire. The decomposition of the structural members is based on the bending moment diagram of the structure for the fire-design combination.

As it is illustrated in Figure 12-4, the beam that is exposed to fire can be decomposed using the combination of three standard beams. The interest is focused on SB1 since it can be easily concluded that the plastic hinges are going to be formed at the beam ends at first. The aforementioned figure presents the moment distribution of the frame for the fire combination $G + \psi_2 Q$, and the plastic hinges that are expected to be formed, during the fire-exposure, at the ends of the beams. The length of the standard beam is defined from the point where the moment diagram becomes zero. At this point it is reminded that the value that is used for the combination factor ψ_2 is equal to 0.8 and that the values for the dead and live loads are presented in Chapter 9. At this point, is noted that for simplicity reasons the same standard beam (having the same length) is used for the left and the right ends of the heated beam. In reality the length should be different, since the bending moment diagram exhibits different values of moment at the ends of the beam (left and right) and, thus, the location of the inflection points is not the same comparing the distance from the corresponding end of the beam. Taking into account the previous, different length for the standard beams should be used for the left and the right end of the beam. Considering the fact that this difference (with respect of the location of the inflection points) is not large, the same standard beam is used for both the ends of the beam. The next step is to determine the moment-rotation laws that characterize the behaviour of SB1 at elevated temperatures. The evaluation of the rotational capacity at elevated temperatures follows, in order to determine the failure criteria during fire exposure.

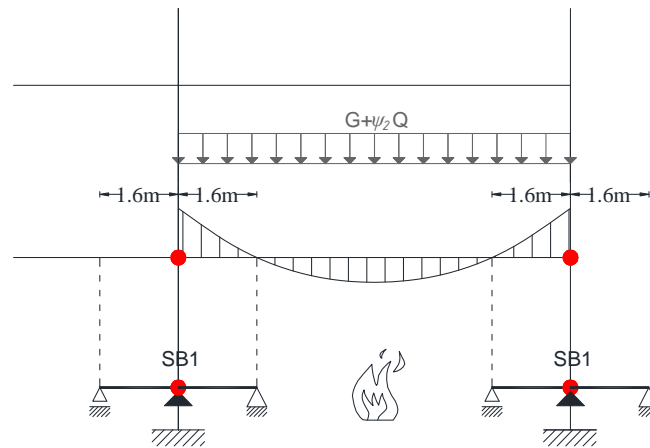


Figure 12-4: Decomposition of the moment resisting frame for the fire combination.

12.2.2 Moment Rotation Curve - Definition of rotational capacity

The moment-rotation curve is a powerful tool for the evaluation of the SB behaviour and subsequently for the definition of the ductility of the member. In this context, the ductility is expressed through the rotational capacity. In order to define the rotational capacity, it is demanding to interpret the SB behaviour through the moment-rotation curve. At room temperature, characteristic points of the curve are connected to changes in the member behaviour. The same holds at elevated temperatures. A characteristic moment-rotation curve of an IPE cross-section, for monotonic static loading is illustrated in Figure 12-5. Point 1 corresponds to the first yield of the section. At this point the moment is equal to M_{el} . After this point, the behaviour comes non-linear according to the material stress-strain law. Point 2 defines the development of the fully plastic moment (M_{pl}) at the mid-span cross-section of the beam and the rotation is equal to θ_{pl1} . As the rotation increases, the phenomenon of plastification spreads to adjacent locations. This is clear in Figure 12-6. During this stage, the behaviour strongly depends on the strain-hardening branch of the steel stress-strain law. The maximum moment (M_{max}) is reached at point 3 where plastic buckling (local or global) occurs at the flange which is under compression. The failure type strongly depends on the initial imperfections of the beam and will be discussed in Section 12.4. After the occurrence of plastic buckling, the behaviour becomes unstable and a descending branch is developed. The steepness of the descending branch depends on the failure type. It is possible that the failure will be due to local or global buckling but it is also possible the local buckling to appear first and in the sequel during the unstable branch, the global buckling to arise. Additionally, the local buckling may also occur in the web. The type of failure affects the tangent of the descending branch. The moment rotation-curve is presented in Figure 12-5, for the plastic local buckling failure type. At elevated temperatures, the moment rotation curve presents the same characteristic points. The shape may be different, since it is strongly dependent on the stress-strain law. In this point of view, the definition of the rotational capacity that follows and it is used at room temperature can be used also at elevated temperatures.

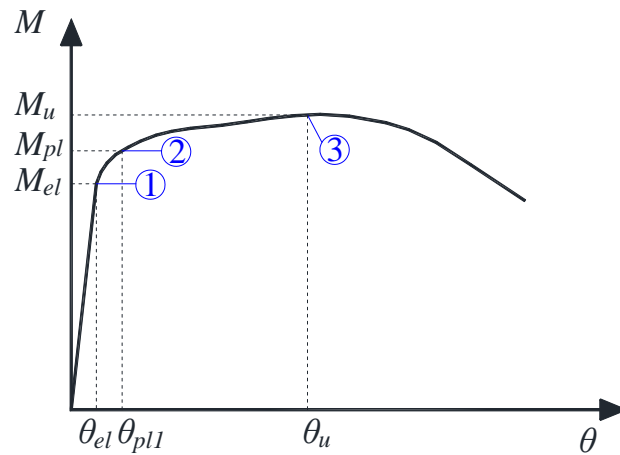


Figure 12-5: Moment-rotation curve for SB1.

According to the literature (Gioncu and Petcu, 1997), unfortunately there is no standard definition for the rotational capacity. Four different approaches are met. According to the first one, the ultimate rotational capacity is reached when the maximum moment is archived in the moment rotation curve. This approach is too conservative. Regarding the second one, the definition of the rotational capacity involves the slope of the descending branch. This presumes the detailed and exact prediction of the post buckling behaviour and the study becomes very complex.

In this dissertation the definition that is used for the rotational capacity is related to the fully plastic moment. According to this definition, the rotational capacity r_α is calculated as the ratio between the inelastic rotation θ_α and the plastic rotation θ_{pl1} , as it is indicated in Figure 12-7, i.e. $r_\alpha = \theta_\alpha / \theta_{pl1}$. Here, the term θ_{pl} corresponds to the plastic moment resistance of the cross-section, defined as:

$$M_{pl} = f_y w_{pl} \quad (12.8)$$

where f_y is the yield stress of the steel at room temperature. The previous relation is modified at elevated temperatures according to the following:

$$M_{pl,T} = f_{y,T} w_{pl}, \quad (12.9)$$

where, $f_{y,T}$ is the yield stress of the steel at temperature T .

The range of the rotation over which the plastic moment resistance of the cross section is retained, is called θ_α . Notice that the characteristic point in which the elastic moment M_{el} is attained, is not used in this definition. Specifically, two choices are available. The first one uses the full plastic moment M_{pl} , while the second one adopts the magnitude $0.9M_{pl}$ as it is demonstrated in Figure 12-7. In the first case the rotational capacity is denoted as r_α , while in the second case the symbol $r_{\alpha,0.9}$ is used. In this study the $r_{\alpha,0.9}$ definition is adopted. According to Gioncu and Petcu (1997), the choice between the two definitions remains a decision of the designer. In this study the definition $r_{\alpha,0.9}$ is used due the fact that at elevated temperatures it is possible that the beam is not able to reach the fully plastic moment $M_{pl,T}$, as it will be explained in the next Sections. In this context, it is

considered more convenient to use the reduced moment in order to be feasible to calculate the rotational capacity in the majority of the cases that are studied. At elevated temperatures the rotational capacity is defined as $r_{\alpha,0.9,T}$, since it depends on the temperature level.

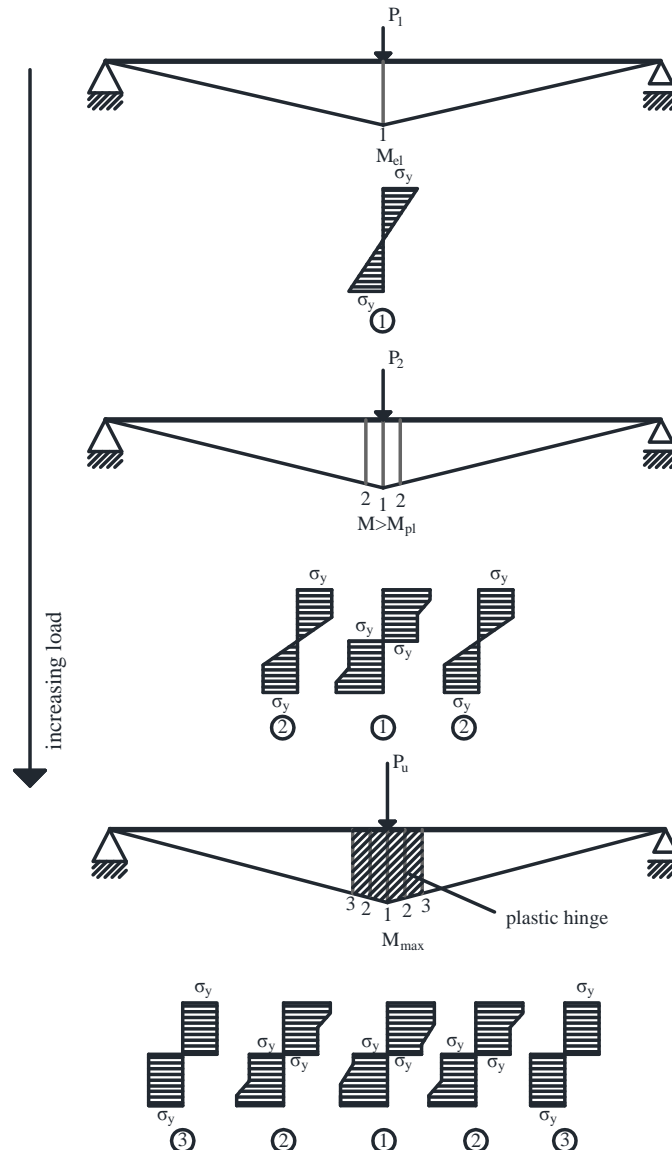


Figure 12-6: Plastification of the SB1.

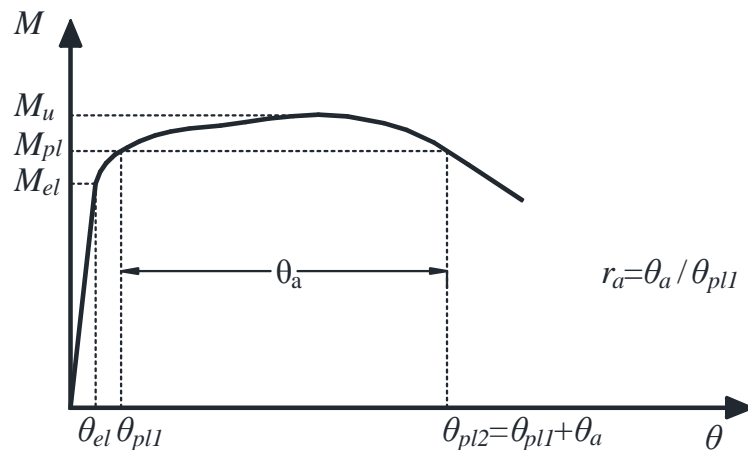


Figure 12-7: Definition of the rotational capacity.

12.2.3 Main factors affecting the member ductility of beams under fire conditions

During the last decades, extensive experimental and analytical research has been conducted for the evaluation of the local ductility of structural steel members at ambient temperature. The research has been focused both on monotonic and on cyclic loading. The study of the literature (Gioncu and Petcu, 1997, Gioncu and Mazzolani, 2002) reveals that the assessment of the member ductility is complicated, since several factors influence the physical phenomenon. The basic factors are summarized in the following:

- Element ductility

The sections that are used in practice are composed by elements that are supported on one or two edges. The support conditions and the slenderness of the plates define the critical stress of the elements and the local buckling modes. Subsequently, the ductility, which is dominated by the appearance of the local buckling phenomena, is also affected.

- Steel properties

According to experimental and numerical results (Gioncu and Petcu, 1997) the increase of the steel yield strength leads to decrease of the rotational capacity. As it has already been explained in Section 12.2.2, the strain-hardening plateau affects the shape of the moment-rotation curve and it is critical for the ductility of the steel members.

- Geometric initial imperfections

Initial imperfections can be local or global. The shape, the wave length, the symmetry and the amplitude of imperfections affect the final failure mode of the member.

- Out-of-plane restrains

Out-of-plane boundary conditions define the effective length of the members regarding the lateral torsional buckling mode. In the case where the member is sufficiently laterally supported, the lateral modes are prevented and the ductility is increased.

- Member type

The behaviour of beam-columns is totally different from that of beams, due to the presence of the axial forces. In general, the presence of compressive forces contributes to the reduction of the rotational capacity of the members.

- Loading type

Two different cases are considered, as they defined by SB1 (Standard Beam 1) and SB2 (Standard Beam 2). The steepness of the moment gradient affects the shape of the moment-rotation curve and subsequently, the ductility of the member.

- Span of the member

In the case where the global buckling is possible, it is clear that the span of the beam plays an important role to the ductility of the member. Considering the case where the beam has sufficient lateral restraints, experimental studies reveal that the region where local buckling occurs is limited to a region that is independent of the beam span.

- Cyclic loading

According to numerical and experimental results (Gioncu and Mazzolani, 2002), the ultimate rotational capacity is reduced during cyclic loading.

- Temperature increase

The reduction of the rotational capacity at elevated temperatures is attributed to the deterioration of the mechanical properties of steel and the “shape” of the stress-strain relationship of steel at elevated temperatures. Moreover the absence of the strain-hardening branch over 400°C is a crucial factor that affects the ductility of the member. The assessment of the rotational capacity at elevated temperatures will be discussed in detail in Section 12.4.

- Temperature gradient in the cross-section

The critical stress of the compressive plates of the cross sections depends on the temperature level. The assumption of the uniform temperature is quite conservative, since the upper part of the cross-section is in reality cooler, compared to the lower one. In this respect, the ductility of the member under monotonic loading can be found to be greater.

12.2.4 Specification of the considered problem - Assumptions

The previous Section emphasizes the difficulty for the assessment of an integrated formula for the determination of the ductility of members. The problem becomes more complex at elevated temperatures and especially in the case of the FAE loading, since the cyclic loading takes place before the fire loading.

The main objective of this Chapter is the assessment of the ductility of beams at elevated temperatures in two different cases. In the first case the rotational capacity of the beams is studied under static, monotonic loading at different temperature levels. Actually, the numerical analysis has two different stages. During the first stage the temperature of the beam increases until the predefined level. In the second stage, static loading is applied. The two different loading stages are described schematically in Figure 12-8. The numerical test is displacement controlled in all cases in this dissertation.

Regarding the second case, first the beam is subjected to cyclic loading and in the sequel the ductility is obtained for static, monotonic loading at elevated temperatures. The analysis has three different stages as it is illustrated in Figure 12-8. The first stage is the

cyclic loading and the other two stages are similar as in the first case. In fact, in the second case, the cyclic loading induces damage to the beam and the goal is the evaluation of the rotational capacity, depending on the ‘level of damage’.

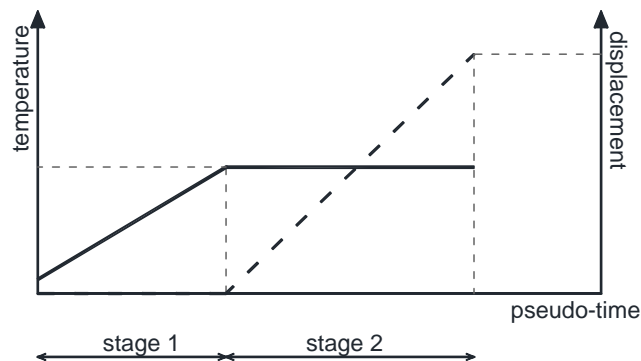


Figure 12-8: Loading procedure- First case.

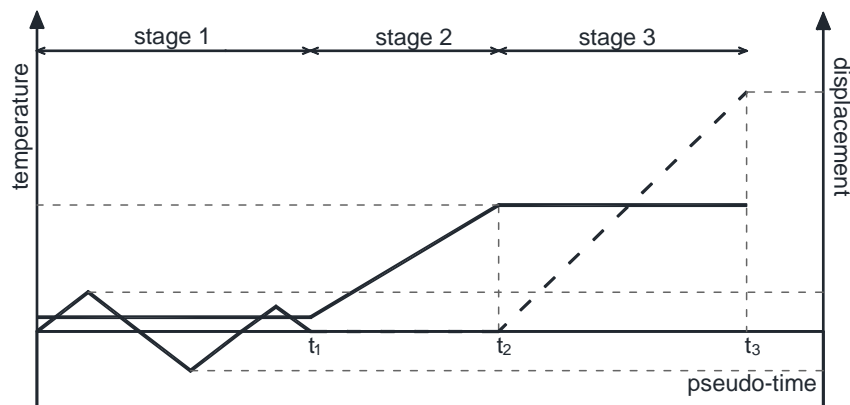


Figure 12-9: Loading procedure- Second case.

The next objective is to define the limits for the determination of fire-resistance of steel frame structures during fire exposure. The limits that arise from the first case are used for undamaged structures, while the corresponding values from the second case are used for structures that are damaged due to earthquake and the fire loading follows.

The problem is handled through geometric non-linear analysis taking into account the temperature dependent non-linear material properties. In both cases the numerical model that is developed considers the initial imperfections and parametric analyses are conducted taking into account different amplitudes of the initial geometrical imperfections. In order to simplify the already complex problem, the following assumptions are adopted for the assessment of the moment-rotation curves:

- The temperature is uniform and constant along the beam.
- No-thermal gradient is considered in the cross-section.
- The beam is free to expand longitudinally, which means that the study does not take into account the effect of thermal compressive forces.

12.3 Validation of the numerical model

Initially, a numerical model is developed for the accurate prediction of the rotational capacity of steel I-beams at elevated temperatures. The basic aim of this Section is to present the validation of the model against experimental results available in the literature (Dharma and Tan, 2007a).

12.3.1 The experimental program-The case study

Objectives of the experimental study

As it was referred in detail in the Chapter 2, a unique experimental program concerning the study of the rotational capacity of steel beams at elevated temperatures, was conducted by Dharma and Tan (2007a). Details for the experimental program are given in Section 2.4. Briefly, it is referred that the purpose of the experimental study was to define the rotational capacity of a two span continuous steel I-beam under uniform loading, at the possible plastic hinge locations under fire conditions. Therefore, according to the study, it was important to assess the fire-behaviour of the beam at the hogging moment region i.e. at the internal supports. In order to simplify the problem, a simply supported beam was considered which was loaded at mid-span. This beam can represent the part of a continuous beam close to the internal support, between the points where the bending moment diagram becomes zero (Figure 12-10). In the case of the simply supported beam the plastic hinge will be formed at mid-span, corresponding actually to the internal support of the continuous beam. It should be noticed that according to the experimental study, the beam has been designed so that it is able to reach the plastic moment capacity at elevated temperatures. In total 9 steel beams were tested. The specimens (simply supported beams) were heated up to the desired temperature level (415 °C or 615 °C) and then they were subjected to a mid-span point load until failure.

The results of the experimental program indicate the effect of the main parameters (web slenderness, the flange slenderness, the effective length) on the rotational capacity at elevated temperatures. More specifically, it is indicated that the difference in shape of the moment rotation curves at elevated temperatures, compared with respect to the corresponding curves at ambient temperature, is due to the introduction of a non-linear segment in the stress strain relationship of steel at elevated temperatures. Also, according to the results of the numerical simulation of the tests, the increased slenderness of the web and flange reduces the rotational capacity at elevated temperatures. Additionally, it is noticed that the reduction of the effective length provides greater rotational capacity and changes the failure mode from lateral torsional buckling to local buckling.

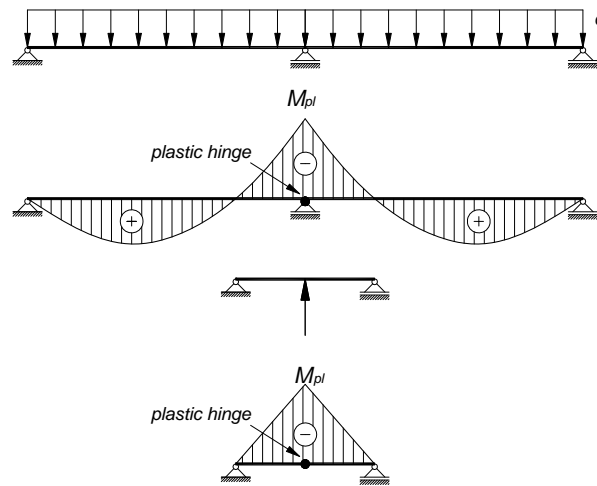


Figure 12-10: Simplification of the problem from a continuous beam to a simply supported beam.

Case study

The structural system that is used in this part of the dissertation is referred to a typical beam specimen of the experimental study by R.B. Dharma and K.H. Tan (2007a). More specifically, the steel I-beam S2-1 is chosen. All the geometrical dimensions and the material properties are considered according to this study. In detail, the total length of the simply supported beam is equal to 3.65m while the distance between the supports is 3.45m. Also, web stiffeners are used at the support and at mid-span, where the load is applied. The beam is laterally restrained at the position of supports at both ends and at mid-span. Therefore, the effective length of the beam for lateral torsional buckling is equal to 1.725m. The cross-section dimensions and the structural system are illustrated in Figure 12-11. The material properties at room temperature are defined from tensile tests and they are presented in Table 12-1.

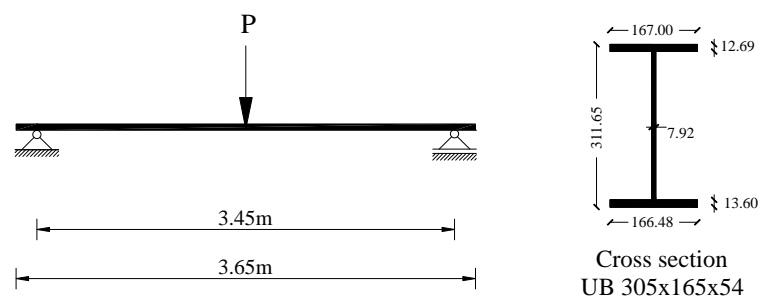


Figure 12-11: The structural system and the cross section (dimensions of the cross section in mm).

It is stressed that the beam is laterally restrained only at the ends and at mid-span and, therefore, the development of plastic lateral-torsional buckling is possible under certain conditions at elevated temperatures. Moreover, plastic local buckling may arise.

	Yield strength $f_{y,20}$ (Mpa)	Ultimate strength $f_{u,20}$ (Mpa)	Elastic modulus E_{20} (Mpa)
web	307.4	491.4	205253
flange	297.6	483.6	203677

Table 12-1: Material properties at ambient conditions.

12.3.2 The numerical model used for the validation

The numerical model is developed using the nonlinear finite element code MSC-MARC (2011). The three-dimensional numerical model (Figure 12-12) utilizes four-node, thick-shell elements. Details about the finite element technology are included in Appendix A. The numerical model takes into account the nonlinear elastic-plastic stress-strain relationship of steel at elevated temperatures. The yield stress, the proportionality limit and the elastic modulus are supposed to be temperature dependent according to EN 1993-1-2.

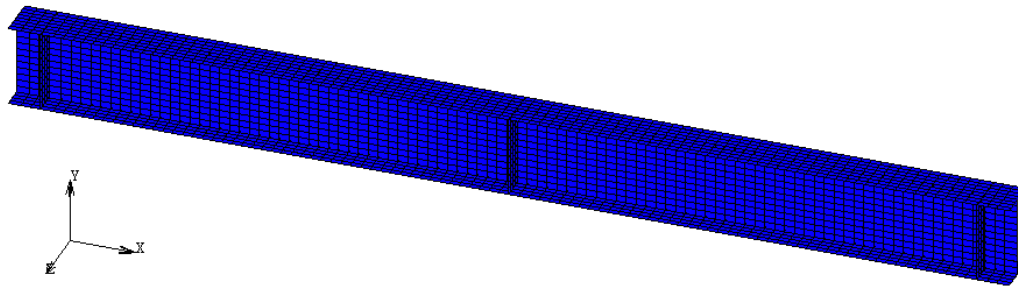
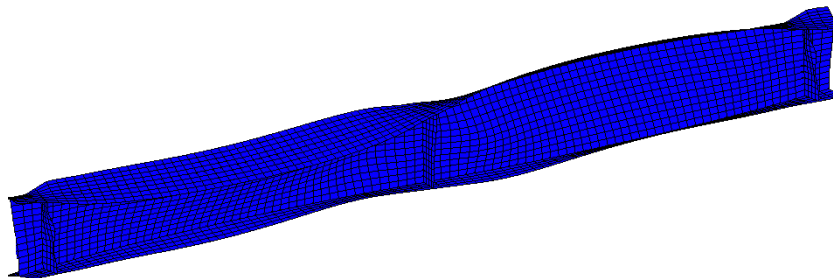


Figure 12-12: The numerical model.

The Von Mises yield criterion is used in the numerical analysis. Additionally, the analysis takes into account the geometric non-linearity.

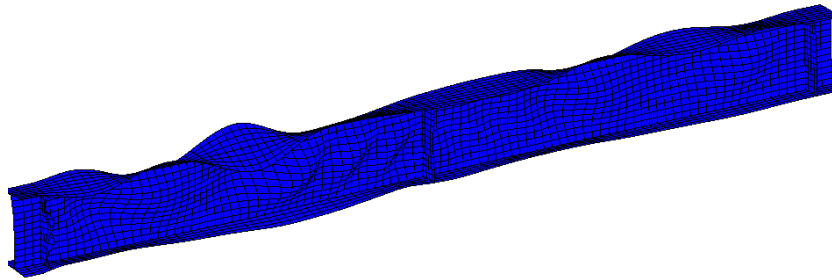
12.3.3 The numerical simulation

Initial imperfections are incorporated in the geometry of the steel beam for a more realistic assessment of its behaviour. There are many different ways to introduce initial geometric imperfections in structural members. A simple way in the context of finite element analysis is to extract the buckling eigenmodes and introduce them as imperfections with specific amplitude. More specifically, the normalized buckling mode is multiplied by a scale factor, leading to certain maximum amplitude and the resulting displacements are added to the initial coordinates of the structural member. For the case studied here, two different eigenmodes are combined (see details in Figure 12-13). The first eigenmode is related with the local buckling along the upper flange of the beam (where compressive stresses arise under the considered loading) while the second buckling eigenmode used is the one corresponding to the development of lateral torsional buckling.



a. Eigenmode corresponding to the lateral torsional buckling.

Figure 12-13: Results of the buckling analysis. (continued)



b. Eigenmode corresponding to the local buckling of the upper flange.

Figure 12-13: Results of the buckling analysis.

The numerical analysis has two different stages following the test procedure that is described in Dharma and Tan (2007a). At the first stage the steel beam is heated with a heating rate equal to $7^{\circ}\text{C}/\text{min}$ until the desired temperature T is reached. It must be noticed that during the heating stage the temperature is supposed to be uniform along the member. At the second stage the temperature remains constant and the beam is submitted to loading at mid-span until failure.

The structural boundary conditions are described in Figure 12-14. At both supports the boundary conditions are applied at the middle node of the web. The vertical y -displacement and the rotation about the longitudinal- x axis (r_x) are restrained at both supports while the x -displacement is restrained only at the left support. The out-of-plane displacements are prevented at the location of the supports and at mid-span.

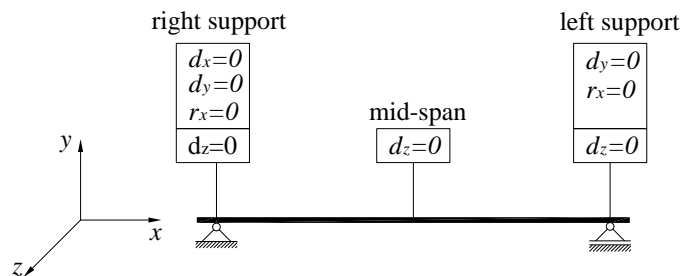


Figure 12-14: The boundary conditions.

12.3.4 Comparison with the test results

The primary objective in this Section is to validate the numerical model against the published experimental results presented in the study of R.B. Dharma and K.H. Tan (2007a). Due to lack of details for the accurate profile of the initial imperfections, an assumption has to be adopted. The amplitude of the initial imperfections that is used for the analysis is supposed to be 0.5mm for the buckling eigenmode which is related to the lateral torsional buckling and 2mm for the eigenmode which is related to the local buckling of the upper flange. These values are in accordance with the maximum values of the measured initial imperfections that are presented in Dharma and Tan (2007a).

For the calibration of the numerical model against the experimental results the material models proposed in EN 1993-1-2 were not followed regarding the ratio between the ultimate stress and the yield stress. This ratio, is limited by EN 1993-1-2 to 1.25. Instead, the actual material properties for the specific steel used in the experiments were followed. More specifically, the tensile coupon tests, for both the web and the flange (Table 1), gave an ultimate strength approximately 1.6 times greater than the yield strength at room temperature. Another point where the recommendations of EN 1993-1-2 were not completely followed was in the temperature above which the hardening of the material should be neglected. This temperature is defined to be 300°C. However, experimental results indicate that steel keeps a significant hardening even in the case of 400°C (Poh, 2001, Kodur and Dwaikat, 2009). For this reason and in order to obtain more realistic results, hardening was taken into account in the numerical model but with an increased ratio between the ultimate and the yield stress. The specific value for this ratio was calculated here to have the value of 1.51, following the analogies yielded by the experimental results. Therefore, in the numerical analysis that is conducted for the calibration of the finite element model, the ultimate strength is supposed to be $f_{u,T} = 1.6f_{y,T}$ for both the web and the flange, for temperatures ranging between 20°C and 400°C and $f_{u,T} = 1.51f_{y,T}$ for temperature of 410°C.

Figure 12-15 illustrates the load-displacement curves obtained numerically and experimentally for the specimen S2-1. A very good agreement is obtained for the initial stiffness and for the maximum load of the system. Moreover, the softening branch is well approximated by the numerical model. An insignificant difference is observed for the maximum strength of the steel beam that can be attributed to the lack of experimental data for the ultimate and the yield strength of steel at elevated temperatures. Also, the slight incompatibility between the numerical and the test results at the unloading branch may attributed to the selection of the specific profile of initial imperfections that is used in the numerical analysis. Additionally, the failure mode that results from the numerical analysis is very close to the experimental results, as it is presented in Figure 12-16. In both cases the failure is due to lateral – torsional buckling of the steel beam.

Taking into account the previous, it is considered that the developed numerical model can predict accurately the behaviour of the steel I-beam at elevated temperatures. Additionally, it is indicated that the shapes of the initial imperfections that were adopted can be used for the purpose of parametric studies.

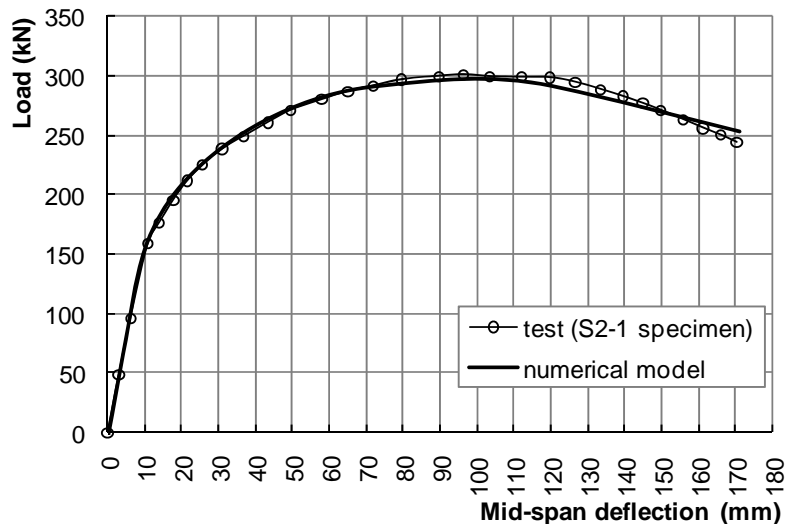
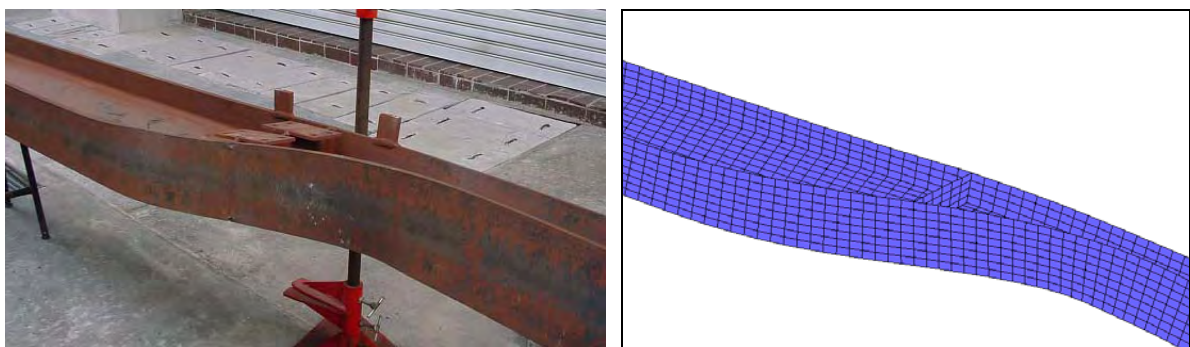


Figure 12-15: Comparison of the numerical analysis results with the test results for the specimen S2-1 at 415°C.



a) test results

b) numerical analysis results

Figure 12-16: Deformed shape of the steel beam at the failure.

12.4 Failure criteria

As it is referred in the previous Sections, the main objective of this Chapter is the definition of the failure criteria of beams for the fire and the FAE loading. In Section 12.4.2 the local ductility is obtained for the fire loading and the results are used in the sequel in Chapter 13. In Section 12.4.3 the corresponding criteria are evaluated for the FAE loading and they are utilized in Chapter 13.

12.4.1 The simplified numerical model used for the assessment of the failure criteria

The model, that was validated in the previous paragraph against experimental results, is now used for the evaluation of the ductility of the structural members of the frame structure that is studied in this dissertation. Specifically, three different issues are addressed. The assessment of the moment-rotation curves, the evaluation of the rotational capacity and the determination of the limit values of rotation at elevated temperatures. In

this Chapter the study is extended to the case where first the cyclic loading takes place in room conditions and the monotonic loading at elevated temperatures follows. For this reason the numerical model should be adjusted in order to take into account the behaviour of steel beams under cyclic loading. The supplementary assumptions are the following:

- The beam is sufficiently laterally restrained and the lateral-torsional buckling is not possible to happen. Subsequently, the initial imperfections that are used are related only to the local buckling failure modes and not to the global one. This consideration is adopted in order to conduct a more rational study that can be used for practice design purposes. Moreover, it is compatible with the situation present in real buildings, where the lateral torsional buckling is usually restrained by the presence of concrete slab.
- The initial imperfections concerning the local buckling of the flanges are symmetric. This assumption is adopted due to the fact that the results of the buckling eigenmode analysis indicate that the first local buckling mode is symmetric. As it is expected, the outcomes of the analysis are not the same with those that would result in the case where asymmetric eigenmodes are employed.
- Geometric imperfections related to web buckling are not considered in order to focus the study to the effect of the imperfections of the flanges. For this reason the out-of-plane displacements of the web are restrained during the buckling eigenmode analysis.
- The strain hardening branch of the stress-strain law of steel (for the temperature range between 20°C -400°C) is not taken into account and isotropic hardening rule is used. This consideration will be clarified in Section 9.4.3.

Geometry

The geometric characteristics of the numerical model used for the determination of the failure criteria of the frame structure, are described in Figure 12-17. At this point it is noted that the length of the beam is equal to 3.2m. The span of the beam plays a crucial role for the determination of the ductility of beams. The length of the beam is determined to be equal to 3.2m, as it explained in Section 12.2.1.

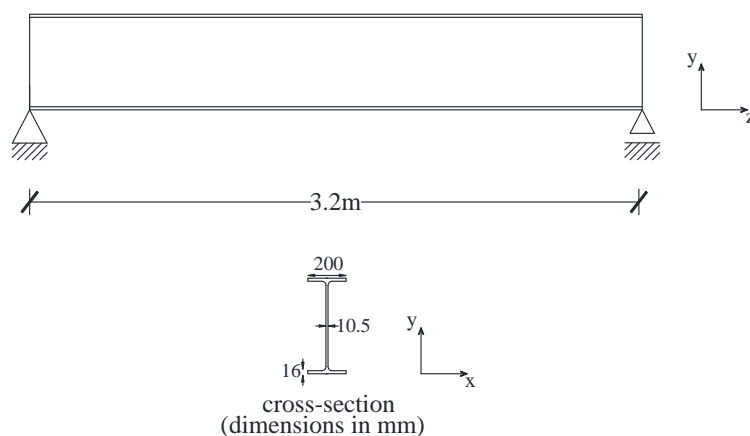
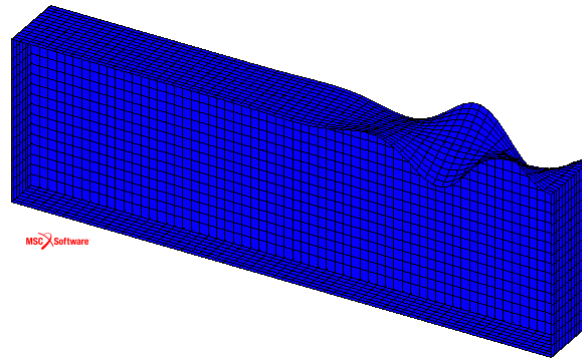


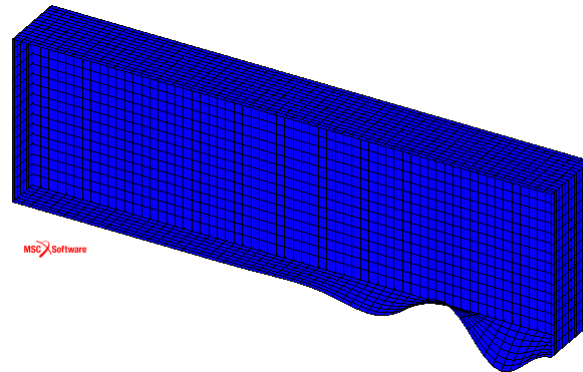
Figure 12-17: Geometry of the numerical model.

Initial imperfections

The initial imperfections that are incorporated in the geometry of the steel beam are depicted in Figure 12-18. Specifically, two different eigenmodes are combined. The first eigenmode is related to the first local buckling mode at the upper flange of the beam, which is anti-symmetric with respect to the x - y plane, while the second eigenmode used is the corresponding mode for the lower flange of the beam. At this point the study includes the imperfections of both flanges, in order to obtain more realistic results in the case of the FAE loading, since the compressive zone shifts during the cyclic loading.



The upper flange eigenmode



the lower flange eigenmode

Figure 12-18: Results of the buckling analysis.

Boundary conditions

Aiming to reduce the computational cost associated with the nonlinear three-dimensional modeling, only half of the total length of the beam is considered, using the appropriate symmetry boundary conditions. Specifically, the displacement d_x and the rotation R_y are fixed and set equal to zero. These simplifications will not affect the results, which will be identical with those of the full model. Therefore, for the simply supported beam, a length equal to 1.6 m is modelled using the following boundary conditions (Figure 12-19).

Concerning the out-of plane displacements, it is noted that they are fixed along the whole length of the beam. The displacement d_z is set equal to zero for all the nodes that lie at the section between the web and the upper/lower flange as it is illustrated in Figure 12-19.

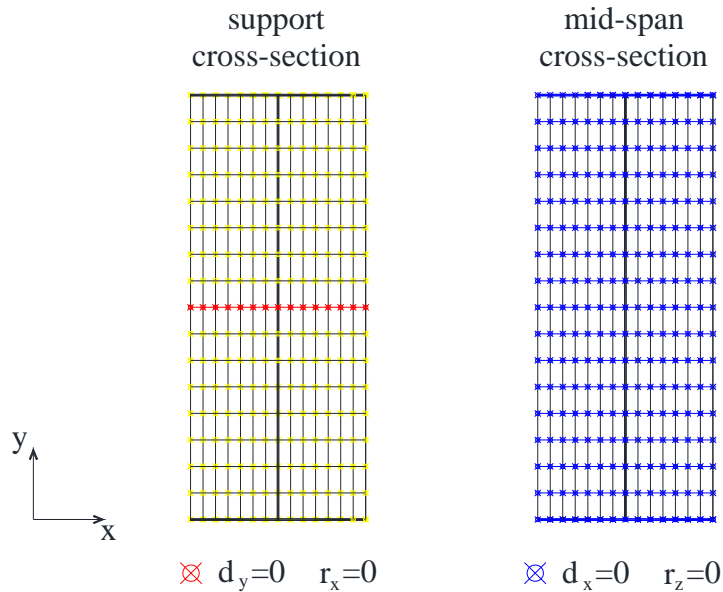


Figure 12-19: Discretization of the cross-section and boundary conditions at the support and at the mid-span.

The first case that is studied concerns the numerical simulation of the three point bending test at elevated temperatures, while the second case concerns the same test for beams that are pre-damaged due to cyclic loading. The next two Sections present the results of the study for the two different cases respectively.

12.4.2 Case 1: Simulation of three point bending test at elevated temperatures

The numerical analysis that is conducted for the simulation of the three point bending test has two different stages. In the first stage the temperature increases until the desired level is attained. During this stage the beam is not loaded as it is described in Figure 12-20. The loading stage follows, while the temperature remains constant. It is noted that the numerical test is displacement controlled.

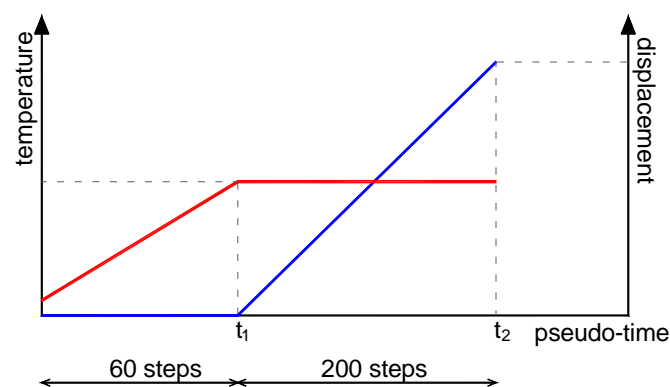


Figure 12-20: Case 1: loading procedure.

The test is conducted at ten temperature levels between 20 °C and 900 °C. Parametric analyses are conducted with respect to the amplitude of initial imperfections. Specifically, three different cases are studied and the amplitude is considered to be 0.5mm, 2mm and

5mm respectively. Also, the case where the model does not include initial imperfections (perfect model) is studied.

Behaviour of the beam during monotonic loading

Figure 12-22 presents the deformed shape of the beam and the equivalent plastic strain fields at various steps of the analysis, for the temperature levels of 20 °C and 400 °C. The amplitude of the initial imperfections is considered to be equal to 2mm in both analyses. The results are presented in order to compare the behaviour of the steel beam at elevated temperatures against that at room temperature. To this end, it is chosen the temperature to be equal to 400 °C due to the considerable reduction of the proportionality limit of steel at this level. It is noted that at 400 °C the yield strength of steel is not reduced while the reduction factor of the proportionality limit is 0.42.

Considering the numerical simulation of the test that is conducted at room temperature, the results of the analysis indicate that initially plastic strains appear at the upper and lower flanges and gradually they are extended to the web for imposed displacement $d=25\text{mm}$. As the loading increases ($d=50\text{mm}$) the plastic hinge is formed at mid-span. The beam would fail due to the occurrence of plastic local buckling at the upper flange ($d=100\text{mm}$) at mid-span. In general, the same remarks hold for the numerical simulation of the test that is conducted at 400 °C. Comparing the results of the analyses that are conducted at different temperature levels, it is observed that the plastification is more extended in the case where $T=400$ °C. Specifically, during the initial loading steps ($d=25\text{mm}$) the results of the analysis show that at room temperature, the plastic hinge is almost formed (a small elastic kernel remains) at mid-span. On the other hand, at the same loading step of the analysis where the temperature is equal to 400 °C, the plastic hinge is not fully developed. As it can be observed in Figure 12-21, the plastic strains appear at both flanges but the web is not fully plastified.

It is interesting to compare the results of the analyses conducted at different temperature levels in terms of equivalent plastic strains and Von Mises stresses at the same time steps. The equivalent Von-Mises stress field of the beam is presented in Figure 12-21. It can be observed that at room temperature the cross-section is fully plastified and the stress is equal to the yield value. On the other hand, the distribution of the stresses is completely different at 400 °C. In the latter case the stresses are smaller, following the stress-strain relationship of steel at elevated temperatures. This indicates that the corresponding values of strain are smaller at 400 °C. For the same imposed displacement the magnitude of the equivalent plastic strains is greater in the analysis that corresponds to the room temperature. The distribution of the equivalent plastic strain is depicted in Figure 12-21.

Moreover, regarding the test that is carried out at 400 °C it can be observed that the region where the plastification takes place is more extended, compared to the test at room temperature and this holds for the entire analysis. This phenomenon is due to the extended plastic branch of steel at 400 °C. Comparing the stress-strain relationships of steel at room temperature and at 400 °C (Figure 6-2), it is clear that the elastic region is limited at

elevated temperatures and that the point where the plastic branch starts corresponds to smaller magnitudes of strain. This indicates that as the temperature increases, the load that is required for the development of plastic strains is reduced. Taking into account the previous, it is expected the length of the plastic hinge to be greater for the test that is conducted at 400 °C.

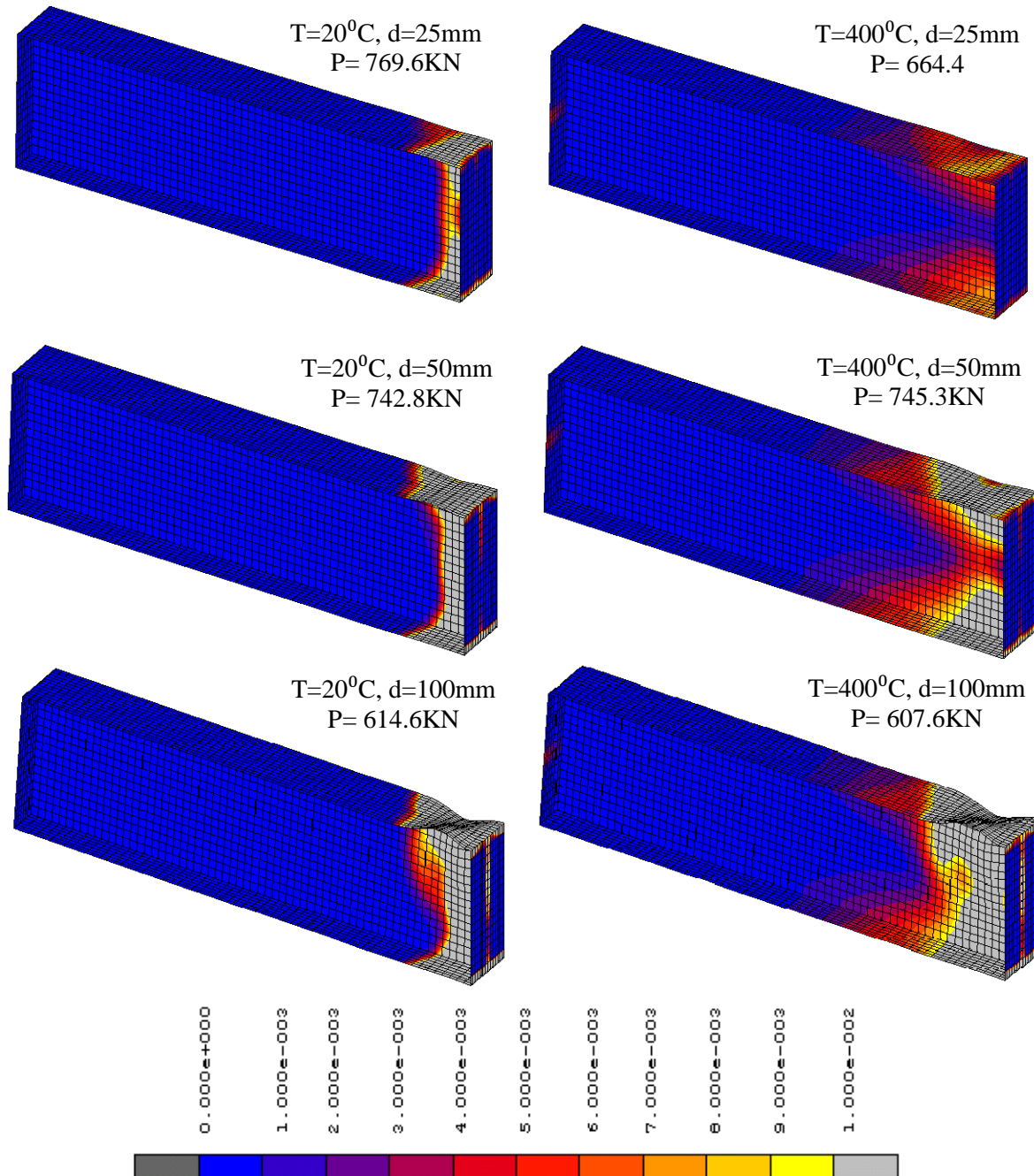


Figure 12-21: Deformed shape of the beam and the distribution of equivalent plastic strain at different increments for temperature equal to $T=20^\circ\text{C}$ and $T=400^\circ\text{C}$ (amplitude of initial imperfections equal to 2mm).

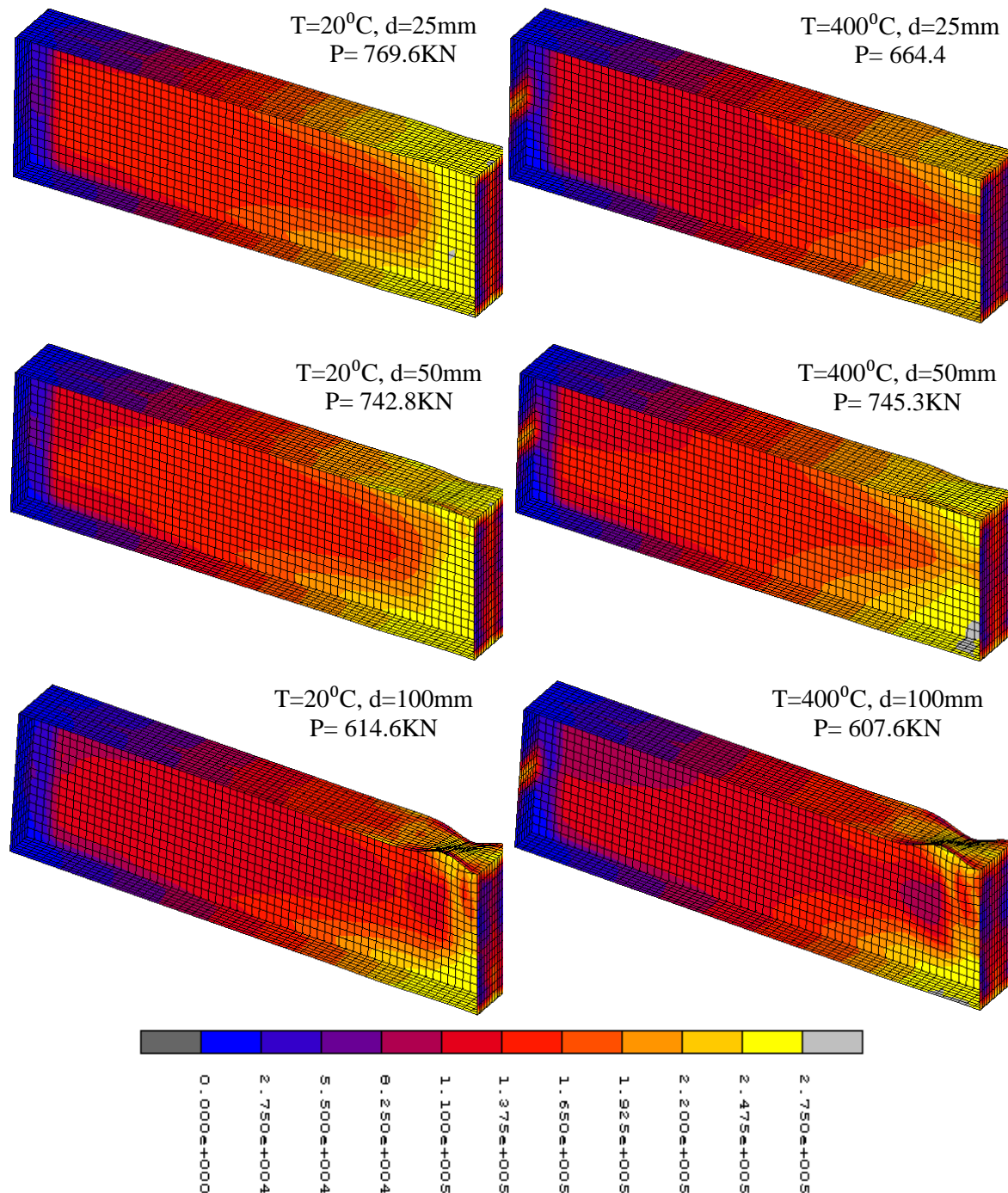


Figure 12-22 : Deformed shape of the beam and the distribution of Von mises at different increments for temperature equal to $T=20^\circ\text{C}$ and $T=400^\circ\text{C}$ (amplitude of initial imperfections equal to 2mm).

Additionally, Figure 12-23 presents the results of the analyses for both temperature levels ($T=20^\circ\text{C}$ and $T=400^\circ\text{C}$) taking into account maximum amplitude of initial imperfections equal to 5mm. In general, the behaviour of the beam remains the same. It can be observed that in this case the local buckling takes place for imposed displacement $d=50\text{mm}$. This is not observed in the previous case where the amplitude was considered to be equal to 2mm. This indicates that as the amplitude of the initial imperfections increases, the beam would fail for lower values of imposed loading.

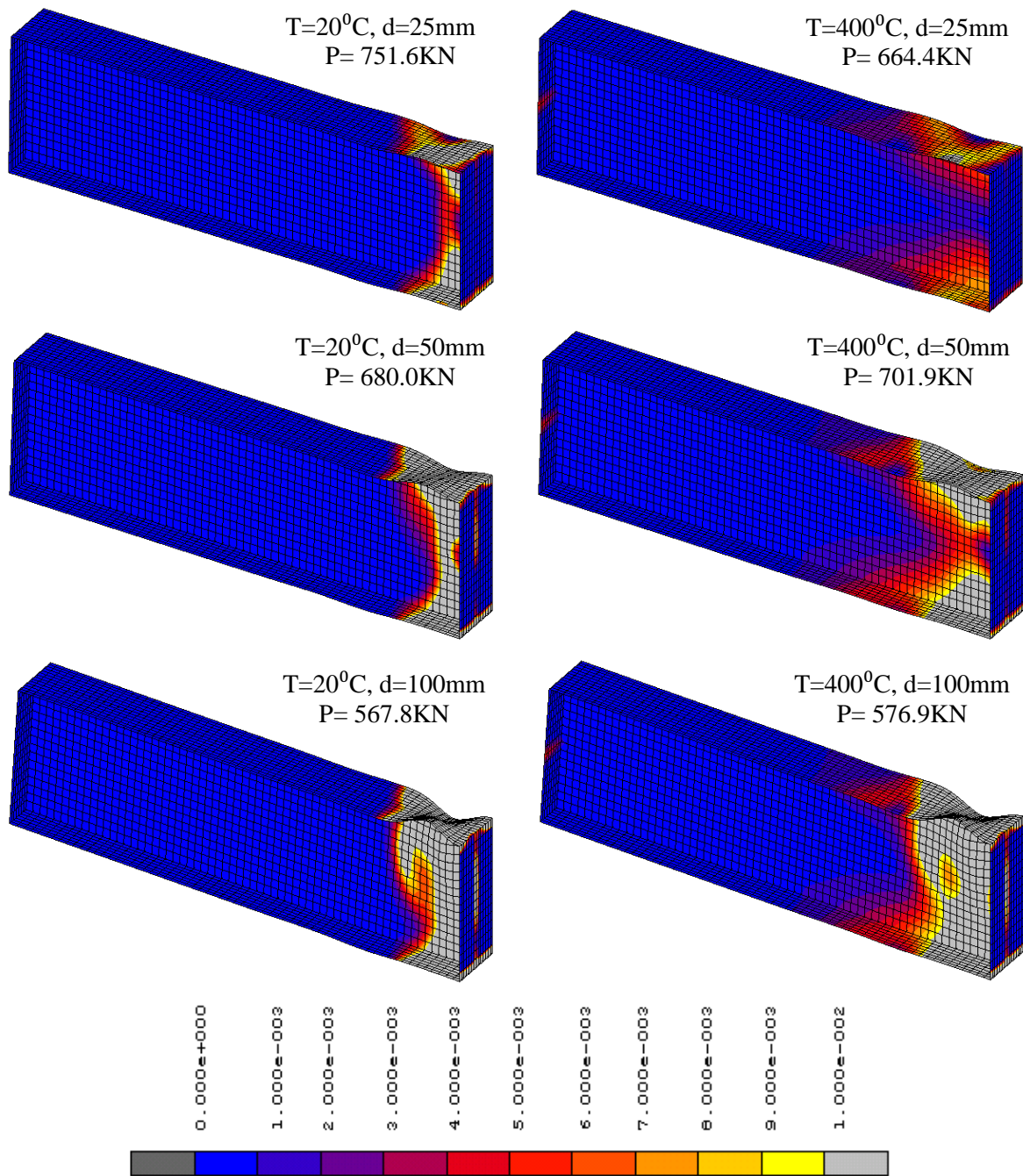


Figure 12-23: Deformed shape of the beam and the distribution of equivalent plastic strain at different increments for temperature equal to $T=20^\circ\text{C}$ and $T=400^\circ\text{C}$ (amplitude of initial imperfections equal to 5mm).

The load-deflection diagrams for the analyses that are conducted at room temperature and at 400°C are presented in Figure 12-24, considering different amplitudes of initial imperfections (2mm and 5mm). First, the analyses are compared with respect to the temperature level. Considering the analyses where the amplitude of initial imperfection is equal to 2mm, it can be observed that for small values of imposed displacement the beam carries greater values of loading at room temperature. This can be explained through the stress distribution (Figure 12-22) in the mid-span cross section. As it is illustrated in the diagrams, the descending branch starts for different values of the imposed displacement. Regarding the analysis at room temperature the plastic local buckling takes place for

$d=12.5\text{mm}$ approximately while the corresponding magnitude at $400\text{ }^{\circ}\text{C}$ is 50mm . Also, it is noted that the ultimate load-bearing capacity is lower when the temperature is equal to $400\text{ }^{\circ}\text{C}$ despite the fact that the yield stress is identical in the cases that are considered here. The maximum load-bearing capacity of the beam is reduced due to the local buckling at the upper flange. The reduction at the temperature of $400\text{ }^{\circ}\text{C}$ can be attributed to the extended strain-hardening branch (branch b in Figure 12-25). The softening branch that follows is identical due to the same type of failure that develops for both cases. In general, the same conclusion holds for the analyses where the amplitude of initial imperfection is equal to 5mm . The failure happens for lower values of imposed loading and again the ultimate capacity is decreased at $400\text{ }^{\circ}\text{C}$.

It is interesting to compare the results of the analyses with respect to the amplitude of initial imperfections. The increase of the amplitude of the initial imperfections leads to premature occurrence of the descending branch and to further reduction of the ultimate capacity of the beam. This amplifies the effect of the local buckling on the reduction of the ultimate capacity as it is stated in the previous. The load-deflection curves indicate that the phenomenon is more intense at elevated temperatures.

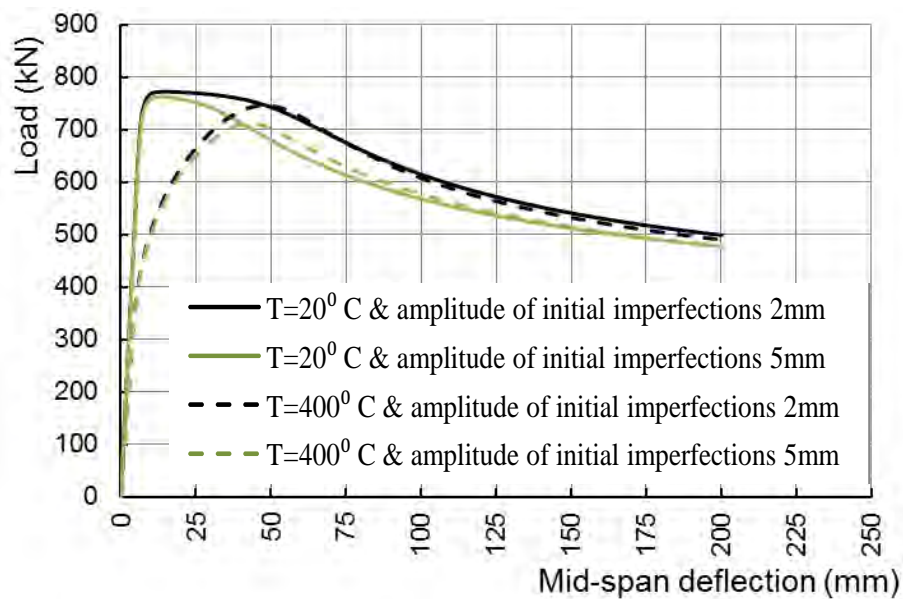


Figure 12-24: Load-deflection curves at $20\text{ }^{\circ}\text{C}$ and $400\text{ }^{\circ}\text{C}$.

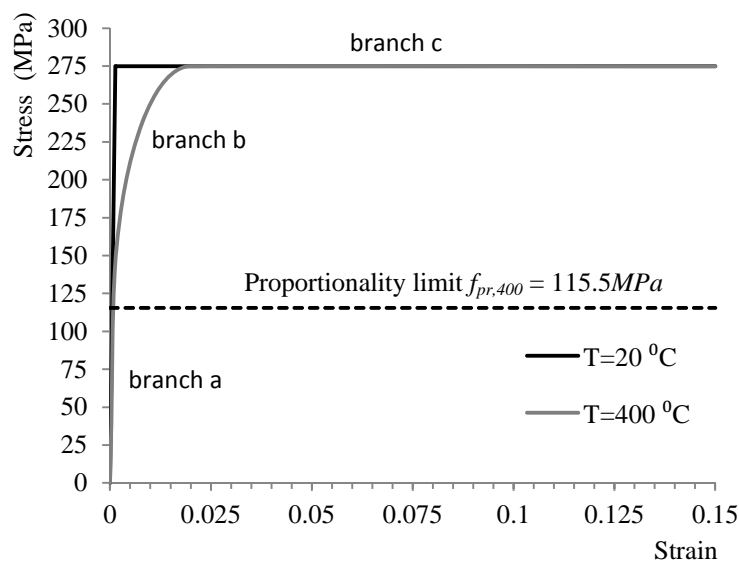


Figure 12-25: The stress-strain relationship of steel (S275) for temperature levels 20 and 400 °C.

Figure 12-26 presents the deformed shape of the beam and the equivalent plastic strain field for the analyses carried out at 500 °C and 700 °C. The amplitude of initial imperfections is considered to be equal to 2mm in both analyses. At this point the comparison is conducted in order to find out the effect of the reduction of the yield stress and the proportionality limit of steel at elevated temperatures. It is noted that the reduction factor of the yield stress of steel is 0.78 and 0.23 for 500 °C and 700 °C respectively. The corresponding values for the proportionality limit are 0.36 and 0.075. The distribution of the equivalent plastic strain is almost similar at the temperatures that are considered here. Moreover, the descending branch that develops is due to plastic local buckling in both cases. It can be observed that as the temperature increases the plastic zone is slightly extended. This is more obvious in Figure 12-27 where the elevation and the plan view of the beam are illustrated for both temperatures at the increment where the imposed displacement is $d=50\text{mm}$. In order to understand in detail the behaviour of the beam at elevated temperatures, the Von-Mises stress distribution is shown in Figure 12-28 and Figure 12-29 for temperatures equal to 500 °C and 700 °C respectively and for different increments of the analyses. In both figures the limit value of the stress corresponds to the proportionality limit while the upper limit is the yield stress of steel with respect to the temperature that is considered in each case. Taking into account these limits, the contours of the colored diagrams can be considered as “dimensionless” and the direct color comparison is possible. The comparison with respect to the temperature level shows that the contours are almost similar for the different temperatures that are considered. This holds for all the increments of the analyses until the occurrence of the descending branch. During the unloading stage (increment where the imposed displacement is equal to 100mm) the stress contours are quite different and this indicates that the slope of the descending branch is not expected to be the same.

In Figure 12-30 the load-deflection curves for both the numerical tests conducted at 500 °C and 700 °C are displayed. As it is expected, the ultimate load-bearing capacity of the beam

is considerably reduced at 700 °C due to the reduction of the yield stress. The comparison is more accurate in the dimensionless curves that are given in the following.

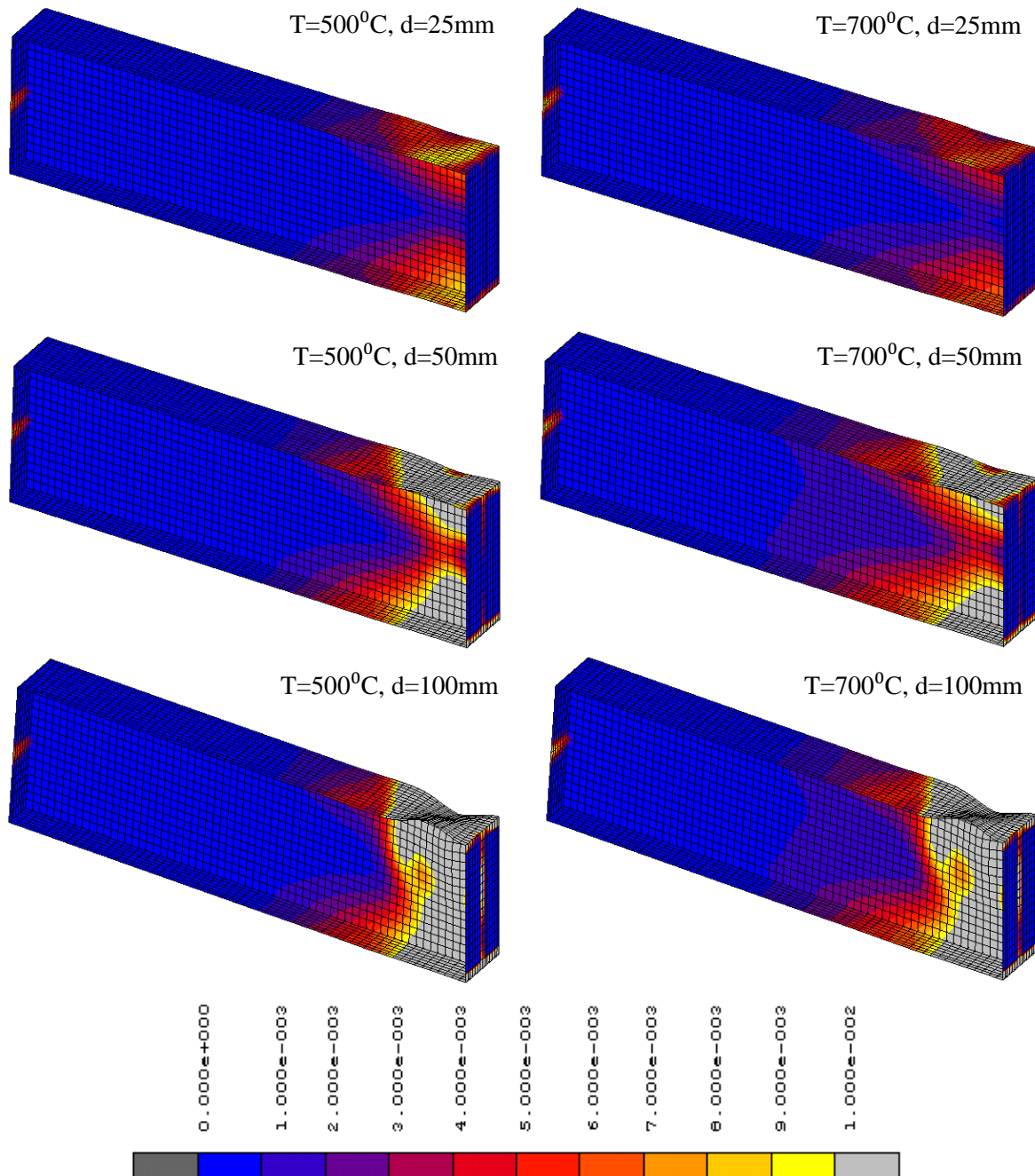
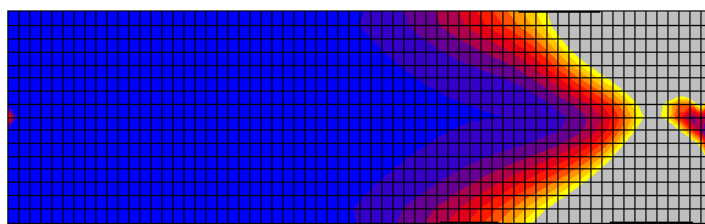
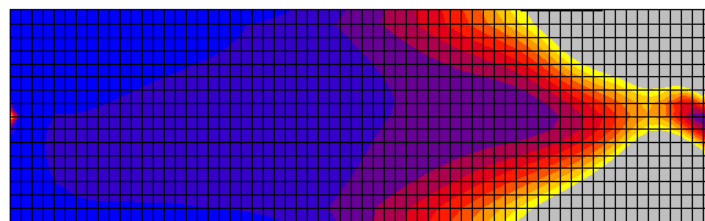


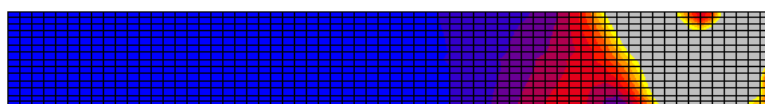
Figure 12-26: Deformed shape of the beam and the distribution of equivalent plastic strain at different increments and for temperature equal to $T=500^{\circ}\text{C}$ and $T=700^{\circ}\text{C}$ (amplitude of initial imperfections equal to 2mm).



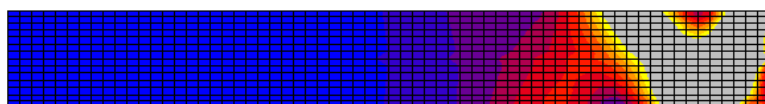
a) Elevation at $T=500^{\circ}\text{C}$



b) Elevation at $T=700^{\circ}\text{C}$



c) Plan view at $T=500^{\circ}\text{C}$



d) Plan view at $T=700^{\circ}\text{C}$

Figure 12-27: Distribution of equivalent plastic strain for $d=50\text{mm}$ (amplitude of initial imperfection equal to 2mm).

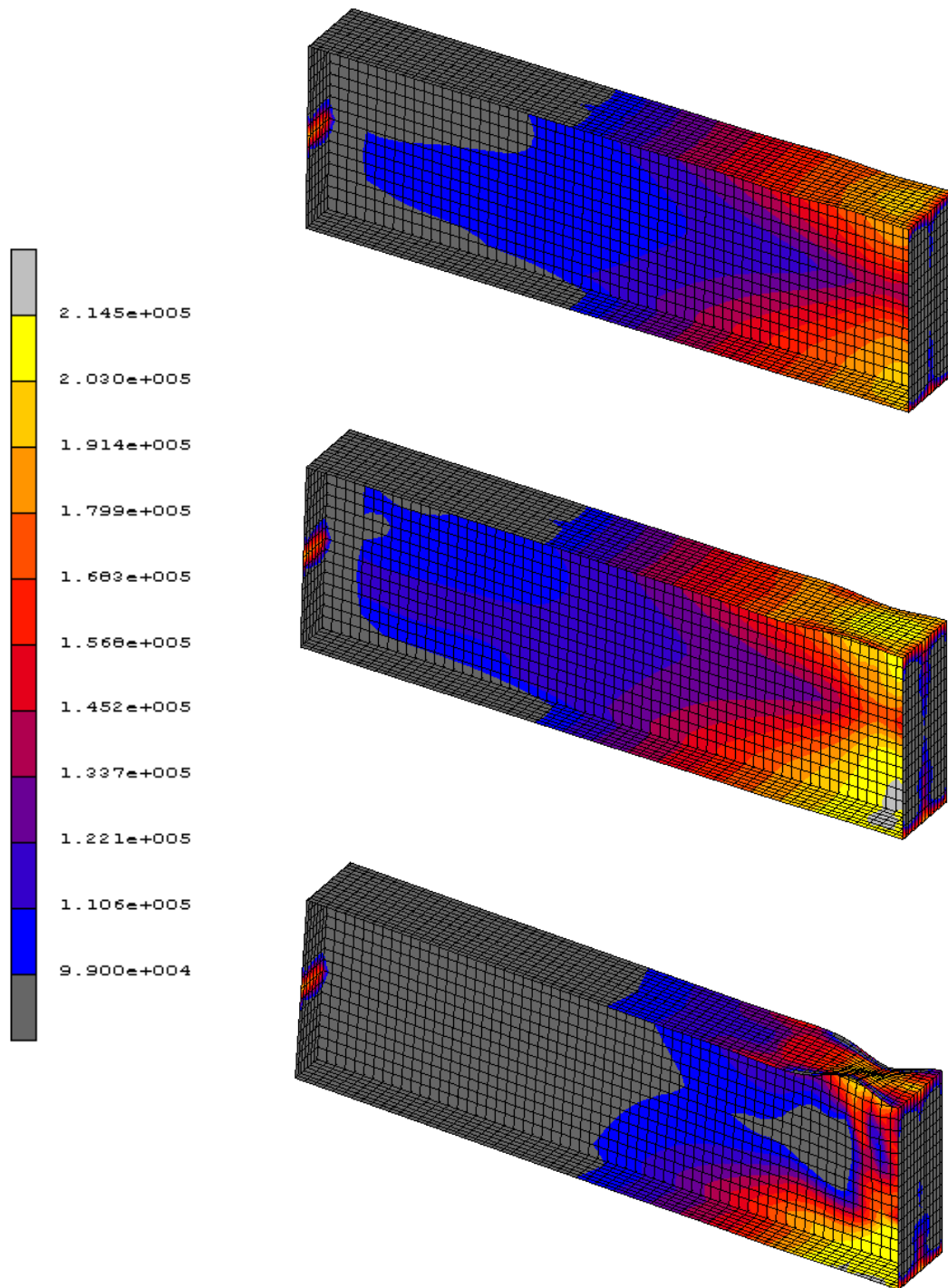


Figure 12-28 Von Mises stress distribution at $T=500^{\circ}\text{C}$ (amplitude of initial imperfection equal to 2mm).

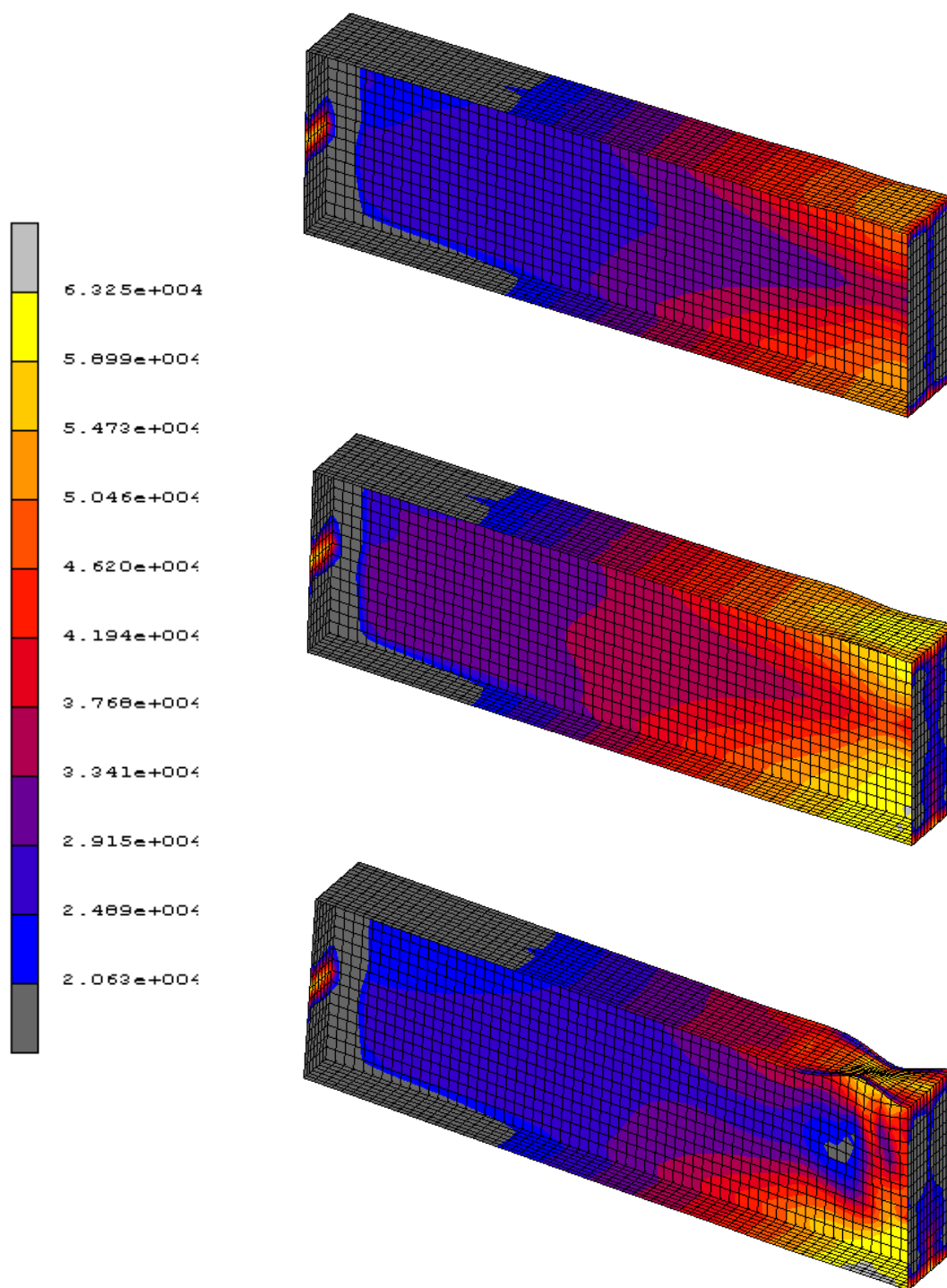


Figure 12-29: Von Mises stress distribution at $T=700^{\circ}\text{C}$ (amplitude of initial imperfection equal to 2mm).

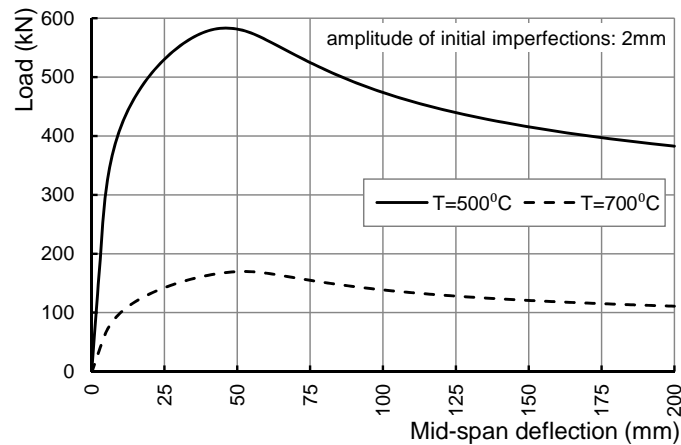
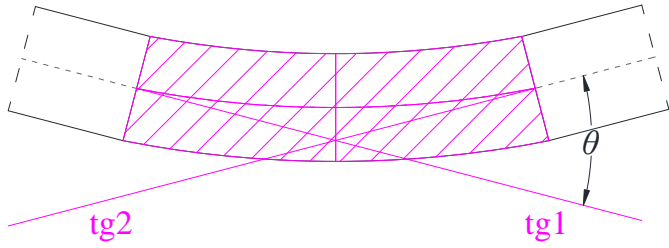
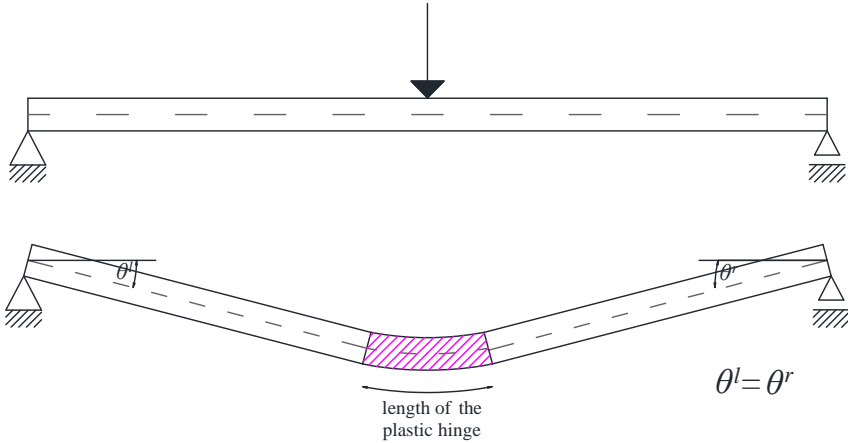


Figure 12-30: Load-deflection curves at 500°C and 700°C (amplitude of initial imperfection equal to 2mm).

At this point the procedure for the evaluation of the rotation as it is used in this thesis should be defined. The rotation that comes from the simulation of the three point bending test is the rotation of the plastic hinge as it is illustrated in Figure 12-31. Specifically, it should be defined as the relative angle α between the tangents (tg1 and tg2) of the deformed shape of the beam at left and right edges of the plastic hinge. This means that initially the limits and the length of the plastic hinge should be determined in order to define the tangent of the deformed shape of the beam at the left and the right edge of the hinge.

The calculation can be simplified if it is taken into account the fact that after the plastic hinge is formed, the rotation (tangent of the vertical deflection curve) is quite constant in the elastic region.. This indicates that it is adequate to calculate the tangent of the beam at the position of the supports and not the rotation at both sides of the plastic hinge region. Furthermore, if the symmetry with respect to the vertical axis of the beam is considered, the calculation is restricted to the evaluation of the rotation angle at one of the supports. The total rotation of the plastic hinge is the double of this value. For design purposes the half of this value should be used, since the plastic hinge is formed at the support position and the interest is focused to the rotation of beams that lie at both sides of the support. This is exactly the rotation as it is defined at the support position of the simply supported beam (Figure 12-31).

Figure 12-32 defines the rotation as it is used in this study. The rotation is obtained from the results of the FEM analyses. Specifically, first the vertical displacements field is obtained for the longitudinal centroid axis of the beam, as it is illustrated in the example of Figure 12-33. The displacement field is differentiated and the rotation on the centroid axis at the support position is obtained.



θ : The relative angle between the tangent lines
 $\theta = \theta^l + \theta^r$

Figure 12-31: Definition of the rotation of the plastic hinge.

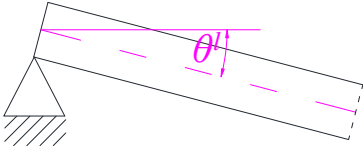


Figure 12-32: Rotation that is used in this study.

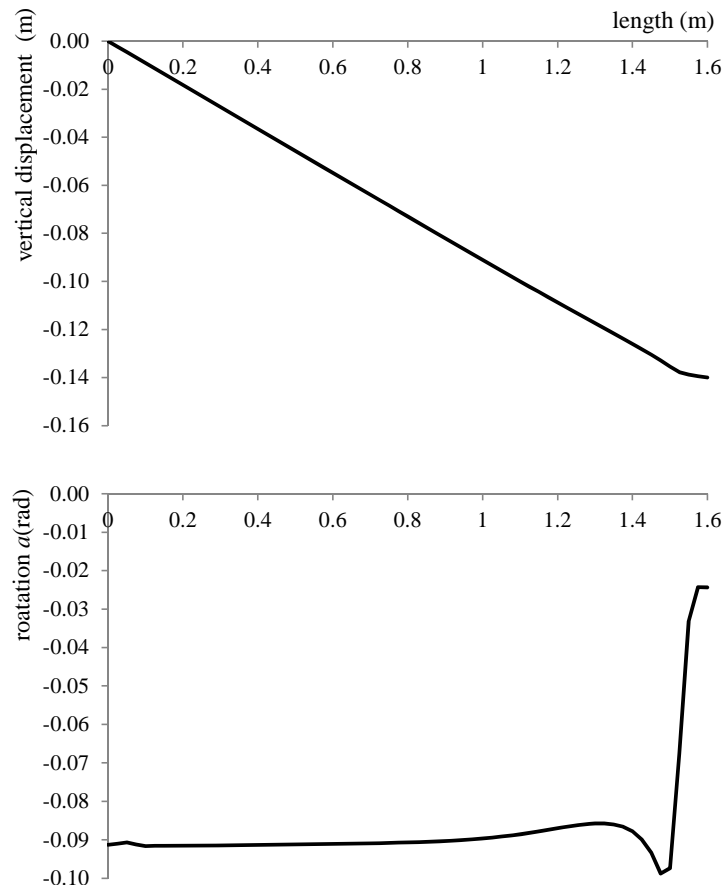


Figure 12-33: Procedure for the evaluation of the rotation.

The moment-rotation curves

The moment-rotation curves for all the temperature levels are presented in Figure 12-34. Imperfections sensitivity study is conducted in order to discover the effect to the ultimate capacity and furthermore to the rotational capacity of the beam. The incorporation of the initial imperfection of the beam geometry results to the reduction of the ultimate load bearing capacity of the beam and this more obvious at elevated temperatures. Table 7.3 presents the moment resistance considering both results from the FEM analyses and the corresponding values according to the calculations based on the plastic resistance of the cross-section. The reduction is calculated with respect to the moment resistance that results from the FEM analysis where the model is considered to be perfect. This comparison is conducted in order to evaluate the possible reduction of the ultimate moment resistance in the case where the imperfections are not considered in the finite element modeling. The comparison shows that the reduction becomes important as the temperature and the amplitude of the initial imperfections increase.

The rotation that corresponds to the ultimate moment capacity of the beam (Table 12-2) is increased as the temperature rises. This can be attributed to the elliptic plastic branch that is incorporated in the stress-strain relationship of steel at elevated temperatures. Due to this

branch, that lies between the elastic and the perfectly plastic one the strain that corresponds to the yield stress is increased compared to the respective value at room temperature. On the other hand as the amplitude of initial imperfections increases, the rotation that corresponds to the ultimate moment capacity is considerably reduced as it is indicated in Table 12-2.

Additionally, it is interesting to notice the effect of the amplitude of the initial imperfections on the descending branch of the curve. The diagrams show that as the magnitude of the initial imperfection increases, the descending branch becomes steeper. This holds for all the imperfect models at both room conditions and at elevated temperatures.

The “perfect” model simulates adequately the phenomenon, until the maximum moment is attained. The results concerning these analyses are not accurate concerning the unstable branch. In general, due to the local instabilities that arise during the physical phenomenon it is more accurate to incorporate the initial imperfections into the beam geometry in order to obtain more realistic results using the finite element method. It can be observed that the gradient of the descending branch is milder, compared to the imperfect models. This can be understood more clearly through the deformed shape of the beam during the descending branch. Figure 12-35 illustrates the local buckling mechanism for the “perfect” and the “imperfect” model (amplitude of initial imperfections 0.5mm) at 200⁰C. The results of the analysis are referred to the same loading step, which corresponds to the descending branch for both models. It is indicated that the local buckling failure mode is completely different for the models that are considered. In the case of the “perfect” model, the upper compressive flange buckles symmetrically with respect to the x - y plane of symmetry of beam. On the other hand, in the case of the “imperfect” model both the upper flange and the web buckle. The buckling of the upper flange is anti-symmetric with respect to the same plane. Moreover, the amplitude and the size of the half-wave length are greater in the case of the imperfect models compared to the perfect one. These different failure modes are reflected to the different descending branches in the diagrams. All the previous hold for all the temperature levels that are studied.

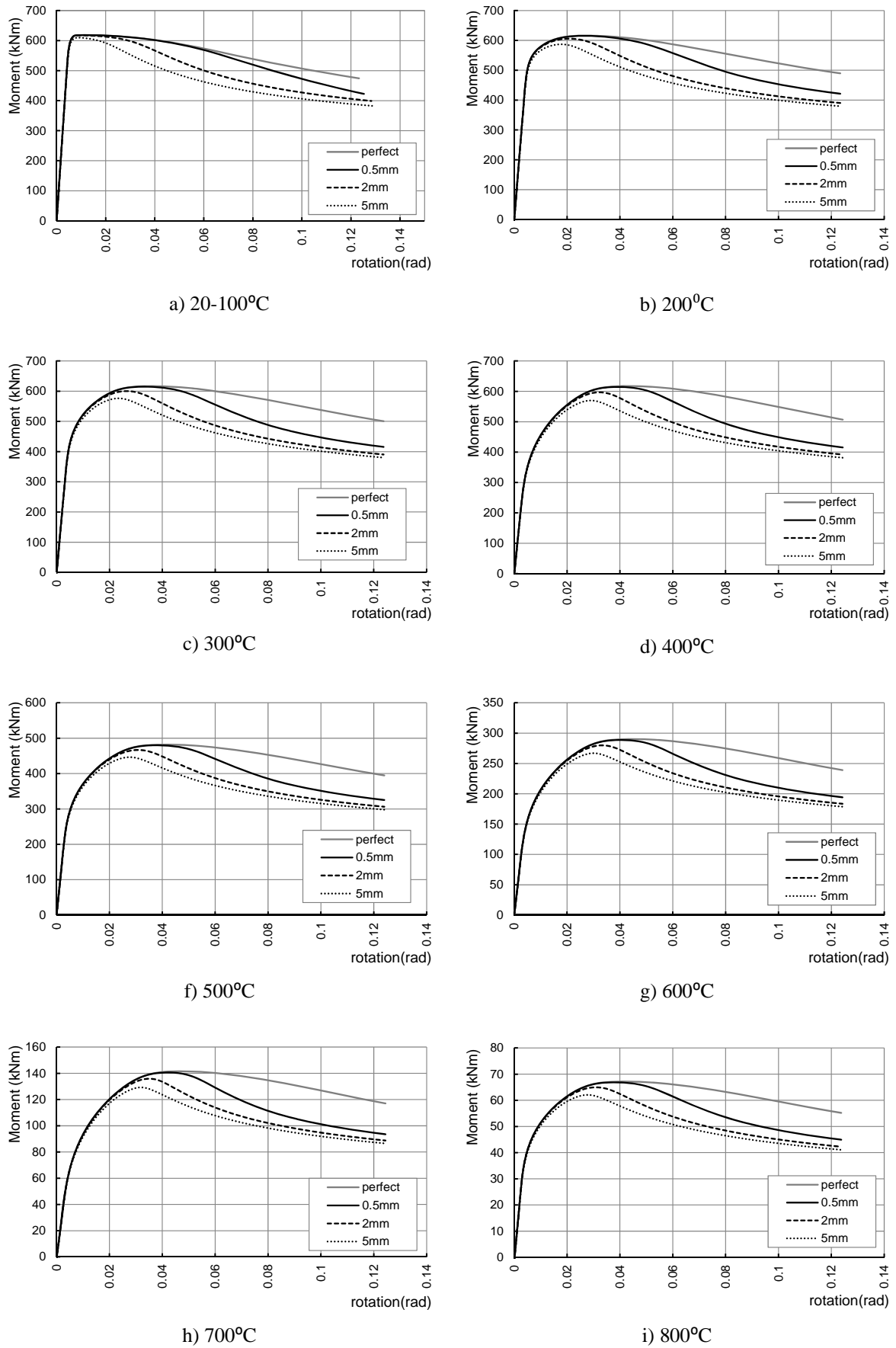


Figure 12-34: Moment-rotation curves at different temperature levels and for various amplitudes of initial imperfections.

T (°C)	20/100	200	300	400	500	600	700	800
M_{pl} (KNm) ¹	603.35	603.35	603.35	603.35	470.61	283.57	138.77	66.37
Perfect model								
M_u (KNm) ²	618.67	616.33	616.86	617.47	481.99	290.24	141.55	67.17
θ_{max} (rad) ⁴	0.011	0.027	0.036	0.043	0.041	0.045	0.047	0.042
Amplitude of initial imperfections 0.5mm								
M_u (KNm) ²	618.62	615.38	614.89	614.58	479.96	288.71	140.62	66.87
Moment reduction ³	0.01%	0.15%	0.32%	0.47%	0.42%	0.53%	0.66%	0.45%
θ_{max} ⁴	0.011	0.026	0.033	0.039	0.038	0.040	0.042	0.038
θ_{max} reduction ⁵	0.00%	4.52%	8.53%	9.87%	8.87%	9.56%	10.29%	8.74%
Amplitude of initial imperfections 2mm								
M_u (KNm) ²	617.56	606.09	600.26	596.75	466.70	279.86	135.88	64.97
Moment reduction ³	0.18%	1.66%	2.69%	3.36%	3.17%	3.58%	4.01%	3.28%
θ_{max} (rad) ⁴	0.010	0.020	0.027	0.032	0.031	0.033	0.035	0.031
θ_{max} reduction ⁵	5.51%	24.97%	25.78%	25.58%	25.35%	24.80%	25.99%	26.46%
Amplitude of initial imperfections 5mm								
M_u (KNm) ²	609.89	587.11	576.34	570.03	446.39	266.95	129.28	62.08
Moment reduction ³	1.42%	4.74%	6.57%	7.68%	7.39%	8.02%	8.67%	7.58%
θ_{max} (rad) ⁴	0.009	0.018	0.023	0.029	0.028	0.030	0.032	0.028
θ_{max} reduction ⁵	16.34%	34.15%	34.58%	32.89%	33.02%	31.89%	32.71%	34.03%

¹ According to the elastic-plastic cross-section analysis

² According to FEM results

³ Reduction with respect to the moment resistance that results from the FEM analysis where the model is considered to be perfect

⁴ Rotation that corresponds to the ultimate moment capacity

⁵ Reduction with respect to the maximum rotation that results from the FEM analysis where the model is considered to be perfect

Table 12-2: The moment resistance of the beam and the maximum rotation at different temperature levels.

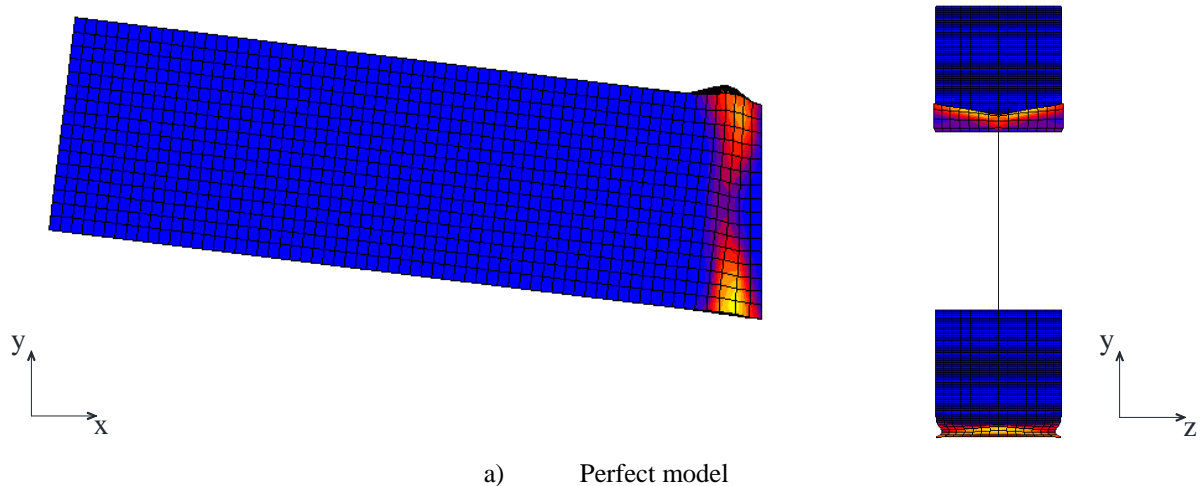


Figure 12 35: Deformed shape and failure mode of the beam during the unloading stage at 200°C. (continued)

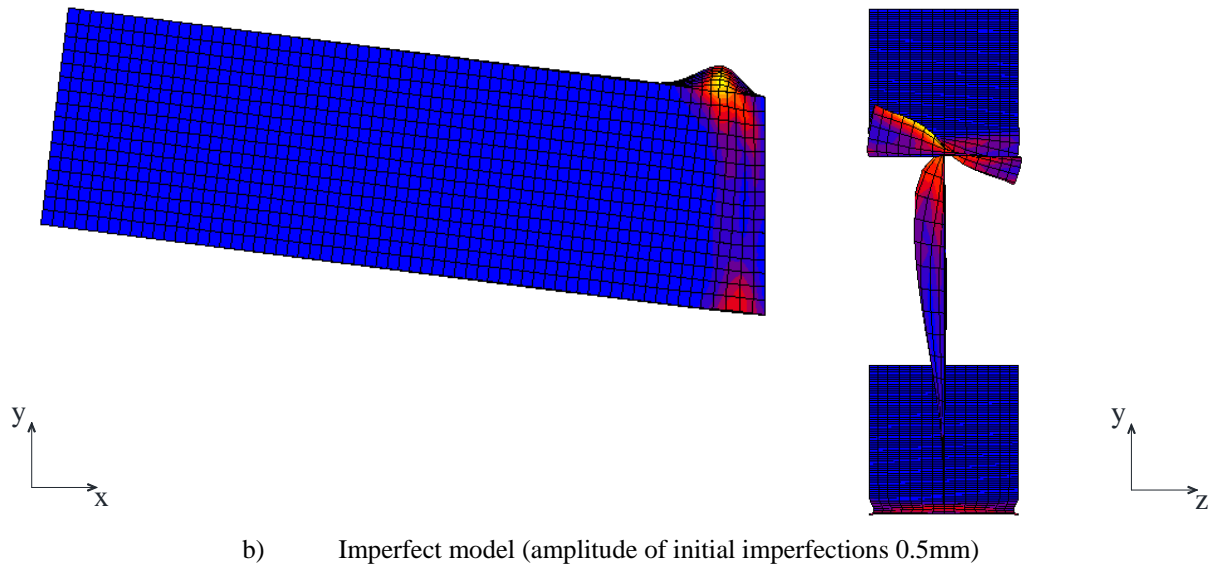


Figure 12-35: Deformed shape and failure mode of the beam during the unloading stage at 200°C.

The available rotation

The next objective is to use the curves obtained in the previous Section in order to evaluate the available rotation of the beam. Figure 12-36 presents the evolution of the available rotation of the beam with the temperature for different amplitudes of initial imperfections and Table 12-3 summarizes the values for $\theta_{pl1,0.9,T}$ and $\theta_{pl2,0.9,T}$ and the available rotation $\theta_{\alpha,0.9,T}$ that result from the FEM analyses. The values of $\theta_{pl1,0.9,T}$ and $\theta_{pl2,0.9,T}$ correspond to $0.9M_{pl,T}$ according to the definition of the rotational capacity that is used in this study. It is noticed that for the models that include initial imperfections, the available rotation of the beam is reduced as the temperature increases. Moreover as the amplitude of the imperfections increases, the available rotation is significantly reduced. It is noticed that for all the considered amplitudes of initial imperfections, the available rotation is slightly increased at 500°C and 800°C. This can be connected to the ratio of the modulus of elasticity to the yield stress at elevated temperatures. As it is shown in Figure 12-1 the same phenomenon is also present in the diagram that gives the evolution of $\sqrt{\frac{k_{E,\theta}}{k_{y,\theta}}}$ with temperature.

In the case of the “perfect” model, the available rotation seems to be an ascending function of the temperature. This is connected to the shape of the descending branch (in the moment-rotation diagram).

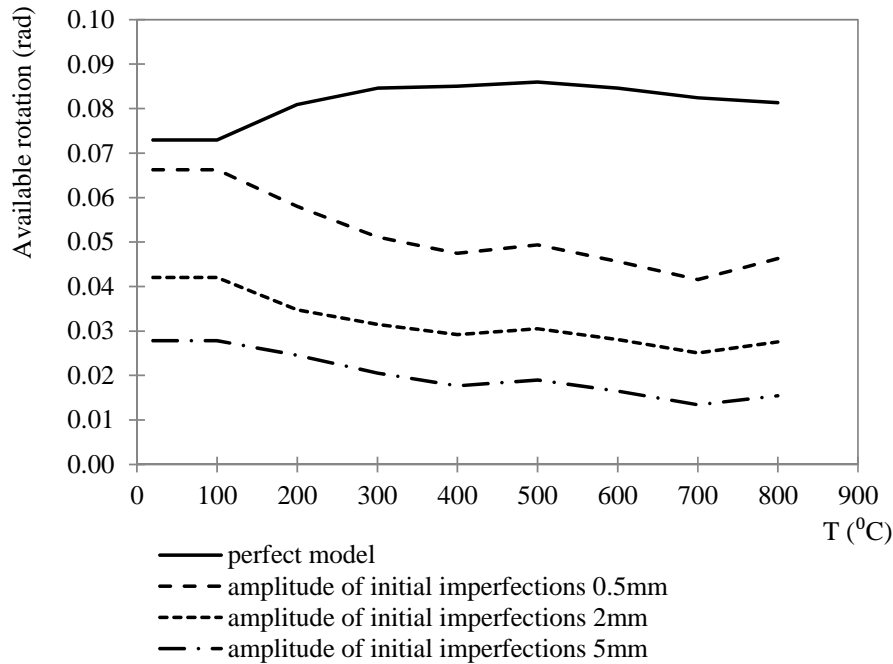


Figure 12-36: The evolution of the available rotation with the temperature and the effect of the amplitude of the initial imperfections.

T	20	200	300	400	500	600	700	800
Perfect model								
$\theta_{pl1,0.9,T}$ (rad)	0.005	0.006	0.012	0.018	0.017	0.020	0.022	0.018
$\theta_{pl2,0.9,T}$ (rad)	0.078	0.087	0.097	0.103	0.102	0.104	0.105	0.099
$\theta_{a,0.9,T}$ (rad)	0.073	0.081	0.085	0.085	0.086	0.085	0.082	0.081
Amplitude of initial imperfections 0.5mm								
$\theta_{pl1,0.9,T}$ (rad)	0.005	0.006	0.012	0.018	0.016	0.020	0.023	0.018
$\theta_{pl2,0.9,T}$ (rad)	0.071	0.064	0.063	0.066	0.066	0.065	0.064	0.064
$\theta_{a,0.9,T}$ (rad)	0.066	0.058	0.051	0.047	0.049	0.046	0.042	0.046
Amplitude of initial imperfections 2mm								
$\theta_{pl1,0.9,T}$ (rad)	0.005	0.007	0.012	0.019	0.017	0.020	0.023	0.018
$\theta_{pl2,0.9,T}$ (rad)	0.047	0.041	0.044	0.048	0.047	0.048	0.048	0.046
$\theta_{a,0.9,T}$ (rad)	0.042	0.035	0.032	0.029	0.030	0.028	0.025	0.028
Amplitude of initial imperfections 5mm								
$\theta_{pl1,0.9,T}$ (rad)	0.005	0.007	0.014	0.021	0.019	0.022	0.025	0.020
$\theta_{pl2,0.9,T}$ (rad)	0.033	0.032	0.034	0.038	0.038	0.039	0.039	0.036
$\theta_{a,0.9,T}$ (rad)	0.028	0.025	0.021	0.018	0.019	0.016	0.013	0.015

Table 12-3: The evaluation of the available rotation of the beam.

The dimensionless moment-rotation curves

In order to compare the results in different temperature levels in a more systematic way, it is necessary to use dimensionless values for the moment and the rotation. The dimensionless moment-rotation curves are presented in Figure 12-37. Considering the moment, $M_{pl,T}$ is used for the regularization, which is the plastic moment resistance

defined as $M_{pl,T} = f_{y,T} w_{pl}$. For the rotation the regularization is based on $\theta_{pl,T}$. This value is taken according to the results of the corresponding analyses according to Table 9.4.

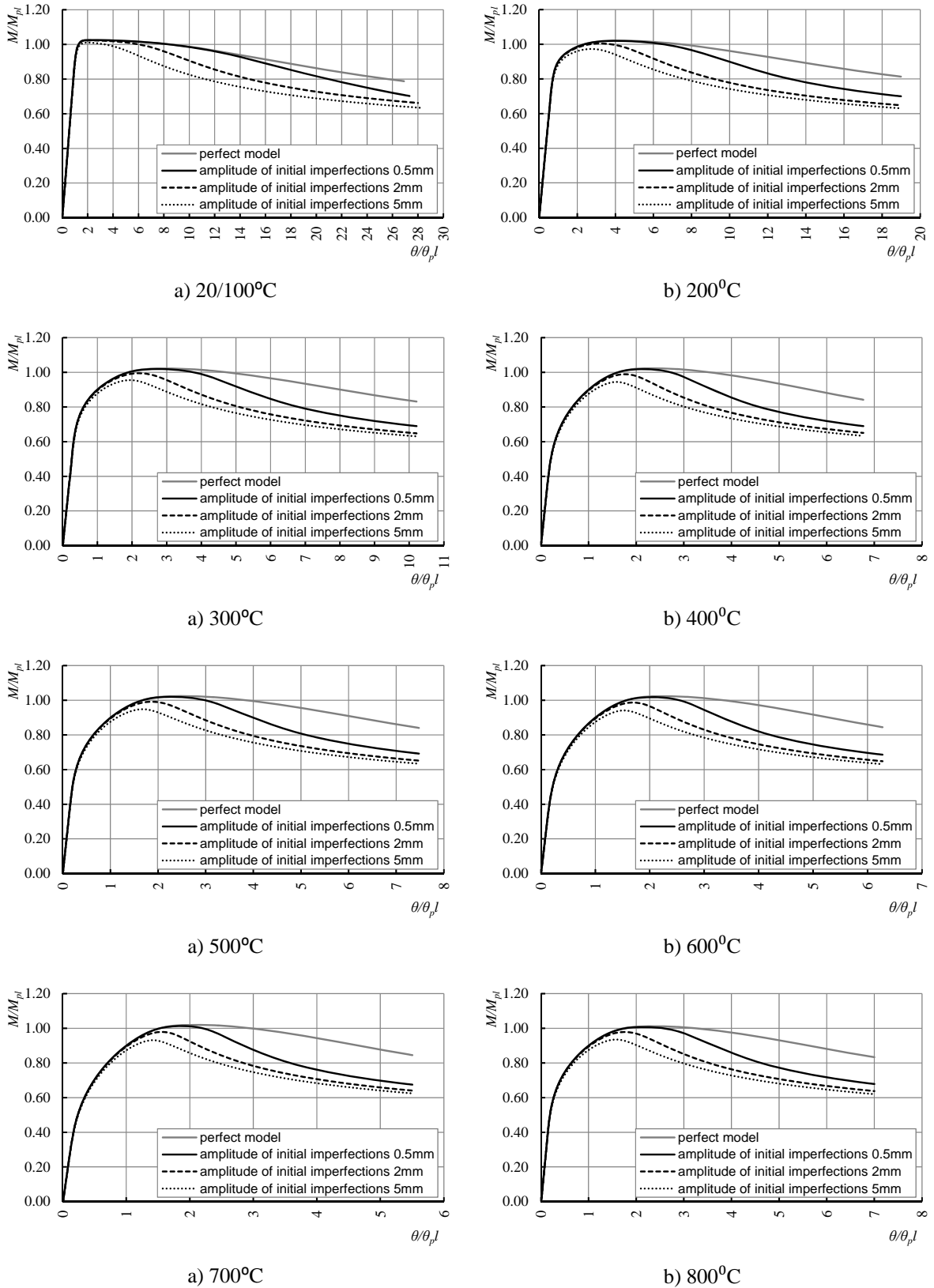


Figure 12-37: Dimensionless moment-rotation curves.

The rotational capacity

Figure 12-38 compares the dimensionless curves at different temperature levels. The comparison is conducted independently for the perfect and the imperfect models. Next, the rotational capacity $r_{0.9,T}$ is evaluated. As it is referred in Section 12.2.2, the rotational capacity is obtained using the value $0.9M_{pl,T}$. In Figure 12-39 it is more clear that the rotational capacity is reduced as the temperature increases and this holds for both the “perfect” and the “imperfect” models. It is noted once more that the rotational capacity is slightly increased at 500°C and 800°C as it is observed in Figure 12-36 for the available rotation. Moreover the rotational capacity is considerably reduced as the amplitude of initial imperfections increases.

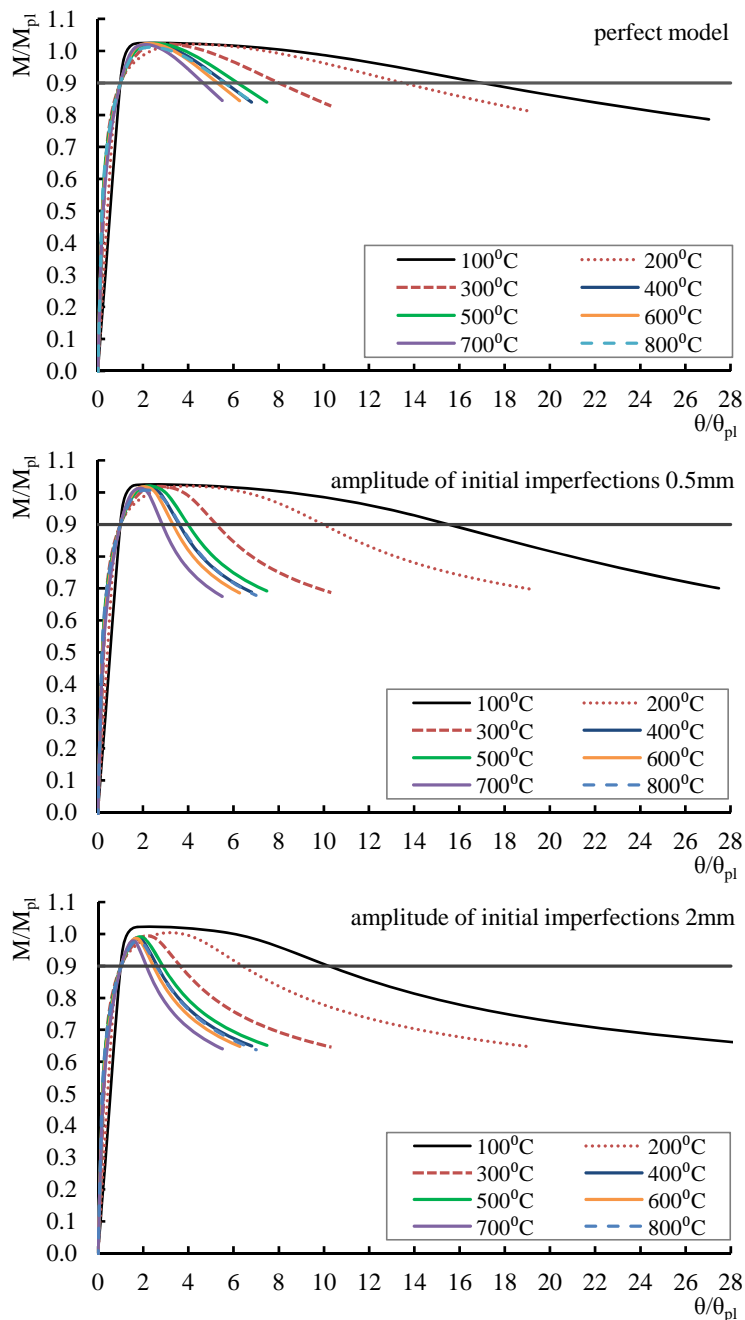


Figure 12-38: Effect of the temperature on the moment-rotation diagrams for different amplitudes of initial imperfections. (continued)

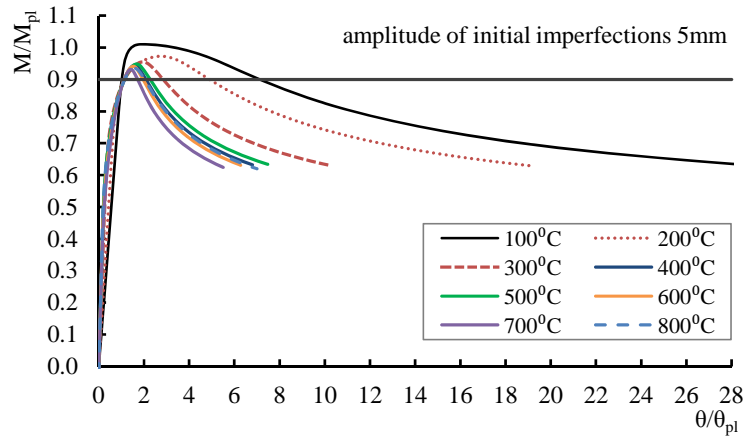


Figure 12-38: Effect of the temperature on the moment-rotation diagrams for different amplitudes of initial imperfections.

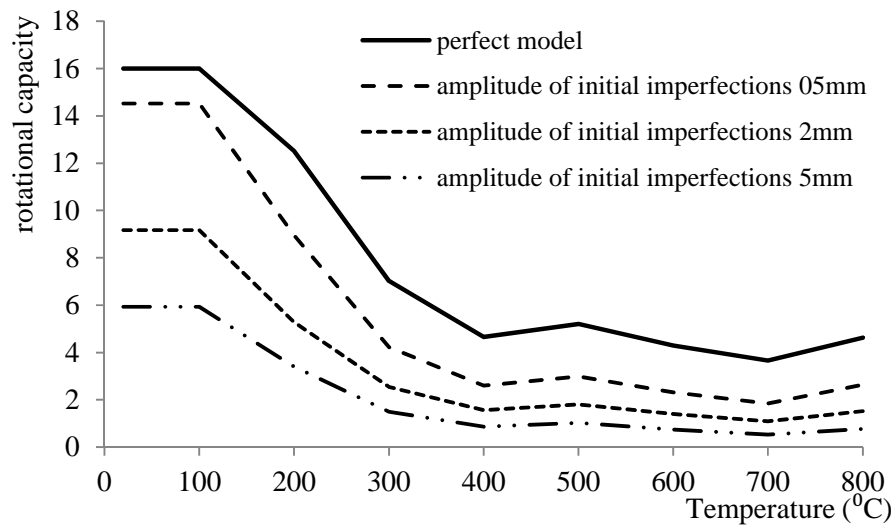


Figure 12-39: The evolution of the rotational capacity with the temperature and the effect of the amplitude of the initial imperfections.

The failure criteria

The final goal is to define the failure criteria for the determination of the fire resistance time of the structure in Chapter 13. The criterion that is proposed in this study is the value of the rotation $\theta_{pl2,0.9,T}$ as it is defined in Section 12.2.2. This value of rotation actually corresponds to the exhaustion of the available rotational capacity of the beam. At the point where this rotation is attained, the moment resistance of the beam becomes equal to $0.9M_{pl,T}$. The term *ultimate available rotation* is used in the following in order to express $\theta_{pl2,0.9,T}$ (see Figure 12-40). Clearly, the criterion depends on the amplitude of the initial imperfections that are considered in the study. It can be observed that the *ultimate available rotation* is not strongly dependent on the temperature. On the other hand as the amplitude of initial imperfection increases, the *ultimate available rotation* is significantly decreased.

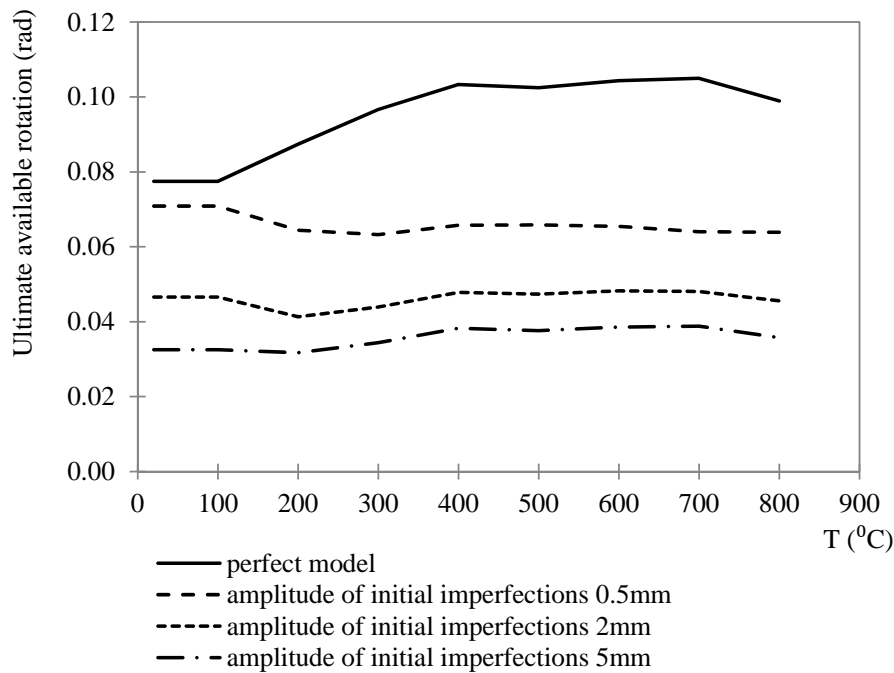


Figure 12-40: The evolution of the ultimate available rotation with the temperature and the effect of the amplitude of the initial imperfections.

12.4.3 Case 2: Simulation of three point bending test at pre-damaged beams (due to cyclic loading) at elevated temperatures

The numerical analysis that is conducted for the simulation of the three point bending test at pre-damaged beams has three different stages. The analysis is displacement controlled. It is specified that the beams are referred as “pre-damaged”, due to the damage that has been induced through the cyclic loading. Consequently, the first stage is the cyclic loading. In the second stage the temperature increases until the desired level is reached. During this stage the thermal actions should be considered. The monotonic loading stage follows, while the temperature remains constant.

The determination of the pattern of the cyclic loading is crucial since the point where this stage stops defines the initial configuration of the beam for the next stage. Actually, three different possibilities can be considered for the point where the cyclic loading is terminated. The behaviour of the beam is depicted through the reaction-displacement curves. The first one (configuration *a*) corresponds to the status where the imposed displacement becomes zero but the reaction is not eliminated. In the second case the beam does not return to the initial position thus the displacement is not equal to zero but the reaction is eliminated. In the third case, at the end of the cyclic loading both the displacement and the reaction are zero (Figure 12-41).

The studied issue is the behaviour of the beam during the thermal loading taking into account the configuration of the beam at the start of this loading. In the case where the initial configuration *a* is taken into account, the beam is actually loaded as the temperature increases and this changes the goal of the test. On the other hand in the case where the

configuration *b* is considered, the beam is not loaded during the rise of the temperature and the test is conducted correctly during the second stage. The same holds also for the initial configuration *c*. The next problem that arises when the configuration *b* is taken into account takes place during the third stage of the monotonic loading. In this case there are two different possibilities. The first one is to continue the loading in the same direction and the second one is to impose the load in the opposite direction. The results are not the same, since the first one corresponds to loading while the second one to unloading conditions. Additionally, the problem becomes more complex if initial imperfections are incorporated in the beam geometry. In order to overcome the problem, configuration *c* is finally adopted. The three different stages are illustrated in Figure 12-41.

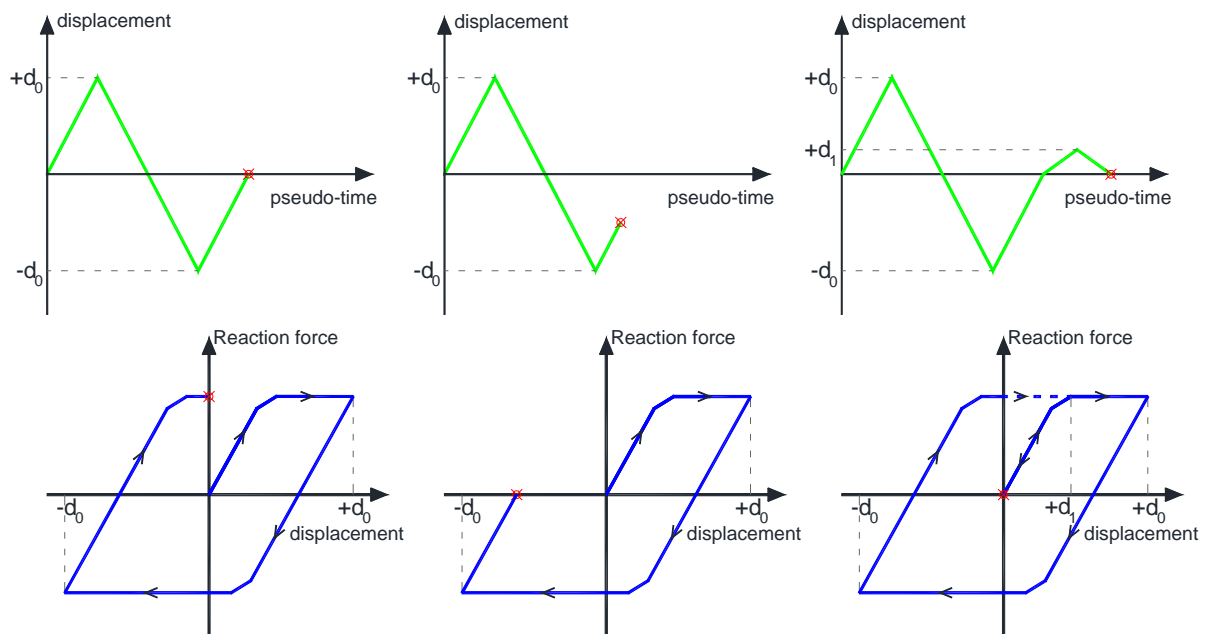


Figure 12-41: Different configurations concerning the cyclic loading.



Figure 12-42: Case 2: loading procedure.

The considered cyclic loading patterns

The cyclic loading is introduced in order to induce a “level” of damage in the beam. Specifically, this simulates the damage that is induced in the frame structure due to earthquake loading. As it is defined in the corresponding Chapter 9, the ‘level of damage’ induced in the frame structure varies and depends on the accelerogram that is used and on the scale factor that is considered. Taking into account the previous, it is obvious that different patterns of cyclic loading should be used in order to simulate different levels of damage induced in the beam.

Five different cyclic loading patterns are studied and they are presented in Figure 12-43. The cyclic loading (displacement controlled) is conducted actually in one and a half cycle. During the first cycle, the amplitude of the imposed displacement varies between 0.02 and 0.05m for the different patterns that are considered, as it is illustrated in Figure 12-43. Specifically, first the maximum value of the displacement is reached, then it is reduced until the negative maximum (same) value is attained and in the following the imposed displacement is eliminated. The final half pattern follows, which is the same for all the considered cases, which has the aim to attain the configuration where both the displacement and the reaction are zero. The designation of the patterns is based on the magnitude of the imposed rotation on the beam as it can be observed in Figure 12-43.

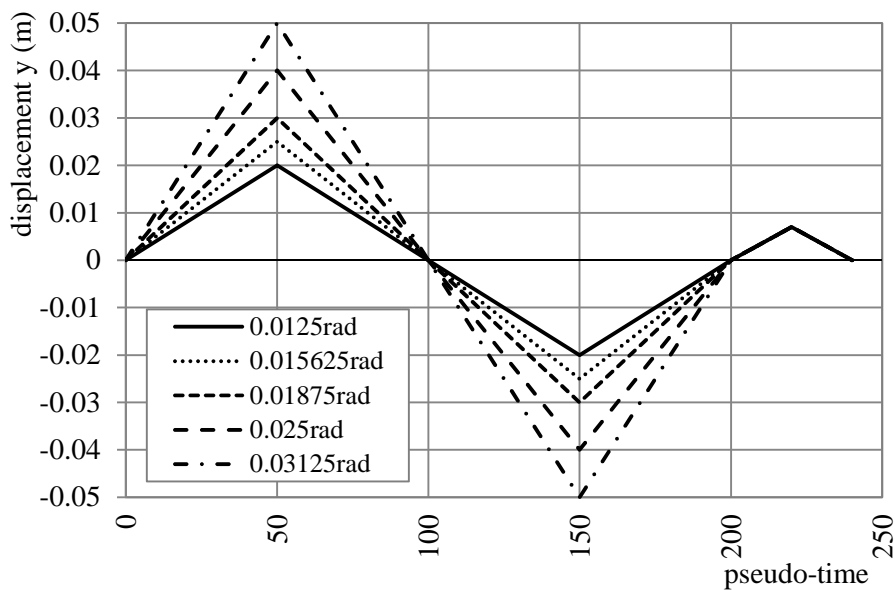


Figure 12-43: Cyclic loading patterns.

It is clear that the results of the analyses that follow (available rotation, rotational capacity and ultimate available rotation) are dependent on the cyclic loading pattern and more accurately on the ‘level of damage’ that is induced in the beam. Considering the previous, it is important to study in detail the deformation and the strain distribution of the beam at the end of the different cyclic loading patterns. The next Section presents the results for the corresponding loading stage.

Behaviour of the beam during the cyclic loading

The reaction force-displacement curves for all the cyclic loading patterns are depicted in Figure 12-44. It is observed that the incorporation of the initial imperfections into the beam geometry affects the behaviour during the cyclic loading and this becomes more clear as the level of the imposed rotation increases. Specifically, the ultimate load-bearing capacity of the beam is reduced when both the amplitude of the initial imperfections and the imposed rotation are increased. This is due to the plastic local buckling that occurs at both flanges and the web. The out-of-plane deflections for both the flanges and the web at the end of the cyclic loading are illustrated in Figure 12-45 and Figure 12-46 respectively. The aforementioned figures present the fields of displacement y and z respectively. Considering the flanges, it is observed that the upper flange appears increased deflections compared to the respective values at the lower one.

Moreover it is noticed that the magnitude of the out-of-plane deflections increases from 1mm to 6mm, as the imposed rotation increases. The local buckling of the flanges is in general symmetric with respect to the x - y plane of symmetry of the beam. On the other hand, the web buckling is not symmetric with respect to the x - z plane of symmetry of the beam. The magnitude of the out-of-plane deflections of the web varies between 0.2mm and 6.5mm. The results presented in Figure 12-45 and Figure 12-46 correspond to the model where the amplitude of the initial imperfections is equal to 2mm. The results are considered representative, since the same phenomena are observed for all the amplitudes of initial imperfections that are studied. Additionally, the aforementioned results are coming from the analyses where the imposed rotation is equal to 18.75mrad. As the imposed rotation becomes greater, the magnitude of the out-of-plane displacements increases. The reverse remark is also true.

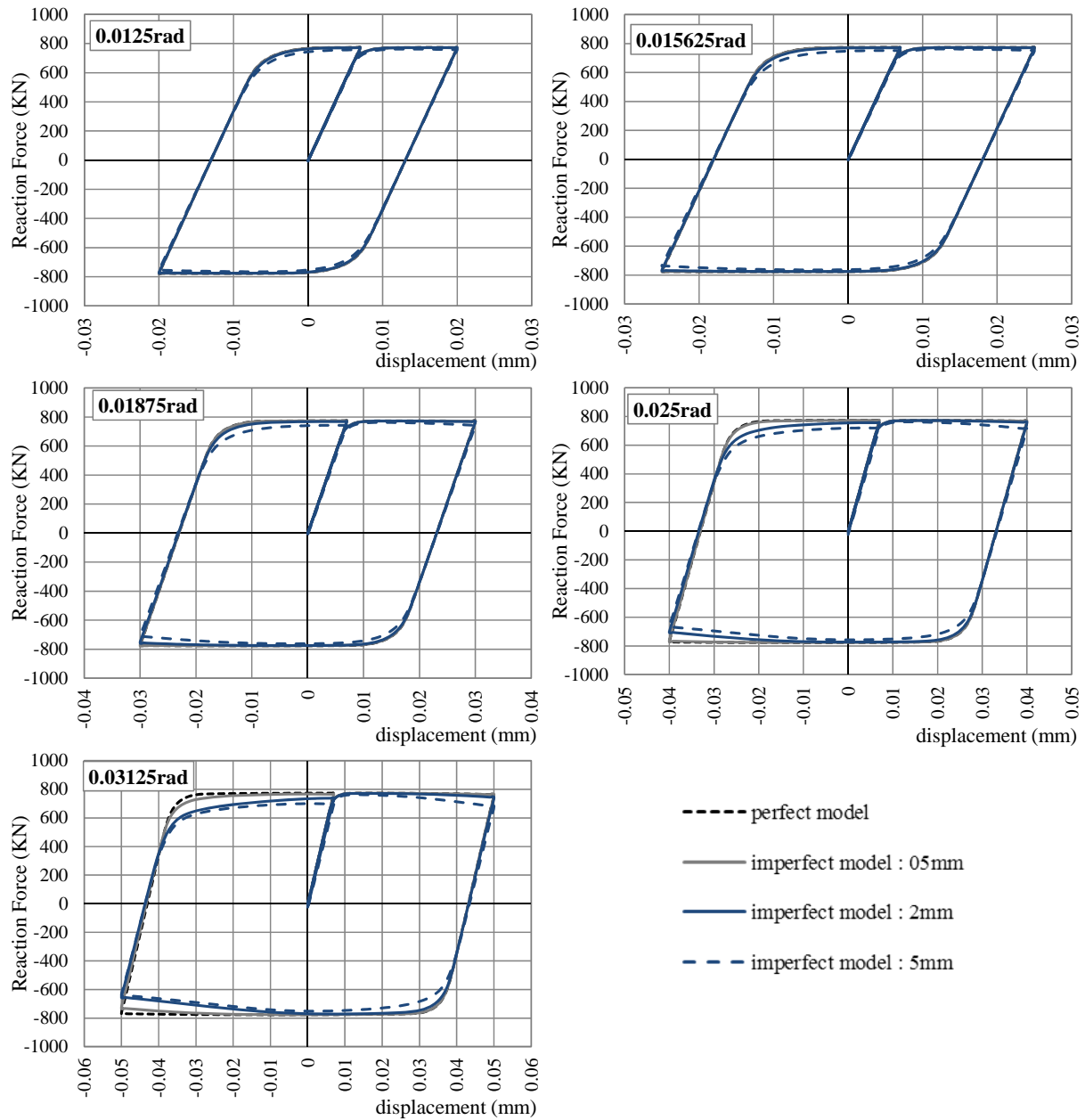


Figure 12-44: Reaction force-displacement curves for the different patterns of cyclic loading.

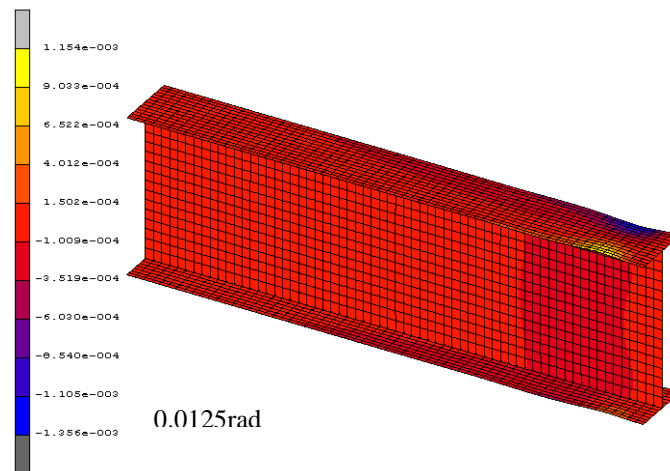


Figure 12-45: Local buckling at the flanges for different cyclic loading patterns. (continued)

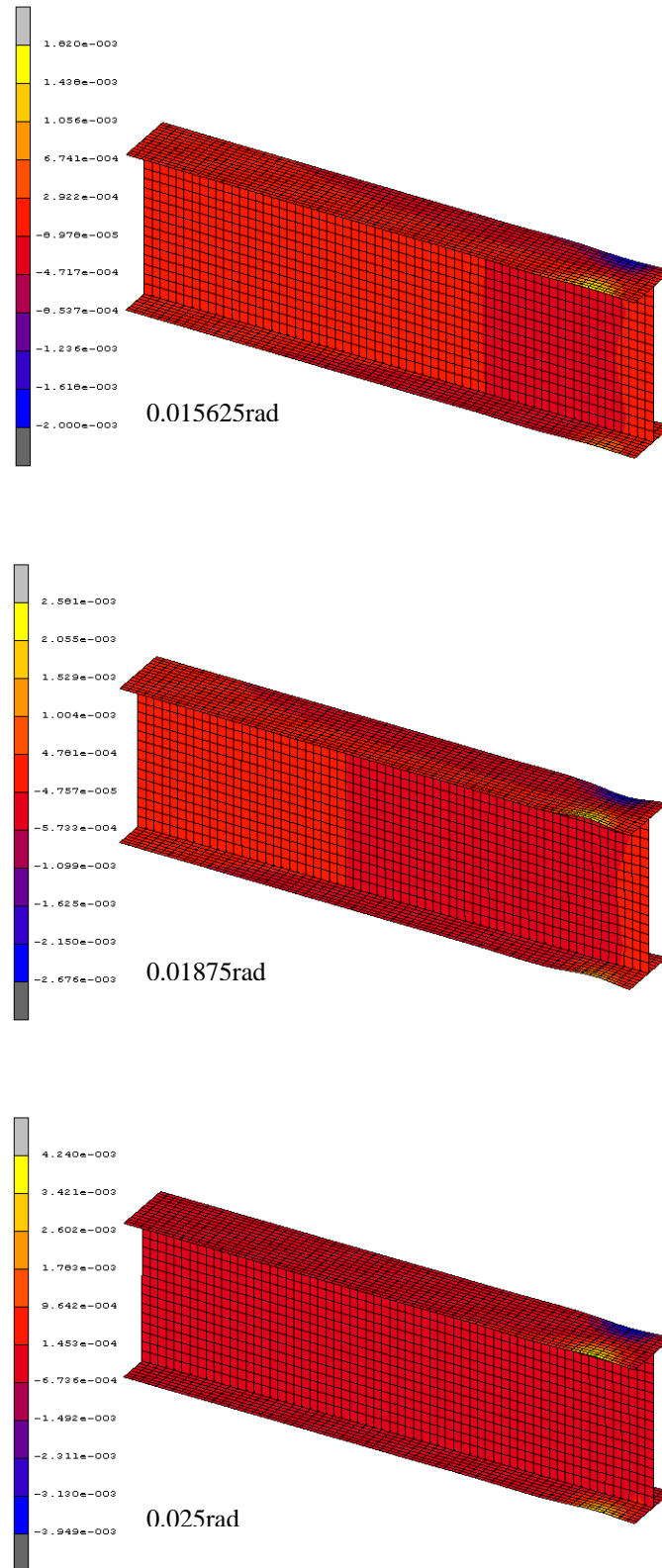


Figure 12-45: Local buckling at the flanges for different cyclic loading patterns. (continued)

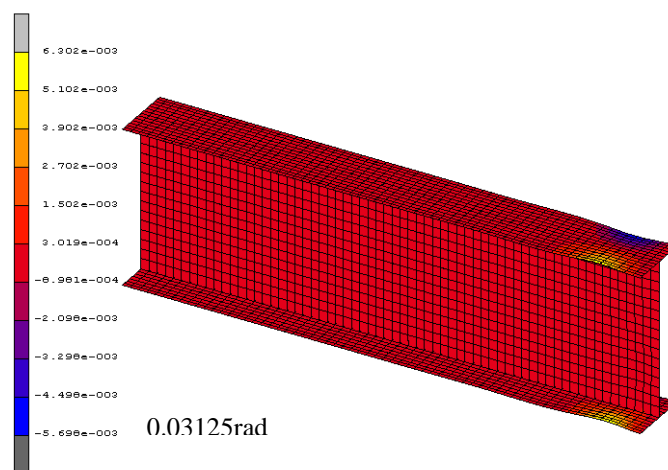


Figure 12-45: Local buckling at the flanges for different cyclic loading patterns.

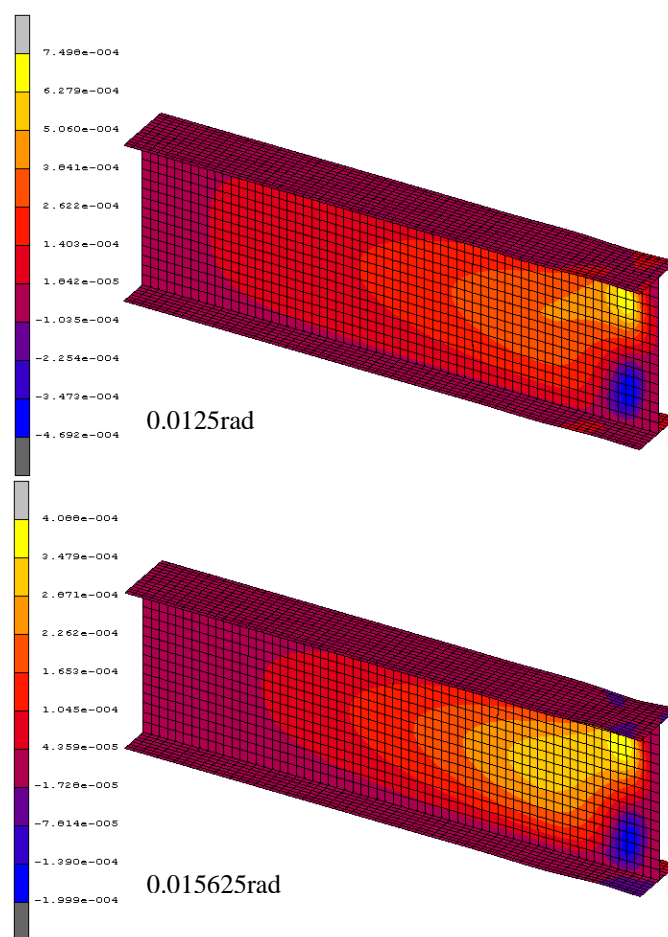


Figure 12 46: Local buckling at the webs for different cyclic loading patterns.(continued)

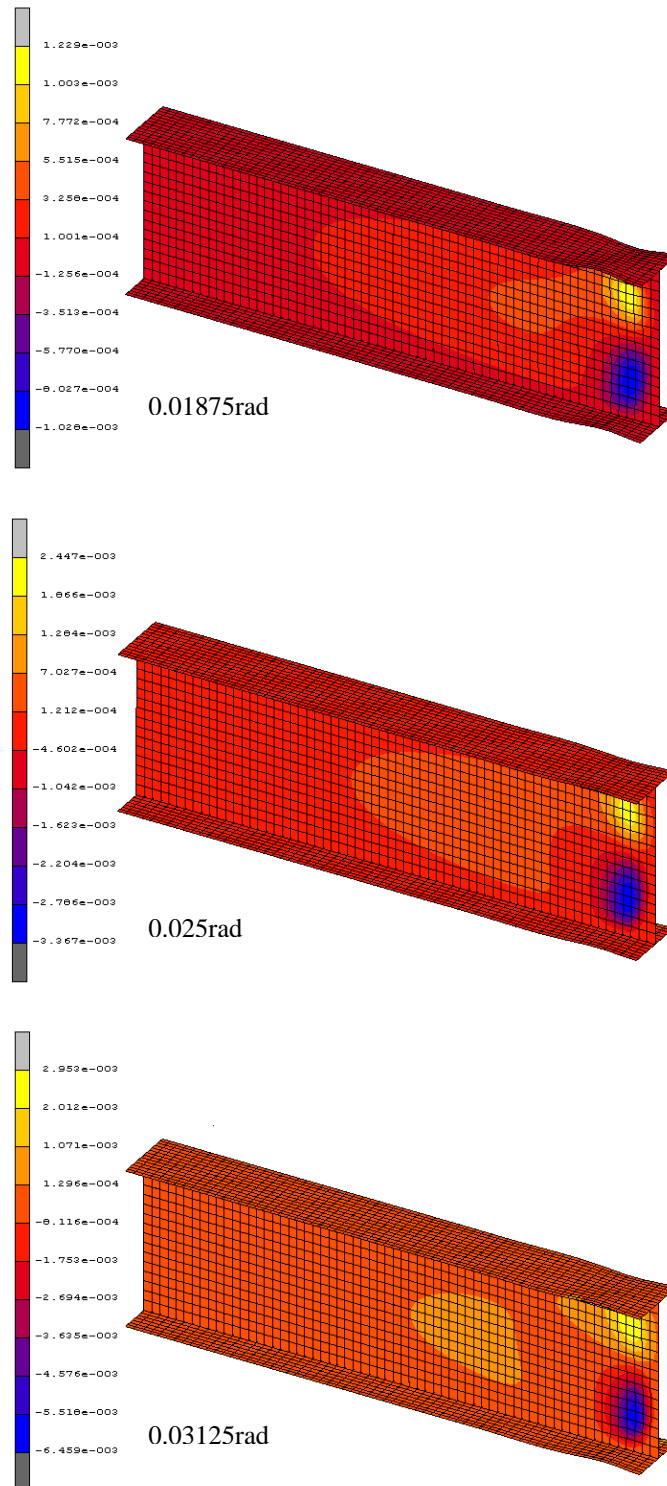


Figure 12-46: Local buckling at the webs for different cyclic loading patterns.

The previous indicate that the amplitude of the initial imperfections that have to be considered in the next stage, of the fire loading, is increased compared to the corresponding values that are considered at the starting point of the combined loading.

The distribution of the equivalent plastic strains at the end of the cyclic loading is illustrated in Figure 12-47. It is clear that the plastic hinge is formed at the mid-span and

this holds for all the considered cyclic-loading patterns. As the amplitude of the imposed rotation becomes greater, the length of the plastic hinge is slightly increased. The results are referred to amplitude of initial imperfections equal to 2mm. The results are qualitatively identical for the rest amplitudes of initial imperfections that are considered in this study. It is noted that as the amplitude of the geometric imperfections increases, the plastic hinge extend expands.

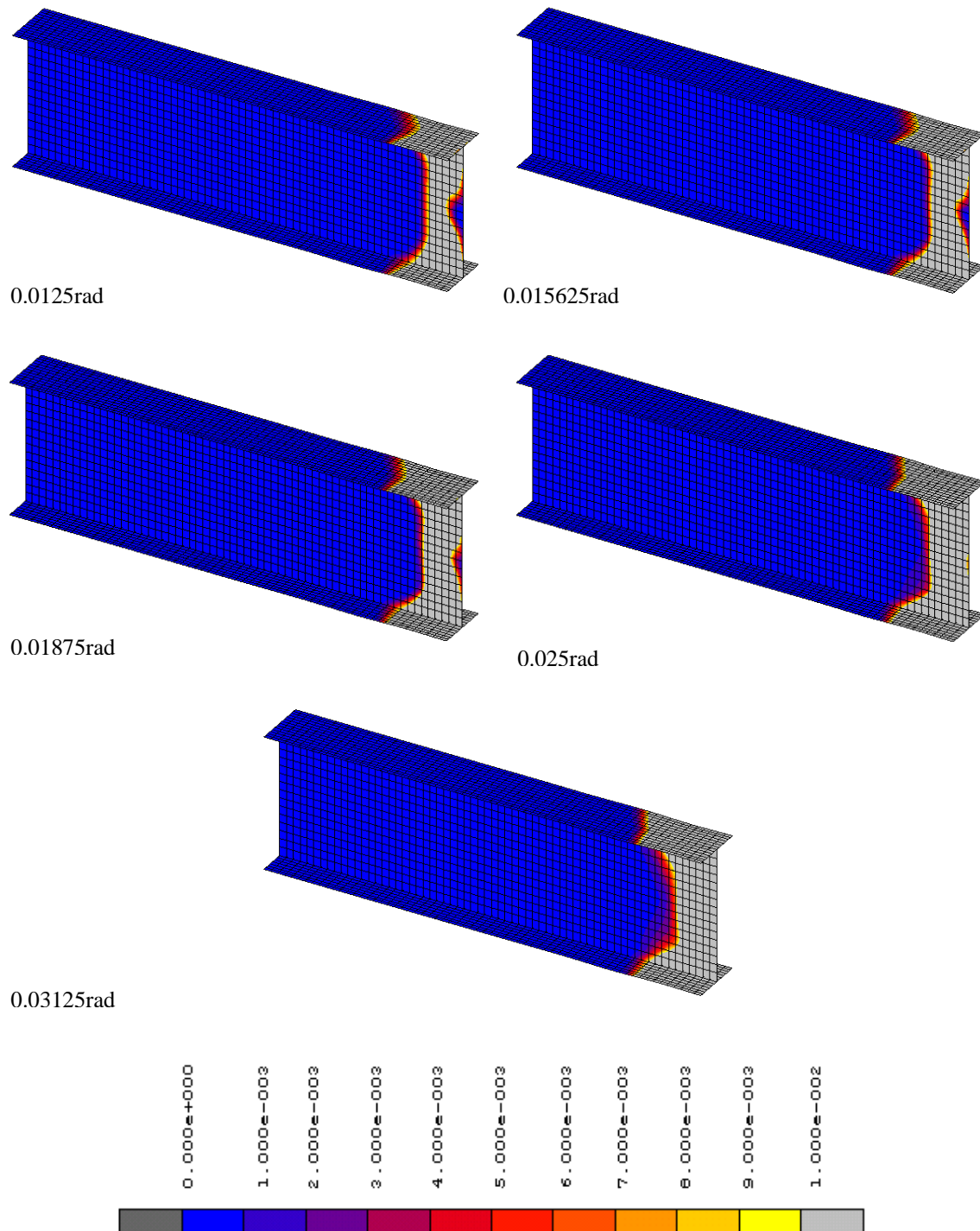


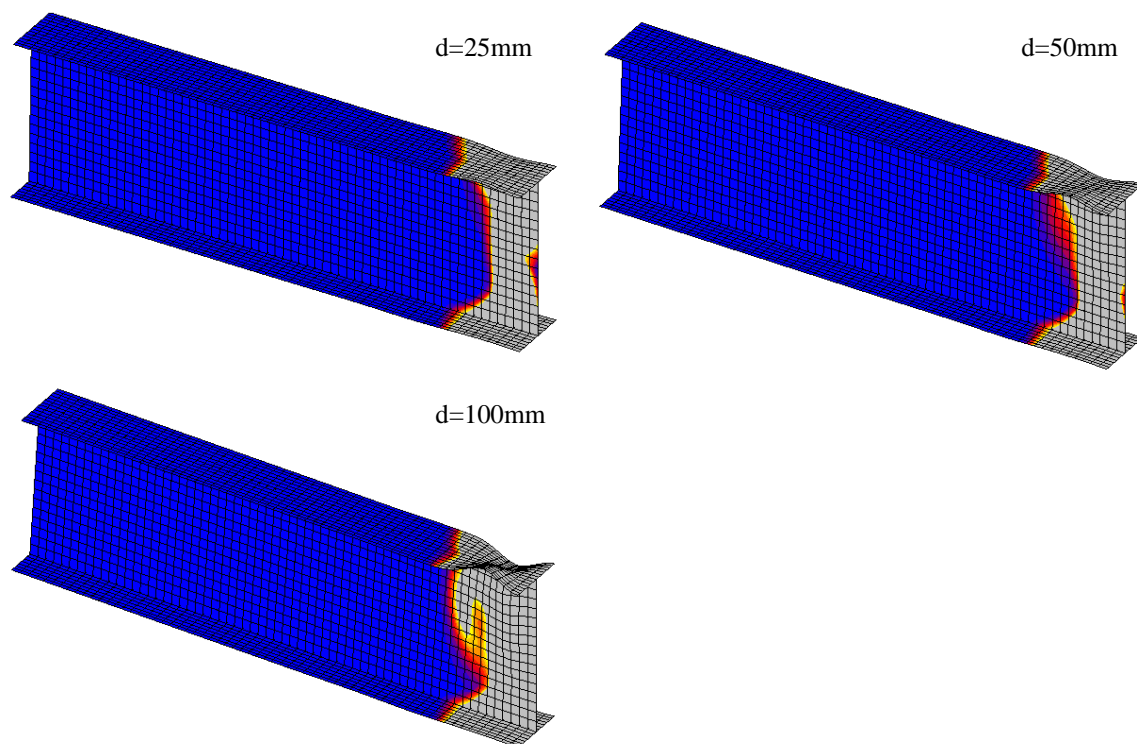
Figure 12-47: The equivalent plastic strain distribution at the end of cyclic loading.

Behaviour of the beam during the thermal loading

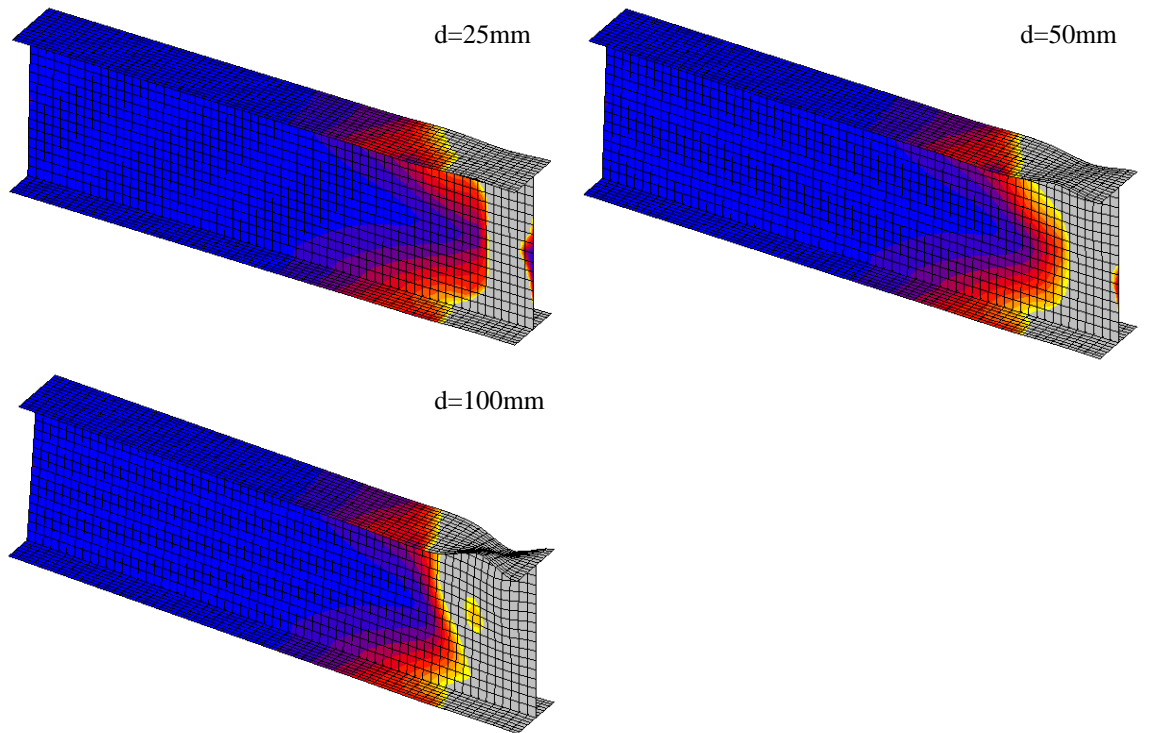
As it is has been explained in the previous, at the end of the cyclic loading the beam returns to the position where both the imposed displacement and the reaction force are zero. During the thermal loading the beam expands. Since the beam expands freely in all directions, there is no additional force introduced during the temperature loading.

Behaviour of the beam during the monotonic loading

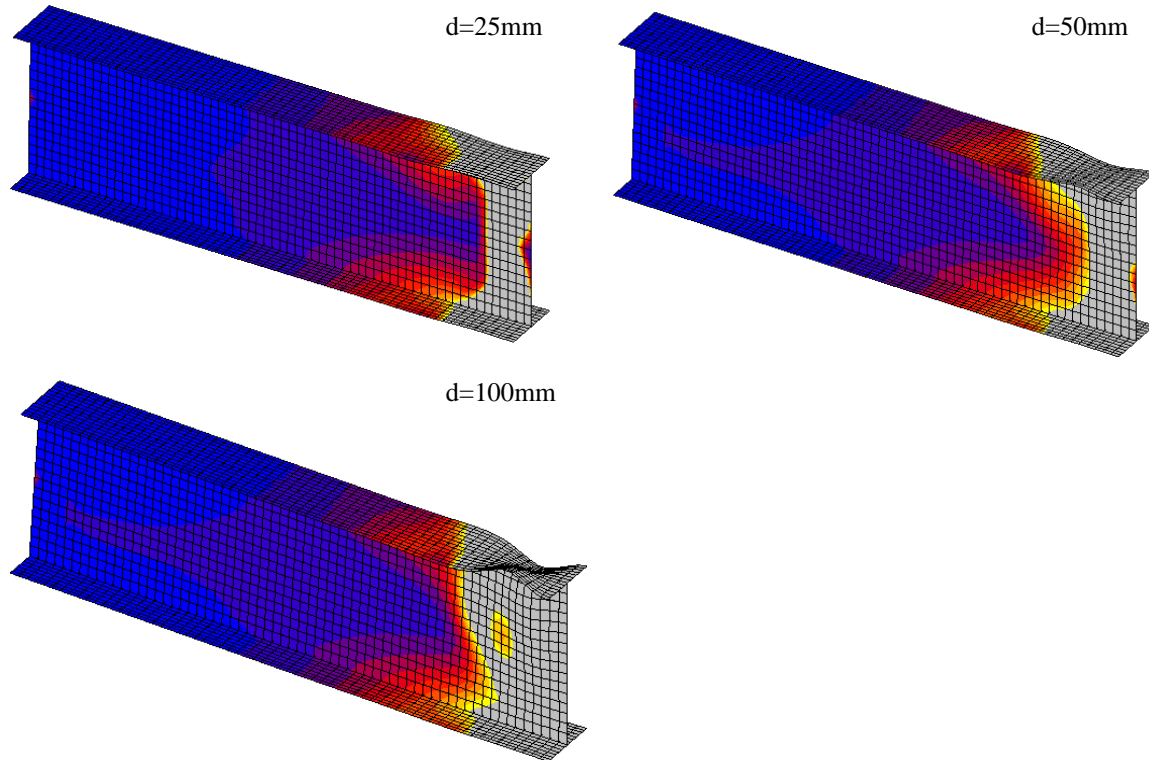
Figure 12-48 presents the evolution of the equivalent plastic strain during the monotonic loading stage at 20°C, 400°C and 600°C. The results concern the analyses where the amplitude of the initial imperfections is equal to 2mm and the imposed rotation of the cyclic loading stage is equal to 18.75mrad. Comparing the equivalent plastic strain distribution at different temperature levels with respect to the same imposed displacement, it is noted that as the temperature increases, the plastified area spreads out. The same phenomenon is observed for all the parametric analyses that are conducted in this study considering the amplitude of the initial imperfections, the cyclic loading patterns and the temperature level. It is noted that the damage concerning the magnitude of the equivalent plastic strains increase as the imposed rotation and the amplitude of the geometric imperfections increase.



a) Imposed rotation during the cyclic loading stage equal to 0.01875rad at T=20°C.



b) Imposed rotation during the cyclic loading stage equal to 0.01875rad at T=400°C.



c) Imposed rotation during the cyclic loading stage equal to 0.01875rad at T=400°C.



Figure 12-48: Evolution of the plastic strain distribution of the beam during the monotonic loading stage at 20°C, 400°C and 600°C.

Moment-rotation curves for the monotonic loading

Figure 12-49, Figure 12-50 and Figure 12-51 depict the moment-rotation curves corresponding to the monotonic loading stage. The comparison is carried-out with respect to the ‘level of damage’ induced during the cyclic loading stage for every temperature level and for different amplitudes of initial imperfections. It is noted that the ultimate moment resistance of the beam is slightly reduced as the ‘level of damage’ increases. This holds for small amplitudes of initial imperfections. As the amplitude increases the reduction becomes important. Table 12-4 presents the ultimate moment resistance of the pre-damaged beam at different temperature levels. It is observed that the reduction of the moment resistance with respect to the calculated plastic resistance of the cross-section is independent of the temperature level and is almost equal to 1%, 5% and 10% for amplitude of initial imperfections 0.5mm, 2mm and 5mm respectively. The previous values correspond to the maximum reduction that is obtained and it is referred to the case where the imposed rotation during the cyclic loading is 31.25rad. Additionally, it can be noticed that the rotation that corresponds to the ultimate moment resistance is reduced as the ‘level of damage’ induced during the cyclic loading is increased. This is valid for all the amplitudes of the initial imperfections that are considered.

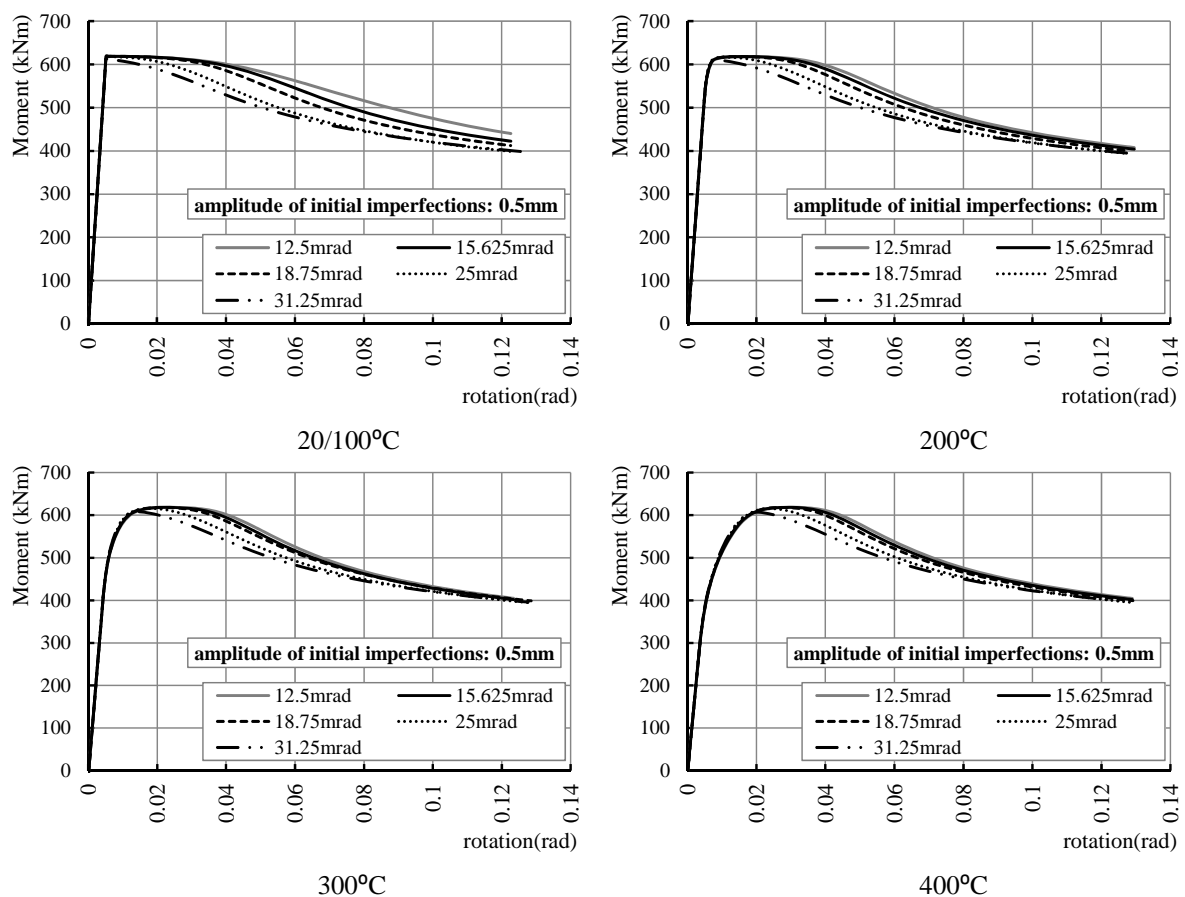


Figure 12-49: Moment-rotation curves for the monotonic loading stage during the numerical simulation of three-point bending test concerning pre-damaged beams (amplitude of initial imperfections equal to 0.5mm).(continued)

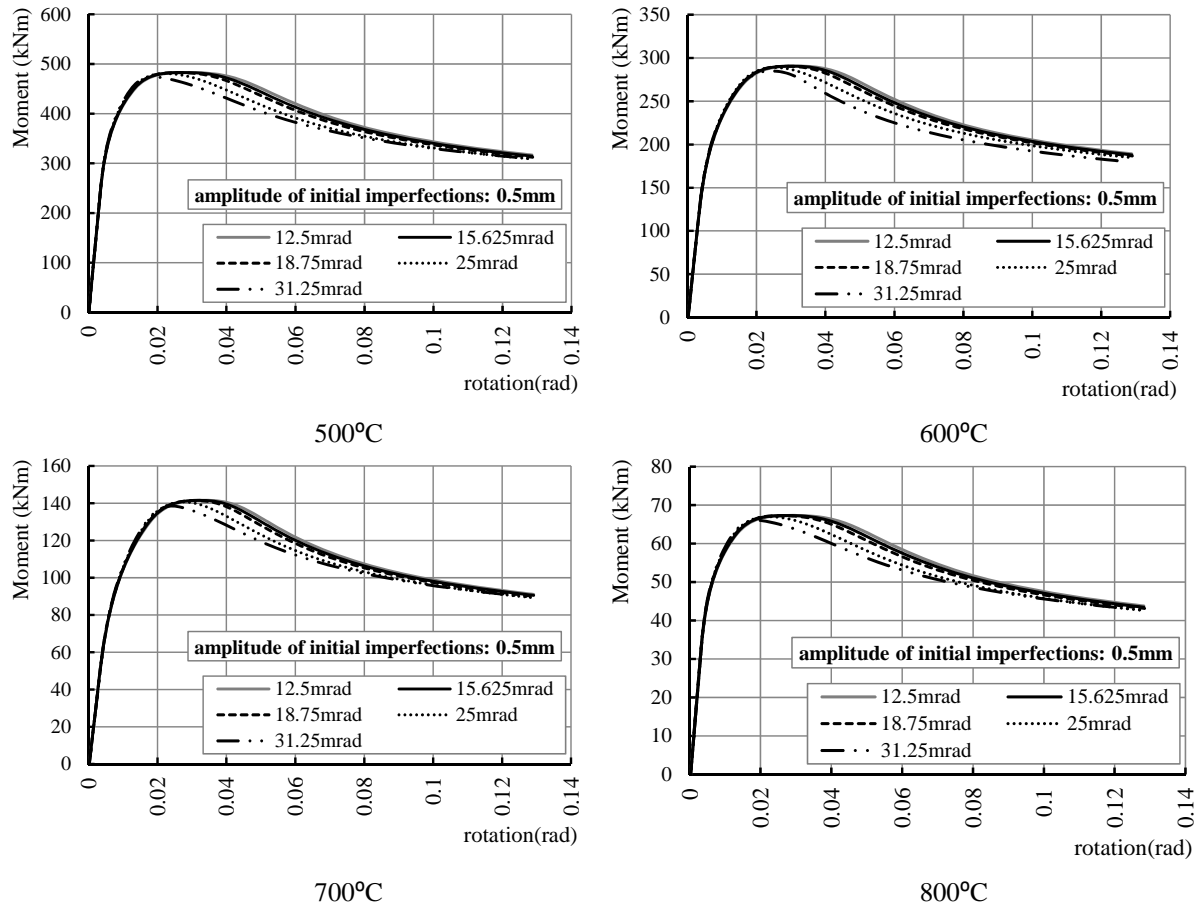


Figure 12-49: Moment-rotation curves for the monotonic loading stage during the numerical simulation of three-point bending test concerning pre-damaged beams (amplitude of initial imperfections equal to 0.5mm).

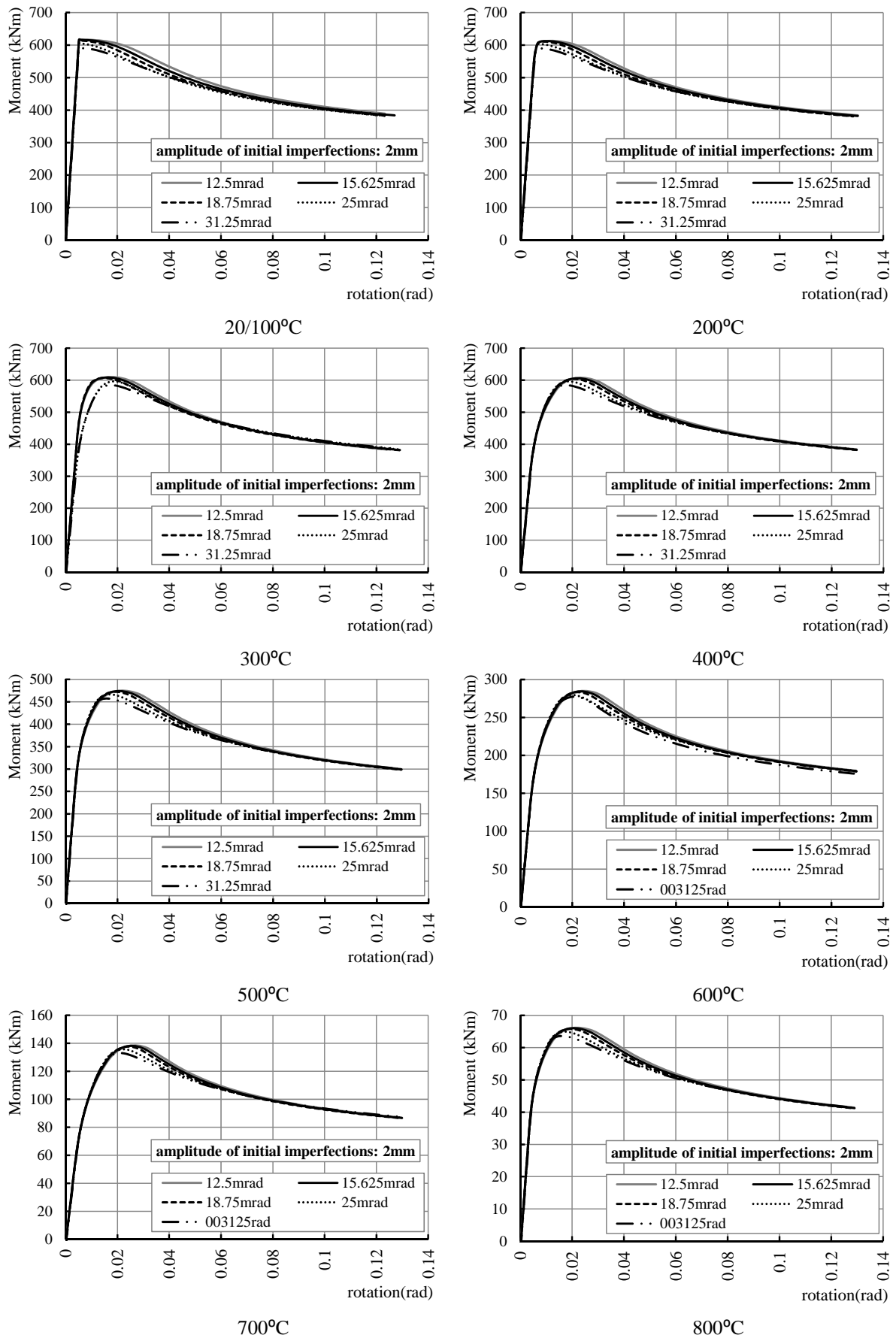


Figure 12-50: Moment-rotation curves for the monotonic loading stage during the numerical simulation of three-point bending analysis test concerning pre-damaged beams (amplitude of initial imperfections equal to 2mm).

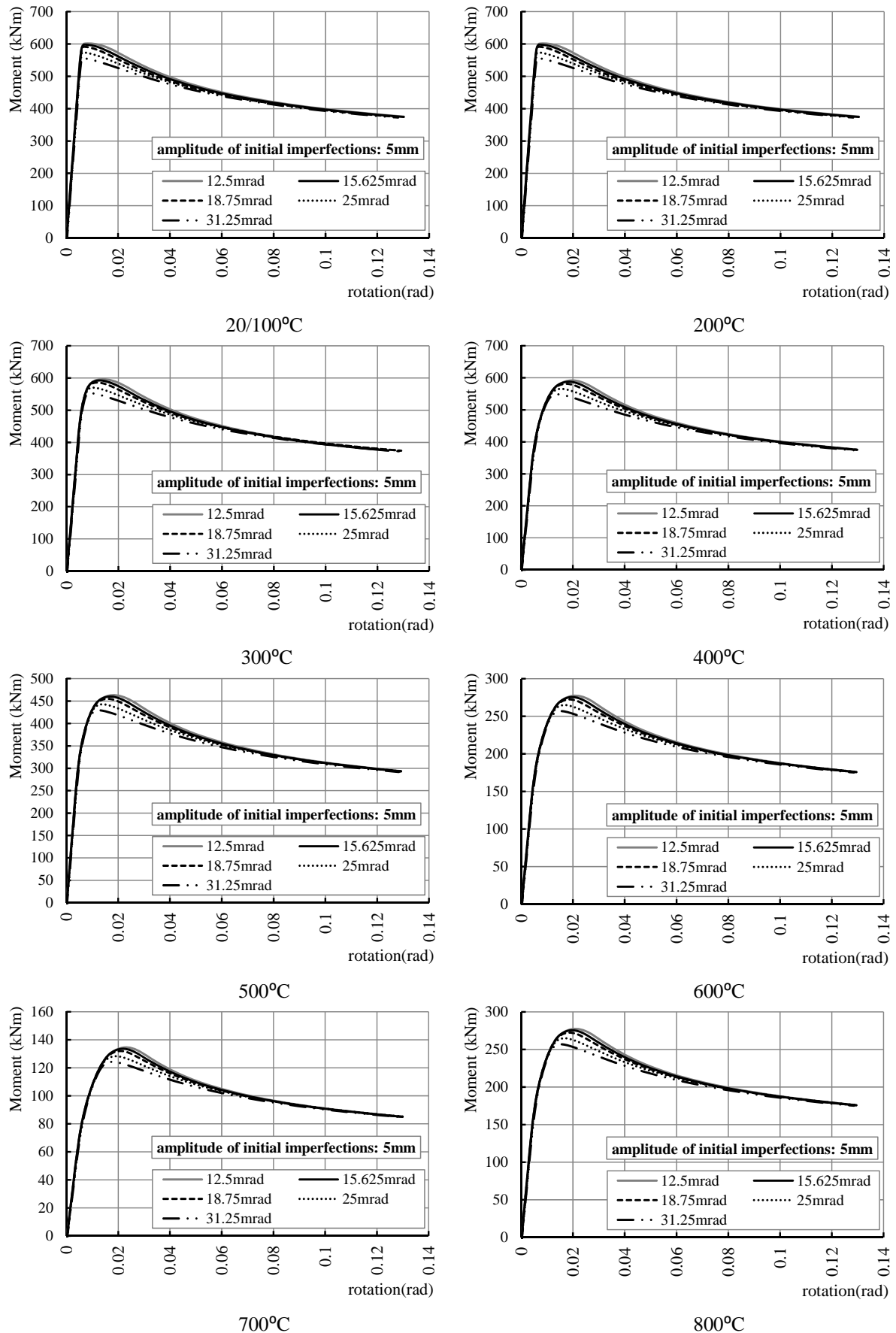


Figure 12-51: Moment-rotation curves for the monotonic loading stage during the numerical simulation of three-point bending test concerning pre-damaged beams (amplitude of initial imperfections equal to 5mm).

T (°C)		20/100	200	300	400	500	600	700	800
Moment resistance (KNm)		618.62	615.38	614.89	614.58	479.96	288.71	140.62	66.87
Amplitude of initial imperfections 0.5mm									
12.5mrad	M _u (KNm)	618.90	618.38	618.56	618.72	483.13	290.72	141.64	67.34
	θ _{max} (rad)	0.008	0.017	0.024	0.030	0.028	0.031	0.033	0.029
15.625mrad	M _u (KNm)	618.94	618.37	618.44	618.58	483.05	290.64	141.60	67.33
	θ _{max} (rad)	0.006	0.016	0.022	0.029	0.027	0.030	0.032	0.027
18.7mrad	M _u (KNm)	618.89	618.19	618.09	618.16	482.73	290.43	141.48	67.28
	θ _{max} (rad)	0.006	0.014	0.021	0.028	0.025	0.028	0.030	0.026
25mrad	M _u (KNm)	618.17	616.79	615.93	615.62	480.88	289.16	140.76	67.02
	θ _{max} (rad)	0.005	0.010	0.018	0.024	0.022	0.025	0.028	0.022
31.25mrad	M _u (KNm)	612.12	610.48	608.34	607.09	474.48	285.02	138.55	66.10
	θ _{max} (rad)	0.005	0.008	0.014	0.021	0.018	0.024	0.024	0.018
Moment reduction (%) ¹		1.05	1.05	0.80	1.06	1.22	1.14	1.28	1.47
Amplitude of initial imperfections 2mm									
12.5mrad	M _u (KNm)	617.04	613.28	609.78	607.39	474.89	285.02	138.51	66.16
	θ _{max} (rad)	0.006	0.011	0.017	0.023	0.022	0.024	0.027	0.022
15.625mrad	M _u (KNm)	616.19	612.55	608.73	606.27	474.03	284.48	138.22	66.04
	θ _{max} (rad)	0.005	0.010	0.016	0.022	0.020	0.023	0.025	0.020
18.7mrad	M _u (KNm)	614.33	610.99	606.90	604.20	472.50	283.48	137.65	65.82
	θ _{max} (rad)	0.005	0.009	0.015	0.021	0.019	0.022	0.024	0.019
25mrad	M _u (KNm)	605.07	603.47	599.62	596.47	466.59	279.75	135.74	64.97
	θ _{max} (rad)	0.005	0.007	0.013	0.019	0.017	0.020	0.022	0.017
31.25mrad	M _u (KNm)	590.54	590.12	587.72	584.88	457.43	277.46	133.04	63.61
	θ _{max} (rad)	0.006	0.007	0.012	0.017	0.016	0.021	0.021	0.016
Moment reduction (%) ¹		4.54	4.10	4.42	4.83	4.69	3.90	5.39	4.87
Amplitude of initial imperfections 5mm									
12.5mrad	M _u (KNm)	605.79	601.78	596.18	591.83	463.13	277.46	134.59	64.49
	θ _{max} (rad)	0.006	0.009	0.014	0.020	0.018	0.021	0.023	0.018
15.625mrad	M _u (KNm)	600.97	598.04	592.49	587.95	460.17	275.60	133.64	64.06
	θ _{max} (rad)	0.005	0.007	0.013	0.019	0.017	0.020	0.022	0.017
18.7mrad	M _u (KNm)	593.37	591.25	586.15	581.39	455.10	272.48	132.04	63.32
	θ _{max} (rad)	0.005	0.007	0.012	0.017	0.016	0.019	0.021	0.016
25mrad	M _u (KNm)	593.37	574.05	570.30	565.58	442.83	264.99	128.31	61.47
	θ _{max} (rad)	0.005	0.007	0.010	0.015	0.014	0.017	0.019	0.015
31.25mrad	M _u (KNm)	557.31	556.25	553.11	548.66	429.65	256.98	124.30	59.41
	θ _{max} (rad)	0.005	0.007	0.009	0.014	0.012	0.015	0.017	0.013
Moment reduction (%) ¹		9.91	9.91	9.61	10.05	10.73	10.48	10.99	11.61

¹The reduction is calculated with respect to the plastic moment resistance of the cross-section

Table 12-4: The moment resistance of the beam and the maximum rotation at different temperature levels considering the amplitude of initial imperfections.

Available rotation

The evolution of the available rotation of the pre-damaged beam with the temperature is illustrated in Figure 12-52. Taking into account specific amplitude of initial imperfections, the available rotation is reduced as the ‘level of damage’ is induced during the cyclic loading is increased. Moreover, it is noticed that the available rotation is strongly dependent on the imperfections that are introduced in the beam geometry, since it is considerably reduced as the amplitude of the initial imperfections increases.

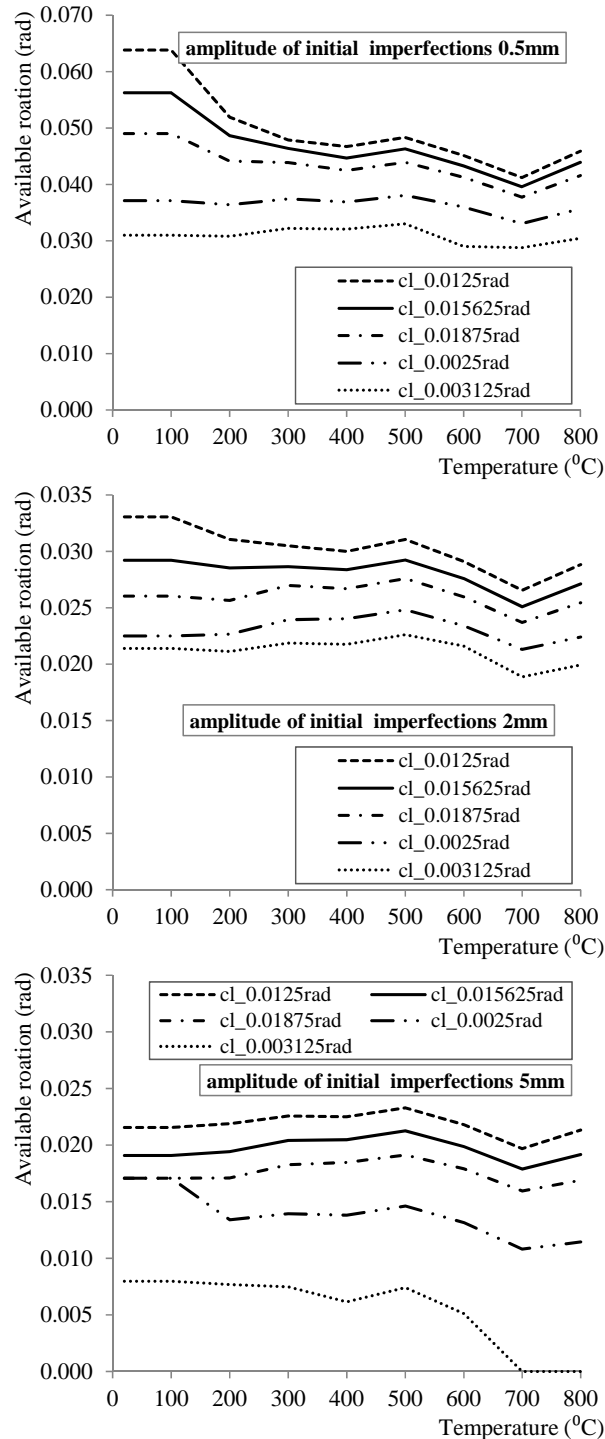


Figure 12-52 Available rotation for beams that are damaged due to cyclic loading.

Dimensionless moment-rotation curves

The dimensionless moment-rotation curves are depicted in Figure 12-53. The results concern the limit cases where the magnitude of the imposed rotation during the cyclic loading is 12.5mrad and 31.25mrad at different temperature levels. It is clear that as the ‘level of damage’ increases, the descending branch appears due to the plastic local that buckling takes place for reduced values of rotation. Additionally, it is noted again as the amplitude of the initial imperfections is getting bigger the ductility of the beam is reduced. The previous are valid for all the temperature levels that are considered in the study.

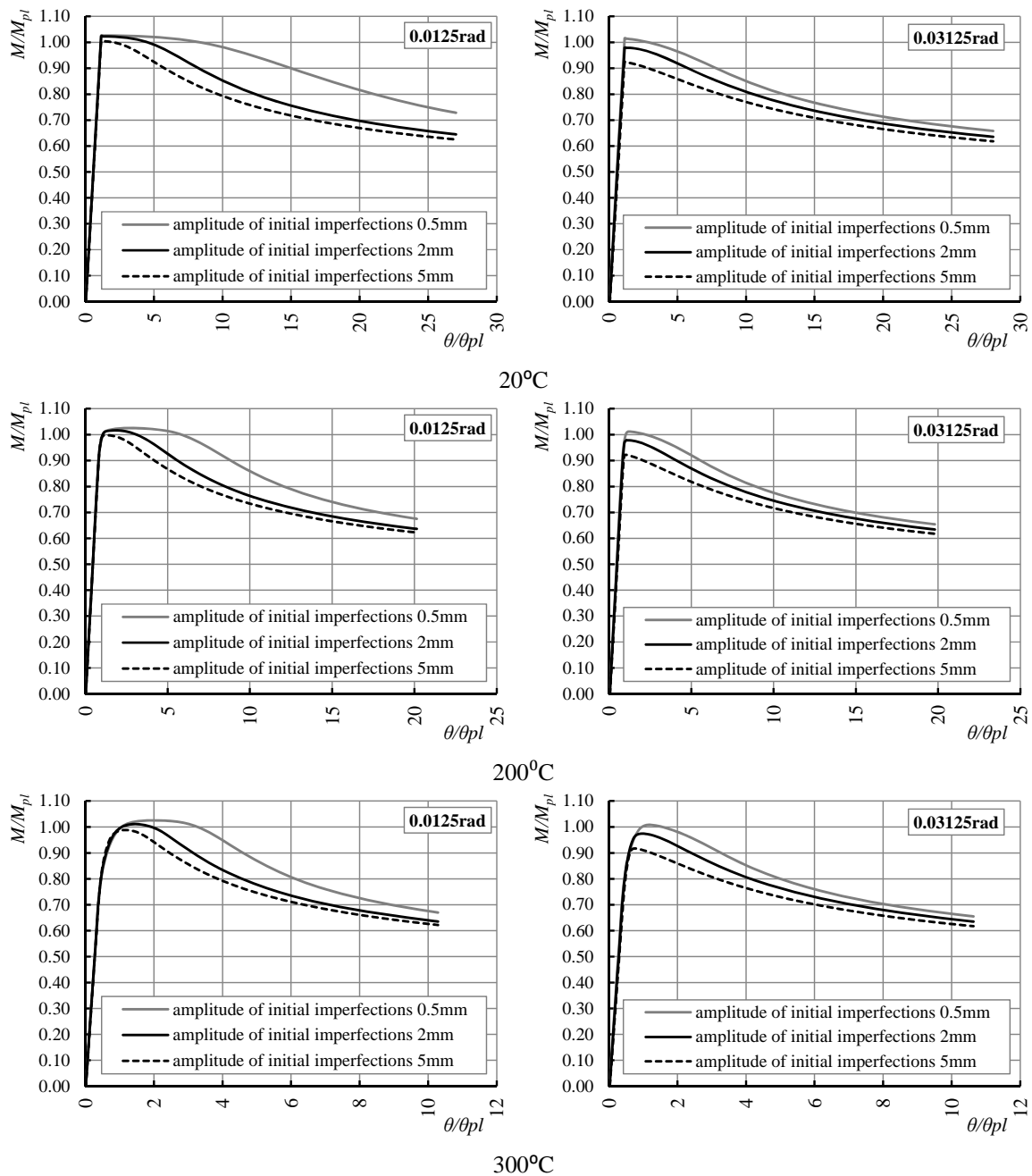


Figure 12-53: Dimensionless moment-rotation curves for the monotonic loading stage during the numerical simulation of three-point bending test at pre-damaged beams.(continued)

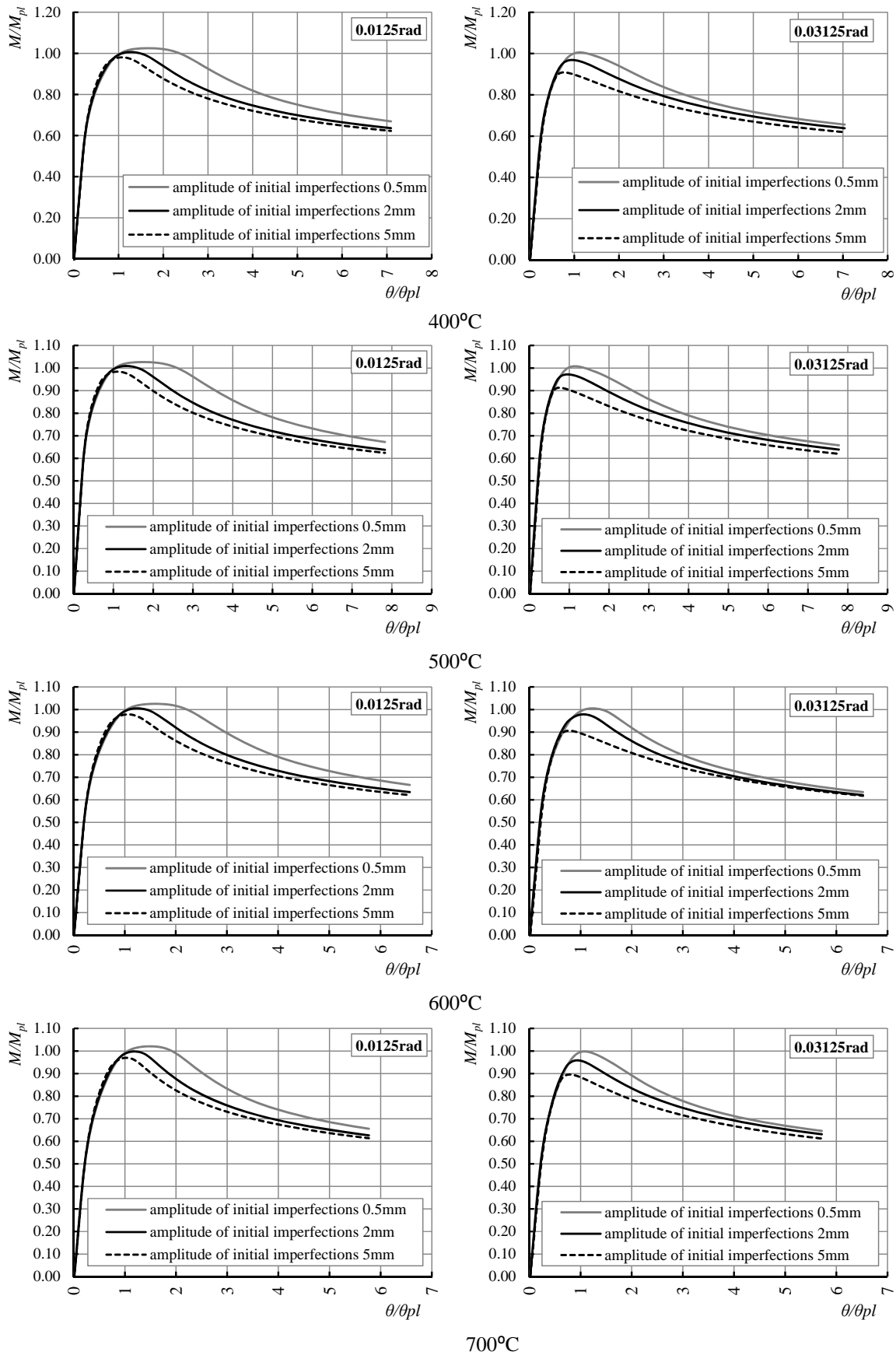


Figure 12-53: Dimensionless moment-rotation curves for the monotonic loading stage during the numerical simulation of three-point bending test at pre-damaged beams.(continued)

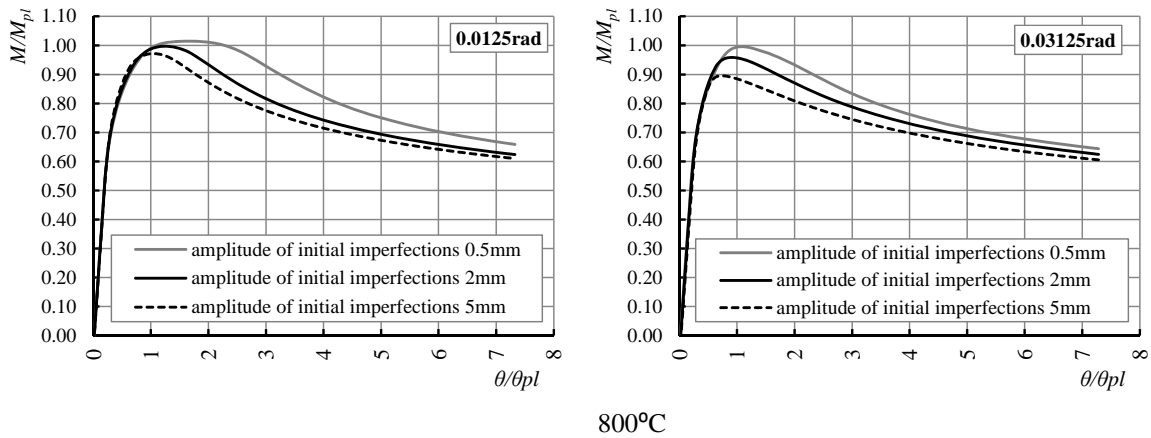


Figure 12-53: Dimensionless moment-rotation curves for the monotonic loading stage during the numerical simulation of three-point bending test at pre-damaged beams.

Figure 12-54 illustrates the comparison of the moment-rotation curves with respect to the temperature level, taking into account different amplitudes of initial imperfections.

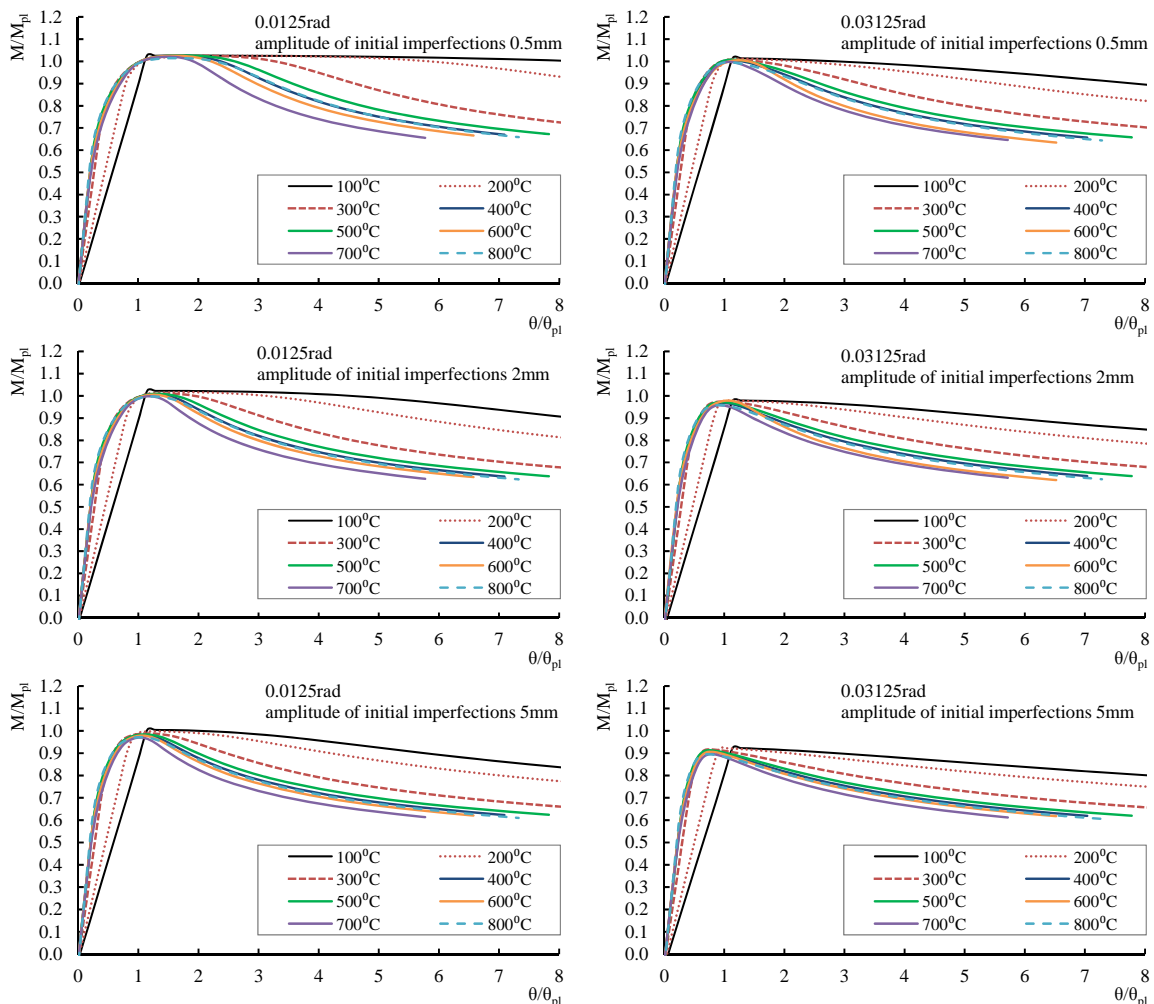


Figure 12-54 The effect of the temperature rise to the behaviour of the pre-damaged beams during the monotonic loading stage depending on the ‘level of damage’ and the amplitude of initial imperfections.

Once more, the limit cases concerning the ‘level of damage’ are presented. At elevated temperatures it is observed that the behaviour of the beam is identical until the point where

the descending branch takes place. As the temperature increases, the descending branch becomes steeper and the ductility of the beam is reduced.

Rotational capacity

The evolution of the available rotational capacity of the beam with temperature is depicted in Figure 12-55 considering the amplitude of the initial imperfections and the magnitude of the imposed rotation during the cyclic loading. It is obvious that the rotational capacity is reduced at elevated temperatures. Moreover, as the ‘level of damage’ s increases the capacity of the beam reduces and this comes more critical as the amplitude of the imperfections is enlarged. It is noted that at 700°C and 800°C, for amplitude of the initial imperfections 5mm and in the case where the magnitude of the imposed rotation during the cyclic loading is equal to 25mrad and 31.25mrad, the moment resistance of the beam does not exceed the value $0.9 M_{pl,T}$. This indicates that the rotational capacity of the beam becomes zero.

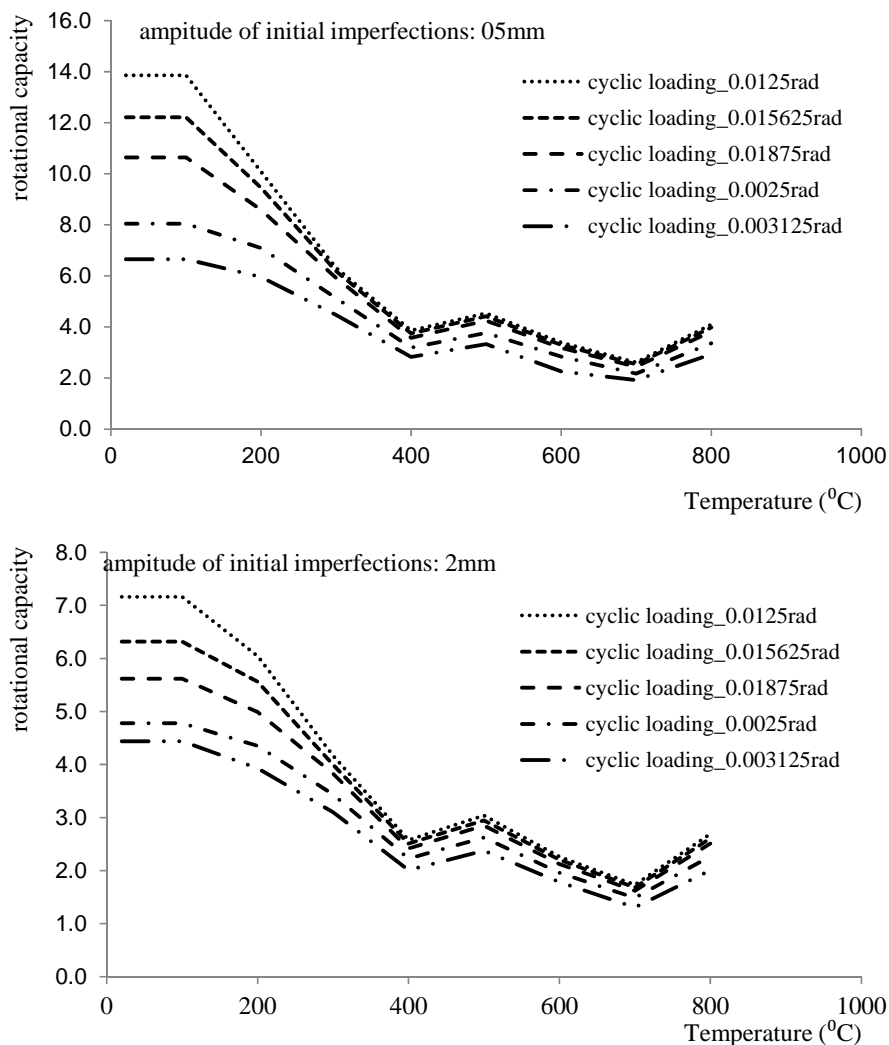


Figure 12 55 Available rotational capacity of the pre-damaged beams for different levels of damage considering the effect of the initial imperfections. (continued)

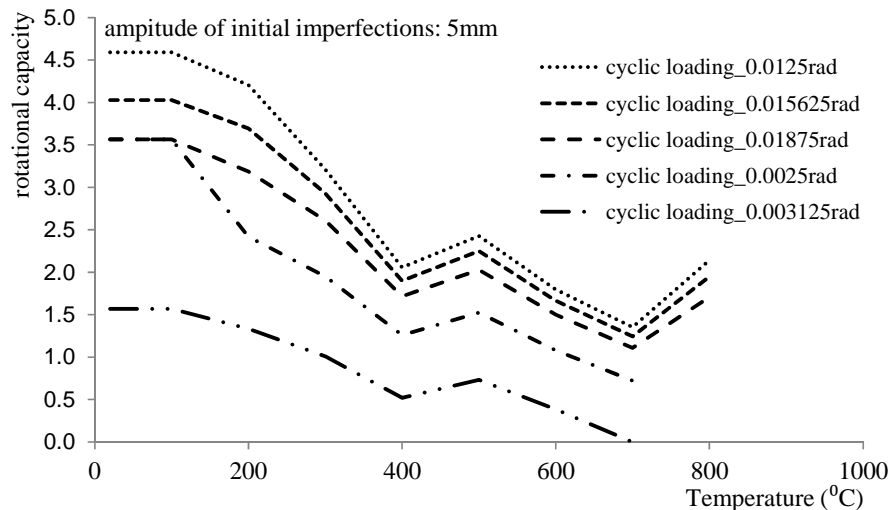


Figure 12-55 Available rotational capacity of the pre-damaged beams for different levels of damage considering the effect of the initial imperfections.

Definition of the ‘level of damage’ induced in the beam due to cyclic loading

The failure criteria, which are defined through the standard beam approach using detailed three-dimensional (shell) models, should be classified according to the ‘level of damage’ induced in beam, during cyclic loading, in order to be utilized for the evaluation of fire-resistance of the frame structure for the FAE loading (Chapter 11). It is reminded that in the latter case beam finite element models are applied. It is clear that two different types of analyses are used and that the results of the different analyses cannot be compared directly. The comparison would be confusing since the formulation of beam elements uses several assumptions that are not present in the shell formulation. In this point of view, a “common reference point” must be specified in order to link the results.

As it has already been explained in Section 9.7, the damage induced in the frames, during seismic loading, is characterized by the maximum recorded value (between the upper and the lower layers) at the end of the analysis. The issue that arises at this point is the *interpretation* of the ‘level of damage’, which is induced in the standard beam (shell finite element analyses) due to cyclic loading, in terms that are comparable to the damage level that characterizes the ‘level of damage’ in the frame structure, where the beam finite element formulation is used.

The correlation that is proposed in this dissertation is based on the plastic strain field, obtained at the end of the cyclic loading stage during the numerical simulation of the pre-damaged beams. The difficulty that arises is that the results the shell finite element analysis indicate the plastic strain distribution in the beam which is not directly comparable with the plastic strain field as it results from the beam finite element analysis where the concentrated plasticity assumption is used. In order to overcome this issue, the standard beam is *re-simulated*, using beam finite elements (the concentrated plasticity assumption is taken into account), and it is submitted to cyclic loading according to the patterns that are defined in Section 12.4.3 (Figure 12-43). In this point of view, the ‘level of damage’ for

the standard beam is obtained at the end of the cyclic loading. This level is identical and comparable with the one that is derived from the analysis of the frame structure at the end of the seismic loading, since the same type of analysis is used and, moreover, the concentrated plasticity assumption is used in both cases.

Taking into account the previous, the following technique is proposed, which is illustrated in Figure 12-56. The simulation of three-point bending test of the standard beam, at various increasing temperatures, is conducted using the finite shell element model (step 1a) and the dimensionless moment-rotation curves are obtained at different temperature levels (step 2a). In the same time, the numerical simulation of the cyclic loading stage for the standard beam is conducted (step 1b), through the beam finite element model, and the same imposed displacement, as in step 1a, is used. In this way the level of damage is calculated (step 2b) which is defined from the maximum equivalent plastic strain developed at the cross-section of the beam at the mid-span. Finally, the (discrete) function of the available rotation with temperature (step 3) is obtained (through the moment-rotation curves found in step 2a) for the specified 'level of damage' that is identified in step 2b. The same procedure is repeated for different amplitudes of imposed rotation (or displacement) during the cyclic loading stage. Actually, the imposed rotation is the parameter that defines the 'level of damage' which finally characterizes the function of the available rotation with temperature. This value is the only link between the different analyses and it has no further explanation. In the next Chapters will be referred as 'level of damage'.

The advantage of the identification of the 'level of damage' is that the same value can be obtained from the finite element analysis of the frame structure using beam elements with concentrated plasticity. Specifically, at the aforementioned analysis the 'level of damage' is derived at the end of the seismic loading. Since the 'level of damage' is defined for the frame structure, the corresponding failure criterion can be utilized

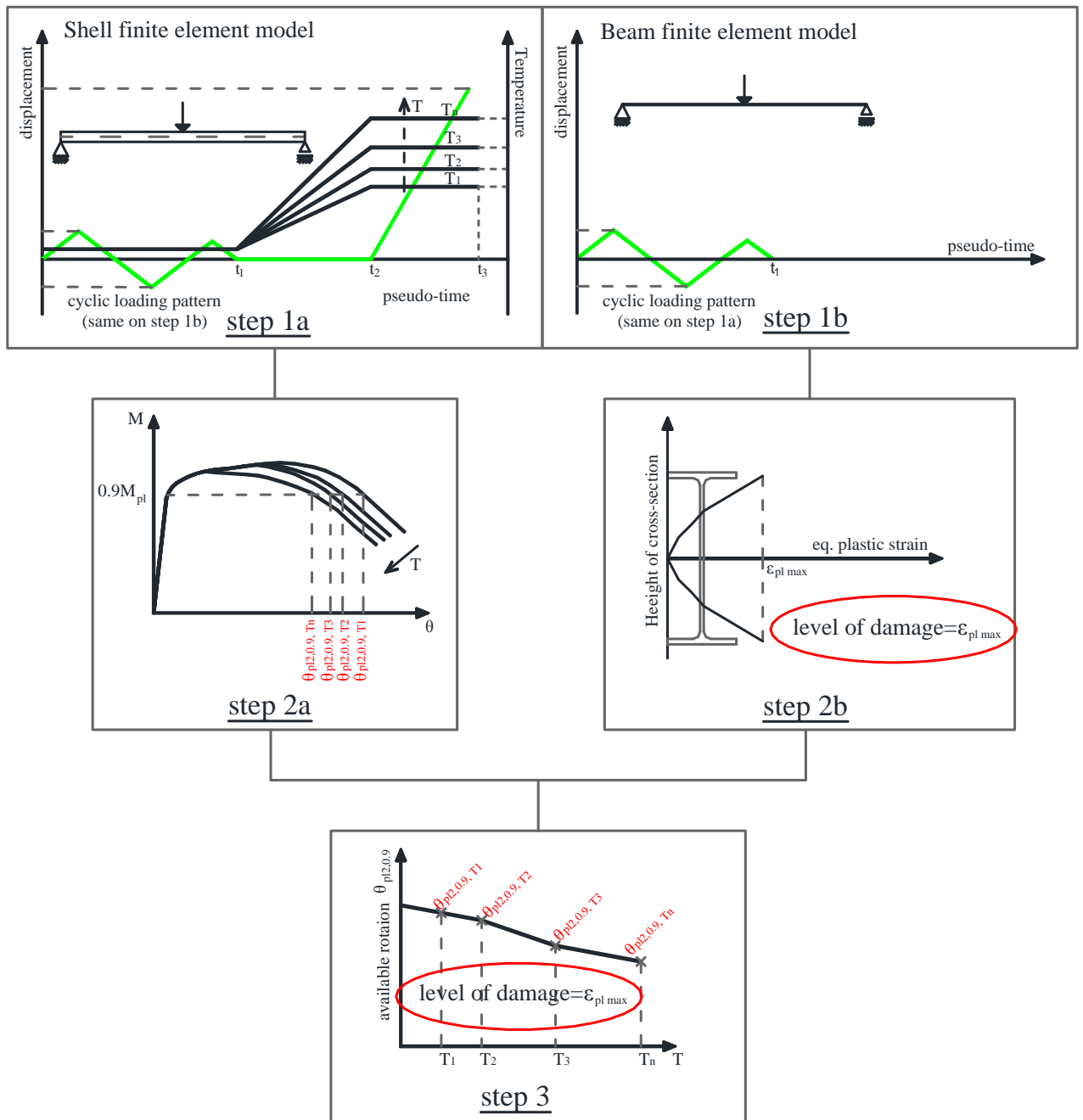


Figure 12-56 Proposed procedure for the definition of the 'level of damage'.

The results of the proposed procedure are presented in Table 12-5. Actually, the magnitude of the imposed rotation during the cyclic loading stage is mapped to the 'level of damage' according to the beam FEM model.

Cyclic loading pattern	'level of damage'
0.0125rad	0.045
0.015625rad	0.055
0.01875rad	0.07
0.025rad	0.11
0.03125rad	0.14

Table 12-5: Identification of the 'level of damage'.

Failure criteria

The failure criteria that are used in Chapter 13 for the determination of the fire resistance of the structure for the FAE loading are presented in Figure 12-57. It is noticed that as the temperature rises, the ultimate available rotation at first is reduced and in the sequel it is slightly increased. On the other hand, the ‘level of damage’ induced due to cyclic loading affects strongly the ultimate available rotation. Specifically, the aforementioned rotation is considerably reduced when the ‘level of damage’ is enlarged and this comes more important as the amplitude of the initial imperfections increases.

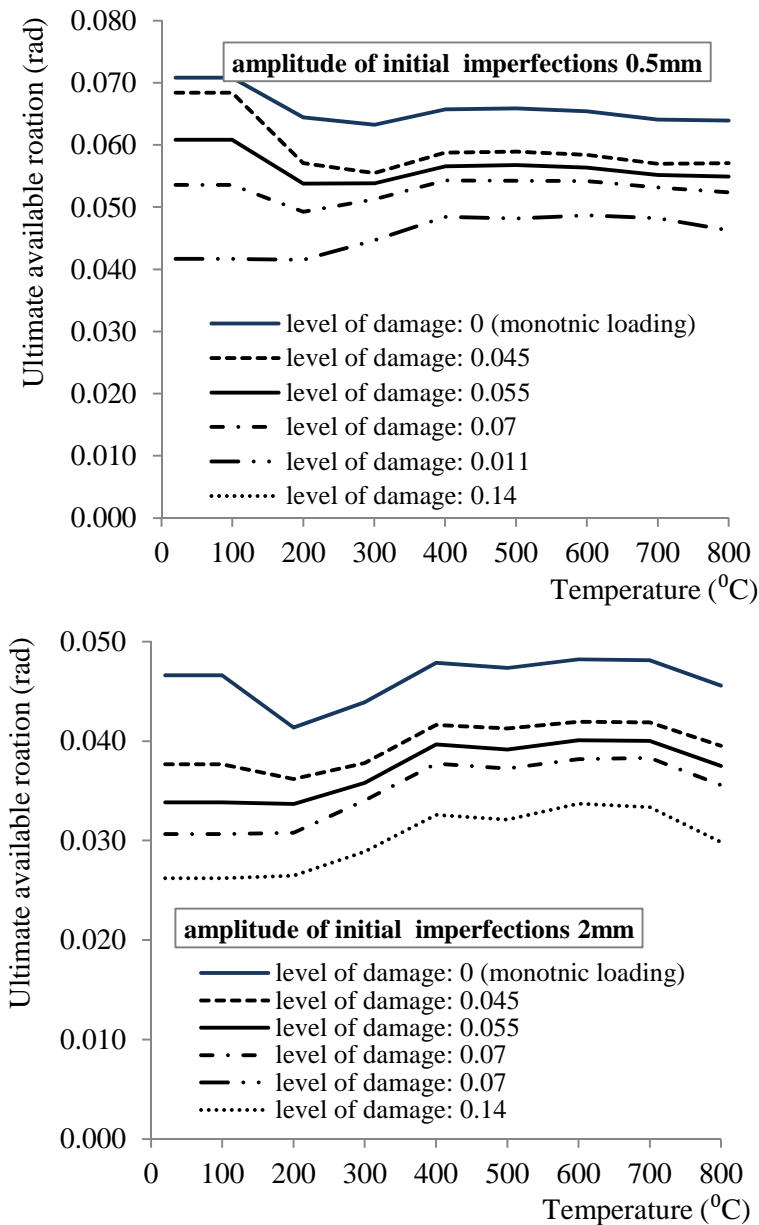


Figure 12-57: Ultimate available rotation of the pre-damaged beams for different levels of damage considering the effect of the initial imperfections. (continued)

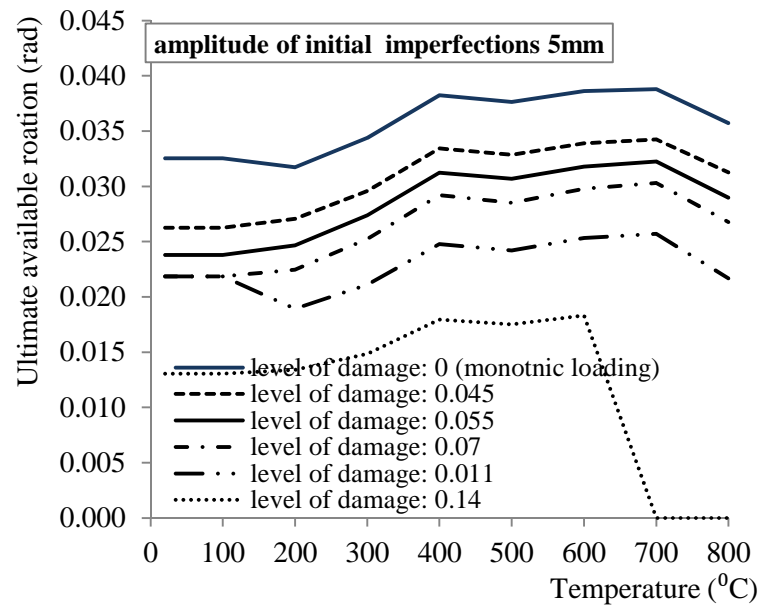


Figure 12-57: Ultimate available rotation of the pre-damaged beams for different levels of damage considering the effect of the initial imperfections.

Chapter 13. Determination of the fire-resistance of the structure for fire and FAE loading

The goal of this Chapter is the determination of the fire-resistance of the structural system for both the *reference* and the FAE scenarios. In this study, the failure of the structural system is defined as the state beyond which the calculated deformations of the structure would cause failure due to the loss of adequate support to one of the members. The fire-resistance of the structural system, in time or temperature domain, is obtained considering criteria that are based on the ductility of the structural members i.e. to the rotational capacity. The criteria, which are defined in Chapter 12, take into account the deterioration of the mechanical properties of steel at elevated temperatures and the initial imperfections of the structural members. Moreover, in the case of FAE loading, where the structural system is damaged due to the seismic action, the criteria take into account the ‘level of damage’ that is induced to the structural members at the end of the earthquake.

13.1 Determination of the fire-resistance

The failure criteria are separated into two categories. In the first category, the failure criteria are defined through the *standard beam* approach under monotonic loading. These criteria are used for the determination of the fire-resistance of the frame structure that is not damaged due to earthquake i.e. in the case of the *reference* fire scenarios. In the second category belong the criteria that depend on the ‘level of damage’ that is induced in the structural members during the cyclic loading and they are defined through the *standard beam* approach under combined cyclic and monotonic loading. In this case, they are classified according to the ‘level of damage’ induced in the beam in order to be utilized for the evaluation of the fire-resistance of the damaged frame structure. The classification of the damage that is induced in the standard beam due to cyclic loading is clarified in Section 12.4.3. The failure criteria, which are defined using the ultimate available rotation (as function of temperature), for both categories are summarized in Figure 13-1 according to the considered amplitude of initial imperfections. It is noted that, in order to homogenize the criteria, the first category is included as the case where the damage level is zero. Moreover, it is underlined that the perfect models are examined only for the case where the beams are not damaged due to cyclic loading.

On the other hand, the classification of the damage that is induced in the structural members of the frame structure during the earthquake loading is defined in Section 9.7. In both cases (standard beam approach and members of frame structure) the ‘level of damage’ is classified according to equivalent plastic strain field (using the maximum equivalent plastic strain value between the upper and the lower flange of the heated beam), thus the damage level that is used in both cases is totally equivalent.

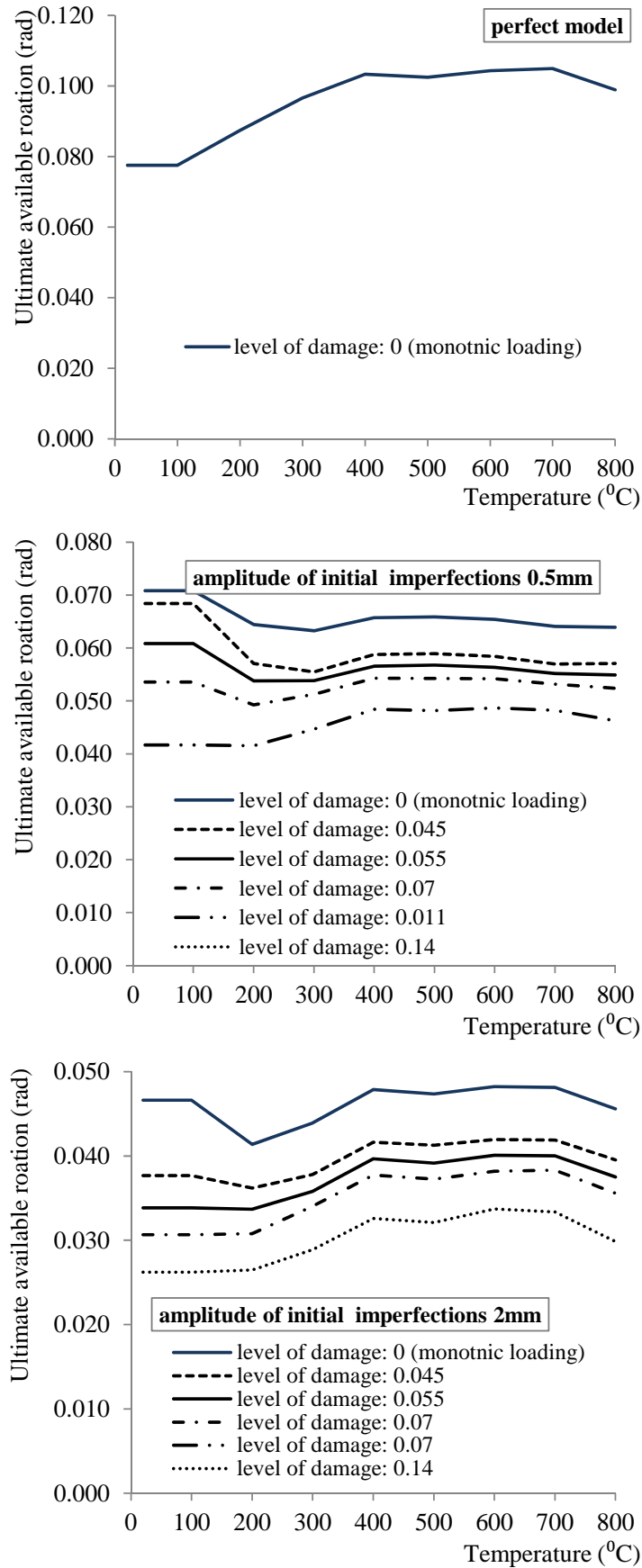


Figure 13 1: Failure criteria according to the standard beam approach for different amplitudes of initial imperfections and for the perfect model. (continued)

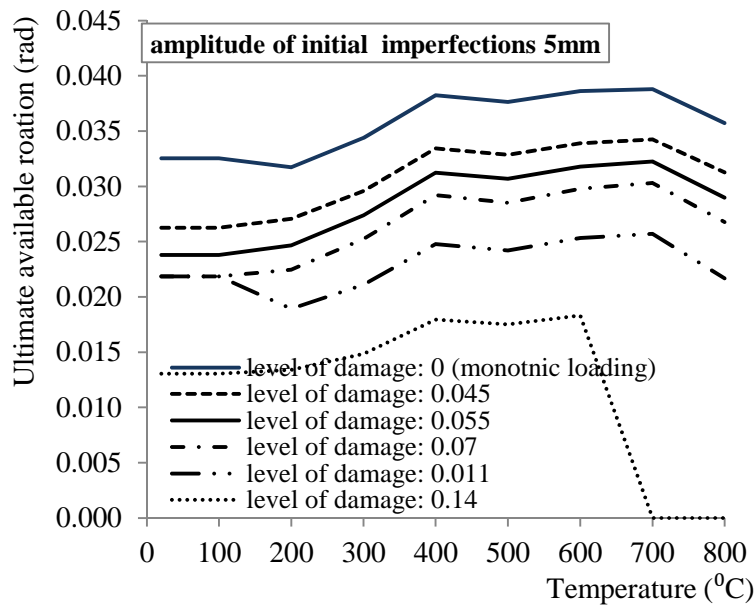


Figure 13-1: Failure criteria according to the standard beam approach for different amplitudes of initial imperfections and for the perfect model.

Taking into account the fact that the criteria are expressed in terms of ultimate available rotation versus temperature, the behaviour of the heated beams that lie in the frame structure is expressed in terms of rotation (at the support locations) versus temperature. In this way, for every heated beam, two different rotation-temperature curves are generated each one corresponding to the each end of the beam. In the case of the *reference* scenarios, the damage level for both the curves of the heated beam is zero and the corresponding criteria should be used. For the cases of PEF scenarios, where the structural system is damaged due to the earthquake, the rotation-temperature curve that corresponds to an individual beam end is characterized by a single damage level according to Table 9-18. The criteria that are used for the determination of the fire resistance in this case, must correspond to the same damage level. Linear interpolation is used for intermediate values of 'level of damage'.

The comparison of the rotation of the heated beam of the frame structure with the limit values of the available ultimate rotation, according to the failure criteria, indicates the *critical value* of rotation and the corresponding *critical temperature*. The critical temperature can be directly connected to the corresponding time of the fire exposure since the temporal evolution of temperature is already known. In this way the fire-resistance time is calculated and it corresponds to the state beyond which the calculated deformations of the structure cause failure due to the loss of adequate support to one of the members. The procedure for the calculation of the fire-resistance in temperature and time domain and the critical value of rotation, illustrated in Figure 13-2.

Figure 13-2 is presents the integrated method for the calculation of the fire resistance of the heated Beam 1A in the case of FAE scenario E6142ya-1.00-FISO. The rotation of the Right and the Left end of Beam 1A during the fire exposure are plotted in two different diagrams. Each diagram includes the failure criteria that are represented though three

different curves of the ultimate available rotation as a function of temperature, for amplitude of initial imperfections equal to 0.5mm, 2mm and 5mm respectively. The failure criteria correspond to a specific 'level of damage' induced to the end of the beam due to earthquake. In the specific case of Figure 13-2, as it is observed in Table 9-18, the 'level of damage' for the beam at the Left end, is equal to 0.0225 and the corresponding value for the Right end is 0.041.

The intersection of the rotation-temperature curve with the ultimate rotational capacity curve indicates the fire resistance in terms of temperature and the critical value of rotation. In this way, for a specific position (Left or Right end), three different intersection points are defined depending on the amplitude of initial imperfections that is taken into account. Then, the fire resistance in time domain is calculated taking into account the time-history temperature of the structural member, according to Figure 13-2. Considering specific amplitude of initial imperfections, the critical fire resistance is the minimum value between the Left and the Right end. For the specific case that is presented in Figure 13-2 the fire resistance (in time and temperature domain) and the critical rotation values are presented in Table 13-1.

The same procedure is repeated for the beam 1B. The minimum fire-resistance between the values that correspond to the different heated beams indicates the ultimate limit state where the failure of the structural system is considered to take place.

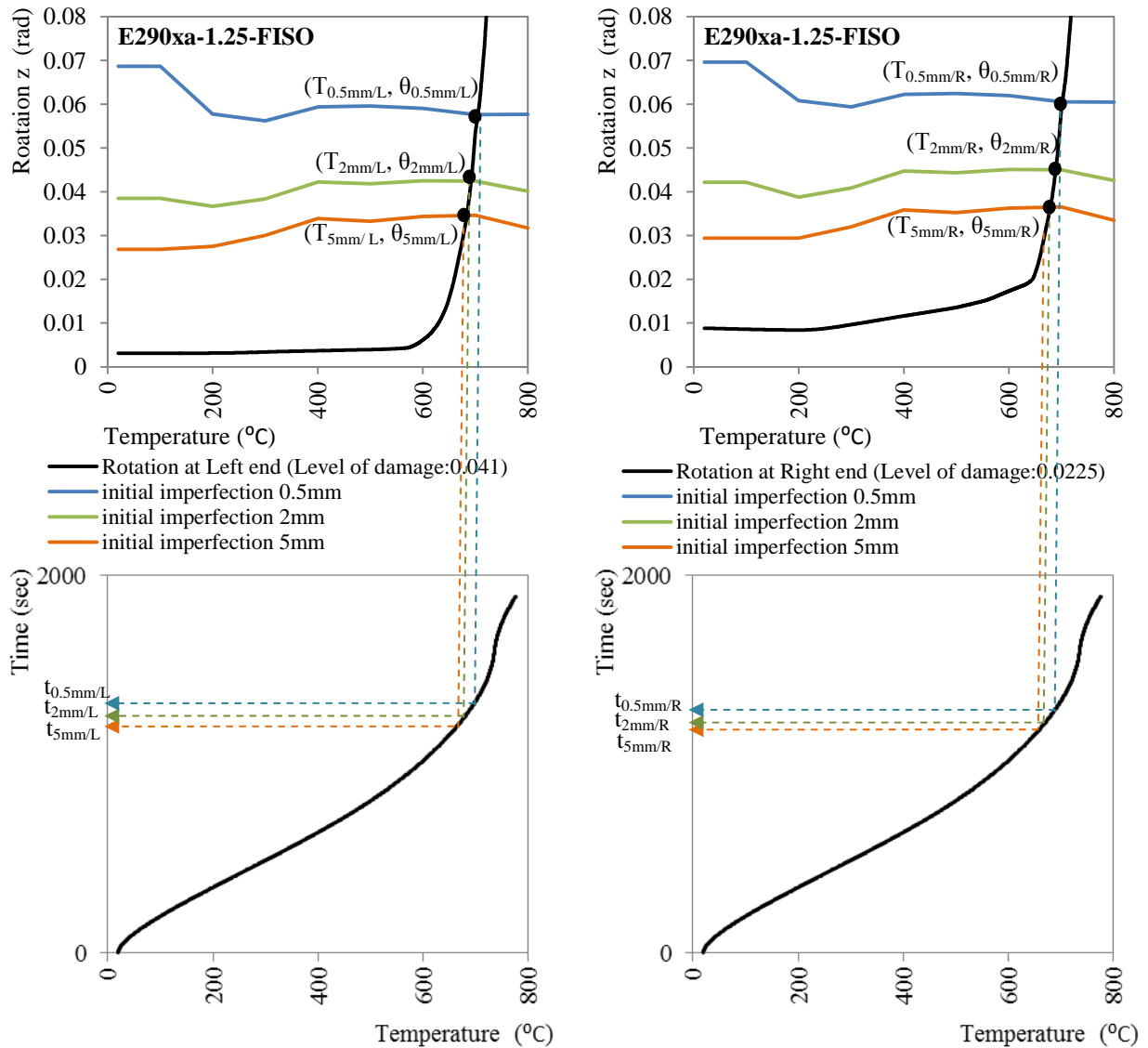


Figure 13-2: Calculation of the fire-resistance of heated beams in terms of temperature and time.

Amplitude of imperfections		
0.5mm	2mm	5mm
$t_{fr} = 1336\text{sec}$	$t_{fr} = 1282\text{sec}$	$t_{fr} = 1244\text{sec}$
$T_{fr} = 699.7^{\circ}\text{C}$	$T_{fr} = 686.6^{\circ}\text{C}$	$T_{fr} = 676.5^{\circ}\text{C}$
$\theta_{cr} = 0.053\text{rad}$	$\theta_{cr} = 0.038\text{rad}$	$\theta_{cr} = 0.030\text{rad}$

Table 13-1: Fire resistance of Bema 1A for the FAE scenario E6142ya-1.00-FISO for different amplitudes of initial imperfections.

13.2 Fire-resistance for the *reference* scenarios

The procedure that is described in the previous section is applied for the determination of the fire-resistance of the structural system for the *reference* fire scenarios. Actually, the fire resistance is calculated taking into account the criteria that correspond to both perfect and imperfect structural members. Considering the ISO-*reference* scenario the results are summarized in Table 13-2.

	Amplitude of initial imperfections			
	No imperfections	0.5mm	2mm	5mm
t_{fr}	1563sec	1388 sec	1323 sec	1291 sec
T_{fr}	733.3 °C	710.7 °C	696.7 °C	688.9 °C
θ_{cr}	0.103 rad	0.064 rad	0.048 rad	0.039 rad

Table 13-2: Fire-resistance of the structural system.

In the case of the natural fire *reference* scenario (SC-00), the structure does not fail. This scenario is not further studied.

13.3 Fire-resistance for the ISO-FAE scenarios

The fire-resistance in temperature domain is presented in Table 13-3. It is noted that the scenarios E290xa/1.75-FISO, E6142ya/1.75-FISO and E612xa/1.75-FISO are not studied due to the excessive ‘level of damage’ that is induced due to earthquake. Specifically, the maximum acceptable ‘level of damage’ that is used in this study for the definition of the failure criteria is 0.14 that corresponds to amplitude of imposed rotation equal to 0.03125rad. The results of the numerical analyses, which are conducted for the definition of the failure criteria, for imposed rotation greater than 0.03125rad are not acceptable due the excessive deformations that take place. In the aforementioned case studies, the level of the induced earthquake damage overcomes the level of 0.14 and, therefore, they are not further studied. It is observed that the fire-resistance, in temperature domain, is slightly reduced as the earthquake becomes more severe and as the amplitude of the considered initial imperfection increases. Moreover, the critical value of rotation is decreased as the scale factor of the earthquake intensity is amplified.

		Seismic action level									
		S.F. 1		S.F. 1.25		S.F. 1.50		S.F. 1.75			
		T(°C)	θ (rad)	T(°C)	θ (rad)	T(°C)	θ (rad)	T(°C)	θ (rad)		
Time-history acceleration record	Amplitude of initial imperfections	290xa	05mm	700.05	0.061	699.68	0.058	695.80	0.053	-	-
		290xa	2mm	688.22	0.046	686.60	0.042	680.22	0.038	-	-
		290xa	5mm	676.65	0.037	676.47	0.035	666.71	0.030	-	-
		293ya	05mm	703.97	0.061	699.57	0.058	696.27	0.054	692.73	0.049
		293ya	2mm	690.77	0.045	687.55	0.043	681.71	0.039	676.99	0.036
		293ya	5mm	681.90	0.037	677.15	0.035	668.88	0.031	660.15	0.027
		6142ya	05mm	700.32	0.057	695.03	0.053	689.06	0.048	-	-
		6142ya	2mm	688.29	0.042	679.03	0.038	671.60	0.035	-	-
		6142ya	5mm	677.89	0.034	665.25	0.030	642.11	0.024	-	-
	6112xa	05mm	704.56	0.062	697.01	0.056	692.13	0.049	-	-	
	6112xa	2mm	691.32	0.042	683.21	0.041	676.58	0.036	-	-	
	6112xa	5mm	681.53	0.037	672.06	0.034	659.20	0.026	-	-	
	1726xa	05mm	701.38	0.060	698.10	0.056	694.02	0.052	691.62	0.049	
	1726xa	2mm	689.74	0.045	684.76	0.041	677.41	0.038	675.12	0.036	
	1726xa	5mm	679.08	0.036	672.59	0.033	661.99	0.029	656.65	0.026	
	1726ya	05mm	701.96	0.061	699.13	0.059	695.93	0.057	695.03	0.055	
	1726ya	2mm	690.13	0.046	686.84	0.044	680.90	0.042	678.96	0.040	
	1726ya	5mm	679.72	0.037	676.18	0.036	667.86	0.034	665.17	0.032	
	5850xa	05mm	707.17	0.062	702.26	0.061	700.01	0.060	695.99	0.056	
	5850xa	2mm	694.16	0.047	690.39	0.046	686.89	0.044	680.48	0.041	
	5850xa	5mm	685.18	0.038	680.10	0.037	675.81	0.036	668.36	0.034	

Table 13-3: Fire-resistance of the frame structure in temperature domain and the critical values of rotation for the ISO-FAE scenarios.

The results are also presented in time domain in Table 13-4 for different amplitudes of initial imperfections (0.5mm, 2mm and 5mm). Two different comparisons are conducted. In the first case, the mean value of the fire-resistance time (taking into account the seven different accelerograms) is compared with the fire-resistance time of the *reference* (ISO) scenario that is obtained using failure criteria which do not take into account initial imperfections. In this case, it is interesting to notice that reduction of the fire-resistance time is considerable for all the amplitudes of initial imperfection that are studied and lies between 14% (for the design earthquake) and 24% when the scale factor 1.75 is used for the escalation of the earthquake intensity.

In the second case, the mean value of the fire-resistance time is compared with the fire-resistance time of the *reference* (ISO) scenario that is obtained using failure criteria which take into account initial imperfections. In this case the comparison is conducted with respect to equal values of initial imperfections. The reduction of the fire-resistance time of the damaged structure with respect to the value that corresponds to the structure that is not damaged due to earthquake is between the 2% and 7% and this magnitude increases as the amplitude of initial imperfection is enlarged.

Amplitude of initial imperfections 0.5mm				
<i>Reference ISO scenario</i>				
Perfect model	1563			
Imperfect model	1388			
ISO-FAE scenarios				
Accelerogram	Seismic action level			
	S.F. 1	S.F. 1.25	S.F. 1.50	S.F. 1.75
290xa	1337	1336	1319	-
293ya	1355	1335	1321	1306
612xa	1339	1316	1291	-
1726xa	1358	1324	1304	-
1726ya	1343	1329	1311	1302
5850xa	1346	1333	1319	1316
6142ya	1371	1347	1337	1320
Mean time	1350	1331	1315	1311
Reduction¹	13.64%	14.82%	15.89%	16.12%
Reduction²	2.75%	4.08%	5.29%	5.55%
Amplitude of initial imperfections 2mm				
<i>Reference ISO scenario</i>				
Perfect model	1563			
Imperfect model	1323			
ISO-FAE scenarios				
Accelerogram	Seismic action level			
	S.F. 1	S.F. 1.25	S.F. 1.50	S.F. 1.75
290xa	1288	1282	1258	-
293ya	1298	1285	1263	1246
612xa	1288	1253	1227	-
1726xa	1300	1269	1244	-
1726ya	1294	1275	1247	1239
5850xa	1296	1283	1260	1253
6142ya	1312	1297	1283	1259
Mean time	1297	1278	1255	1249
Reduction¹	17.05%	18.25%	19.73%	20.07%
Reduction²	2.00%	3.42%	5.17%	5.57%
Amplitude of initial imperfections 5mm				
<i>Reference ISO scenario</i>				
Perfect model	1563			
Imperfect model	1291			
ISO-FAE scenarios				
Accelerogram	Seismic action level			
	S.F. 1	S.F. 1.25	S.F. 1.50	S.F. 1.75
290xa	1245	1244	1210	-
293ya	1264	1246	1218	1189
612xa	1249	1205	1133	-
1726xa	1262	1228	1186	-
1726ya	1253	1230	1195	1177
5850xa	1276	1243	1214	1205
6142ya	1258	1257	1242	1216
Mean time	1258	1236	1200	1197
Reduction¹	19.51%	20.91%	23.24%	23.43%
Reduction²	2.55%	4.25%	7.07%	7.30%

¹ Reduction with respect to the fire resistance of the *reference* scenario considering criteria that do not take into account initial imperfections

² Reduction with respect to the fire resistance of the *reference* scenario considering criteria that take into account initial imperfections

Table 13-4: Fire-resistance of the frame structure in time domain (sec) for the ISO-FAE scenarios for different amplitude of imperfections - Comparison with the *reference* ISO-fire *reference* scenario.

13.4 Fire-resistance for the natural- FAE scenarios

The fire-resistance of the structural system, in temperature domain, and the corresponding values of the critical rotation for the natural-FAE scenarios are presented in Table 13-5. The fire resistance is decreased slightly as the earthquake intensity is enlarged. Reduction to the critical values of rotation is also noticed. The interpretation of the results in time domain (Table 13-6) indicates that the fire resistance time is increased as the earthquake becomes more severe. The phenomenon is related to the temporal redundant that takes place to the appearance of the maximum value of the HRR as the percent of the broken/open windows in the fire-compartment is increased. This remark is misleading since the results are dominated by the temporal delay that takes place as the percentage of the non-structural damage is increased. This is absolutely related to the spread of fire in the compartment and can be attributed to the modeling technique that was used in this study. At this point, it should be taken into account the fact that the fire-resistance of the structure should be determined during the post-flashover stage and the growth phase should be excluded. In other words, the equivalent time used in order to express the fire-resistance of the structures, cannot be directly compared to the real time needed for the evacuation of the building. At this point, it should be also taken into account the fact that the ISO-fire curve is a prescriptive fire curve that is based on the equivalent time and it is used for the simulation of the post-flashover stage. For this reason, it is clear that, in the case of the natural FAE-scenarios, it is difficult to determine the fire-resistance in time domain. The time that arises from the numerical analyses, is real time and it does not express the fire-resistance of the structure. In order to utilize the results of the natural-FAE scenarios, the critical temperature that defines the failure of the structure is “translated” in equivalent ISO-fire time. In this way, the results are almost identical with the case of the ISO FAE-scenarios. The upper bound considering reduction of the fire-resistance time (with respect to the fire-resistance time of the ISO *reference* scenario that is obtained using failure criteria which do not take into account initial imperfections) is calculated approximately 25%.

		Earthquake intensity level														
		S.F. 1				S.F. 1.25				S.F. 1.50				S.F. 1.75		
		SC-25		SC-50		SC-50		SC-75		SC-125		SC-150				
		T(°C)	θ (rad)	T(°C)	θ (rad)	T(°C)	θ (rad)	T(°C)	θ (rad)	T(°C)	θ (rad)	T(°C)	θ (rad)	T(°C)	θ (rad)	
Time-history acceleration record	290xa	05mm	-	-	699.07	0.061	698.81	0.058	699.71	0.058	695.44	0.053	695.59	0.053	-	-
		2mm	-	-	684.16	0.046	681.72	0.042	685.41	0.042	678.48	0.038	678.68	0.038	-	-
		5mm	-	-	668.52	0.037	667.93	0.035	674.56	0.035	664.97	0.030	665.43	0.030	-	-
	293ya	05mm	-	-	703.60	0.061	698.71	0.058	699.46	0.058	695.89	0.054	695.93	0.054	691.69	0.049
		2mm	-	-	687.65	0.045	683.48	0.043	686.35	0.043	680.10	0.039	680.20	0.039	674.42	0.036
		5mm	-	-	675.02	0.037	669.34	0.035	675.37	0.035	667.27	0.031	667.57	0.031	656.71	0.027
	6142ya	05mm	-	-	699.89	0.057	693.13	0.053	694.31	0.053	687.44	0.048	687.50	0.048	-	-
		2mm	-	-	685.02	0.042	672.02	0.038	676.99	0.038	668.93	0.035	669.05	0.035	-	-
		5mm	-	-	671.07	0.037	671.069	0.030	663.07	0.030	611.30	0.024	589.60	0.024	-	-
	6112xa	05mm	-	-	704.11	0.062	695.58	0.056	696.49	0.056	691.21	0.049	691.33	0.049	-	-
		2mm	-	-	688.17	0.046	676.79	0.041	681.19	0.041	674.74	0.036	674.90	0.036	-	-
		5mm	-	-	674.53	0.037	663.40	0.034	669.71	0.034	657.17	0.026	657.57	0.026	-	-
	1726xa	05mm	-	-	700.45	0.060	697.16	0.056	697.80	0.056	693.27	0.052	693.01	0.052	690.14	0.049
		2mm	-	-	686.12	0.045	679.76	0.041	683.12	0.041	675.02	0.038	674.37	0.038	671.86	0.036
		5mm	-	-	671.47	0.036	664.90	0.033	670.22	0.033	659.35	0.029	658.48	0.029	646.54	0.026
1726ya	05mm	-	-	701.27	0.061	698.18	0.059	698.91	0.059	695.38	0.057	695.30	0.057	694.28	0.055	
	2mm	-	-	686.60	0.046	682.79	0.044	685.39	0.044	678.95	0.042	678.56	0.042	676.60	0.040	
	5mm	-	-	671.64	0.037	668.61	0.036	673.97	0.036	665.83	0.034	665.60	0.034	662.88	0.032	
5850xa	05mm	-	-	707.24	0.062	700.50	0.061	701.98	0.061	699.89	0.060	699.56	0.060	694.70	0.056	
	2mm	-	-	691.78	0.047	686.23	0.046	688.77	0.046	685.32	0.044	684.53	0.044	676.39	0.041	
	5mm	-	-	679.51	0.038	671.58	0.037	677.40	0.037	673.30	0.036	671.99	0.036	663.46	0.034	

Table 13-5: Fire-resistance of the frame structure in temperature domain and the critical values of rotation for the Natural-FAE scenarios.

Amplitude of initial imperfections 0.5mm							
Natural-FAE scenarios							
Accelerogram	Seismic action level						
	S.F. 1		S.F. 1.25		S.F. 1.50		S.F. 1.75
	SC-25	SC-50	SC-50	SC-75	SC-75	SC-100	SC-100
290xa	-	1567	1567	1808	1803	2100	-
293ya	-	1577	1566	1808	1803	2101	2096
612xa	-	1569	1554	1801	1791	2092	-
1726xa	-	1579	1559	1804	1797	2096	-
1726ya	-	1570	1563	1806	1800	2098	2095
5850xa	-	1572	1565	1807	1803	2100	2099
6142ya	-	1587	1570	1811	1809	2104	2099
Mean time	-	1574	1563	1806	1801	2099	2097

Amplitude of initial imperfections 2mm							
Natural-FAE scenarios							
Accelerogram	Seismic action level						
	S.F. 1		S.F. 1.25		S.F. 1.50		S.F. 1.75
	SC-25	SC-50	SC-50	SC-75	SC-75	SC-100	SC-100
290xa	-	1536	1531	1789	1780	2083	-
293ya	-	1543	1534	1790	1782	2085	2079
612xa	-	1537	1511	1778	1767	2074	-
1726xa	-	1544	1522	1783	1775	2080	-
1726ya	-	1540	1528	1786	1775	2079	2077
5850xa	-	1541	1533	1789	1780	2083	2081
6142ya	-	1551	1540	1793	1789	2089	2081
Mean time	-	1542	1528	1787	1778	2082	2080

Amplitude of initial imperfections 5mm							
Natural-FAE scenarios							
Accelerogram	Seismic action level						
	S.F. 1		S.F. 1.25		S.F. 1.50		S.F. 1.75
	SC-25	SC-50	SC-50	SC-75	SC-75	SC-100	SC-100
290xa	-	1504	1503	1774	1761	2071	-
293ya	-	1517	1506	1775	1764	2073	2063
612xa	-	1509	1483	1758	1691	2010	-
1726xa	-	1516	1495	1768	1750	2064	-
1726ya	-	1510	1498	1768	1753	2065	2055
5850xa	-	1510	1504	1773	1762	2071	2069
6142ya	-	1527	1510	1778	1773	2077	2069
Mean time	-	1513	1500	1771	1751	2062	2064

Table 13-6: Fire-resistance of the frame structure in time domain (sec) for the Natural-FAE scenarios for different amplitude of imperfections.

Amplitude of initial imperfections 0.5mm							
<i>Reference</i> scenario (ISO)							
Prefect model	1563						
Natural-FAE scenarios							
Accelerogram	Seismic action level						
	S.F. 1		S.F. 1.25		S.F. 1.50		S.F. 1.75
	SC-25	SC-50	SC-50	SC-75	SC-75	SC-100	SC-100
290xa	-	1333	1332	1336	1317	1318	-
293ya	-	1354	1331	1335	1319	1319	1302
612xa	-	1337	1308	1313	1285	1285	-
1726xa	-	1356	1318	1322	1300	1300	-
1726ya	-	1339	1325	1327	1308	1307	1296
5850xa	-	1343	1329	1332	1317	1317	1313
6142ya	-	1371	1339	1346	1337	1335	1314
Mean time	-	1348	1326	1330	1312	1312	1306
Reduction¹	-	13.78%	15.16%	14.90%	16.07%	16.09%	16.43%

Amplitude of initial imperfections 2mm							
<i>Reference</i> scenario (ISO)							
Prefect model	1563						
Natural-FAE scenarios							
Accelerogram	Seismic action level						
	S.F. 1		S.F. 1.25		S.F. 1.50		S.F. 1.75
	SC-25	SC-50	SC-50	SC-75	SC-75	SC-100	SC-100
290xa	-	1272	1263	1277	1251	1252	-
293ya	-	1286	1270	1281	1257	1258	1237
612xa	-	1276	1228	1246	1218	1218	-
1726xa	-	1288	1245	1261	1238	1238	-
1726ya	-	1280	1256	1268	1239	1237	1228
5850xa	-	1282	1267	1277	1253	1252	1244
6142ya	-	1302	1280	1290	1277	1274	1244
Mean time	-	1284	1258	1271	1248	1247	1238
Reduction¹	-	17.87%	19.49%	18.65%	20.18%	20.22%	20.78%

Amplitude of initial imperfections 5mm							
<i>Reference</i> scenario (ISO)							
Prefect model	1563						
Natural-FAE scenarios							
Accelerogram	Seismic action level						
	S.F. 1		S.F. 1.25		S.F. 1.50		S.F. 1.75
	SC-25	SC-50	SC-50	SC-75	SC-75	SC-100	SC-100
290xa	-	1216	1214	1237	1204	1206	-
293ya	-	1239	1219	1240	1212	1213	1178
612xa	-	1225	1176	1198	1048	994	-
1726xa	-	1237	1199	1220	1179	1180	-
1726ya	-	1226	1204	1222	1186	1183	1146
5850xa	-	1227	1217	1235	1207	1207	1198
6142ya	-	1255	1227	1247	1233	1228	1199
Mean time	-	1232	1208	1228	1181	1173	1180
Reduction¹	-	21.17%	22.71%	21.41%	24.42%	24.95%	24.49%

¹Reduction with respect to the fire resistance of the *reference* scenario considering criteria that do not take into account initial imperfections

Table 13-7: Fire-resistance of the frame structure in time domain (sec) for the Natural-FAE scenarios for different amplitude of imperfections - Comparison with the *reference* ISO-*reference* scenario.

Figure 13-3 summarizes the results, concerning the fire-resistance of the structural system in time domain. The fire-resistance is plotted against the average inter-storey drift (with respect to the different accelerograms that are used) of the ground floor that is induced in the structural system during the corresponding earthquake excitation. It is noted that the increase of the average drift corresponds to more severe seismic actions. The results are referred to both the ISO and the *natural*-FAE scenarios for different amplitudes of initial imperfections. It can be concluded that as the earthquake return period increases and, subsequently, the earthquake becomes more severe, the fire-resistance of the structural system is slightly reduced. Moreover, for the more rare earthquake actions it almost remains constant (comparison between the fire-resistance time that corresponds to drift 0.0169 and 0.0211). This remark holds for all the amplitudes of initial imperfections that are studied. The reduction of the fire-resistance becomes more important as the amplitude of the initial imperfections increases.

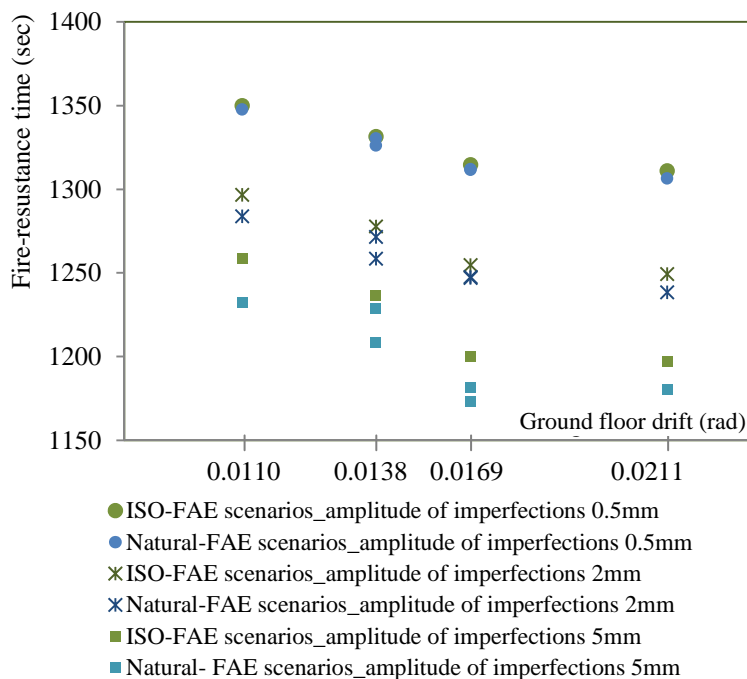


Figure 13-3: Comparison of fire-resistance time for ISO and Natural FAE scenarios (in ISO-fire time).

13.5 Conclusions

In this Chapter the fire-resistance of the structural system is calculated, in both time and temperature domain, for the *reference* and the FAE scenarios. The calculation is based on the failure criteria that are defined in Chapter 13. First, it is noticed that the structural system does not fail for the natural *reference* scenarios. The results of the natural –FAE scenarios are interpreted in ISO-fire time in order to represent in a realistic way the fire-resistance of the structural system. It is concluded that the upper limit of the reduction of the fire-resistance of the structure for the FAE loading, with respect to the fire resistance of the *reference* scenario (considering criteria that do not take into account initial imperfections) is approximately 25% for both the ISO and the natural FAE scenarios. The reduction is important and this indicates that the structural system should be re-designed in

order to take into account the FAE loading. Finally it is noticed that the calculation of the fire-resistance of the structural system, for both fire and FAE scenarios, should be based on ductility criteria that take into account the effect of the initial imperfection. In the case of the FAE loading, it is important the criteria to be dependent on the 'level of the damage' that is induced in the structural system due to the seismic action.

Chapter 14. Summary, conclusions and suggestions for further research

14.1 Summary and conclusions

The dissertation addresses the problem of the behavior of steel structures under the Fire after Earthquake loading. The problem is handled numerically. The study is focused on a four-storey library building. It is emphasized that the study takes into account the damage that is induced due to earthquake to both structural and non-structural members. The basic objective is the assessment of both the fire behavior and the fire-resistance of the structure in the case where the structure is damaged due to earthquake and, supplementary, in the case where the structure is not damaged. The last case is considered as the *reference case* and it is used for comparison of the behavior of the damaged structure with the undamaged one.

It is important to notice that the building is designed to resist the gravity and the earthquake loading according to European codes and, subsequently, follows the capacity design requirements that are specified in EN 1998-1-1. Here, a brief review of the dissertation and the main conclusions that are derived, are presented.

The first issue was the presentation of the library building and the definition of both PEF scenarios and *reference* scenarios. The Post Earthquake Fire (PEF) scenarios were used in order to study the effect of the non-structural damage to the fire evolution in the enclosure. In this study the PEF scenarios were defined through the non- structural damage that is induced due to earthquake. Specifically, two different issues were considered which are the functionality of the fire-sprinkler system and the breakage of the windows. The *reference* scenarios were defined to be the cases where the sprinkler-system is entirely functional and the one where none of the windows is broken due to earthquake. Finally, ten different PEF and two *reference* scenarios were generated.

The next issue was the presentation of the numerical model that was developed for the numerical simulation of the natural PEF scenarios in the first floor of the library building. The simulation was conducted in FDS using the principles of CFD. At this point the study was focused on the effect of non-structural damage to the fire evolution in the enclosure. It was observed that as the area of the damaged (open) windows is increased, the maximum value of the total HRR is amplified and this indicates that the peak value that is recorded depends on the available oxygen in the fire enclosure. Moreover, it was concluded that the position of the damaged windows does not affect the evolution of the total HRR with time and that the active percentage of the fire-sprinkler system affects strongly the total HRR in the fire-compartment. The results concerning the temperature “near” the structural members indicated that the temperature is highly non-uniform along the members and that it changed rapidly during the fire-exposure. A FSI (Fire Structure Interface) model was

proposed in order to overcome the difficulties which arise due to the strong spatial non-homogeneity and the intense time variation of the gas-temperature profile in the fire-compartment. The “dual-layer” model was developed in order to “condense” the results (concerning the spatial and temporal gas-temperature evolution) and the fire-compartment was divided into eleven virtual zones. The model was based on the idea of the “two-zone” models, as they are proposed in EN-199-1-2, and adopted the assumption that each virtual zone is further divided into two layers of uniform temperature: the upper (hotter) layer and the lower (colder) layer. It was concluded that the “dual-layer” post-processing model can describe effectively the temperature distribution in the fire-compartment. The advantage lies in the fact that the phenomenon is depicted in a simple way through three different variables which are the temperature of the upper and the lower layers and the layer height. In the sequel, the temperature profile of the structural members was calculated for both the *reference* and PEF scenarios, using the gas-temperature that results from the dual-layer model, depending on the virtual zone and the layer where they are located. The calculation of the temperature profile of the structural members was based on the simplified models that are proposed in EN 1991-1-2.

The design of the structural system for the gravity and earthquake loadings followed. The numerical model and the techniques that were used for the simulation of the structural behavior under the FAE loading, was the next issue. The behavior of the structure for the design earthquake was verified through the results of the pushover analysis which indicated that the system follows the capacity design rules for the formation of the plastic mechanism. Moreover, the behavior of the structural system was studied in detail through non-linear dynamic analyses, based on the direct integration of the equations of motion. The seismic action was modelled using seven different time-history accelerograms which were compatible with the design spectrum. The accelerograms were further scaled in order to represent more severe earthquakes using scale factors for the PGA. The results of the IDA analysis indicate that the maximum inter-storey drifts angles were recorded in the second level of the structure. Only in the case where the most severe earthquake was used, the first level became the critical one. Finally, the response of the structural system was verified with respect to the limit values for the drifts that are recommended in FEMA 356. Taking into account both the permanent and the transient drifts, the response of the structure was found to be bounded between the I.O. and the L.S. performance levels.

The next issue was the detailed study of the fire behavior of the structural system for both the ISO and the natural *reference* scenarios. At this point of the study, the structure was considered to be undamaged. The study of the temporal variation of the axial force and vertical deflection at the mid-span of the beam indicate clearly the different stages that take place during the fire exposure. Three different stages were identified which were the *restrained thermal expansion*, the *increase of curvature* and the *catenary action* stages. The results were obtained also in terms of stresses (Von Mises), strains and bending moments, at the ends and at mid-span of the heated beams, during the fire exposure. It was concluded that the structural system fails due to the formation of a local unstable

mechanism at both heated beams.

The study continues with the presentation of the numerical simulation of the behavior of the structural system under the FAE loading. The first issue was the definition of the FAE scenarios. The scenarios were divided into two main categories, depending on the representation of the fire action: the ISO-FAE scenarios and the Natural-FAE scenarios. Totally 28 different ISO-FAE scenarios were generated, depending on the accelerogram that was used and the scale factor of the earthquake intensity. The fire action was simulated through the ISO-fire curve in all the cases. The definition of the Natural-FAE scenarios was based on the idea that the structure can suffer different PEF scenarios as the earthquake becomes stronger. Specifically, it was considered that, as the intensity of the seismic action is scaled-up, using the appropriate scale factors for the PGA, different levels of non-structural damage are expected and these were directly connected to the different PEF scenarios. Thus, each Natural-FAE scenario is defined from a scaled accelerogram and the expected PEF scenario. Totally 49 different Natural-FAE scenarios were defined. The results of the numerical analyses indicate the failure mechanism of the structural system under the FAE scenarios. In all the cases that were studied, the same failure mechanism (local unstable mechanism at both beams that were exposed to fire) took place as the one that was observed in the *reference* fire scenarios. The results were presented in terms of mid-span deflection and rotation at the support locations of the heated beams. It was observed that the maximum recorded values of the compression forces are not influenced by the 'level of damage' that is induced during the earthquake but they are affected from the PEF scenario that is used. Moreover, the temporal evolution of the equivalent plastic strain fields and the Von Mises stresses were studied in detail in order to understand thoroughly the formulation of the unstable mechanism at the heated beams. In general, it was concluded that numerical analysis stops due to convergence failure. This is actually the result of a formation due to the formulation of the unstable local mechanism at the heated beams. Finally, it was concluded that the fire resistance of the structural system cannot be easily defined and that it is demanding to define integrated criteria in order to calculate the fire-resistance of the structural system during fire exposure.

Next, the dissertation was focused on the definition of the failure criteria for the determination of the fire-resistance of the structure under fire and FAE loading. To this end, three-dimensional shell finite element models were proposed, for the simulation of the behaviour of I-beams at elevated temperatures. First, the models were validated against published experimental results. The ductility of the beams was obtained through three-point bending tests (monotonic loading), using the standard beam approach. In the sequel, parametric analyses were conducted, with respect to the amplitude of the initial imperfections, at elevated temperatures, mainly in order to define the ductility of the members, in terms of rotational capacity and rotational (failure) criteria. The criterion that was proposed in this study is determined through the value of the rotation that corresponds to the exhaustion of the available rotational capacity of the beam. The term *ultimate available rotation* was used to identify this rotation. It was concluded that, clearly, the

criterion depends on the amplitude of the initial imperfections and that it is not strongly temperature dependent. On the other hand, it was observed that as the amplitude of initial imperfection increased, the *ultimate available rotation* was significantly decreased. The study was further extended to the evaluation of the rotational capacity of pre-damaged beams at elevated temperatures. Different cyclic loading patterns were introduced in order to induce a specified “level” of damage in the beam. Cyclic loading was used in order to simulate the damage that is induced at the ends of the beams that belong in the frame structure due to earthquake loading. In this case the ductility of the beams was obtained through virtual three-point bending tests (monotonic loading), which follow the cyclic loading stage. Parametric analyses were conducted with respect to the amplitude of the initial imperfections and to the different cyclic loading patterns, at elevated temperatures. The results indicated that as the temperature rises, the ultimate available rotation at first is reduced and in the sequel it is slightly increased. On the other hand, the ‘level of damage’ induced due to cyclic loading affects strongly the ultimate available rotation. Specifically, the aforementioned rotation is considerably reduced when the ‘level of damage’ is escalated and this becomes more important as the amplitude of the initial imperfections increases. Taking into account the previous, it is concluded that the failure criteria can be separated into two categories. In the first category the failure criteria are defined through monotonic loading and they can be used for the determination of the fire-resistance of the frame structure that is not damaged due to earthquake i.e. in the case of the *reference* fire scenarios. The criteria that depend on the ‘level of damage’ that is induced in the structural members during the cyclic loading belong in the second category. In this case, they are classified according to the ‘level of damage’ induced in the beam in order to be utilized for the evaluation of the fire-resistance of the damaged frame structures

In the last part of the dissertation, the fire-resistance of the structure for the *reference* and the FAE scenarios is determined, in time and temperature domain, taking into account the failure criteria that were previously defined. In the case of the *reference* (ISO) fire scenario, the fire resistance was calculated to be equal to 1563 sec, 1388 sec, 1323 sec and 1291st sec for the case where the imperfections are not considered and for amplitude of initial imperfections 0.5 mm, 2 mm and 5 mm, respectively. In the case of the natural fire *reference* scenario the structure did not fail. Regarding the ISO-FAE scenarios, the results indicate that the reduction of the fire-resistance time (with respect to the fire-resistance time of the ISO *reference* scenario that is obtained using failure criteria which do not take into account initial imperfections) is considerable for all the amplitudes of initial imperfection that are studied, and lies between 14% (for the design earthquake) and 24% when the most severe earthquake is considered. In the case of the natural FAE scenarios, the results indicate that the fire-resistance, in time domain, is increased as the earthquake becomes more severe and the level of the non-structural damage is amplified. This remark is misleading since the results are dominated by the temporal delay that takes place as the percentage of the non-structural damage is increased. This is absolutely related to the spread of fire in the compartment and can be attributed to the modeling technique that was used in this study. At this point, the fire-resistance of the structure should be determined

during the post-flashover stage. Therefore, the growth phase should be excluded. In other words, the equivalent time used in order to express the fire-resistance of the structures, cannot be directly compared to the real time needed for the evacuation of the building. Additionally, it is noticed that the ISO-fire curve, which is a prescriptive fire curve based on the equivalent time and that it is used for the simulation of the post-flashover stage, should be also taken into account. For this reason, it is clear that in the case of the natural FAE-scenarios it is difficult to determine the fire-resistance in time domain. The time that arises from the numerical analyses, is *real* time and it does not express the fire-resistance of the structure. In order to utilize the results of the natural-FAE scenarios, the critical temperature that defines the failure of the structure is “translated” into the equivalent ISO-fire time. In this way, the results are almost identical with the case of the ISO FAE-scenarios. The upper bound of the reduction of the fire-resistance time of the damaged structure (with respect to the fire-resistance time of the ISO *reference* scenario that is obtained using failure criteria which do not take into account initial imperfections) is approximately 25%.

14.2 Innovative points of the dissertation

This dissertation provides an integrated procedure for the study of the behaviour of a steel structure under the combined FAE loading.

The study starts from the modeling of the fire enclosure. The simulation is conducted numerically through the principles of CFD. The modeling procedure takes into account the damage especially the windows and the sprinkler system, which is induced due to earthquake, to the non-structural members. The non-structural damage is simulated through the malfunction of the fire-extinguishing system and the breakage of the windows. The results of the CFD analyses indicate the effect of the non-structural damage to the flow of gas in the compartment and, subsequently, to the temperature distribution in the enclosure. It is easily concluded that, in all the cases, the gas-temperature distribution in the compartment presents spatial non-homogeneity and that the temporal evolution is strongly “non-linear”. Then, the gas-temperature field “near” the structural members is obtained. The study does not utilize further (the transition of the results to the subsequent structural analysis) the spatial gas-temperature evolution that is calculated “near” the structural members due to the problems that are connected to this approach. The main issue is the extremely non-uniform temperature distribution along the members and the intense temporal variation. This approach would require an identical mesh in both the structural and the CFD model. This would lead to excessive computational cost for the CFD analysis and it is not finally used. Taking into account the previous, it is emphasized the requirement of a simplified FSI model. The “dual layer” post-processing model that is developed is based on the gas-temperature distribution along the height of the fire-compartment, at discrete *plan-view* points. The model “compresses” the point data to (spatial) virtual zones, which are divided into in two layers (with respect to the height of the fire-compartment) of uniform temperature: the upper (hot) layer and the lower (cold) layer. The main advantage of this technique is that actually, only three different variables (height of interface, upper and lower layer temperature) are required during the post-

processing stage of the CFD analysis. In this scientific field the innovative points of the dissertation are the following:

- Investigation of the effect of non-structural damage, induced due to earthquake, to the spatial and temporal gas-temperature “near” the structural members. The results indicate the exact profile of the gas-temperature along the members during the fire-exposure.
- Development of the “dual-layer model” that is based on the assumption of the two-zone models that are proposed in EN 1991-1-2. The model can be utilized in the post-processing stage of the CFD analysis and it is concluded that it consists a good approximation for the prediction of the gas-temperature evolution in virtual zones of the fire-compartment.

In the sequel, a numerical model is proposed for the simulation of the behaviour of the structural system during the FAE loading. The integrated numerical model that is proposed simulates accurately the behaviour of the structure for both the fire and the seismic loading and it can be utilized for design purposes taking into account the FAE loading. The model incorporates the dynamic characteristics that are required for the simulation of the response of the structure during the seismic action and in the same time it includes the temperature dependent mechanical and thermal properties of steel at elevated temperatures. Specifically, the two-dimensional model that is developed, utilizes beam finite elements and it is formulated taking into account the concept of concentrated plasticity. Moreover, the dissertation proposes techniques for the numerical analysis in the case of FAE loading. The techniques are referred to the problems that arise in this case. The first problem is connected to the different scale of the duration of earthquake and fire events. In order to encounter this issue it is proposed to divide the analysis into two separate ones. In the first analysis, the structure is subjected to the seismic action while in the second one the analysis restarts and the deformed structure is exposed to fire for 60 minutes. In this way, the desired time step is utilized in the corresponding analyses. It is noted that at the start point of the fire analysis, where the analysis restarts, the code “reads” the output file of the seismic analysis, which includes all the results of the previous stage. In this case, where the problem is solved through two subsequent analyses, the problem that arises is related to simulation of the earthquake excitation. Specifically, when the analysis is restarted, the output file of the seismic analysis, which is actually the input file for the fire analysis, includes the non-zero values for the acceleration or the displacement for the corresponding DOF of the support nodes of the frame. This indicates that the prescribed values are used in the second (fire) analysis and the structural system actually is submitted to a ground motion of constant acceleration. In order to overcome this problem, it is proposed to eliminate the ground acceleration of the earthquake analysis. The technique that is proposed is to stabilize the ground displacement artificially. The stabilization is proposed to be gradual and a second order curve is used. Moreover, in this case the earthquake excitation is applied as time-history displacement at the lateral-translational DOF (direction of the ground motion) to the support nodes of the numerical model. The innovative points of the dissertation in this field are the following:

- Development of an “integrated” two-dimensional beam finite element model that incorporates the required dynamic characteristics and includes the temperature-dependent mechanical and thermal properties of steel at elevated temperatures. The model is formulated taking into account the concentrated plasticity concept. Moreover, it can be used for the simulation of the fire response of the damaged structural systems. The model can be used for design purposes.

- The numerical analysis technique that is proposed for the simulation of structural behavior under the FAE loading. The methodology proposes to divide the analysis into two separate ones in order to use the appropriate time-step. Moreover, it is proposed to eliminate the ground-acceleration at the end of the earthquake analysis. To this end the ground displacement is first calculated by the double time-integration of the ground acceleration. Then the ground displacement is stabilized artificially and finally it is applied to the appropriate DOF to the support nodes of the numerical model.

The dissertation proposes three-dimensional models for the determination of the ductility of beams at elevated temperatures. Initially, the model is validated against experimental results. In the sequel, the numerical model is modified in order to take into account the possible local buckling and the corresponding initial imperfections and the lateral torsional buckling is restrained. In this way, it is compatible with the situation present in real buildings, where the lateral torsional buckling is usually restrained by the presence of concrete slab. The ductility is determined, in rotational capacity terms, through the numerical simulation of the three-point bending test and the standard beam approach is used. The numerical simulation is conducted for both damaged and undamaged beams. In the first case, the damage is induced in the beam through different cyclic loading patterns. In this way both the rotational capacity and the failure (rotational) criteria are determined. The failure criteria are based on the rotation that corresponds to the exhaustion of the rotational capacity of the beam. It is concluded that the failure criteria slightly vary as the temperature increases. On the other hand it is concluded that the criteria are strongly dependent on the considered amplitude of the initial imperfections and to the ‘level of damage’ that is induced during the cyclic loading. Moreover, the failure criteria, which are defined through the standard beam approach using detailed three-dimensional (shell) models, are classified according to the ‘level of damage’ induced in beam, during cyclic loading, in order to be utilized for the evaluation of the fire-resistance of the frame structure for the FAE loading. The procedure proposed in order to define the ‘level of damage’ that is induced in the standard beams is the following: First, the simulation of three-point bending test of the standard beam at elevated temperatures is conducted using the finite shell element model and the dimensionless moment-rotation curves are obtained at different temperature levels. In the same time, the numerical simulation of the cyclic loading stage for the standard beam is conducted through a beam finite element model with the same characteristics, and the same imposed displacement is used. In this way the ‘level of damage’ is calculated, which is defined from the maximum equivalent plastic strain

developed at the cross-section of the beam (beam finite element model) at the mid-span. Finally, the evolution of the available rotation with temperature is obtained. The same procedure is repeated for different amplitudes of imposed rotation (or displacement) during the cyclic loading stage. Actually, the imposed rotation is the parameter that defines the ‘level of damage’ which finally characterizes the evolution of the available rotation with temperature. In this dissertation it is referred as the “‘level of damage’”.

On the other hand, considering the frame structure, the maximum equivalent plastic strain at the plastic hinge locations at the end of the seismic excitation is used. In this way, the damage level is completely localized. It is concluded that, in both cases (standard beam approach and members of frame structure) the ‘level of damage’ is classified according to the equivalent plastic strain field (using the maximum equivalent plastic strain value between the upper and the lower flange of the heated beam), thus the damage level that is used in both cases is equivalent.

The dissertation is finalized with the calculation of the fire-resistance of the structure, in time and temperature domain, for the *reference* and the FAE scenarios that are studied. The calculation of the fire resistance time is based on the comparison of the rotation at the ends of the heated beams of the frame structure with the limit values of the available ultimate rotation, according to the failure criteria. In this way, the critical value of rotation and the corresponding critical temperature are indicated. The critical temperature can be directly connected to the corresponding time of the fire exposure since the temporal evolution of temperature is already known. In this way, the fire-resistance time is calculated and it corresponds to the state beyond which the calculated deformations of the structure cause failure due to the loss of adequate support to one of the members.

The innovative points of the dissertation in the scientific field are the following:

- Assessment of the ductility, in terms of rotational capacity, of damaged, due to cyclic loading, steel I-beams at elevated temperatures. The study takes into account different amplitudes of initial imperfections and different levels of damage through scaled imposed cyclic-loading patterns. The results are systematically classified with respect to the imposed ‘level of damage’.

- Assessment of the failure criteria that can be used for the determination of the fire-resistance time of structures under fire and FAE loading. The criteria are defined through the standard beam approach under monotonic loading. Moreover, they are defined for both damaged and undamaged beam in order to be utilized for damaged and undamaged structural systems respectively. The criteria are determined by the value of the rotation that corresponds to the exhaustion of the available rotational capacity of the beam. The term ultimate available rotation is used to identify this rotation. Finally, the criteria are systematically classified with respect to the imposed ‘level of damage’ and in the case of the undamaged beams the ‘level of damage’ is set equal to zero.

- Utilization of the failure criteria for the determination of the fire-resistance of the structural system. This is based on the identification of the 'level of damage' that is induced in both the standard beams, due to cyclic loading and to the frame structure, due to earthquake loading. In the first case, a systematic procedure is proposed for the estimation of the 'level of damage'. According to this procedure, the dimensionless moment-rotation curves are obtained through finite shell element model at different temperature levels. In the same time, the numerical simulation of the same cyclic loading test is conducted using a beam finite element model with the same characteristics. In this way 'level of damage' is calculated, which is defined from the maximum equivalent plastic strain developed at the cross-section of the beam (beam finite element model) at the mid-span. The procedure is repeated for different amplitudes of imposed rotation during the cyclic loading stage. The advantage of the identification of the 'level of damage' is that the same value can be obtained from the finite element analysis of the frame structure using beam elements with concentrated plasticity. Specifically, at the aforementioned analysis the 'level of damage' is derived at the end of the seismic loading. Since the 'level of damage' is defined for the frame structure, the corresponding failure criterion can be utilized.

- Estimation of the fire-resistance of the structure for fire and FAE loading, using the rotational failure criteria that are proposed in this dissertation. The calculation of the fire resistance is based on the rotations at the ends of the heated beams, and the subsequent comparison with the available ultimate rotation. In this way, the fire-resistance of the structure depends on the 'level of damage' that is induced during the earthquake and the level of initial imperfections that are taken into account for the determination of the ultimate available rotation.

14.3 Suggestions for further research

The dissertation is finalized with some suggestions for future research, which are summarized in the following:

- Experimental study for the behavior of steel beams under monotonic loading, at elevated temperatures, in the case that they are damaged due to cyclic loading at ambient temperature.

- Parametric (numerical) analyses for the determination of the rotational capacity and assessment of the failure criteria for different cross-section types and structural systems. The parameters that should be studied are the slenderness ratios (for both flange and web), the grade of steel and the length of the beam. Investigation of the influence of the temperature gradient in the cross-section.

- Parametric (numerical) analyses for the calculation of the rotational capacity, for both damaged and not-damaged, steel I-beams at elevated temperatures taking into account the effect of axial forces. Additionally, the failure criteria should be modified accordingly.

- Experimental and numerical study of the behavior of fire-protected steel beams (using

fire-proof paintings) under monotonic loading, at elevated temperatures, in the case that they are damaged due to cyclic loading at ambient temperature. It is expected that during the cyclic loading stage the fire-proof painting may be “damaged”. Consequently, the behavior will be different at elevated temperatures comparing with the protected beam.

- Study of the failure modes and calculation of the fire-resistance time of steel frame structures of different typologies under the combined loading of fire after earthquake.

Appendix A. Finite Element Modeling

Finite element library

(According to Marc Volume B: element library, MSC Marc (2011a))

Element 98

This is a straight beam in space which includes transverse shear effects with linear elastic material response as its standard material response, but it also allows nonlinear elastic and inelastic material response. Large curvature changes are neglected in the large displacement formulation. Linear interpolation is used for the axial and the transverse displacements as well as for the rotations. This element can be used to model linear or nonlinear elastic response by direct entry of the cross-section properties.

This element can be used to model inelastic and nonlinear elastic material response when employing numerical integration over the cross section. Standard cross sections and arbitrary cross sections can be entered if the element is to use numerical cross-section integration. Inelastic material response includes plasticity models, creep models, and shape memory models, but excludes powder models, soil models, concrete cracking models, and rigid plastic flow models. Elastic material response includes isotropic elasticity models and nonlinear elasticity models, but excludes finite strain elasticity models like Mooney, Ogden, Gent, Arruda-Boyce, Foam, and orthotropic or anisotropic elasticity models. Arbitrary nonlinear material response can be used when special subroutines are used.

Numerical Integration

The element uses a one-point integration scheme. This point is at the midspan location. This leads to an exact calculation for bending and a reduced integration scheme for shear. The mass matrix of this element is formed using three-point Gaussian integration.

Degrees of Freedom

- 1 = u_x = global Cartesian x-direction displacement
- 2 = u_y = global Cartesian y-direction displacement
- 3 = u_z = global Cartesian z-direction displacement
- 4 = θ_x = rotation about global x-direction
- 5 = θ_y = rotation about global y-direction
- 6 = θ_z = rotation about global z-direction

Output of Strains

Generalized strain components are as follows:

Axial stretch ϵ

Local γ_{xz} shear

Local γ_{yz} shear

Curvature about local x-axis of cross section κ_{xx}

Curvature about local y-axis of cross section κ_{yy}

Twist about local z-axis of cross section κ_{zz}

Output of Stresses

Generalized stresses:

Axial force

Local T_x shear force

Local T_y shear force

Bending moment about x-axis of cross section

Bending moment about y-axis of cross section

Torque about beam axis

Layer stresses:

Layer stresses in the cross section are only available if the element uses numerical cross-section integration (and the section is not pre-integrated) and are only printed if explicitly requested or if plasticity is present.

1 = σ_{zz}

2 = τ_{zx}

3 = τ_{zy}

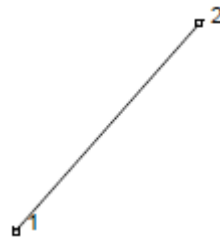


Figure A- 1: Finite element of type 98.

Element 75

This is a four-node, thick shell element with global displacements and rotations as degrees of freedom. Bilinear interpolation is used for the coordinates, displacements and the rotations. The membrane strains are obtained from the displacement field and the curvatures from the rotation field. Element 75 takes into account transverse shear effects. The transverse shear strains are calculated at the middle of the edges and interpolated to the integration points. Under this way, a very efficient and simple element is obtained which exhibits correct behaviour in the limiting case of thin shells. Element 75 can be used in curved shell analysis as well as in the analysis of complicated plate structures.

Because of its simple formulation compared with the standard high order shell elements, it is less expensive and, therefore very attractive in nonlinear analysis. The element is not very sensitive to distortion, particularly if the corner nodes lie in the same plane. It is noted that all constitutive relations can be used with this element and that the specific element can be collapsed to triangle element.

Geometrical basis

Element 75 is defined geometrically by the (x,y,z) coordinates of the four corner nodes. Due to the bilinear interpolation, the surface forms a hyperbolic paraboloid which is allowed to degenerate a plate. The following picture shows Element 75.

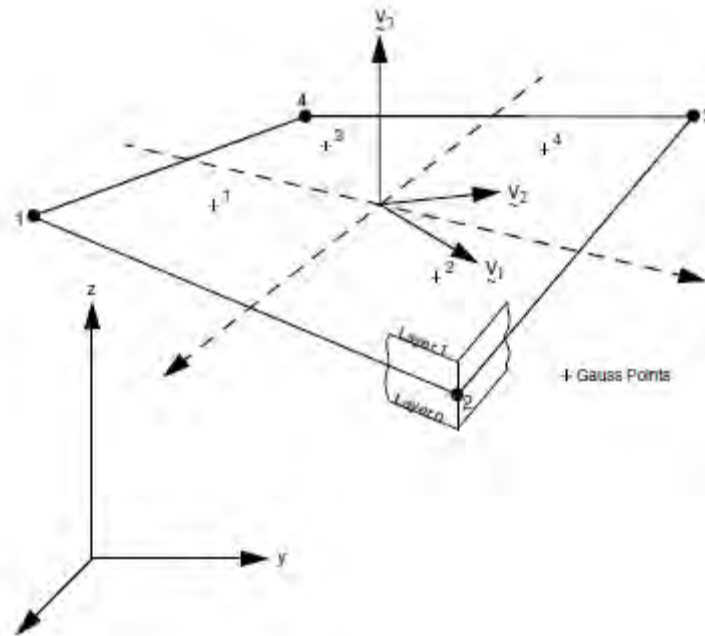


Figure A- 2: Finite element of type 75.

Numerical Integration

Integration through the shell thickness is performed numerically using Simpson's rule. The user can specify the number of the integration points. The default option is 11 points.

Degrees of Freedom

- 1 = u_x = global Cartesian x-direction displacement
- 2 = u_y = global Cartesian y-direction displacement
- 3 = u_z = global Cartesian z-direction displacement
- 4 = φ_x = rotation about global x-direction
- 5 = φ_y = rotation about global y-direction
- 6 = φ_z = rotation about global z-direction

Output of Strains

The Generalized strains components are:

- Middle surface stretches: $\varepsilon_{11}, \varepsilon_{22}, \varepsilon_{12}$
- Middle surface curvatures: k_{11}, k_{22}, k_{12}
- Transverse shear strains: γ_{23}, γ_{31}

The above are calculated at the local system $\tilde{V}_1, \tilde{V}_2, \tilde{V}_3$ of the element.

Output of Stresses

For element 75 the stresses $\sigma_{11}, \sigma_{22}, \sigma_{12}, \sigma_{23}, \sigma_{31}$ are calculated in the local system of the element $(\tilde{V}_1, \tilde{V}_2, \tilde{V}_3)$. The stresses are given at equally spaced layers though thickness. The first layer is on positive direction \tilde{V}_3 .

*Structural procedures library***Dynamic transient analysis based on the direct integration of the equations of motion**

Direct integration is a numerical method for solving the equations of motion of a dynamic system. It is used for both linear and nonlinear problems. In nonlinear problems, the nonlinear effects can include geometric, material, and boundary nonlinearities. The equations of motion of the structural system are defined as follows:

$$Ma + Cv + Ku = F \quad (\text{A.1})$$

Where M , C and K are mass, damping and stiffness matrices respectively and a , v , u and F are acceleration, velocity displacement and force vectors. Various direct integration operators can be used to integrate the equations of motion in order to obtain the response of the structural system. Marc offers four direct integration operators listed below.

- Newmark-beta operator
- Houbolt operator
- Generalized-Alpha operator
- Central Difference operator

In this dissertation the Newmark-beta Operator is used. This operator is probably the most popular direct integration method used in finite element analysis. The Newmark-beta operator can effectively obtain solutions for linear and nonlinear problems for a wide range of loadings. The procedure allows for change of time step, so it can be used in problems where sudden impact makes a reduction of time step desirable. This operator can be used with adaptive time step control. When using the Newmark-beta operator, the frequencies of the fundamental modes are important to the response. The time step in this method should not exceed 10 percent of the period of the highest relevant frequency in the structure. Otherwise, large phase errors will occur. The phenomenon usually associated with a too large time step is strong oscillatory accelerations. With even larger time steps, the velocities start oscillating. With still larger steps, the displacement eventually oscillates. In nonlinear problems, instability usually follows oscillation.

The generalized form of the Newmark-beta operator is the following:

$$u^{n+1} = u^n + \Delta t v^n + (1/2 - \beta)\Delta t^2 a^n + \beta\Delta t^2 a^{n+1} \quad (\text{A.2})$$

$$v^{n+1} = v^n + (1 - \gamma)\Delta t a^n + \gamma\Delta t a^{n+1} \quad (\text{A.3})$$

Where superscript n denotes a value at the n^{th} time step and u, v, a take on their usual meanings. The particular form of the dynamic equations corresponding to the trapezoidal rule, $\gamma = 1/2, \beta = 1/4$ results in:

$$\left(\frac{4}{\Delta t^2}M + \frac{2}{\Delta t}C + K\right)\Delta u = F^{n+1} - R^n + M\left(a^n + \frac{4}{\Delta t}v^n\right) + Cv^n \quad (\text{A.4})$$

where the internal force R is:

$$R = \int_V \beta^T \sigma dV \quad (\text{A.5})$$

The previous equation allows the allows implicit solution of the system

$$u^{n+1} = u^n + \Delta u \quad (\text{A.6})$$

Notice that the operation matrix includes K , the tangent stiffness matrix. Hence any nonlinearity results in a reformulation of the operator matrix. Additionally, if the time step changes, this matrix must be recalculated because the operator matrix also depends on the time step.

Mass Matrix

The mass matrix is a discrete representation of the system mass. System mass can be defined through either distributed masses and concentrated masses. Distributed masses are defined for elements through the mass density material property. Marc offers both consistent and lumped element masses element matrices. The consistent mass matrix is given by:

$$[m] = \int \rho [N]^T [N] dV \quad (\text{A.7})$$

where ρ is mass density and $[N]$ is the shape function matrix is the shape function matrix. Marc uses the Hinton, Rock, Zienkiewicz lumping scheme to produce a diagonal mass matrix. The salient features of this scheme are as follows.

The diagonal coefficients of the consistent mass matrix are computed. The total mass of the element m is also computed. A scale factor s is computed by adding the translational diagonal coefficients that are mutually parallel and in the same direction. All diagonal coefficients are then scaled by m/s , thereby preserving the total mass of the element..

Damping

In a transient dynamic analysis, damping represents the dissipation of energy in the structural system. It also retards the response of the structural system. Marc allows to enter two types of damping in a transient dynamic analysis: Modal damping and Rayleigh damping. Rayleigh damping is used for the direct integration method.

During time integration, Marc associates the corresponding damping fraction with each mode. The program bases integration on the usual assumption that the damping matrix of the system is a linear combination of the mass and stiffness matrices, so that damping does

not change the modes of the system. For direct integration damping, you can specify the damping matrix as a linear combination of the mass and stiffness matrices of the system. Numerical damping is used to damp out unwanted high-frequency chatter in the structure. If the time step is decreased (stiffness damping might cause too much damping), use the numerical damping option to make the damping (stiffness) coefficient proportional to the time step. Thus, if the time step decreases, high-frequency response can still be accurately represented. This type of damping is particularly useful in problems where the characteristics of the model and/or the response change strongly during analysis (for example, problems involving opening or closing gaps). Element damping uses coefficients on the element matrices and is represented by the equation:

$$C = \sum_{i=1}^n \left\{ a_i M_i + \left(\beta_i + \gamma_i \frac{\Delta t}{\pi} \right) K_i \right\} \quad (\text{A.8})$$

where,

C - is the global damping matrix

M_i - is the mass matrix of i^{th} element

K_i - is the stiffness matrix of the i^{th} element

a_i - is the mass damping coefficient on the i^{th} element

β_i - is the usual stiffness damping coefficient on the i^{th} element

γ_i - is the numerical damping coefficient on the i^{th} element

Δt - is the time increment

If the same damping coefficients are used throughout the structure the above equation is equivalent to Rayleigh damping.

Rayleigh damping coefficients

Briefly, the Rayleigh damping is a procedure for the construction of the classical damping matrix (Chopra, 2007). The damping matrix is divided into the mass-proportionality and the stiffness proportionality damping matrices as it is indicated in the following:

$$[C] = a_0[M] + a_1[K] \quad (\text{A.9})$$

where $[C]$ is the classical damping matrix of the structural system, $[M]$ is the mass matrix and $[K]$ is the stiffness matrix. The constants a_0 and a_1 have units of sec^{-1} and sec respectively. The stiffness-proportionality damping appeals to intuition because it can be interpreted to model the energy dissipation arising from the story deformations. In contrast,

mass-proportionality damping is difficult to justify physically because the air damping it can be interpreted to model is negligibly small for most structures. The coefficients a_0 and a_1 are determined from the following relations:

$$a_0 = \zeta \frac{2\omega_i\omega_j}{\omega_i + \omega_j} \quad a_1 = \zeta \frac{2}{\omega_i + \omega_j} \quad (\text{A.10})$$

where ω_i and ω_j are the natural frequencies of the i th and j th modes respectively and ζ is the damping ratio which is considered to be the same for both modes. Applying this procedure to practical problems, the modes i and j with specified damping ratio should be chosen to ensure reasonable values for the damping ratios in all the modes contributing significantly to the response of the structural system. In this study the natural frequencies of the first and the second modes are considered in order to calculate the Rayleigh damping coefficients a_0 and a_1 . The values that are resulting are:

$$a_0 = 0.55 \text{sec}^{-1} \quad a_1 = 0.0034 \text{sec}^{-1} \quad (\text{A.11})$$

The values that are used in the study are summarized in Table A-1.⁴ The damping ratio of the third mode is calculated according to the following:

$$\zeta_3 = \frac{\alpha_0}{2\omega_3} + \frac{\alpha_1\omega_3}{2} \quad (\text{A.11})$$

Additionally in the aforementioned table, the computed damping ratios for the third are presented. It is concluded that the Rayleigh damping coefficients that are based on the first and the second modes, are predicting reasonable value for the third mode of the structural system.

Mode	f_n (sec ⁻¹)	ω_n (rad/sec ⁻¹)	ζ
1	1.138	7.150	0.050
2	3.527	22.161	0.050
3	7.017	44.089	0.059

Table A- 1: The natural frequencies and the Rayleigh damping coefficients

⁴ The values of the natural frequencies are resulting from the eigenmode analysis that is presented in section 9.5.

Appendix B. Results of CFD modeling

Gas-temperature “near” the structural members

The outcomes of the CFD analyses concerning the temperature recorded “near” the structural members are illustrated in the following figures (Figure B- 1to Figure B- 40), for completeness reasons. Specifically, snapshots (800th sec, 120th sec, 160th sec and 2000th sec) of the temperature distribution, for both beams and columns, are presents along the axis of the members. The results are referred to SC-25A, SC-50A, SC-50A, SC-50B, SC-50C, SC-100, SC-SP20 and SC-SP40. The corresponding results for SC-75 are included in Chapter 8. Moreover, the results for the *reference* scenarios (SC-00 and SC-SP100) are not included here for due to the facts that the values are considerably low (below 200 °C).

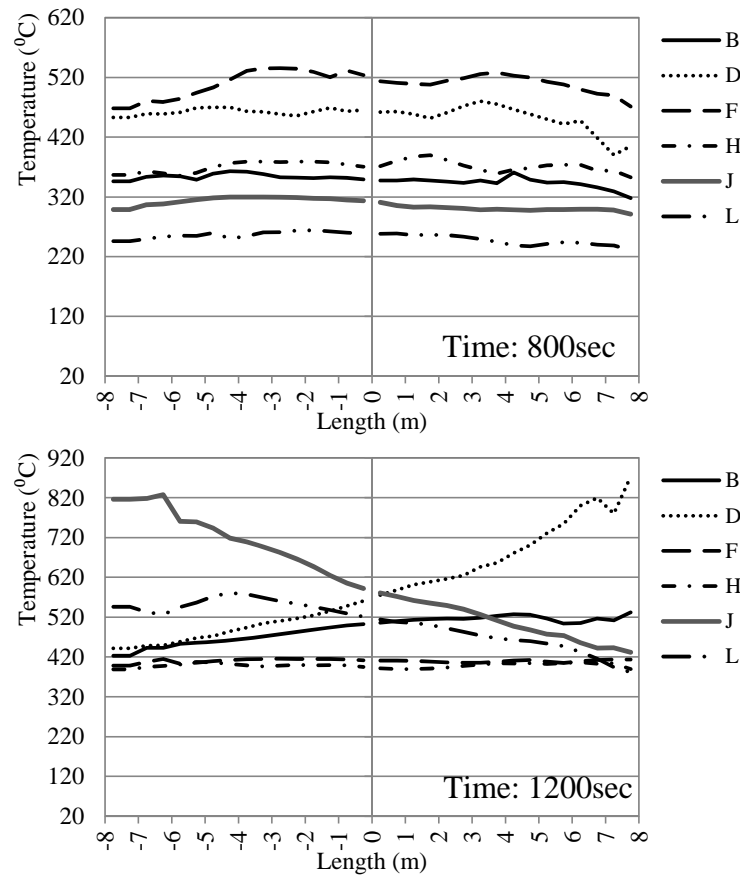


Figure B- 1: Temperature distribution along the axis of the beams that lie at different frames for the SC-25A.(continued)

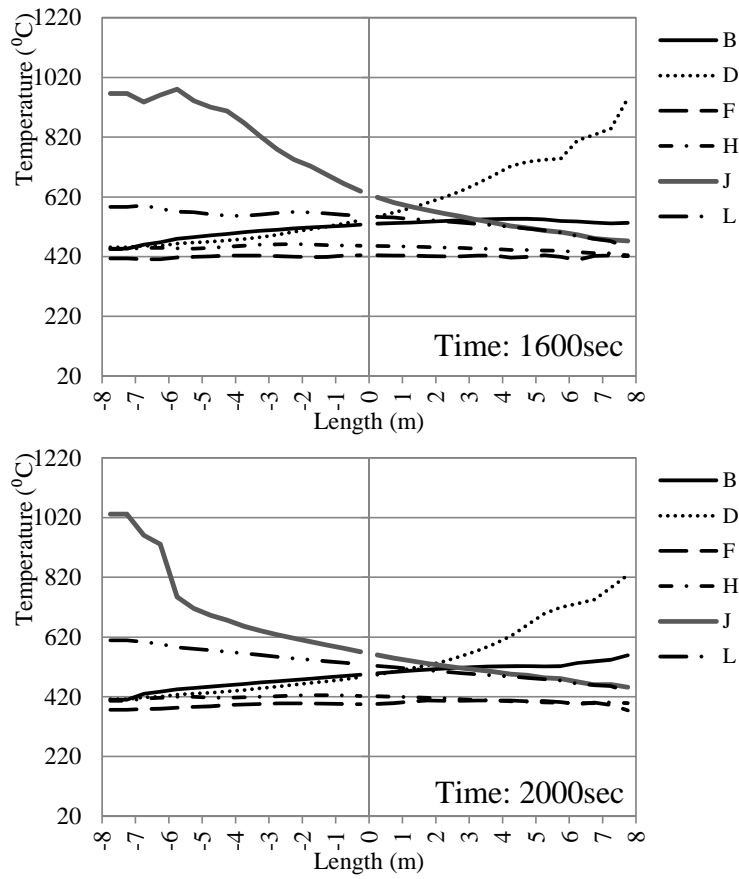


Figure B- 1: Temperature distribution along the axis of the beams that lie at different frames for the SC-25A.

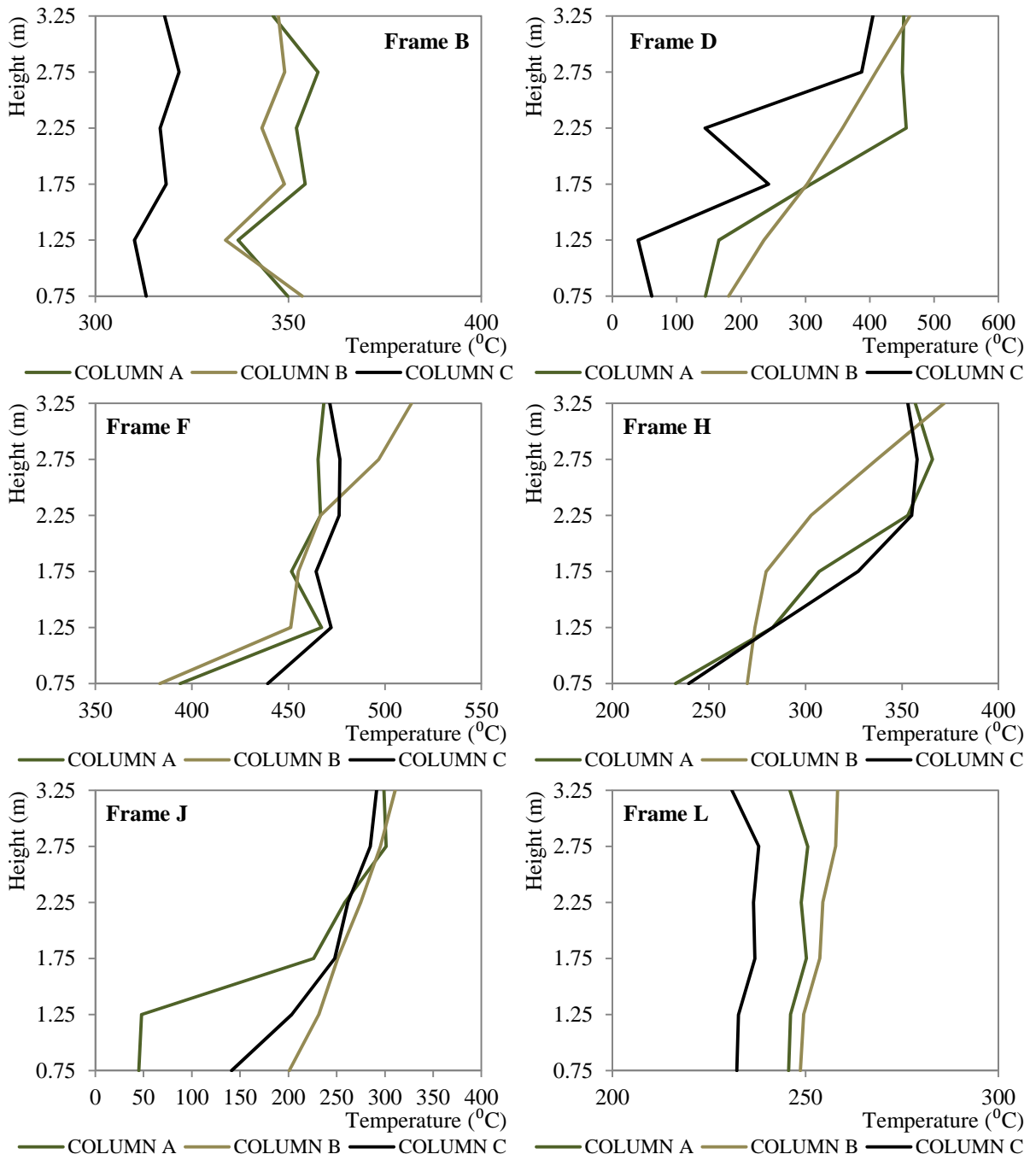


Figure B- 2: Temperature distribution along the axis of the columns in different frames for the SC-25A/
Time=800sec.

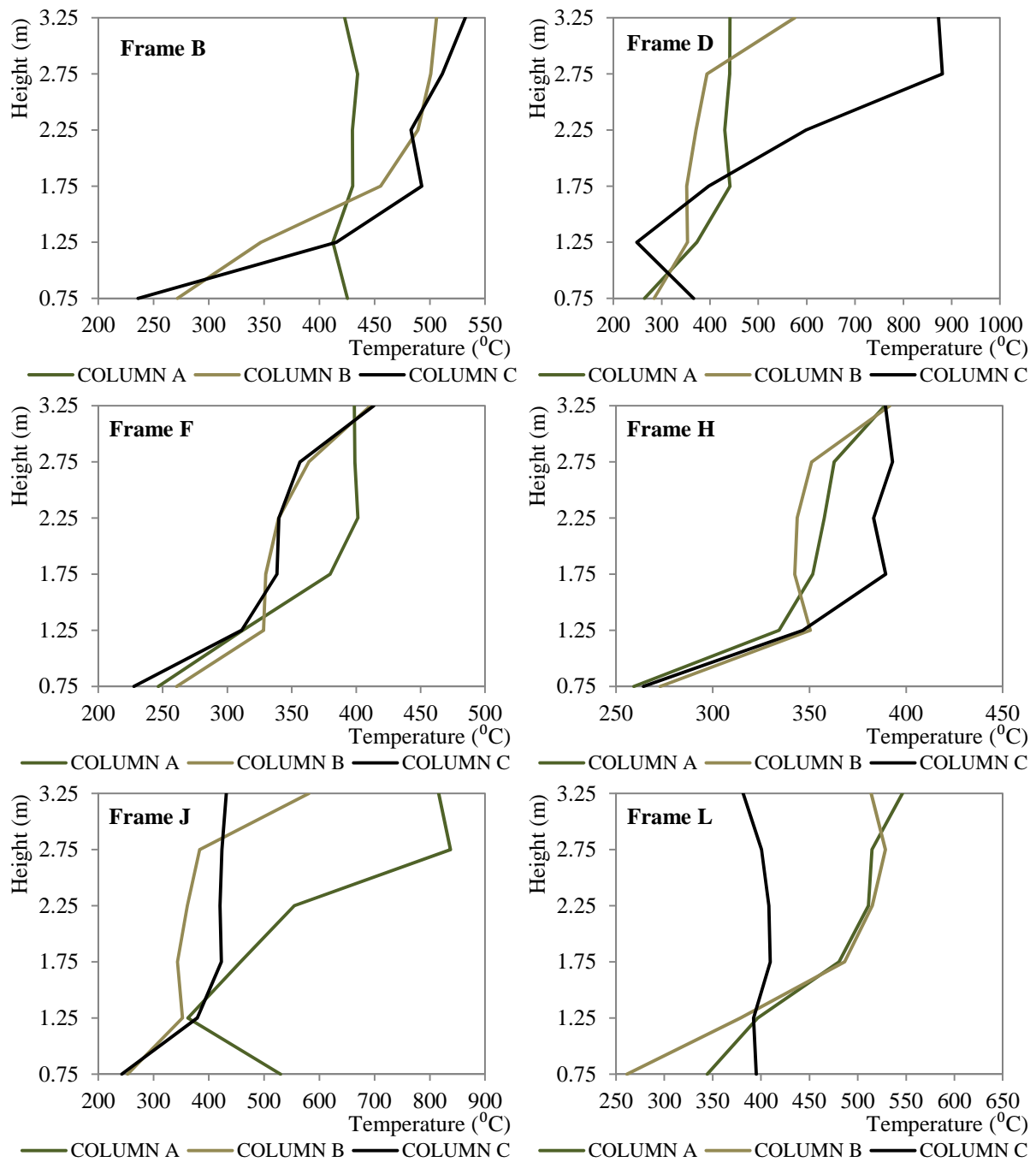


Figure B- 3: Temperature distribution along the axis of the columns in different frames for the SC-25A/
Time=1200sec.

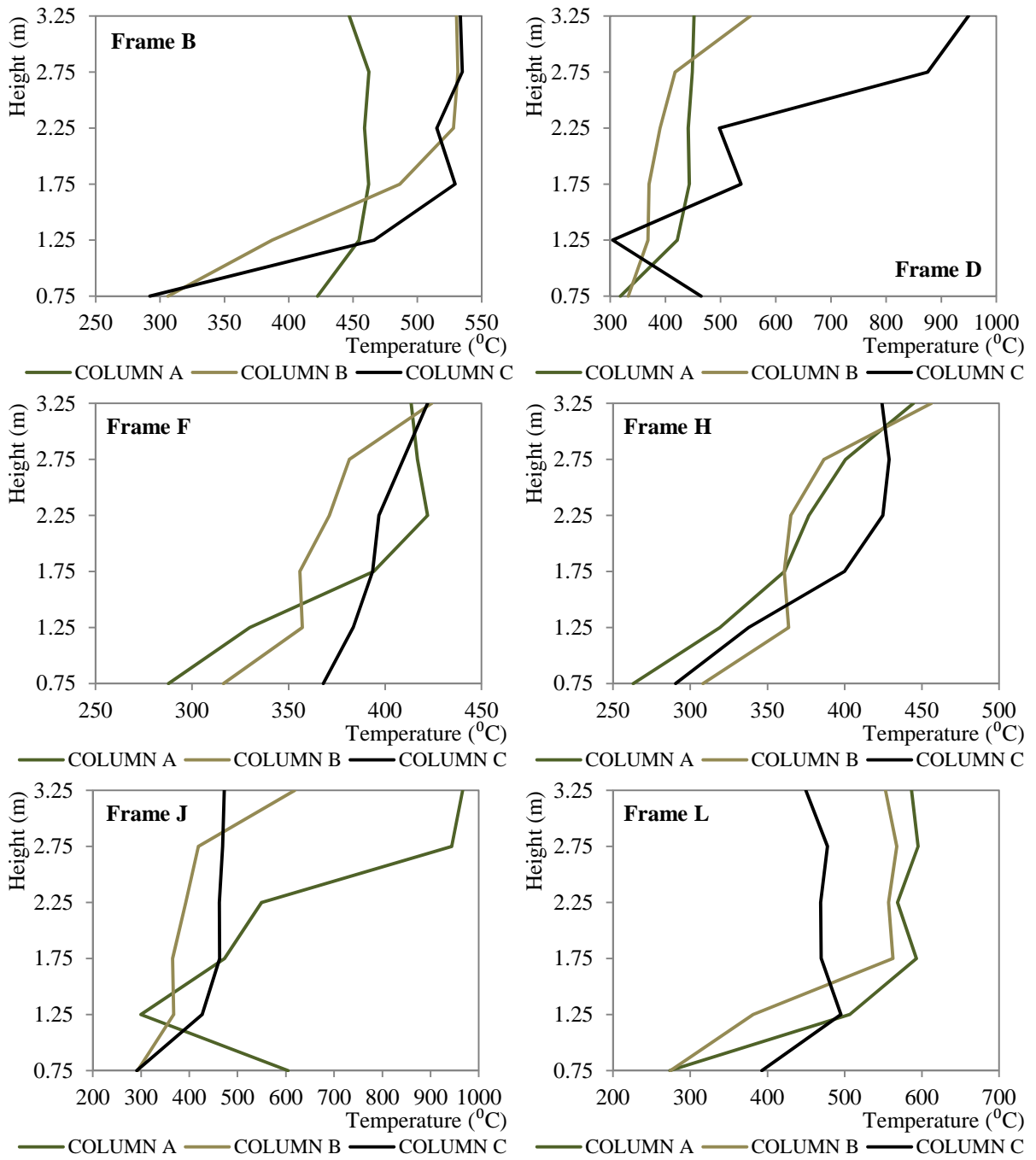


Figure B- 4: Temperature distribution along the axis of the columns in different frames for the SC-25A/
Time=1600sec.

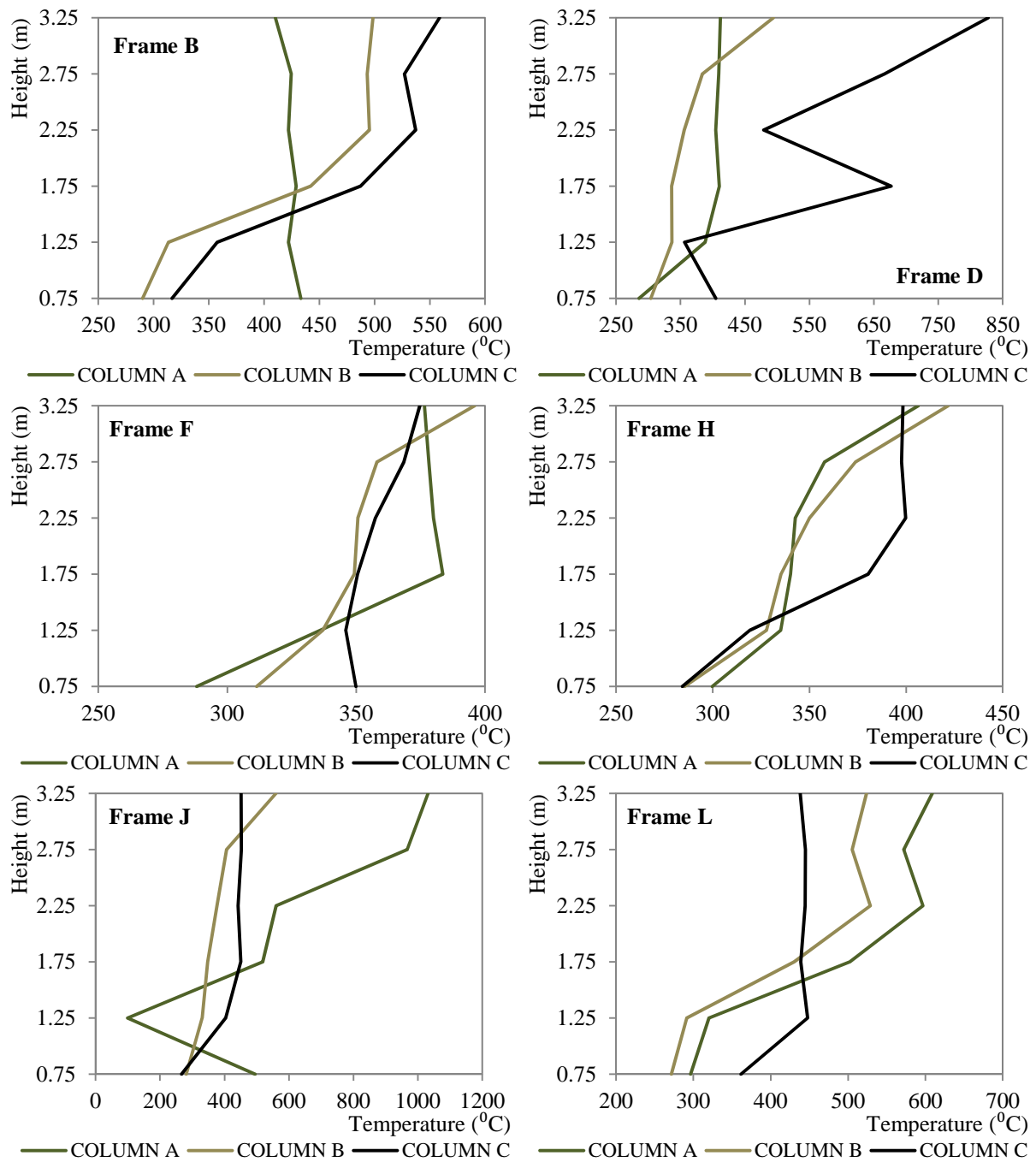


Figure B- 5: Temperature distribution along the axis of the columns in different frames for the SC-25A/
Time=2000sec.

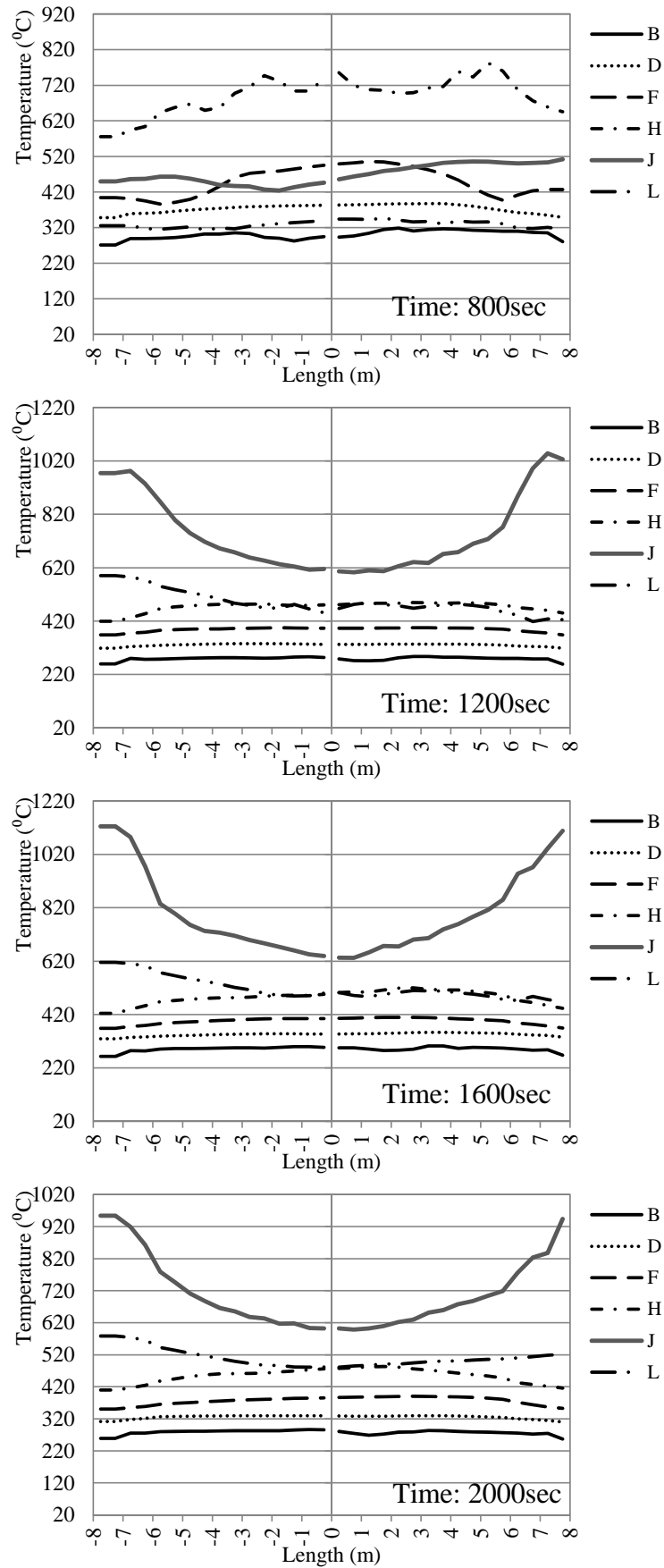


Figure B- 6: Temperature distribution along the axis of the beams that lie at different frames for the SC-25B.

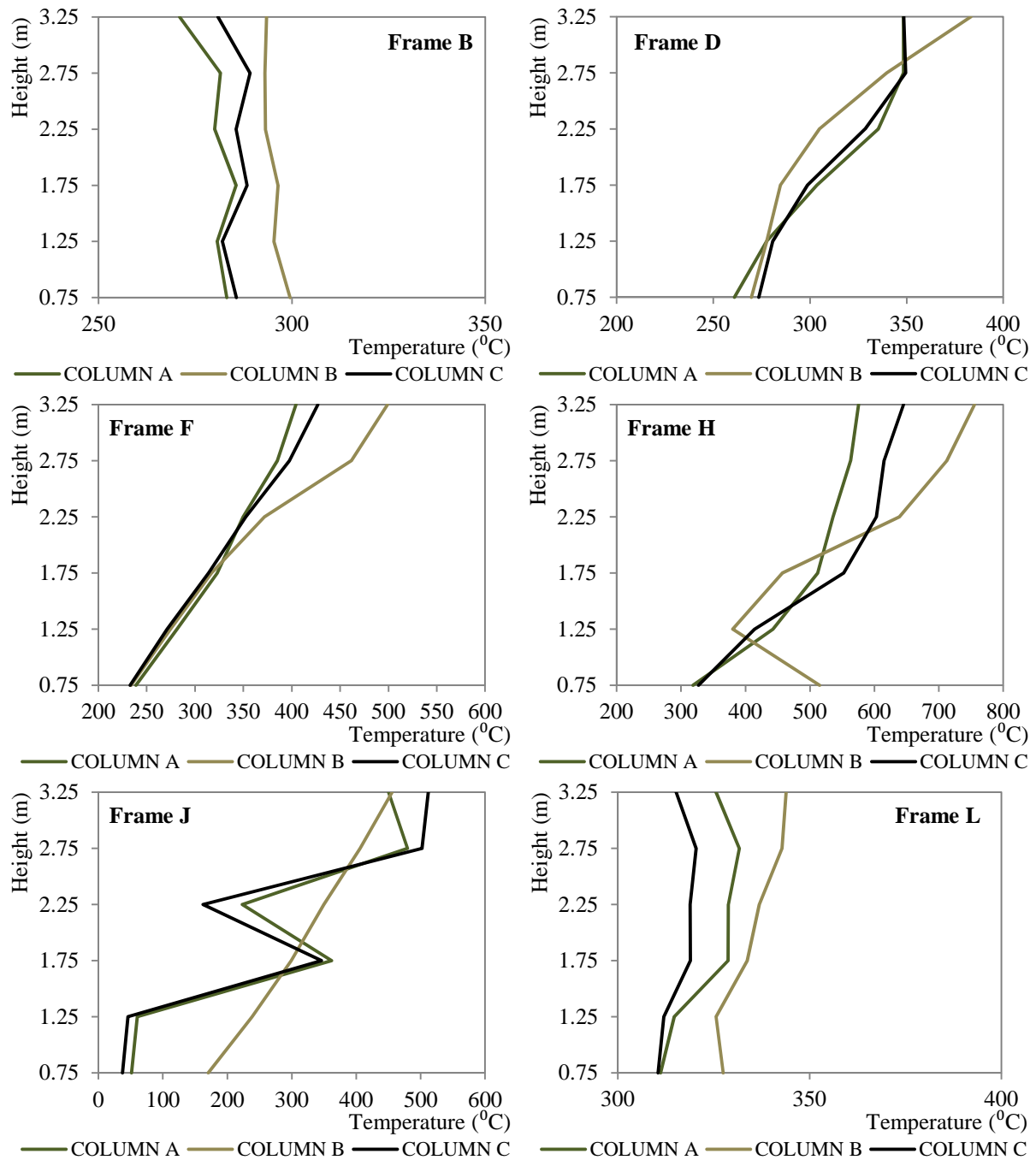


Figure B- 7: Temperature distribution along the axis of the columns in different frames for the SC-25B/ Time=800sec.

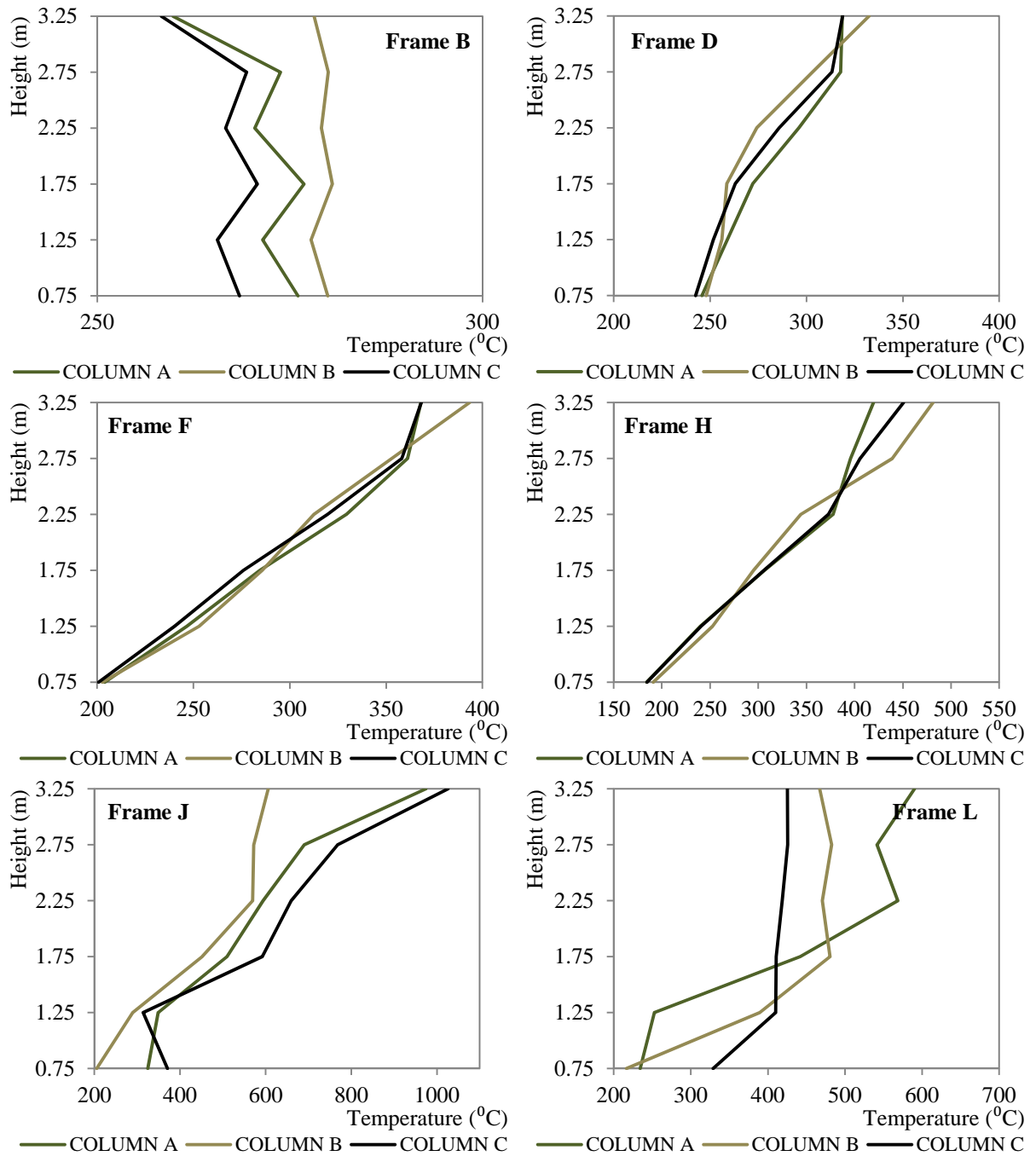


Figure B- 8: Temperature distribution along the axis of the columns in different frames for the SC-25B/
Time=1200sec.

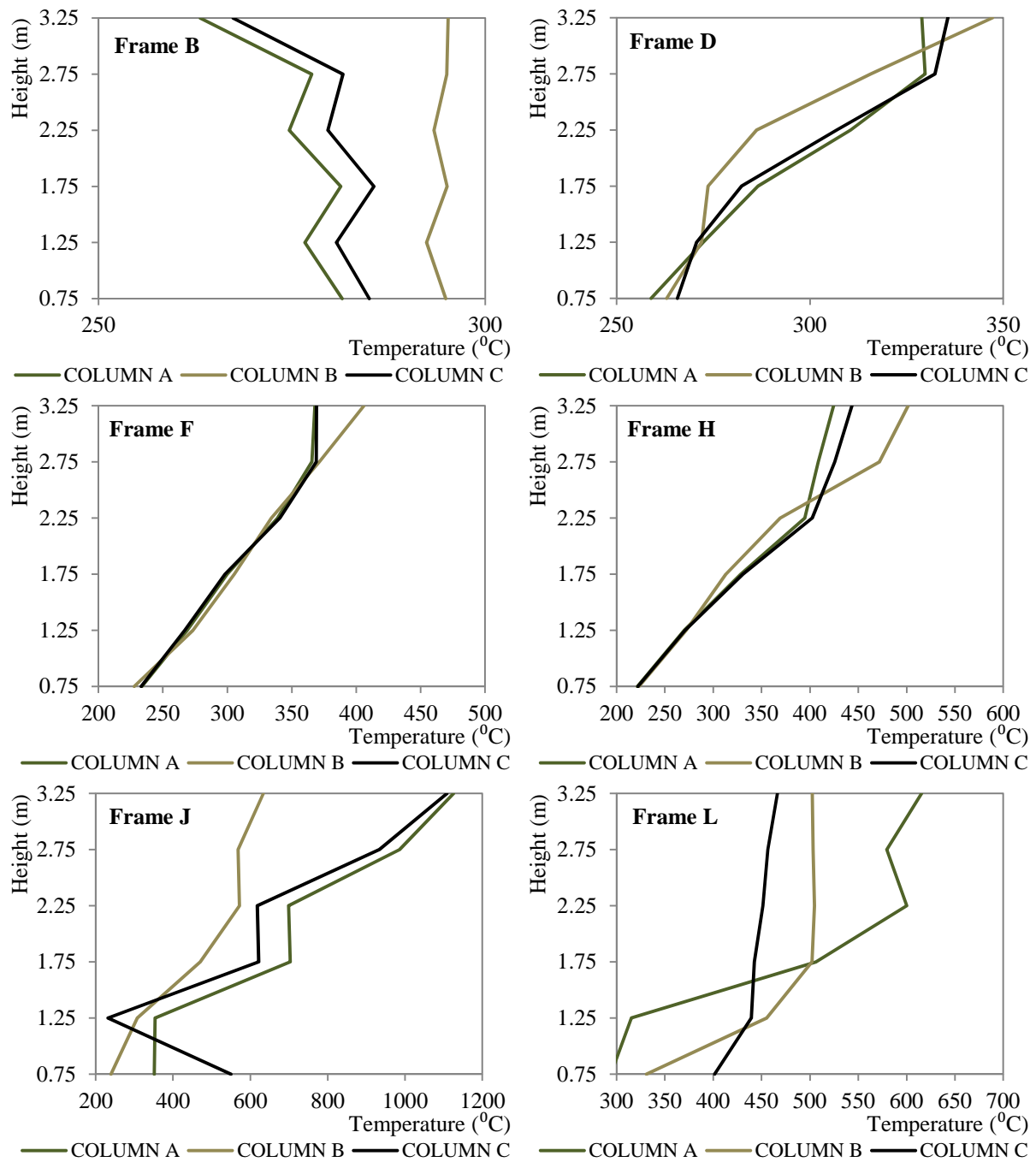


Figure B- 9: Temperature distribution along the axis of the columns in different frames for the SC-25B/
Time=1600sec.

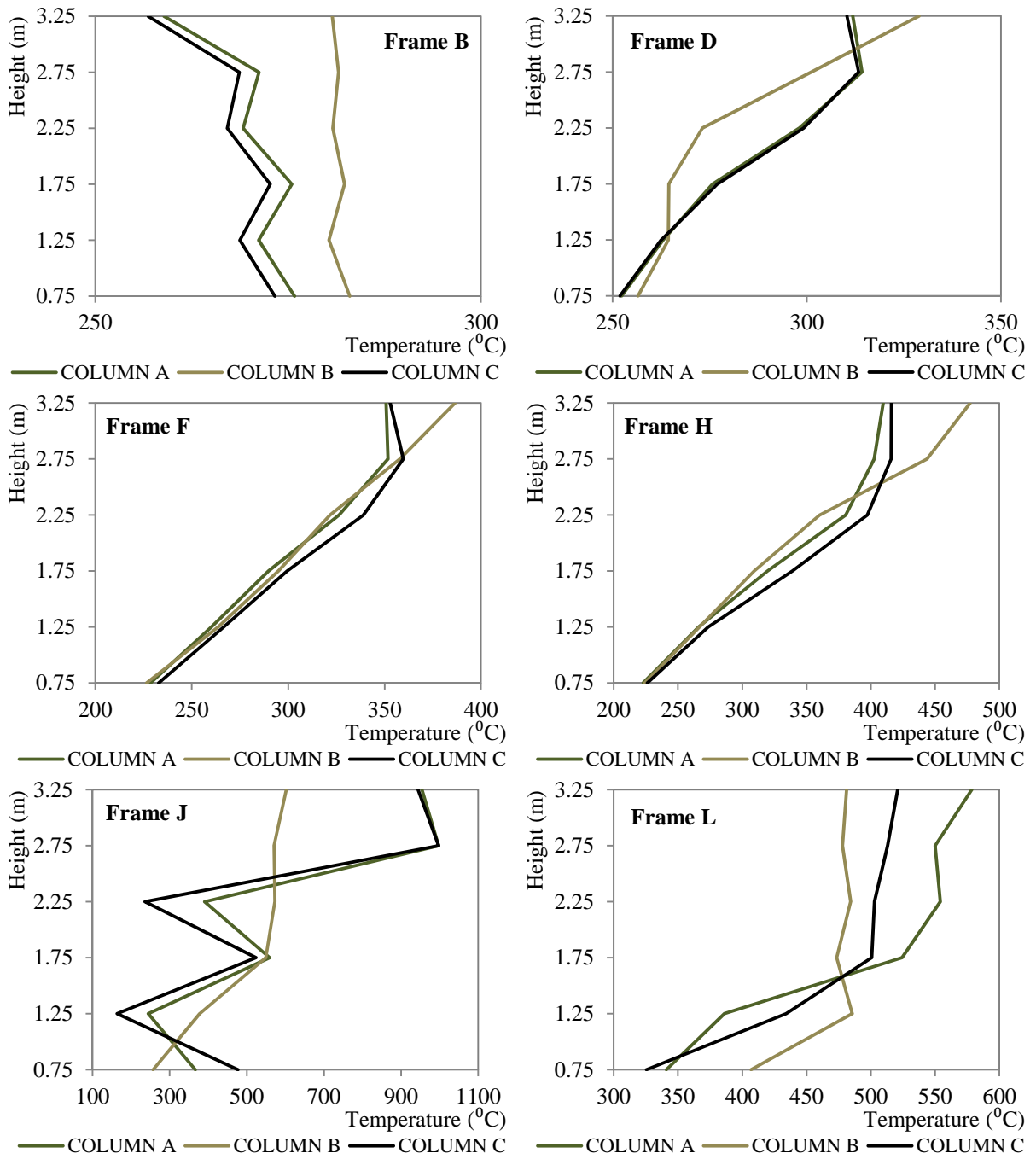


Figure B- 10: Temperature distribution along the axis of the columns in different frames for the SC-25B/
Time=2000sec.

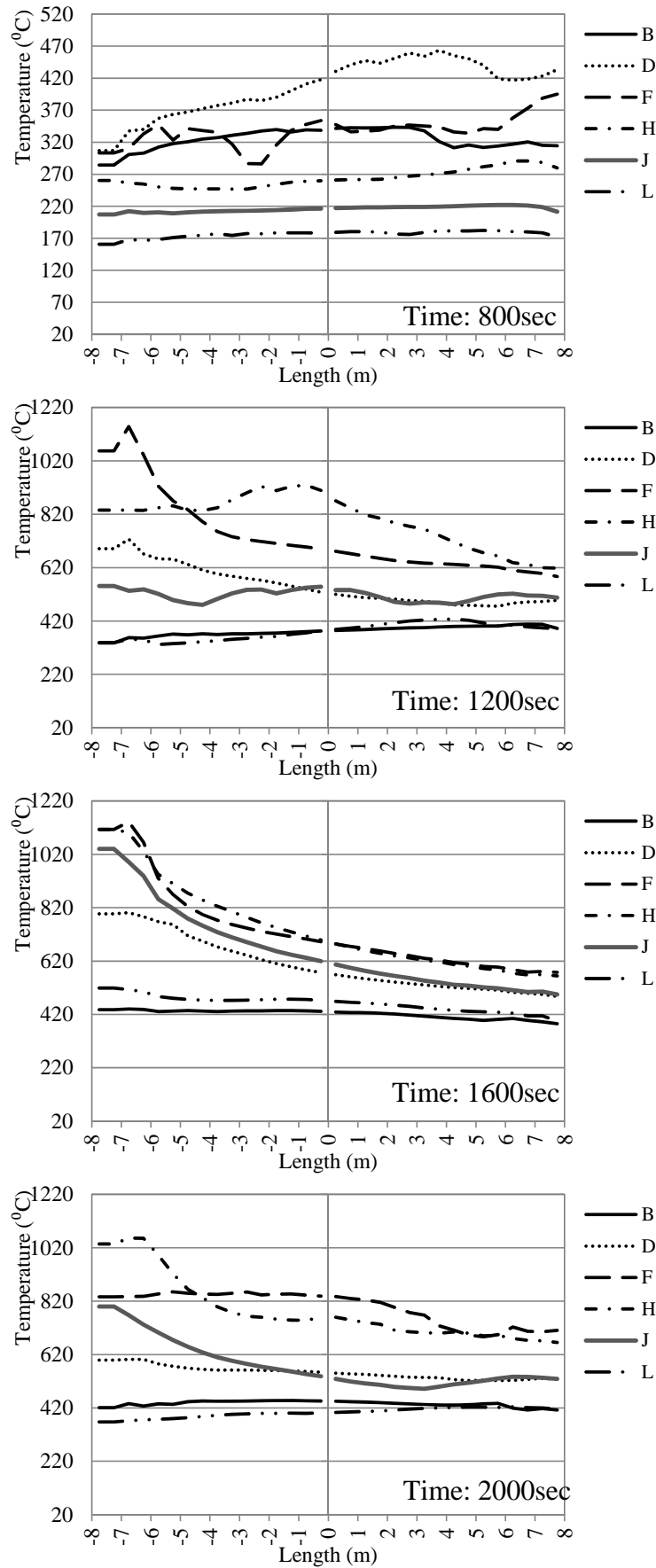


Figure B- 11: Temperature distribution along the axis of the beams that lie at different frames for the SC-50A.

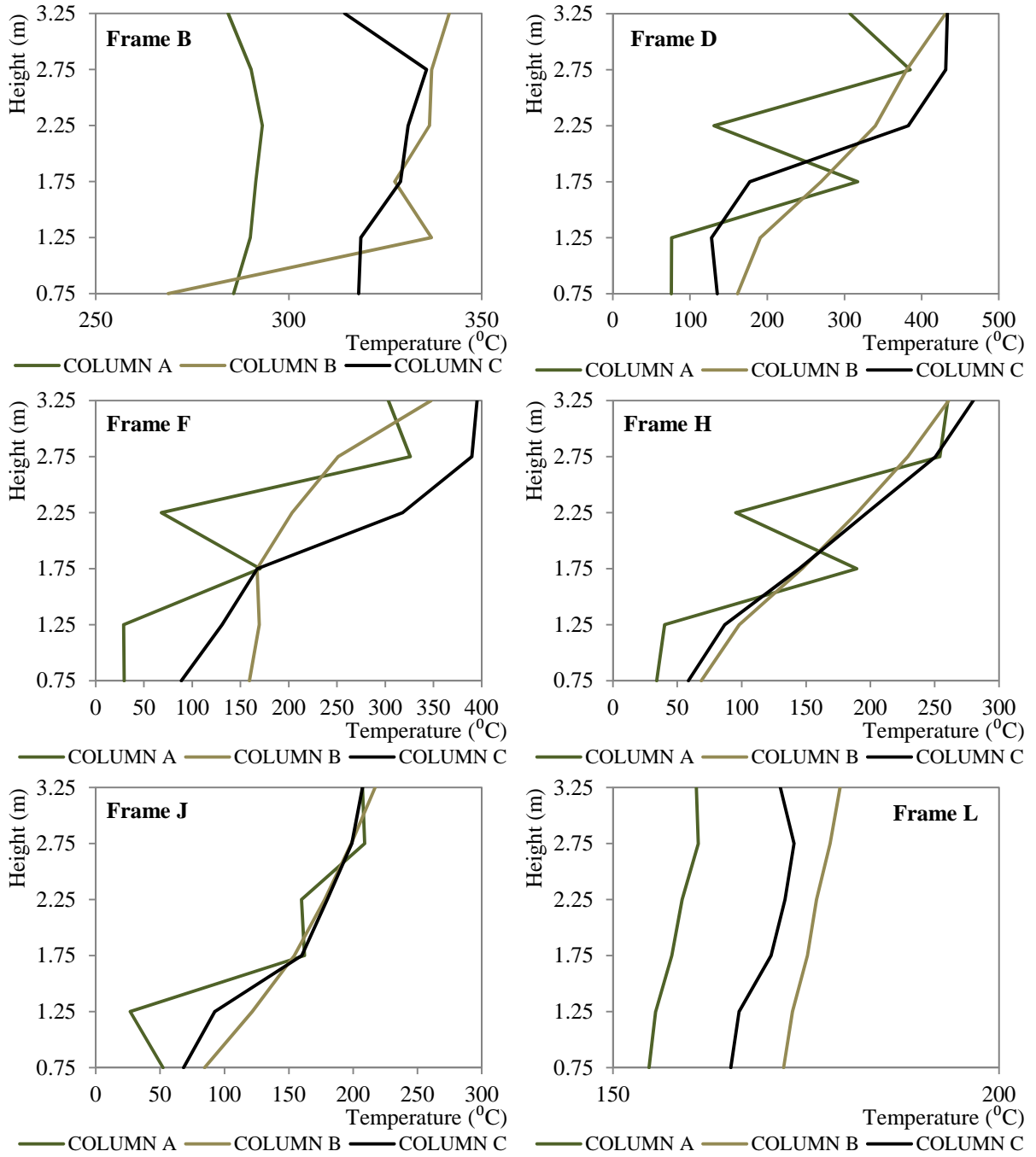


Figure B- 12: Temperature distribution along the axis of the columns in different frames for the SC-50A/
Time=800sec.

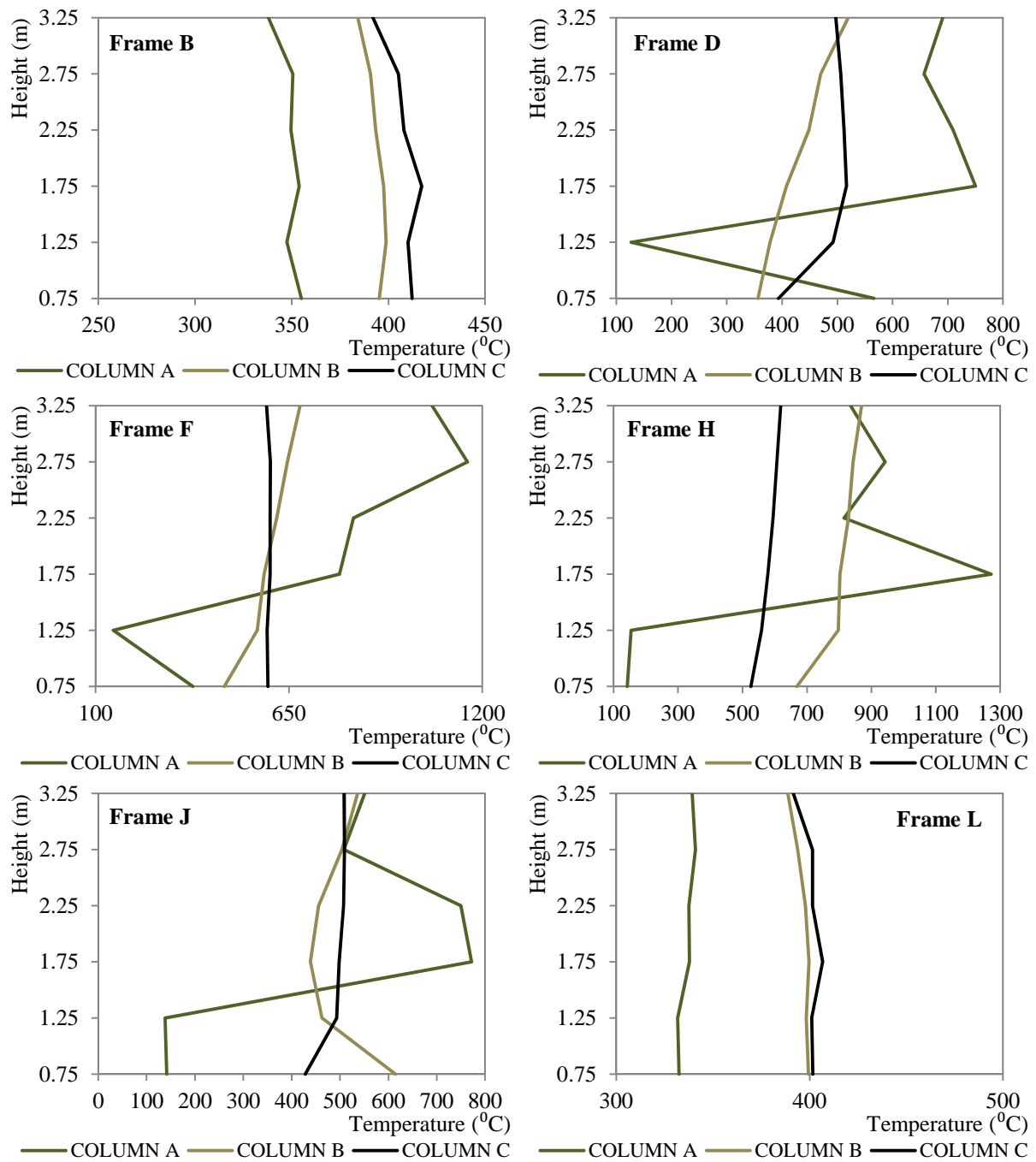


Figure B- 13: Temperature distribution along the axis of the columns in different frames for the SC-50A/
Time=1200sec.

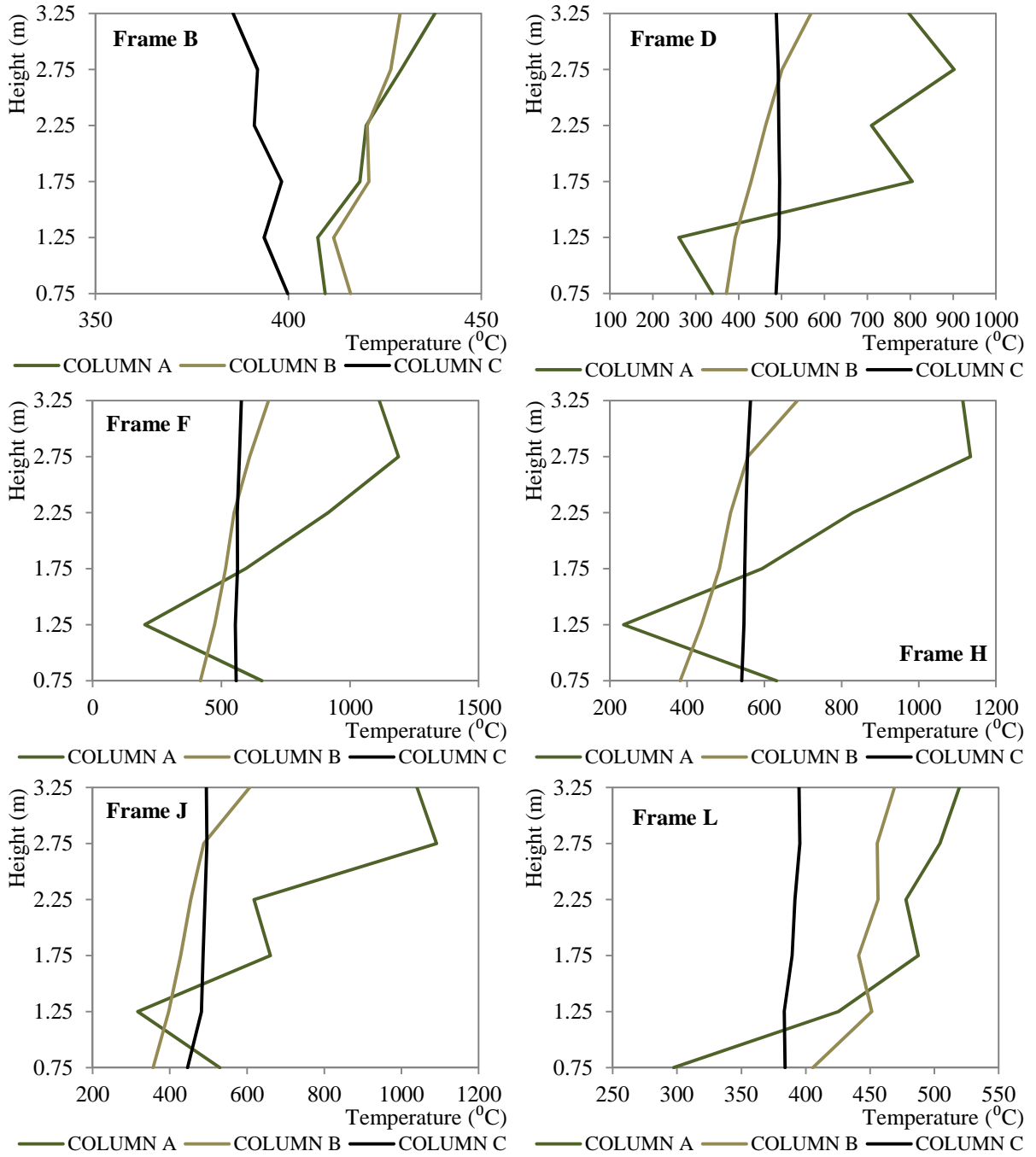


Figure B- 14: Temperature distribution along the axis of the columns in different frames for the SC-50A/
Time=1600sec.

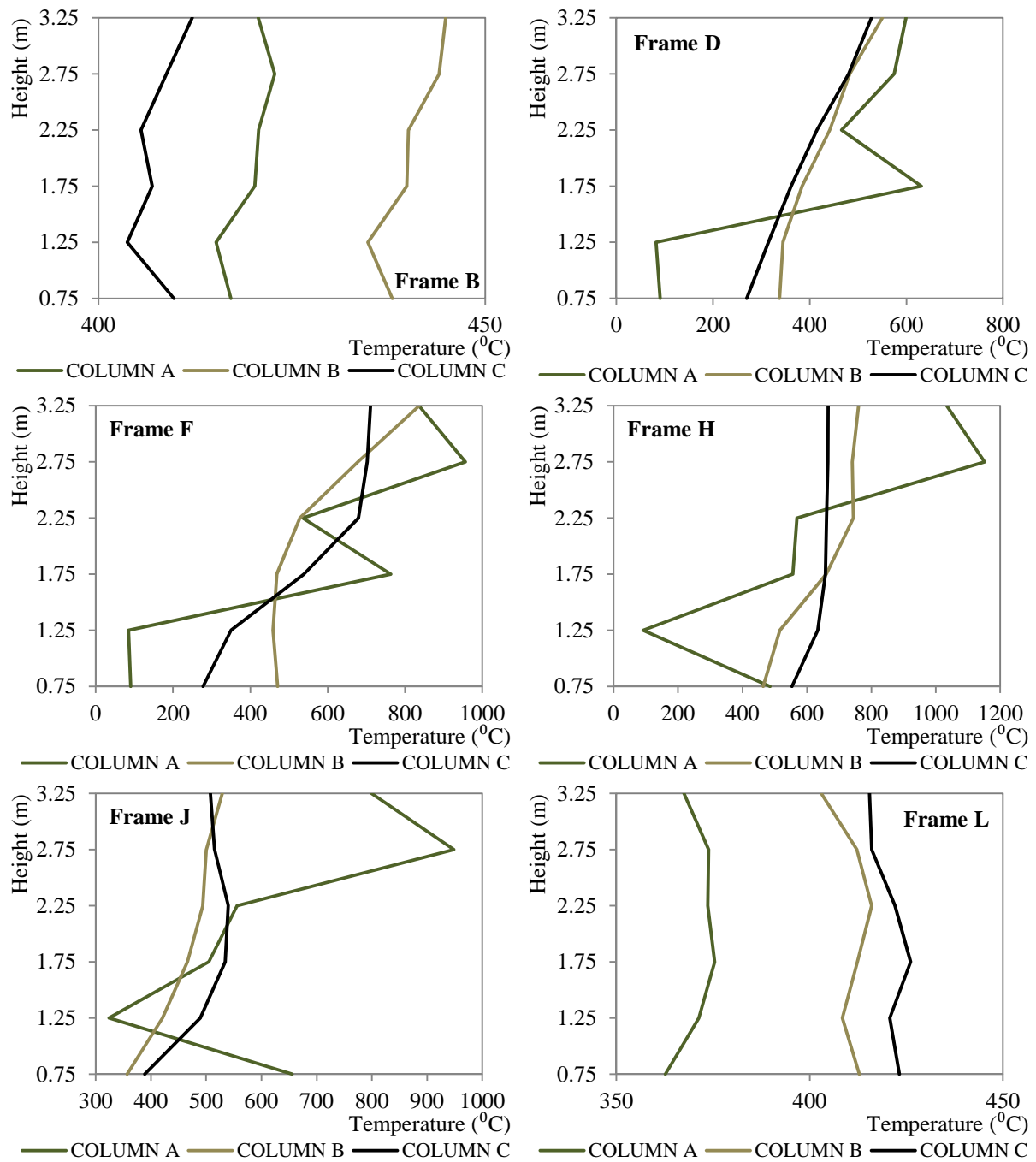


Figure B- 15: Temperature distribution along the axis of the columns in different frames for the SC-50A/
Time=2000sec.

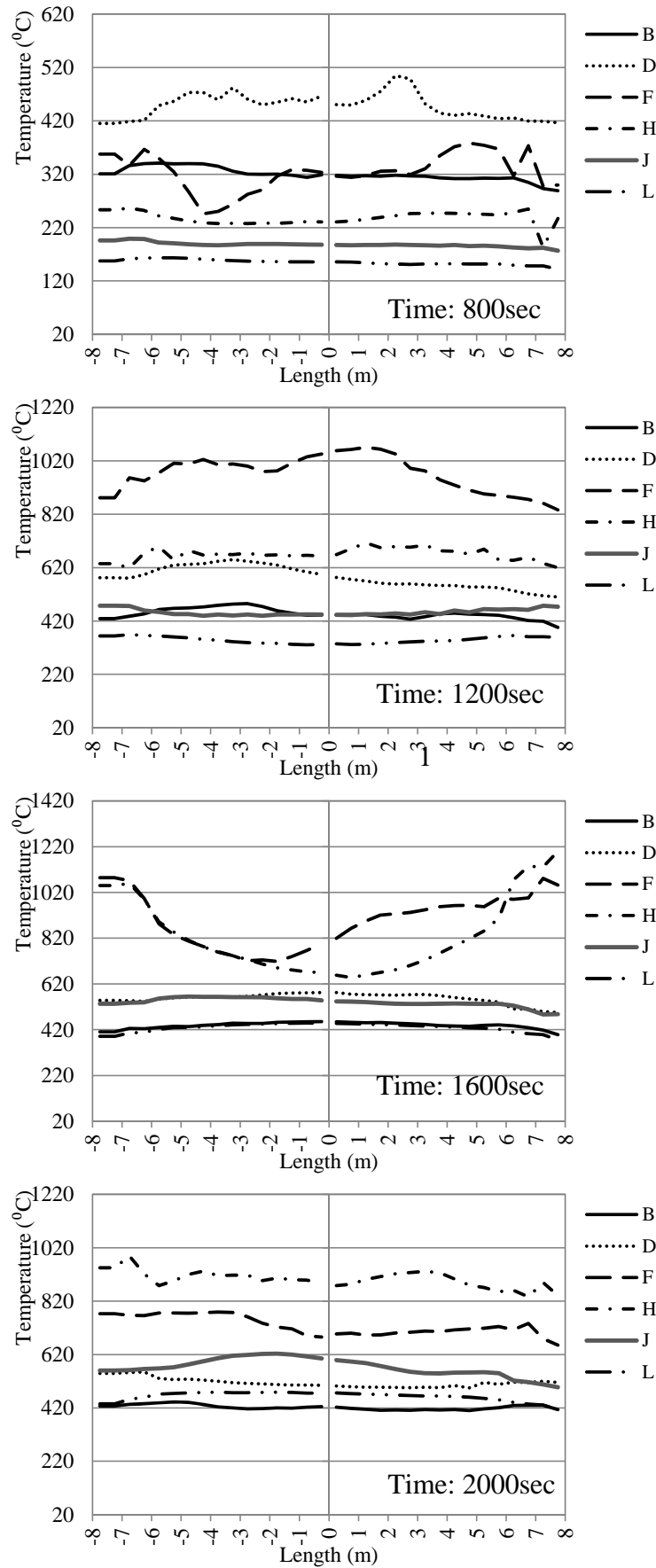


Figure B- 16: Temperature distribution along the axis of the beams that lie at different frames for the SC-50B.

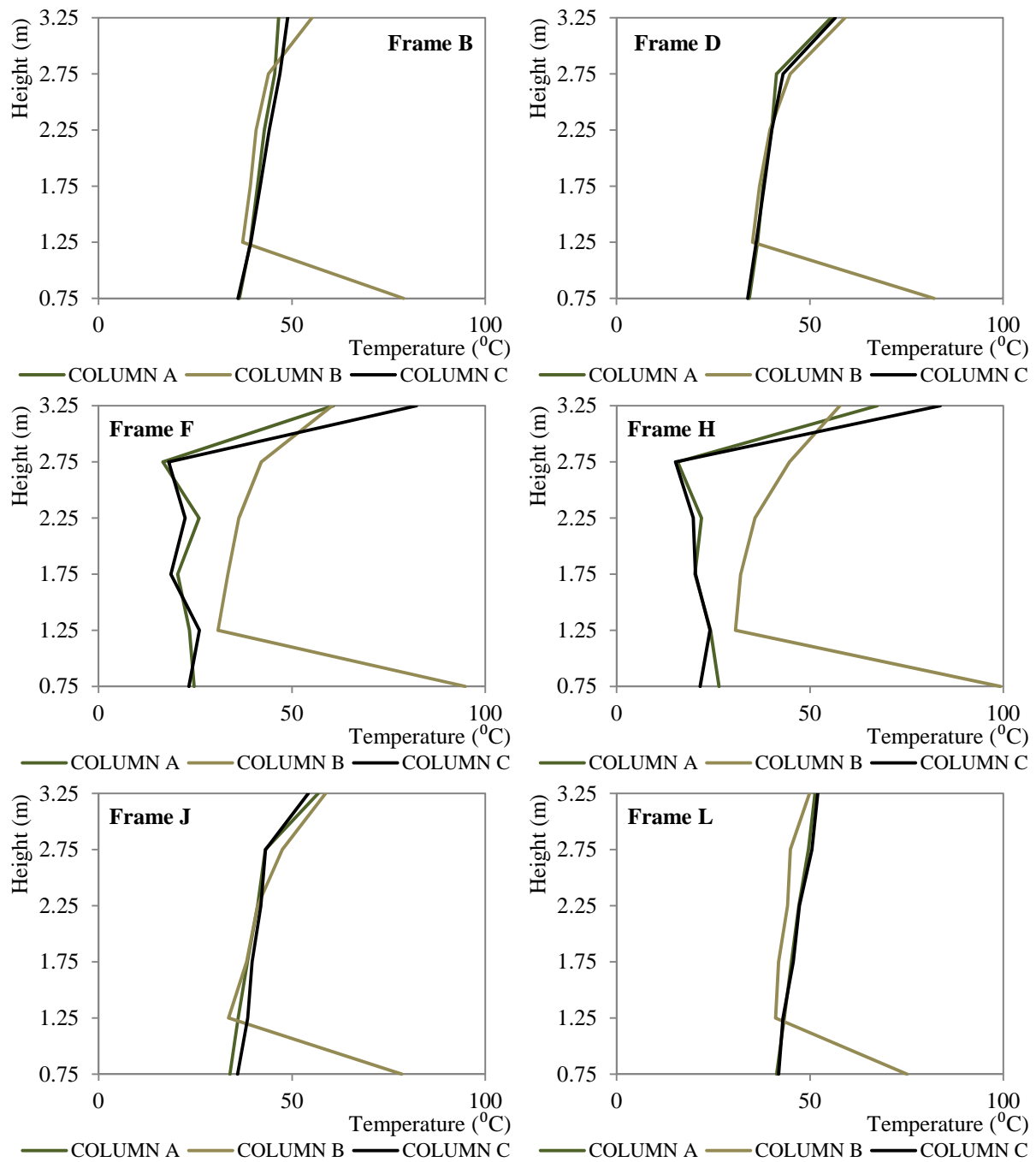


Figure B- 17: Temperature distribution along the axis of the columns in different frames for the SC-50B/
Time=800sec.

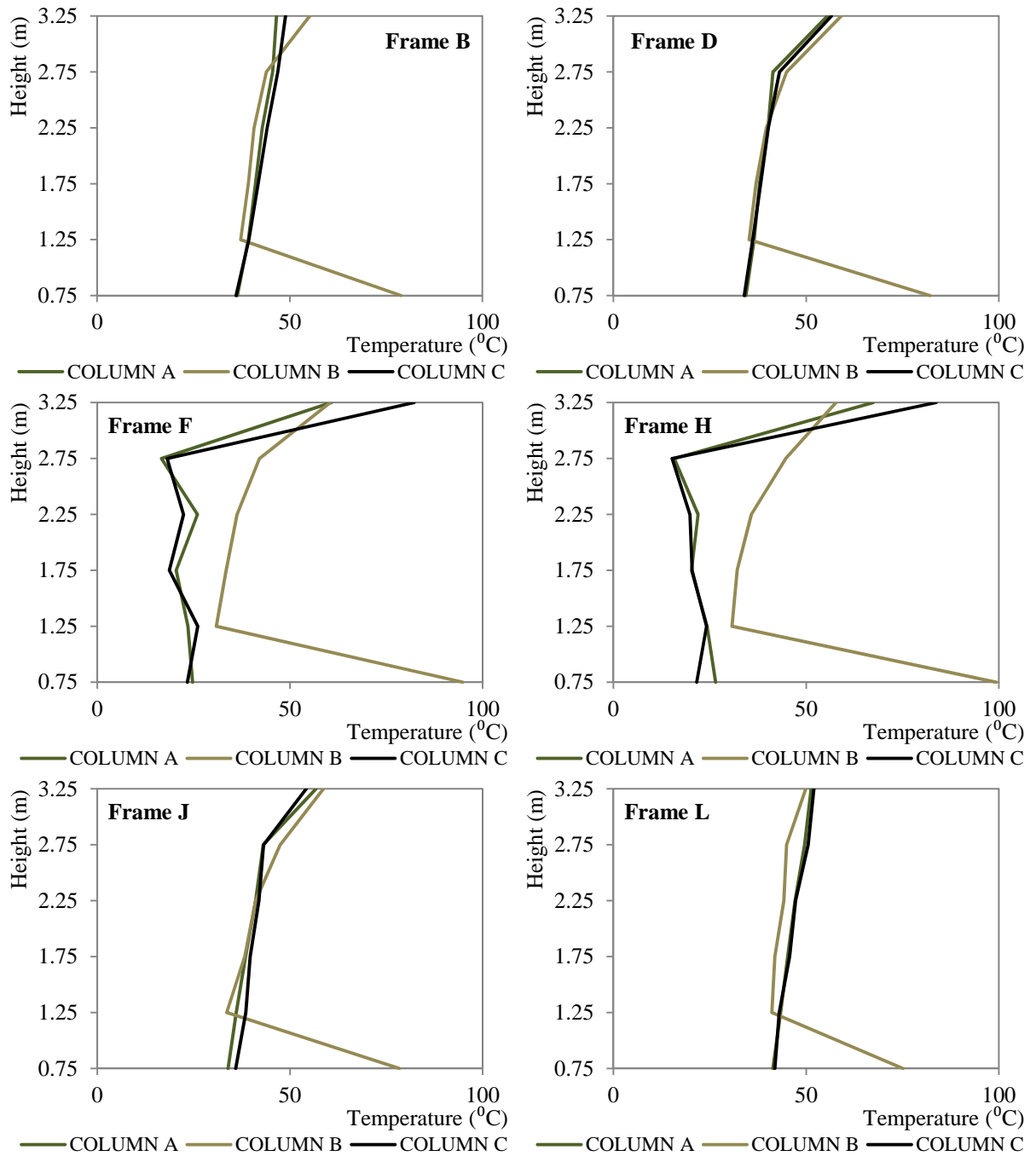


Figure B- 18: Temperature distribution along the axis of the columns in different frames for the SC-50B/
Time=1200sec.

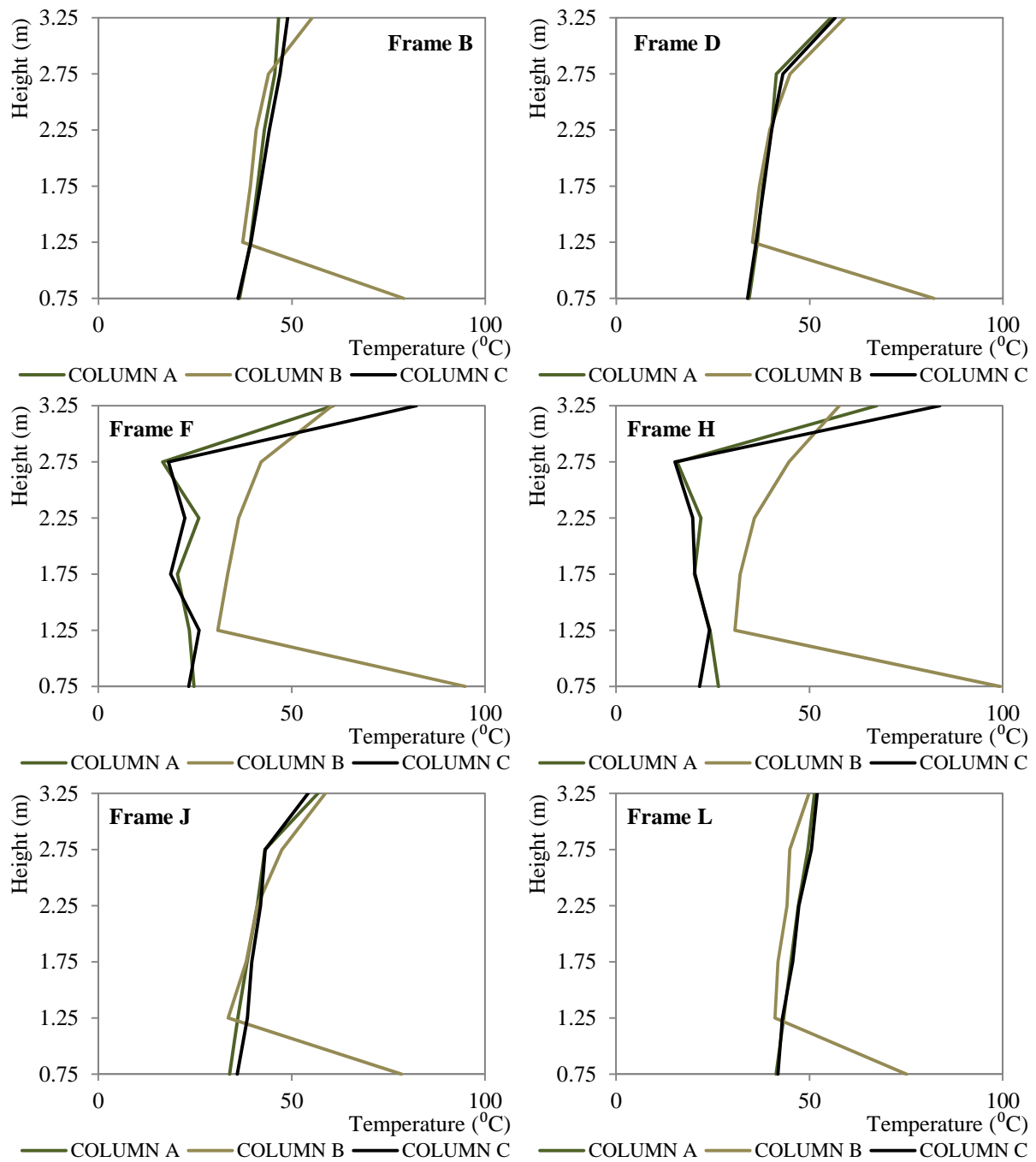


Figure B- 19: Temperature distribution along the axis of the columns in different frames for the SC-50B/
Time=1600sec.

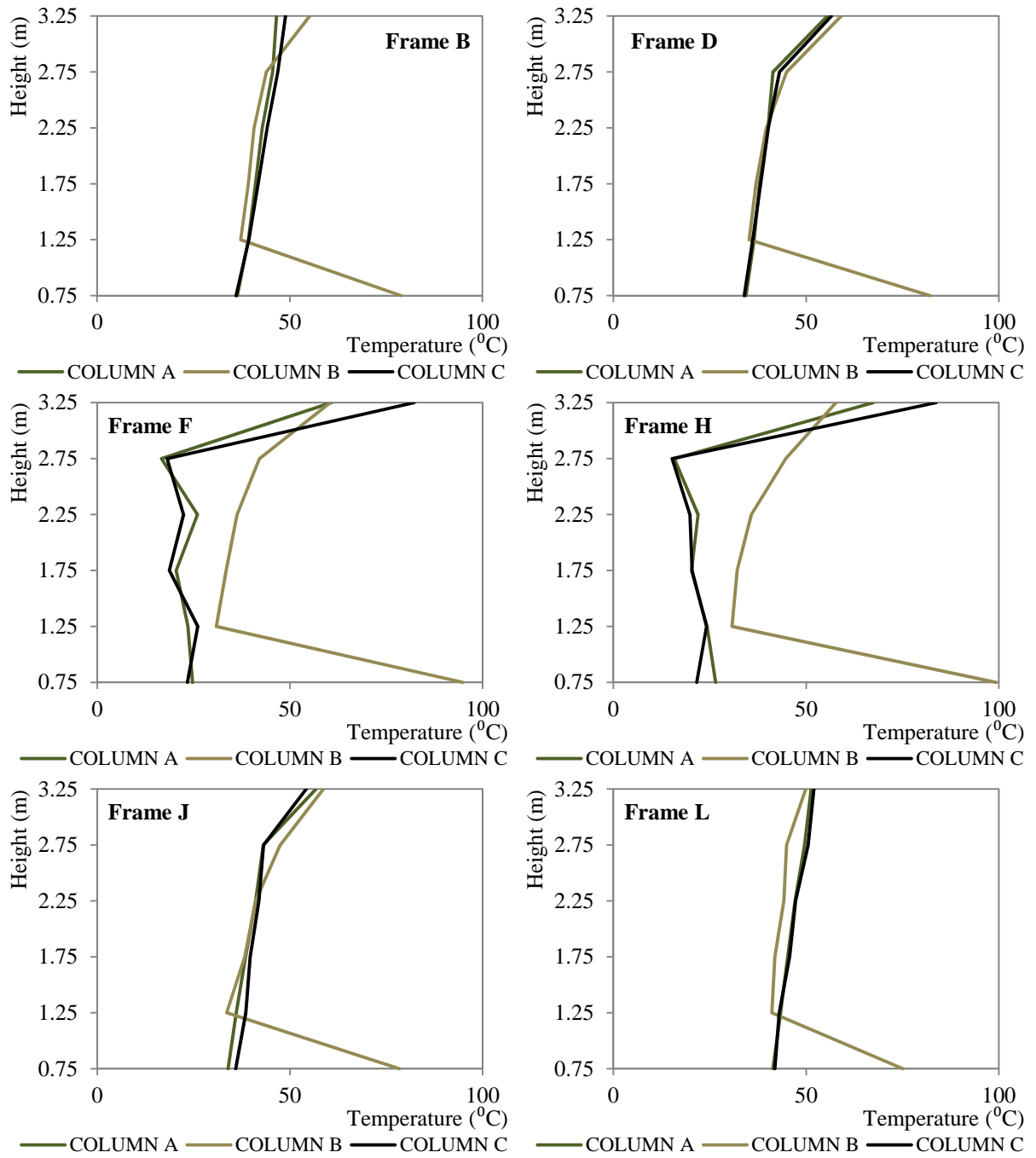


Figure B- 20: Temperature distribution along the axis of the columns in different frames for the SC-50B/
Time=2000sec.

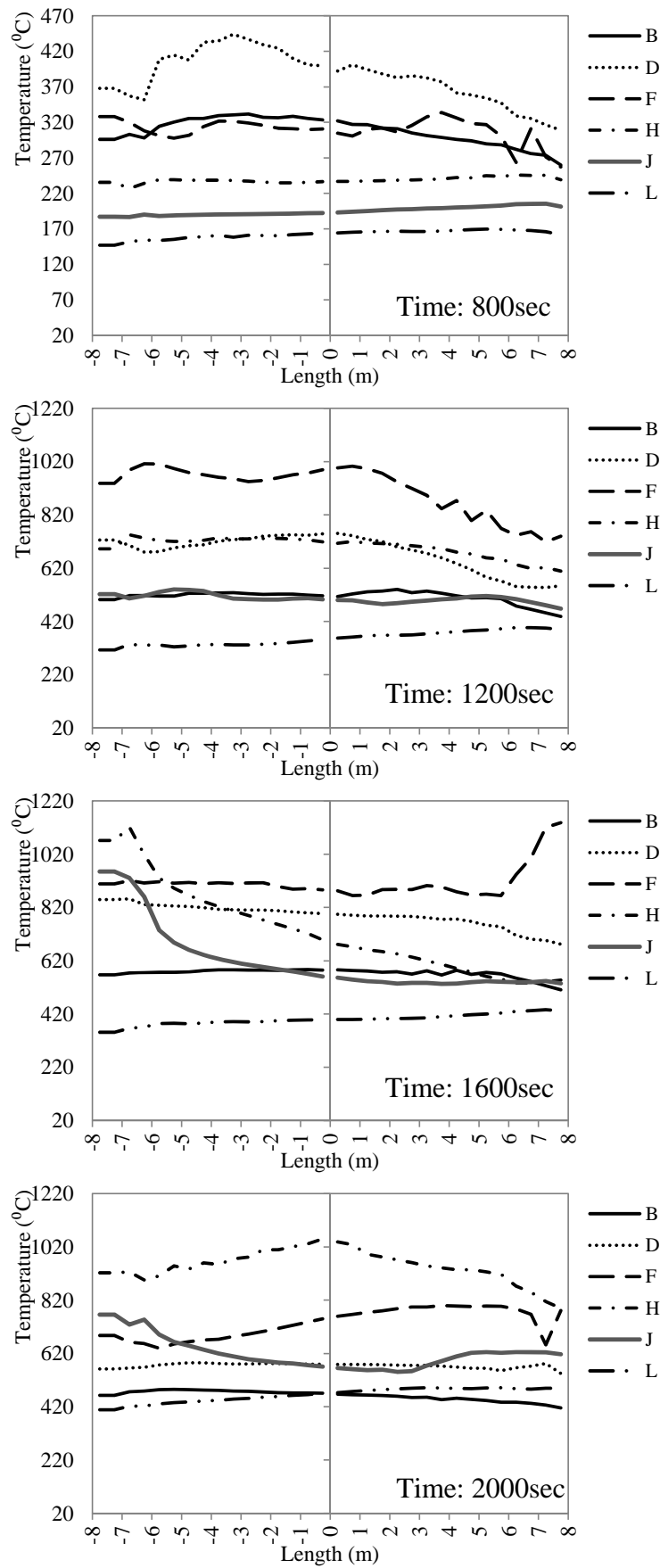


Figure B- 21: Temperature distribution along the axis of the beams that lie at different frames for the SC-50C.

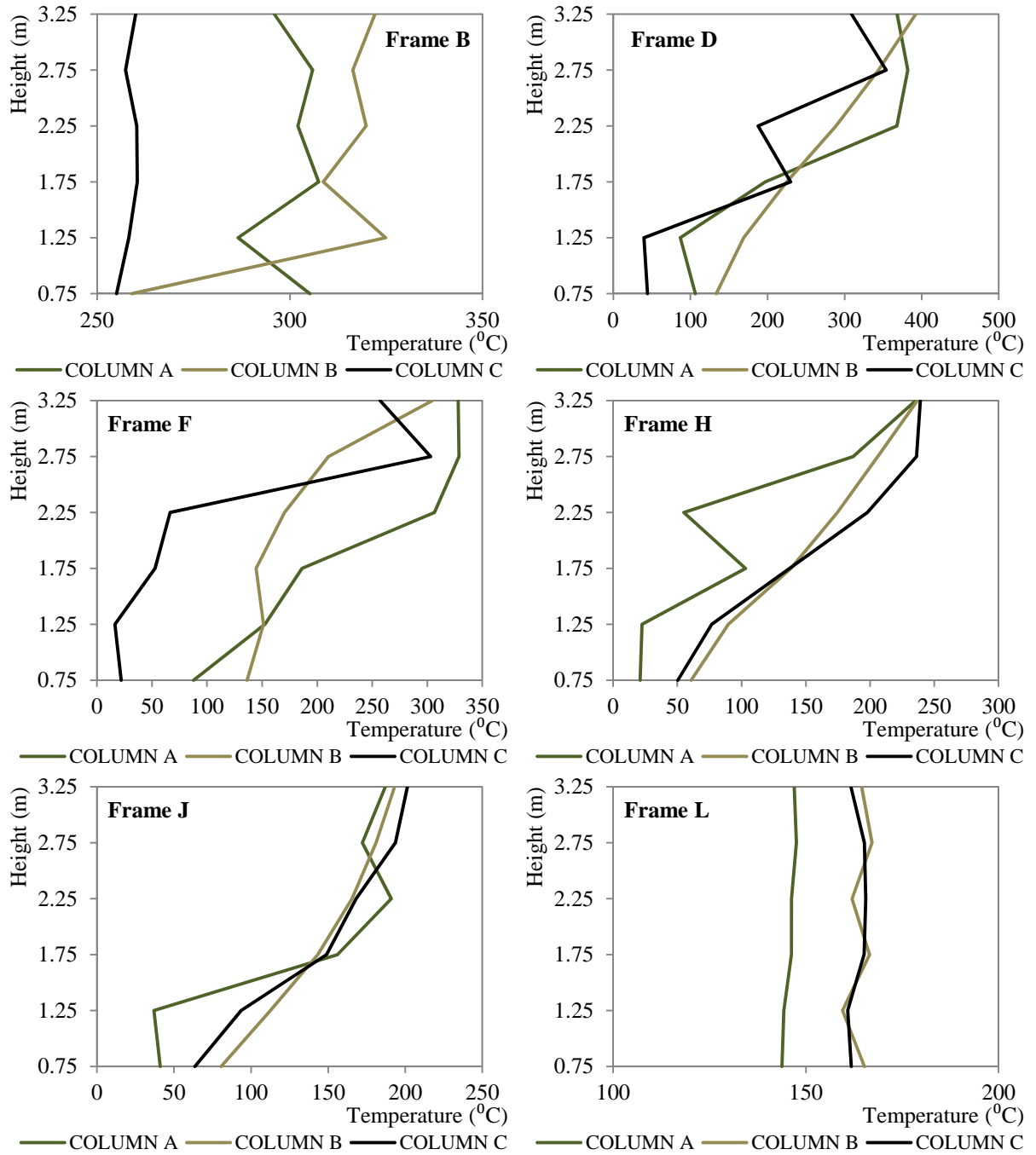


Figure B- 22: Temperature distribution along the axis of the columns in different frames for the SC-50C/
Time=800sec.

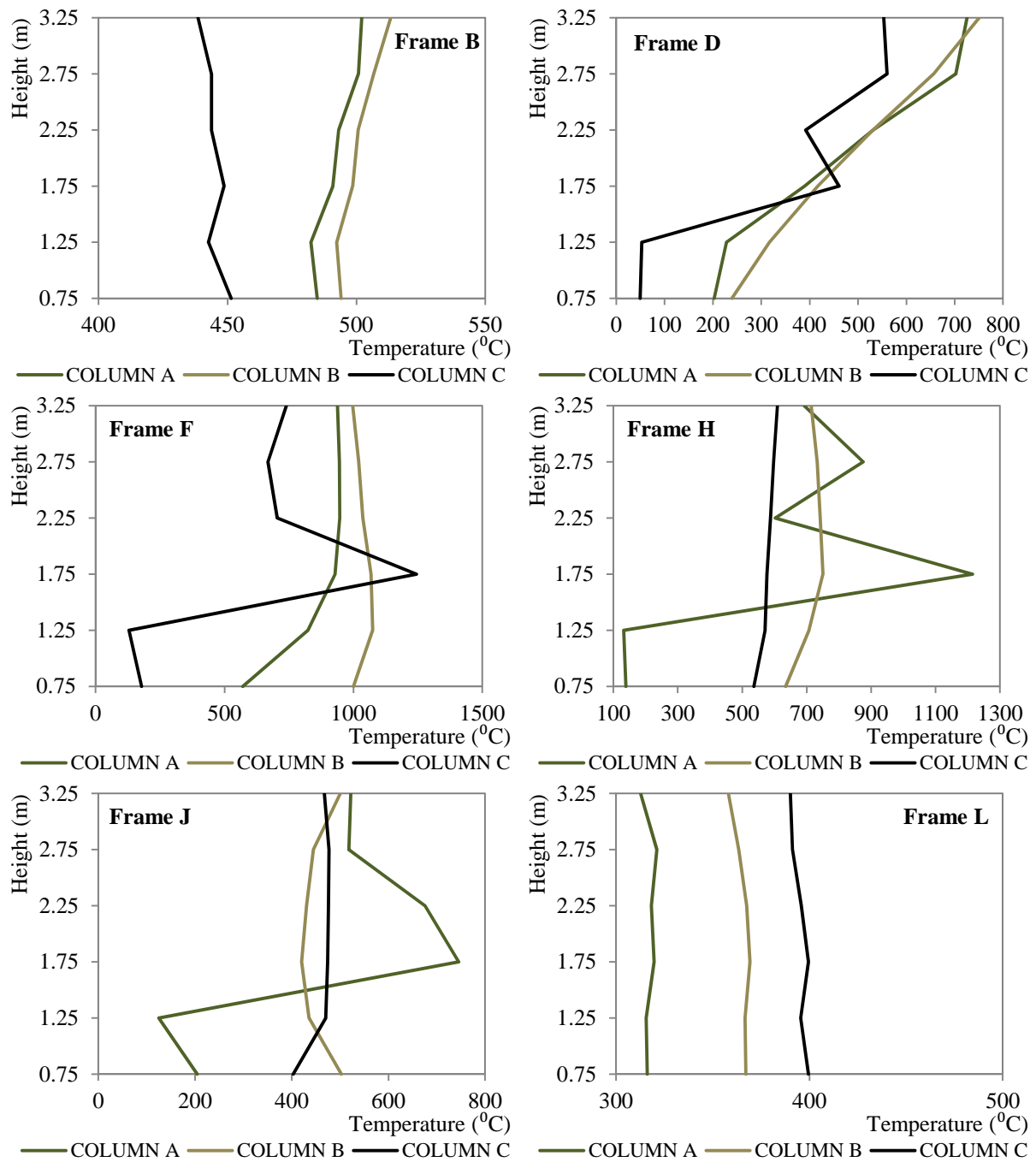


Figure B- 23: Temperature distribution along the axis of the columns in different frames for the SC-50C/
Time=1200sec.

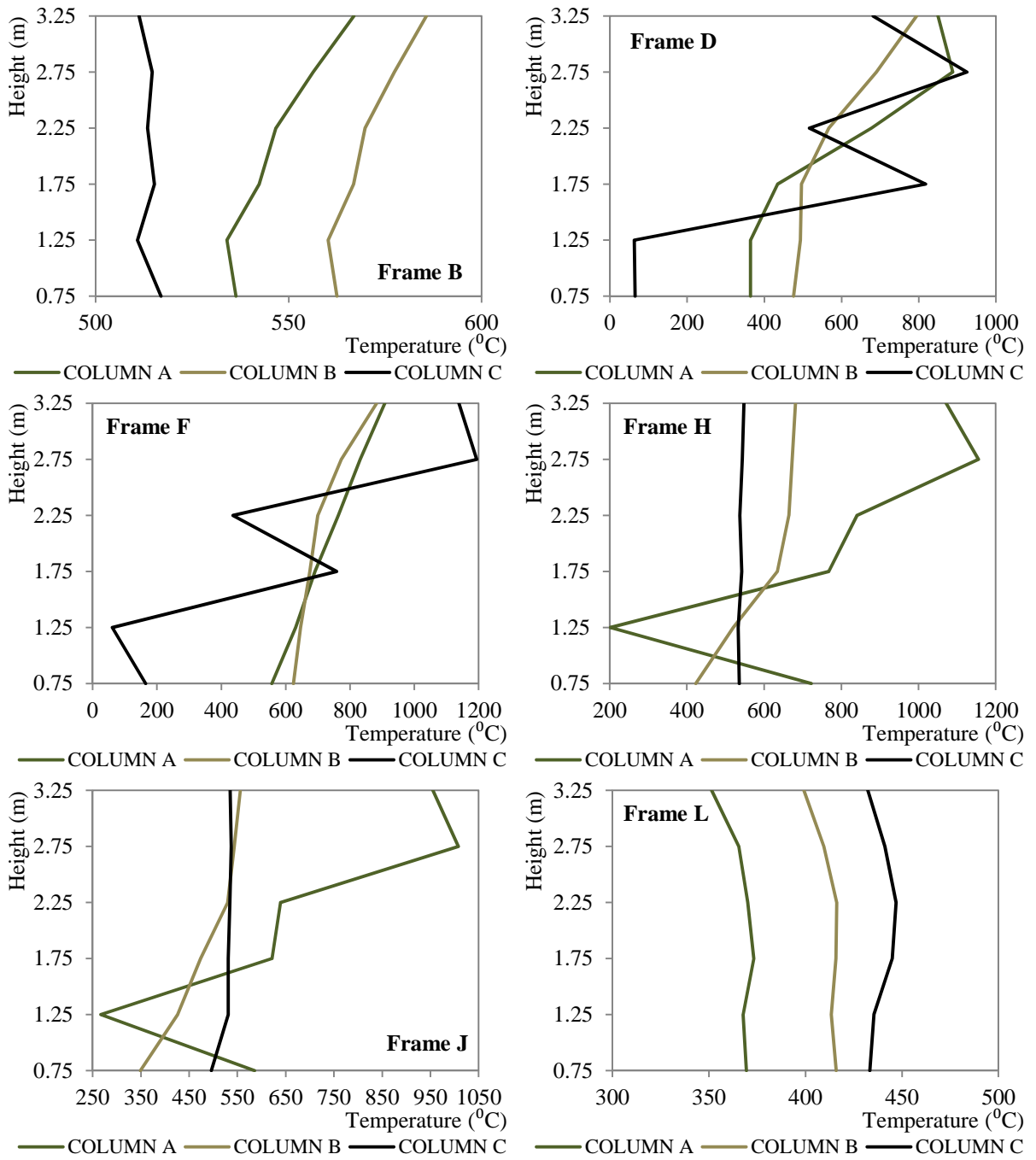


Figure B- 24: Temperature distribution along the axis of the columns in different frames for the SC-50C/
Time=1600sec.

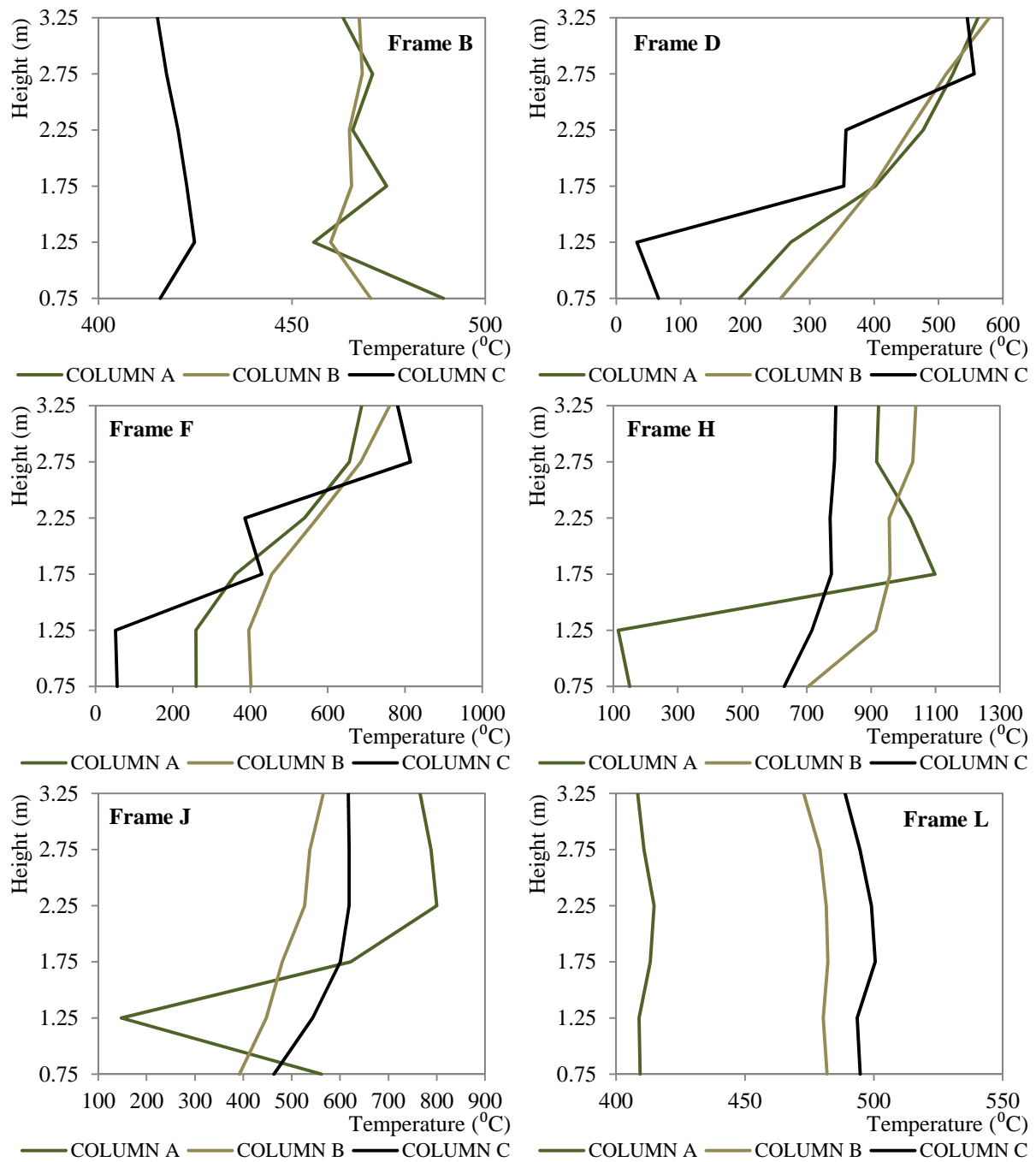


Figure B- 25: Temperature distribution along the axis of the columns in different frames for the SC-50C/
Time=2000sec.

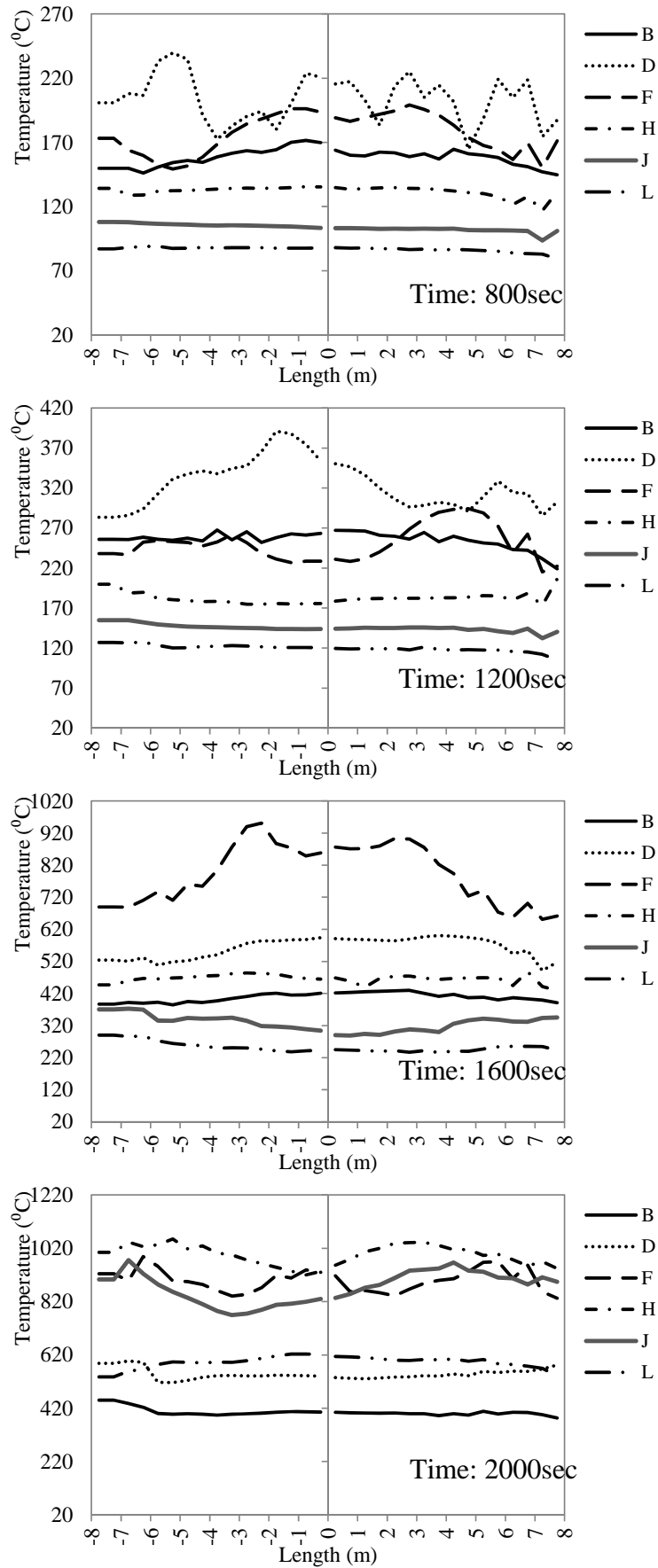


Figure B- 26: Temperature distribution along the axis of the beams that lie at different frames for the SC-100.

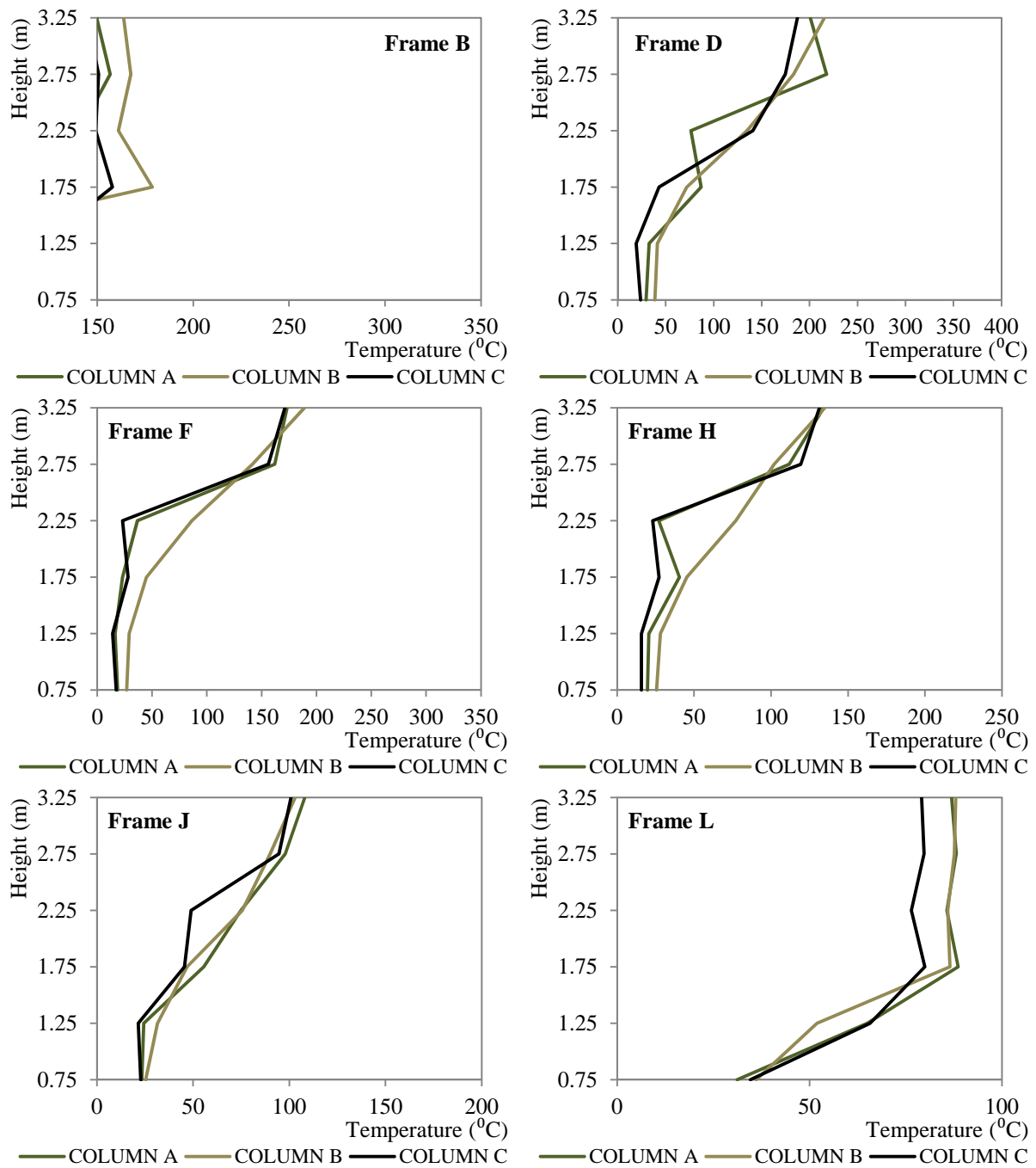


Figure B- 27: Temperature distribution along the axis of the columns in different frames for the SC-100/
Time=800sec.

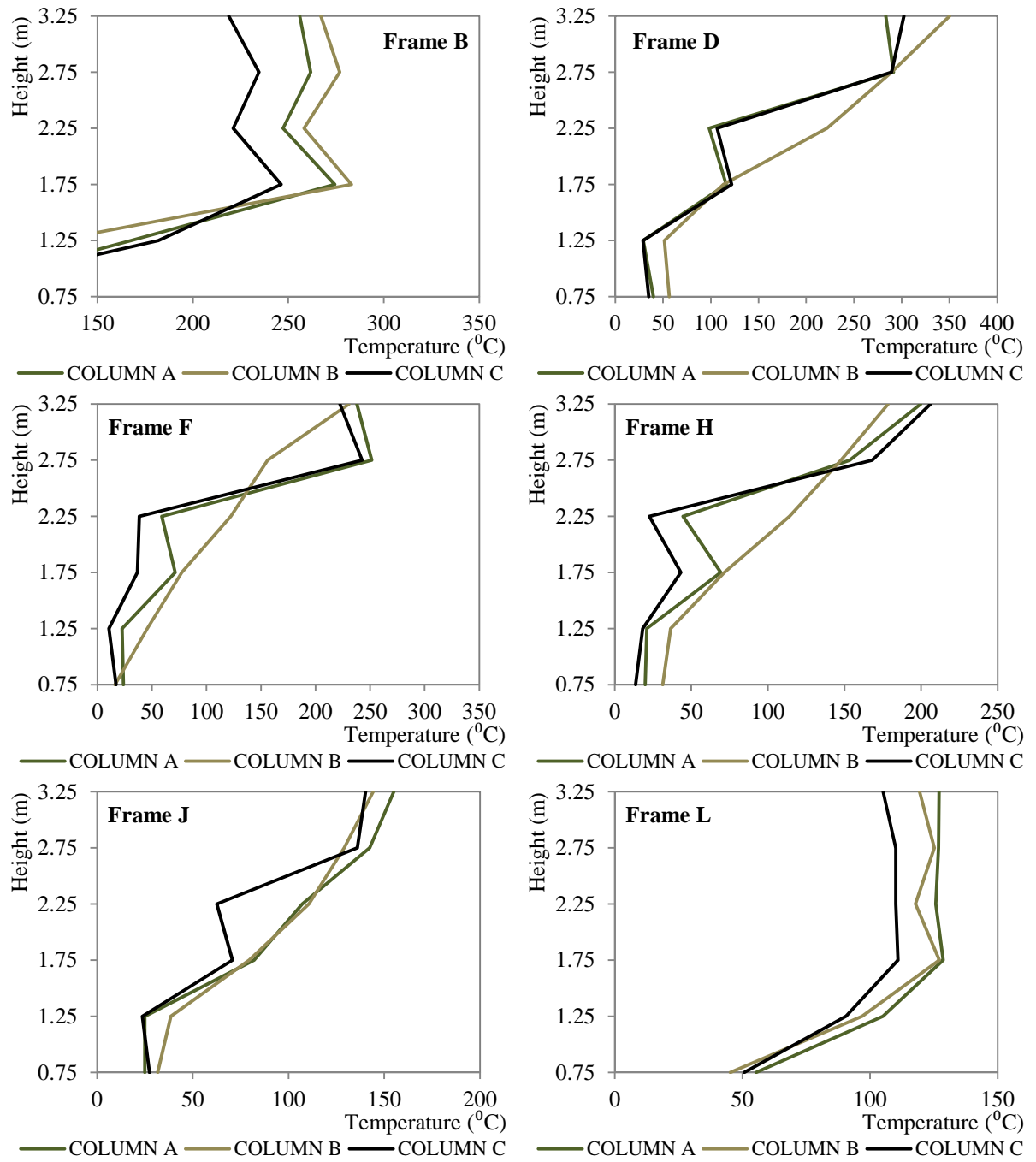


Figure B- 28: Temperature distribution along the axis of the columns in different frames for the SC-100/
Time=1200sec.

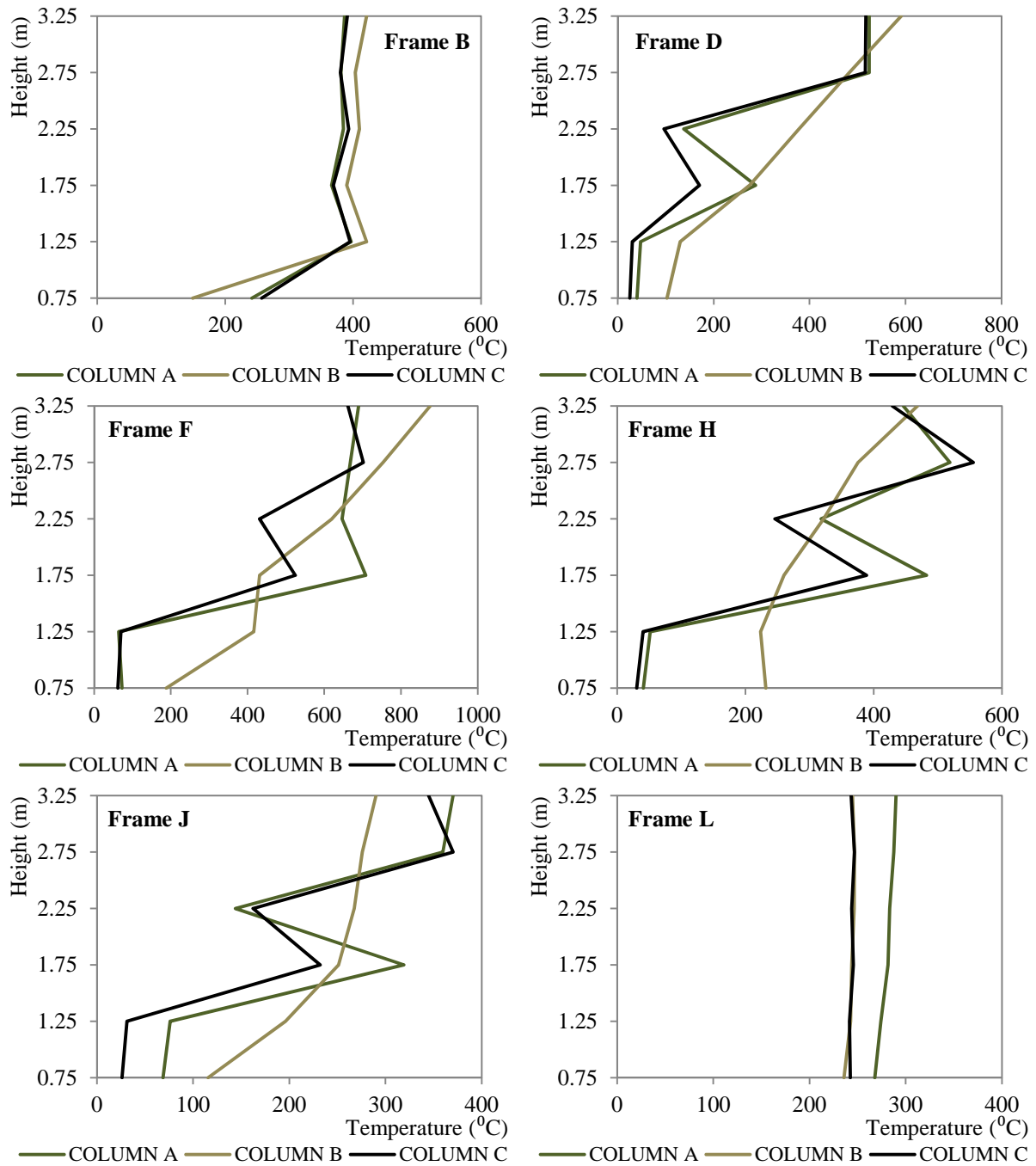


Figure B- 29: Temperature distribution along the axis of the columns in different frames for the SC-100/
Time=1600sec.

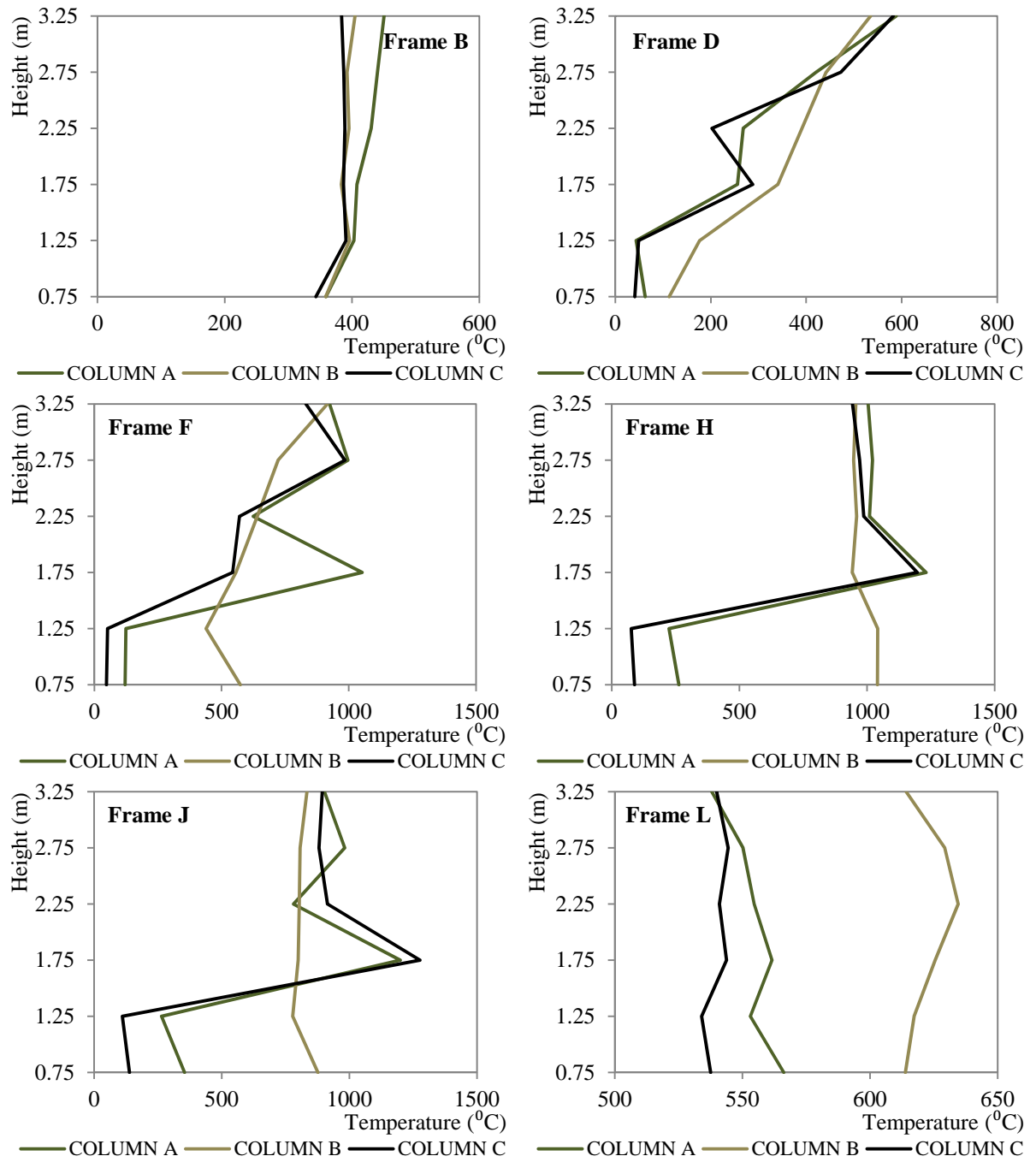


Figure B- 30: Temperature distribution along the axis of the columns in different frames for the SC-100/
Time=1800sec.

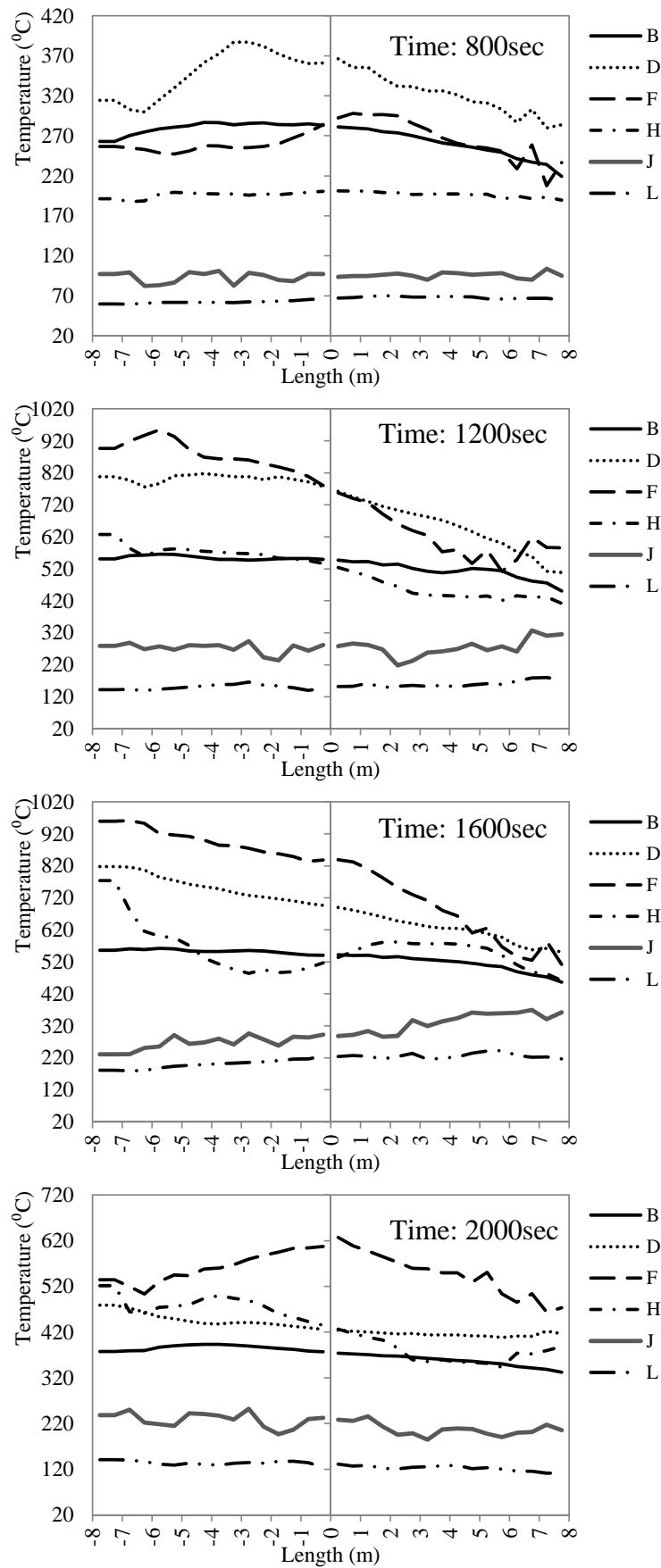


Figure B- 31: Temperature distribution along the axis of the beams that lie at different frames for the SC-SP40.

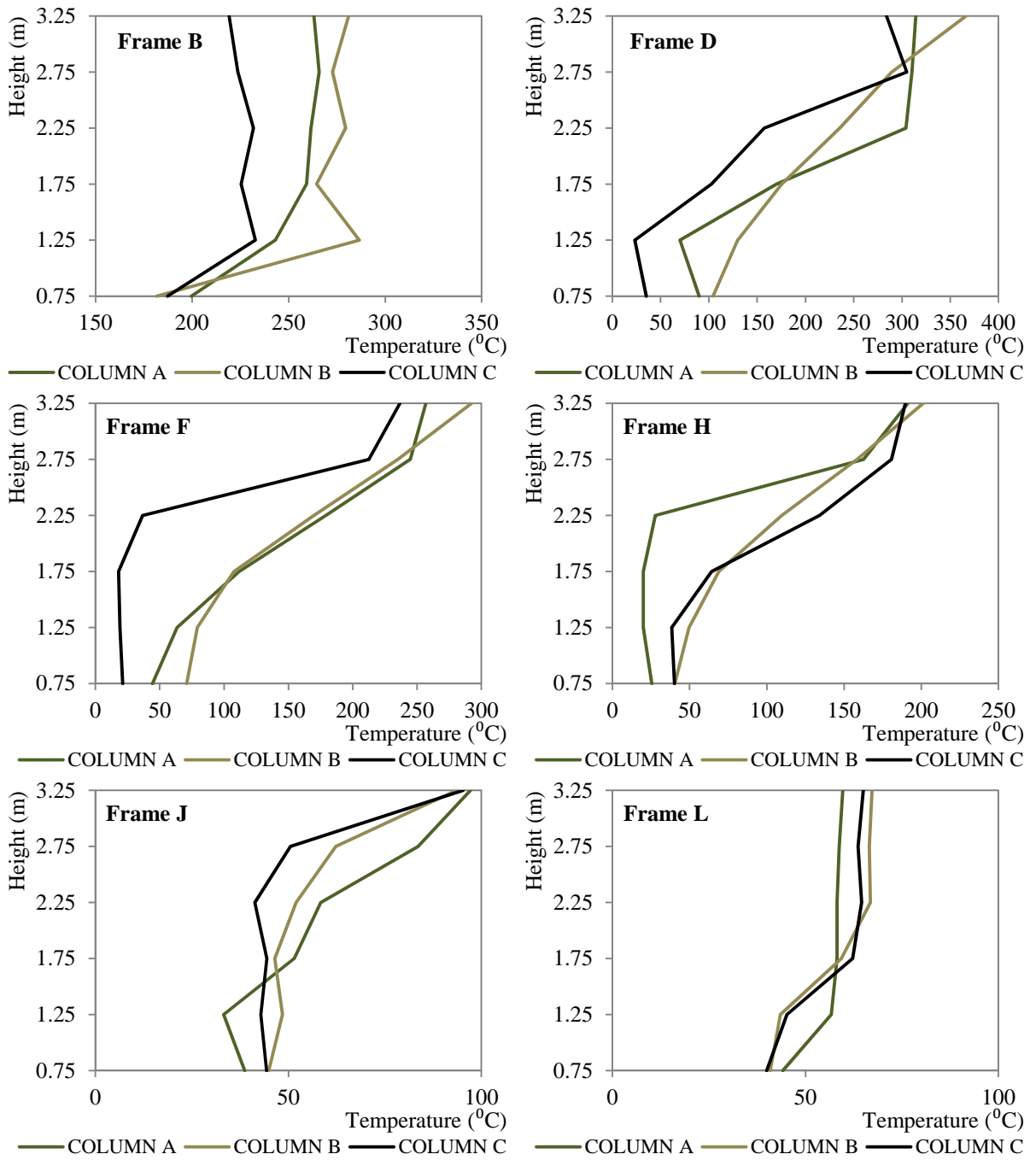


Figure B- 32: Temperature distribution along the axis of the columns in different frames for the SC-SP40/
Time=800sec.

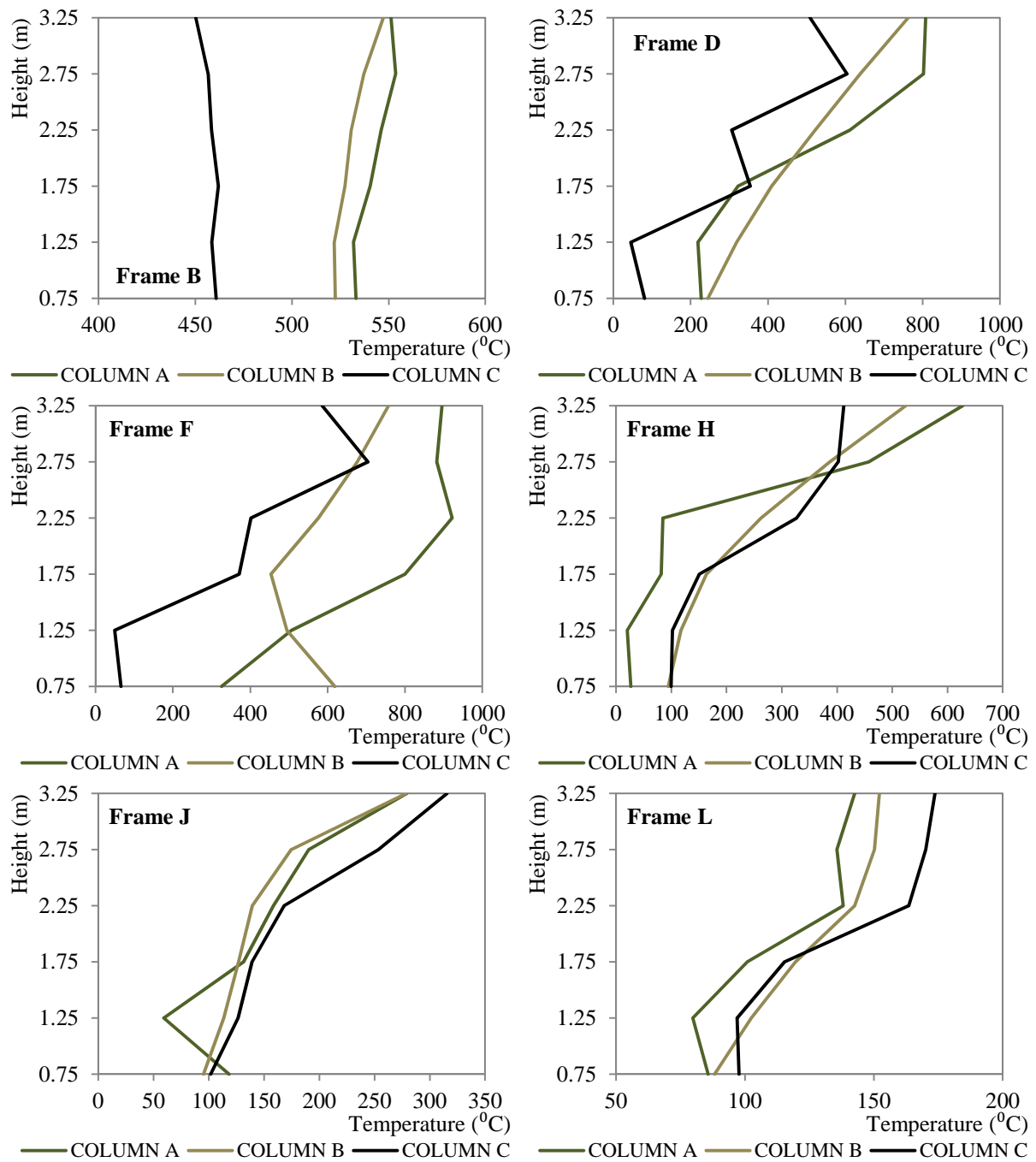


Figure B- 33: Temperature distribution along the axis of the columns in different frames for the SC-SP40/
Time=1200sec.

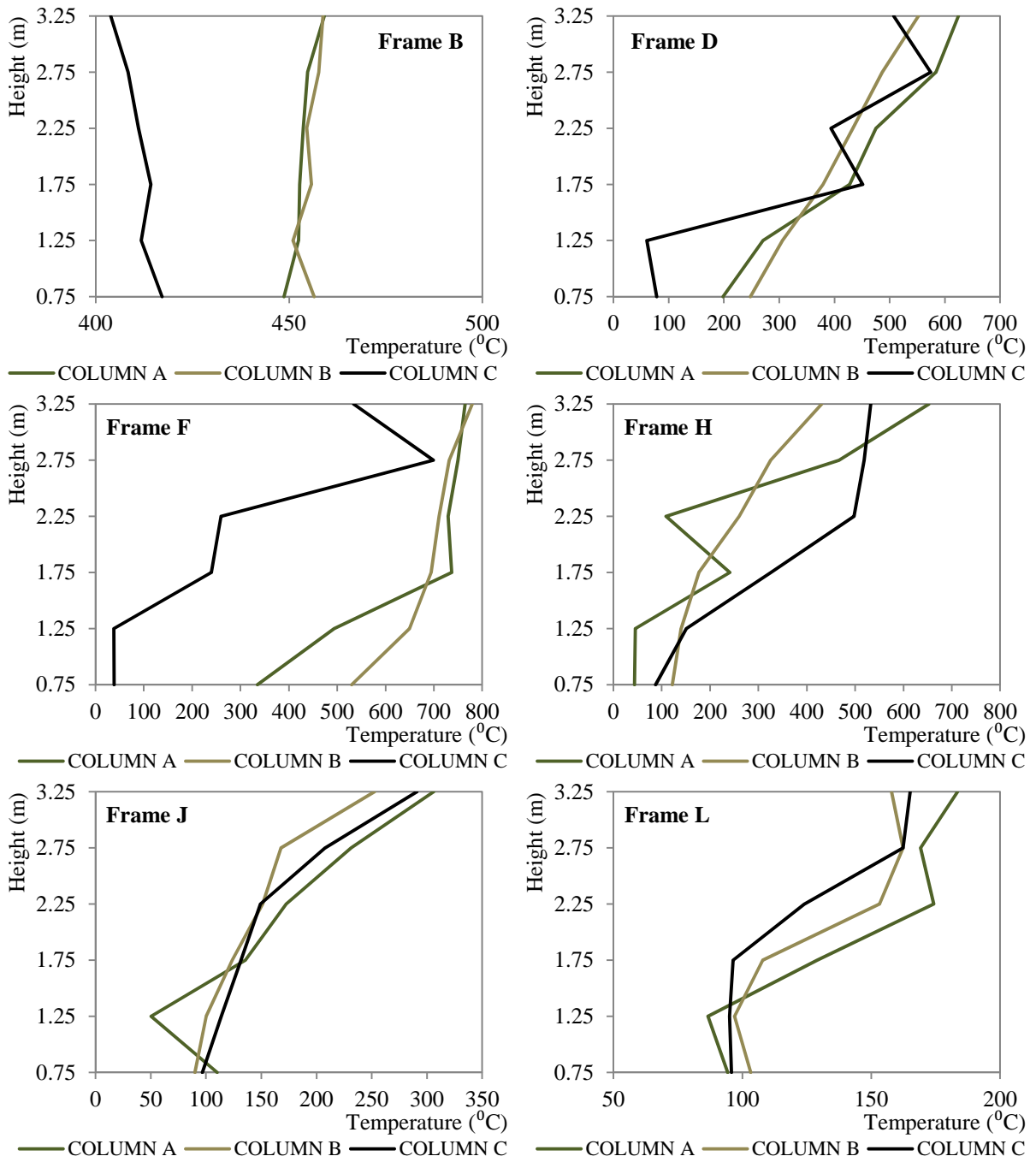


Figure B- 34: Temperature distribution along the axis of the columns in different frames for the SC-SP40/
Time=1600sec.

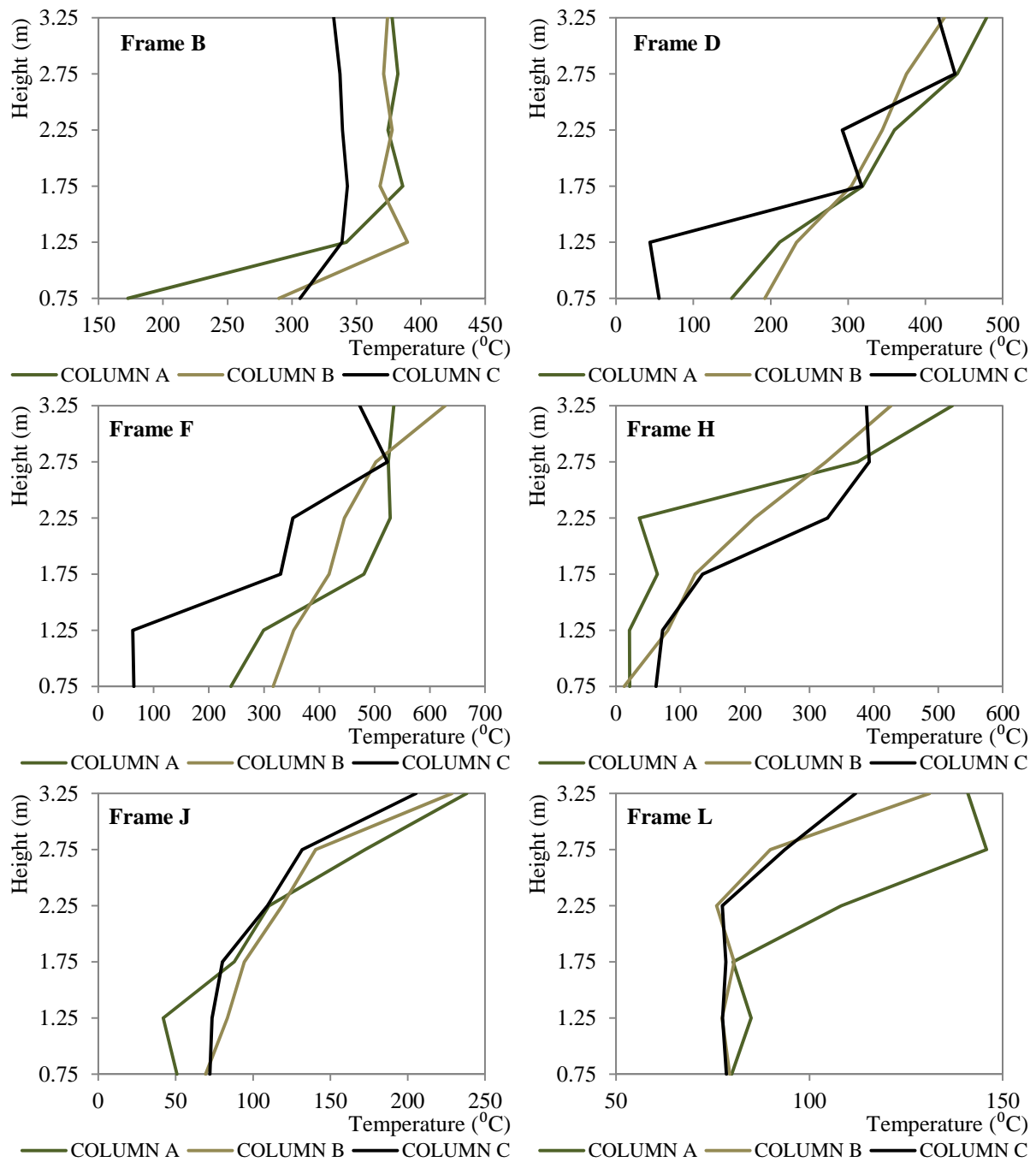


Figure B- 35: Temperature distribution along the axis of the columns in different frames for the SC-SP40/
Time=2000sec.

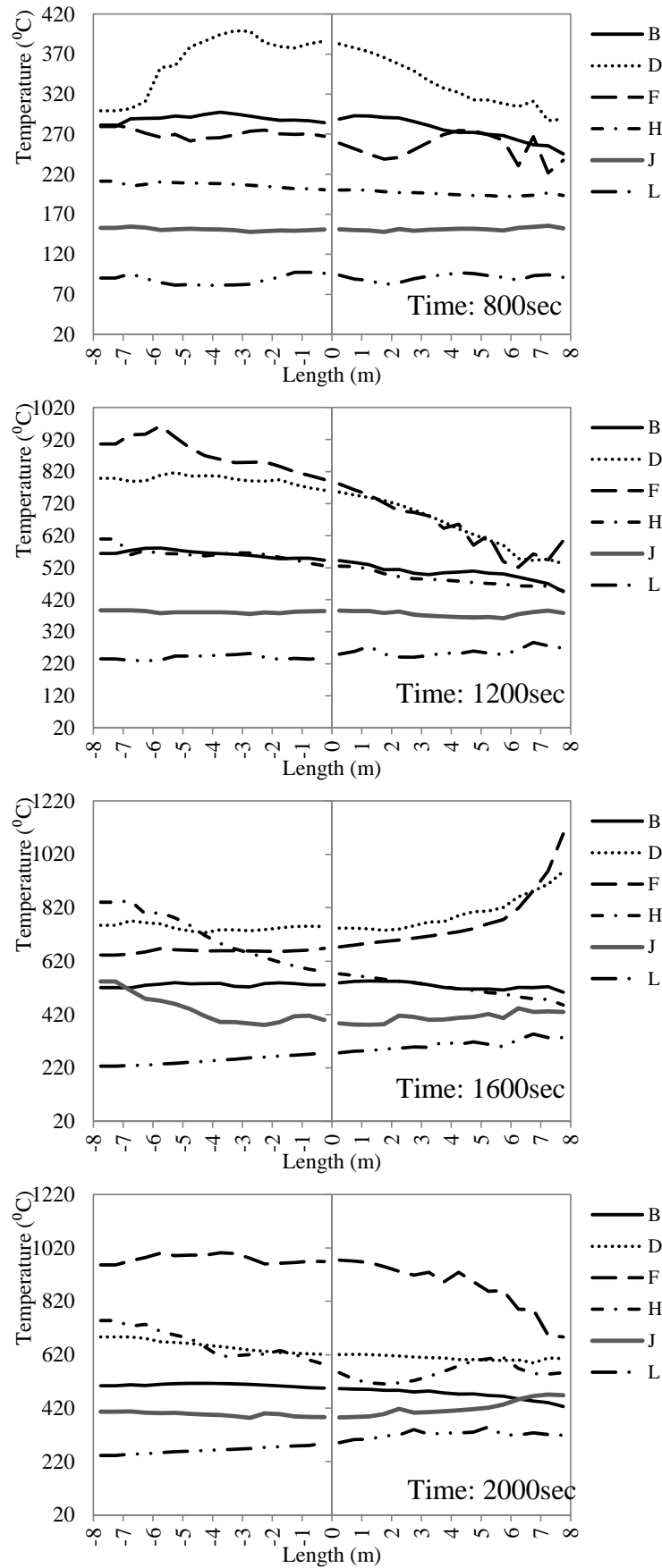


Figure B- 36: Temperature distribution along the axis of the beams that lie at different frames for the SC-SP20.

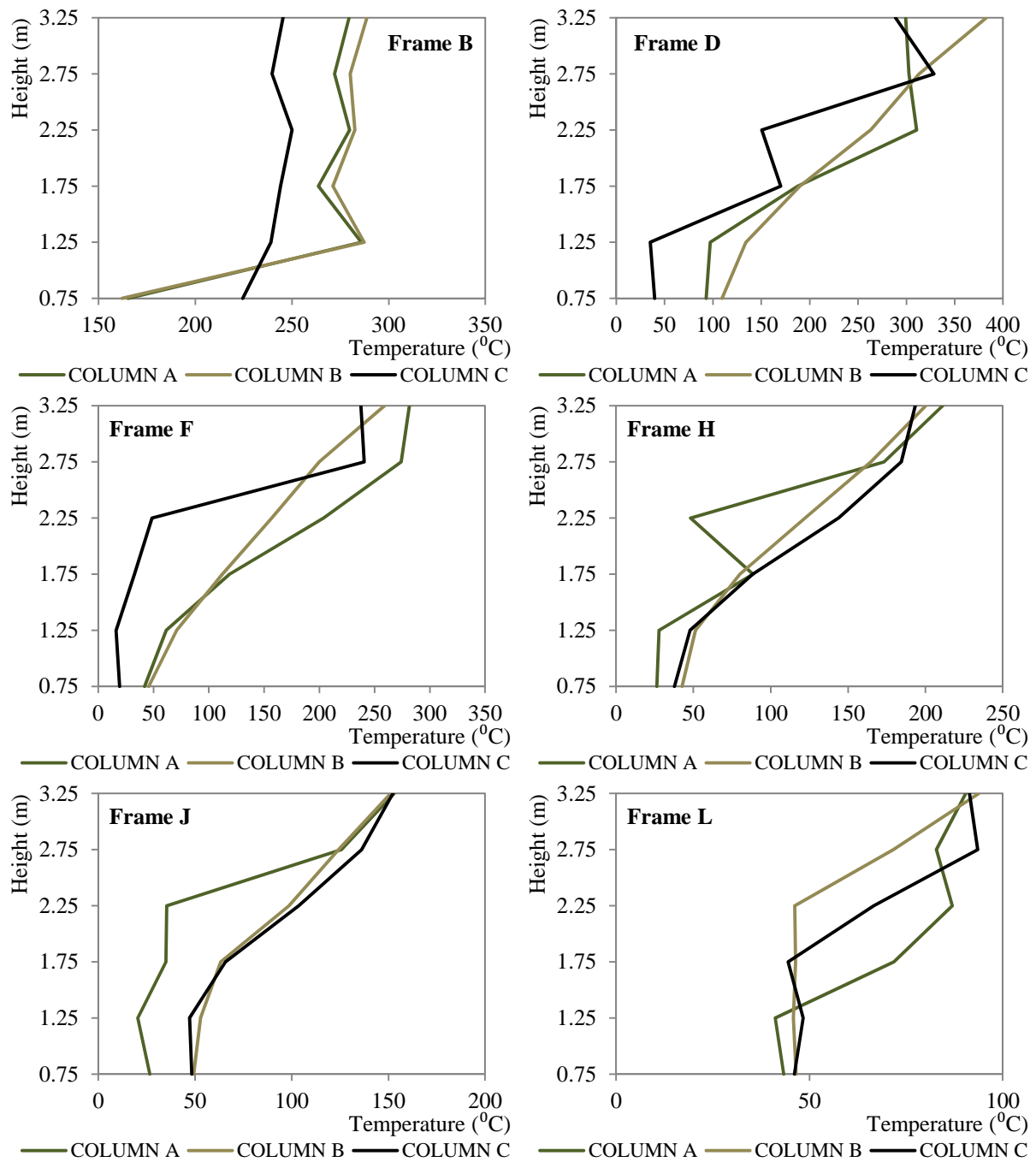


Figure B- 37: Temperature distribution along the axis of the columns in different frames for the SC-SP20/
Time=800sec.

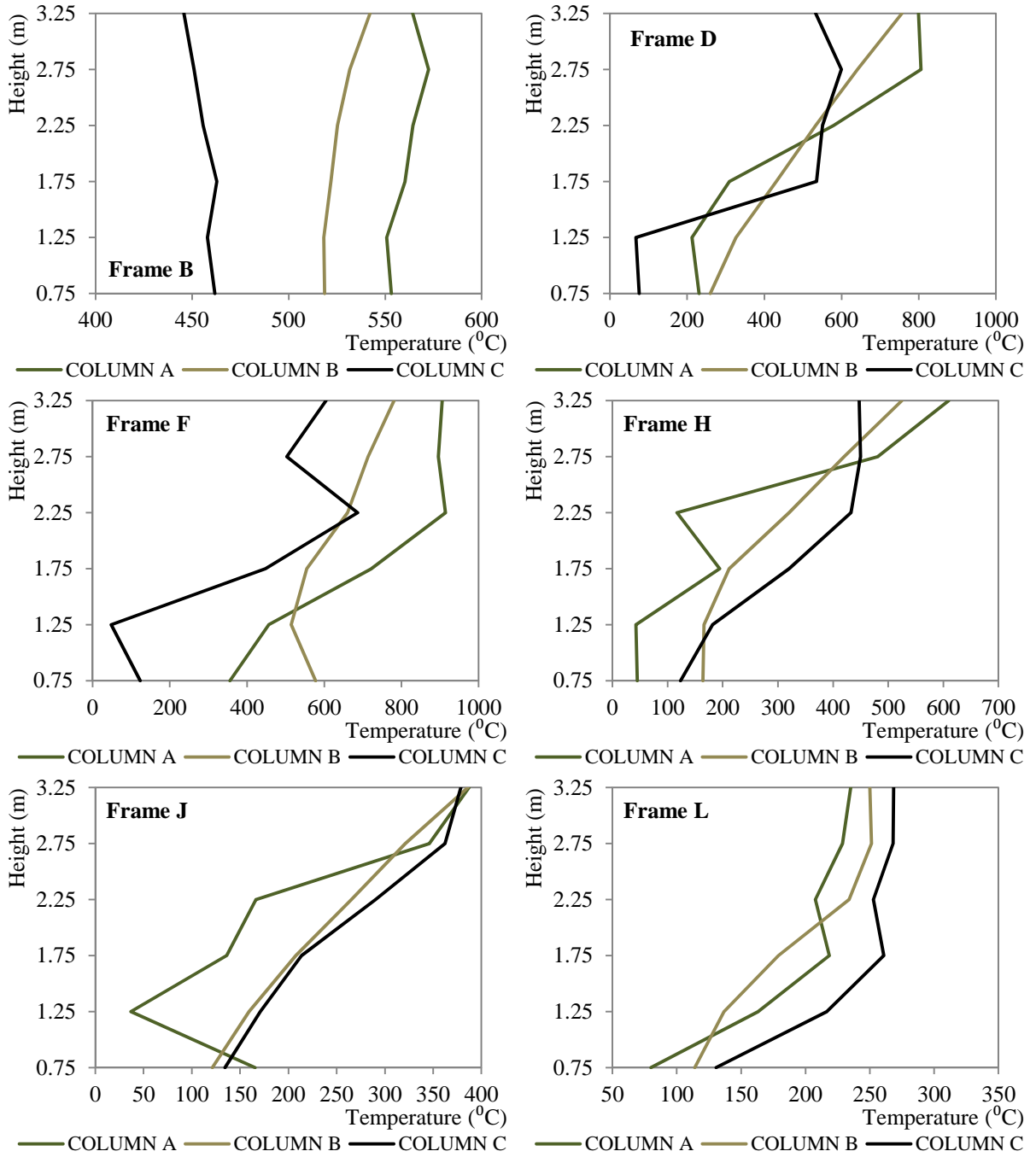


Figure B- 38: Temperature distribution along the axis of the columns in different frames for the SC-SP20/
Time=1200sec.

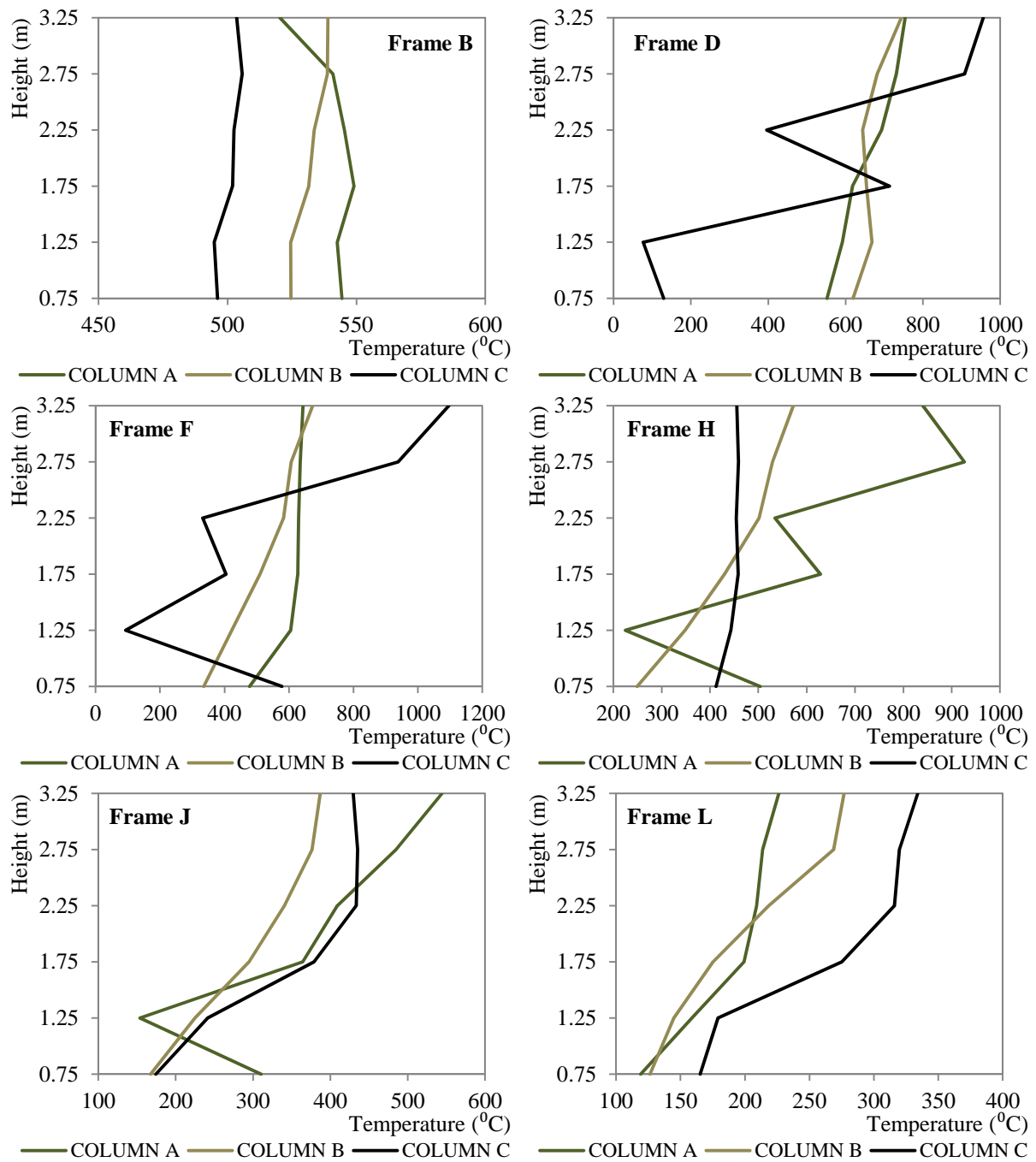


Figure B- 39: Temperature distribution along the axis of the columns in different frames for the SC-SP20/
Time=1600sec.

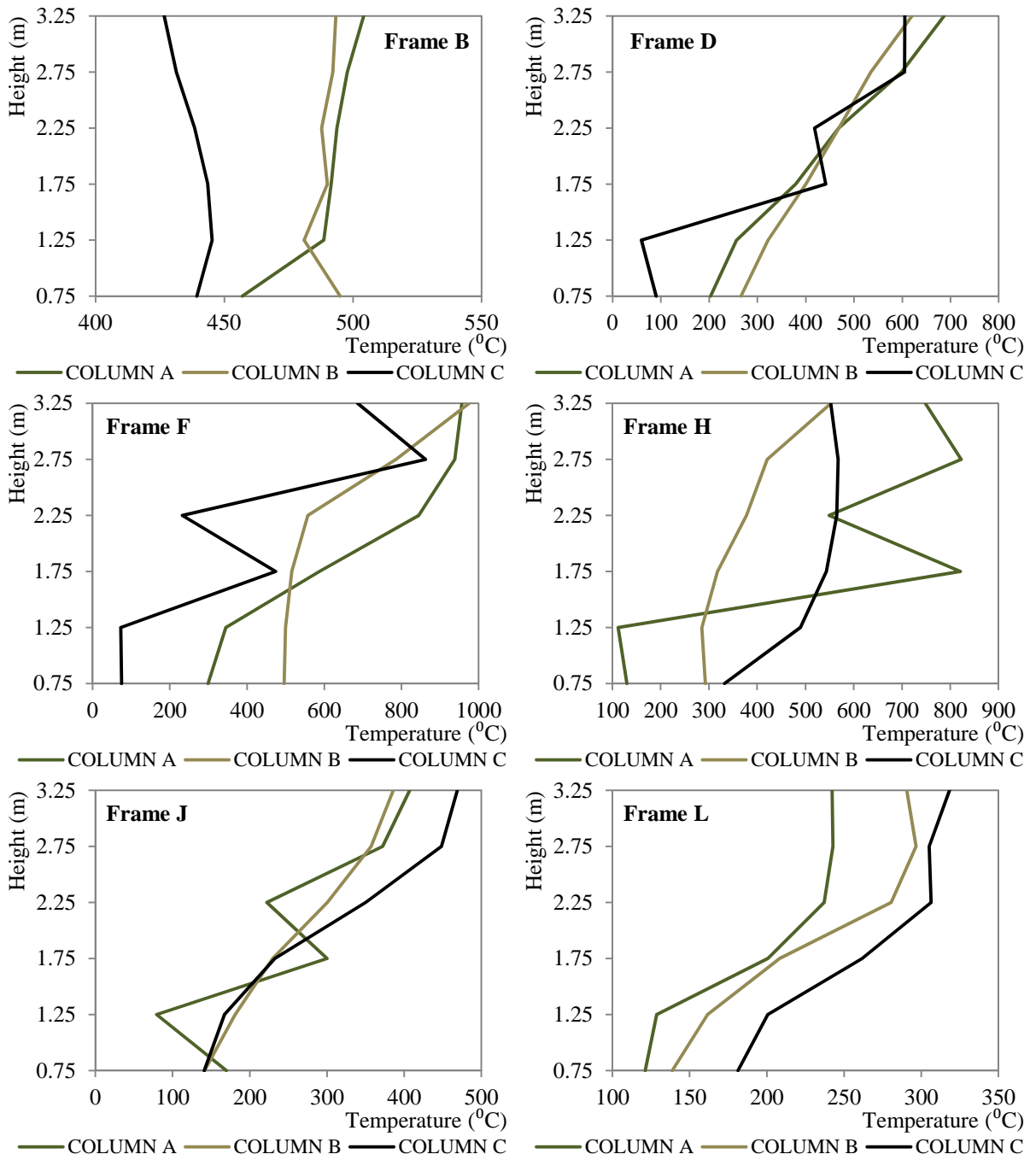


Figure B- 40: Temperature distribution along the axis of the columns in different frames for the SC-SP20/
Time=2000sec.

Output of “dual-layer” post-processing model

The result of the post-processing “dual-layer” model are presented in the following figures (Figure B- 41 to Figure B- 46) for the SC-25A, SC-50A, SC-50C, SC-100, SC-SP40 and SC-SP-40. Each diagram illustrates the temporal evolution of the gas-temperature for the Upper and Lower layers and the interface height.

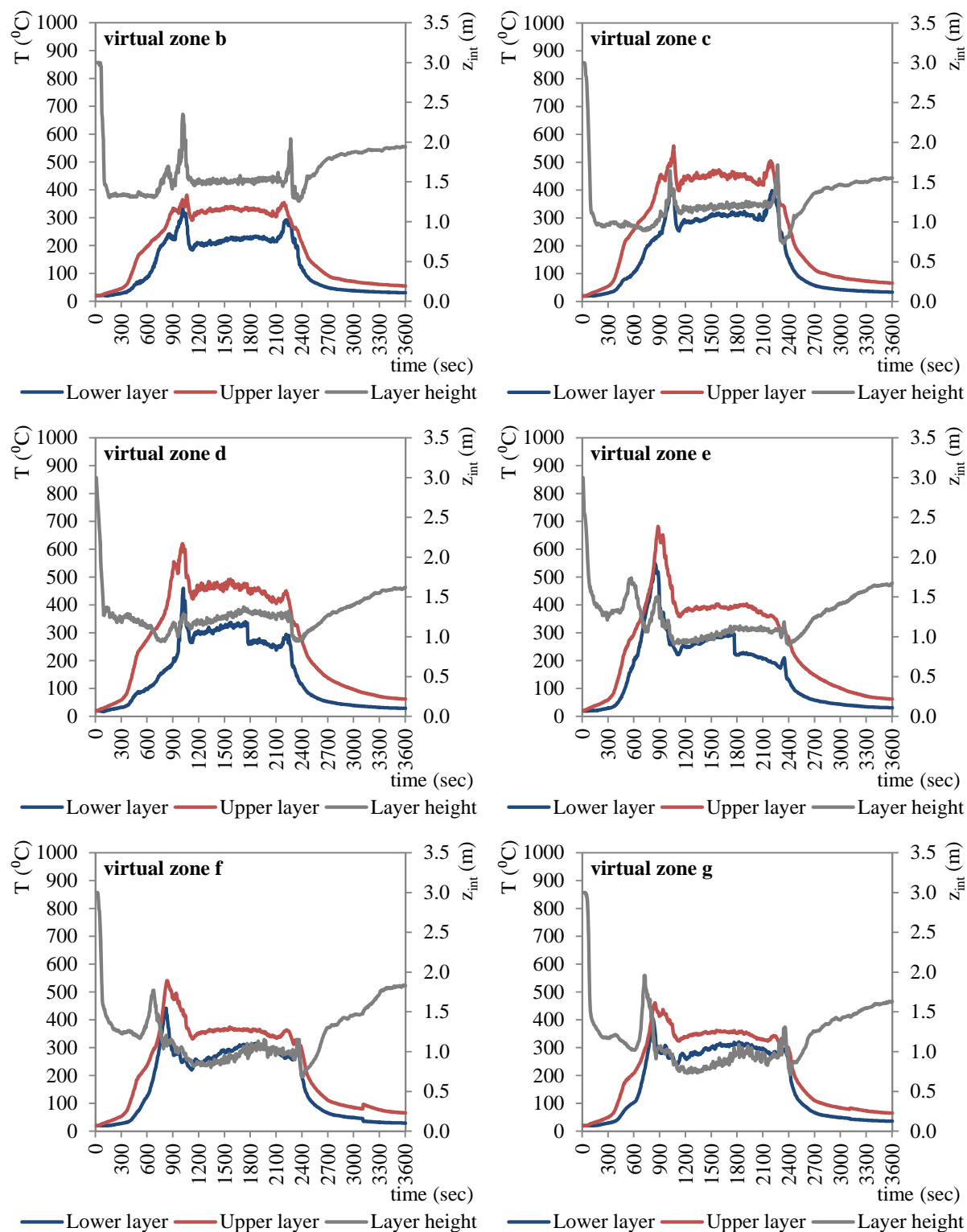


Figure B- 36: Upper-Lower temperature and layer height at different virtual zones for SC-25B.(continued)

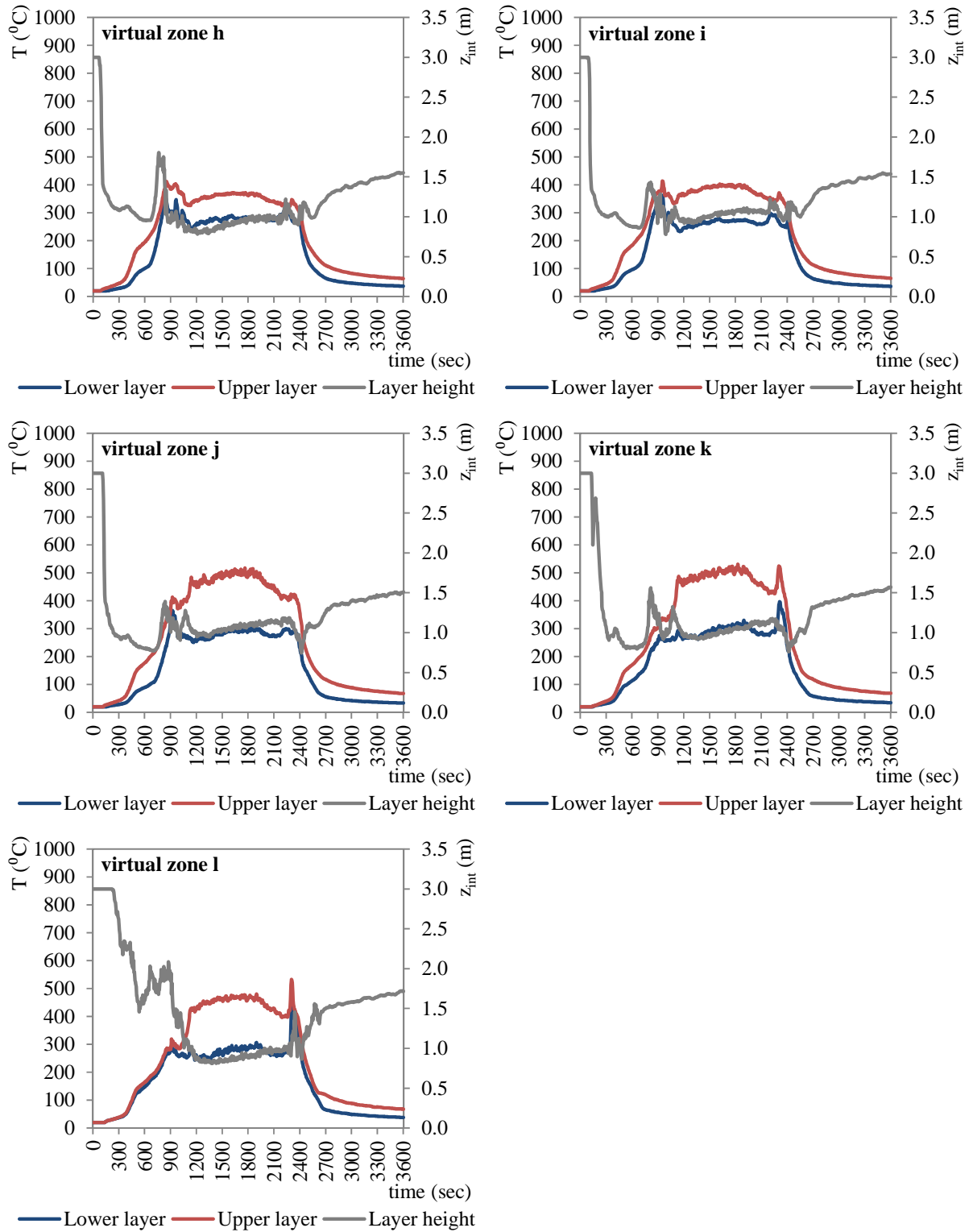


Figure B- 41: Upper-Lower temperature and layer height at different virtual zones for SC-25B.

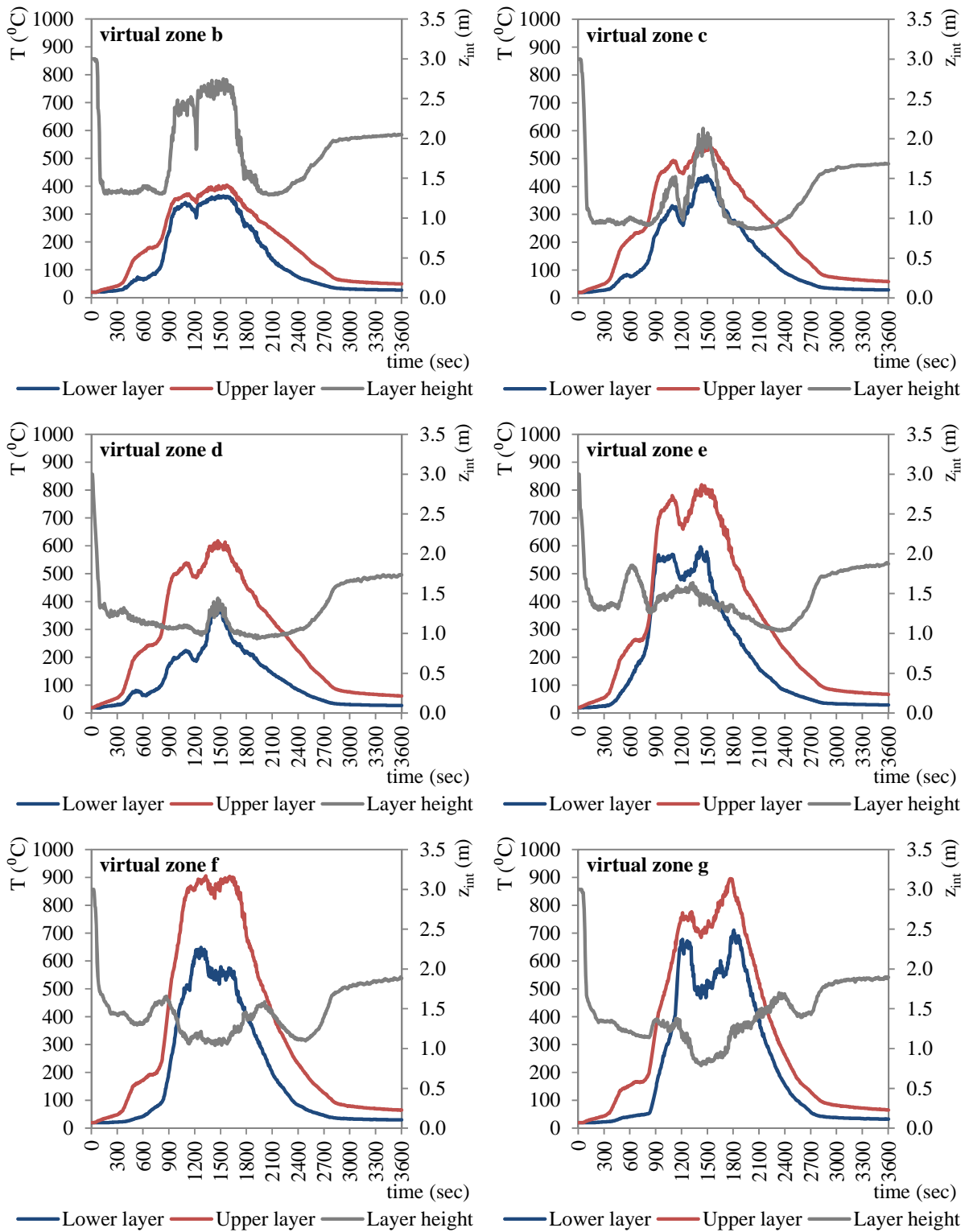


Figure B- 37: Upper-Lower temperature and layer height at different virtual zones for SC-50A.(continued)

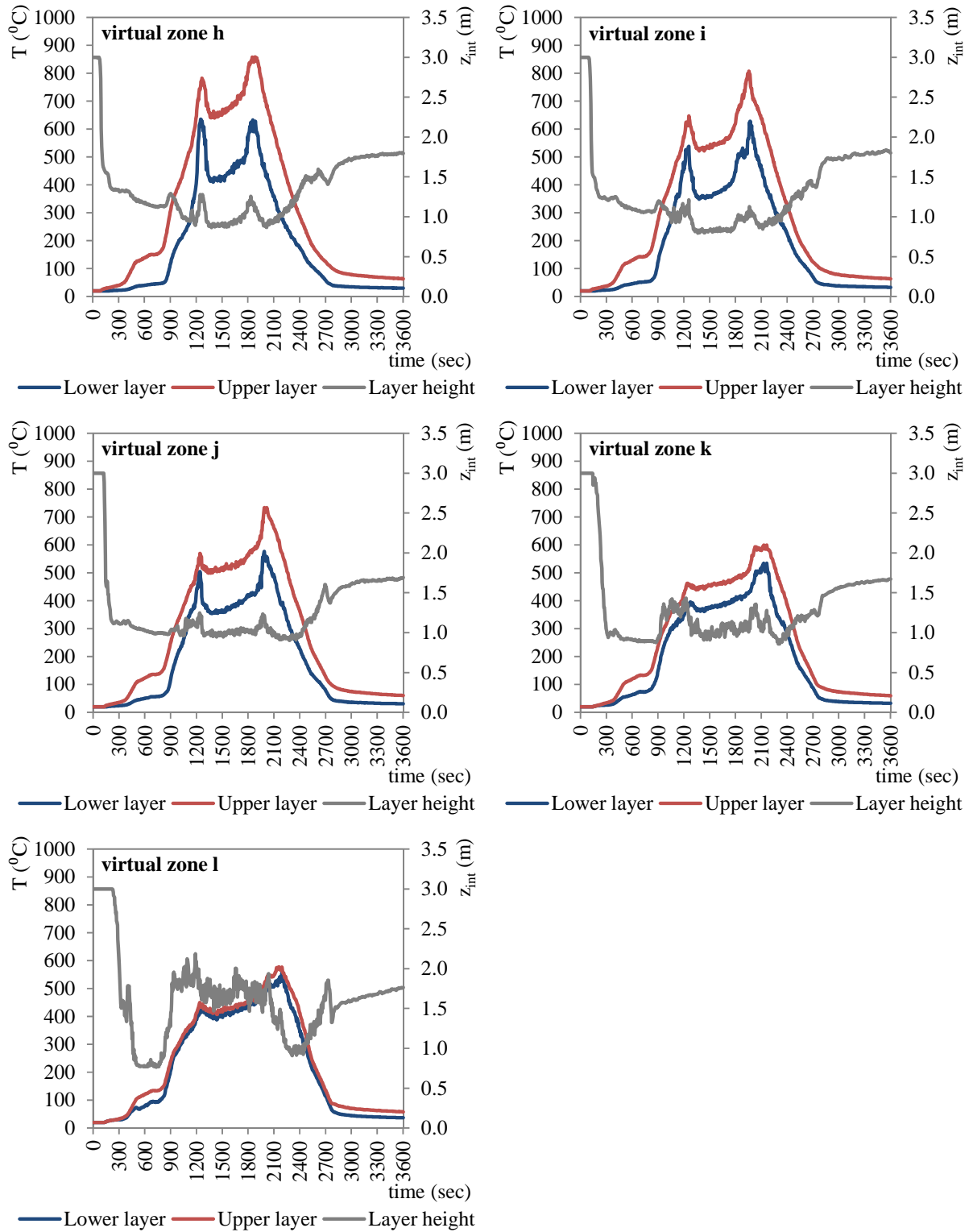


Figure B- 42: Upper-Lower temperature and layer height at different virtual zones for SC-50A.

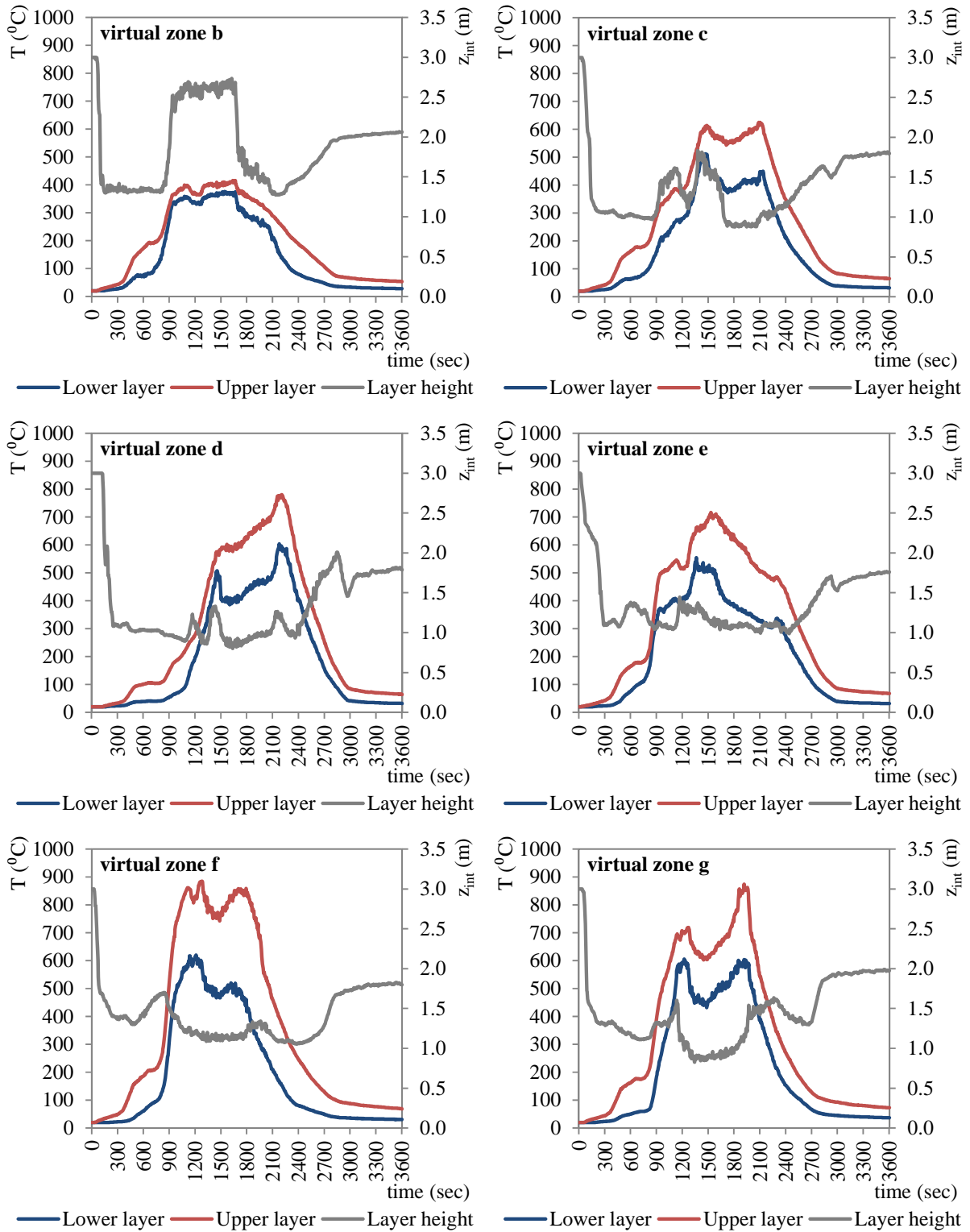


Figure B- 38: Upper-Lower temperature and layer height at different virtual zones for SC-50C. (continued)

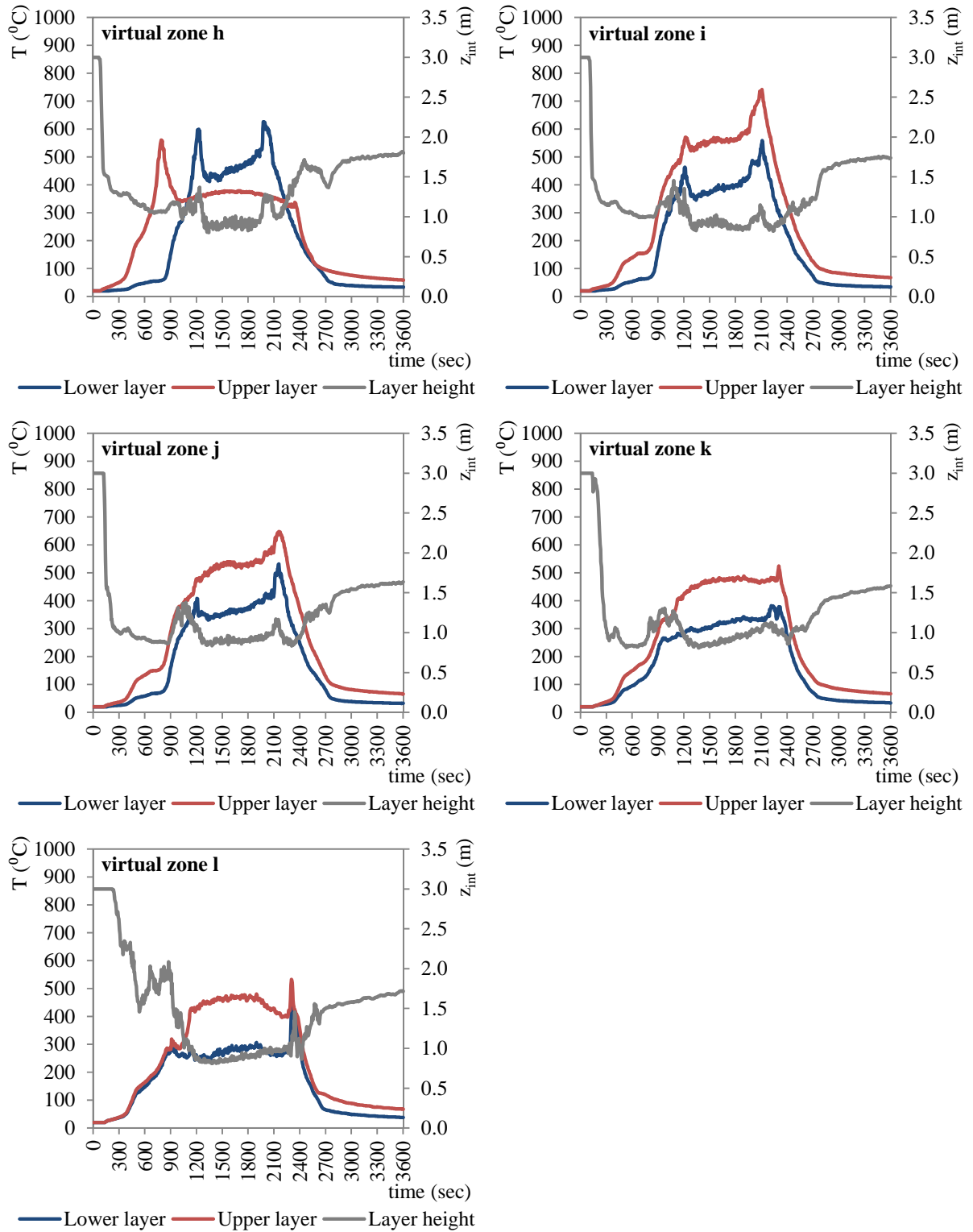


Figure B- 43: Upper-Lower temperature and layer height at different virtual zones for SC-50C.

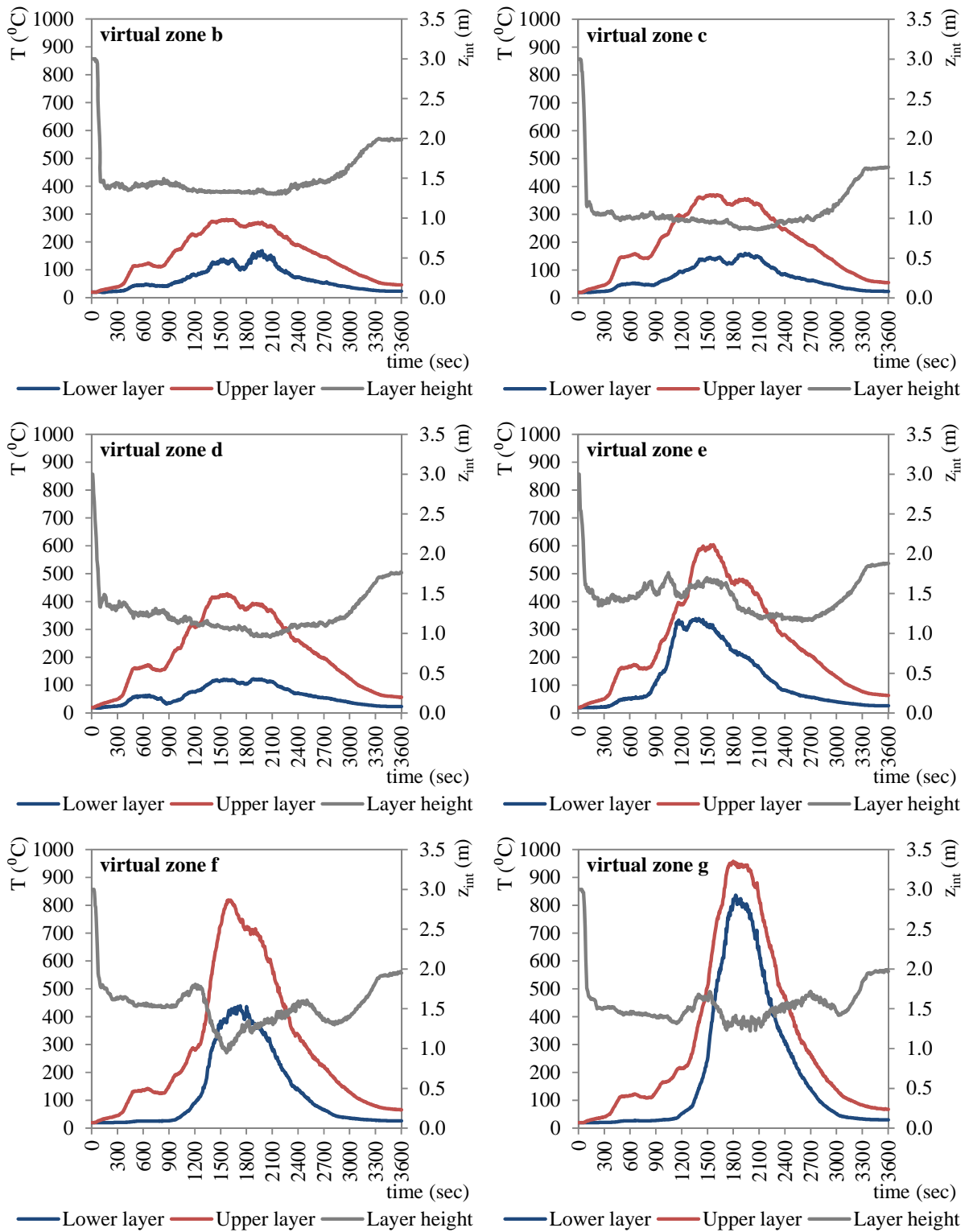


Figure B- 39: Upper-Lower temperature and layer height at different virtual zones for SC-100. (continued)

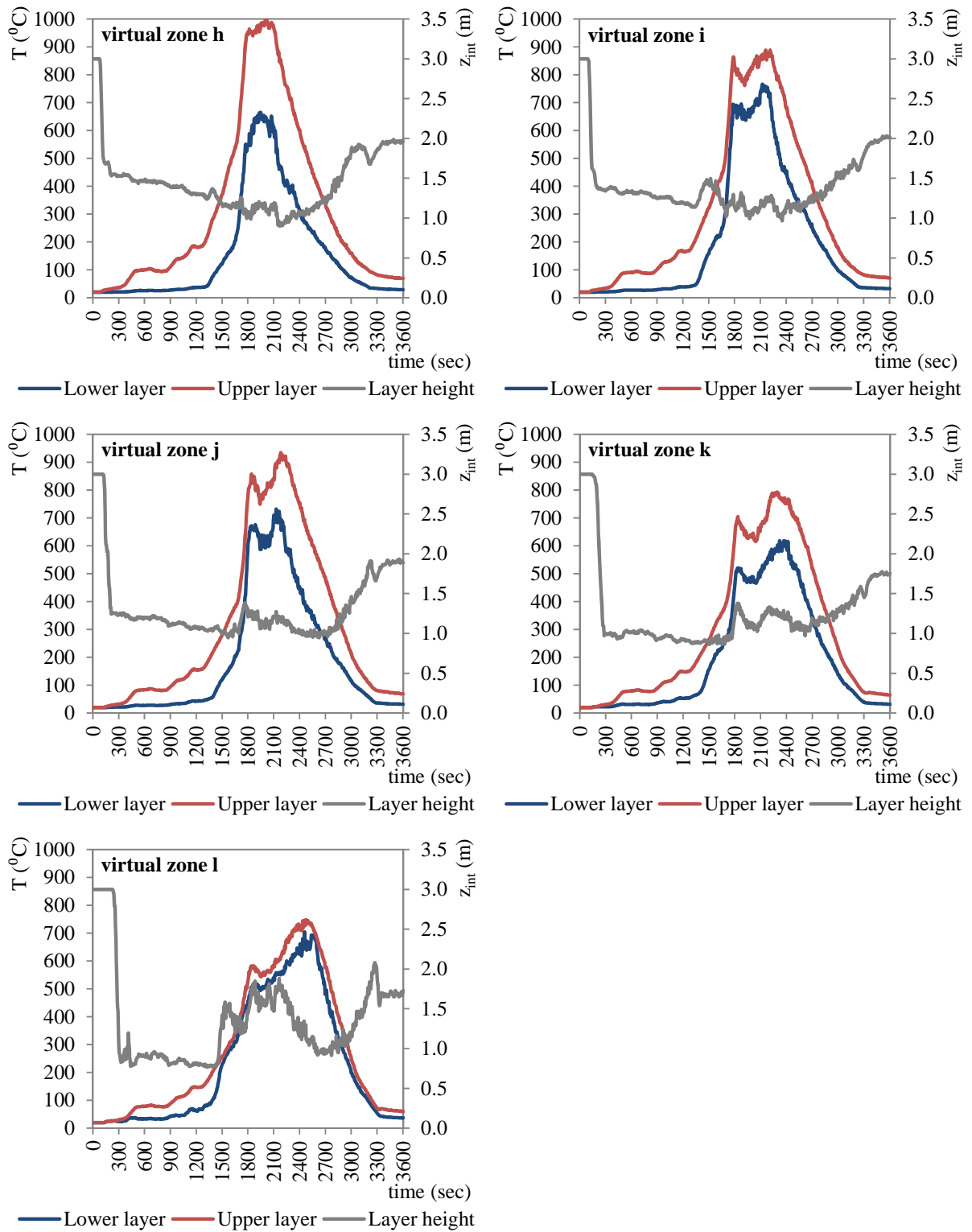


Figure B- 44: Upper-Lower temperature and layer height at different virtual zones for SC-100.

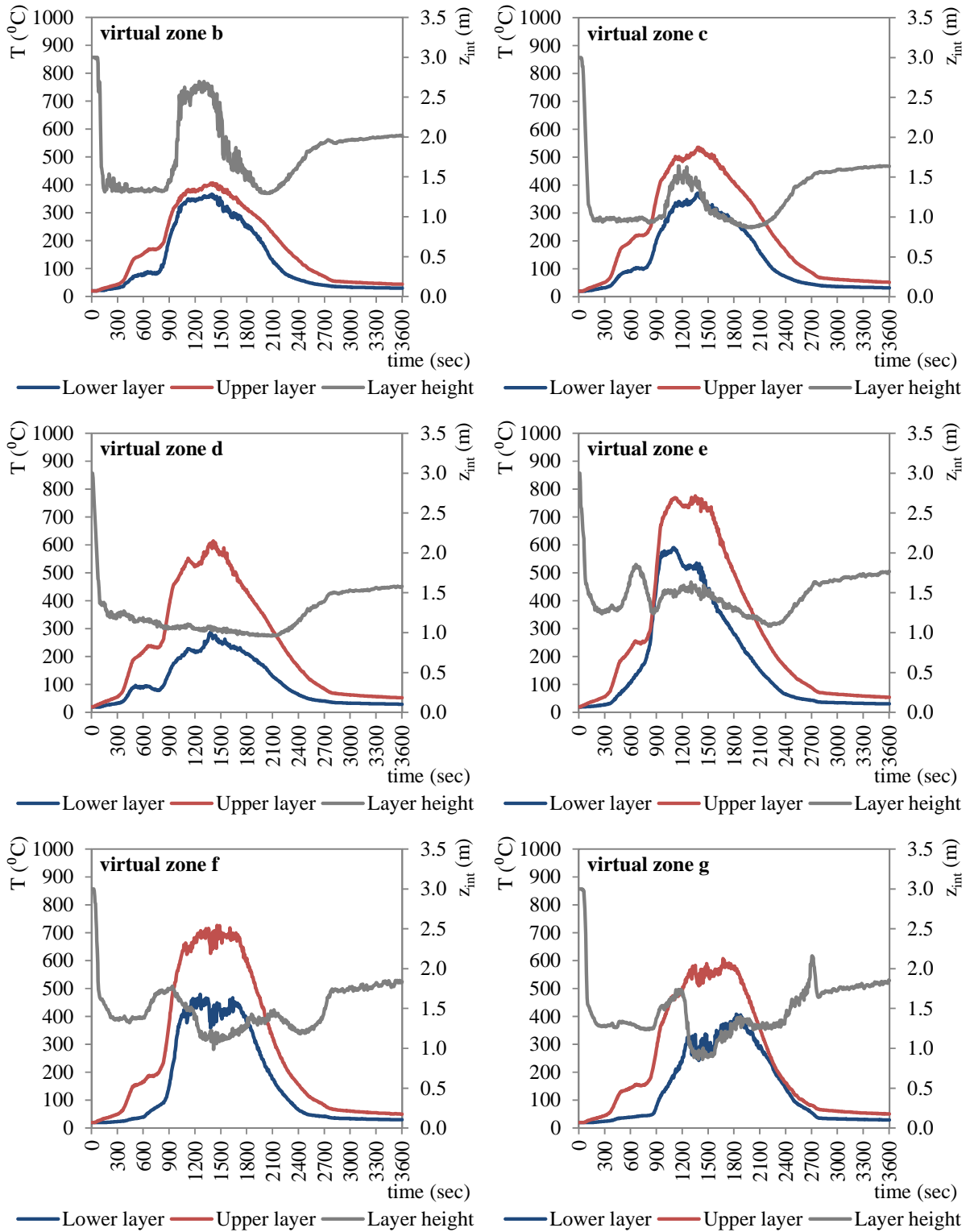


Figure B- 40: Upper-Lower temperature and layer height at different virtual zones for SC-SP40. (continued)

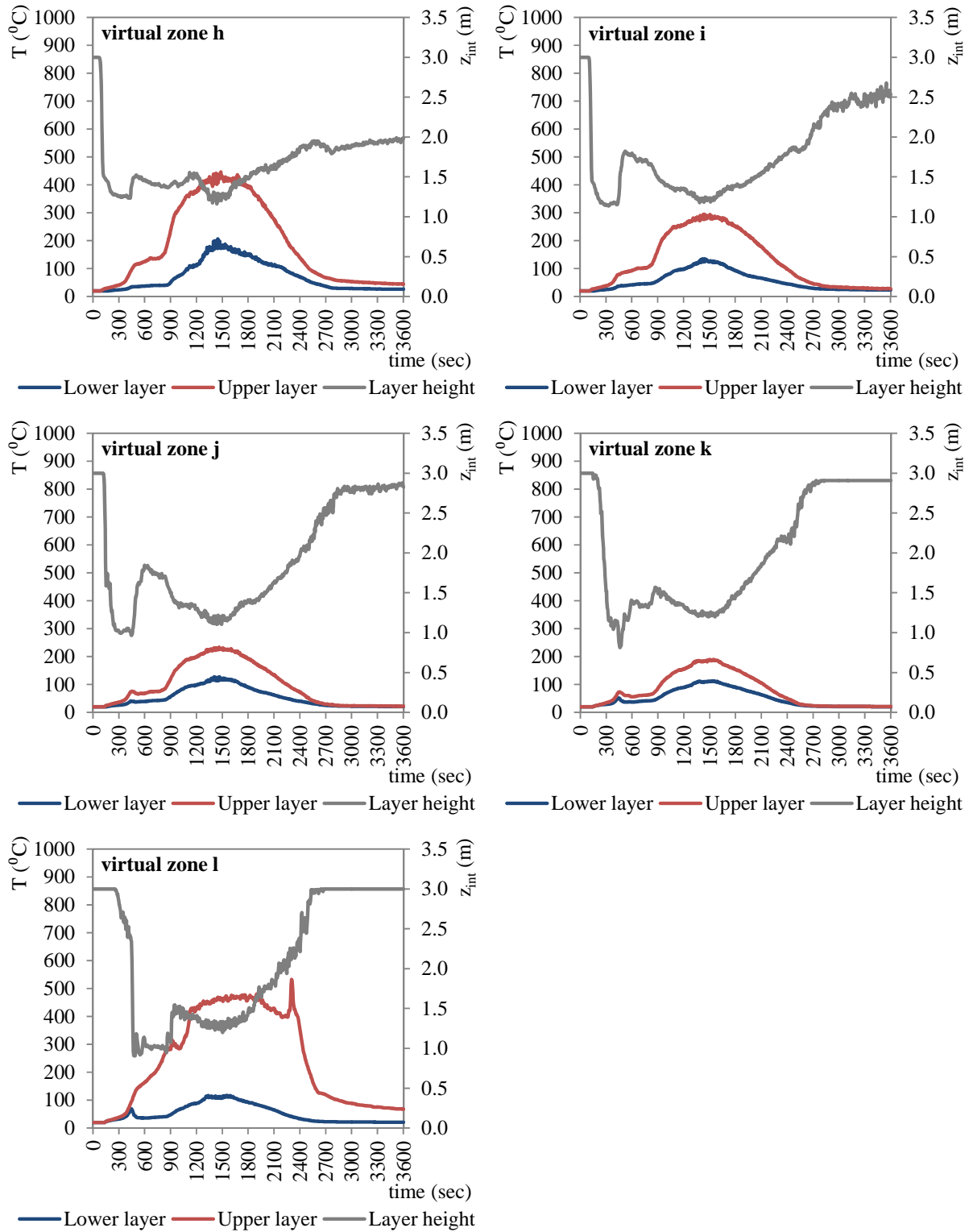


Figure B- 45: Upper-Lower temperature and layer height at different virtual zones for SC-SP40.

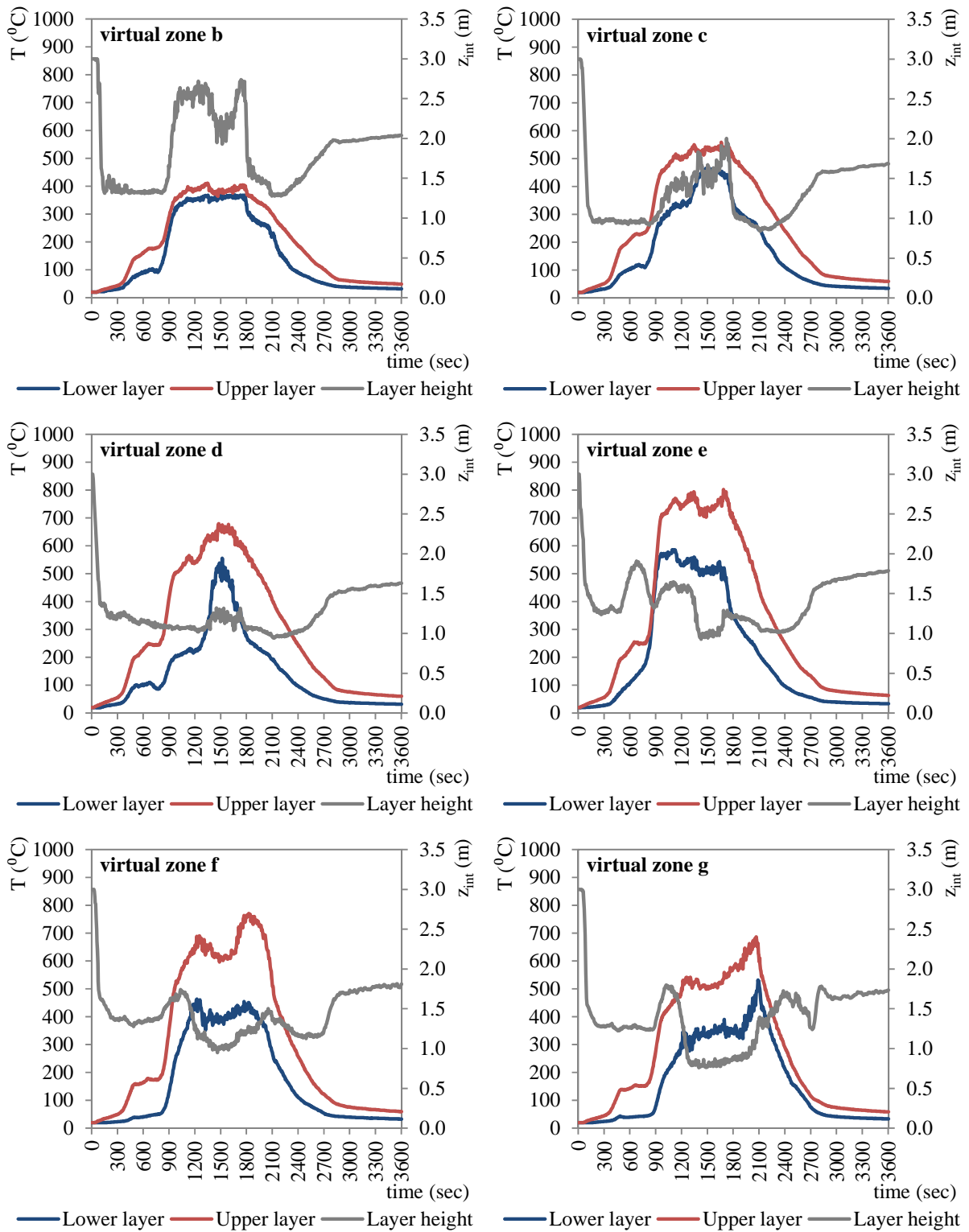


Figure B- 41: Upper-Lower temperature and layer height at different virtual zones for SC-SP20. (continued)

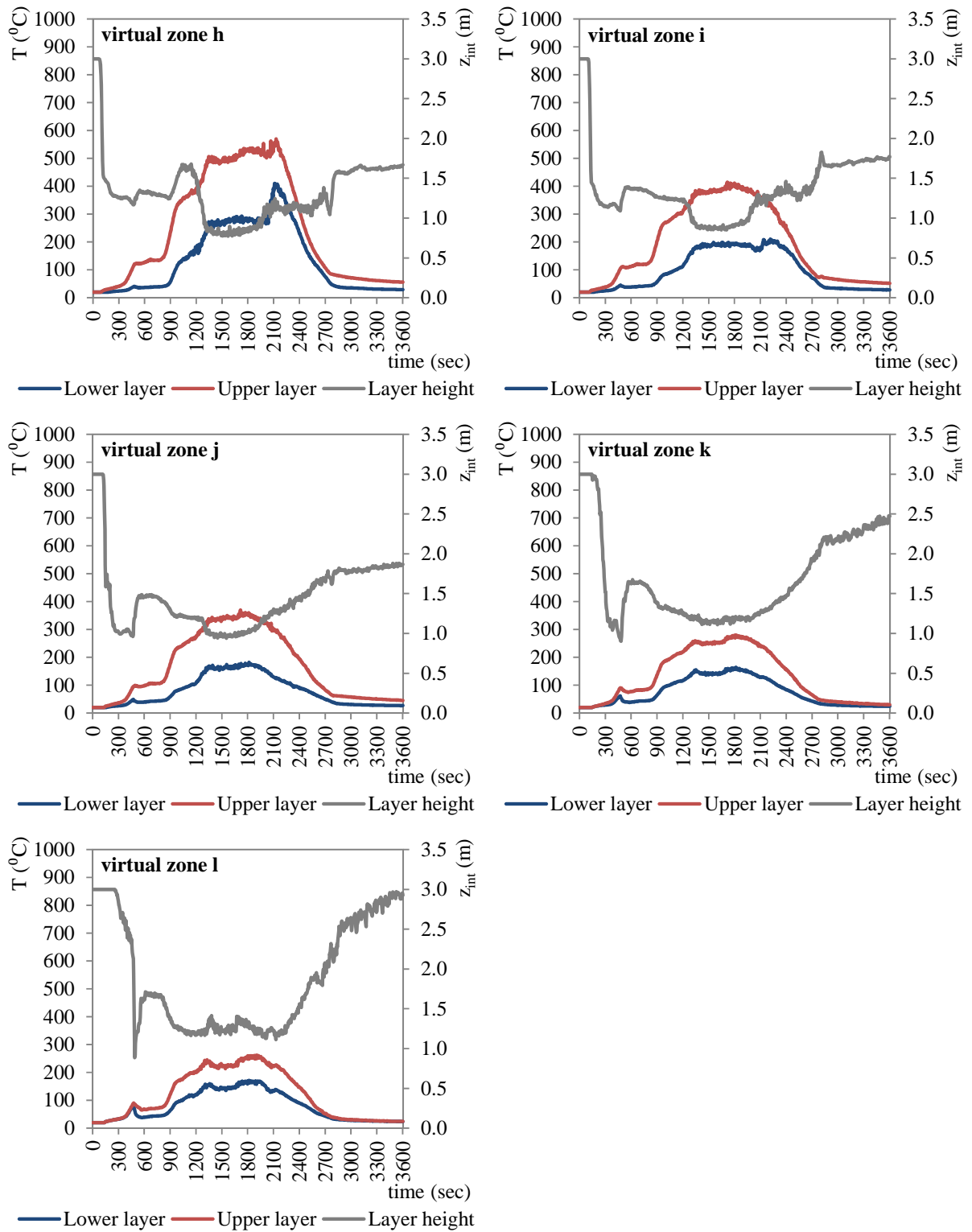


Figure B- 46: Upper-Lower temperature and layer height at different virtual zones for SC-SP20.

References

- Abaqus v6.10, (2011). User's Manual, Simulia, Providence, RI, USA
- Ambraseys, N., Smit, P., Sigbjornsson, R., Suhadolc, P., Margaris, B. (2002) Internet-Site for European Strong-Motion Data, European Commission, Research-Directorate General, Environment and Climate Programme.
- Antoniou, S., Pinho, R. (2004) Development and verification of a displacement-based adaptive pushover procedure, *Journal of Earthquake Engineering*, 8: 643-661.
- ATC – Applied Technology Council (1995), Guidelines and commentary for seismic rehabilitation of buildings. ATC Report 33-03, California.
- ATC – Applied Technology Council (1996), Seismic evaluation and retrofit of concrete buildings, Vol. 1, ATC-40, Applied Technology Council, Redwood City.
- Babrauskas V., (2002), Ignition of Wood: A Review of the State of the Art, *J. Fire Protection Engineering*, 12: 163-189.
- Bazzurro, P., Cornell, CA. (1994) Seismic hazard analysis for non-linear structures. I: Methodology, *ASCE Journal of Structural Engineering*, 120(11): 3320–3344.
- Bazzurro, P., Cornell, CA. (1994) Seismic hazard analysis for non-linear structures. II: Applications, *ASCE Journal of Structural Engineering*, 120(11): 3345–3365.
- Bracci, JM., Kunnath, SK., Reinhorn, AM. (1997) Seismic performance and retrofit evaluation of reinforced concrete structures, *ASCE Journal of Structural Engineering*, 123(1): 3-10.
- Burgess, I.W., El-Rimawi, J.A., Plank, R.J. (1990) Analysis of beams with non uniform temperature profile, *Journal of Constructional Steel Research*, 16: 169–192.
- Burgess, I.W., El-Rimawi, J.A., Plank, R.J. (1991) Studies of the behaviour of steel beams in fire, *Journal of Constructional Steel Research*, 19: 285–312.
- Cadorin, J.F., Pintea, D., Dotreppe, J.C., Franssen, J. (2003) A tool to design steel elements submitted to compartment fires – Ozone V2. Part2: Methodology and application, *Fire safety Journal*, 28: 439-451.
- CFX 5.7.1, ANSYS, Inc., 275 Technology Drive, Canonsburg, PA 15317, 2005.
- CFX 5.7.1, ANSYS, Inc., 275 Technology Drive, Canonsburg, PA 15317, 2005.
- Chen, S., Lee, G.K., Shinozuka, M. (2004) Hazard mitigation for earthquake and subsequent fire, ANCEER annual Meeting: Networking of Young Earthquake Engineering Researchers and Professionals, Honolulu, Hawaii.

- Chi-ming, L., Chien-Jung, C., Ming-Ju, T., Meng-Han, T., Ta-Hui, L. (2013) Determinations of the fire smoke layer height in a naturally ventilated room, *Fire Safety Journal*, 58: 1–14.
- Chopra, A. (2007) *Dynamics of Structures – Theory and applications to earthquake engineering*, 3rd edition, Pearson, Prentice Hall. Upper Saddle River, New Jersey.
- Collier, P.C.R. (2008) Post –earthquake performance of passive fire protection systems, *Proceedings of fifth international Conference in Fire, Singapore*, 748-759.
- Cooke, G.M.E., Latham, D.J. (1987) The inherent fire resistance of a loaded steel framework, *Fire Research Station paper PD 57/87*, Building Research Establishment.
- Cosenza, E., Manfredi, G. (2000), Damage indices and damage measures, *Progress in Structural Engineering and Materials*, 2: 50-59.
- D’Aniello, M., Landolfo, R., Piluso, V., Rizzano G. (2012) Ultimate behaviour of steel beams under non-uniform bending, *Journal of Constructional Steel Research*, 78: 144-158.
- Daali, M.L., Korol, R.M. (1995) Prediction of local buckling and rotational capacity at maximum moment, *Journal of Constructional Steel Research*, 32: 1-13.
- Davies, J.M., (2006) Stain hardening, local buckling and lateral torsional buckling in plastic hinges, *Journal of Constructional Steel Research*, 62: 27-34.
- De Matteis, G., Landolfo, R., Dubina, D., Stratan, A. (2000) Influence of the structural typology on the seismic performance of steel framed buildings, In *Moment Resistant Connections of Steel Frames in Seismic Areas*, Mazzolani FM (ed.). E & FN Spon: New York, 513–538.
- Della Corte, G., Landolfo, R. and Mazzolani F.M. (2003) Post-earthquake fire resistance of moment resisting steel frames, *Fire Safety Journal*, 38: 593-612.
- Dharma, R.B., Tan, K.H. (2007a) Rotational capacity of steel I-beams under fire conditions Part II: Numerical simulations, *Engineering Structures*, 29 : 2403–2418.
- Dharma, R.B., Tan, K.H. (2007b) Rotational capacity of steel I-beams under fire conditions Part I: Experimental study, *Engineering Structures*, 29: 2391–2402.
- Drysdale, D. (2002) *An Introduction to Fire Dynamics*. John Wiley and Sons, New York, 2nd edition.
- Dubina, D., Ciutina, A., Stratan, A., Dinu, F. (2000) Ductility demand for semi-rigid joint frames. In *Moment Resistant Connections of Steel Frames in Seismic Areas*, Mazzolani FM (ed.). E & FN Spon: New York, 371–408.
- Elghazouli, A.Y., Izzuddin, B.A. (2000) Response of idealised composite beam-slab system under fire conditions, *Journal of Constructional Steel Research*, 56: 199–224.
- Elnashai, A.S. (2001) Advanced inelastic static (pushover) analysis for earthquake applications, *Structural Engineering and Mechanics*, 12: 151-169.
- Elnashai, AS. (2002) Do we really need inelastic dynamic analysis?, *Journal of Earthquake Engineering*, 6(1): 123-30.

References

El-Rimawi, J.A., Burgess, I.W., Plank, R.J. (1997) The influence of connection stiffness on the behaviour of steel beams in fire, *Journal of Constructional Steel Research* 43(1–3): 1–15.

Engineering Research Center, University of California Berkeley, USA, 2011.
(www.opensees.berkeley.edu).

European Committee for Standardization (CEN), (1998), EN 1998, Eurocode 8: Design provisions for earthquake resistance of structures. (Abbreviation in the document as EN 1998).

European Committee for Standardization (CEN), (2001), EN 1991-1-2. Eurocode 1: Actions on structures exposed to fire – Part 1-2. General actions – structural fire design. (Abbreviation in the document as EN 1991-1-2).

European Committee for Standardization (CEN), (2002), EN 1991-1-1, Eurocode 1: Actions on structures-Part 1-1: General actions – Densities, self-weight, imposed loads for buildings. (Abbreviation in the document as EN 1991-1-1).

European Committee for Standardization (CEN), (2003), EN 1993-1-2, Eurocode 3: Design of steel structures – Part 1-2. General rules – structural fire design. (Abbreviation in the document as EN 1993-1-2).

European Committee for Standardization (CEN), (2004), EN 1998-1-1, Eurocode 8: Design of structures for earthquake resistance – Part 1. General rules seismic actions and rules for buildings. (Abbreviation in the document as EN 1998-1-1).

European Committee for Standardization (CEN), (2005), EN 1994-1-2, Eurocode 4: Design of composite steel and concrete structures – Part 1-2. General rules – structural fire design. (Abbreviation in the document as EN 1994-1-2).

European Committee for Standardization (CEN), (2005a), EN 1993-1-1, Eurocode 3: Design of steel structures – Part 1-1. General rules and rules for buildings. (Abbreviation in the document as EN 1993-1-1).

European Committee for Standardization (CEN), (2006), EN 1990/A1, Eurocode: Basis of structural design. (Abbreviation in the document as EN 1990).

Faggiano, B., Espoto, M., Mazzolani, F.M. and Landolfo, R. (2007) Fire analysis of steel portal frames damaged after earthquake according to performance based design, *Urban Habitat Constructions under Catastrophic Events*, Cost C26, Workshop, Prague, Czech Republic.

Faggiano, B., Espoto, M., Zaharia, R., Pintea, D. (2008) Structural analysis in case of fire after earthquake, *Urban Habitat Constructions under Catastrophic Events*, Cost Action C26, Malta University Publishing :75-80.

Fajfar, P. (1998) Trends in seismic design and performance evaluation approaches. In: *Proceedings of 11th European Conference on Earthquake Engineering*. Rotterdam: AA Balkema, 237-249

Fajfar, P. (1999) Capacity spectrum method based on inelastic demand spectra, *Earthquake Engineering and Structural Dynamics*, 28: 979-993.

- Fajfar, P. (2000) A Nonlinear Analysis Method for Performance-Based Seismic Design, *Earthquake Spectra*, 16(3): 573-592.
- Fajfar, P., (1998a) Trends in seismic design and performance evaluation approaches, In 11th Euroean Conference on Earthquake Engineering, Paris, Balkema, Rotterdam, Incited Lectures, 237-249.
- Fajfar, P., Fisehineer, M. (1988) N2 Method for nonlinear seismic analysis of regular structures, *Proceedings of 9th World Conference on Earthquake Engineering*, Tokvo-Kvoto. Japan, 5: 111-116.
- Federal Emergency management Agency (FEMA) (2000) Fema 356 Prestandard and commentary for the seismic rehabilitation of buildings, Washington, D.C.
- FEMA 350 (2001) Seismic design criteria for new moment-resisting steel frame construction. Federal Emergency Management Agency.
- Federal Emergency management Agency (FEMA) (2008) Fema P695 Quantification of Building Seismic Performance Factors. Federal Emergency Management Agency, Washington, D.C.
- Ferracuti, B., Pinho, R., Savoia, M., Francia, R. (2009) Verification of displacement-based adaptive pushover through multi-ground motion incremental dynamic analyses, *Engineering Structures*, 31: 1789-1799.
- FM Global, 2013, www.fmglobal.com
- Fong, Y.Y., Fong, N.K. (2003) Scale Modelling of Smoke Movement in Linear Atrium, *International Journal on Engineering Performance-Based Fire Codes*, 5(4): 149-151.
- Forney, G., (2007) User's guide for Smokeview Version 5 – A tool for visualizing Fire Dynamics Simulation Data, National Institute of Standards and Technology.
- Franssen, J.M., Kodur, V.K.R., Mason, J. (2000) User's manual for SAFIR2001, A computer program for analysis of structures submitted to the fire, University of Liege, Belgium.
- Franssen, J-M., Vila Real, P. (2010), *Fire Design of steel Structures*, ECCS Eurocode Design Manuals, Ernst & Sohn – Awiley Company.
- Freeman, S.A., Nicoletti, J.P., Tyrell. J.V. (1975) Evaluation of existing buildings for seismic risk - A case study of Puget Sound Naval Shipyard Bremerton, Washington, *Proceedings of the United States National Conference on Earthquake Engineering Berkeley*, 113-22.
- Garcia, J.R. , Miranda, E., (2002) Evaluation of approximate methods to estimate maximum inelastic displacement demands, *Earthquake Engineering and Structural Dynamics*, 31: 539–560.
- Garcia, J.R., Miranda, E. (2005) Performance -based assessment of existing structures accounting for residual displacements, Report at The John A. Blume Earthquake Engineering Center.

References

Ghobarah, A. (2001) Performance-based design in earthquake engineering: state of development, *Engineering Structures*, 23: 878-884.

Gioncu, V., Mazzolani, F.M. (2002) *Ductility of seismic resistant steel structures*, Taylor and Francis Group, Spon Press, London and New York.

Gioncu, V., Mosoarca, M., Anastasiadis, A. (2012) Prediction of available rotational capacity and ductility of wide-flange beams: Part 1: DUCTROT-M computer program, *Journal of Constructional Steel Research*, 69:8-19.

Gioncu, V., Mosoarca, M., Anastasiadis, A. (2012) Prediction of available rotational capacity and ductility of wide-flange beams: Part 2: Applications, *Journal of Constructional Steel Research*, 68: 176-191.

Gioncu, V., Petcu, D. (2007a) Available rotational capacity of wide flange beams and beam-columns Part 1. Theoretical approaches, *Journal of Constructional Steel Research*, 43:161-217

Gioncu, V., Petcu, D. (2007b) Available rotational capacity of wide flange beams and beam-columns Part 1. Experimental and Numerical tests, *Journal of Constructional Steel Research*, 43: 219-244.

Gissi, E. (2010) *An introduction to Fire Simulation with FDS and Smokeview*, Creative Commons Licence, <http://www.emanuelegissi.eu>.

Graf, S. H. (1949) *Ignition Temperatures of Various Papers, Woods, and Fabrics*, (Oregon State College Bull. 26), Oregon State College, Corvallis.

Gulkan, P., Sozen, M.A. (1974) Inelastic response of RC structures to earthquake motion, *ACI*, 71: 609-614.

Gupta, B., Kunnath, SK. (2000) Adaptive spectra-based pushover procedure for seismic evaluation of structures, *Earthquake Spectra*, 16(2): 367-91.

Hamins, A., Mcgrattan, K., Prasad, K., Maranghides, A., Mcallister, T. (2005) Experiments and Modeling of unprotected steel elements to a fire, *Fire Safety Science. Proceedings. Eighth (8th) International Symposium. International Association for Fire Safety Science (IAFSS)*. Beijing, China, Intl. Assoc. for Fire Safety Science, Boston, MA, Gottuk, D. T.; Lattimer, B. Y., Editor(s)(s): 189-200.

Iervolino, I, Maddaloni, G, Cosenza, E (2008) Eurocode 8 compliant real record sets for seismic analysis of structures, *Journal of Earthquake Engineering* 12: 54–90.

Iervolino, I. Galasso, C., and • Cosenza, E. (2010), REXEL: computer aided record selection for code-based seismic structural analysis, *Bulletin of Earthquake Engineering*, 8:339–362.

Janssens, M.L., Tran, H.C. (1992) Data Reduction of Room Tests for Zone Model Validation, *Journal of Fire Science*, 10(164): 528–555.

Kaewkulchai, G., Williamson, EB. (2004) Beam element formulation and solution procedure for dynamic progressive collapse analysis. *Computer and Structures*, 82 (7–8): 639–51.

- Kappos, A. (1997) Seismic damage indices for RC buildings: evaluation of concepts and procedures, *Progress in Structural Engineering and Materials*, 1: 78-87.
- Keller, W.J. (2012) Thermomechanical response of steel moment-frame beam-column connections during post-earthquake Fire Exposure, Dissertation in Lehigh University.
- Keski-Rahkonen, O., Hostikka, S. (2002) Zone model validation of room fire scenarios, International Collaborative Project to Evaluate Fire Models for Nuclear Power and Plant Applications, Gaithersburg, May 2-3.
- Khandelwal, K., El-Tawil, S., Sadek, F. (2009) Progressive collapse analysis of seismically designed steel braced frames, *Journal of Constructional Steel Research*, 65(3): 699–708.
- Kim J, Youngho Lee Y, Choi H. (2011), Progressive collapse resisting capacity of braced frames. *Struct Des Tall Spec Build*;20(2):257–70.
- Kim, S., D'Amore, E. (1999) Push—over analysis procedures in earthquake engineering, *Earthquake Spectra*, 15: 417-434.
- Kirby, BR. (1997) Large scale fire tests: the British Steel European collaborative research programme on the BRE 8-storey frame, *Proceedings of the Fifth International Symposium on Fire Safety \science*, Melbourne, Australia: 1129-1140.
- Kirby, BR., (1996) The Behaviour of a Multi-Storey Steel Framed Building Subject to Fire Attack - Experimental Data; British Steel Swinden Technology Centre, United Kingdom, 1998. Also data from BRE, Cardington, on the Corner Fire Test and Large Compartment Fire Test.
- Knobloch, M., Fontana, M. (2006) Strain-based approach to local buckling of steel sections subjected to fire, *Journal of Constructional Steel Research*, 62:44-67.
- Kodur, V. and Dwaikat, M. (2009) Response of steel beam-columns exposed to fire, *Engineering Structures*, 31: 369-379.
- Kodur, V., Garlock, M., Iwankiw (2012), *Structures in Fire: State-of-the-art*, Research and training needs, *Fire Technology*, 48: 825-839.
- Kuhlmann, U., (1989) Definition of flange slenderness limits on the basis of rotational capacity values, *Journal of Constructional Steel Research*,14: 21-40.
- Kumar, S., Miles, S., Welch, S., Vassart, O., Zhao, B., Lemaire, A.D., Noordijk, L.M., Fellingner, J.H., Franssen, J.M., (2008) FIRESTRUCT, Integrating advanced three-dimensional modelling methodologies for predicting thermo-mechanical behaviour of steel and composite structures subjected to natural fires, RFCS project PFS-PR-02110, European Commission report.
- Lawson, R.S., Vance, V., and Krawinkler, H. (1994) Nonlinear static pushover analysis, why, when and how?, *Proceedings of 5th US National Conference on Earthquake Engineering*, Chicago, 1: 283-292.
- Leelataviwat, S., Goel, S.C., Stojadinovic, B. (1999), Toward performance-based design, *Journal of Structural Engineering*, 1: 183-194.

References

- Li, G., Wang, P., Jiang, S. (2007) Non-linear finite element analysis of axially restrained steel beams at elevated temperatures in a fire, *Journal of Constructional Steel Research*, 63: 1175–1183.
- Li, G.Q., Wnag, W.Y. (2008) Experimental behaviour of steel columns with partial damage of fire retardant coating in fire, *Proceedings of the international Conference in Fire, Singapore*: 738-747.
- Li, T.Q., Choo, B.S., Nethercot, D.A., (1995) Determination of rotational capacity for steel and composite beams, *Journal of Constructional Steel Research*, 32: 303-332.
- Liu, T.C.H. (1998) Effect of connection flexibility on fire resistance of steel beams, *Journal of Constructional Steel Research*, 45(1): 99–118.
- Liu, T.C.H. (1999) Fire resistance of unprotected steel beams with moment connections, *Journal of Constructional Steel Research*, 51: 61–77.
- Liu, T.C.H., Davies, J.M. (2001) Performance of steel beams at elevated temperatures under the effect of axial restraints, *Steel Composite Structures*, 1(4): 427–40.
- Luco, N., Cornell, C.A. (2000) Effects of connection fractures on SMRF seismic drift demands. *ASCE Journal of Structural Engineering*, 126: 127–136.
- Luco, N., Cornell, C.A. (1998) Effects of random connection fractures on demands and reliability for a 3-storey pre-Northridge SMRF structure, *Proceedings of the 6th U.S. National Conference on Earthquake Engineering*, EERI: El Cerrito, CA: Seattle, Washington, 244: 1–12.
- Manoukas, G., Athanatopoulou, A. and Avramidis, I. (2011a) Multimode pushover analysis for asymmetric buildings under biaxial seismic excitation based on a new concept of the equivalent single degree of freedom system, *Soil Dynamics and Earthquake Engineering*, 38: 88-96.
- Manoukas, G., Athanatopoulou, A. and Avramidis, I. (2011) Static Pushover Analysis Based on an Energy-Equivalent SDOF System. *Earthquake Spectra*: February 2011, Vol. 27, No. 1, pp. 89-105.
- McGrattan, K., Hostikka, S., Floyd J., Baum, H., Rehm R., Mell W., McDermott R. (2010a) *Fire Dynamics Simulator (Version 5) Technical Reference Guide Volume 1: Mathematical Model*, NIST Special Publication 1018-5, NIST, U.S. Government Printing Office, Washington.
- McGrattan, K., McDermott, R., Hostikka S., Floyd J. (2010b) *Fire Dynamics Simulator (Version 5) User's Guide*, NIST Special Publication 1019-5, NIST, U.S. Government Printing Office, Washington.
- McGrattan, K., (2005) *Fire Modelling: Where Are We? Where Are We Going?* *Fire Safety Science*, 8:53–68.
- Merci, B., Van Maele, K. (2008) Numerical simulations of full-scale enclosure fires in a small compartment with natural roof ventilation, *Fire Safety Journal*, 43: 495–511.
- Mousavi, S., Bagchi, A., Kodur, V.K.R. (2008) Post-Earthquake Fire Hazard to building structures, *Canadian Journal of Civil Engineering*, 35: 689-698.
- MSC Software Corporation, *MSC Marc, Volume A: Theory and User Information*, Version 2011.

- MSC Software Corporation, MSC Marc, Volume B: Element Library, Version 2011.
- Najjar, S. R., Burgess, I. W. (1996) A nonlinear analysis for three-dimensional steel frames in fire conditions, *Engineering Structures*, 18(1): 77-89.
- Novozhilov, V. (2001) Computational fluid dynamics modeling of compartment fires, *Progress in Energy and Combustion Science*, 27: 611-66.
- Novozhilov, V. (2001) Computational fluid dynamics modeling of compartment fires, *Progress in Energy and Combustion Science*, 27: 611-666.
- OpenSees v2.2, (2011) Open System for Earthquake Engineering Simulation, Pacific Earthquake
- Oran, E.S., Boris, J.P. (1987) *Numerical Simulation of Reactive Flow*, Elsevier Science Publishing Company, New York, 2, 11.
- Pantousa, D., Mistakidis, E. (2011) The effect of the geometric imperfections on the rotational capacity of steel beams at elevated temperatures, 7th GRACM international congress on computational mechanics, Athens.
- Pessiki, D., Kwon, K., Lee, B.J. (2006) Fire load behaviour of steel building columns with damaged spray-applied fire resistance material, *Fourth International Workshop on Structures in Fire*, Portugal: 235-245.
- Poh, K.W. (2001) Stress-strain temperature relationship for structural steel, *Journal of Materials in Civil Engineering*, 13: 371-379.
- Pope, N.D., Bailey, C.G. (2006) Quantitative comparison of FDS and parametric fire curves with post-flashover compartment fire test data, *Fire Safety Journal*, 41: 99-110.
- Prasad, K., Baoum H.R. (2005) Federal Building and fire safety investigation of the world Trade Center disaster: Fire structure interface, National Institute of standards and technology Report NCSTAR 1-5G, Gaithersburg, MD.
- Prasad, K., Baoum, H.R. (2005) Coupled fire dynamics and thermal response of complex building structures, *Proceedings of the Combustion Institute*, 30: 2255-2262.
- Purkiss, J.A. (2007) *Fire safety engineering, Design of structures*, ELSEVIER, Butterworth-Heinemann, Oxford, UK.
- Quintiere, J.G., Steckler, K., Corlet, D., (1984) An assessment of fire induced flows in Compartments, *Fire science and Technology*, 4(1): 1-14.
- Raunaq Hasib, Rajiv Kumar, Shashi, Surendra Kumar, Simulation of an experimental compartment fire by CFD, *Building and Environment* 42 (2007) 3149-3160
- Rehmand, R.G., Baum, H.R. (1978) The Equations of Motion for Thermally Driven, Buoyant Flows. *Journal of Research of the NBS*, 83: 297-308, 2, 11, 17, 21.
- Rein, G., Abecassis Empis, C., Carvel, R. (2007) *The Dalmarnock Fire Tests: Experiments and Modelling*, School of Engineering and Electronics, University of Edinburgh.

References

- Rein, G., Wolfram, J., Torero, J. (2011) Modelling of the growth phase of Dalmarnock fire test one, 12th International Fire and Materials Conference, San Francisco.
- Reinhorn, AM. (1997) Inelastic analysis techniques in seismic evaluations. In: Krawinkler H, Fajfar P, editors. Seismic design methodologies for the next generation of codes, Balkema: 277-87.
- Richard Liew, J.Y. , Tang, L.K., Holmaas, T., Choo, Y.S. (1998) Advanced analysis for the assessment of steel frames in fire, *Journal of Constructional Steel Research*,47:19–45.
- Sasaki, K.K., Freeman, S.A., Paret., T.F. (1996) Multi—modal pushover procedure (MMP) - A method to identify the effects of higher modes in a pushover analysis, *Proceedings of 6th US national Conference on Earthquake Engineering, EERI, Oakland California, 12*
- Saudi, M., Sozen., M.A., (1981) Simple nonlinear analysis of RC structures, *Journal of Structural Division- ACSE, 107 (ST5): 937-951.*
- Scawthorn, C., Eidinger, J.M., Schiff, A. (2005), *Fire following earthquake, The Americal Society of Civil Engineers ASCE, USA*
- Sherman, C.P., Cheung Richard, K.K.,Yuen, G.H., Yeoh Grace, W.Y., Cheng (2004) Contribution of soot particles on global radiative heat transfer in a two-compartment fire, *Fire Safety Journal*,39: 412–428.
- Suard, S. (2011) Verification and validation of a CFD model for simulations of large-scale compartment fires, *Nuclear Engineering and Design*,241: 3645– 3657.
- Sun, R., Huang, Z., Burgess, I. (2012) The collapse behaviour of braced steel frames exposed to fire, *Journal of Constructional Steel Research*,72: 130–142.
- T. Rinne, J. Hietaniemi, S. Hostikka. *Experimental Validation of the FDS Simulations of Smoke and Toxic Gas Concentrations. VTT Working Papers 66, 2007.*
<http://www.vtt.fi/inf/pdf/workingpapers/2007/W66.pdf>
- Teran-Gilmore, A. (1998) A parametric approach to performance-based numerical seismic design, *Earthquake spectra, 14(3): 501-518.*
- Tondini, N., Vassart, O., Franssen J-M. (2012) Development of an interface and FE software, 7th International Conference on structures in Fire, Zurich, Switzerland.
- Usmani, A.S., Rotter, J.M., Lament, S., Sanad, A.M., Gillie, M. (2001) Fundamental principles of structural behaviour under thermal effects, *Fire Safety Journal, 36: 721–144.*
- Vaari, J., Hostikka, S., Sikanen,T., Paajanen, A. (2012) Numerical simulations on the performance of water-based fire suppression systems, *VTT Technology 54.*
- Vamvatsikos, D., Cornell, C.A. (2002) Incremental dynamic analysis, *Earthquake Engineering and Structural Dynamics*,31: 491–514.

- Wainman, D.E., Kirby, B.R. (1987) Compendium of UK Standard Fire Test Data, Unprotected Structural Steel—1, Ref. No. RS/RSC/S10328/1/98/B, British Steel Corporation (now Corus), Swinden Laboratories, Rotherham.
- Wainman, D.E., Kirby, B.R. (1988) Compendium of UK Standard Fire Test Data, Unprotected Structural Steel—2, Ref. No. RS/RSC/S1199/8/88/B, British Steel Corporation (now Corus), Swinden Laboratories, Rotherham
- Wang, C.Y. C., Lennon, T., Moore, D. B. (1995) The Behaviour of Steel Frames Subject to Fire, *Journal of Constructional Steel Research*, 35 : 291-322.
- Wang, Y. C., Moore, D. B. (1995) Steel frames in fire: analysis, *Engineering Structures*, 17(6): 462-472.
- Wang, Y.C., (2002) *Steel and Composite Structures. Behaviour and design for fire safety*, Taylor and Francis Group, Spon Press, London and New York.
- Wickström, U., Duthinh, D., McGrattan, K. (2007) Adiabatic surface temperature for calculating heat transfer to fire exposed structures, *Interflam 2007. (Interflam '07). International Interflam Conference, 11th Proceedings. September 3-5, 2007, London, England, (2): 943-953.*
- Yamawaki, K., Kimatura, H., Tsuneki, Y., Mori, N., Fukai, S. (2000) Introduction of performance-based design, *12th World Conference on Earthquake Engineering*, Auckland.
- Yang, D., Hu, L.H., Jiang, Y.Q., Huo, R., Zhu, S., Zhao, X.Y. (2010) Comparison of FDS predictions by different combustion models with measured data for enclosure fires, *Fire Safety Journal*, 45: 298–313.
- Yassin, H., Iqbal, F., Bagchi, A., Kodur, V.K.R. (2008) Assessment of post-earthquake fire performance of steel-frame buildings, *Proceedings of 14th World Conference on Earthquake Engineering*, Beijing, China.
- Yeoh, G.H., Yuen K.K. (2009) *Computational Fluid dynamics in Fire engineering*, ELSEVIER, Butterworth-Heinemann, Oxford, UK.
- Yeoh, G.H., Yuen, R.K.K., Chueng, S.C.P., Kwok, W.K. (2003) On modelling combustion, radiation and soot processes in compartment fires, *Building and Environment*, 38: 771 – 785.
- Yeoh, G.H., Yuen, R.K.K., Lo, S.M., Chen, D.H. (2003) On numerical comparison of enclosure fire in a multi-compartment building, *Fire Safety Journal*, 38: 85–94.
- Yin, Y.Z., Wang, Y.C. (2004) A numerical study of large deflection behaviour of restrained steel beams at elevated temperatures, *Journal of Constructional Steel Research*, 60: 1029–1047.
- Yin, Y.Z., Wang, Y.C. (2005a) Analysis of catenary action in steel beams using simplified hand calculation method, Part 1: theory and validation for non-uniform temperature distribution, *Journal of Constructional Steel Research*, 61: 213-234.

References

Yin, Y.Z., Wang, Y.C. (2005a) Analysis of catenary action in steel beams using simplified hand calculation method, Part 1: theory and validation for uniform temperature distribution, *Journal of Constructional Steel Research*, 61: 183-211.

Yun, S.Y., Hamburger, R.O., Cornell, C.A, Foutch, D.A. (2002) Seismic performance for steel moment frames. *ASCE Journal of Structural Engineering*, submitted.

Zaharia, R., Pintea, D. (2009) Fire after earthquake analysis of steel moment resisting frames, *International Journal of Steel Structures*, 9: 275-284.

Zaharia, R., Pintea, D., Dubina, D. (2007) Fire analysis and design of a composite steel-concrete structure, *Steel and Composite Structures*, Taylor & Francis Group, London UK.

Zaharia, R., Pintea, D., Dubina, D. (2008) Fire after earthquake- a natural fire approach, *Proceedings of the fifth International Conference EUROSTEEL*, Austria.

Zaharia, R., Pintea, D., Dubina, D. (2009) Fire analysis of structures in seismic areas, *Proceedings of the International Conference on Application of Structural Fire Engineering*, Prague, Czech Republic.

Zografopoulou, K., Pantousa, D., Mistakidis, E. (2013a) Numerical simulation of natural fire in an industrial building considering earthquake damage of non-structural members, *Proceedings of ASFE, Application of Structural Fire Engineering*, 19-20 April 2013, Prague, Czech Republic

Zografopoulou, K., Pantousa, D., Mistakidis, E. (2013b) The fire–after–earthquake event in an industrial building, part 1: simulation of the natural fire, *Proceedings of 10th HSTAM International Congress on Mechanics Chania*, 25– 27 May, Crete, Greece.

This research has been co-financed by the European Union (European Social Fund – ESF) and Greek national funds through the Operational Program "Education and Lifelong Learning" of the National Strategic *Reference* Framework (NSRF) - Research Funding Program: Heracleitus II. Investing in knowledge society through the European Social Fund